Magma chamber assembly and dynamics of a supervolcano: Whakamaru, Taupo Volcanic Zone, New Zealand

by

Naomi E. Matthews

Thesis submitted to the University of Oxford
for the degree of Doctor of Philosophy

Department of Earth Sciences
and University College
University of Oxford

Trinity, 2011

Supervised by Prof. David M. Pyle, University of Oxford
Co-supervised by Prof. Colin J.N. Wilson, Victoria University, New Zealand

Whakamaru – To give shelter to, or safeguard (Maori)

The high priest, Ngatoroirangi, was caught in a blizzard while climbing Mount Ngauruhoe.
He prayed to his sisters in Hawaiki to send him fire to save him from freezing.
The flames they sent south emerged first at White Island, then Rotorua and Taupo
before finally bursting at Ngatoroirangi's feet.
Thus Ngatoroirangi is credited with bringing volcanic activity to Aotearoa, New Zealand,
not as a curse upon the land, but as a blessing.

Figure: *Maui Fishing New Zealand Out of the Ocean*, W. Dittmer, 1970
Source: Alexander Turnbull Library, Wellington New Zealand (PUBL-0088-049)

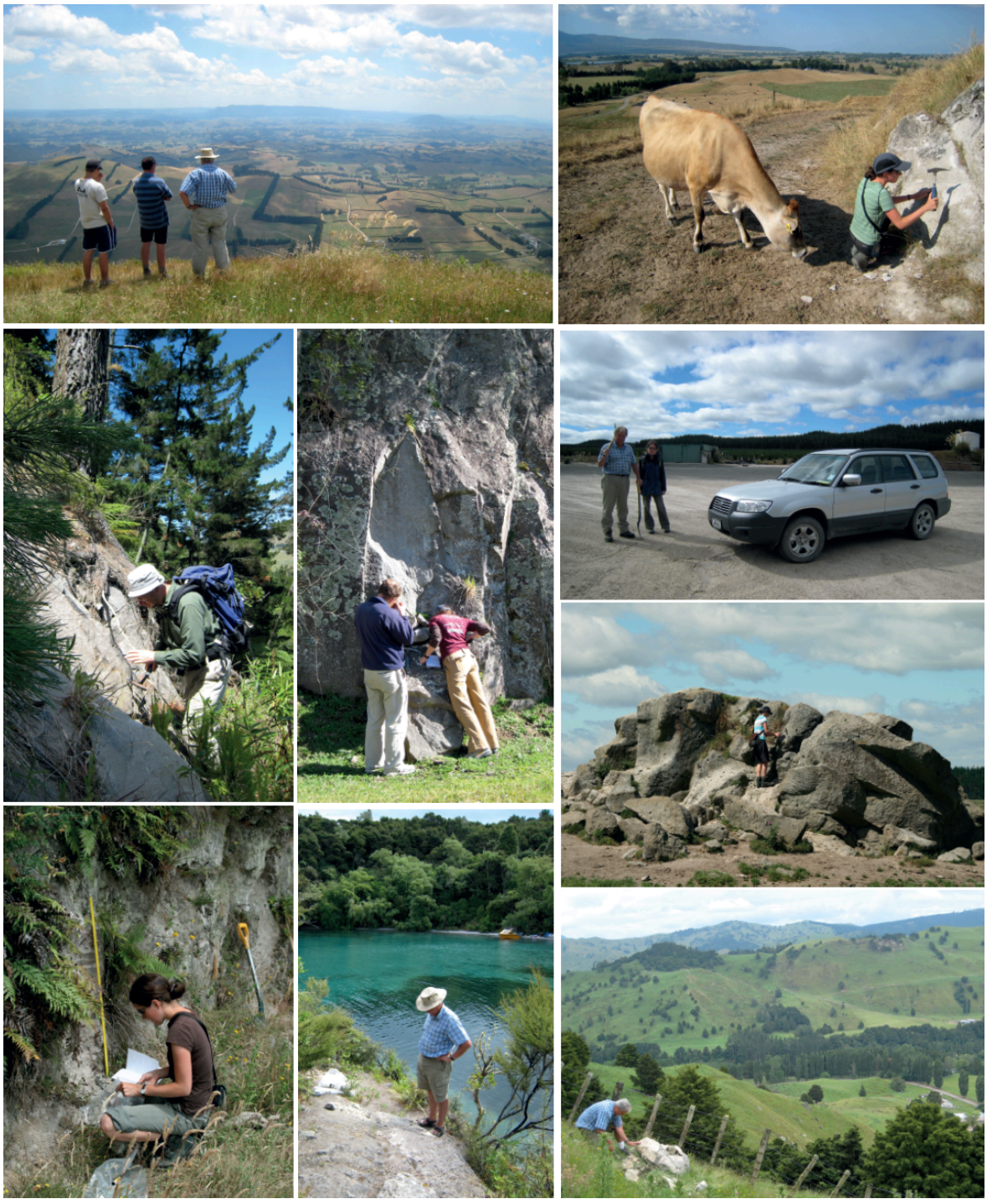









Photographs on previous pages, captions listed from top left:

Page iv: Photographs of proximal Whakamaru Group Ignimbrite fieldwork, Taupo Volcanic Zone, New Zealand: View from top of Paeroa Range (Ryan and Peter Macdonald and Murray Matthews); Sampling ignimbrite near Rerewhakaaitu with the assistance of Daisy the cow; Colin Wilson sampling on the Paeroa scarp; Colin Wilson and Alexa Van Eaton examining Whakamaru Ignimbrite at Maraetai hydro-electric dam site; Murray and Naomi Matthews in Kaingaroa Forestry area; Sampling Rangitaiki Ignimbrite off SH5; Sampling Whakamaru Ignimbrite in Kaingaroa Forestry; Whakamaru Ignimbrite at Boat Harbour, northern shore of Lake Taupo; Sampling Manunui pumice near Benneydale.

Page v: Photographs of Distal Rangitawa Tephra and Younger Toba Tuff (YTT) fieldwork: Investigating Rangitawa Tephra at Rangitawa Stream; Sampling distal Rangitawa Tephra at Mairangi, Chatham Island; Alan Palmer at Mount Curl; Murray Matthews at Mairangi North, Chatham Island; Logging the YTT deposit in Jurreru Valley, southern India, Archaeological trench JWP3; Emma Gatti and Naomi Matthews sampling basal YTT, Jurreru; Sampling YTT at Middle Son Valley, northern India; Clive Oppenheimer investigating the reworked YTT sequence, Jurreru Valley; View across Middle Son Valley, India.

Abstract

Magma chamber assembly and dynamics of a supervolcano:

Whakamaru, Taupo Volcanic Zone, New Zealand

Naomi E. Matthews

University College, Oxford
Doctor of Philosophy, Trinity 2011

This thesis employs crystal-specific techniques, combined with field observations, petrology, geochemistry and numerical modelling to reconstruct the magmatic system associated with the ~ 340 ka Whakamaru supereruption, New Zealand. Comparisons are drawn with the ~ 74 ka Youngest Toba Tuff (YTT) supereruption.

Whakamaru Group Ignimbrites contain five pumice types, characterised by different mineralogies and crystal contents. Pumice petrography and geochemistry indicate that basaltic magma mixing occurred, possibly triggering eruption. Geothermobarometers suggest an eruption temperature of ~ 770°C and magma storage at ~ 5 km depth. High-resolution thermal records from Ti-in-quartz analysis indicate a thermal pulse of ~ 100°C prior to eruption. Diffusion timescales show multiple recharge events with the most significant event occurring ~ 35 y prior to eruption. Zircon U-Pb data show that most crystallisation occurred at ~ 400 ka, with antecrysts and xenocrysts incorporated. Zircon trace-element data suggest multiple recharge events and complex mixing over ~ 100 ky, consistent with an incrementally growing reservoir. Oxygen-isotope data illustrate that zircon, quartz and feldspar crystallised together in equilibrium, with isotopically homogenous magma sources feeding the reservoir over time.

Whakamaru and YTT tephra thickness and grain-size data were used in ash dispersal modelling. Results indicate the YTT eruption had a ~ 35 km column height and erupted volumes of 1500 – 1900 km^3, with deposition from a co-ignimbrite phase; whereas Whakamaru had a Plinian column ~ 45 km high with SE dispersal and a minimum volume of ~ 400 km^3. The widespread dispersal of large volumes of fine ash from both eruptions would have had global environmental consequences.

The data are integrated to reconstruct a new Whakamaru magma reservoir model. The complex crystal records indicate the system was characterised by long periods of incremental assembly, mixing, recycling of material, and reactivation during multiple recharge episodes which perturbed the system and primed the magma for eruption.

Extended abstract

Magma chamber assembly and dynamics of a supervolcano:
Whakamaru, Taupo Volcanic Zone, New Zealand

Naomi E. Matthews

University College, Oxford
Doctor of Philosophy, Earth Sciences
Trinity 2011

This thesis describes the magmatic system associated with the voluminous (~ 1500 km^3) Whakamaru supereruption which erupted from central Taupo Volcanic Zone (TVZ), New Zealand, at ~ 340 ka. Geochemical compositions of crystals contained in eruption products (pumices) provide information on magma chamber processes occurring over hours to millions of years before eruption, with changes in magmatic conditions being effectively recorded in crystal growth zones. The interrogation of such records contained in quartz, feldspar and zircon crystals using high-resolution micro-analytical techniques is a major focus of this thesis. The integration of crystal records with data from comprehensive field studies, petrology, glass chemistry and numerical modelling enables reconstruction of temporal records of thermochemical changes in the magmatic system leading up to eruption. Extensive fieldwork was conducted throughout the TVZ, in the Wanganui region (North Island), on Chatham Island, and in India.

The primary aim was to achieve a better understanding of magma assembly, storage, crystallisation, mixing, fractionation and eruption-triggering mechanisms. Eruption magnitude, ash dispersal patterns and environmental impacts of the supereruption were also explored, and comparisons drawn with the ~ 74 ka Youngest Toba Tuff (YTT) eruption (the largest to have occurred globally in the last 2 Ma), Sumatra, thereby furthering current understanding of the systems that drive supereruptions.

Proximal deposits of the Whakamaru supereruption, the Whakamaru Group Ignimbrites, are divided into five ignimbrite units on the basis of physical characteristics and geographical distributions: the Whakamaru, Rangitaiki, Te Whaiti, Manunui and Paeroa Range ignimbrites. The relationships between these ignimbrite units and the sequence of eruption is uncertain, although earlier work (Brown et al., 1998a) suggests that they were all erupted over a period of < 5 ky. Here sampling and detailed analysis focused on pumices rather than bulk ignimbrite, as these are considered to represent quenched fragments of the vesiculated rhyolite magma, with variations in glass composition between pumices reflecting variations within the parent magma reservoir(s). Pumices were selected on the basis of mineralogy, clast size and lack of alteration. Bulk ignimbrite was sampled where deposits were strongly welded or pumice-poor. Distal tephra associated with the eruption, the Rangitawa Tephra, was sampled at locations in the Wanganui region and on Chatham Island, at high resolution through the stratigraphic sequence. Sampling was guided by earlier work by Brown (1994) and Holt et al. (2010) for Whakamaru Group Ignimbrites and Rangitawa Tephra respectively.

Whole-rock (XRF) data for pumices extracted from these ignimbrite units confirm that the system involved five distinct pumice or 'magma' types (*A, B, C, D* and *mixed basaltic* types). Glass compositions (by EPMA and LA-ICP-MS) are similar, indicating that the pumice types, defined with whole-rock geochemistry, reflect different mineralogies or crystal content. Each of the five ignimbrite units contains varying amounts of each of these pumices (as previously identified by Brown et al., 1998a), with type *A* being dominant (~ 90%) and showing the greatest compositional range (possibly attributed to mixing with basaltic magma). Fractional crystallisation modelling indicates that types *B* and *C* evolved from type *A*, but that type *D* evolved separately with extensive biotite crystallisation, and may therefore represent a related but subsidiary magma chamber. On the basis of glass chemistry and biotite compositions, the Rangitawa Tephra ashfall deposit correlates with the Whakamaru type *A* magma with a minor component of Rangitaiki type *A*, and is clearly directly associated with the eruption. Pumice petrography, whole-rock chemistry and glass major- and trace-element compositions also provide evidence for basaltic magma mixing and mingling with the host rhyolite (as recorded in the mixed basaltic pumices).

Detailed analysis of quartz crystals extracted from pumices of the Whakamaru Group Ignimbrite deposits is a particular focus of this thesis. Various geothermometers were applied to reconstruct the thermal evolution of the system. Data from Fe-Ti oxides, feldspar-melt, amphibole, Ti-in-quartz and Ti-in-zircon geothermometers indicate a wide temperature range of 655 – 975°C, with an eruption temperature (mode) of ~ 770°C. High-resolution Ti-in-quartz analysis using CL-EPMA calibration and synchrotron μ-XRF techniques, provides a high-resolution thermal record (using the TitaniQ formulation) for the Whakamaru magma reservoir and indicates a thermal pulse of ~ 100°C (or alternatively a significant pressure drop) prior to eruption. Thermodynamic considerations show that > 1000 km^3 of mafic magma underplating the rhyolitic reservoir would be required to generate such a temperature increase. Diffusion modelling over the significant quartz core-rim interface, using a new 2D Lattice Boltzmann technique, provides an average timescale of ~ 35 y (between event and eruption), while other boundaries indicate earlier events occurring at intervals of up to 2000 y. These results are consistent with quartz-derived timescales for the larger YTT eruption and the smaller TVZ Earthquake Flat eruption, suggesting that magma recharge events occur over similar timescales irrespective of magma volumes. The quartz record thus provides evidence for sequential recharge events which perturb the system in terms of P/T/melt composition.

Zircon-derived records of magma storage timescales and magmatic evolution (by SHRIMP-RG) provide further information on magma assembly and storage prior to eruption. Most zircon crystallisation occurred at ~ 400 ka, although older zircons up to ~ 700 ka were also identified and interpreted as being antecrystic (providing evidence for assimilation of older plutonic rocks). Zircons > 100 Ma in age are interpreted as being xenocrysts inherited from basement metasedimentary rocks (consistent with geochronology for Torlesse and Waipapa Terranes). The zircon age spectra provide an estimated residence time of ~ 60 ky for most of the magmatic system, although this is difficult to constrain due to the presence of inherited antecrysts and xenocrysts. Zircon trace-element data and thermal records provide evidence for complex compositional and thermal fluctuations over a timescale of > 100 ky. These data suggest that there were multiple recharge events and complex mixing and recycling into the system, consistent with an incrementally growing reservoir. Oxygen isotope data for zircon, quartz and feldspar (by SIMS) from the same pumice clasts illustrate that these mineral phases

crystallised together in isotopic equilibrium and suggest that isotopically homogenous magma sources fed the reservoir over time prior to eruption.

Analysis of distal and ultra-distal tephra deposits from the Whakamaru and YTT eruptions provides insight into tephra dispersal mechanisms and potential eruption impacts. Primary YTT ashfall deposits in India are 4 – 5 cm thick, as measured at Jwalaparum, Kurnool district, and the Middle Son Valley, Madhya Pradesh, both at distances of > 2000 km from the source caldera. Distal Rangitawa Tephra is 15 – 30 cm thick at distances of ~ 900 km from source, as preserved on Chatham Island, New Zealand. Stratigraphy (tephra thickness at terrestrial and ocean localities) and grain-size data were used as inputs into a numerical ash dispersal model (HAZMAP), making assumptions concerning the total grain-size distribution, particle aggregation, average wind direction and strength, eruption column shape and vent size. Modelling results for YTT show a relatively low column height of about 35 km and provide a new estimate of erupted volumes of 1500 – 1900 km^3 (DRE). Results also suggest that distal deposits identified in India were deposited by a co-ignimbrite phase of the eruption. Whakamaru ash-dispersal modelling indicates a Plinian column about 45 km high, with dispersal to the SE by strong prevailing winds, and a minimum erupted volume of ~ 400 km^3. The widespread dispersal of large volumes of fine and very-fine ash from both eruptions would have had global environmental consequences, with potential climatic impacts (particularly for the equatorial YTT eruption). Both eruptions would have resulted in the burial of land surfaces with major impacts on groundwater and sedimentary systems. Human health impacts for the YTT eruption would have been significant, due to the high proportion of respirable ash, even at great distances from source.

Integration of the complementary lines of evidence investigated in this thesis enables the reconstruction of a new magma reservoir model for the Whakamaru system. Crystal records (mainly derived from zonation patterns in quartz, zircon and feldspar) provide evidence for complex thermochemical changes during the assembly and growth of the silicic magma reservoir. The large volume of magma accumulated in the reservoir system at a depth of ~ 5 – 10 km (as derived from amphibole geothermobarometry and quartz melt inclusion data), and was fed by mafic recharge magma from depths > 15 km. Assimilation and recycling of older crustal material (e.g., older plutonics and basement rocks), and remobilisation of completely crystalline parts of the reservoir (e.g., side-wall crystal

mush), also played a role in the petrogenesis of the rhyolitic magma. The complex crystal records indicate that the system was characterised by long periods of incremental assembly, reactivation, stirring, mixing and recycling of material and multiple recharge pulses resulting in significant perturbations (P/T/composition) of the system which ultimately primed the magma for eruption over timescales of less than a hundred to thousands of years. The direct evidence for mafic recharge (mixed and mingled basaltic pumice clasts) suggests that a final mafic recharge event (causing abrupt P/T change) may have been the eruption-triggering mechanism.

The data presented in this thesis provide insight into the complexity of magmatic processes which can be reconstructed from crystal records. The applications of crystal zonation studies, and diffusion and thermodynamic modelling, together with field and petrological studies have proved valuable in constraining pre-eruptive processes and enabling the development of the new model for the Whakamaru magma reservoir.

Acknowledgements

Foremost I thank my supervisors, David Pyle and Colin Wilson, for their invaluable advice, ideas and guidance throughout my research. Special thanks goes to Victoria Smith, for her informal supervision without which this thesis could not have attained its present form. I gratefully acknowledge funding from the Woolf Fisher Trust, New Zealand, which made this work possible. Additional funding for travel came from the Burdett-Coutts fund, University College and the Geological Society Geochemistry Group. I am grateful to David Pyle and Vicki Smith for the opportunities to undertake exciting fieldwork in Argentina (during the Chaitén eruption, 2008), India (2009) and South Korea (2010). I thank Conall Mac Niocaill and Kathy Cashman for examining this thesis.

This research involved a wide range of laboratory work in Oxford and elsewhere, and I thank the following people for their assistance and input: Norman Charnley, Steve Wyatt, Owen Green and Christopher Jackson at the University of Oxford, John Craven at the NERC Ion Microprobe Facility, Edinburgh, Nick Pearce and Henry Lamb at University of Aberystwyth, Stuart Kearns and Horst Marschall at Bristol University, Stephen Reed at the University of Cambridge, John Watson at the Open University, Rob Spiers at the University of Canterbury, Tina Geraki at the Diamond Light Source, and Joe Wooden at the USGS-Stanford SHRIMP-RG facility.

I thank Chris Huber, Georgia Tech, for his enthusiasm, advice and hospitality and invaluable input into the diffusion modelling. Bruce Charlier is thanked for his company in the ionprobe lab and assistance with zircon work. Antonio Costa is thanked for his help and input with tephra dispersal modelling. Vincent van Hinsberg is acknowledged for his help with a_{TiO2} modelling, and Kim Berlo and Vicki Smith for their company during long hours at the synchrotron. Mark Ghiorso is thanked for his input with MELTS-modelling and interest in my research. Jim Cole is also thanked for providing the initial inspiration for this thesis, and for providing access to the sample collection and data of Stu Brown.

I thank my father for his enthusiasm and invaluable help in the field in New Zealand, and for his long hours of proofreading. Colin Wilson is also thanked for his insight and assistance with TVZ fieldwork on numerous occasions. I am grateful for the advice and help with Rangitawa Tephra fieldwork in the Wanganui region and Chatham Island from Alan Palmer and Katherine Holt, Massey University. Toba ash fieldwork in India was supported by Adam Durant, Clive Oppenheimer, Emma Gatti, Mike Petraglia, Michael Haslam among others.

Finally, I thank Team Volcano and Team Coffee (Dave, Gio, Seb, Ben, Laura, Alan, Susi and John) for their friendships and encouragement. The Missing Bean for bringing flat whites to Oxford and revolutionising my world! My kiwis in Oxford - Joel, Anna, Matt, Holly and Dave - for making me feel at home. Jess and Eveliina for their wonderful friendships, continual support and laughter, I couldn't have done this without you. Mum, Dad and Rachel for their continual encouragement, advice and love. And to Nick for his love, support and the wonderful conversations at the end.

Contents

Chapter 1: Introduction – Supervolcanoes, the Taupo Volcanic Zone and the Whakamaru Supereruption

Chapter 2: Glass and mineral chemistry of the Whakamaru Group Ignimbrites and Rangitawa Tephra

Chapter 3: Quartz zoning and the pre-eruptive evolution of the Whakamaru magma system

Chapter 4: Timescales of magma recharge and reactivation of large silicic magma systems from Ti diffusion in quartz

Chapter 5: Zircon crystallisation histories - investigating processes and timescales of silicic magma generation

Chapter 6: Ultra-distal tephra deposits from supereruptions: Toba and Whakamaru

Chapter 7: Summary and conclusions

Appendices

List of Figures

List of Tables

Chapter 1

Introduction – Supervolcanoes, the Taupo Volcanic Zone and the Whakamaru Supereruption

1. Introduction

Volcanoes represent a significant natural hazard with the capacity to cause major environmental damage, loss of life and social disruption. Four recent eruptions have demonstrated the range of their effects: Chaitén (Chile, 2008) with widespread destruction of infrastructure and agriculture; Merapi (Indonesia, 2010) with significant loss of life; and Eyjafjallajökull (Iceland, 2010) and Puyehue (Chile, 2011) with severe civil disruption. Yet the magnitude of these eruptions is insignificant when compared to "supereruptions", which eject $\geq 10^{15}$ kg of magma (dense-rock equivalent, DRE) or > 1000 km^3 of pumice and ash (Mason et al., 2004; Sparks et al., 2005; Miller and Wark, 2008). Numerous such eruptions have occurred in the geological past with global consequences, affecting ecosystems and climate (e.g., Rampino and Self, 1992; Self, 2006), and potentially impacting human populations (as in the case of the ~ 74 ka Toba supereruption; e.g., Ambrose, 1998). There are no first-hand observations of supereruptions so investigations must take advantage of detailed physical volcanology studies and application of micro-analytical techniques which enable examination of erupted deposits in unprecedented detail. Crystals record magma chamber processes occurring over hours to millions of

years, and these can be interrogated for information on pre-eruption magmatic processes and eruption-triggering mechanisms. This is a central theme of this thesis.

The Taupo Volcanic Zone (TVZ), New Zealand, is the most frequently active zone of rhyolitic volcanism on Earth, and the source of four catastrophic supereruptions over the past 1.6 Ma (Wilson et al., 1995a; 2009). The TVZ erupts small and large volumes of rhyolite at very frequent intervals (Wilson et al., 2009), and is thus an ideal place to test models of how exceedingly large volumes of silicic magma are generated and assembled prior to eruption. Current models of supervolcano development include rapid rejuvenation of silicic mushes, which have developed piecemeal over time and are only homogenised immediately prior to eruption, versus progressive growth of a large melt reservoir with extended magma storage periods over hundreds of thousands of years.

This thesis explores these models by focusing on the largest TVZ supereruption, the ~ 340 ka Whakamaru eruption (most recent age estimate is 347 ± 4 ka; Leonard et al., 2010; Section 1.5), and drawing comparisons with the well-documented ~ 74 ka Toba (Sumatra) supereruption (Chapters 4 and 6). The Whakamaru supereruption is of particular interest as it is the largest eruption to have occurred in New Zealand, and its physical and geochemical complexities suggest that it holds crucial information regarding the manner in which supervolcanoes develop and their mechanisms of operation.

Crystals preserved in erupted deposits provide records of pre-eruptive events in magma reservoirs which can be deciphered particularly in terms of temperature, pressure, degassing processes and compositional changes. High-spatial-resolution micro-analytical techniques applied to crystals extracted from the erupted deposits (Section 1.3) are

therefore useful in addressing fundamental questions in supervolcano research. Recent studies have focused on U-Th and U-Pb analysis of zircons (e.g., Charlier and Zellmer, 2000; Vazquez and Reid, 2004; Charlier et al., 2005, 2007; Simon and Reid, 2005; Wilson and Charlier, 2009) to place time constraints on pre-eruptive crystallisation timescales; analysis of melt inclusions to constrain pre-eruptive conditions (magmatic P, T, fO_2 and H_2O; e.g., Wallace et al., 1999; Liu, Y. et al., 2006; Baker, 2008; Chesner and Luhr, 2010); detailed analysis of plagioclase-feldspar crystal stratigraphies and Sr-isotopic zonation (Davidson and Tepley, 1997; Davidson et al., 2001; Charlier et al., 2008) to reconstruct the pre-eruption histories of crystal recycling, magma mixing and contamination; and quantification of pre-eruption timescales using diffusion modelling techniques (e.g., Morgan et al., 2004; Costa and Dungan, 2005; Morgan and Blake, 2006; Martin et al., 2008; Costa et al., 2010; Saunders et al., 2010; Matthews et al., 2011a). The present work extends these applications in addressing the manner in which large volumes of magma accumulate, timescales over which pre-eruption magmatic processes occur, mechanisms which finally trigger eruption (e.g., silicic or mafic magma recharge, and gas influx), ash dispersal mechanisms and environmental impact.

1.1 Project aims and objectives

This thesis presents the results of detailed crystal-specific analyses including trace-element and oxygen isotopic analysis of zircon, quartz and feldspar; analysis of major and trace elements in glass; and crystal zonation studies. By combining previously published data with new petrological observations, comprehensive field studies and numerical models, the aim is to achieve a better understanding of shallow crystallisation, magma assembly, storage, mixing and eruption-triggering processes associated with the Whakamaru supereruption.

The primary objectives of the study were:

- To analyse major and trace elements in matrix glass and minerals of pumices extracted from the Whakamaru Group Ignimbrites to characterise the magma and correlate the distal ashfall units to specific phases of the supereruption;
- To establish the pre-eruptive state of the magma body or bodies using Fe-Ti oxide geothermometry, amphibole geothermometry (Ridolfi et al., 2010), feldspar-melt (Putirka, 2005; 2008), Ti-in-quartz (Wark and Watson, 2006) and Ti-in-zircon (Watson et al., 2006) techniques (core-to-rim), providing a thermal record of intensive conditions in precursor melt-rich bodies or melt-poor crystal-mush zones;
- To apply diffusion modelling techniques to trace-element micro-zonation patterns in quartz in order to reconstruct eruption-triggering timescales;
- To undertake U-Pb dating of zircon crystals extracted from representative pumice samples in order to constrain the magma residence time of the Whakamaru supereruption and address the long-term history of magma assembly and storage;
- To analyse trace-element patterns in dated zircon crystals and thereby reconstruct a history of conditions within the source magma chamber(s), e.g., periods of replenishment, reheating, crystal-mush rejuvenation, fractional crystallisation and melt segregation;
- To measure oxygen isotope signatures of zircon, quartz and feldspar to determine the degrees of isotopic fractionation and crystal recycling, constrain core-rim variations, and to identify magma sources;
- To investigate grain-size characteristics and glass chemistry of distal co-ignimbrite ashfall deposits from both the Whakamaru and Toba supereruptions to constrain eruption depositional processes, magnitudes and dispersal mechanisms of tephra.

In particular, the aims of the crystal-specific analyses are to constrain models for the thermal dynamics of crustal magma chambers, and to shed light on possible driving mechanisms for such eruptions. In turn, this may provide new insights into how and where such systems develop and mature. In order to address these objectives, this thesis is divided into six further chapters:

- Chapter 2: Geochemistry of proximal ignimbrites and distal tephra
- Chapter 3: Geothermometry and magmatic thermal evolution
- Chapter 4: Recharge timescales from Ti-diffusion in quartz
- Chapter 5: Zircon-derived magma storage timescales and evolution
- Chapter 6: Tephra dispersal modelling and environmental impact
- Chapter 7: Conclusions and magma reservoir model

1.2 Supervolcanoes and supereruptions

The term 'supereruption' was first used by Rampino and Self (1992), in reference to those eruptions that eject magma with a mass greater than 10^{15} kg, equivalent to a volume of > 450 km^3 (Mason et al., 2004; Sparks et al., 2005; Self, 2006; Miller and Wark, 2008). In comparison, the largest eruptions of recent historic times have released 10 – 30 km^3 of magma (Self, 2006; see Table 1.1 and Fig. 1.1 for comparison with smaller historic eruptions).

Supereruptions also exclusively refer to relatively short-term explosive events (e.g., Francis and Oppenheimer, 2004; Mason et al., 2004), with a volcanic explosivity index (VEI) of 8+ (Newhall and Self, 1982; where the magnitude is calculated by $\log_{10}$[(erupted

mass, kg)$^{-7}$]; Pyle, 2000), producing fragmental vesiculated deposits with bulk volumes > 1000 km^3 (Miller and Wark, 2008). A supervolcano is defined as a volcano that has produced at least one explosive supereruption (Miller and Wark, 2008). These volcanoes form negative topographic features (calderas) due to catastrophic collapses into the underlying large-volume chamber evacuated during eruption. Caldera size correlates broadly with eruption size (Smith, 1979), with supervolcano calderas being up to 100 km across (Miller and Wark, 2008).

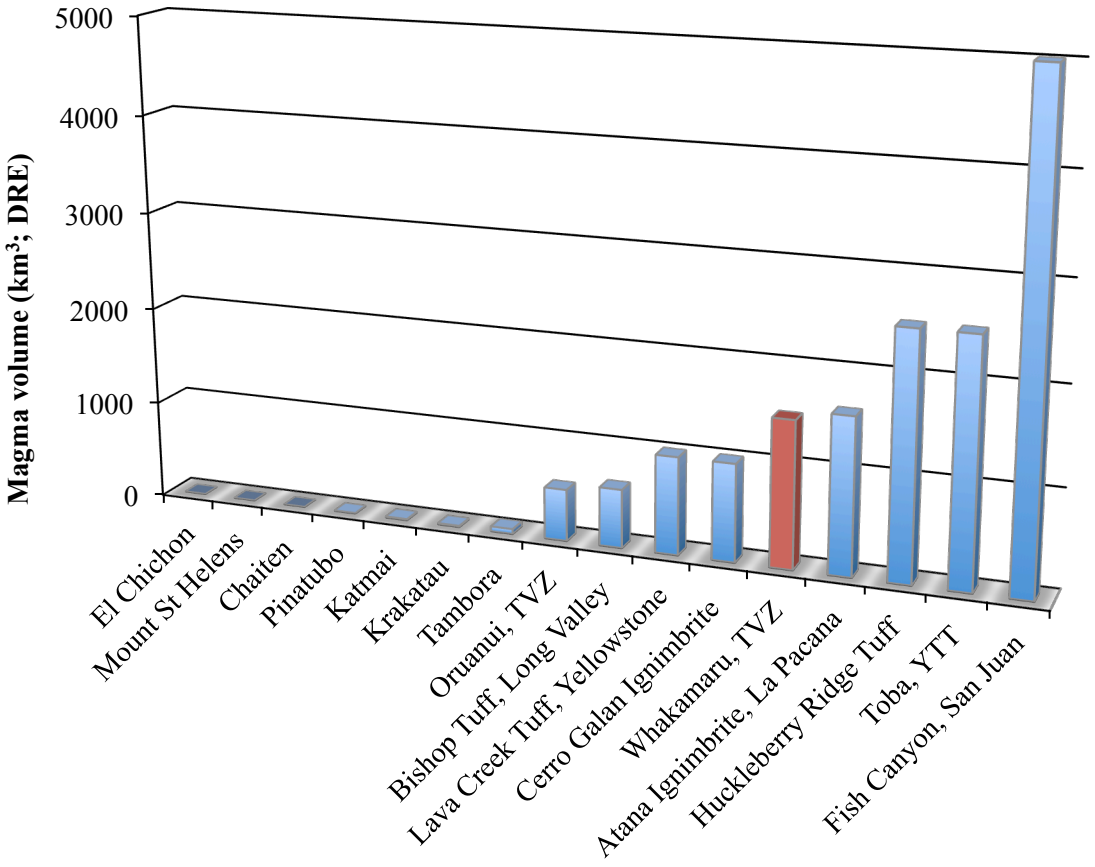

Fig. 1.1: Comparison of historically 'large' explosive eruptions such as Pinatubo, Tambora and Krakatau, with supereruptions involving > 450 km^3 magma (equivalent to ~ 1000 km^3 bulk deposit; Mason et al., 2004); eruption volumes and references listed in Table 1.1. Whakamaru eruption is indicated in red – representing the largest TVZ eruption, but smaller than eruptions from Toba, Yellowstone and San Juan volcanic fields.

Supereruptions represent a considerable volcanic hazard, with the capacity to cause significant environmental and human impact (refer to Chapter 6 for further discussion). The global frequency of volcanic eruption correlates inversely with eruption size, and supereruptions therefore occur extremely infrequently, averaging one every ~ 100,000 y (Mason et al., 2004). There have, however, been ten such eruptions in the Quaternary (last 2.5 Ma; Mason et al., 2004). The youngest well-documented supereruption is the ~ 26.5 ka Oruanui eruption (TVZ) and the largest eruption in the past 2.5 Ma is the Youngest Toba Tuff (YTT) supereruption from Toba, Sumatra (see Table 1.1 and references therein).

Table 1.1: ***Comparison of magma volumes for historic large explosive eruptions and documented supereruptions***

Eruption	Magma volume (km^3)	Year/age	Ref.
El Chichón	1	1982	1
Mount St Helens	0.5	1980	2
Chaiten	0.7	2008	3
Pinatubo	5	1991	4
Katmai, Alaska	11	1912	5
Krakatau	12	1883	6
Tambora	50	1815	7
Oruanui, TVZ	530	26.5 ka	8
Bishop Tuff, Long Valley	600	760 Ma	9
Lava Creek Tuff, Yellowstone	1000	640 ka	10
Cerro Galan, Argentina	1000	2.2 Ma	11
Whakamaru, TVZ	1500	340 ka	12
Atana, La Pacana, Chile	1600	4 Ma	13
Huckleberry Ridge Tuff	2500	2.05 Ma	10
Toba, YTT	2500	74 ka	14
Fish Canyon	5000	28 Ma	15, 16

Notes: Magma volume quoted as DRE. References: (1) Rose and Durant, 2008; (2) Pallister et al., 1992; (3) Watt et al., 2009a; (4) Scott et al., 1996; (5) Hildreth, 1983; (6) Yokoyama, 1981; (7) Self et al., 2004; (8) Wilson et al., 2006; (9) Bailey, 1976; (10) Christiansen, 2001; (11) Folkes et al., 2011; (12) Brown et al., 1998a; (13) Lindsay et al., 2001; (14) Rose and Chesner, 1987; (15) Lipman et al., 1997; (16) Bachmann et al., 2002. Note that the recent age estimate for the Oruanui eruption is 27.1 ± 0.9 ka (Lowe et al., 2008, 2010).

1.2.1 Eruption characteristics

Supereruptions are fed by magmas with high explosive potential, due to high volatile content (mostly H_2O) and high viscosity (silica-rich dacitic and rhyolitic magmas; Miller and Wark, 2008). Supervolcanoes are distinguished from other volcanoes capable of explosive eruptions (Table 1.1) in that they accumulate very large volumes of eruptible magma in shallow chambers, which may be only minor components of even larger underlying magma reservoirs (e.g., Hildreth, 1979a, 1981; Smith, 1979; Bergantz, 1989; Bachmann and Bergantz, 2006, 2008; Reid, 2008). They are usually located in areas of thick, low-density crust in continental and old island-arc areas which inhibit buoyant ascent of dense, low-silica magmas and therefore promote long-term reservoir growth and fractionation processes (Smith, 1979; Hildreth, 1981, 2004; Bachmann and Bergantz, 2008; Miller and Wark, 2008). The thermal energy required as a driving mechanism for such systems is thought to be derived from deeper-level, hotter basaltic and andesitic magmas (Smith, 1979; Hildreth, 1981; Lowenstern and Hurwitz, 2008).

Explosive eruptions are thought to be triggered by one or more of the following factors: (1) gas saturation in crystallising magma; (2) replenishment by magma recharge and mixing (causing thermal or chemical perturbations); (3) escape of gas-rich, crystal-poor magma from crystal mush and storage of low-density magma beneath the chamber roof; or (4) tectonic triggers (i.e., earthquakes and faulting) which may fracture chamber walls or destabilise a stagnant crystal-mush (e.g., Anderson, 1976; Sparks et al., 1977; Blake, 1984; Pallister et al., 1992; Linde and Sacks, 1998; Cottrell et al., 1999; Bachmann and Bergantz, 2003; Jellinek and DePaolo, 2003; Davis et al., 2007; de Silva et al., 2008; Watt et al., 2009b; de la Cruz-Reyna et al., 2010).

Fundamental questions concerning supervolcanoes are centred around the mechanisms by which magmas can accumulate to vast quantities over extended time periods (Miller and Wark, 2008) without eruption being triggered by any one of the above perturbations; and the mechanism(s) which finally trigger eruption. Other challenges in supervolcano research relate to how supereruptions are initiated and finish, and their duration; the distributions and volumes of pyroclastic deposits; how rapidly such volumes of magma and gas are erupted; and the links between eruption sequences and evacuation of the magma reservoir system (Wilson, 2008).

1.2.2 Ignimbrites and co-ignimbrite ash

Ignimbrite and ashfall deposits are the characteristic and dominant products of supereruptions. Explosive eruptions eject a mixture of fragmented magma and gases which exits the vent at high velocities (up to 600 m s^{-1}), then slows rapidly as it enters the atmosphere, and mixes with and heats air (Sparks et al., 1997). If enough air is incorporated the erupted mixture becomes positively buoyant with respect to the surrounding atmosphere and rises until it reaches a level of neutral buoyancy (Sparks, 1986; Woods, 1988). At this level the particle-laden plume spreads laterally and particles are sedimented from the plume to generate Plinian fall deposits (the largest observed plumes have reached heights of ~ 45 km, and modelled examples may exceed 50 km: Wilson et al., 1978; Woods, 1988; Wilson, 2008). Various models have been developed for the deposition of Plinian fall deposits through which ash dispersal patterns provide information on mass flux, gas content and maximum column height as discussed further in Chapter 6 (e.g., Sparks and Wilson, 1976; Wilson, 1976; Wilson et al., 1978; Carey and Sparks, 1986; Sparks, 1986; Wilson and Walker, 1987; Valentine and Wohletz, 1989; Woods and Bursik, 1991; Bonasia et al., 2010; Costa et al., 2010).

Pyroclastic flows are generated by plume collapse triggered either by instabilities in the rising plume or by failure of the emergent mixture to become or remain buoyant. Such flows can travel at speeds exceeding 100 m s^{-1} and form ignimbrites (or 'ash-flow tuffs'). Ignimbrite-forming flows are dense, topographically controlled, poorly sorted, hot, particulate mixtures which form gravity currents (e.g., Smith, 1960; Ross and Smith, 1961; Sparks et al., 1973; Wilson, 1980). In addition, buoyant, ash-rich eruption plumes are generated simultaneously with large pyroclastic flows, which generate coeval co-ignimbrite fall deposits (dominated by fine ash, and generated above moving flows rather than at the primary vent; Sparks and Walker, 1977; Woods and Wohletz, 1991; Wilson, 2008).

Ignimbrite deposits are generated through two currently accepted models - *en masse* and *progressive aggradation*. In *en masse* deposition the flow is characterised by a high-yield-strength 'plug', which moves over a basal laminar shear zone (Sparks, 1976, 1978; Branney and Kokelaar, 2002). Ignimbrites deposited in this manner are massive units with little internal stratigraphy, emplaced over a thin, inversely graded layer (Branney and Kokelaar, 2003). *Progressive aggradation* describes pyroclastic flows as highly concentrated and non-turbulent, with the resulting deposit being attributed to incremental deposition from density-stratified currents (Branney and Kokelaar; 1992; Legros and Marti, 2001).

The cooling history of pyroclastic flow deposits generated through both mechanisms is recorded through welding and densification of the ignimbrite (Grunder and Russell, 2005). Welding of the deposit is caused by sintering and deformation of juvenile components (glass and pumice) relating to emplacement conditions of the deposit, volatile resorption

and compression (e.g., Smith, 1960; Riehle et al., 1995; Sparks et al., 1999; Grunder et al., 2005). Densely welded ignimbrites display a strong eutaxitic texture, whereas the poorly welded ignimbrites show some pumice flattening, and are highly porous and unconsolidated (Wilson and Hildreth, 2003). Poorly welded ignimbrites are thought to be produced by pyroclastic flow emplacement below the minimum welding temperature, although other factors such as water and volatile content also play a role in the degree of welding (Grunder and Russell, 2005).

This thesis focuses on analysis of proximal ignimbrites and distal co-ignimbrite and Plinian ash deposits associated with the Whakamaru supereruption.

1.3 Crystal-specific micro-analysis

Voluminous ignimbrites provide a snapshot view of large, batholith-scale magma chambers that have undergone syn-eruptive drawdown (e.g., Hildreth, 1981, 1984). Crystal-specific analysis is a particularly valuable tool for use with these large-volume, crystal-rich ignimbrites which are commonly altered by devitrification and are therefore not appropriate for whole-rock analysis (Wilson, 2008). In-situ crystal analysis using electron-microprobe (EPMA) and ion-probe techniques provides quantitative data on distinct zones within crystals, enabling a time-controlled reconstruction of magmatic evolution throughout crystal growth (e.g., Davidson and Tepley, 1997).

In addition to compositional zoning, textural discontinuities, reaction rims, and inclusion zones are also inferred to reflect changes in magmatic conditions, with compositional changes being produced by changes in intrinsic variables (H_2O content, temperature, pressure, and eruptive/convective cycles in magma chamber) or by open-system processes such as recharge and contamination (Davidson and Tepley, 1997). The crystal assemblage in each pumice clast extracted from ignimbrite deposits, with application of detailed crystal-specific analyses, can therefore potentially provide valuable chemical, isotopic and P-T-$X H_2O$ information pertaining to the source magma chamber (Davidson and Tepley, 1997; Anderson et al., 2000). These features are exploited in the work described here.

1.4 The Taupo Volcanic Zone

1.4.1 Tectonic setting

The TVZ was first recognised by Hochstetter in 1864, who used the term 'Taupo Zone' to describe the area of young eruptive centres and geothermal systems between White Island and Ruapehu (Fig. 1.2). This zone trends NNE-SSW for ~ 300 km, is up to 60 km wide, and is the result of subduction of the oceanic Pacific lithosphere westward beneath continental crust of the Australian plate at a rate of ~ 50 mm y^{-1} around a relative pole of rotation at 62 °S, 174 °E (Chase, 1978; Cole and Lewis, 1981; Wallace et al., 2004; Spinks et al., 2005). The entire TVZ is currently rifting at rates ranging from ~ 7 mm y^{-1} at the southern end, to ~ 15 mm y^{-1} at the Bay of Plenty coastline to the north (Rowland and Sibson, 2001; Wallace et al., 2004; Rowland et al., 2010).

The central TVZ (Fig. 1.2) is an actively rifting arc segment that has produced rhyolite eruptions at millennial frequency during the late Quaternary (Wilson et al., 1995a, 2009). Mechanisms proposed for rifting within the central TVZ include pure tectonic faulting, mafic dike intrusion and associated faulting and fissuring, and rhyolite dike intrusion (Villamor and Berryman, 2001; 2006; Berryman et al., 2008; Rowland et al., 2010). In addition, regional-scale uplift and subsidence are associated with inflation and deflation of silicic magma bodies, and regional-scale basin development in association with rhyolitic caldera-forming eruptions (Rowland et al., 2010). The central TVZ is thought to be the most productive and active rhyolitic volcanic zone on Earth, with eruption rates from large caldera-forming events at ~ 3.8 km^3 ky^{-1} since 2 Ma (similar to eruption rates for intracontinental silicic volcanic provinces such as Yellowstone: 3.0 km^3 ky^{-1} over the last 2.1 Ma; Wilson et al., 2009). Rhyolitic caldera-forming events represent 82% of the

volume erupted from the TVZ (Wilson et al., 2009). It is thus the ideal location to study the processes that govern the rates of rhyolitic magma production, storage and eruption.

The very high heat flux (800 mW m^{-2}) in the central, rhyolite-dominated portion of the TVZ (Stern, 1987; Bibby et al., 1995; Hochstein, 1995; Stern et al., 2006) causes the brittle-to-ductile transition to occur at 6 – 7 km depth (Bryan et al. 1999). Geophysical techniques show that the TVZ is distinguished by a broad gravity low with large negative residual gravity anomalies superimposed, indicating thick sequences of low-density volcaniclastic sediments and marking the location of rhyolitic calderas (Stern, 1979; Rogan, 1982; Davey et al., 1995; Fig. 1.2).

Seismic refraction data indicate that the quartzo-feldspathic upper crust extends to only 15 – 16 km depth (Harrison and White, 2004; Stratford and Stern, 2004; Stern et al., 2010) beneath the central TVZ. Volcanic sediments with P-wave velocities of 2.0 – 3.5 km s^{-1} reach a maximum thickness of 3 km beneath central TVZ (Rowland et al., 2010). Low P-wave velocities (6.9 – 7.3 km s^{-1}; Stratford and Stern, 2004) recorded from below 15 – 16 km may indicate mantle with significant amounts of melt, or highly intruded mafic crust with ~ 2% melt (Harrison and White, 2004). Existing models of TVZ lithospheric structure (Fig. 1.3; Harrison and White, 2006; Stratford and Stern, 2006) are consistent with large volumes of mafic magma being emplaced at depths > 15 km (Rowland et al., 2010).

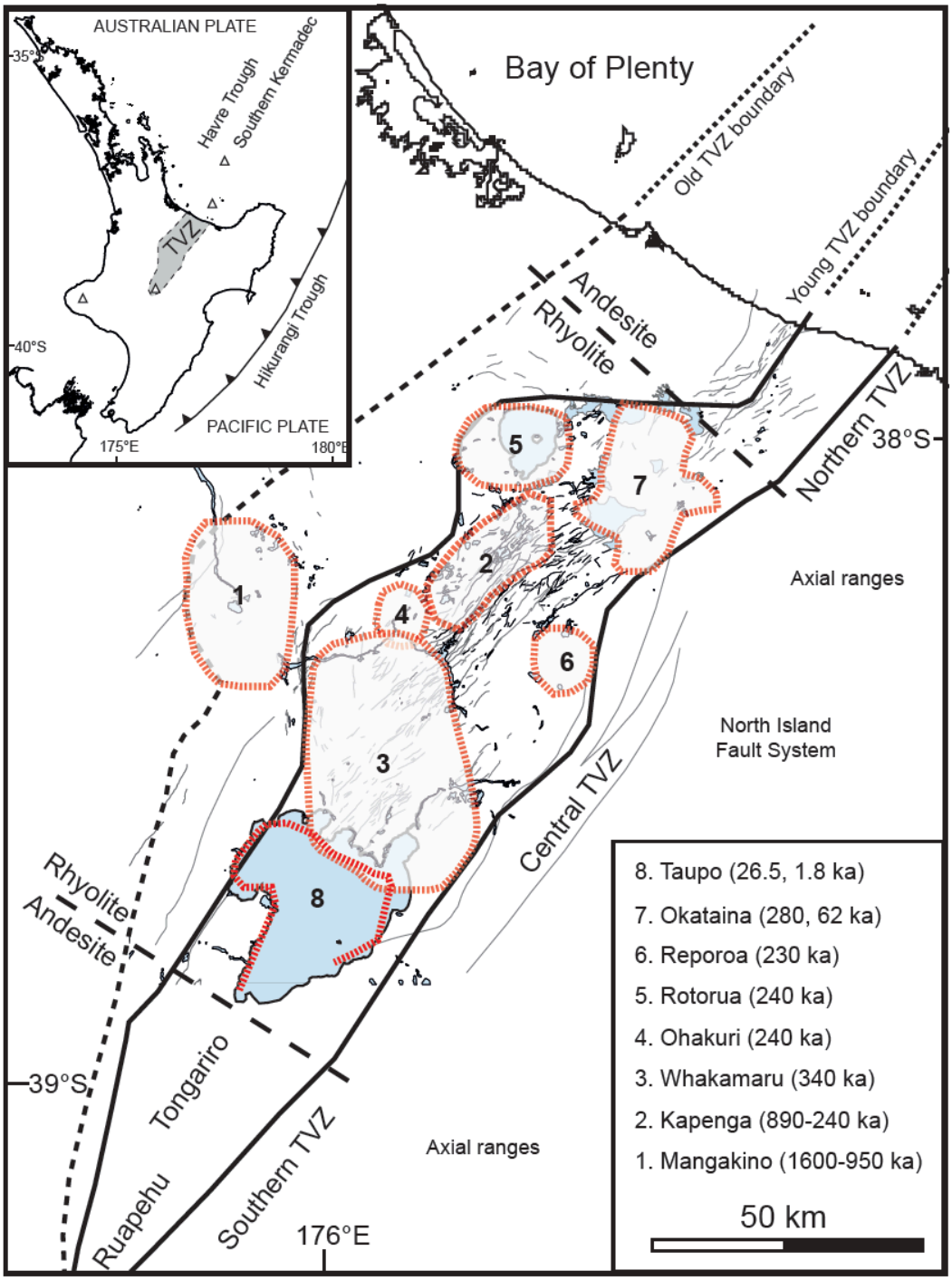

Fig. 1.2: Summary map of the Taupo Volcanic Zone (TVZ) showing the division of the zone into the three main segments: andesite-dominated at northern and southern extremities of zone, and the central rhyolite-dominated zone. Inferred caldera outlines of eight recognized calderas are marked by dashed red lines and identified in key (with eruption ages). Solid and black dashed lines marked Old TVZ and Young TVZ represent the boundaries around vent sites and caldera margins active from 1.6 to 0.34 Ma, and from 0.34 Ma to present, respectively. Modified from Wilson et al. (1995a) and Gravley et al. (2007). Inset map shows North Island and location of the subduction zone plate boundary between the Pacific and Australian plates.

1.4.2 Regional geology of TVZ

The TVZ has a pronounced segmentation into three major zones, with the northern and southern extremities characterised by andesite composite cones, and a 125 km long central segment dominated by rhyolite volcanism (Fig. 1.2; Wilson et al., 1995a; Rowland et al., 2010). Upper-crustal rhyolite magma reservoirs are part of a complex magmatic system distributed across the entire central TVZ from the base of the seismogenic zone (~ 6 km) to depths of ~ 16 km, below which the mafic magmatic system extends to depths of ~ 30 km (Fig. 1.3; Stern et al., 2006; Rowland et al., 2010).

Mafic magma is able to intrude through the entire crustal section in the TVZ, as shown by its reaching the surface via dike injection; interacting with melt-dominant rhyolite bodies and triggering rhyolitic eruption (e.g., Blake et al., 1992; Nairn et al., 2005; Wilson et al., 2006; Shane et al., 2007, 2008a); and interacting and hybridising with greywacke basement (e.g., McCulloch et al., 1994; Charlier et al., 2008; 2010). TVZ rhyolitic volcanism is therefore thought to differ from the mush model which involves a density structure that inhibits mafic magmas from interacting with the rhyolite melt-dominant zone or reaching the surface (Hildreth, 1981, 2004; Hildreth and Wilson, 2007). Furthermore, there is an apparent sharp demarcation of the floor to the rhyolite magma bodies, as evidenced by ponding of mafic magma immediately below crystal-poor rhyolite, and a frequent lack of crystal concentration gradients in the rhyolites (Wilson et al., 2009).

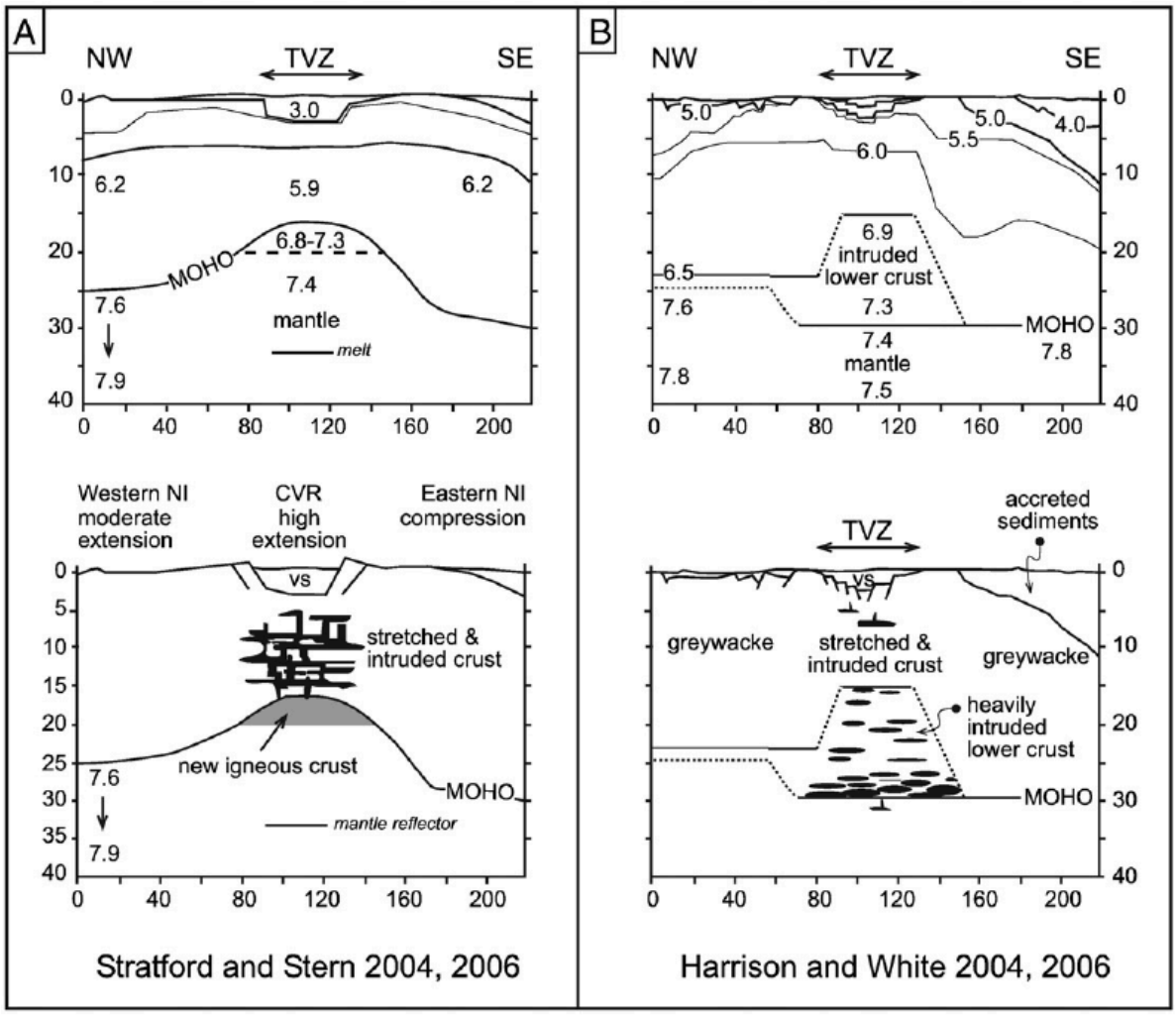

Fig. 1.3: Lithospheric-scale velocity models (showing V_p values in km s^{-1}) and geological interpretations of the central North Island structure; (A) Stratford and Stern (2004, 2006); (B) Harrison and White (2004, 2006). Length dimensions are in km. Data acquired during the Central North Island Passive Seismic Experiment (CNIPSE) and North Island Geophysical Transect (NIGHT) (Henrys et al., 2003). Figure modified from Rowland et al. (2010).

Mesozoic basement metasediments ('greywacke') crop out east and west of the TVZ and underlie the volcanic fill within the zone, either as rifted blocks with intrusions or as tectonically stretched crust (Rowland et al., 2010). The basement lithology for modelling of TVZ assimilation is dominantly Mesozoic greywackes of the Gondwana accretionary wedge: the Torlesse and Waipapa Terranes (100 – 170 Ma; Mortimer, 1994, 2004; Adams et al., 2009). Xenoliths and xenocrysts from greywacke occur in eruptive units from

within the southern and central TVZ (Graham, 1987; Nairn et al., 1994; Graham et al., 1998; Krippner et al., 1998; Charlier et al., 2005, 2010). There is much uncertainty concerning the extent of basement greywacke beneath the TVZ, however, with some authors suggesting that these rocks are continuous across the TVZ, albeit locally intruded by plutons and feeder intrusions (e.g., Grindley, 1960; Heise et al., 2007), while others consider that the entire sub-volcanic crust has been replaced by intermediate to silicic intrusives (e.g., Evison et al., 1976; Stern, 1985).

Older plutonics are also contributors to silicic magma generation, in addition to greywacke as a crustal protolith (Charlier et al., 2010). Granitic xenoliths have been recorded in several silicic deposits in central TVZ which are either co-genetic with the host eruption magma or incorporated from the crust during caldera collapse (e.g., Ewart and Cole, 1967; Brown et al., 1998b; Burt et al., 1998; Charlier et al., 2003).

1.4.3 Eruptive history and temporal variations

The present-day TVZ represents the latest stage in a complex history of subduction zone and arc volcanism in the New Zealand region which commenced at ~ 23 Ma with a NW-SE arc in the north of the North Island, and shifted at ~ 16 Ma to the present-day NNE-SSW trending zone aligned with the active Kermadec arc (Fig. 1.2; Herzer, 1995; Herzer and Mascle, 1996; Mortimer et al., 2007; Rowland et al., 2010). The earliest period of TVZ activity began at ~ 2 Ma with andesitic eruptions, joined from ~ 1.6 Ma by voluminous rhyolitic activity (Houghton et al., 1995; Wilson et al., 1995a; Briggs et al., 2005; Spinks et al., 2005). (Note: the abbreviations adopted for “year(s)” here are as follows: “a” when referring to an age (time before present); and “y” when referring to a time period).

Caldera-forming silicic volcanism occurred during three main periods: 2.0 – 0.34 Ma, 0.34 Ma – 65 ka and < 65 ka (Wilson et al., 1995a). These periods are classified as follows: *Old TVZ*, defined as products from 2.0 Ma to 0.34 Ma; *Young TVZ* representing centres active during and after the Whakamaru-group eruptions from 0.34 Ma to ~ 64 ka (Wilson et al., 1995a); and *Modern TVZ* comprising activity during and since the ~ 61 ka Rotoiti eruption and considered to represent the current state of TVZ (Houghton et al., 1995, Wilson et al., 1995a). The history of caldera-related TVZ eruptions is described in Table 1.2.

Table 1.2: ***Large-volume, caldera-related eruptions from the central TVZ***

Volcanic centre	Deposit name (ignimbrite)	Magma volume (km^3)	Age (ka)	Reference
		TVZ supereruptions:		
Taupo	Oruanui	530	26.5	Wilson, 2001; 2008
Whakamaru	Whakamaru Group	1500	347	Wilson et al., 1986; Brown et al., 1998a
Mangakino	Kidnappers	1200	1010	Wilson, 1986; Wilson et al., 1995b
Mangakino	Ongatiti	400	1210	Wilson, 1986
		Caldera-forming eruptions:		
Taupo	Taupo	35	1.8	Wilson and Walker, 1985
Okataina	Rotoiti	80	61	Nairn, 1972
uncertain	Mokai	40	210	Milner et al., 2003
Reporoa	Kaingaroa	100	230	Nairn et al., 1994; Beresford and Cole, 2000
Ohakui	Ohakuri	100	240	Gravley et al., 2007
Rotorua	Mamaku	145	240	Milner et al., 2003
Kapenga	Pokai	100	275	Karhunen, 1993; Gravley et al., 2007
Okataina	Matahina	150	280	Bailey and Carr, 1994
Kapenga	Chimp	50	300	Karhunen, 1993
Kapenga	Waiotapu	100	710	Wilson et al., 2009
Kapenga	Rahopaka	30	720	Houghton et al., 1995
Kapenga	Tikorangi	30	890	Hildyard et al., 2000
Mangakino	Marshall	50	950	Wilson, 1986
Mangakino	Rocky Hill	200	1000	Wilson, 1986
Mangakino	Ahuroa	100	1180	Wilson, 1986

Notes: Magma volumes are quoted as DRE; See also compilation of large-volume eruptions in Wilson et al. (2009). Age data from Houghton et al. (1995) and Leonard et al. (2010) for the Whakamaru eruption.

Eight calderas are recognised, including single-collapse calderas Reporoa, Rotorua and Ohakuri; compound and multiple nested collapses Okataina, Taupo and Whakamaru; and composite structures Mangakino and Kapenga (Fig. 1.2; Houghton et al., 1995; Wilson et al., 1995a; Spinks et al., 2005), which are together responsible for 25 caldera-forming plus numerous smaller eruptions in the last 1.6 Ma (Wilson et al., 2009). The central TVZ has generated four supereruptions over the last 1.6 Ma (Table 1.2): ~ 26.5 ka Oruanui (~ 530 km^3; Wilson, 2001; Wilson et al., 2006), 347 ka Whakamaru (~ 1500 km^3; Briggs, 1976a; Wilson et al., 1986; Brown et al., 1998a), 1.01 Ma Kidnappers/Rocky Hill pair (Wilson et al., 1995a; Schipper, 2004), and ~ 1.2 Ma Ongatiti (Briggs et al., 1993; Houghton et al., 1995; Brown and Smith, 2004).

Three caldera-forming eruptions (Rotoiti, Oruanui and Taupo) have occurred within the TVZ during the most recent period, and Holocene eruptive activity is concentrated at the 'active' centres of Taupo and Okataina at the southern and northern ends of the central TVZ respectively (Fig. 1.2; Wilson et al., 1995a). Three unrest periods over the last 100 y have been observed at Taupo (1922, 1964-65, 1983: Grindley and Hull, 1986; Otway, 1986: Smith and Webb, 1986; Webb et al., 1986; Otway et al., 2002) involving earthquake swarm activity and detectable surface deformation and faulting. Such caldera unrest during non-eruptive periods has been attributed to the accumulation or movement of magma and/or aqueous fluids at depth (Smith et al., 2007; Rowland et al., 2010).

Eruption styles, volumes and rates are distinctly different in the northern and southern TVZ in comparison to those of the central TVZ segment, with differences that reflect fundamentally different magmatic plumbing networks within the crust (cf. Charlier et al., 2005; Price et al., 2005). Rhyolitic eruptions within central TVZ seem to occur irregularly

in time and space, with no evidence for geographic separation of basalts from rhyolites (Rowland et al., 2010), whereas major caldera-forming eruptions there appear to cluster in time on a range of scales, and may also erupt coevally (e.g., Houghton et al., 1995; Gravley and Wilson, 2006; Gravley et al., 2007).

1.4.4 TVZ geochemistry

Eruptions in the central TVZ are volumetrically skewed heavily towards rhyolite, with lesser amounts of andesite > dacite > basalt as surficial eruptive units (Cole, 1990; Wilson et al., 1995a). Isotopic data indicate that the silicic melts are generated from highly fractionated primitive basalt which has been contaminated by the metasedimentary crust (< 25%; McCulloch et al., 1994; Graham et al., 1995), although evidence for silicic magma components derived from direct crustal melting is also recorded (Charlier et al., 2008; 2010). The high volumes of mafic magma required to generate the rhyolites, by whatever pathway of fractionation or crustal melting may apply, are almost entirely trapped within or immediately below the quartzo-feldspathic crust. A characteristic feature of the central TVZ is, however, that mafic melts do reach and interact with the melt-dominant magma bodies at shallow depths (4 – 8 km) and are not entirely confined within a deeper mush zone (cf. Hildreth, 1981; 2004). Mafic magma evidently interacted with the melt-dominant body for the Rangitaiki ignimbrite member of the Whakamaru group (Brown et al., 1998a; Matthews et al., 2011a; refer to Chapters 2, 3 and 4), for example, as well as in younger eruptions of the Taupo and Okataina volcanoes (e.g., Blake et al., 1992; Leonard et al., 2002; Wilson et al., 2006; Shane et al., 2007).

Geochemical studies of individual rhyolitic eruptions have indicated limited geochemical and compositional zonation within pyroclastic deposits, with this being interpreted as evidence for chemical and thermal homogeneity in rhyolitic magma chambers due to high heat flow and short magma residence times (e.g., Houghton et al., 1995; Nairn et al., 2004; Smith et al., 2004; Shane et al., 2005). Studies of Taupo and Okataina calderas demonstrate that the melt-dominant rhyolite magma bodies were stored prior to eruption at shallow levels (~ 4 – 10 km; Dunbar et al., 1989; Liu, Y. et al., 2006; Shane et al., 2008a; Johnson et al., 2011). Data from petrological and zircon studies indicate that these rhyolite reservoirs may accumulate over short time frames of hundreds to thousands of years, and are relatively short-lived compared to mafic magmatic activity in the lower crust (Sutton et al., 2000; Charlier et al., 2005; Shane et al., 2008a; Wilson and Charlier, 2009).

1.5 Whakamaru supereruption

The Whakamaru supereruption represents the largest known eruption in the history of the TVZ, involving > 1500 km^3 of high-silica rhyolite magma (Brown et al., 1998a) which erupted at 347 ± 4 ka from a large (~ 40 km across) source caldera to the north of the present day Lake Taupo (Figs 1.2, 1.4; Briggs, 1976a; Froggatt et al., 1986; Wilson et al., 1986; Brown, 1994; Pillans et al., 1996; Brown et al., 1998a; Leonard et al., 2010; Saunders et al., 2010; Matthews et al., 2011a). This location has been inferred on the basis of the distribution of ignimbrites in outcrops and drill-holes, lithic studies and distribution of lithic breccias (Brown, 1994), geophysical models (gravity and magnetic anomalies; Rogan, 1982; Wilson et al., 1986) and anisotropy of magnetic susceptibility (AMS) flow directions (Lamarche and Froggatt, 1993).

1.5.1 The Whakamaru Group Ignimbrites

The deposits of the Whakamaru supereruption comprise five different ignimbrite members classified separately according to their field characteristics (Table 1.3) and spatial distribution around the source caldera (Fig. 1.4) as outlined here. These deposits are known collectively as the "Whakamaru Group Ignimbrites" and have been previously characterised by field, magnetic, petrological and geochemical investigations (Hatherton, 1954; Ewart, 1965; Martin, 1965; Briggs, 1976a, b; Wilson et al., 1986; Lamarche and Froggatt, 1993; Brown et al., 1998a; Brown and Fletcher, 1999; Matthews et al., 2011a).

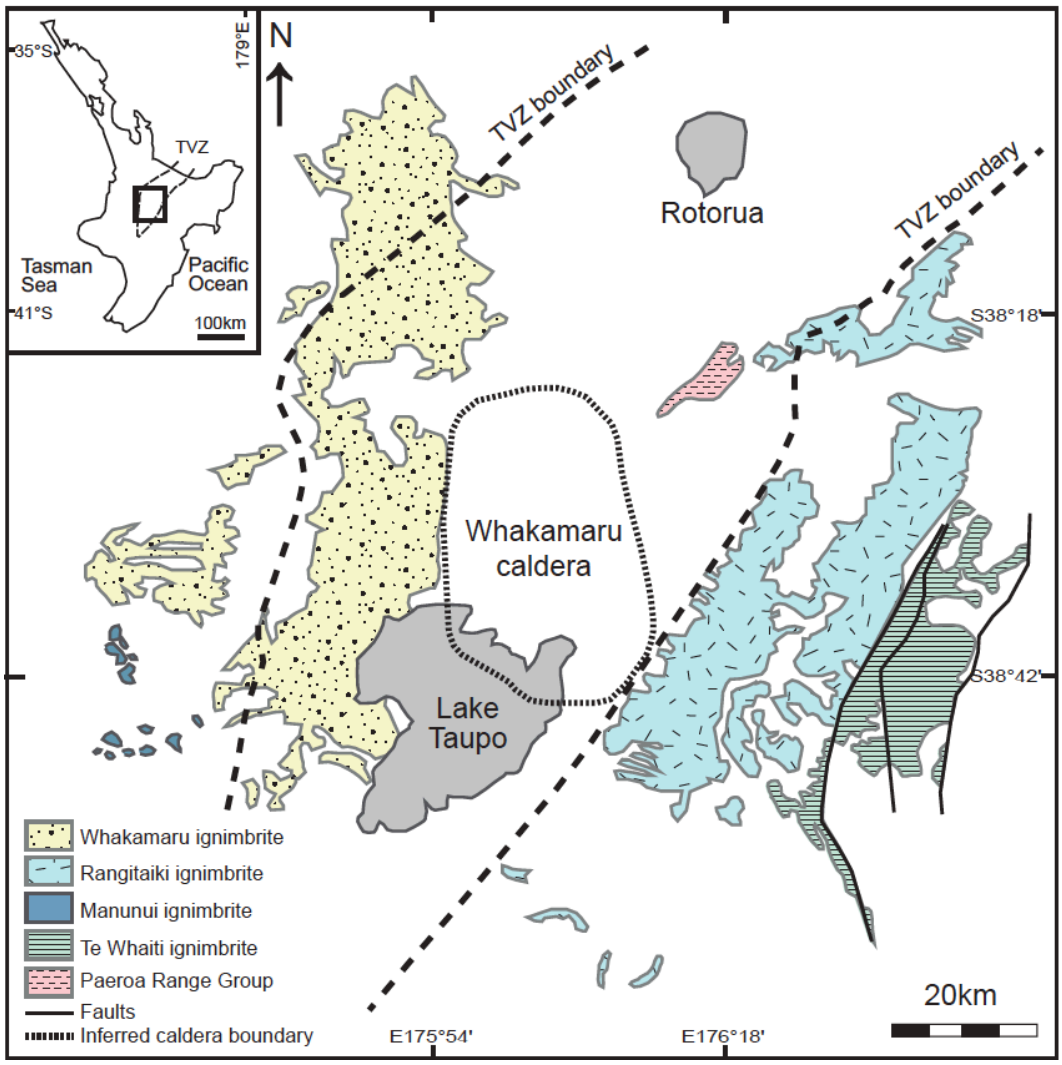

Fig. 1.4: Sketch map showing location of Whakamaru caldera and the distribution of Whakamaru Group Ignimbrites, central TVZ (after Brown et al., 1998a). Dashed black lines indicate boundary of TVZ. Inset map shows North Island of New Zealand and location of TVZ.

These studies identified stratigraphic subdivisions within the ignimbrites on the basis of mineralogy and modal analyses (e.g., Ewart, 1965; Briggs, 1973; Brown, 1994), and elucidated significant petrographic trends, including an increase in crystal content and size, and a decrease in plagioclase : quartz with increasing stratigraphic height.

The ignimbrite members are named as follows: *Whakamaru* and *Manunui* ignimbrites are located to the west of Lake Taupo, *Rangitaiki* and *Te Whaiti* ignimbrites to the east, and the *Paeroa Range* ignimbrites in the centre of the TVZ rift, north of Lake Taupo (Fig. 1.4). The ignimbrite deposits cover a total area of 13,000 km^2 (Brown, 1994) outcropping over the eastern and western margins of the TVZ (Fig. 1.4), and are largely buried by younger volcanic deposits along the central TVZ axis.

The large volumes and high crystal content (~ 15 – 45 %) of the Whakamaru Group Ignimbrites typically make these deposits distinctive throughout the TVZ. In addition to the proximal ignimbrite deposits, there is also a co-ignimbrite and Plinian ashfall phase, the *Rangitawa Tephra*, which has been correlated with the Whakamaru eruption (see Section 1.5.2 and further description in Chapters 2 and 6). The term *Whakamaru Group Ignimbrites* is used here to refer to all of these five ignimbrite units dated at ~ 347 ± 4 ka (Leonard et al., 2010; other age constraints from Ar-Ar, K-Ar and fission track methods are presented in Table 1.4) associated with the Whakamaru supereruption. Characteristics of the group are discussed in the following sections, summarised in Table 1.3 and their distribution is mapped in Fig. 1.4 and 1.5.

Table 1.3: ***Characteristics and relationships of the Whakamaru Group Ignimbrites***

Ignimbrite	Characteristic features	Interpretation of relationships
Whakamaru *(Section 1.5.1.1)*	Crystal-rich, coarse-grained non-welded to welded ignimbrite, containing large (< 12 mm) resorbed quartz crystals. Contains vapour-phase altered pumices and predominantly vent-derived (quartz-rich welded ignimbrite) lithic fragments.	Whakamaru and Rangitaiki ignimbrites may represent two eruptive episodes over a significant time period (Brown, 1994). It has been postulated that initial phases of the Whakamaru eruption deposited the Te Whaiti and Manunui, followed by Whakamaru and Rangitaki ignimbrites (Wilson et al., 1986; Brown, 1994).
Rangitaiki *(Section 1.5.1.2)*	Coarse-grained, crystal-rich, welded ignimbrite. Similar to Whakamaru in lithology and appearance. Contains mafic-mixed and mingled pumices.	Field evidence suggests continuity between the 'early' Manunui and Te Whaiti and the 'later' Whakamaru and Rangitaiki ignimbrite units (Brown, 1994).
Te Whaiti *(Section 1.5.1.3)*	Fine-grained, relatively crystal-poor, welded ignimbrite. Typically vapour-phase altered. Contains predominantly locally-derived lithics (more closely resembles Manunui ignimbrite).	Corresponds to lowermost parts of lower Rangitaiki ignimbrite (east of TVZ). No well-defined contact between this and Rangitaiki.
Manunui *(Section 1.5.1.4)*	Light coloured, and welded to non-welded. Less crystal- and pumice-rich than Whakamaru and Rangitaiki ignimbrites. Contains common metasedimentary (regolith-derived) lithic fragments.	Postulated as the fine-grained, distal equivalent of Whakamaru (Blank, 1965; Martin, 1965; Briggs, 1973). Exposed in medial- distal areas where upper, less-welded units (Whakamaru and Rangitaiki) have been removed by erosion.
Paeroa Range *(Section 1.5.1.5)*	Coarse lithic breccias. Three distinct ignimbrite units: Te Kopia, Te Weta and Paeroa ignimbrites (from oldest to youngest).	Breccias suggest that the source caldera may be a larger structure extending further north than mapped (Brown, 1994). Mineralogy differs from other ignimbrites due to presence of sanidine.

Note: Characteristic features are from field data supplemented by descriptions by Brown (1994).

Table 1.4: ***Summary of published dates for the Whakamaru Group Ignimbrites and correlatives***

Unit	Dating method	Age (Ma)	1sd	*Ref*
Whakamaru	Ar-Ar	0.320	0.01	1
	ZFTA	0.370	0.03	2
	FTA	0.330	0.05	3
	Ar-Ar	0.330	0.004	4
	K-Ar	0.360	0.01	2
	Ar-Ar	**0.347**	**0.004**	10
Manunui	Ar-Ar	0.310	0.03	1
	Ar-Ar	0.275	0.04	4
	Ar-Ar	0.307	0.03	4
Rangitaiki	ZFTA	0.360	0.04	2
Te Whaiti	ZFTA	0.390	0.04	2
	FTA	0.300	0.04	3
Paeroa	Ar-Ar	0.330	0.01	1
	ZFTA	0.370	0.02	2
	Ar-Ar	0.337	0.004	4
	Ar-Ar	0.331	0.003	4
Te Weta	Ar-Ar	0.360	0.01	2
Te Kopia	ZFTA	0.380	0.09	2
	Ar-Ar	0.340	0.01	1
Rangitawa Tephra	ZFTA	0.340	0.04	2
	GFTA	0.370	0.07	5
	ZFTA	0.370	0.05	5
	GFTA	0.380	0.04	6
	GFTA	0.390	0.01	7
	TL	0.348	0.07	8
	ZFTA	0.350	0.05	9
	ZFTA	0.340	0.03	2

Notes: Ar-Ar = ^{39}Ar-^{40}Ar method; K-Ar = conventional potassium-argon dating; FTA = fission-track dating; ZFTA = zircon fission-track dating; GFTA = glass shard fission-track dating; TL = thermoluminescence dating. References: (1) Houghton et al., 1995; (2) Kohn et al., 1992; (3) Kohn, 1973; (4) Pringle et al., 1992; (5) Pillans and Kohn, 1981; (6) Seward, 1974; (7) Boellstorff and Te Punga, 1977; (8) Pillans et al., 1996; (9) Holt, 2008; (10) Leonard et al., 2010. Age in bold is the most recent age estimate for the Whakamaru eruption (derived from Ar-Ar dating of feldspar from pumice sample P1920).

1.5.1.1 Whakamaru ignimbrite

Whakamaru ignimbrite is variably welded, relatively coarse-grained and crystal-rich with large resorbed quartz crystals (up to ~ 12 mm diameter), vapour-phase-altered pumices and vent-derived lithic inclusions (Ewart, 1965; Martin 1965; Brown, 1994). The thickest (~ 300 m) and most complete sections of the Whakamaru ignimbrite are exposed along the Waikato River between Maraetai and Arapuni hydro-electric dams towards the western margin of TVZ (Fig. 1.4; Briggs, 1976a; Brown et al., 1998a). Thick Whakamaru ignimbrite deposits have also been identified in geothermal drill-holes in central TVZ (Grindley, 1965).

1.5.1.2 Rangitaiki ignimbrite

The Rangitaiki ignimbrite is mapped on the eastern side of the TVZ, cropping out over much of the Kaingaroa plateau and areas east of Lake Taupo (Fig. 1.4). This ignimbrite is characteristically coarse-grained, crystal- and pumice-rich, and variably welded, and is similar in appearance to the Whakamaru ignimbrite. Both the Whakamaru and Rangitaiki ignimbrites are thought to represent a more crystal-rich textural end-member, containing large resorbed quartz crystals and common quartz-rich, welded ignimbrite lithic fragments (Brown et al., 1998a).

1.5.1.3 Te Whaiti ignimbrite

The Te Whaiti ignimbrite is exposed further east of the Rangitaiki ignimbrite (Fig. 1.4) and is restricted to welded to non-welded remnant valley pond deposits in the distal areas extending into the axial greywacke ranges (Ewart and Healy, 1965; Wilson et al., 1986; Brown, 1994). It is fine-grained, relatively crystal-poor, often strongly welded, and contains predominantly locally-derived lithics, thus more closely resembling the Manunui

ignimbrite (Section 1.5.1.4). The Te Whaiti ignimbrite is also distributed further south than the other ignimbrites, and forms thick welded deposits up to ~ 50 km from the inferred caldera margin (Fig. 1.4). This ignimbrite was initially considered as a fine-grained distal equivalent of the Rangitaiki ignimbrite (Martin, 1961; Kohn, 1973), although Wilson et al. (1986) suggested that these deposits represent two ignimbrite eruptions separated by a significant time period. Brown (1994) postulated that the Te Whaiti ignimbrite corresponds to the lower parts of the Rangitaiki, with field evidence for a gradational boundary between the two ignimbrites.

Both the Te Whaiti and the Rangitaiki ignimbrites overlie basement greywacke (Ewart and Healy, 1966; Brown, 1994). There are no complete sections through these ignimbrites on the eastern side of TVZ (Wilson et al., 1986; Brown et al., 1998a) and hence the stratigraphy must be inferred from numerous partial sections.

1.5.1.4 Manunui ignimbrite

Manunui ignimbrite is found as strongly welded but patchy outcrops in distal localities on the western boundary of the TVZ (Fig. 1.4), cropping out in the Hauhungaroa Range and lowlands to the west of Lake Taupo with a type locality ~ 16 km east of Taumarunui (Martin, 1961; see Appendix 1 sampling localities). The Manunui ignimbrite has a distinctly different lithology to the more crystal-rich Whakamaru ignimbrite deposits. Manunui deposits are fine-grained, non-welded to strongly welded, less crystal- and pumice-rich, and contain angular metasedimentary (regolith-derived) lithic fragments (Table 1.3). These deposits were regarded by Blank (1965) as merely the distal equivalents of ignimbrite sheets in the Mangakino and Taupo basins, whereas Grindley (1960), Martin (1961) and Wilson et al. (1986) considered them to be separate ignimbrites, and they have

since been included with the Whakamaru Group Ignimbrites. The Manunui and Te Whaiti units underlie the Whakamaru and Rangitaiki units, respectively (Wilson et al., 1986).

1.5.1.5 Paeroa Range ignimbrites

The Paeroa Range ignimbrites (Fig. 1.4) have been studied in detail by Keall (1988). The area was mapped by Grindley (1960) and Martin (1961) who named the deposits the *Paeroa Range Group ignimbrites*, comprising (from oldest to youngest) the Te Kopia, Te Weta and Paeroa ignimbrites. These three ignimbrite units are similar in terms of petrographic and geochemical characteristics and have been interpreted as being eruptive products of a single magma chamber, being emplaced by low- to moderate-energy pyroclastic flows (Keall, 1988). The distribution of ignimbrite facies, in conjunction with very proximal facies (lithic breccias), led Keall (1988) to suggest that these ignimbrites erupted from two source calderas located nearby (with the Te Kopia ignimbrites being erupted from a source caldera at the northern end of the Paeroa Range fault scarp, while the Te Weta and Paeroa ignimbrites were erupted from a southern source). These ignimbrites yield identical ages within uncertainty to the Whakamaru units (Houghton et al., 1995) and display geochemical similarities to the Whakamaru Group, indicating that they can be directly correlated to the Whakamaru eruption, and here they are considered collectively as “Paeroa Range ignimbrites”.

The relationship between the five Whakamaru Group Ignimbrites has not yet been definitively constrained. Wilson et al. (1986) suggested that there were three eruption phases: firstly Manunui/Te Whaiti; secondly Whakamaru/Rangitaiki; and Paeroa and Rangitawa Tephra as a final phreatoplinian phase. There is no field evidence for time breaks between the ignimbrite units, and it is currently thought that the Manunui–

Whakamaru pair and the Te Whaiti–Rangitaki pair represent the deposits of single eruptions (C. Wilson, *pers. comm.,* 4 July 2011). On the basis of field evidence, Brown et al. (1998a) suggest that all ignimbrites were erupted over a period of < 10 ky. Ar-Ar dating (Table 1.4) indicates that there is no significant time break between the ignimbrite units, and Brown (1994) suggests that the ignimbrite eruptions occurred over a period of < 5 ky.

1.5.2 Rangitawa Tephra

The *Rangitawa Tephra* unit (formerly the *Mt Curl Tephra*; Milne, 1973; Pillans and Kohn, 1981; Froggatt, 1982; Froggatt et al., 1986; Wilson et al., 1986; Kohn et al., 1992) has previously been linked to the ~ 340 ka Whakamaru supereruption on the basis of glass shard major-element chemistry, ferromagnesian mineralogy, and similarity of paleomagnetic dates and zircon fission-track ages (Kohn et al., 1992; Pillans et al., 1996; Table 1.4). Mineralogically, Rangitawa Tephra is characterised by dominantly glass shards, plagioclase, orthopyroxene, quartz and minor biotite, hornblende, clinopyroxene, magnetite, apatite and zircon.

The Rangitawa Tephra represents an important stratigraphic marker in mid-Pleistocene marine and terrestrial sequences in New Zealand and has been fission-track dated at 340 ± 40 ka (near the end of OIS 10; Kohn et al., 1992; Pillans et al., 1996; Holt et al., 2010), corresponding to the age of the Whakamaru eruption. It is characterised by a coarse crystal-rich base and crystal-poor, vitric upper part at the Mount Curl and Rangitawa Stream type sections (Fig. 1.6) which has been previously interpreted as initial ashfall grading up into co-ignimbrite ash (Froggatt et al., 1986). The crystal-rich nature of the fall deposit is, however, thought to preclude it from being a simple co-ignimbrite ashfall

(Wilson et al., 1986; Kohn et al., 1992). There is no evidence, however, for any pre- or syn-ignimbrite fall deposits in the proximal area (Wilson et al., 1986; Brown, 1994), on which to base any stratigraphic correlations.

The volume of ashfall dispersed across the Pacific Ocean is estimated to be ~ 700 km^3 (bulk; Froggatt et al., 1986) which was deposited primarily to the southeast of the source caldera and forms a ~ 15 – 30 cm thick horizon on Chatham Island (Fig. 1.6; Section 6.3.1; Matthews et al., 2011b). The recent study of grain size characteristics, glass chemistry, and computational modelling indicates that the distal tephra was deposited by an eruption column of ~ 40 km height, with dispersal by strong winds to the SE of the source caldera (Matthews et al., 2011b). Refer to Chapter 6 for detailed analysis of Rangitawa Tephra characteristics and dispersal modelling.

1.5.3 Whakamaru Group pumice and magma types

In addition to the five ignimbrite types described above, a distinct set of associated *Whakamaru Group* pumice types has also been identified. The ignimbrite members share similar geochemistry and petrography and each contains varying amounts of five distinct pumice types associated with different whole-rock XRF compositions and crystal contents (Wilson et al., 1986; Brown et al., 1998a). These pumices have been classified as *types A*, *B*, *C*, *D* and *mixed basaltic pumices* (high-alumina basalt; Brown et al., 1998a) and this nomenclature is used here (refer to Table 2.2 for definitions).

Unless specifically dealing with one particular pumice type, the term *Whakamaru Group pumice* is used here generically to describe the five-pumice group as a whole. Similarly, pumices may be referred to according to their host ignimbrite type. *Whakamaru Group*

pumice thus refers to the five pumice types irrespective of ignimbrite type; while *Whakamaru pumice*, for example, refers to pumices hosted in the Whakamaru ignimbrite, irrespective of pumice type.

These pumice types have been previously interpreted as 'magma types' and therefore as evidence that the magmas underwent complex crystallisation processes in multiple chambers (Brown et al., 1998a). Here 'magma' types are referred to by pumice type as their definitions are based on XRF data which includes both melt and crystals, whereas glass chemistry for each type is similar (refer to Section 2.3.3). Magma type is thus related to pumice type, with "type *A* magma" referring to that from which type *A* pumice was derived, and so on. The terms "magma" and pumice" are therefore able to be used interchangeably in the present context. As with the pumices, previous reconstruction of the magmatic system suggests that *type A* magmas are volumetrically dominant, with *types B* and *C* related to type *A* by two-stage fractional crystallisation (Brown et al., 1998a). *Type D* magmas are rare, with elevated Rb and Sr, and are thought to represent a separate crustal melt or cumulate rock (Brown et al., 1998a). Refer to Section 2.4.4 for further discussion.

Brown et al. (1998a) provided evidence that the less-evolved, low-silica rhyolites represent magmas that underwent significant fractionation at shallow crustal levels to produce the dominant volumes of more evolved rhyolites ultimately erupted. Analysis of Sr isotopes has indicated limited (~ 1%) assimilation of greywacke basement accompanied by fractional crystallisation (Brown, 1994). The Whakamaru supereruption is therefore thought to have involved non-systematic tapping of a complex magmatic system and eruptive mixing of pumice clasts (Brown et al., 1998a).

1.6 Sampling strategy

The Whakamaru eruption produced a complex range of ignimbrite and tephra deposits of varying thicknesses and spatial distributions (Figs 1.4, 1.5, 1.6). In order to avoid confusion the sampling criteria for the present study are summarised here. The full sample database is provided in Appendix 1 and proximal sampling localities are marked in Fig. 1.5. The sample database was supplemented by 120 pumices previously collected and analysed by Brown (1994).

1.6.1 Ignimbrite sampling

Ignimbrite sampling was guided by localities outlined by Brown (1994). For the proximal ignimbrite deposits, attention focused mainly on the *Whakamaru* and *Rangitaiki* members of the Whakamaru Group Ignimbrites because they are volumetrically dominant and the other ignimbrite members were too intensely welded, vapour-phase altered, and pumice-poor to allow detailed analysis. These two ignimbrites provided 83% of the samples analysed. Less attention was given to Manunui, Paeroa Range and Te Whaiti ignimbrites because the former two ignimbrites are volumetrically small and pumice-poor, and the latter is too strongly welded and altered to enable pumice extraction. Together, these provided 17% of the samples analysed. Bulk ignimbrite was sampled where the deposit was strongly-welded or pumice-poor. Both pumices and bulk ignimbrite samples were analysed petrographically (Appendix 2).

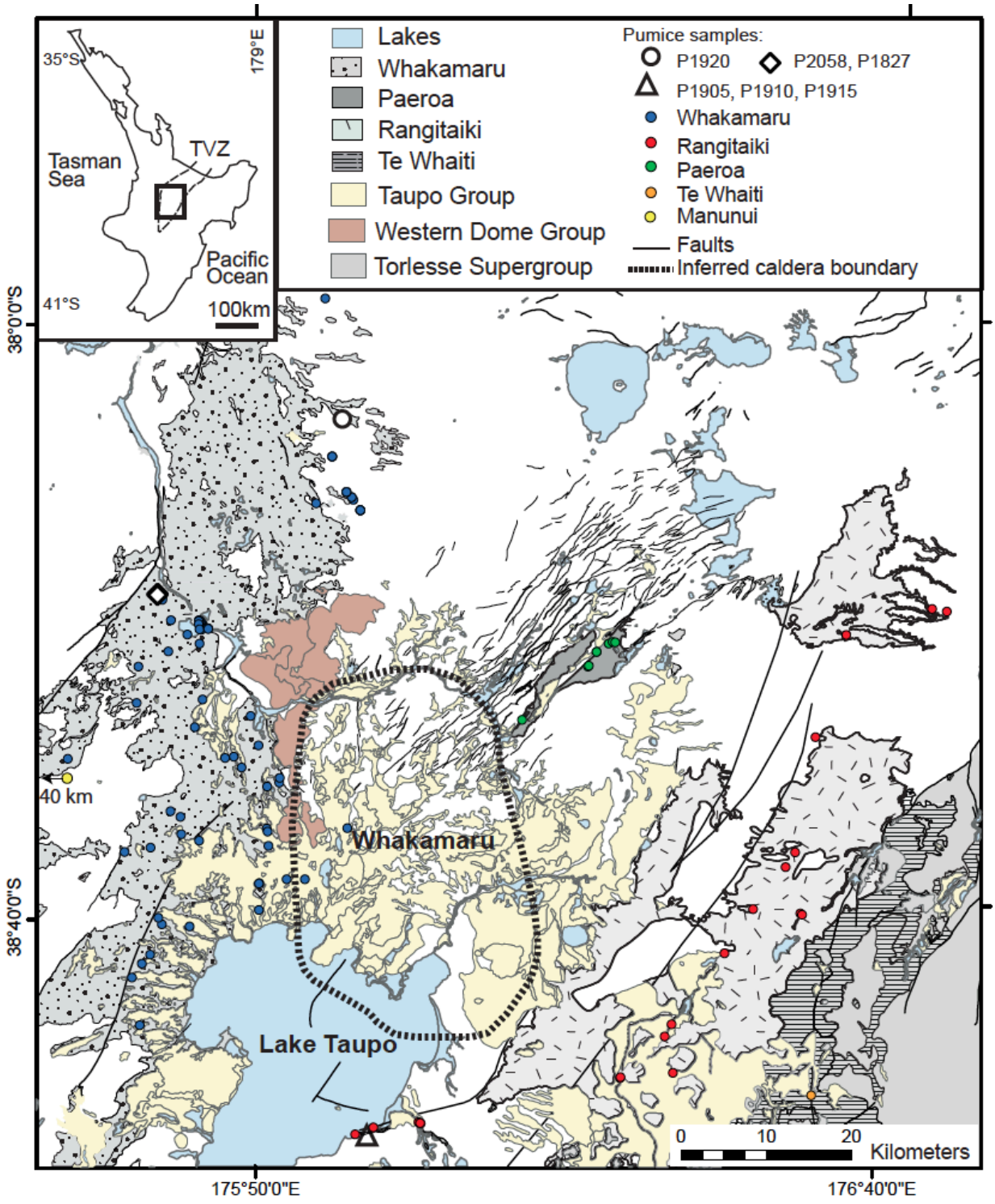

Fig. 1.5: Detailed geological map showing Whakamaru Group Ignimbrite distribution and inferred caldera boundary (from Wilson et al., 1986; Brown, 1994; Brown et al., 1998a). Sampling locations are marked by coloured circles coded by ignimbrite type, and selected Whakamaru and Rangitaiki samples for detailed analysis are also marked (white symbols). The distribution of the younger Western Dome Group and Taupo Group deposits are also shown by brown and yellow shading respectively. Inset map shows the location of the TVZ in central North Island, New Zealand. Base map from Leonard et al. (2010).

1.6.2 Pumice sampling

Pumice sampling focused on clasts selected on the basis of mineralogy, clast size, lack of alteration and major-element geochemistry. Pumice fragments were used for detailed analysis rather than bulk ignimbrite (cf. Saunders et al., 2010) as these are considered to represent quenched fragments of the vesiculated rhyolite magma, with variations in glass composition between pumices reflecting variations within the parent magma reservoir(s) that were quenched in at the time of eruption (Hildreth, 1981). Stratigraphic control on samples is limited due to the patchy exposures and difficulties with correlation across the large distances.

This study focuses primarily on type *A* pumice as it represents the volumetrically dominant magma type (~ 89% of pumice sampled). Type *D* is also of interest because it may represent a co-erupted but possibly separate (and subsidiary) chamber on the basis of its contrasting isotopic and trace-element characteristics (Brown et al., 1998a). Types *B* and *C*, in contrast, are likely to represent only second-order variants produced by convective fractionation in a dominantly type *A* magma reservoir (Brown et al., 1998a). The sample database included ~ 89% type *A*, 4% type *B*, 4% type *C*, and 3% type *D* pumices (Appendix 3). Detailed crystal-specific analyses focused on a selection of six representative pumices from the Whakamaru and Rangitaiki ignimbrites as discussed in the following chapters.

1.6.3 Tephra sampling

Any consideration of tephra invokes the concepts of "proximal" and "distal" deposits. In the Whakamaru context, proximal deposits are defined here as being within the area bounded by the greatest distance at which ignimbrites are still preserved – i.e., within ~ 50 km of the vent (ignimbrite deposits are also proximal in this context). Distal tephra deposits occur beyond that, with "ultra-distal" deposits being those recorded at extreme distances, such as Chatham Island, > 900 km from source (discussed in Chapter 6).

The Rangitawa Tephra was sampled at the type locality at Mount Curl and Rangitawa Stream, Wanganui Region, North Island (Fig. 1.6, Appendix 1: sites R025 and R024 respectively: Te Punga, 1952), located ~ 200 km from the source. Samples were taken at high resolution (2 cm increments) throughout the ~ 55 – 70 cm thick tephra horizon (focusing on the Rangitawa Stream locality, as tephra at Mount Curl is more altered, with hydrated glass shards).

Samples were also collected from the most distal on-land exposures on Chatham Island, ~ 900 km from source (Fig. 1.6) at locations previously documented by Holt et al. (2010). The tephra is present as a distinctive macroscopic horizon within terrestrial deposits, commonly preserved within peat and outcrops at coastal exposures. These distal tephra samples were collected at 1 cm increments through the ~ 15 – 30 cm tephra layer.

Distal ash deposits of the large Oruanui eruption from Taupo caldera (Wilson, 2001; Wilson et al., 2006), the "Kawakawa Tephra", are also preserved on the Chatham Islands (Holt et al., 2010) and this was sampled for comparative purposes.

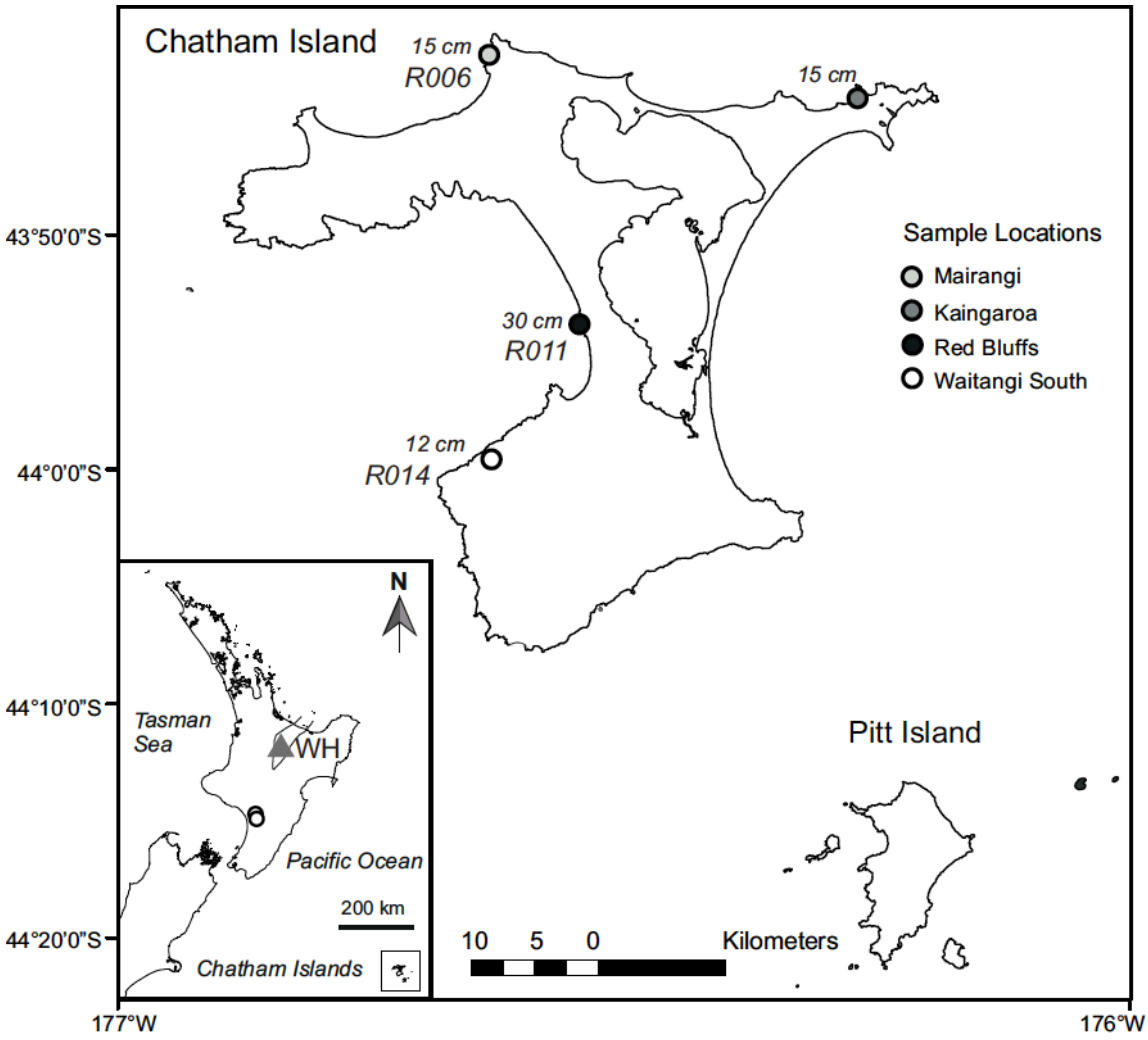

Fig. 1.6: Map of Chatham Island, New Zealand, showing distal Rangitawa Tephra sampling localities and measured thickness; Inset shows Chatham Islands location in relation to mainland New Zealand (marked by black box), Rangitawa Stream and Mount Curl localities marked by open circles, and Whakamaru caldera marked by grey triangle. Base map from Forsyth et al. (2008).

Both bulk pumice and tephra samples and single crystals were analysed. The methodologies employed and results are discussed in the following chapters. All observational, analytical and numerical approaches are combined to elucidate and quantify processes operating within this large silicic magma system prior to eruption.

Chapter 2

Glass and mineral chemistry of the Whakamaru Group Ignimbrites and Rangitawa Tephra

2.1 Introduction

Glass and mineral chemistries of pumices extracted from the Whakamaru eruption deposits (Section 1.5) provide information and insight into pre-eruptive processes and magma storage. Although the focus of this thesis was to use the record preserved in quartz and zircon crystals, the glass and other mineral phases have been analysed to provide further understanding of the magmatic processes. Furthermore, the geochemical characteristics of pumices from proximal ignimbrite deposits may also be used as fingerprints which enable correlation of distal ash deposits (the Rangitawa Tephra, Section 1.5.2) to a particular phase of the eruption. Previous work has been unable to establish how this distal ashfall is related to the ignimbrites or to a specific eruption phase. Here, data from whole-rock compositions, glass and mineral chemistry are also used to characterise the Whakamaru magma types.

Detailed major- and trace-element data of glass shards from both distal and proximal outcrops were collected to assess the chemical variation within and between deposits. Comparison between characteristic compositions of glass shards, typically comprising > 95% of distal deposits, enables the correlation of proximal and distal deposits. Correlations between ignimbrite units and the correlative tephra deposits are strengthened here using additional mineral chemistry data, particularly the ferromagnesian mineral assemblage (biotite, orthopyroxene, amphibole), following the approach of Hildreth and Mahood (1985), de Silva and Francis (1989), Shane (1998, 2000), Shane et al. (2003) and Smith et

al. (2011). Mineral chemistry is also used to assist in reconstruction of pre-eruption magmatic processes and to distinguish between the different ignimbrite units and/or eruption phases. Here data from the modally-dominant feldspar crystals are presented (refer to Chapter 3 for the analysis of quartz crystallisation histories). The geological setting of the TVZ and full descriptions of the Whakamaru Group Ignimbrites are provided in Sections 1.4 and 1.5, and distal ashfall deposits are discussed further in Chapter 6.

2.2 Methods

2.2.1 Sampling

Pumices from non-welded parts of the Whakamaru and Rangitaiki ignimbrites were sampled extensively (140 samples; Appendix 1; selected field photographs in Fig. 2.1). Proximal and distal sampling localities referred to here are listed in Table 2.1, and mapped in Figs 1.5 and 1.6 (Chapter 1) respectively. The new data presented here are also compared with 120 pumices previously analysed by Brown et al. (1998a). Rangitawa Tephra sampling localities are described fully in Chapter 6 (refer to Table 6.3 and Fig. 6.6).

Table 2.1: ***Selected Whakamaru Group Ignimbrite and Rangitawa Tephra samples***

Sample	Eruption unit	Pumice type	Location	Lat/long
(a) Proximal:				
P1905, P1910, P1912, P1915	Rangitaiki	*A*	Hinemaiaia Dam, TVZ	38°52’09.522" S, 176°03'13.140" E
P1826, P1885, P1886,P1889f	Whakamaru	*A*	Waipapa Rd, TVZ	38°13'26.328" S, 175°56'44.052" E
P1920, P1921	Whakamaru	*A*	Northern Lake Taupo, TVZ	38°12'19.950" S, 175°55'35.450" E
P1917f	Whakamaru	*B*	Northern Lake Taupo, TVZ	38°37'18.840" S, 175°49'32.268" E
T5/4	Whakamaru	*C*	Pureora Forest, TVZ	38°11'34.080" S, 175°24'37.512" E
SB1119	Whakamaru	*D*	Edsel Road, TVZ	38°19'30.600" S, 175°41'03.566" E
P1827	Whakamaru	*D*	Edsel Road, TVZ	38°19'30.600" S, 175°41'03.566" E
(b) Distal:				
R025	Rangitawa	-	Mt Curl, New Zealand	39°58'14.284" S, 175°27'03.039" E
R024	Rangitawa	-	Rangitawa Stream	40°07'53.414" S, 175°27'34.960" E
R011	Rangitawa	-	Red Bluffs, Chatham Is.	43°54'05.220" S, 176°32'33.060" W
R006	Kawakawa	-	Mairangi Nth, Chatham Is.	43°42'19.740" S, 176°38'14.100" W

Notes: Distal tephra samples are taken at 1 cm increments at each locality on Chatham Island (R011, R006), and at 2 cm increments at Mt Curl (R025) and Rangitawa Stream (R024) sites.

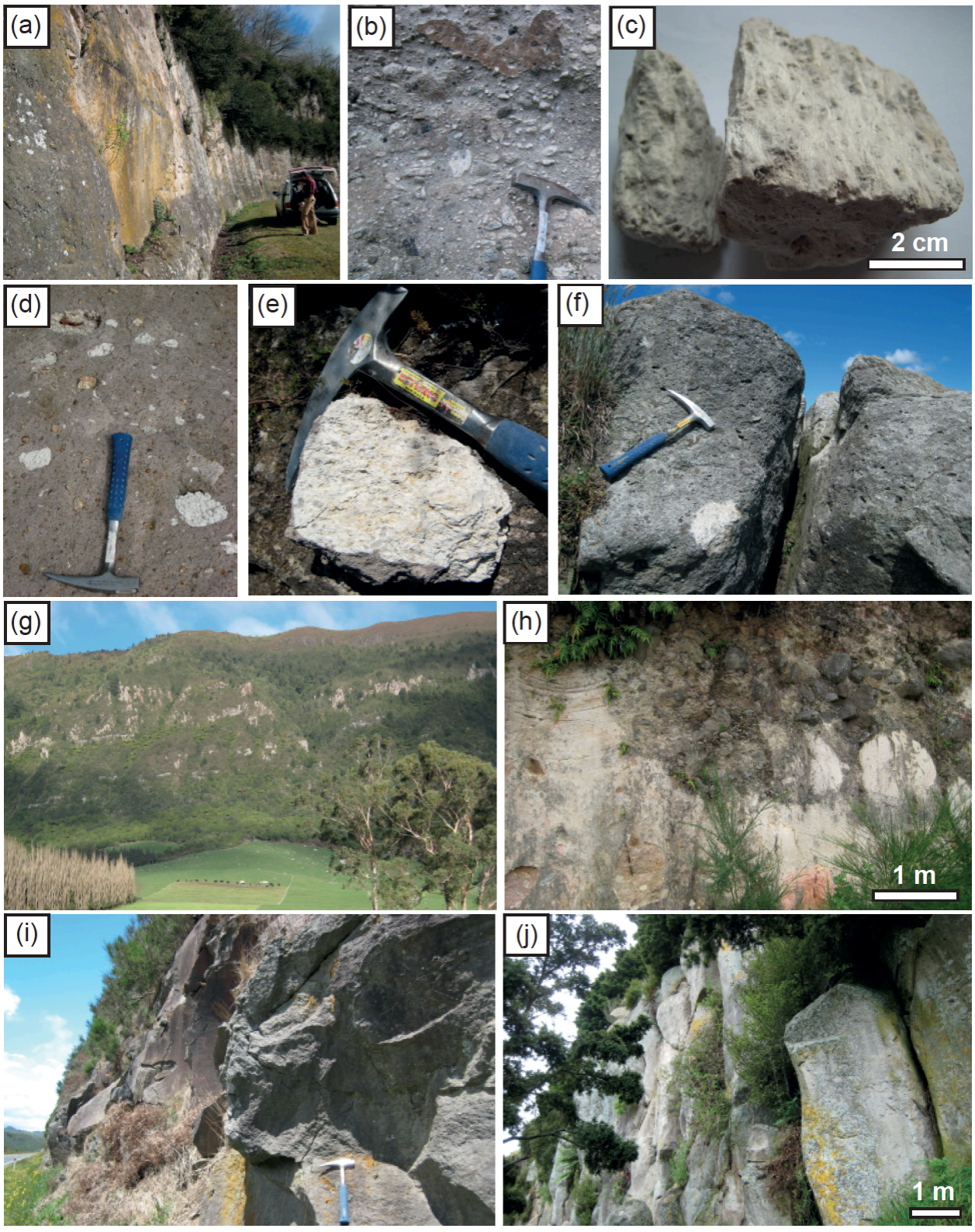

Fig. 2.1: Field photographs of Whakamaru Group Ignimbrites. (a) Welded Whakamaru Ignimbrite at Maraetai Dam; (b) Unwelded, pumice-rich Whakamaru Ignimbrite near Tokoroa; (c) Type *D* Whakamaru pumice, sample SB1119; (d) Rangitaiki Ignimbrite at Hinemaiaia Dam; (e) Rangitaiki pumice from Hinemaiaia Dam; (f) Welded Rangitaiki Ignimbrite, located adjacent Matea Road, near SH5; (g) View of Paeroa Range ignimbrites; (h) Paeroa lithic breccia; (i) Strongly-welded basal Te Whaiti Ignimbrite, SH5; (j) Welded Manunui Ignimbrite, Eastward Road type section (non-welded above this exposure).

2.2.2 Petrographic analysis and BSE imaging

Thin sections of all pumice samples were examined by optical microscopy. Petrographic descriptions for selected Whakamaru Group pumices are provided in Appendix 2, and selected petrographic images are presented in Fig. 2.2. Polished thin sections were cut from each pumice clast prior to crushing. After petrographic examination, crystals (feldspar, quartz, orthopyroxene, biotite, amphibole and Fe-Ti oxides) were extracted from pumices, mounted in epoxy resin and polished, and features documented using a JEOL SEM at the University of Oxford. Back-scattered electron (BSE) images were also collected, enabling specific zones to be targeted for further analysis.

2.2.3 X-ray Fluorescence

Pumices ~ 5 – 40 cm diameter were selected for individual X-ray fluorescence (XRF) analysis (Appendix 3). Most pumices were sampled from the Whakamaru and Rangitaiki ignimbrites (Appendix 1), as these units are less welded, less vapour-phase altered and more pumice-rich than the other ignimbrites (see Section 1.5.1 for ignimbrite classification). Samples were washed in deionised water to remove any adhering matrix and weathering rind, and oven dried at 110°C for several days prior to crushing. Pumices were then crushed to chips in a steel jaw crusher, or by covering in paper and lightly hammering. After removal of any weathered pieces, samples were reduced to powder in an agate Tema mill.

Major and trace elements were determined in this powder from 98 pumice samples (Appendix 3) using an ARL 8420+ wavelength-dispersive XRF spectrometer at the Open University, Milton Keynes, UK, following the techniques of Ramsey et al. (1995). Detection limits for trace element analyses are as follows: 2 ppm for Rb, Sr, Y, Zr, Co,

Mo; 1.5 ppm for Nb; 3 ppm for U, Ni, Cu, Zn, Ga; 4 ppm for Th and Cr; 5 ppm for Pb, Sc, V and As; and 12 ppm for Ba. Approximate 2sd analytical precisions (relative %) found by replicate analyses of the same disc for elements at concentrations typical in the rhyolites were: SiO_2 ± 0.13%, TiO_2 ± 0.04%, Al_2O_3 ± 0.03%, Fe_2O_3 ± 0.05%, MnO ± 0.001%, MgO ± 0.02%, CaO ± 0.04%, Na_2O ± 0.02%, K_2O ± 0.01%.

2.2.4 Electron Microprobe Analysis

The glass phase was separated from proximal pumices and distal tephra samples using standard procedures. Proximal pumice samples were first cleaned by immersion in distilled water in an ultrasonic bath, then dried prior to crushing, grinding and wet sieving to a grain size of < 125 μm. Standard procedures for separation of glass shards from distal ash were followed, involving sieving and removal of crystal content. Glass shards were mounted in epoxy discs, polished and carbon coated for analysis. Major-element compositions of the glass shards (Appendix 4) and minerals were determined using a wavelength-dispersive JEOL 8600 electron microprobe (EPMA) equipped with four spectrometers, at the Research Laboratory for Archaeology and the History of Art, University of Oxford. In order to reduce the impact of alkali loss on the analysis of glass shards (> 20 μm), an accelerating voltage of 15 kV, a low beam current of 6 nA, and a defocussed (10 μm) beam were used.

Minerals (biotite, orthopyroxene and hornblende) were analysed using a beam current of 15 nA and a 1 – 5 μm beam. For feldspar analysis, analytical spacing along core-to-rim profiles ranged from 20 – 25 μm using the mechanical stage (location of profiles are illustrated in annotated BSE images; Appendix Fig. A2.1; major-element EPMA data provided in Appendix 5). An accelerating voltage of 20 kV and 40 nA beam current were

used, with count times as follows: 10 s for Si, 15 s for Al, 120 s for Fe, 240 s for Mg, 10 s for Ca, 12 s for Na, 30 s for K (following analytical settings of Smith et al., 2009). The high beam currents and long count times for Mg (240 s), and Ti (120 s) were used to obtain lower detection limits (~ 50 ppm) on these low-abundance elements. The instrument was calibrated for each set of beam conditions using a suite of mineral standards. The calibration was verified using secondary standards from the Max Planck Institute (glass; Jochum et al., 2006) and the Smithsonian Institution (minerals). Totals of glass analyses were > 95% and, due to variable secondary hydration, all analyses presented here are normalised to 100% (Appendix 4). Biotite analytical totals were typically > 92 wt% and slightly lower for some of the smaller crystals in the distal deposits (only biotite data with totals > 94 wt% are presented here).

2.2.5 Laser-Ablation Inductively-Coupled-Plasma Mass Spectrometry

Trace-element compositions of glass shards (full dataset provided in Appendix 4) were acquired using laser-ablation inductively-coupled-plasma mass spectrometry (LA-ICP-MS) with a Coherent GeoLas ArF 193 nm Excimer laser ablation system coupled to the Thermo Finnegan Element 2 sector field ICP-MS at the University of Aberystwyth. Analyses were performed on glass shards previously analysed by EPMA, using a 20 μm diameter laser beam with a fluence of 10 J cm^{-2}, a repetition rate of 5 Hz, and a 24 s acquisition time. A 10 μm beam was used for smaller shards by moving the mount in small (2.5 μm) increments during the ablation. Back-scattered electron images taken prior to EPMA were used to relocate individual glass shards on the polished grain mounts in the laser-ablation system. The minor ^{29}Si isotope (4.67%) was used as the internal standard for calculation of unknown concentrations, with the SiO_2 contents of shards having been determined by EPMA, normalised to an anhydrous basis. Methods for the quantification

of the analyses are given in Perkins and Pearce (1995), Perkins and Pearce (1997) and Pearce et al. (2004, 2007 and *submitted*). Calibration was achieved against the NIST SRM 612 standard using the concentrations given in Pearce et al. (1997). Analyses were performed in two batches on the same day, and there was no difference in the range and means of data from either batch. Detection limits for many elements were ~ 0.01 – 0.5 ppm, and accuracy was ~ 75% RSD. In homogeneous materials LA-ICP-MS has a precision (reproducibility) of better than 10% at ~ 1 ppm, and accuracy is typically better than 10%. Further details of the LA-ICP-MS instrumentation, calibration and analytical methods have been described by Pearce et al. (1996, 1999, 2004, 2007).

2.3 Results

2.3.1 Petrology

The pumice samples studied in detail here (Table 2.1) are characterised by a mineral assemblage of plagioclase, quartz >> orthopyroxene, amphibole > biotite >> magnetite, ilmenite and trace zircon (full petrographic descriptions of selected pumice and ignimbrite samples are provided in Appendix 2). Total phenocryst contents in the selected pumices range from ~ 15 – 25% (crystal content in bulk ignimbrite is up to 45%; Appendix 2). Plagioclase phenocrysts typically display complex oscillatory zoning and occur as fractured aggregates (Fig. 2.2a, b). Quartz crystals are mostly anhedral, which is assumed to be due to resorption caused by changing conditions prior to eruption (Fig. 2.2c; see Chapter 3 for further analysis of quartz). They are also extensively fractured, most likely due to fragmentation through melt-inclusion explosion during pre-eruptive heating and/or decompression, and syn-eruptive shattering (Tait, 1992; Best and Christiansen, 1997; Gualda et al., 2004; Bindeman, 2005). Ferromagnesian minerals (amphibole,

orthopyroxene and/or biotite; Fig. 2.2d) occur as aggregates with feldspar or as free crystals. Fe-Ti oxides are present both as free crystals and hosted within orthopyroxene and amphibole phenocrysts. Sanidine is generally absent, although trace amounts have been found in the Paeroa Range ignimbrites (see Section 1.5.1.5).

Whakamaru pumice is dominantly type *A* in composition (Section 1.5.3; Table 2.2) and contains aggregates of strongly zoned plagioclase phenocrysts (Fig. 2.2a, b) and ferromagnesian phases dominated by biotite rather than amphibole. Plagioclase crystals are subhedral to euhedral, and often contain inclusions of orthopyroxene and melt. Whakamaru and Rangitaiki pumice samples occasionally contain strongly zoned plagioclase phenocrysts which are partly rimmed with granophyric intergrowths or contain discrete plutonic inclusions (with a mineral assemblage that is quartz- and plagioclase-rich, with biotite as the main ferromagnesian mineral; e.g., sample P1909; Fig. 2.2g, h), indicating that some portions of the magma reservoir were completely crystalline and subsequently remobilised prior to or during eruption (also noted by Brown et al., 1998a).

Some Whakamaru Group pumices display petrographic textures that imply contact with, and intermingling of, mafic magma and silicic melt (see photomicrographs of mixed-basaltic pumice, Fig. 2.2e,f). In addition, basaltic andesite and andesitic enclaves are common, containing sieved or strongly oscillatory-zoned plagioclase and aggregates of pyroxene, and crystal clots of amphibole respectively (see Fig. 3.2b). These mafic-mingled pumices and features are most commonly observed in the Rangitaiki ignimbrite.

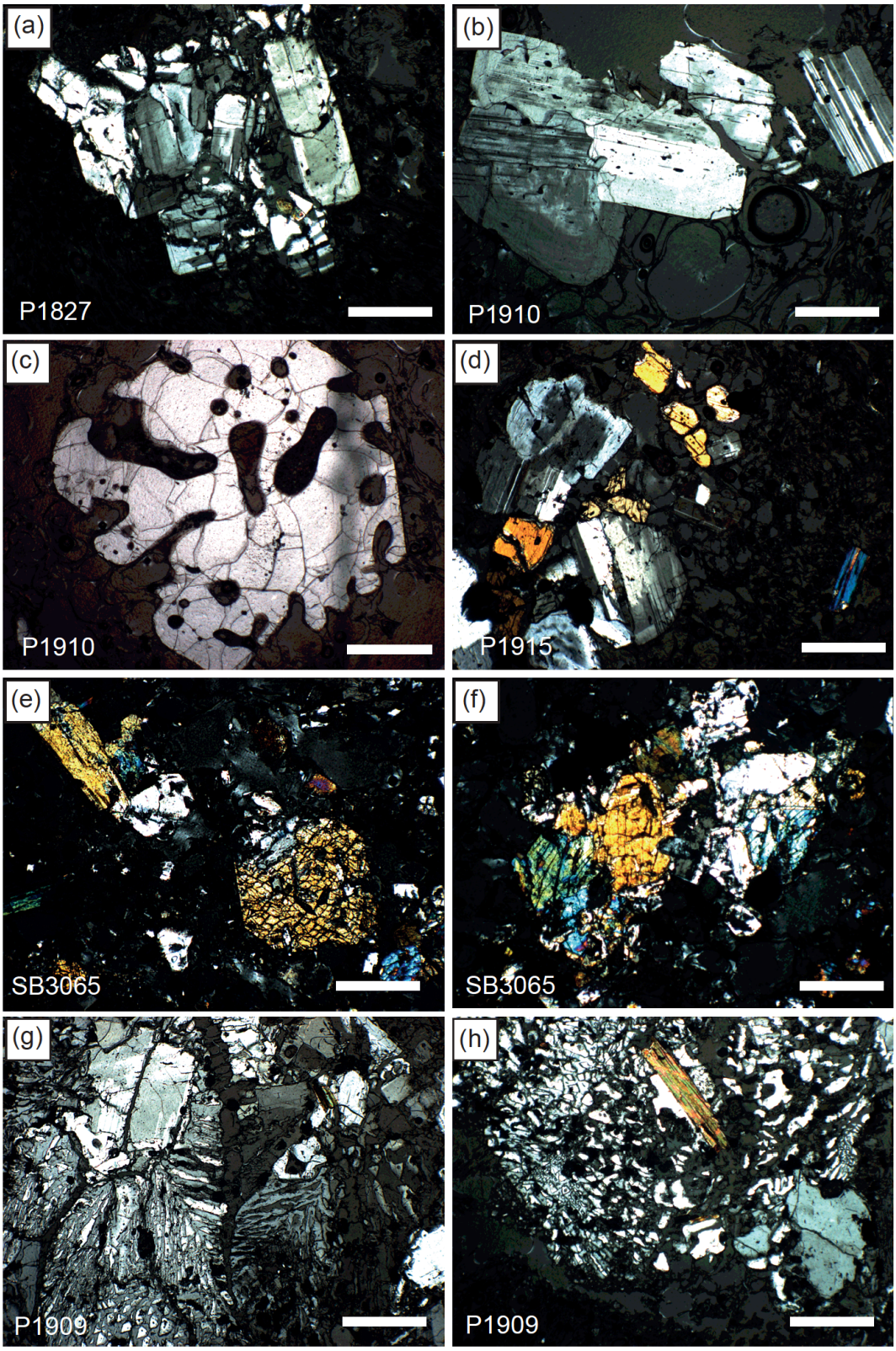

Fig. 2.2: Whakamaru and Rangitaiki thin-section images, all in cross-polarised light (CPL) with 500 µm scale bar. (a) Strongly fractured feldspar aggregate in Whakamaru pumice P1827; (b) feldspar aggregate in Rangitaiki pumice P1910; (c) resorbed and fractured quartz in Whakamaru pumice sample P1910; (d) plagioclase, biotite and orthopyroxene crystal aggregate in Rangitaiki pumice P1915; (e)-(f) mixed-basaltic Rangitaiki pumice, sample SB3065, with pyroxene and plagioclase aggregates; (g)-(h) plutonic enclave in pumice P1909 with granophyric intergrowths of quartz and feldspar, and euhedral biotite laths.

2.3.2 Whole-rock chemistry

2.3.2.1 Pumice types

Whakamaru Group pumice clasts range in composition from basaltic (~ 51.7 wt% SiO_2) in mafic inclusions/mingled bands, to high-silica rhyolite (~ 77 wt% SiO_2; TAS plot Fig. 2.3; Appendix 3) and lie on a calc-alkaline trend. Whole-rock geochemistry for individual pumice clasts is characterised by the following compositional ranges: 51.66 – 77.12 wt% SiO_2 (Fig. 2.3), 0.82 – 9.76 wt% CaO, 12.77 – 19.39 wt% Al_2O_3 (Fig. 2.5), and 1.15 – 10.95 wt% FeO^T; and 21 – 288 ppm Rb, 50 – 585 ppm Sr (Fig. 2.4), 55 – 226 ppm Zr and 394 – 1417 ppm (by XRF; *n = 200*; Appendix 3).

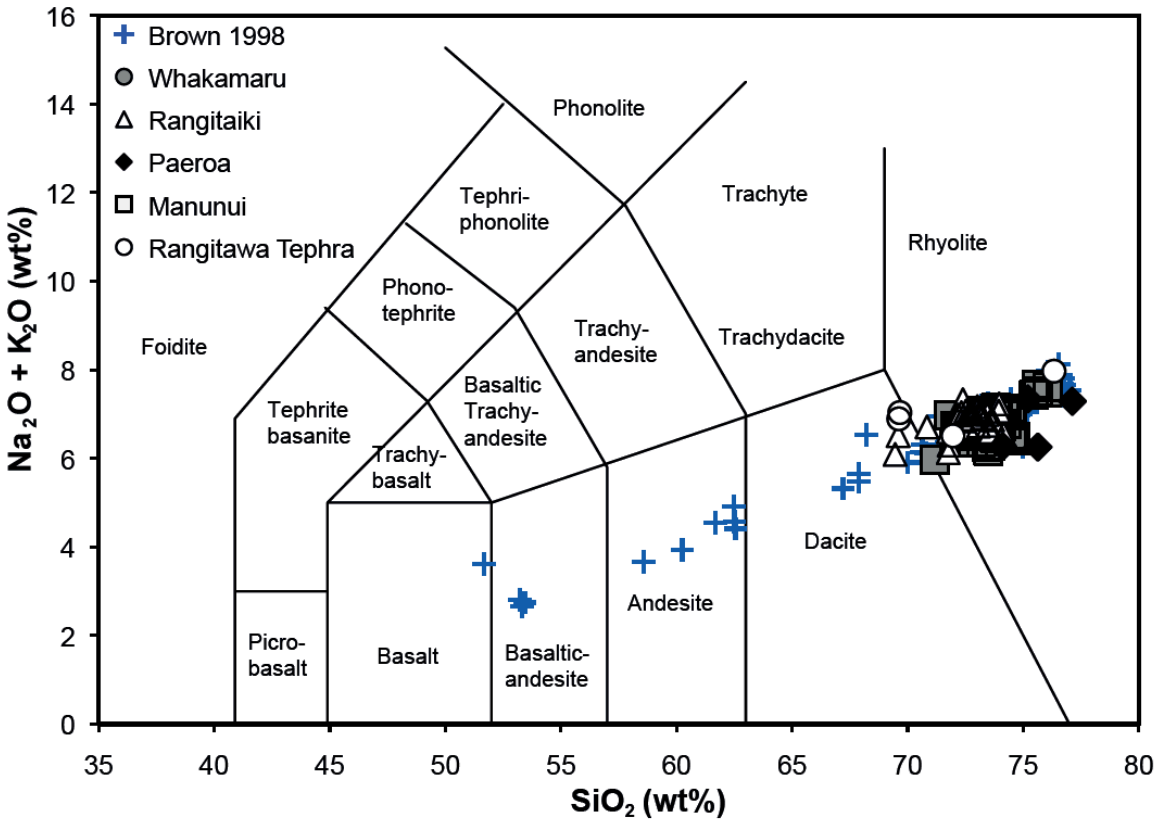

Fig. 2.3: Total-alkali versus silica (TAS) plot of XRF data for Whakamaru Group pumices and distal Rangitawa Tephra compared with Whakamaru data from Brown et al. (1998a).

The pumice compositional groupings (Brown et al., 1998a; refer to Section 1.5.3) are confirmed by XRF data, showing the four types *A, B, C* and *D* (Fig. 2.4; see summary of pumice types in Table 2.2) in addition to high-alumina basalt (mixed and mingled pumices). As mentioned in Section 1.5.3, Whakamaru Group pumices are dominantly type *A* compositions with minor amounts of *B, C* and *D* – as shown by the Sr versus Rb plot (Fig. 2.4).

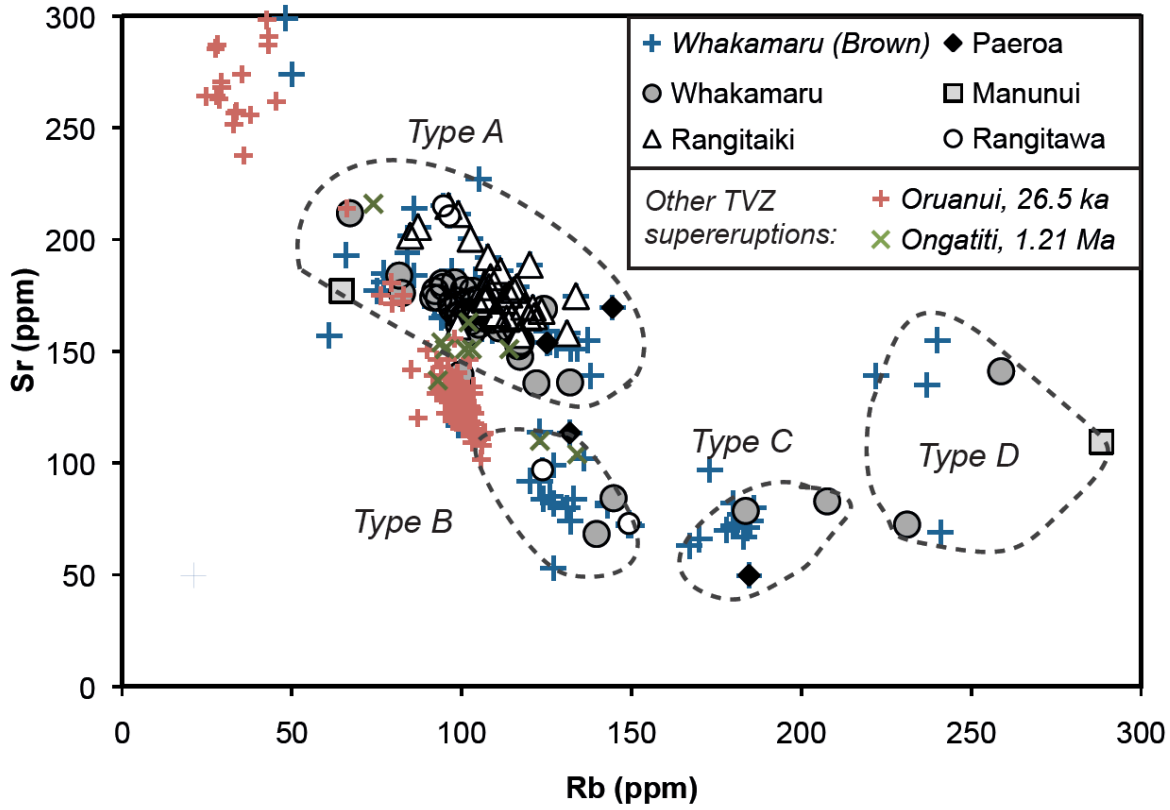

Fig. 2.4: Plot of Sr versus Rb for Whakamaru Group pumices, showing four main pumice types *A, B, C, D*, as first defined by Brown et al. (1998a) on the basis of XRF data for single pumices. Whakamaru whole-rock chemistry is compared here with data for Whakamaru Group pumices from Brown et al. (1998a) and for two other TVZ supereruptions: Ongatiti data from Brown (1994) and Oruanui data from Wilson et al. (2006).

Table 2.2: ***Summary of Whakamaru Group pumice types***

Pumice/ magma type	Description	Mineralogy	Crystal content (vol.%)	XRF	Glass chemistry	Whak	Rang	Man	Paeroa	Representative samples
Type A	Large complexly zoned plagioclase, abundant resorbed quartz. Euhedral opx crystals.	Plagioclase > quartz >> orthopyroxene > hornblende >> biotite, Fe-Ti oxides	~ 10 - 40	Low Rb, high Sr	High Ba, high FeO, wide compositional range	✓	✓	✓	✓	P1905, P1910, P1912, P1915, P1920, P1921, P1885, P1886
Type B	Crystal-rich. Biotite is the dominant ferromagnesian mineral. Quartz smaller and less resorbed than in type *A*.	Plagioclase > quartz > biotite > Fe-Ti oxides	~ 25 - 30	Low Rb, low Sr	Low FeO^T, low CaO	✓			✓	P1917f, R2/2, RA1/3
Type C	Biotite is the dominant ferromagnesian mineral. Quartz smaller and less resorbed than type *A*. Similar to type *B*.	Quartz > plagioclase > biotite > Fe-Ti oxides	~ 10 - 15	High Rb, low Sr	Low FeO^T, low CaO	✓			✓	T5/3, T5/4, Pa1/1, Pa3/3
Type D	Crystal-rich. Appearance similar to type *A*. Large and abundant quartz and plagioclase phenocrysts. Quartz resorbed.	Plagioclase > quartz > biotite > Fe-Ti oxides > hornblende > orthopyroxene	~ 30	Very-high Rb	Low FeO^T, low Ba	✓		✓		SB1119, P1827
Mixed-basaltic	Inclusions/enclaves and/or poorly-mixed and mingled streaks in rhyolitic pumices.	Plagioclase > orthopyroxene > clinopyroxene >> hornblende > magnetite	~ 25	52 - 68 wt% SiO_2, low Rb/Sr	Low SiO_2, low K_2O	✓	✓			SB3065

Notes: Whak = Whakamaru; Rang = Rangitaiki; Man = Manunui; Paeroa = Paeroa Range

Notes: Crystal content in vol.% estimated from thin section. FeO^T refers to total FeO. 'Type' classification from Brown et al. (1998a). Data from fieldwork observations, petrographic analysis, XRF and EPMA, supplemented by previous observations by Brown et al. (1998a).

Brown et al. (1998a) found that type *C* pumices were mainly restricted to the Manunui ignimbrite. Assuming the Wilson et al. (1986) postulation that this unit erupted first (Section 1.5.1.4), type *C* pumices would therefore have been involved in the earlier eruption phases and later replaced by types *A*, *B* and *mixed pumices* (refer to Section 1.5.3 for definitions).

The less common *mixed* pumices appear in hand specimen as typically darker, grey-white with dark streaks. They are moderately vesicular, and contain quartz and a greater proportion of plagioclase and ferromagnesian minerals (clinopyroxene, orthopyroxene, and minor hornblende; Table 2.2) than types *A – D*. Mixed pumices range from thoroughly mixed to mingled (incompletely mixed; Brown et al., 1998a) and have high-alumina basalt to andesite whole-rock compositions (Fig. 2.3).

2.3.2.2 Comparison with other TVZ ignimbrites

The major- and trace-element plots (Figs 2.4, 2.5) based on whole-rock geochemistry compare Whakamaru Group pumice chemistry with published data for the ~ 26.5 ka Oruanui and ~ 1.21 Ma Ongatiti supereruptions from TVZ (Brown et al., 1998a; Wilson et al., 2006). Oruanui deposits also contain basaltic mingled through to high-silica rhyolite pumices and are characterised by a similar range in SiO_2 content (52.27 – 76.66 wt%), but are distinguished from Whakamaru by lower K_2O (0.02 – 0.69 wt%) and Sr (102 – 348 ppm), and higher Zr contents (86 – 282 ppm; XRF data for Oruanui from Wilson et al., 2006). The steeper trend of Whakamaru data in comparison to Oruanui data highlights the importance of fractionation in addition to mixing with a basaltic end-member for the Whakamaru magmatic system (Fig. 2.5).

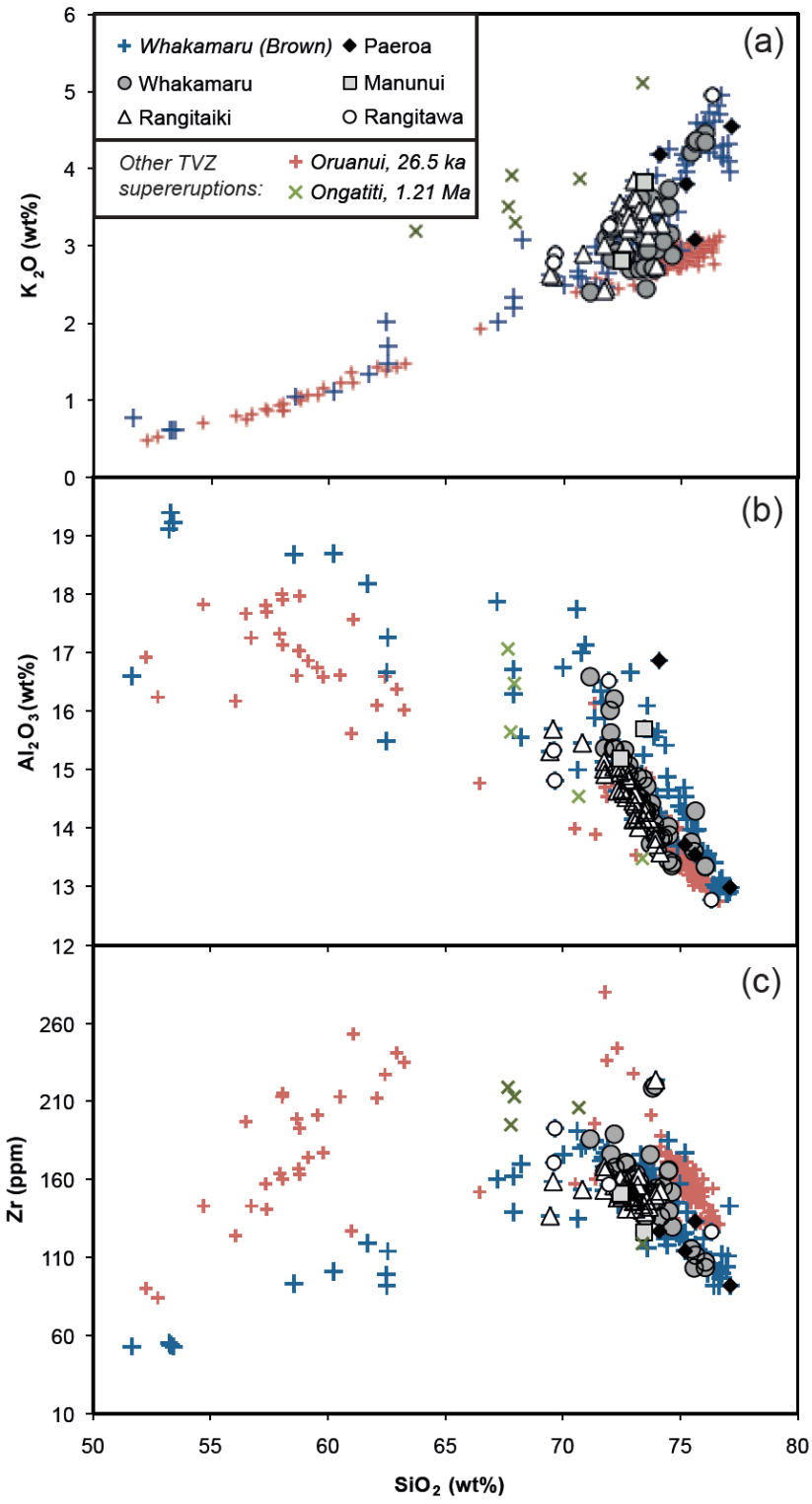

Fig. 2.5: Whole-rock geochemistry (XRF) plots for Whakamaru pumices: (a) K_2O versus SiO_2 showing high-K_2O characteristic of Whakamaru pumices relative to Oruanui pumices; (b) Al_2O_3 versus SiO_2 showing effect of alteration on some pumice clasts (glass devitrifies to clays); (c) Zr versus SiO_2 showing compatible behaviour of Zr in rhyolite pumices, data which plots off the main trend are from mixed-basaltic pumices. Oruanui data from Wilson et al. (2006); Ongatiti from Brown (1994). Additional Whakamaru data from Brown et al. (1998a).

2.3.3 Glass

2.3.3.1 Glass major elements

Major-element glass chemistry for each pumice type (*A, B, C, D* and *mixed basaltic*) is summarised in Table 2.3. A summary of the full major- and trace-element compositions of both proximal pumices and distal tephra samples is presented in Tables 2.4 and 2.5 respectively, Figs 2.6 and 2.7, the full data set is provided in Appendix 4, and tephra is discussed fully in Chapter 6.

Unaltered pumices were analysed where possible, but many were vapour-phase altered and/or weathered as is evident from their geochemistry. Alteration of proximal deposits has caused some alkali exchange, compromising Na_2O and K_2O concentrations, although data that indicated severe alteration were omitted. The focus here is therefore on the other elements that are not typically affected (analyses which indicate alteration by anomalous K_2O values are not shown in Fig. 2.6). Divergent trends which are distinct from the expected liquid line of descent are particularly evident from elevated Al_2O_3 values (due to alteration of glass to clays; Brown, 1994).

Anhydrous glass compositions of pumices from the proximal Whakamaru and Rangitaiki pumices range 76.8 – 78.9 wt% SiO_2 (Figs 2.6 and 2.7), 0.3 – 0.9 wt% CaO, 0.2 – 1.4 wt% FeO^T (n = 280; Table 2.4; Appendix 4). The Rangitaiki pumices are typically depleted in CaO, Na_2O and Sr relative to Whakamaru pumices, suggesting that more plagioclase fractionation has occurred in these samples.

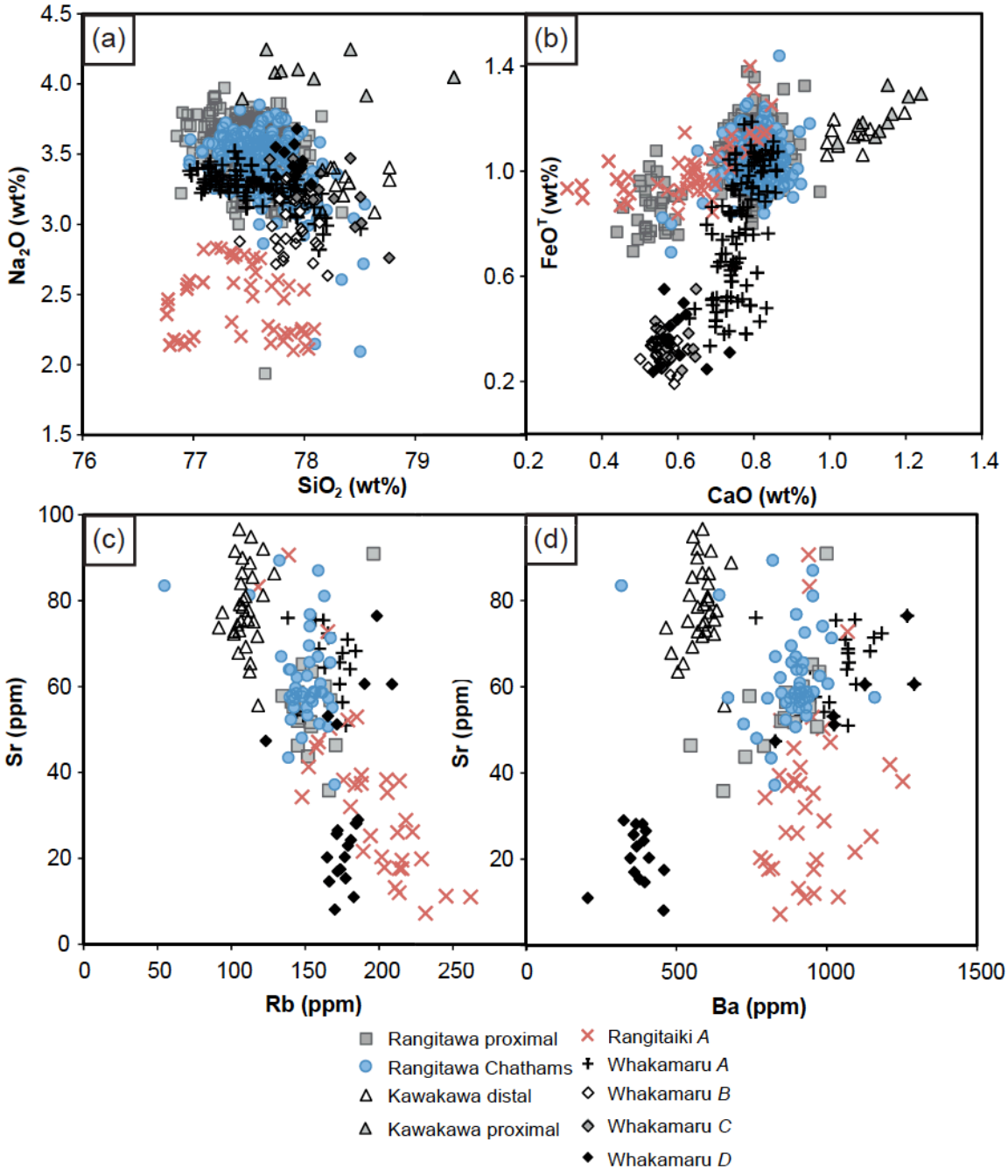

Fig. 2.6: Compositions of Rangitawa glass shards at distal locality on Chatham Island (R011) compared with the more proximal Rangitawa Stream locality (R024), North Island, and proximal pumices from the Rangitaiki and Whakamaru members of the Whakamaru group ignimbrites. Glass chemistry for all units shown as (a) SiO_2 – Na_2O plot; (b) FeO^T – CaO plot; (c) Rb – Sr plot; (d) Ba – Sr plot. The Rangitaiki member tends to be depleted in CaO and Sr with respect to the Whakamaru member. Distal Kawakawa Tephra (R006, Chatham Island), and more proximal Kawakawa (from the type section; Aokautere Ash, Manawatu; Holt et al., 2010) are marked for comparison. K_2O may have been slightly affected by alteration (Whakamaru analyses clearly affected by alteration are omitted). Proximal Kawakawa data shows the effect of alteration (with alkali exchange causing high Na_2O glass values as shown in (a)).

Major-element glass compositions of distal Rangitawa Tephra samples (from Rangitawa Stream and Chatham Island; Fig. 2.6; Tables 2.1, 2.5) do not show the same compositional range as the proximal members with 76.9 – 78.5 wt% SiO_2 (Fig. 2.6a), 3.8 – 5.8 wt% K_2O (Fig. 2.7), 1.9 – 4.0 wt% Na_2O, 0.4 – 1.0 wt% CaO (Fig. 2.6b), 0.7 – 1.4 wt% FeO^T (*n=474*; averages provided in Table 2.4 and 2.5; see also EPMA data in Nelson et al., 1985; Lowe et al., 2001; Holt et al., 2010). Stratigraphically, Rangitawa Tephra glass chemistry is homogenous throughout the sequence, with a slightly increasing trend of Na_2O and decreasing MgO and CaO up-section (Fig. 2.8). Tephra at site R024 shows two populations in terms of CaO glass chemistry (Figs 2.6b, 2.8). The composition of the Rangitawa Tephra is similar to the Rangitaiki and Whakamaru ignimbrites (type *A*) sampled. It has a closer chemical affinity to Whakamaru type *A* magma, however, with high CaO, Na_2O and Sr (Fig. 2.6).

Table 2.3: ***Summary of glass chemistry (by EPMA) for Whakamaru pumice types and mixed-basaltic pumice***

Pumice sample	P1921		P1917f		T5/4		SB1119		SB3065	
Ignimbrite	Wh	*1sd*	Wh	*1sd*	Wh	*1sd*	Wh	*1sd*	Wh	*1sd*
Type	*A*	*(n=18)*	*B*	*(n=30)*	*C*	*(n=14)*	*D*	*(n=30)*	*Basalt/ mixed*	*(n=13)*
SiO_2	77.35	*0.26*	77.91	*0.16*	78.20	*0.30*	77.88	*0.10*	65.84	*2.57*
TiO_2	0.15	*0.02*	0.07	*0.02*	0.06	*0.02*	0.06	*0.01*	0.44	*0.12*
Al_2O_3	12.73	*0.13*	12.46	*0.14*	12.35	*0.17*	12.67	*0.10*	17.50	*2.91*
FeO	0.75	*0.23*	0.31	*0.05*	0.34	*0.08*	0.39	*0.13*	3.78	*1.02*
MnO	0.03	*0.02*	0.03	*0.03*	0.03	*0.02*	0.03	*0.02*	0.11	*0.06*
MgO	0.08	*0.02*	0.02	*0.02*	0.03	*0.01*	0.03	*0.01*	0.81	*0.30*
CaO	0.77	*0.05*	0.56	*0.03*	0.59	*0.04*	0.58	*0.03*	5.05	*1.78*
Na_2O	3.31	*0.16*	3.01	*0.20*	3.22	*0.20*	3.47	*0.12*	4.19	*0.46*
K_2O	4.83	*0.17*	5.38	*0.17*	4.97	*0.10*	4.89	*0.10*	1.49	*0.47*
P_2O_5	-	-	0.02	0.02	0.02	*0.02*	-	-	0.16	*0.06*
Cl	-	-	0.21	0.07	0.19	*0.04*	-	-	0.62	*0.23*
Total	96.25	*1.70*	95.23	*2.05*	95.77	*1.71*	95.80	*0.63*	97.70	*1.28*

Notes: Major element glass chemistry in wt%, quoted anhydrous (normalised to 100%); multiple analyses of glass shards performed on each pumice samples and results are quoted as averages and standard deviations of n analyses.

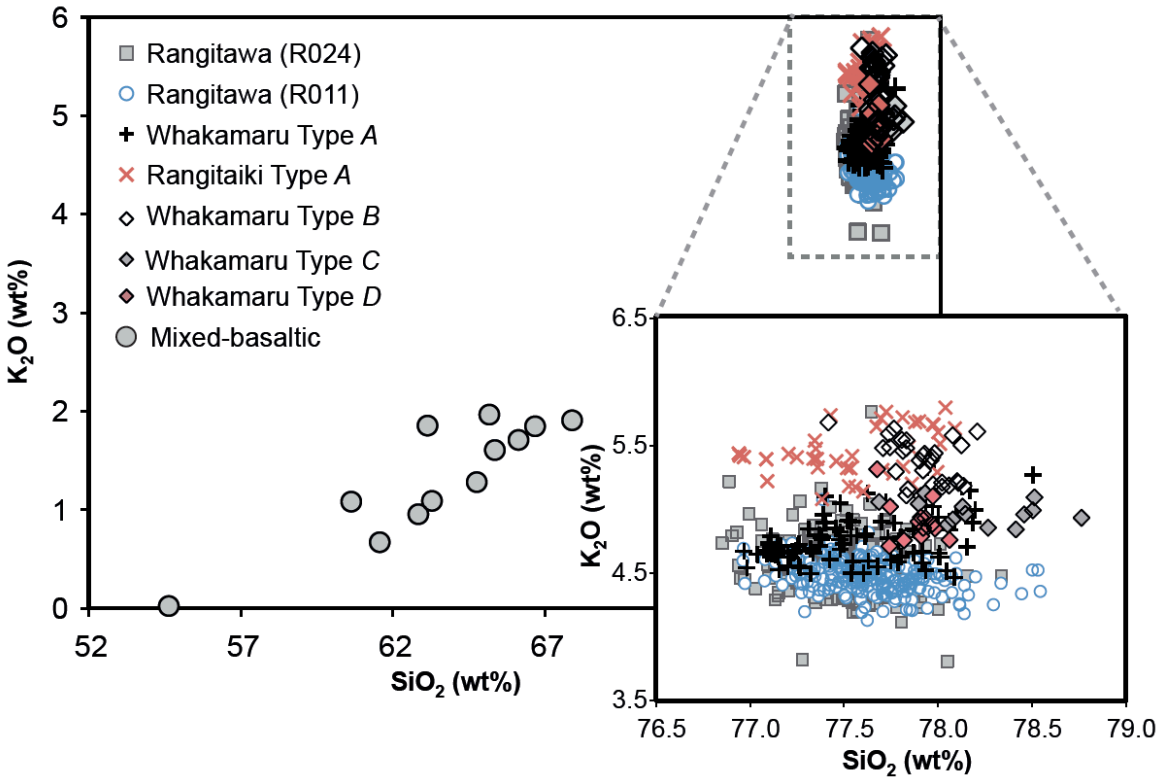

Fig. 2.7: Plot of SiO_2 versus K_2O for glass shards of Whakamaru Group pumices. Pumice types *A, B, C, D* and mixed-basaltic are shown, in addition to Rangitawa Tephra data. Glass chemistry measured by EPMA, results presented anhydrous. Inset shows detail of high-silica glass shards (expansion of the section indicated by dashed rectangle).

Glass chemistry of distal Kawakawa Tephra from the ~ 26.5 ka Oruanui eruption on Chatham Island is shown for comparison (Fig. 2.6). Glass from Kawakawa Tephra is characterised by 78.2 – 78.8 wt% SiO_2, 2.9 – 3.4 wt% K_2O, 3.1 – 3.4 wt% Na_2O, 1.0 – 1.2 wt% CaO, 1.1 – 1.2 wt% FeO^T (n = 34; Fig. 2.6). It forms a separate compositional grouping in terms of glass chemistry with lower K_2O, Rb and Ba, and higher FeO, Na_2O and Sr, than Rangitawa Tephra (Fig. 2.6) allowing these units to be distinguished geochemically. Proximal Kawakawa Tephra glass is clearly altered (alkali-exchange has resulted in an increase in K_2O and a decrease in Na_2O; Fig. 2.6a) and therefore cannot be robustly used for correlation.

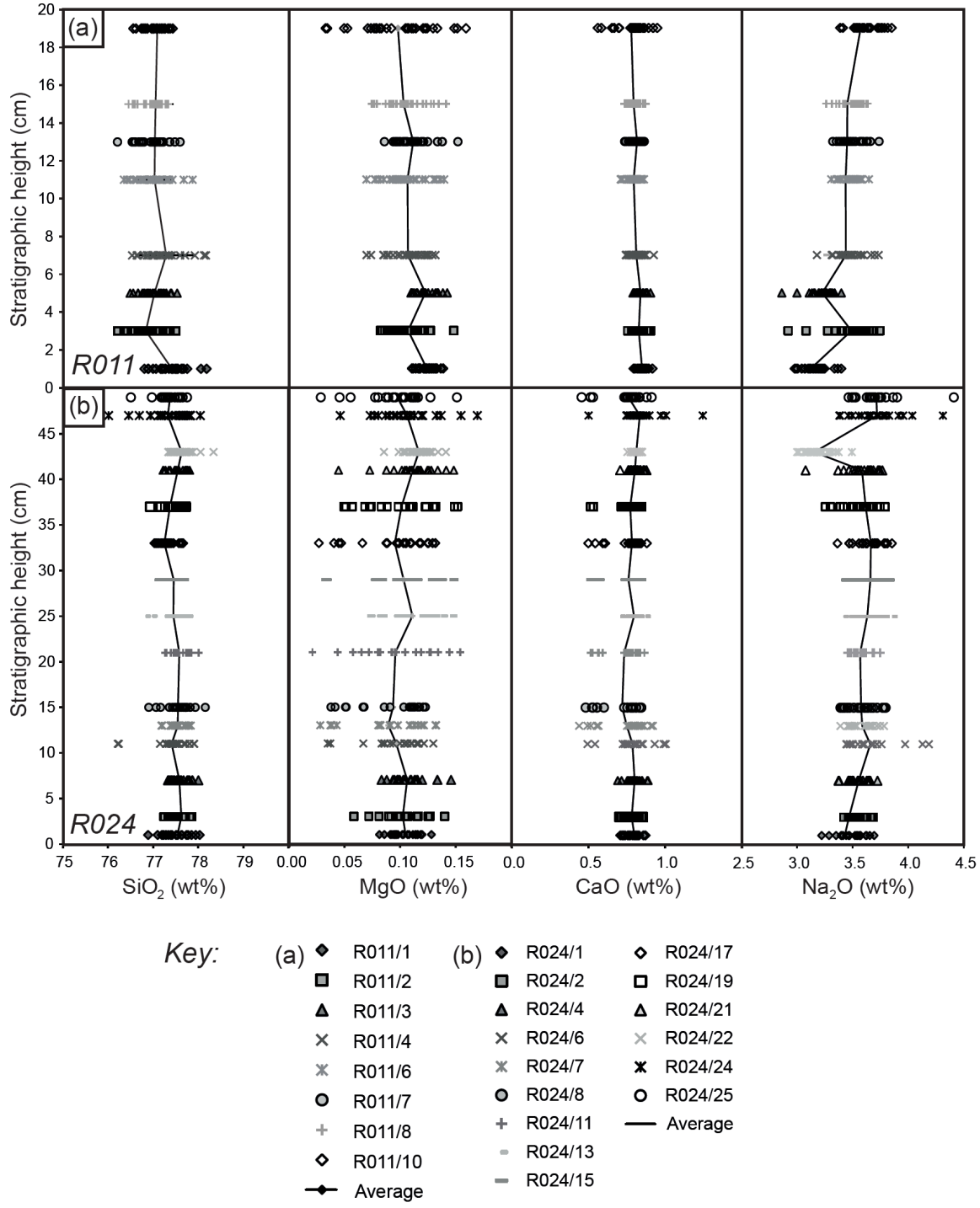

Fig. 2.8: Glass chemistry for distal Rangitawa Tephra showing stratigraphic changes; (a) Rangitawa Tephra at Red Bluffs (R011); Chatham Island; (b) Rangitawa Stream locality (R024), North Island. Locality details provided in Table 2.1.

Table 2.4: ***Proximal Whakamaru Group pumice glass chemistry (EPMA, LA-ICP-MS)***

	Rangtaiki - type *A*		**Whakamaru - type *A***		**Whakamaru - type *B***		**Whakamaru - type *C***		**Whakamaru - type *D***	
EPMA	**P1905, 1910, P1912, P1915**		**P1885, P1886, P1920, P1921**		**P1917f**		**T5/4**		**P1827, SB1119**	
(wt%)	***(n = 62)***	***1sd***	***(n = 103)***	***1sd***	***(n = 30)***	***1sd***	***(n = 14)***	***1sd***	***(n = 26)***	***1sd***
SiO_2	77.55	*0.40*	77.55	*0.36*	77.91	*0.16*	78.20	*0.30*	78.08	*0.41*
TiO_2	0.16	*0.02*	0.15	*0.02*	0.07	*0.02*	0.06	*0.02*	0.07	*0.03*
Al_2O_3	12.46	*0.30*	12.63	*0.21*	12.46	*0.14*	12.35	*0.17*	12.50	*0.32*
FeO	1.03	*0.11*	0.79	*0.23*	0.31	*0.05*	0.34	*0.08*	0.31	*0.08*
MnO	0.04	*0.04*	0.03	*0.02*	0.03	*0.03*	0.03	*0.02*	0.02	*0.02*
MgO	0.13	*0.04*	0.08	*0.03*	0.02	*0.02*	0.03	*0.01*	0.02	*0.01*
CaO	0.61	*0.15*	0.76	*0.05*	0.56	*0.03*	0.59	*0.04*	0.57	*0.05*
Na_2O	2.47	*0.25*	3.25	*0.12*	3.01	*0.20*	3.22	*0.20*	3.38	*0.19*
K_2O	5.47	*0.18*	4.76	*0.18*	5.38	*0.17*	4.97	*0.10*	4.88	*0.09*
H_2O*	3.63	*0.74*	3.47	*0.85*	4.77	*2.05*	4.23	*1.71*	2.56	*1.00*
LA-ICP-MS	**P1905, P1910**		**P1920**						**P1827, SB1119**	
(ppm)	***(n=38)***	***1sd***	***(n=18)***	***1sd***					***(n=21)***	***1sd***
Rb	199	*37*	165	*13*					176	*16*
Sr	34.4	*19.6*	65.2	*8.1*					31.6	*20.0*
Y	25.4	*3.5*	27.0	*2.6*					27.4	*4.9*
Zr	140	*16*	150	*15*					93	*20*
Nb	8.6	*1.1*	9.2	*1.3*					9.1	*1.1*
Cs	9.0	*2.2*	7.7	*0.8*					8.8	*1.1*
Ba	939	*110*	1039	*99*					579	*348*
La	28.7	*3.0*	35.1	*14.3*					32.3	*4.3*
Ce	54.9	*6.6*	58.7	*10.6*					61.2	*7.7*
Pr	5.7	*0.8*	6.4	*1.3*					7.1	*2.9*
Nd	22.0	*2.9*	23.6	*3.5*					25.3	*4.2*
Sm	4.65	*1.21*	4.85	*1.68*					5.39	*2.17*
Eu	0.27	*0.49*	0.41	*0.34*					0.16	*0.35*
Gd	4.80	*1.90*	4.99	*1.02*					4.82	*1.25*
Tb	0.63	*0.28*	0.73	*0.15*					0.72	*0.23*
Dy	4.53	*1.33*	5.01	*1.02*					5.17	*1.30*
Ho	1.07	*0.31*	0.97	*0.18*					1.04	*0.30*
Er	3.41	*0.89*	3.56	*0.94*					3.26	*0.88*
Tm	0.57	*0.34*	0.44	*0.18*					0.65	*0.22*
Yb	3.40	*1.07*	3.77	*0.77*					3.76	*0.93*
Lu	0.54	*0.22*	0.55	*0.13*					0.67	*0.22*
Hf	5.19	*1.15*	5.32	*0.72*					4.17	*0.75*
Ta	1.14	*0.36*	1.10	*0.25*					1.37	*0.33*
Pb	28.50	*32.45*	14.68	*2.00*					20.99	*3.01*
Th	20.59	*2.83*	22.13	*3.24*					23.39	*4.25*
U	4.29	*0.65*	4.25	*0.49*					4.68	*0.75*

*Notes: Numbers are quoted as averages of n analyses, with 1 standard deviation, and results are presented as anhydrous. *H_2O by difference. All major elements determined by EPMA at University of Oxford, and trace elements by LA-ICP-MS (no trace-element data were collected for pumice types B and C).*

Table 2.5: ***Distal Rangitawa and Kawakawa Tephra glass chemistry (EPMA, LA-ICP-MS)***

	Rangitawa Tephra (distal and medial)						*Kawakawa Tephra (distal)*			
	R011/1 (base)		**R011/10 (top)**		**R024/25 (top)**		**R006/2 (base)**		**R006/5 (top)**	
EPMA (wt%)	***(n = 28)***	***1sd***	***(n = 29)***	***1sd***	***(n = 24)***	***1sd***	***(n = 24)***	***1sd***	***(n = 18)***	***1sd***
SiO_2	77.93	*0.26*	77.67	*0.26*	77.37	*0.27*	78.34	*0.24*	78.24	*0.24*
TiO_2	0.15	*0.02*	0.12	*0.05*	0.14	*0.05*	0.12	*0.02*	0.13	*0.02*
Al_2O_3	12.29	*0.19*	12.27	*0.16*	12.22	*0.19*	12.70	*0.13*	12.67	*0.11*
FeO	1.04	*0.11*	0.99	*0.11*	1.10	*0.15*	1.16	*0.08*	1.14	*0.09*
MnO	0.03	*0.03*	0.03	*0.04*	0.06	*0.04*	0.05	*0.03*	0.05	*0.03*
MgO	0.12	*0.01*	0.10	*0.03*	0.10	*0.03*	0.13	*0.01*	0.13	*0.01*
CaO	0.85	*0.03*	0.78	*0.10*	0.76	*0.11*	1.09	*0.05*	1.09	*0.08*
Na_2O	3.12	*0.22*	3.57	*0.30*	3.71	*0.19*	3.41	*0.16*	3.41	*0.16*
K_2O	4.46	*0.10*	4.47	*0.19*	4.53	*0.24*	3.00	*0.13*	3.16	*0.25*
H_2O*	5.32	*0.83*	5.99	*1.28*	5.87	*0.72*	5.32	*0.80*	5.02	*1.20*
LA-ICP-MS										
(ppm)	***(n=20)***	***1sd***	***(n=10)***	***1sd***	***(n=21)***	***1sd***	***(n=14)***	***1sd***	***(n=20)***	***1sd***
Rb	139	*20*	153	*13*	152	*15*	107	*8*	108	*13*
Sr	59.8	*7.8*	59.0	*13.7*	54.8	*10.8*	71.1	*13.8*	77.6	*16.2*
Y	25.4	*6.6*	31.1	*12.1*	25.0	*6.9*	26.0	*4.0*	24.9	*4.0*
Zr	132	*27*	140	*30*	119	*22*	121	*27*	135	*34*
Nb	8.3	*1.2*	8.6	*0.8*	8.3	*1.0*	8.0	*2.9*	9.3	*4.5*
Cs	6.7	*0.9*	7.1	*1.0*	7.4	*0.6*	5.8	*0.6*	5.9	*1.1*
Ba	886	*150*	825	*85*	855	*110*	567	*46*	563	*91*
La	27.7	*2.2*	29.5	*2.7*	28.7	*4.3*	24.7	*2.9*	25.1	*3.2*
Ce	50.0	*2.1*	58.2	*26.0*	52.8	*7.9*	45.3	*5.1*	46.9	*6.4*
Pr	5.3	*0.4*	5.9	*0.7*	5.6	*1.0*	5.6	*1.0*	5.5	*0.8*
Nd	20.4	*3.1*	24.3	*5.1*	21.8	*6.0*	22.8	*5.7*	23.2	*4.9*
Sm	4.16	*1.17*	4.49	*1.81*	4.47	*1.07*	4.85	*2.17*	5.00	*1.56*
Eu	0.55	*0.25*	0.76	*0.70*	0.38	*0.34*	0.77	*0.72*	0.80	*0.45*
Gd	3.74	*1.00*	4.96	*1.95*	4.08	*1.42*	4.83	*1.03*	5.13	*1.30*
Tb	0.69	*0.21*	0.77	*0.36*	0.71	*0.39*	0.83	*0.38*	0.77	*0.33*
Dy	4.26	*1.63*	4.79	*2.28*	4.63	*1.23*	5.75	*1.67*	5.07	*1.70*
Ho	0.98	*0.26*	1.16	*0.41*	1.02	*0.29*	1.13	*0.42*	1.19	*0.41*
Er	3.04	*0.70*	3.80	*1.13*	3.32	*1.21*	2.71	*1.10*	3.57	*0.88*
Tm	0.48	*0.16*	0.66	*0.36*	0.57	*0.44*	0.70	*0.41*	0.53	*0.38*
Yb	3.58	*0.88*	3.82	*1.22*	3.31	*0.88*	3.40	*0.66*	3.31	*0.89*
Lu	0.58	*0.14*	0.62	*0.21*	0.46	*0.19*	0.67	*0.25*	0.49	*0.26*
Hf	4.90	*1.49*	4.87	*1.07*	4.39	*1.09*	4.84	*1.13*	5.63	*1.69*
Ta	1.25	*0.51*	1.16	*0.52*	0.98	*0.33*	0.90	*0.44*	1.03	*0.40*
Pb	20.4	*3.25*	17.4	*2.84*	22.4	*4.53*	19.4	*6.40*	19.0	*6.84*
Th	20.6	*2.71*	20.8	*5.45*	21.5	*10.6*	13.8	*1.97*	15.7	*3.12*
U	3.93	*0.32*	3.87	*0.23*	4.15	*0.49*	3.07	*0.39*	2.95	*0.24*

*Notes: All Whakamaru major elements by EMPA at University of Oxford; trace elements by LA-ICP-MS. Numbers are quoted as averages of n analyses, with 1 standard deviation. *H_2O by difference.*

2.3.3.2 Glass trace elements

The proximal Whakamaru and Rangitaiki pumices (for samples in Table 2.1a) have glass trace-element compositions of: 13 – 317 ppm Rb, 7 – 91 ppm Sr, 11-180 ppm Zr, 58 – 1291 ppm Ba, 4 – 95 ppm Ce and 2 – 35 ppm Nd (*n* = 90; Fig. 2.6c, d; Table 2.4). Distal Rangitawa Tephra glass is characterised by 50 – 197 ppm Rb, 36 – 90 ppm Sr (Fig. 2.6c,d), 77 – 243 ppm Zr, 317 – 1159 ppm Ba, 40 – 130 ppm Ce and 14 – 42 ppm Nd (*n* = 80; Table 2.5). Distal Kawakawa tephra has trace elements concentrations of 60 – 130 ppm Rb, 29 – 97 ppm Sr (Fig. 2.6c, d), 100 – 253 ppm Zr, 328 – 682 ppm Ba, 34 – 64 ppm Ce and 14 – 40 ppm Nd (*n* = 34; Table 2.5). It is therefore distinguished from Rangitawa by lower Rb (Fig. 2.6c) and Ba concentrations (Fig. 2.6d).

Trace-element patterns and ratios for proximal Whakamaru Group pumices are similar to Rangitawa Tephra (Figs 2.6, 2.9), with the exception of type *D* pumice which forms a separate compositional grouping. Whakamaru glass shards show a trend of enrichment in incompatible elements, including fluid-mobile elements (e.g. Ba; Fig. 2.6a), with type *D* glass creating a steeper trend on a different fractionation path.

Table 2.6: ***Chondrite-normalised REE ratios for selected pumices and tephra units***

Sample	SB1119	P1827	P1910	P1905	P1920	R011	R024	R006	SB3065
Unit	Whak	Whak	Rang	Rang	Rang	Tephra	Tephra	Kawa	Rang
Type	*D*	*D*	*A*	*A*	*A*				*Basalt*
Gd/Yb_N	1.03	1.09	1.20	1.10	1.07	1.05	0.99	1.25	1.49
La/Sm_N	3.70	4.10	4.08	3.75	4.49	3.94	4.02	3.15	2.47
Eu/Eu*	0.05	0.22	0.16	0.17	0.25	0.34	0.27	0.48	0.83

Notes: Glass REE values from LA-ICP-MS, normalised to C1 chondritic meteorite (McDonough and Sun, 1995). Eruption units are abbreviated as follows: Whak = Whakamaru; Rang = Rangitaiki; Kawa = Kawakawa.

Rare-earth element (REE) characteristics of proximal Whakamaru and Rangitaiki pumices are compared with Rangitawa Tephra in Fig. 2.10. Whakamaru and Rangitaiki pumices

show similar REE distributions, characterised by relatively flat HREE patterns (Gd/Yb_N = 0.52 – 1.03; Table 2.6), and moderately enriched LREE pattern (La/Sm_N = 1.98 – 3.70; Table 2.6). All pumices have a negative Eu anomaly (where Eu/Eu* < 1; Table 2.6; see Section 5.3.3 for Eu/Eu* calculation), with type *D* pumice having the most significant Eu anomaly (Fig. 2.10a), suggestive of more advanced plagioclase crystallisation and melt fractionation (which is consistent with the modal mineralogy).

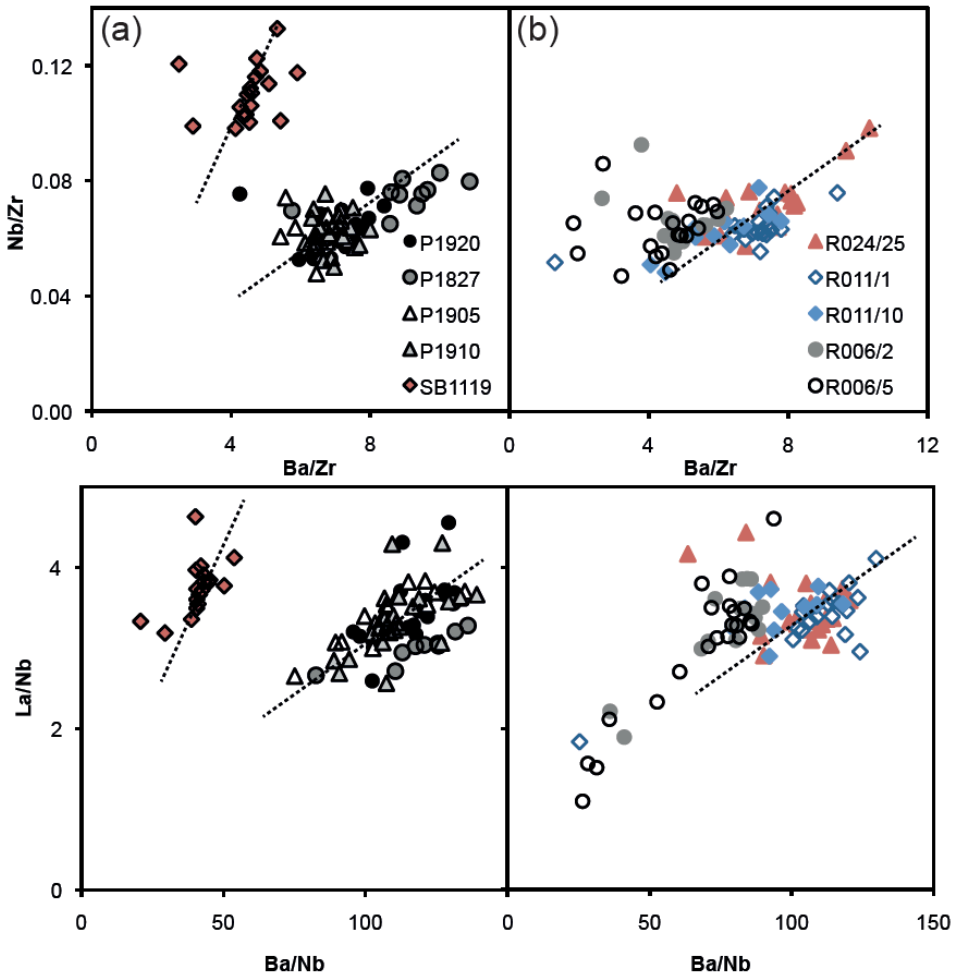

Fig. 2.9: Trace-element ratio plots for glass from (a) Whakamaru pumices and (b) Rangitawa Tephra. All glass analysed by LA-ICP-MS. Major- and trace-element averages provided in Table 2.3 (samples are as follows: Rangitawa R011/1 = base; R011/10 = top; R024/25 = top; Kawakawa R006/2 = base; R006/5 = top). Type *D* pumice (SB1119) forms a discrete grouping of higher Nb, lower Ba compositions; Kawakawa Tephra (R006) is clearly separate from Rangitawa Tephra, with lower Ba and La. Dashed lines indicate incompatible element enrichment trends, Rangitawa Tephra shows the same compositional trend as the type *A* Whakamaru pumices, and type *D* forms a separate compositional trend.

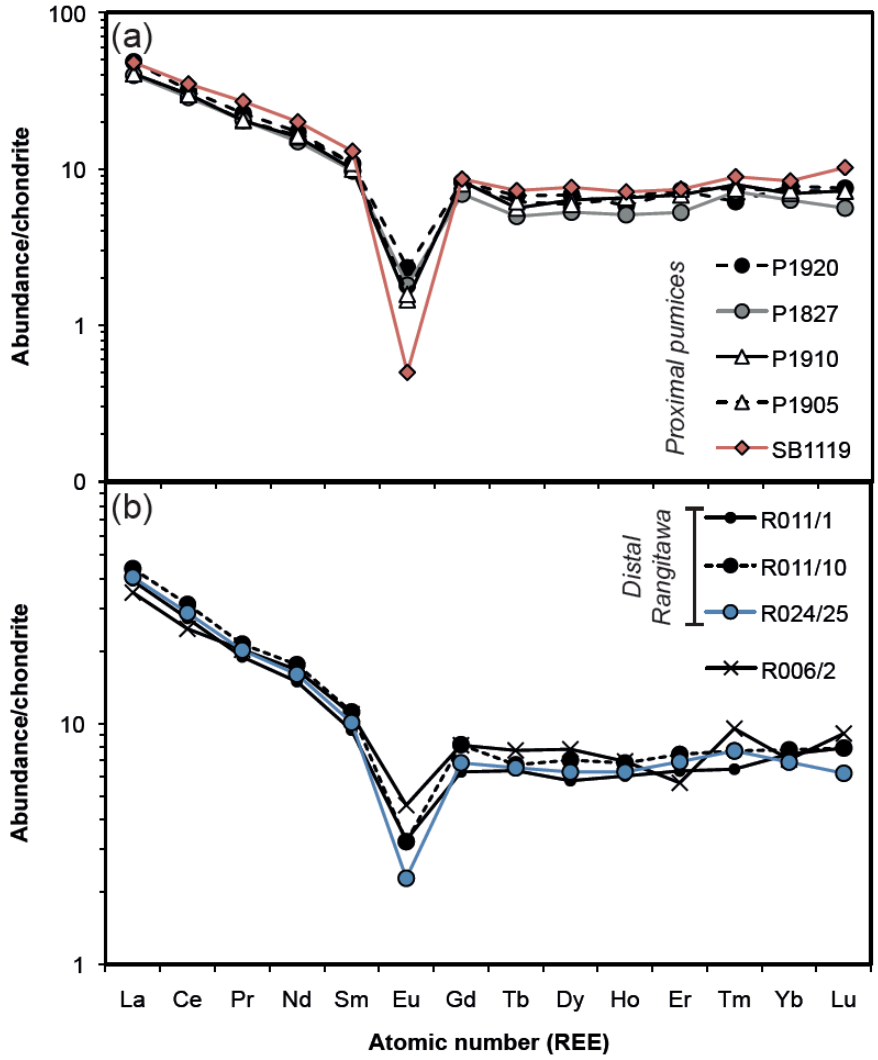

Fig. 2.10: Chondrite-normalised trace-element plots for glass from (a) Whakamaru and Rangitaiki pumices (where SB1119 is rare type *D* pumice); (b) Rangitawa Tephra, with Kawakawa Tephra (R006) for comparison. REE data are plotted here as averages of *n* analyses, and the full datasets are provided in Tables 2.4 and 2.5.

Rangitawa Tephra shows REE patterns similar to type *A* Whakamaru pumices, with flat HREE patterns (Gd/Yb_N = 0.18 – 2.09), and more enriched LREE patterns (La/Sm_N = 2.11 – 8.91; Table 2.6). Rangitawa Tephra also shows a more pronounced Eu anomaly than distal Kawakawa Tephra (Fig. 2.10; sample R006/2). REE ratios for a basaltic inclusion in Rangitaiki pumice (Table 2.6; from Brown, 1994) are characterised by a very minor Eu anomaly, and HREE abundances lower than for glass from types *A* and *D* pumices. Brown

(1994) suggested that the similarities in REE patterns between the Rangitaiki basaltic inclusion, other TVZ basaltic rocks (Gamble et al., 1993) and type *A* rhyolite precluded crystal fractionation from this basalt as a viable mechanism for producing the Whakamaru Group rhyolite (cf. McCulloch et al., 1994).

2.3.4 Mineral Chemistry

2.3.4.1 Biotite

Biotite occurs as coarse (up to ~ 3 mm diameter) euhedral crystals in proximal Whakamaru Group pumices, while only fine (< 10 μm diameter) thin sheets of biotite are found in the distal deposits on the Chatham Islands. Biotite was usually found to be weathered and oxidised in proximal deposits, so few crystals were analysed due to the difficulty of finding unaltered crystals (analyses with low totals, even allowing for 3 – 4 wt% H_2O within the crystal lattice, and variable K_2O contents are indicative of alteration; Scott, 1971).

Average biotite compositions for all pumice types and the Rangitawa Tephra are reported in Table 2.7. Results are compared with data from Brown et al. (1998a) in Fig. 2.11a, which shows a bimodal population with respect to Mg-number (Mg*, defined as % atomic Mg/(Mg+Fe)). The least evolved rhyolite pumices contain the high-Mg* biotite, with Mg* > 45. Mg* ranges 30 – 54 (average 41 ± 5; 1sd: see examples in Table 2.7 and full dataset in Appendix 6). Whakamaru Group biotite composition ranges 16.22 – 26.83 wt% FeO; 0.13 – 0.78 wt% MnO; and 5.08 – 12.20 wt% MgO (*n = 78*; Fig. 2.11a). Biotite in distal tephra deposits on Chatham Island have similar compositions to Whakamaru type *A* biotite, with 18.69 – 22.31 wt% FeO; 0.13 – 0.30 wt% MnO; 10.93 – 12.35 wt% MgO; and Mg* 47 – 54 (Fig. 2.11a; Table 2.7; Appendix 6).

Table 2.7: ***Average biotite compositions from type A, B, C and D pumices and tephra***

Sample	P1910		P1826		P1917f		T5/4		SB1119		R024	
Unit type	Rang *type A*		Whak *type A*		Whak *type B*		Whak *type C*		Whak type *D*		Rang Tephra	
(wt%)	*(n = 11)*	*1sd*	*(n = 8)*	*1sd*	*(n = 23)*	*1sd*	*(n = 16)*	*1sd*	*(n = 12)*	*1sd*	*(n = 5)*	*1sd*
SiO_2	36.63	*0.37*	36.8	*0.75*	35.62	*0.77*	35.82	*0.72*	36.05	*1.55*	35.90	*0.09*
TiO_2	4.07	*0.29*	4.47	*0.18*	4.11	*0.2*	4.12	*0.26*	4.03	*0.43*	4.48	*0.93*
Al_2O_3	13.99	*0.84*	14.48	*0.89*	13.93	*1.06*	13.73	*1.28*	15.14	*3.03*	13.12	*0.10*
FeO	23.03	*1.53*	22.19	*0.88*	22.89	*0.97*	22.98	*1.38*	22.68	*2.17*	20.98	*1.70*
MnO	0.37	*0.08*	0.34	*0.14*	0.39	*0.04*	0.38	*0.07*	0.41	*0.15*	0.23	*0.07*
MgO	8.78	*1.03*	9.3	*0.55*	8.26	*0.41*	8.36	*0.61*	7.99	*1.13*	11.59	*0.63*
CaO	0.05	*0.04*	0.07	*0.08*	0.09	*0.1*	0.05	*0.04*	0.15	*0.1*	0.06	*0.01*
Na_2O	0.41	*0.05*	0.57	*0.13*	0.48	*0.07*	0.44	*0.07*	0.37	*0.09*	0.45	*0.04*
P_2O_5	0.1	*0.09*	0.19	*0.21*	0.38	*0.03*	0.4	*0.03*	-	-	-	-
K_2O	8.61	*0.33*	8.42	*0.48*	8.16	*0.36*	8.25	*0.66*	7.64	*1.27*	8.62	*0.10*
Total	96.00	*1.27*	96.83	*0.68*	94.3	*1.1*	94.54	*1.46*	95.02	*0.91*	96.15	*0.28*
*Mg**	40.44	*4.34*	42.75	*1.45*	39.15	*0.51*	39.32	*0.52*	38.44	*1.81*	49.66	*3.39*
Cations (based on 22 O)												
Si	5.78	*0.07*	5.74	*0.08*	5.63	*0.64*	5.77	*0.12*	5.77	*0.19*	5.61	*0.04*
Ti	0.48	*0.03*	0.52	*0.02*	0.49	*0.06*	0.50	*0.03*	0.49	*0.05*	0.53	*0.11*
Al	2.60	*0.13*	2.66	*0.16*	2.59	*0.35*	2.61	*0.25*	2.85	*0.54*	2.41	*0.00*
Fe	3.04	*0.22*	2.89	*0.13*	3.03	*0.37*	3.10	*0.17*	3.04	*0.31*	2.74	*0.24*
Mn	0.05	*0.01*	0.04	*0.02*	0.05	*0.01*	0.05	*0.01*	0.06	*0.02*	0.03	*0.01*
Mg	2.07	*0.21*	2.16	*0.12*	1.95	*0.24*	2.01	*0.14*	1.91	*0.28*	2.70	*0.13*
Ca	0.01	*0.01*	0.01	*0.01*	0.01	*0.02*	0.01	*0.01*	0.03	*0.02*	0.01	*0.00*
Na	0.13	*0.02*	0.17	*0.04*	0.15	*0.03*	0.14	*0.02*	0.11	*0.03*	0.14	*0.01*
K	1.73	*0.05*	1.67	*0.10*	1.65	*0.20*	1.70	*0.13*	1.56	*0.27*	1.72	*0.03*
Sum	15.89	*0.06*	15.88	*0.08*	15.75	*0.76*	15.89	*0.11*	15.81	*0.21*	15.88	*0.08*

Notes: Results presented as averages of n analyses, with ± 1sd compositions; only results with totals > 94 wt% accepted. Rang = Rangitaiki ignimbrite; Whak = Whakamaru ignimbrite; Type refers to 'pumice type' A, B, C and D as described in Section 1.5.3. Mg refers to Mg-number calculated by Mg/(Mg+Fe). Full dataset provided in Appendix 6. Reference materials from the Smithsonian Institution (minerals) were run as secondary standards during all analytical runs.*

2.3.4.2 Orthopyroxene

Orthopyroxene contained in the Whakamaru and Rangitaiki pumices is dominantly enstatite (Fig. 2.11b; Table 2.8; Appendix 7). In terms of Wo and En, orthopyroxene compositions from different pumice and ignimbrite types are remarkably uniform considering the compositional variability in pumice chemistry (Fig. 2.11b). Across all pumice types, orthopyroxene ranges between $Wo_{1.6–4.0}$ and $En_{50.0–70.8}$ (see Appendix 7).

Table 2.8: ***Orthopyroxene compositions for Whakamaru Group pumices and tephra***

Sample	**P1920, P1921, P1886, P1885, P1788**		**P1905, P1908**		**R011, R024**	
Unit	**Whak**	***(n = 79)***	**Rang**	***(n = 35)***	**Rangitawa**	***(n = 35)***
Pumice type	***Type A***	***1sd***	***Type A***	***1sd***	**Tephra**	***1sd***
EPMA (wt%)						
SiO_2	51.85	*1.42*	51.96	*0.60*	51.97	*0.21*
TiO_2	0.12	*0.06*	0.12	*0.05*	0.11	*0.04*
Al_2O_3	0.71	*1.15*	0.62	*0.51*	0.36	*0.13*
FeO	25.69	*0.78*	24.55	*2.51*	26.68	*0.63*
MnO	1.28	*0.11*	1.17	*0.23*	1.32	*0.08*
MgO	18.85	*0.70*	19.10	*2.23*	18.60	*0.37*
CaO	0.98	*0.19*	0.98	*0.15*	0.92	*0.09*
Na_2O	0.02	*0.02*	0.03	*0.11*	0.02	*0.02*
K_2O	0.02	*0.01*	0.04	*0.15*	0.02	*0.01*
P_2O_5	0.01	*0.02*	0.00	*0.00*	0.01	*0.02*
Total	99.53	*1.57*	98.58	*1.49*	100.00	*0.48*
Cations (based on 6O)						
Si	1.98	0.03	2.00	0.02	1.98	0.02
Ti	0.00	0.00	0.00	0.00	0.00	0.00
Al	0.03	0.05	0.03	0.02	0.02	0.03
Fe	0.82	0.03	0.79	0.09	0.81	0.16
Mn	0.04	0.00	0.04	0.01	0.04	0.01
Mg	1.07	0.03	1.09	0.11	1.05	0.04
Ca	0.04	0.01	0.04	0.01	0.08	0.19
Na	0.00	0.00	0.00	0.01	0.00	0.00
Wo	2.04	*0.40*	2.07	*0.31*	1.94	*0.19*
En	54.33	*1.25*	55.66	*4.71*	39.16	*0.90*
Fs	43.64	*1.42*	42.27	*4.80*	58.90	*1.00*
Mg#	*56.66*	*1.31*	*57.98*	*4.70*	*57.01*	*6.52*

Notes: All major-element data collected by EPMA. Total includes Na_2O, K_2O and P_2O_5 with values of ~ 0.01 – 0.02 wt%. Whak = Whakamaru; Rang = Rangitaiki. Full dataset in Appendix 7.

Crystals also show only minor core-to-rim zonation in composition, with both normal and reverse zoning patterns observed (Appendix 7; as was also reported by Ewart et al., 1975, and Brown, 1994). Rare high En compositions (< 1 % of crystals analysed) are mainly restricted to mixed Rangitaiki pumices (Fig. 2.11b). These Mg- and Ca-rich crystals are characterised by cores of ~ 25.3 wt% MgO and 1.2 wt% CaO. Rangitawa Tephra orthopyroxene has the same compositions as crystals from type *A* Whakamaru and some type *A* Rangitaiki pumices, with $Wo_{1.5–2.2}$ and $En_{50.3–55.6}$ (Fig. 2.11b).

2.3.4.3 Amphibole

Hornblende occurs as euhedral to subhedral (0.5 – 1 mm diameter), green-brown pleochroic crystals in Whakamaru and Rangitaiki pumices. Crystals commonly contain oxide inclusions and are often intergrown with plagioclase phenocrysts. Compositionally, they are dominantly classified as magnesio-hornblende (86% of crystals analysed), with rare tschermakitic hornblende and magnesio-hastingsitic hornblende crystals also identified (Appendix 10). Major-element geochemistry is as follows: 39.93 – 49.82 wt% SiO_2, 0.22 – 3.43 wt% TiO_2, 5.15 – 14.27 wt% Al_2O_3, 10.71 – 15.21 wt% MgO, and 9.08 – 16.47 wt% CaO (*n = 164*; Appendix 10). Hornblende in Rangitawa Tephra is compositionally similar: 39.55 – 47.06 wt% SiO_2, 1.34 – 1.80 wt% TiO_2, 6.62 – 13.24 wt% Al_2O_3, 11.22 – 13.72 wt% MgO, and 10.44 – 11.20 wt% CaO (*n = 17*; Appendix 10). There is no systematic variation in hornblende chemistry with stratigraphic height through the Whakamaru Group Ignimbrites (previously noted by Brown, 1994).

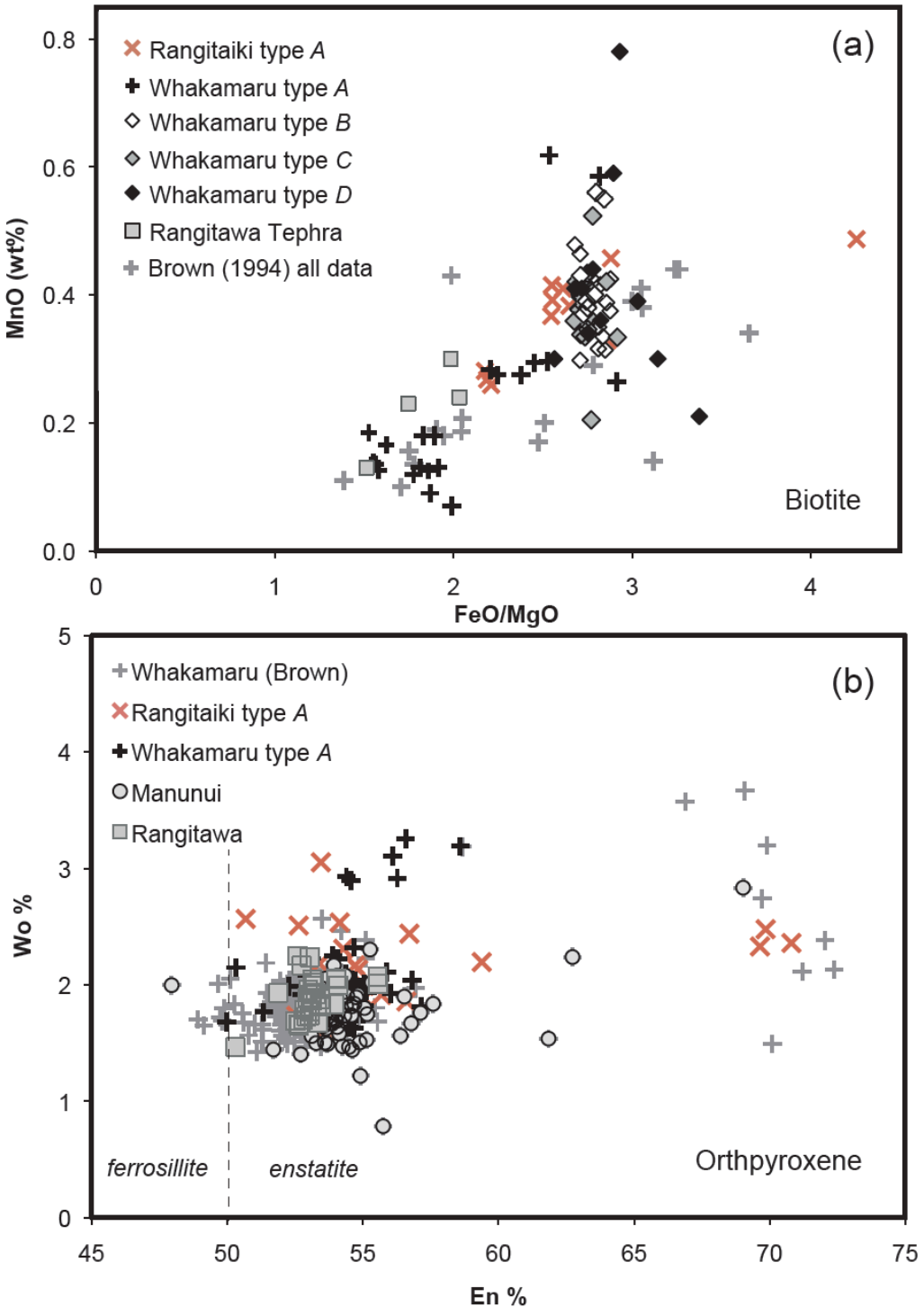

Fig. 2.11: (a) Biotite compositions for proximal Whakamaru and Rangitaiki type *A*, *B*, *C* and *D* pumices and Rangitawa Tephra biotite (from site R024); (b) Orthopyroxene compositions for Rangitaiki, Whakamaru and Manunui pumices in comparison to crystals extracted from Rangitawa Tephra (from sites R024 and R011). Data averages are provided in Tables 2.7 and 2.8 and full datasets in Appendix 6 and 7, respectively.

2.3.4.4 Plagioclase feldspar

Plagioclase feldspar is a ubiquitous phenocryst in most subduction zone volcanic rocks, and crystallises over a large range of magmatic compositions, physical conditions and timescales (e.g., Blundy and Shimizu, 1991; Smith et al., 2009). Plagioclase zoning is therefore a valuable source of information about magma chamber processes and recharge events (e.g., Davidson and Tepley, 1997; Wiebe et al., 2007; Smith et al., 2009; 2010).

Plagioclase is a common phase in Whakamaru Group pumices (~ 30 – 40% of the crystal assemblage; Appendix 2), and typically occurs as large subhedral to euhedral laths up to 4 mm long, which are often fragmented. Plagioclase phenocrysts display typical oscillatory zoning and more complex zoning patterns, often with numerous resorption horizons which are likely to be associated with significant pressure, temperature or compositional changes within the magma (e.g., Andrews et al., 2008; Smith et al., 2009). Plagioclase is typically characterised by fine oscillatory zoning often punctuated by dissolution surfaces, patchy zones, and sieve textures (visible in BSE imagery; Fig. 2.12) all of which correspond to multi-stage crystallisation histories likely to be associated with large-amplitude pressure/temperature/compositional changes as discussed below. Rare crystals display sieved core textures (e.g., P1910-14; Appendix 5) or strongly resorbed cores (e.g., P1827-1, P1827-13; Appendix 5).

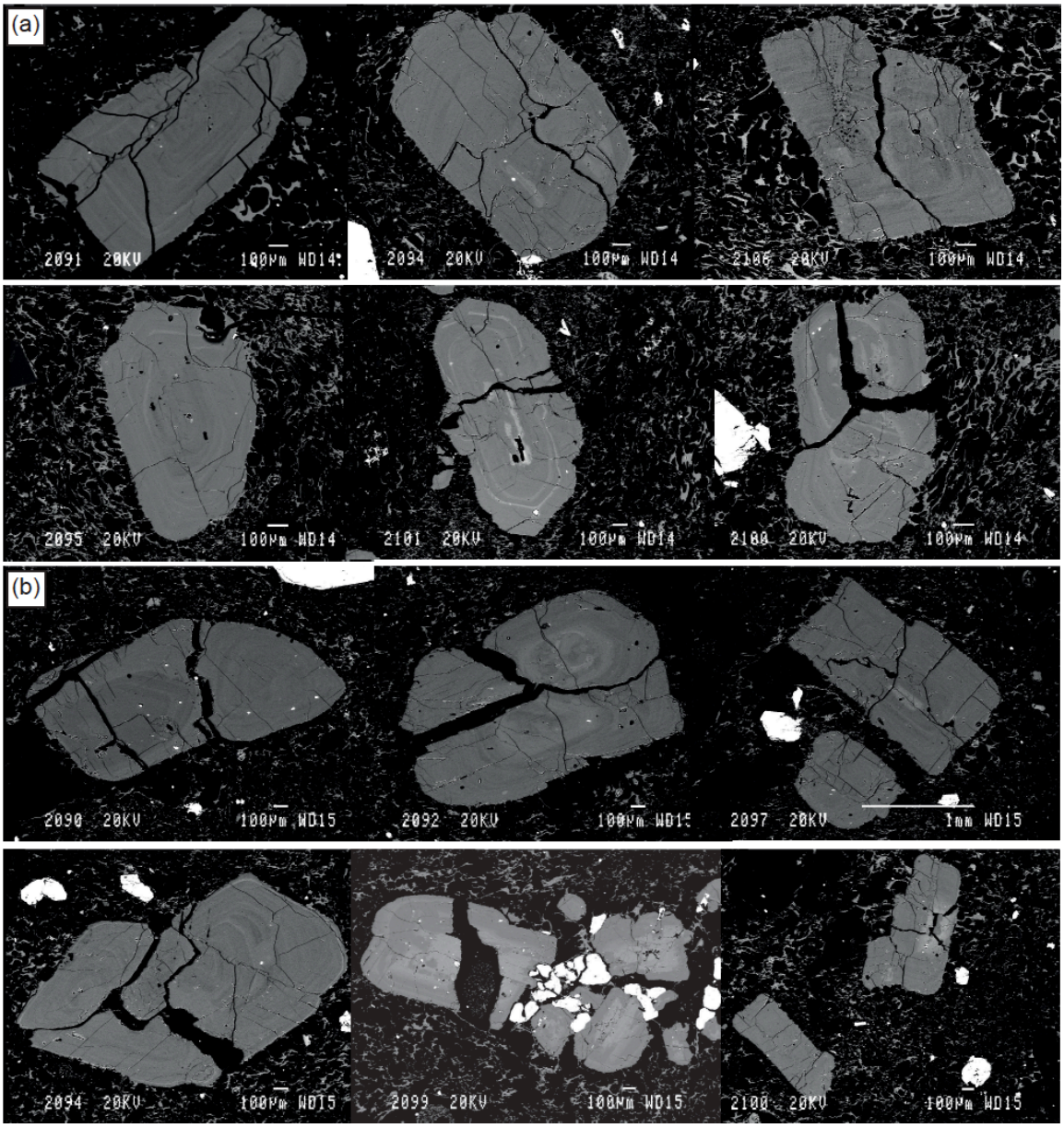

Fig. 2.12: SEM-BSE images of selected plagioclase feldspar phenocrysts in samples (a) P1905 and (b) P1915; images from thin section; note vesicular glassy groundmass of pumice; bright white minerals are Fe-Ti oxides.

Feldspar compositions span a wide range, An_{12} to An_{80}, and the average composition across all crystals analysed is $An_{32}Ab_{61}Or_6$ (*n = 112*; Fig. 2.13; full dataset in Appendix 5). On the basis of anorthite (An) composition, the plagioclase crystals are classified here as Groups 1, 2 and 3 (Fig. 2.13). The groups are defined as: Group 1 = $Ab_{19-34}An_{65-80}Or_{0-1}$; Group 2 = $Ab_{38-64}An_{29-61}Or_{0-10}$; Group 3 = $Ab_{65-81}An_{12-35}Or_{0-15}$. Most plagioclase is Group

2 (~ 50%) and 3 (~ 49%) in composition, whereas Group 1 feldspar crystals are rare (<1%) and restricted to mixed pumices and calcic cores. Group 3 feldspars are dominantly from type *D*, Manunui, Paeroa, and some Rangitaiki pumices. Rangitaiki feldspars display a much broader compositional range than feldspar from Whakamaru pumice, with a higher proportion of Group 1 feldspars (with high An contents, suggesting less-evolved magma characteristics and a mixed pumice origin; Fig. 2.13) and feldspars of all three compositional groups.

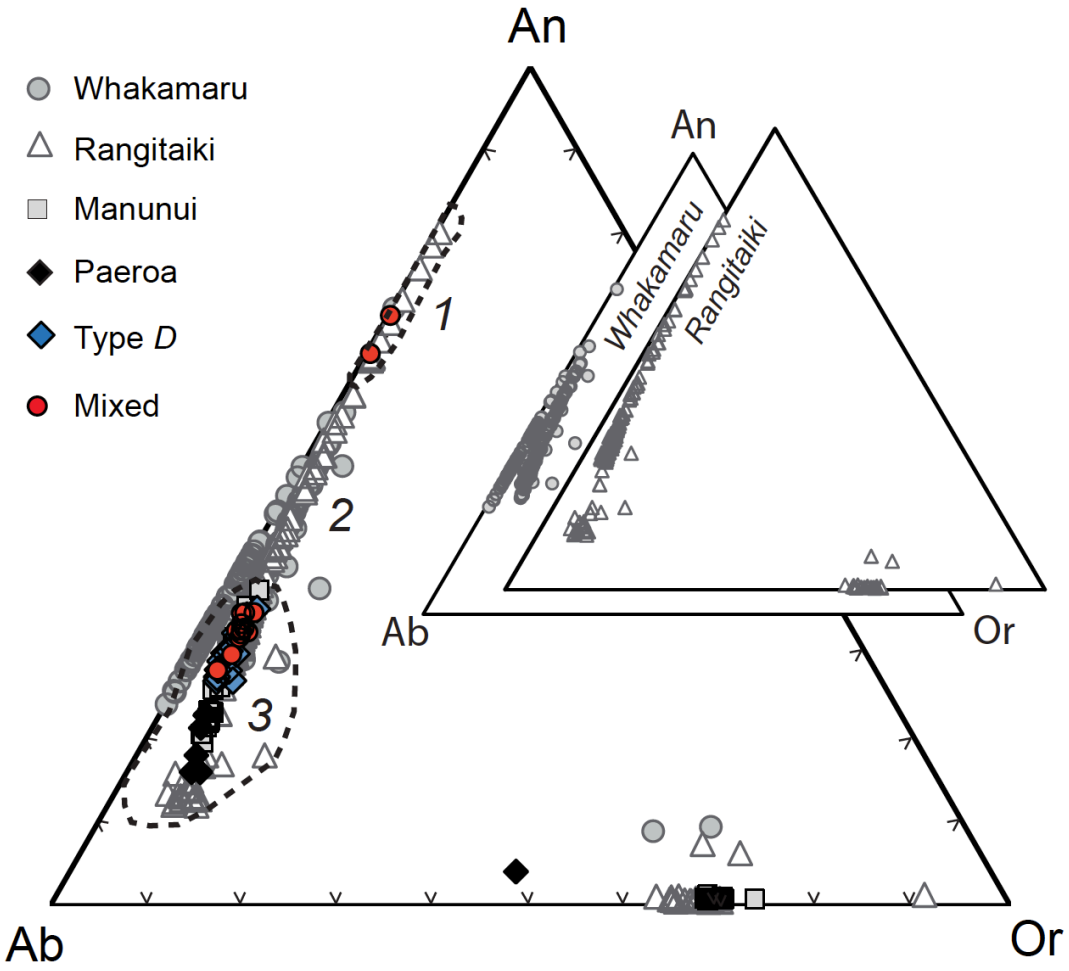

Fig. 2.13: Ternary classification diagram Ab-An-Or for feldspars from Whakamaru, Rangitaiki, Manunui and Paeroa Range pumices, in addition to type *D* and *mixed pumices*. Feldspar compositions form three compositional groupings labeled *1*, *2* and *3*. Feldspars with high An-content (Group *1*) are mainly from mixed Rangitaiki pumices. Rangitaiki feldspars also form a separate compositional grouping from Whakamaru feldspar at high Ab-contents (Group *3*). Rare sanidine also identified. Inset shows Whakamaru and Rangitaiki feldspars plotted separately, with Rangitaiki feldspar showing a wider compositional range.

Plagioclase also displays some inter-crystal variability (Figs 2.14 – 16; Appendix 5). Compositional profiles across plagioclase crystals highlight the complexities of chemical fluctuations during crystal growth (e.g., Fig. 2.14). Many feldspars are characterised by oscillatory zoning (~ 45% of crystals analysed), visible in BSE imaging and major-element transects (with no systematic core-rim change in An content but with abrupt fluctuations in An number from rim to core of up to 10 mol% An over 20 µm; Figs 2.15 – 2.17; Appendix 5).

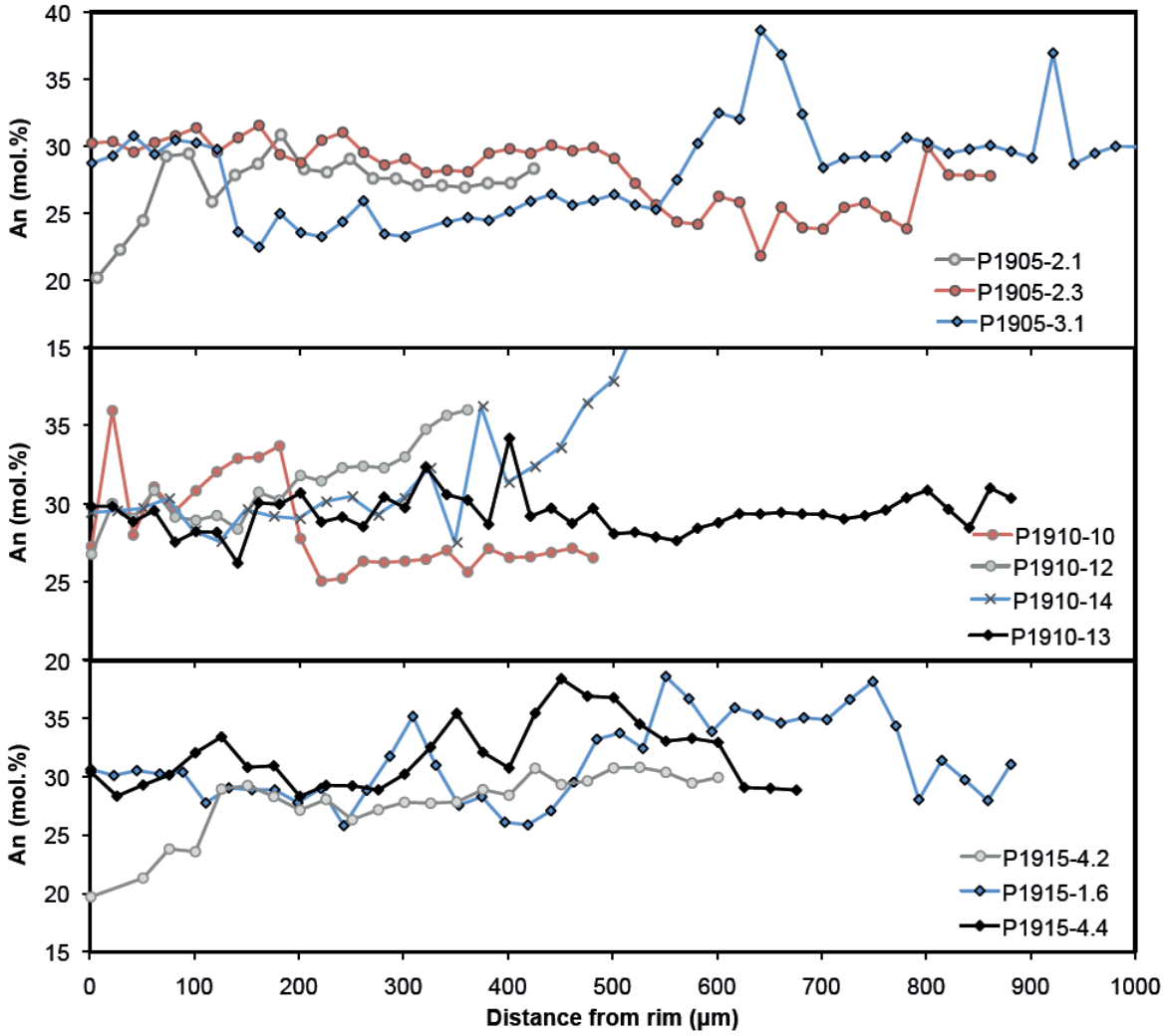

Fig. 2.14: Feldspar An-transects for crystals extracted from three Rangitaiki pumice clasts; patterns include normal, reversed and oscillatory zoning, with no systematic correlation in An-zoning between crystals. Most crystal are characterised by rims of ~ An_{30}, although rare normally-zoned crystals have less calcic rims (An_{20}) e.g., feldspars P1905-2.1 and P1915-4.2.

Although complex zoning is observed in some crystals, the average rim composition (An_{28}) is similar to the average core composition (An_{30}; Table 2.9). Some rare crystals display more pronounced zoning, with changes of ~ 10 – 20 mol % An from the rim to core (e.g., P1915-4.2 has rim of An_{20} and a core of An_{30}; P1827-13 rim = An_{22} and core = An_{47}; Table 2.9). These rare feldspars may be xenocrystic (BSE imagery shows distinct resorbed cores surrounded by euhedral rim growth; Appendix Figs A2.1), and not in equilibrium with the melt immediately prior to eruption. Crystal core compositions vary widely, with the most Ca-rich cores, $An_{90\text{-}100}$, probably representing xenocrysts inherited from a more mafic magma. Numerous resorption horizons and fluctuations in X_{An} are visible in BSE imagery (Figs 2.15, 2.16; Appendix 5). Most commonly (~ 90% of feldspar analysed) crystals show three major resorption horizons (see Figs 2.15, 2.16) followed by normal An zoning.

Table 2.9: ***Rim/core compositions and zoning patterns for selected feldspar crystals***

Sample	Feldspar rim compositions An	Feldspar core compositions An	Zoning
P1915-4.2	20	30	Normal
P1915-4.4	28	29	Oscillatory
P1915-3.4	31	31	Oscillatory
P1915-1.6	31	38	Normal
P1915-1.2	29	28	Oscillatory
P1905-4.3	32	27	Reverse
P1905-3.1	29	27	Normal
P1905-2.3	30	24	Reverse
P1905-2.1	20	28	Normal
P1910-10	30	25	Oscillatory
P1910-12	27	36	Normal
P1910-14	29	40	Normal
P1910-28	27	27	Oscillatory
P1910-13	30	30	Oscillatory
P1827-15	35	31	Oscillatory
P1827-13	22	47	Normal
Average	**28**	**30**	

Note: Average rim and core compositions are calculated omitting the rare reverse-zoned crystals

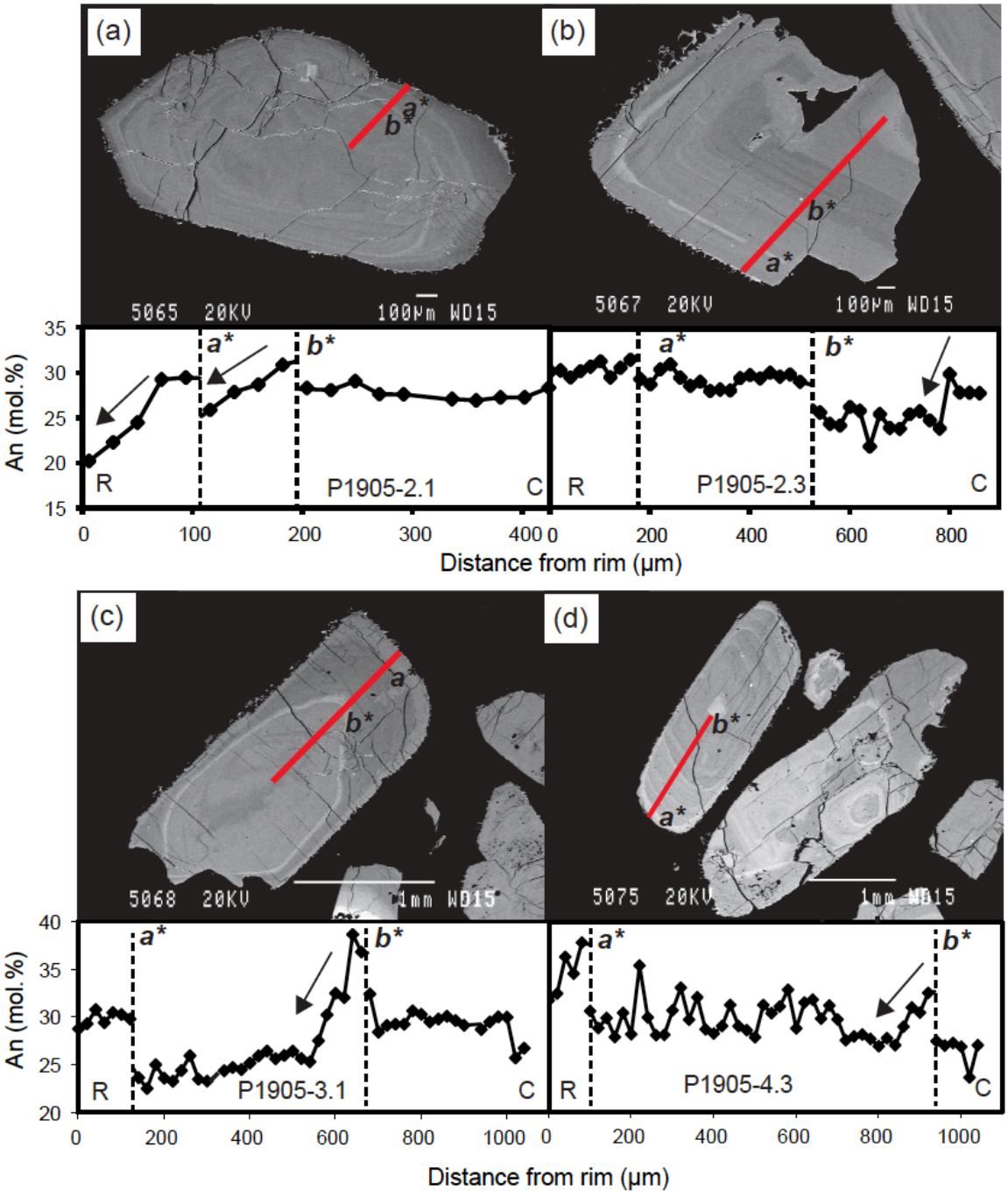

Fig. 2.15: Feldspar transects from rim to core (by EPMA) of selected crystals from Rangitaiki pumice sample P1905; SEM-BSE images are annotated with transect (marked by red line). An (mol.%) changes across crystal are shown in profiles. Rim (R) and core (C) marked on profiles. Arrows indicate zones of normal An zoning as a result of fractional crystallisation; dashed vertical lines show significant resorption boundaries, also marked on BSE image by a* or b* (with increasing age of horizon). These major resorption horizons do not necessarily represent common events between crystals.

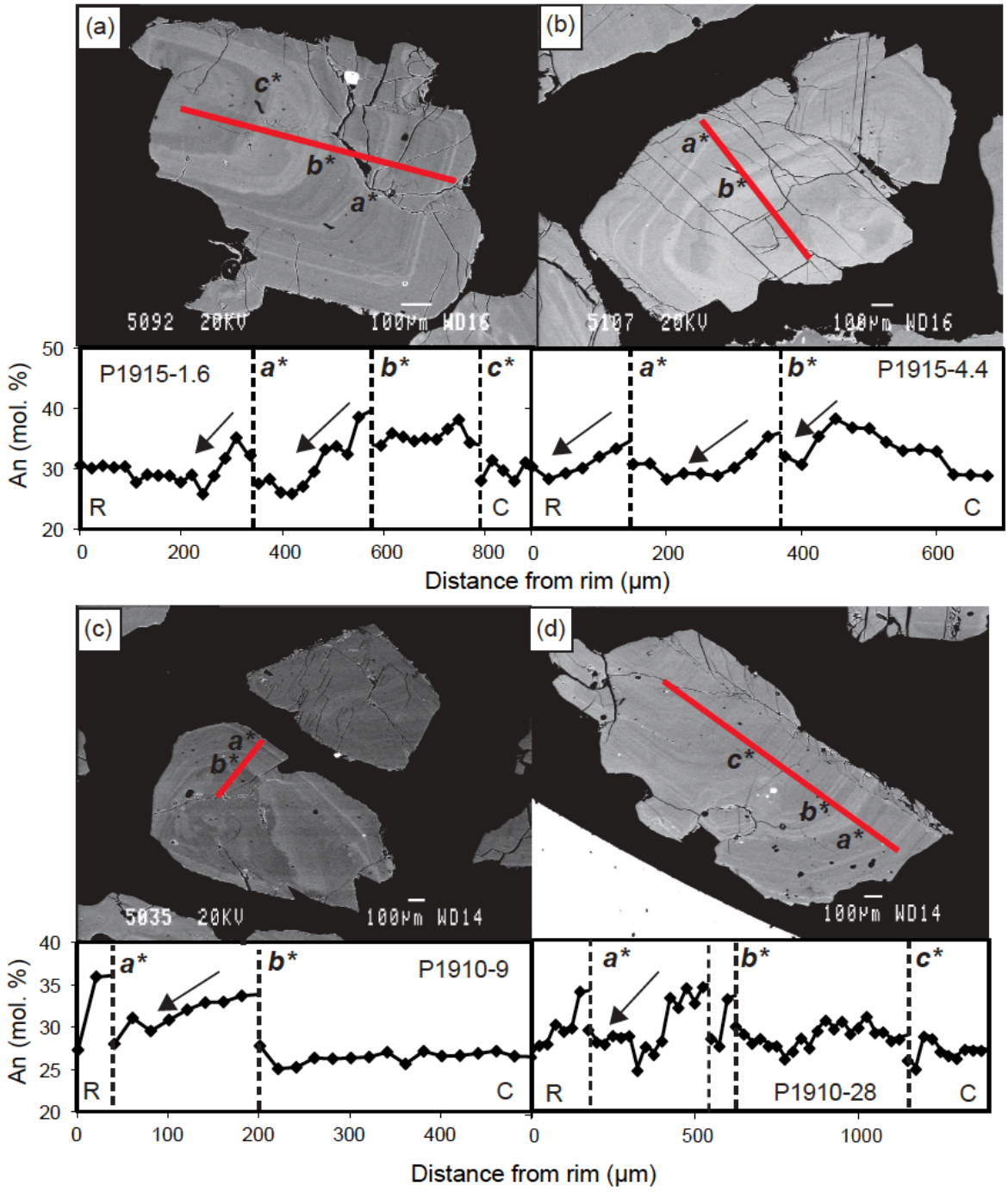

Fig. 2.16: Feldspar transects from rim to core (by EPMA) of selected crystals from pumice samples P1915 and P1910; SEM-BSE images are annotated with transect (marked by red line). An (mol.%) changes across crystal are shown in profiles. Rim (R) and core (C) marked on profiles. Arrows indicate zones of normal An zoning as a result of fractional crystallisation; dashed vertical lines show significant resorption boundaries, also marked on BSE image by a*, b* or c* (with increasing age of horizon).

2.4 Discussion

2.4.1 Glass chemistry: linking Rangitawa Tephra to Whakamaru ignimbrite

Only some of the pumice types (*A, B, C* and *D*), as defined based on whole-rock chemistry, have different glass chemistries (Table 2.2; Fig. 2.6). Rangitaiki type *A* and Whakamaru type *A* show compositional overlap in terms of CaO and FeO^T (Fig. 2.6b) but with divergent trends, suggesting that these magma bodies are related but evolved separately prior to eruption (see Section 2.4.4.2). Types *B, C* and *D* form a separate compositional grouping in terms of major elements, and type *D* pumice shows distinct trace-element characteristics (Fig. 2.6c, d) suggesting it represents a separate magma body which contributed to the Whakamaru eruption (with type *A* being volumetrically dominant, ~ 89%). This is consistent with Sr-isotopic systematics which also showed that type *D* was separate (Brown et al., 1998a). Variations in whole-rock composition of the pumice types appear to mostly reflect variations in crystal content and mineralogy (Table 2.2; as discussed further in Section 2.4.4.2). Mafic mixed pumices (Table 2.3) are geochemically distinct and provide direct evidence for the involvement of basaltic magma in the large silicic magma system, most likely representing a syn-eruptive phenomenon or being directly associated with the eruption trigger.

Post-emplacement alteration of eruption deposits is common near source, where deposits are thick and take time to cool once emplaced, often with fluid moving through them (e.g., Donoghue et al., 2008) causing vapour phase alteration (Scott, 1971). It appears that the distinct K_2O and Na_2O compositions of some samples of the proximal Whakamaru Group Ignimbrites are result of alkali exchange (Scott, 1971). Furthermore, these compositions did not plot along typical crystallisation trends. This alteration of the thick, often welded,

near-source ignimbrite deposits makes it hard to correlate proximal and distal deposits of very large eruptions (e.g., Alloway et al., 2005).

Distal Rangitawa Tephra glass chemistry compares well with non-altered data from proximal Whakamaru and Rangitaiki pumices, as shown by the overlapping fields in the K_2O-SiO_2, CaO-FeO, Sr-Rb and Sr-Ba plots (Fig. 2.6) and the Qz-Ab-Or ternary plot (Fig. 2.17). The chemical compositions of Rangitawa glass shards are most similar to those of the Whakamaru type *A* pumices, as shown by the CaO and Sr plots, for example (Fig. 2.6). The low CaO glass population observed at the Rangitawa Stream locality (see Fig. 2.8) most likely relates to Rangitaiki type *A* magma, and Whakamaru pumice types *B, C* and *D* do not appear to have contributed significantly to the distal tephra. The chemical similarity between the Rangitawa Tephra and volumetrically-dominant type *A* magma indicates that the distal tephra is certainly associated with the eruption of this magma (during emplacement of Whakamaru and Rangitaiki ignimbrites).

The distal tephra displays less compositional diversity than the proximal Whakamaru ignimbrite deposits, as can be seen in Figs 2.6 and 2.9. This relatively limited compositional variation of distal tephra suggests that the magma that fed the Plinian or co-ignimbrite phase was relatively homogeneous compared to the other phases recorded in the proximal ignimbrite (see Brown et al., 1998a, and Chapter 6 for further discussion of eruption phases). Long-range transport might also have reduced the compositional variability in distal ash, however, with only certain size/composition fractions or eruptive phases being transported distally. Ignimbrite phases typically display more chemical diversity (e.g., Bishop Tuff; Hildreth and Wilson, 2007) as they tap more compositionally diverse magma. Sampling is limited given the volume of material erupted, however,

which means that there is a higher probability of analysing material from the dominant pumice type and therefore may not reflect the contribution of minor and trace compositions to the distal ash deposits.

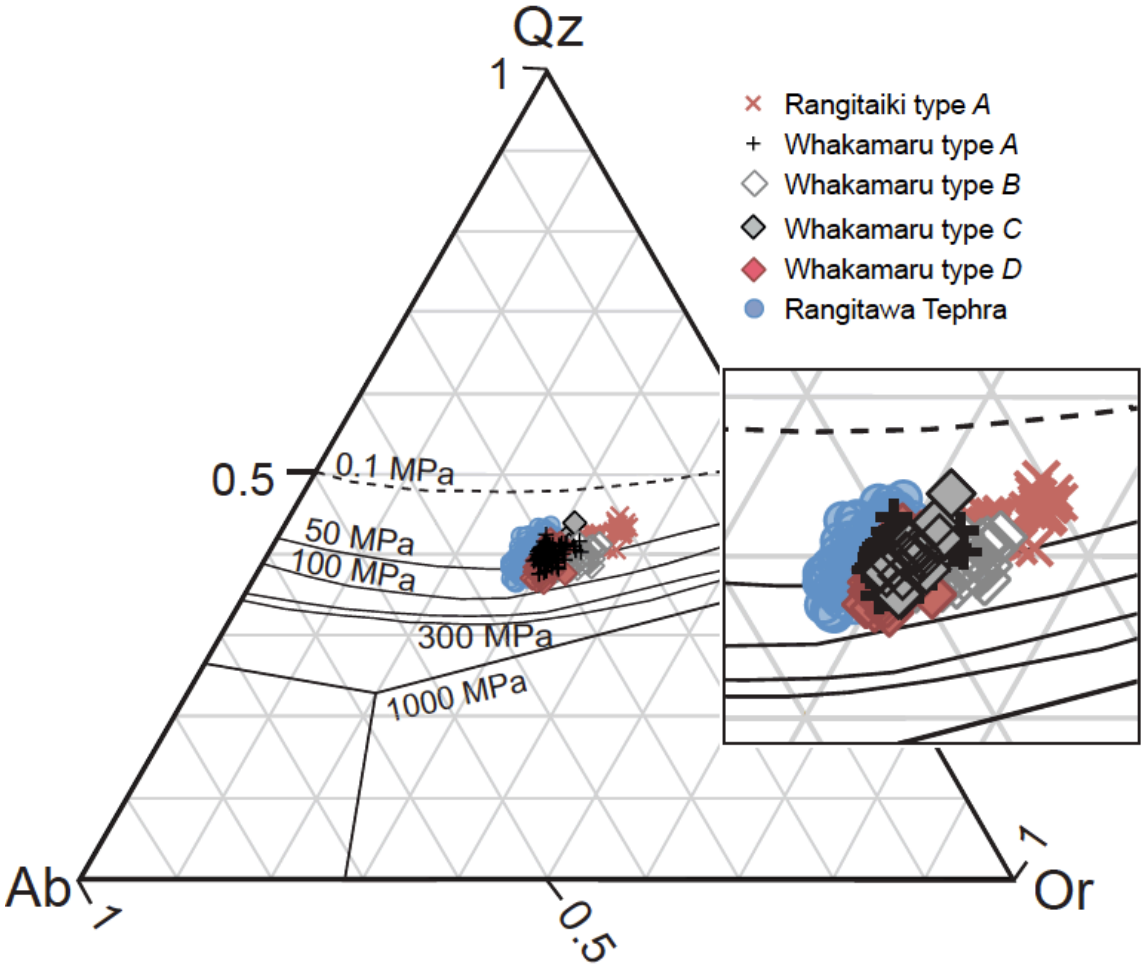

Fig. 2.17: Qz–Ab–Or ternary plot ('haplogranite' system; after Blundy and Cashman, 2001) showing glass compositions for pumice types in comparison to Rangitawa Tephra. Cotectic lines and compositions of H_2O-saturated minima and eutectics are after Blundy and Cashman (2001) for a range of water pressures. All pumices and tephra glass shards show similar eutectic compositions (see Section 3.3.5 for further discussion of magmatic pressures). The magmas are quartz-bearing and H_2O-saturated. Pressures ≤ 40 MPa may reflect disequilibrium crystallisation (Blundy and Cashman, 2008). Inset shows results for pumice types in detail.

The composition of Rangitawa Tephra is also compared here with deposits from the Oruanui eruption, the Kawakawa Tephra, to assess whether large eruptions from New

Zealand share the same chemical affinities (Fig. 2.6). Rangitawa Tephra is clearly different from the Kawakawa Tephra in terms of major- and trace-element compositions. It is more evolved than Kawakawa with higher K_2O, Rb and Ba, and lower CaO, FeO^T and Sr compositions, forming a separate compositional group (Fig. 2.6). This is in marked contrast to other supereruption deposits (e.g., Toba, where the three major ashfall deposits all show similar chemical affinities; Smith et al., 2011; see Chapter 6).

2.4.2 Ferromagnesian minerals – fingerprinting the tephra

Biotite forms two main compositional groupings (as illustrated by Fig. 2.11, and confirming earlier results from Brown et al., 1998a) – Whakamaru type *A* biotite has low FeO/MgO and MnO, and types *B*, *C* and *D* form a second group characterised by higher FeO/MgO and MnO contents. Biotite from Rangitaiki type *A* pumice shows compositions which overlap with both groups. Rangitawa Tephra biotite and orthopyroxene compositions both correlate with the Whakamaru type *A* compositions. This further strengthens the correlation between the tephra and type *A* magma made on the basis of similarities in glass composition (Section 2.4.1).

The elevated Mg and Ca compositions in some rare orthopyroxene crystals (Fig. 2.11b) in Whakamaru Group pumices are suggestive of either an input of mafic magma, or xenocrystic orthopyroxene being incorporated into the magma. Furthermore, the limited compositional variation of orthopyroxene (Fig. 2.11b) indicates that the magmas involved represent a single magma batch with one dominant orthopyroxene population, and minor contamination by a more mafic magma. Rare high-Mg hornblendes in mixed pumices and basaltic enclaves are also interpreted as being derived from a pre-eruptive basaltic component.

2.4.3 Plagioclase chemistry

2.4.3.1 Variations in X_{An} and oscillatory zoning

Major-element plagioclase compositions (mole fraction of An, X_{An}) are known to be sensitive to numerous parameters including temperature, pressure, H_2O content and melt composition (Blundy and Wood, 1991; Ginibre et al., 2002a, b; Putirka, 2005, 2008). Variations in composition of crystals from core to rim can therefore be used to trace magmatic evolution, providing information on recharge and assimilation processes. These variables can change concurrently, however, and it is therefore difficult to gain insight into processes operating within the system based on major-element concentrations alone (refer to Section 3.3.4 for discussion of feldspar-melt equilibria geothermometry).

Plagioclase crystals within individual Whakamaru Group pumice clasts show diverse compositional changes core-to-rim, with no systematic correlations in zoning patterns between crystals (Fig. 2.14). Small oscillations in An can be explained through thermal perturbations and/or fluctuations in the magma water content (e.g., Ginibre et al., 2002a, b; Putirka, 2005). The general consistency in feldspar rim compositions (Table 2.9) suggests that plagioclase continued crystallising in equilibrium with the melt up until eruption (oxygen isotope data strengthens this argument; Section 5.4.3). The resorption and crystallisation of zones with high-An content within crystals from some of the Rangitaiki pumices (Fig. 2.13) suggests crystallisation within slightly hotter, more primitive magmas which most likely reflects magma recharge events (similar zoning is seen within the quartz which is explored further in Chapters 3 and 4). Oscillatory zoning is generally attributed to local kinetic effects in a boundary layer at the crystal-melt interface (Ginibre et al., 2002a), although interpretation remains controversial.

The variability between crystals within a single pumice (e.g., samples P1905, P1910 and P1915; Fig. 2.14; Appendix 5) suggests that plagioclase was recording localised changes within the magma reservoir and therefore cannot be used to reconstruct temporal changes for the magma system as a whole. Furthermore, diffusion modelling for Whakamaru plagioclase crystals shows diverse timescales (Saunders et al., 2010), which indicates that most crystals experience a unique history. An alternative explanation may be that there was a sufficiently diverse range of histories that would require analysis of a very large number of crystals in order to reconstruct the overall magma reservoir history.

2.4.3.2 Resorption events

Three noticable plagioclase resorption events are typically observed in BSE imagery and major-element profiles and indicated in Figs 2.15 and 2.16 (by the points labeled a*, b* and c*). These resorption horizons are likely to correspond to significant changes in temperature, pressure, oxygen fugacity and/or melt composition possibly during magma recharge (Nixon and Pearce, 1987; Davidson and Tepely, 1997; Ginibre et al., 2002, 2002a), but these variables cannot be distinguished on the basis of the present data set (additional trace-element data would be required). The resorption horizons cannot be correlated between crystals with any certainty and therefore do not necessarily represent common events. The final resorption horizon, however, may correspond to the significant resorption event and P/T/composition change observed in quartz crystals from the same pumice samples (refer to Chapter 3). Each resorption horizon is typically overgrown by a normally-zoned region, which may be attributed to fractional crystallisation. The minor resorption surfaces visible in BSE imagery (Figs 2.15, 2.16) are more likely to be caused by minor changes in pressure or temperature.

2.4.4 Melt composition and magma evolution

The identification of mixed, mingled and banded basaltic pumice clasts and basaltic enclaves within rhyolite pumices provides direct evidence for the involvement of mafic magma in the petrogenesis of the large-volume rhyolite magma chamber system. Furthermore, the wide compositional range of type *A* Whakamaru and Rangitaiki magma (Fig. 2.6) is suggestive of mixing with basaltic magma. Such mafic magma interaction has been frequently observed in other large rhyolitic systems. A notable example is the identification of mingled basaltic andesite pumices and cognate basaltic inclusions in the Rattlesnake Tuff, Oregon, interpreted as recharge magma which mingled with the rhyolite while being stalled beneath a silicic cap (Streck and Grunder, 1997). Rare banded pumices and mafic mingling features observed in deposits of the rhyolitic Kos Plateau Tuff are also interpreted as indicative of a reheating event caused by the intrusion of hydrous mafic magma at the base of a rhyolitic mush zone, triggering eruption (Bachmann, 2010). Furthermore, basaltic - silicic magma interaction is common in smaller events from the TVZ (e.g., Wilson et al., 2006; Shane et al., 2008a).

The evolution of the rhyolitic magma of the Whakamaru Group Ignimbrites is discussed here in terms of fractional crystallisation processes.

2.4.4.1 Partition coefficients

Partition coefficients (*D*) of trace elements between plagioclase and melt depend primarily on X_{An} and to a lesser extent on temperature (Blundy and Wood, 1991; Bindeman et al., 1998). Established partitioning relationships can be used in conjunction with compositional data from plagioclase crystals to reconstruct the evolution of the coexisting melt during plagioclase crystallisation (e.g., Blundy and Shimizu, 1991). Partition coefficients (D_{Sr} and

D_{Ba}) for plagioclase are calculated using the D-T-X_{An} partitioning equation from Blundy and Wood (1991) and plagioclase rim compositions (X_{An}):

$$RT\ln D_{Sr} = 26800 - 26700 \times X_{An} \quad [2.1]$$

$$RT\ln D_{Ba} = 10200 - 38200 \times X_{An} \quad [2.2]$$

where R is the universal gas constant (8.314 J K^{-1}), and T is absolute temperature (°K; estimated from Fe-Ti oxides; Section 3.3.4). Measurement of X_{An} and trace-element (Ba, Sr) contents of magmatic plagioclase permits calculation of the Ba and Sr contents of the coexisting liquid. Using the above equations, a temperature of 770°C (Section 3.3.4), X_{An} = 0.28 (average feldspar rim composition; Table 2.9), and initial melt compositions Sr = 90 ppm and Ba = 1050 ppm, calculations yield: D_{Sr} = 9.302 and D_{Ba} = 0.944. Modelled plagioclase fractional crystallisation using these partition coefficients is shown in Fig. 2.19.

For comparison, partition coefficients were also calculated using Whakamaru feldspar trace element data from Brown (1994) using equation [2.3]:

$$D_i = \frac{C^{\text{mineral}}_{\text{element}_i}}{C^{\text{melt}}_{\text{element}_i}} \quad [2.3]$$

where D_i is the partition coefficient for element i, and C is the concentration of the trace element i in the plagioclase rim and melt (McIntire, 1963; Rollinson, 1993). Results of this calculation for Whakamaru plagioclase are as follows: D_{Sr} = 2.954; D_{Rb} = 0.019; D_{Ba} = 0.606, which differ considerably from the above. There are problems with this approach however, particularly as partition coefficients can vary significantly according to temperature, pressure, composition and fO_2 of the melt (Rollinson, 1993), and plagioclase is most sensitive to X_{An} (Blundy and Wood, 1991). The use of zoned minerals can

introduce additional errors, although this is less significant here due to the limited element concentration variation in crystals from core to rim and the use of average values. Melt composition is known to be the most important factor controlling mineral/melt partition coefficients (Rollinson, 1993), and the data are well constrained here by EPMA and LA-ICP-MS analysis.

2.4.4.2 Fractional crystallisation

Fractional crystallisation (FC) modelling assumes Rayleigh fractionation, as described by equation [2.4]:

$$\frac{C_L}{C_O} = F^{(D-1)} \qquad [2.4]$$

where C_O is the initial concentration of a trace element in the primary (parental) magma, C_L is its concentration in the liquid, F is the fraction of melt remaining and D is the bulk partition coefficient of the fractionating assemblage (Rollinson, 1993). The crystallisation vectors based on equation [2.4] with 5% and 10% crystallisation increments are shown in Figs 2.18 and 2.19 for Whakamaru Group pumices with: (1) fractional crystallisation of the bulk assemblage; and (2) plagioclase-dominant equilibrium fractionation. Calculations use partition coefficients, D, as calculated for plagioclase in Section 2.4.4.1 (using Blundy and Wood, 1991), and published estimates for the other mineral phases in rhyolite (from Pearce and Norry, 1979; Mahood and Hildreth, 1983; Nash and Crecraft, 1985; Rollinson, 1993).

Comparison of glass and whole-rock trace-element (XRF) data shows FC trends (indicated by the modelled FC trends between glass and whole-pumice pairs; Fig. 2.18). Bulk FC modelling fitting whole-rock to glass compositions (Fig. 2.18) shows that type *A* and *B*

pumice glass can be produced by dominantly plagioclase crystallisation (50 – 65% modal plagioclase, 10% biotite, 10 – 20% orthopyroxene and minor hornblende). In contrast, the divergent trend of type *D* pumice (due to Rb being compatible in these more evolved pumices) can only be produced by significant biotite crystallisation and more crystal-rich magma (modal 42 – 65% biotite and 35 – 55% plagioclase). This is consistent with the biotite-rich nature of type *D* pumices. This modelling suggests extensive crystallisation, however, which is not consistent with observed modal mineralogy for each pumice (see Table 2.2). Thus, the XRF composition is heavily influenced by the incorporation of a large proportion of xenocrystic or antecrystic crystals (cf. Charlier et al., 2005).

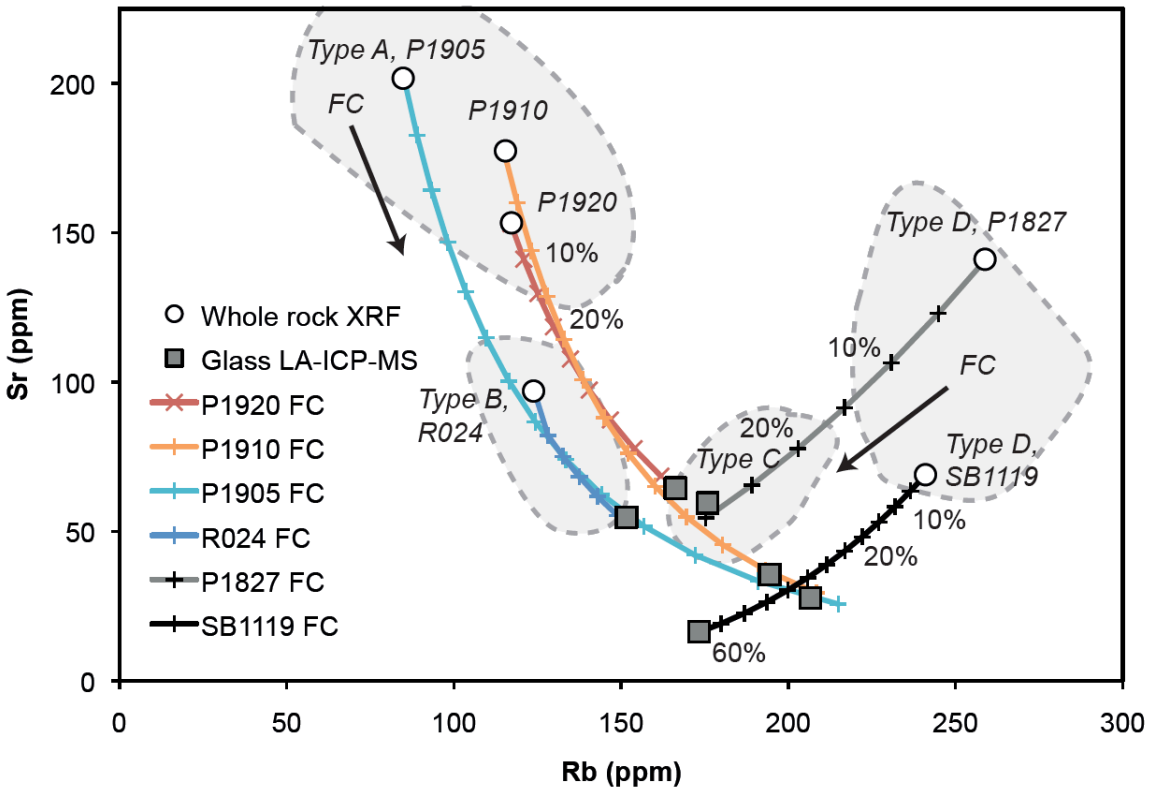

Fig. 2.18: Comparison of Rb and Sr trace-element data from whole-rock XRF and glass LA-ICP-MS analysis (glass data shown by grey squares). Coloured lines show modelled fractional crystallisation (for bulk assemblages as described in text above) with 5% crystallisation increments, linking data for same pumice samples. Grey dashed lines show compositional range of pumice types. Note that types *C* and *D* pumice shows different fractional crystallisation trends from types *A* and *B* that can only be produced by significant biotite crystallisation. FC = fractional crystallisation.

Fractional crystallisation modelling of the glass data is depicted in Fig. 2.19, where plagioclase FC is modelled using both the Blundy and Wood (1991) formulation (equations [2.1] and [2.2]) and partition coefficients calculated from Whakamaru feldspar-melt pairs (equation [2.3]). The Rb-Sr plot shows that type *A* Whakamaru and Rangitaiki melts are distinct (Fig. 2.19a), with the compositional range in Rangitaiki type *A* melts being produced from ~ 10 – 45% plagioclase fractionation of the Whakamaru melt. Type *D* pumice lies slightly off this trend, and is more reflective of the bulk modelling curve (Fig. 2.19b), with 30 – 50 % fractional crystallisation of a modal mineralogy of ~ 70% plagioclase, 10% biotite, 15% orthopyroxene, 4% hornblende and 1% alkali feldspar. Rangitawa Tephra correlates directly with Whakamaru type *A* melt chemistry (Fig. 2.19), with 10 – 20% fractional crystallisation required to produce the range in glass trace-element compositions.

The calculations presented here assume simple fractional crystallisation for melt evolution. A more relevant process for this viscous mush-melt system would be the "assimilation and fractional crystallisation" model (AFC; Bowen, 1928) whereby wall-rock assimilation also plays a role in petrogenesis. Additional complexities could also be described by the "RTF" magma chamber model (Replenished, periodically Tapped, continuously Fractionated magma chamber; O'Hara, 1977; O'Hara and Matthews, 1981).

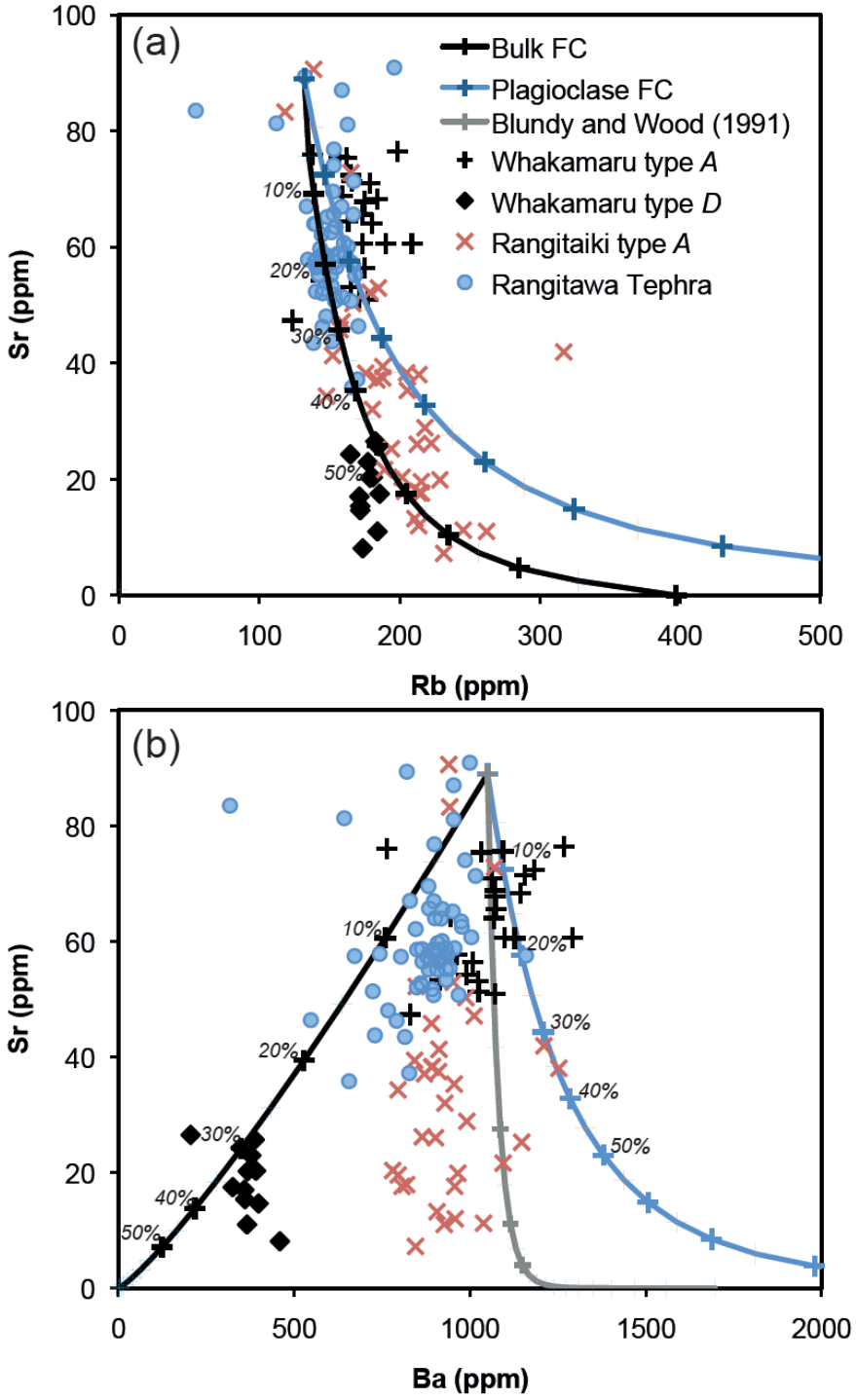

Fig. 2.19: Trace-element fractional crystallisation modelling for Whakamaru and Rangitaiki pumices in comparison to Rangitawa Tephra, based on glass chemistry (by LA-ICP-MS). Partition coefficients for plagioclase are calculated from plagioclase-melt pair (blue line) and Blundy and Wood (1991) formulation (grey line; b). These are compared with bulk assemblage fractional crystallisation (with normalised modal mineralogy as follows: 70% plagioclase, 15% orthopyroxene, 10% biotite, 3% hornblende, 1% alkali feldspar and 1% clinopyroxene). Fractional crystallisation shown in 10% increments (marked by crosses). Note that trace-element data for pumice types *B* and *C* were not collected and therefore their relationships cannot be evaluated. The trace-element dataset does, however, clearly show that Rangitawa Tephra is most likely derived from Whakamaru type *A* magma.

2.5 Conclusions

Whakamaru Group Ignimbrite deposits are characterised by high-silica rhyolite and comprise five separate pumice or 'magma' types on the basis of whole-rock geochemistry, defined as types *A, B, C, D*, and *mixed-basaltic*, where *A* is the most dominant pumice type. The similar glass chemistry of *A*, *B* and *C* pumice types (defined on whole-rock chemistry) implies that they were likely the same melt, while *D* crystallised separately. The whole-rock chemistry appears to mostly reflect variable modal mineralogy and crystal content. Fractional crystallisation modelling shows that the whole-rock composition is not clearly related to the glass composition via crystallisation of the modal mineral assemblage indicating that there is a substantial amount of xenocrystic and antecrystic material incorporated into the magmas. Rayleigh fractional crystallisation modelling shows that Rangitaiki melt can be produced from Whakamaru melt by up to ~ 45% plagioclase crystallisation, while type *D* Whakamaru pumice is distinct, requiring fractionation of biotite in addition to advanced plagioclase fractionation (also consistent with anomalously high Rb contents, the plagioclase- and biotite-rich crystal assemblage, and the pronounced Eu/Eu* anomaly shown by glass chemistry; Fig. 2.10). This suggests, therefore, that the Whakamaru magmatic system is dominantly one magma body (zoned in terms of crystal content and mineralogy), with a separate melt pocket (type *D*) which was isolated from the main reservoir and evolved separately at a late stage.

These results are consistent with previous interpretations by Brown et al. (1998a), which suggest that type *D* was unrelated to types *A* or *B* by crystal fractionation and may have formed in a separate subjacent chamber that was incorporated into the eruption. Fractional crystallisation modelling based on whole-rock data indicate that types *B* and *C* were generated by two-stage fractional crystallisation from type *A*, with 30 – 40% fractionation

of a plagioclase-dominant assemblage to produce type *B* magma, which in turn underwent fractionation of a plagioclase + quartz assemblage to produce the highly evolved type *C* magmas (Brown et al., 1998a).

The mixed/mingled basaltic pumice clasts indicate that mafic magma interacted with the silicic melt immediately prior to eruption and possibly triggered the eruption (see Chapter 3 and 4 for further discussion of magma volumes, the magnitude of the subsequent thermal perturbation and timescales of recharge). Periodic mafic recharge has also been suggested for the construction and triggering of other large silicic eruptions in the TVZ (e.g., the Okataina Caldera Complex; Schmitz and Smith, 2004; Shane et al., 2005).

The wide range in plagioclase compositions and numerous resorption events suggests crystallisation over a range of temperature and pressure conditions, and could be related to changes in melt composition over time due to recharge. Crystal histories of quartz and zircon are discussed in detail in Chapters 3, 4 and 5.

Glass, biotite and orthopyroxene within the Rangitawa Tephra deposit have major-element compositions which correspond directly to the components from type *A* pumice within the Whakamaru and Rangitaiki ignimbrite deposits. These similarities in compositions therefore suggest that this widely dispersed ash, deposited > 900 km from the vent, was deposited during the emplacement of the Whakamaru ignimbrite. Dispersal of the ash is discussed and modelled in Chapter 6.

Appendix A2.1: BSE images of feldspar crystals with EPMA transects

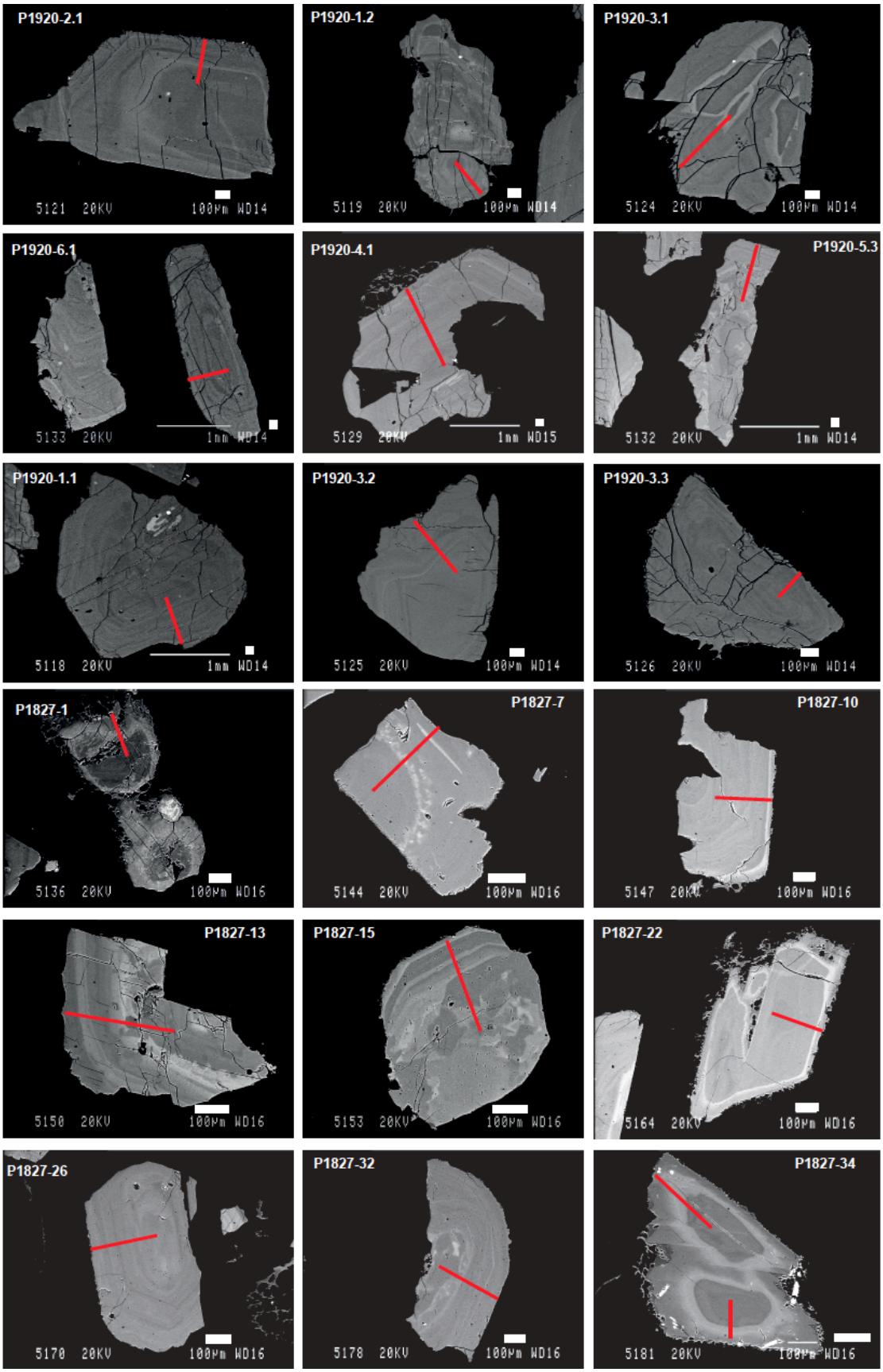

SEM-BSE images of feldspar crystals extracted Whakamaru pumices (sample P1920 and P1827). Red lines mark EPMA transects (data provided in Appendix 5). Scale bar is 100 µm for all images.

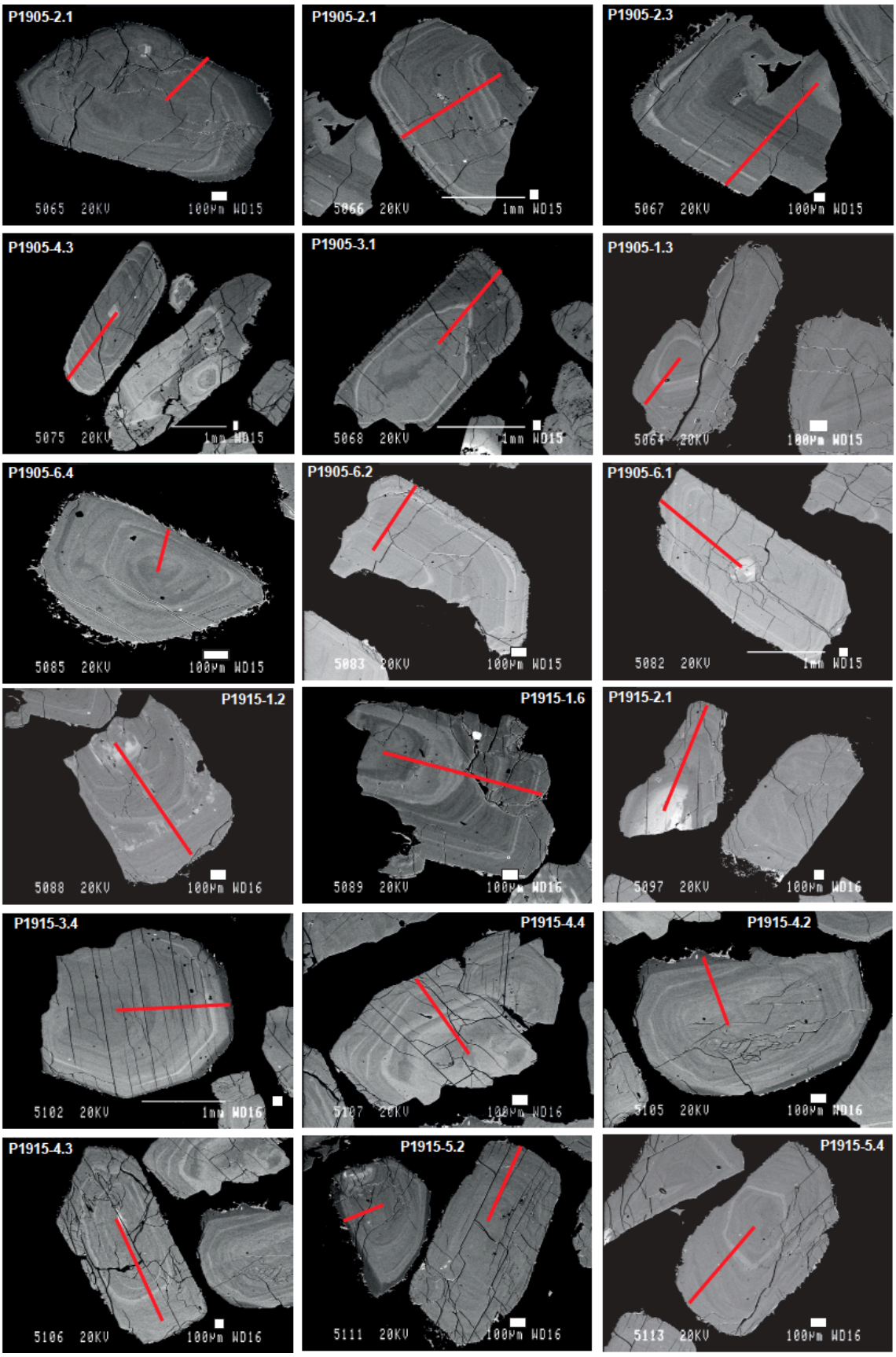

SEM-BSE images of feldspar crystals extracted from Rangitaiki pumices (sample P1905 and P1915). Red lines mark EPMA transects (data provided in Appendix 5). Scale bar is 100 µm for all images.

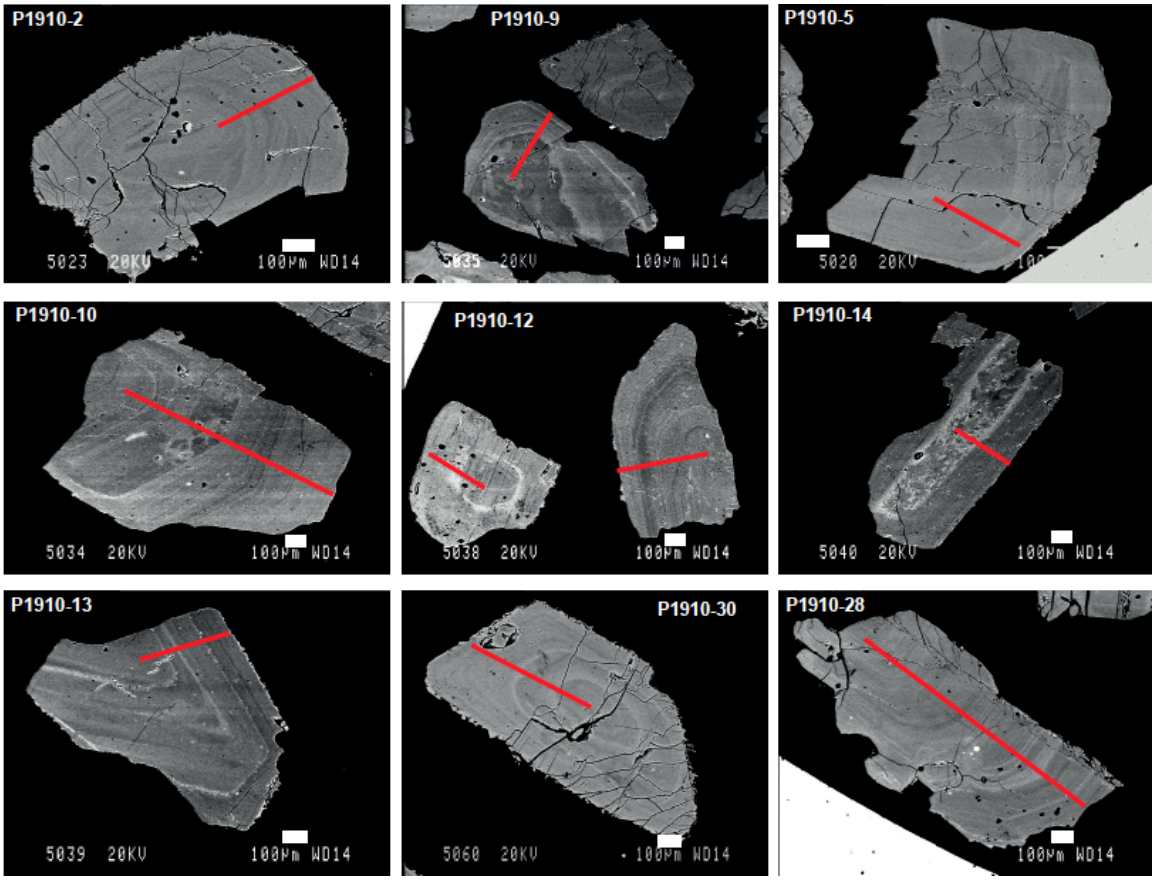

SEM-BSE images of feldspar extracted from Rangitaiki pumice sample P1910. Red lines mark EPMA transects (data provided in Appendix 5). Scale bar is 100 µm for all images.

Chapter 3

Quartz zoning and the pre-eruptive evolution of the Whakamaru magma system[1]

3.1 Introduction

The chemical zonation of crystals in igneous rocks provides an important archive of information that may be used in the reconstruction of magma reservoir processes. Detailed petrographic and geochemical analysis of such zoning can provide constraints on complex thermal and pressure histories and changes in host melt composition or physical parameters of the overall magma reservoir during crystal growth (e.g., Wallace et al., 1999; Anderson et al., 2000; Humphreys et al., 2006; Liu, Y. et al., 2006; Smith et al., 2009). In particular, in silicic systems, trace-element concentrations in quartz and their related cathodoluminescence (CL) emission properties have the potential to provide valuable petrological clues concerning crystallisation conditions (Götze et al., 2004; Wark and Watson, 2006).

CL imaging reveals complex zoning in magmatic quartz crystals (e.g., Peppard et al., 2001; Liu, Y. et al., 2006; Wark and Watson, 2006; Wiebe et al., 2007; Rusk et al., 2008;

[1] Much of the material in this chapter is published in Matthews, N.E., Pyle, D.M., Smith, V.C., Wilson, C.J.N., Huber, C. and van Hinsberg, V., 2011a. Quartz zoning and the pre-eruptive evolution of the ~340-ka Whakamaru magma systems, New Zealand. Contributions to Mineralogy and Petrology. In press, doi:10.1007/s00410-011-0660-1.

Shane et al., 2008b; Smith et al., 2010). These variations in quartz CL intensity are interpreted empirically as relating directly to Ti content, reflecting changes in melt chemistry and/or temperature/pressure during crystallisation (Peppard et al., 2001; Wark and Watson, 2006; Thomas et al., 2010). Complex histories are thus indicated by the wide variety of quartz CL zoning patterns observed, indicating detailed temperature/pressure/composition records present in single pumice clasts. However complex, such histories are central to reconstructing the assembly of the erupted magma body.

Questions about this magma assembly process include: (1) whether large silicic magma systems form by rapid rejuvenation of, or melt extraction from, silicic mushes (e.g., Murphy et al., 2000; Vazquez and Reid, 2002; Bachmann and Bergantz, 2003, 2006; Charlier et al., 2007; Knesel and Duffield, 2007; Wark et al., 2007; Wilson and Charlier, 2009); (2) whether they developed piecemeal over time and were homogenised immediately prior to eruption (e.g., Petford and Gallagher, 2001; Annen and Sparks, 2002; Glazner et al., 2004; Annen et al., 2006) or formed by progressive growth of a large melt reservoir with long magma residence times (e.g., Halliday et al., 1989; Davies et al., 1994; Reid et al., 1997; Simon and Reid, 2005; de Silva et al., 2007; Hildreth and Wilson, 2007; Huber et al., 2009); and (3) what processes finally trigger their eruption. Crystal zonation data can highlight the roles of thermal, pressure and compositional perturbations in assembling and priming the magma body for eruption and thus provide insights into these questions.

This chapter presents new geochemical data on the trace-element zonation and CL properties of quartz from pumices extracted from specific members of the large-volume

Whakamaru Group Ignimbrites (Froggatt et al., 1986; Wilson et al., 1986; Pillans et al., 1996; Brown et al., 1998a). Quartz zonation patterns are explored here to investigate magmatic conditions leading up to the Whakamaru eruption (or eruptions), and document the complexity of underlying magma chamber processes. Results are compared with studies of magmatic quartz crystals in other TVZ rhyolites (Liu, Y. et al., 2006; Shane et al., 2008b; Smith et al., 2010) and the Bishop Tuff (Peppard et al., 2001; Wark et al., 2007), although the cumulative volume of the Whakamaru group eruptions is at least twice that of those events. It is thus an ideal case study to investigate whether very large magmatic systems may be assembled in a similar way to smaller silicic systems, and whether the timescales over which the processes operate are comparable (see Chapter 4).

3.2 Samples and methods

Measurements of Ti concentrations are applied together with interpretations of CL images (Watt et al., 1997; Götze et al., 2001, 2004; Peppard et al., 2001) to studies of Ti zonation in quartz crystals extracted from five pumices sampled from the two most widespread and pumice-rich Whakamaru Group Ignimbrites, Rangitaiki and Whakamaru (Fig. 3.1). Published models are used to reconstruct possible crystallisation temperature and pressure records (Wark and Watson, 2006; Thomas et al., 2010), together with diffusion modelling of Ti concentration profiles (Chapter 4), in order to provide constraints on the thermal/pressure histories of the melts prior to eruption. Other factors that may have contributed to the quartz zoning (pressure and composition, in addition to temperature) are considered as existing models may have limitations (Wilson et al., 2011).

3.2.1 Samples

Five pumice samples (three Rangitaiki; two Whakamaru: sample localities in Fig. 3.1) were selected for detailed quartz CL study (Table 3.1). Pumices were selected on the basis of mineralogy, clast size, lack of alteration and major-element geochemistry.

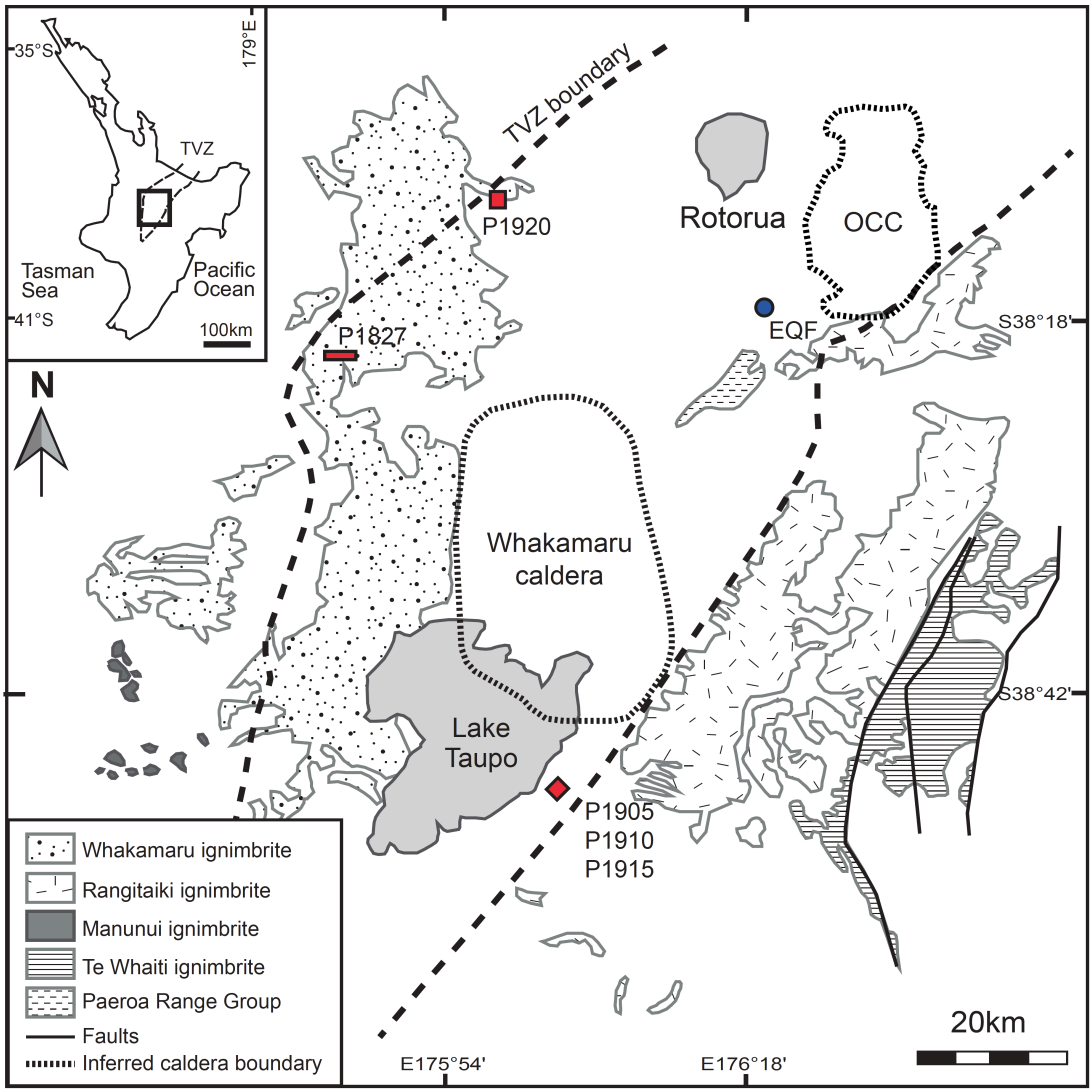

Fig. 3.1: Sketch map showing location of Whakamaru caldera and the distribution of Whakamaru Group Ignimbrites, central TVZ (after Brown et al., 1998a). Pumice sample localities are marked by red symbols. Rangitaiki samples are P1905, P1910, P1915 (collected from Hinemaiaia B Dam) and Whakamaru samples are P1920 (from Sutton Road) and P1827 (Type *D* pumice collected from Edsel Road). Inset map shows North Island of New Zealand and location of TVZ. The Okataina Caldera Complex (OCC) and Earthquake Flat pumice sample (EQF) are also marked (blue circle), as referred to in Chapter 4.

Type *A* pumice is the main focus of this quartz study as it represents the volumetrically dominant magma type (~ 89% of pumice sampled; Section 1.6.2). Type *D* is also of interest because it may represent a co-erupted but separate (and subsidiary) chamber on the basis of its contrasting isotopic and trace element characteristics (Brown et al., 1998a). Types *B* and *C*, in contrast, are likely to represent only second-order variants produced by convective fractionation in a dominantly type *A* magma reservoir (Brown et al., 1998a). The discussion here of quartz zoning patterns and crystallisation histories therefore relates mainly to types *A* and *D* Whakamaru Group pumices, with one of the samples being of mixed basaltic type (Table 3.1, Section 1.5.3).

Table 3.1: ***Summary of single pumice samples used for quartz study***

Pumice sample	Unit	Pumice Type	Pumice mineralogy	Ti melt (av. ppm)	FM	T (°C)	Ti (ppm) rutile saturated melt	a_{TiO2} (from melt FM)	a_{TiO2} (from oxides)
P1905	Rang	*A*	Feldspar,qtz>>hbl, opx>biotite>>mag, ilm	800 *(n = 11)*	1.74	763	1116	0.72	0.53
P1910	Rang	*A*	Feldspar, quartz> opx>>mag, ilm	827 *(n = 26)*	1.59	768	1125	0.74	0.62
P1915	Rang	*Mixed*	Feldspar, qtz>pyx, hbl>>oliv, oxides (mafic clots)	821 *(n = 32)*	2.01	763	1195	0.69	0.65
P1920	Whak	*A*	Feldspar, qtz>> opx>> mag, ilm	790 *(n = 43)*	1.55	789	1403	0.54	0.67
P1827	Whak	*D*	Feldspar, qtz>> biotite>>mag, ilm	610 *(n = 23)*	1.42	740	**1210 ± 133**	**Av. = 0.67 ± 0.09**	**Av. = 0.66 ± 0.09**

Note: Pumice type is based on Brown et al. (1998a) classification scheme as outlined in Section 1.5.3 and Table 2.2. SiO_2 and TiO_2 values are from whole-rock XRF analysis. FM is the melt composition parameter (calculated from Hayden and Watson, 2007). For a given temperature, TiO_2 solubility increases as FM increases, or as the melt becomes more mafic; and for a given melt composition as represented by FM, TiO_2 solubility increases with temperature (Hayden and Watson, 2007). The single temperature used to calculate rutile saturation and a_{TiO2} is derived from average Fe-Ti oxide temperatures (using Ghiorso and Evans, 2008). The a_{TiO2} values in the final column are derived directly from oxide compositions.

Quartz crystals were extracted by lightly crushing, sieving and hand-picking under an optical microscope. Approximately 40 quartz crystals from each pumice sample were extracted, of which 92 were imaged by CL and analysed by EPMA. Quartz crystals in Whakamaru and Rangitaiki pumices are commonly embayed and/or fractured and thus only crystal fragments could usually be retrieved. Individual quartz fragments were chosen such that the glass selvedges were still intact on one face of the fragments, to ensure that the complete core-to-rim crystal zonation was captured. These were mounted in epoxy resin, polished and carbon coated for imaging and analysis. Backscattered-electron (BSE) images of the mounts were made for ease of navigation, using a JEOL SEM at the University of Oxford.

3.2.2 Ti in quartz

Ti concentrations in quartz were measured using a JEOL JXA-8800R electron microprobe at the Begbroke Science Park, University of Oxford, with a 15 kV accelerating voltage, 200 nA beam current, and a beam diameter of 10 μm. In order to obtain reliable Ti results at low abundance, Ti was analysed on two spectrometers simultaneously, using count times of 800 s on the peaks and backgrounds. Merging the Ti counts from the spectrometers resulted in low detection limits (< 10 ppm) and low uncertainties (± 11 ppm; 1sd) for Ti. The JEOL 8600 electron probe in the Research Laboratory for Archaeology and the History of Art, University of Oxford, was also used with a high beam current (100 nA), extended count times (900 s on peak and background), and a 10 μm beam diameter. Transects for Ti analyses were chosen on the basis of CL zoning, in particular targeting the core-rim interface. Analyses were spaced at 100 μm (av.) intervals (spacing ranged from 45 to 200 μm depending on crystal size) along core-to-rim profiles.

3.2.3 TitaniQ geothermobarometry

The Ti content of hydrothermally grown quartz has been proposed to be a function of both temperature (Wark and Watson, 2006) and pressure, with a ± 100 MPa pressure change corresponding to ± 20°C change in temperature and *vice versa* (Thomas et al., 2010). The proposed pressure dependency means that higher Ti contents may indicate higher temperatures, but may also imply lower pressures or a combination of the two effects. The content of Ti in quartz (Ti_{qtz}) was proposed by Wark and Watson (2006) to be related primarily to temperature and Ti activity of the melt, using equation [3.1], where T = temperature (K); and a_{TiO2} = activity of Ti in the quartz.

$$T = \frac{-3765}{\log(Ti_{qtz} / a_{TiO_2}) - 5.69} \qquad [3.1]$$

This geothermometer was calibrated experimentally by Wark and Watson (2006) by synthesising quartz in the presence of rutile and hydrous silicate melt, at temperatures of 600 – 1000°C and at 1.0 GPa.

The Ti concentration in quartz may also have a significant pressure dependency, as described by equation [3.2] (output converted to MPa here) where a = 60952 ± 3177, b = 1.52 ± 0.39, c = 1741 ± 63, R is the universal gas constant (8.3145 J K^{-1}), T is temperature in K, and $XQtz_{TiO2}$ is the mole fraction of TiO_2 in quartz (Thomas et al., 2010).

$$P(kbar) = \frac{(-a + bT + RT\ln a_{TiO_2} - RT\ln XQtz_{TiO_2})}{c} \qquad [3.2]$$

The parameters *a*, *b* and *c* have been established by a least-squares fit of experimental Ti-in-quartz solubilities (Thomas et al., 2010). As noted in this chapter and discussed by Wilson et al. (2011), however, the application of the P and T dependency of Ti solubilities proposed by Thomas et al. (2010) leads to implausible results, especially with regard to pressure (refer to Section 3.4.2). Ti partitioning and thus Ti values in the quartz may also be affected by compositional changes in the chamber, which affects the effective solubility of Ti in the melt.

3.2.4 Constraining Ti activity

None of the Whakamaru Group deposits contain rutile, so an estimate of activity of Ti in the melt (a_{TiO2}) was calculated as

$$a_{TiO_2} = \frac{Ti_{melt}}{Ti_{rut-melt}} \qquad [3.3]$$

where Ti_{melt} is the Ti measured in the melt (matrix glass), and $Ti_{rut\text{-}melt}$ is the Ti content of rutile-saturated melt (ppm). $Ti_{rut\text{-}melt}$ was determined using the method of Hayden et al. (2005) and equation [3.4], where *FM* is given by equation [3.5] (Hayden and Watson, 2007; Table 3.1).

$$\log(Ti_{rut-melt}) = 7.95 - \frac{5305}{T} + (0.124 \times FM) \qquad [3.4]$$

$$FM = \frac{Na + K + 2(Ca + Mg + Fe)}{Al \times Si} \qquad [3.5]$$

Temperatures and oxygen fugacities (fO_2) were estimated using the Fe-Ti oxide geothermometer of Ghiorso and Evans (2008) with the Fe-Ti oxide data (Appendix 9) being supplemented by values from Brown et al. (1998a) (recalculated using the Ghiorso and Evans (2008) formulation). Magnetite-ilmenite pairs were tested for Mg-Mn equilibrium using the Bacon and Hirschmann (1988) method and only pairs meeting the equilibrium criterion were used here. These calculations indicate that rutile should saturate at Ti concentrations of 1210 ± 133 ppm (Table 3.1), giving an average value of a_{TiO2} of 0.67 ± 0.09 (1sd), with a range of 0.54 to 0.74. Results are consistent with Oruanui rhyolite (0.74 ± 0.07; Wilson et al., 2011), Bishop Tuff (0.63 ± 0.03; Wark et al., 2007; and 0.53 ± 0.02 to 0.51 ± 0.10; Reid et al., 2011), and the range for large silicic systems of $0.5 < a_{TiO2} < 0.6$ reported by Hayden and Watson (2007). Pressures were calculated using both average and end-member a_{TiO2} values and equation [3.2], see Table 3.1 and Section 3.4.2.

Problems arise with this methodology as the Ti activity is calculated using equation [3.4], which is dependent on temperature. In order to avoid this problem, equations [3.1] and [3.4] can be simultaneously fitted, although this requires knowledge of the Ti content of the melt from which the crystal zone grew. It cannot be determined whether the concentration of the bulk rock is in equilibrium with the cores of the quartz crystals so this introduces an additional error in a_{TiO2} calculations.

The activity of rutile in the melt can also be constrained from the coexisting oxides (e.g., method employed by Reid et al., 2011). Using end-member thermodynamic properties from the 2004 version of the Holland and Powell (1998) dataset, and mixing and disorder models for the oxides from White et al. (2000, 2002) and Ghiorso and Evans (2008),

temperature, oxygen fugacity and a_{TiO2} can be fitted simultaneously from the set of independent reactions:

$$2\ FeTiO_3 = Fe_2TiO_4 + TiO_2 \quad [3.6]$$

$$6\ FeTiO_3 + O_2 = 2\ Fe_3O_4 + 6\ TiO_2 \quad [3.7]$$

$$6\ Fe_2O_3 = 4\ Fe_3O_4 + O_2 \quad [3.8]$$

and the activities of the respective end members in the oxide solid solutions (see Appendix 8). The use of a full thermodynamic model including non-ideality in mixing and disorder for the oxides allows for calculations of all equilibria despite the low activities for some of the end members involved. Across all pumice samples, the oxide calculation gives a weighted average a_{TiO2} = 0.66 ± 0.09 (1sd; Table 3.1, Appendix 8). There are, however, uncertainties with this methodology. If it is accepted that the oxides re-equilibrate on a short timescale to reflect different conditions (e.g., Venezky and Rutherford, 1999; Devine et al., 2003), then the oxides do not reflect conditions during growth of the quartz crystals, except for their outermost portions (if no resorption). Their present composition can therefore only provide information on a_{TiO2} for final quartz growth. The average a_{TiO2} value is, however, essentially the same when calculated by either method.

The presence of coexisting oxides throughout quartz crystallisation indicates that Ti activity was buffered. However, the buffered value of a_{TiO2} will vary with changes in melt composition, temperature and pressure. In an attempt to quantify these relative changes in Ti activity, melt and coexisting oxide compositions were modelled using rhyolite-MELTS

(Gualda et al., 2010). Changes in melt composition and TiO_2 content predict an increase in a_{TiO2} for the preferred *P-T* path (increasing *T* with decreasing *P*), but oxide compositions predict a decrease. The magnitude of the difference for the full range of quartz crystallisation conditions is predicted to be of the order of $\Delta a_{TiO2} = 0.2$. Nonetheless, this systematic change in a_{TiO2} is insufficient to explain the differences in Ti concentrations between core and rim, and does not modify the trends in temperature that are calculated here from TitaniQ thermometry, although it suggests a smaller temperature range when using the Δa_{TiO2} from modelled oxide compositions.

These uncertainties in a_{TiO2} values mean that TitaniQ temperatures must be interpreted as temperature *estimates* only. They do, however, provide reliable and useful constraints on relative changes. Owing to the contradictory results from the modelling of Δa_{TiO2} with changing *P-T* conditions, this model is not preferred for calculating absolute temperatures. Instead, a fixed, rounded a_{TiO2} value of 0.7 is used, with interpretations being restricted to consideration as relative rather than absolute temperature values.

3.2.5 Feldspar-melt and amphibole geothermobarometry

Feldspar-melt equilibrium temperatures for each sample were calculated using the Putirka (2008) geothermometer, by pairing matrix glass compositions (Appendix 4; Section 2.3.3) with plagioclase rim data (Appendix 5). Values from Putirka (2008) calculations are interpreted with caution, however, as feldspar-melt equilibria are dependent on dissolved volatile contents (which are not specifically constrained here), and feldspar rims may not be in equilibrium in the melt when erupted (e.g., Saunders et al., 2010). Amphibole geothermobarometry was applied to the full set of amphibole data from Brown et al. (1998a) using the Ridolfi et al. (2010) formulation. These pre-existing data cannot provide

the high-resolution thermal history that may be obtained from application of TitaniQ to zoned quartz, but provide a useful overall comparison in terms of the eruptive temperatures and pressures of the host magma.

3.2.6 CL zoning and Ti correlation

Quartz CL brightness is known to have a linear correlation with both Ti and Al concentrations (Liu, Y. et al., 2006; Wark and Watson, 2006; Rusk et al., 2008; Shane et al., 2008b) suggesting they are important contributors to CL activity in magmatic quartz. Thus, greyscale values (numerical values assigned to zone brightness) of CL images can be used as a proxy for Ti content, and continuous Ti profiles across all crystal zones can be interpolated from a greyscale calibrated by individual EPMA Ti measurements.

CL images were obtained using a CL detector mounted on a JEOL electron microprobe at the University of Bristol, using a 22 nA beam current, 15 kV, and 42 s capture time, with image resolution of 1020 × 790 pixels. CL mosaics of entire quartz crystals from thin sections were also captured using a SEM with attached CL detector at the University of Cambridge.

CL greyscale profiles were calibrated against measured Ti content along each profile as described in Section 3.4.1. The correlation between greyscale and EPMA Ti concentrations used in the calibration was statistically significant, with R^2 values of 0.75 – 0.99. Each CL image was calibrated separately due to differences (contrast and brightness) in the original CL image capture parameters.

The calibrated-greyscale profiles (Fig. 3.10) provide a highly resolved record of the Ti uptake during quartz crystallisation. These estimated temperature profiles express the changes in Ti concentrations purely in terms of temperature, using TitaniQ, and therefore ignore dependencies on pressure and melt composition that must accompany any temperature changes and hence affect the absolute figures. Whatever the causes, the core to rim traverses clearly provide a detailed record of changes (temperature, pressure and/or composition perturbations) throughout growth of the crystals concerned (many of the Whakamaru crystals are shattered so only a few complete core-to-rim traverses are preserved, but the crystallisation history can be reconstructed from the fragments).

3.3 Results

3.3.1 Pumice petrography

The petrology of Whakamaru and Rangitaiki pumice is described in detail in Section 2.3.1 and Appendix 2 (and previously by Brown et al., 1998a). The selected pumice samples referred to here are characterised by a mineral assemblage of plagioclase, quartz >> hornblende, orthopyroxene > biotite >> magnetite, ilmenite and zircon (Table 3.1). Total phenocryst contents in the selected pumices range from ~ 15 to 25%. Fe-Ti oxides are present both as free crystals and hosted within orthopyroxene phenocrysts.

Some Rangitaiki pumice displays petrographic textures that imply contact with, and intermingling of, mafic magma and silicic melt (Section 2.3.1). In addition, basaltic andesite and andesitic enclaves are common, containing sieved or strongly oscillatory-zoned plagioclase and aggregates of pyroxene, and crystal clots of amphibole respectively (Fig. 3.2). The selected Whakamaru pumices also contain some aggregates comprised of

strongly zoned plagioclase phenocrysts and a ferromagnesian assemblage that is dominated by biotite rather than amphibole. Plagioclase compositions range from An_{25} to An_{43} across the selected samples (see Chapter 2, Section 2.3.4.4, and Appendix 5 for full geochemistry and descriptions).

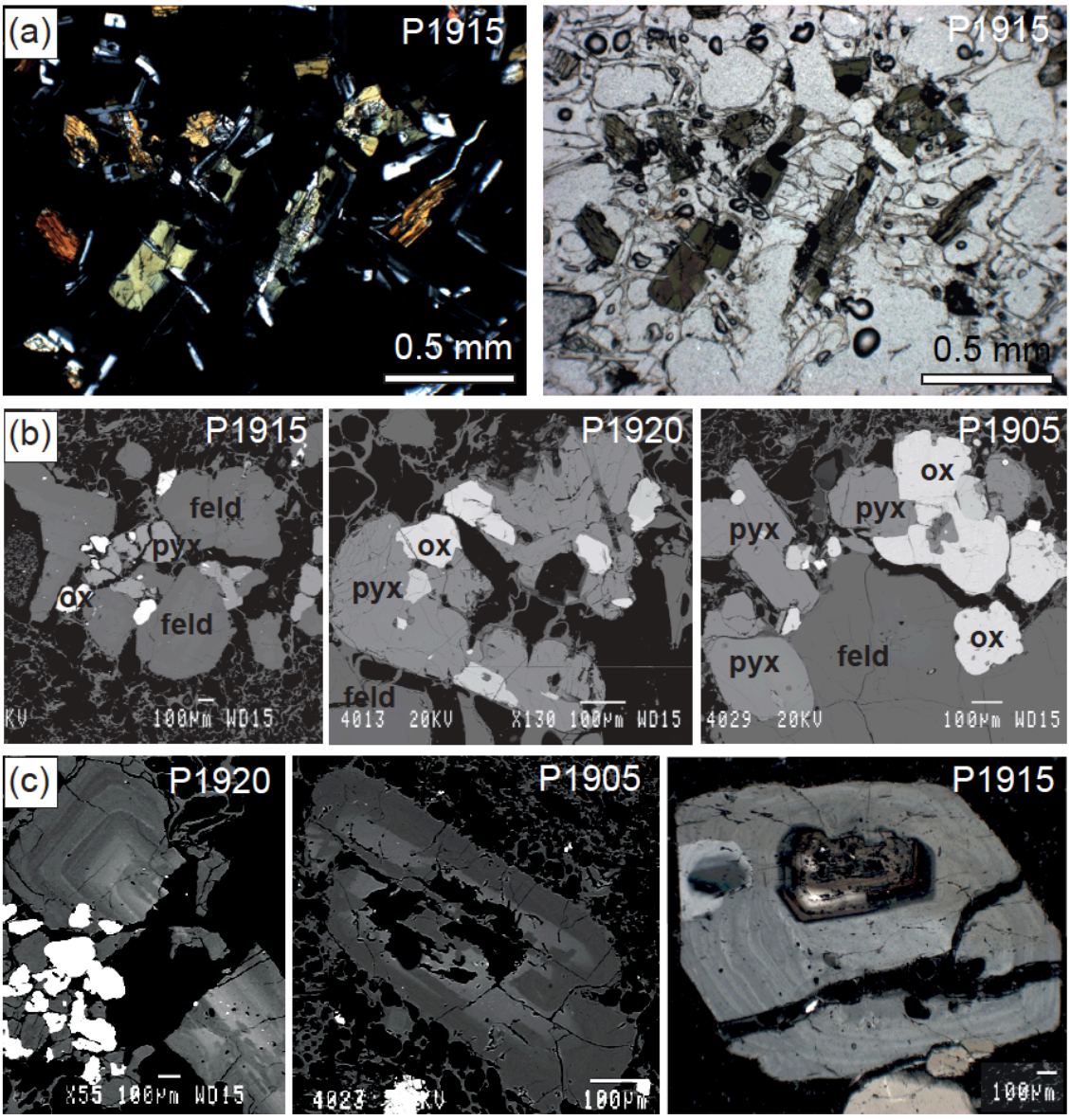

Fig. 3.2: Petrographic and BSE-SEM images of pumice clasts: (a) Pyroxene-rich layers in sample P1915 in crossed-polarised light (CPL) and plain-polarised light (PPL); (b) Crystal clots of pyroxene (pyx), Fe-Ti oxides (ox) and feldspars (feld) in samples P1915, P1920 and P1905; (c) Strong oscillatory zoning, fracturing and seive textures in plagioclase phenocrysts, indicating open system processes.

3.3.2 Glass compositions

Matrix glass fragments derived from the selected Whakamaru and Rangitaiki pumices are characterised by 74.9 – 78.9 wt% SiO_2, 0.30 – 1.00 wt% CaO, 4.46 – 6.83 wt% K_2O, 2.03 – 3.39 wt% Na_2O and 0.18 – 1.58 FeO^T (*n* = 97; Table 3.2; quoted anhydrous; see Appendix 4). Glass TiO_2 ranges 0.08 – 0.22 wt% across all pumice clasts, and this small variability is likely to have little influence on the assumption of near-fixed a_{TiO2}. Refer to Section 2.3.3 for full glass chemistry results for Whakamaru and Rangitaiki pumice types *A, B, C* and *D*.

Whole-rock geochemistry of the mafic inclusions in mingled Whakamaru pumices is characterised by 51.7 – 53.4 wt% SiO_2, 8.06 – 9.76 wt% CaO, 0.62 – 0.78 wt% K_2O, and 2.04 – 2.84 wt% Na_2O (Table 3.3). Glass chemistry for Rangitaiki mixed-basaltic pumice (sample SB3065) is characterised by 44.8 – 69.2 wt% SiO_2, 1.14 – 18.76 wt% CaO, 1.14 – 18.76 wt% K_2O, 0.03 – 4.79 wt% Na_2O and 0.57 – 16.56 FeO^T (*n* = 30; Appendix 4a; averages provided in Table 3.3).

Table 3.2: ***Proximal Whakamaru pumice glass chemistry (by EPMA and LA-ICP-MS)***

Sample	P1905		P1910		P1827		P1920		SB1119	
Unit	Ra		Ra		Wh		Wh		Wh	
EPMA (wt%)	*(n = 33)*	*1sd*	*(n = 24)*	*1sd*	*(n = 16)*	*1sd*	*(n = 20)*	*1sd*	*(n = 16)*	*1sd*
SiO_2	76.85	*0.09*	77.87	*0.26*	78.70	*0.12*	77.88	*0.40*	77.86	*0.25*
TiO_2	0.15	*0.02*	0.16	*0.02*	0.11	*0.02*	0.15	*0.03*	0.06	*0.02*
Al_2O_3	12.64	*0.05*	12.35	*0.22*	12.20	*0.15*	12.43	*0.24*	12.77	*0.21*
FeO	0.94	*0.05*	0.98	*0.07*	0.29	*0.08*	0.72	*0.26*	0.33	*0.08*
MnO	0.02	*0.01*	0.04	*0.05*	0.02	*0.02*	0.02	*0.03*	0.03	*0.02*
MgO	0.12	*0.02*	0.10	*0.02*	0.01	*0.01*	0.07	*0.03*	0.02	*0.01*
CaO	0.41	*0.06*	0.65	*0.03*	0.63	*0.04*	0.75	*0.05*	0.58	*0.04*
Na_2O	2.25	*0.13*	2.21	*0.06*	3.18	*0.05*	3.15	*0.17*	3.34	*0.23*
K_2O	6.62	*0.11*	5.64	*0.10*	4.87	*0.11*	4.83	*0.26*	5.01	*0.14*
Total	95.88	*0.43*	96.86	*0.36*	96.95	*0.51*	96.59	*0.76*	95.85	*1.22*
LA-ICP-MS										
(ppm)	*(n=20)*	*1sd*	*(n=24)*	*1sd*	*(n=11)*	*1sd*	*(n=22)*	*1sd*	*(n=18)*	*1sd*
Rb	207	*37*	194	*35*	176	*25*	166	*13*	173	*14*
Sr	27.8	*27.7*	35.6	*18.7*	59.5	*8.5*	64.5	*8.0*	16.5	*8.0*
Y	26.1	*4.1*	24.8	*2.7*	22.7	*5.2*	26.7	*2.7*	29.2	*2.8*
Zr	139	*14*	141	*17*	124	*23*	148	*16*	83	*10*
Nb	8.5	*1.2*	8.7	*1.0*	9.3	*1.7*	9.2	*1.2*	9.1	*0.9*
Cs	8.0	*1.0*	10.5	*3.1*	8.0	*1.8*	7.7	*0.7*	8.9	*1.0*
Ba	912	*103*	961	*106*	1090	*148*	1040	*94*	369	*58*
La	28.7	*1.9*	28.8	*3.5*	28.1	*3.8*	34.3	*13.8*	33.9	*2.8*
Ce	54.7	*4.6*	54.9	*7.6*	52.5	*7.6*	58.5	*10.1*	64.1	*4.3*
Pr	5.7	*0.7*	5.7	*0.8*	5.7	*0.9*	6.3	*1.3*	7.5	*3.1*
Nd	22.2	*2.3*	21.8	*3.1*	20.4	*3.6*	23.5	*3.4*	27.3	*3.2*
Sm	4.81	*1.40*	4.42	*1.04*	4.30	*2.11*	4.79	*1.61*	5.75	*1.81*
Eu	0.26	*0.29*	0.24	*0.59*	0.30	*0.20*	0.39	*0.32*	0.08	*0.38*
Gd	4.75	*1.08*	4.95	*2.32*	4.10	*0.86*	4.90	*1.02*	5.11	*1.19*
Tb	0.67	*0.22*	0.61	*0.30*	0.54	*0.19*	0.73	*0.14*	0.78	*0.20*
Dy	4.35	*1.09*	4.65	*1.44*	3.89	*0.93*	5.01	*0.98*	5.61	*1.03*
Ho	1.07	*0.29*	1.06	*0.33*	0.83	*0.42*	0.95	*0.18*	1.16	*0.23*
Er	3.56	*1.01*	3.25	*0.74*	2.52	*0.50*	3.48	*0.94*	3.53	*0.94*
Tm	0.55	*0.18*	0.59	*0.43*	0.53	*0.24*	0.46	*0.18*	0.66	*0.23*
Yb	3.47	*1.06*	3.33	*1.02*	3.02	*0.72*	3.71	*0.75*	4.01	*0.83*
Lu	0.53	*0.18*	0.53	*0.26*	0.41	*0.11*	0.55	*0.14*	0.75	*0.17*
Hf	4.94	*0.85*	5.44	*1.26*	4.77	*1.02*	5.21	*0.79*	3.97	*0.68*
Ta	1.11	*0.25*	1.19	*0.42*	1.20	*0.34*	1.10	*0.24*	1.43	*0.31*
Pb	29.9	*46.83*	28.3	*9.83*	20.4	*3.82*	14.7	*1.94*	20.5	*3.09*
Th	20.2	*2.46*	21.0	*2.92*	18.3	*2.70*	21.7	*3.36*	25.3	*2.37*
U	4.25	*0.66*	4.36	*0.63*	4.50	*1.39*	4.22	*0.48*	4.97	*0.46*

Note: All major elements by EMPA; trace elements by LA-ICP-MS. Numbers are quoted as averages of n analyses, with 1 standard deviation (1sd). Ra refers to Rangitaiki pumice, Wh is Whakamaru.

Table 3.3: ***Chemistry of mafic inclusions and mixed-basaltic pumice***

	Whole-rock XRF			Glass av. (EPMA)	
Sample code	SB3065/1	SB3065/2	SB3065/3	SB3065	
(wt%)	Basalt incl.	Basalt incl.	Basalt incl.	*Av. (n = 40)*	*1sd*
SiO_2	53.24	53.30	53.44	58.63	*8.9*
TiO_2	0.67	0.62	0.67	0.27	*0.2*
Al_2O_3	19.10	19.39	19.22	23.04	*8.5*
FeO	9.68	9.69	9.66	2.88	*2.8*
MnO	0.15	0.14	0.13	0.08	*0.1*
MgO	5.91	5.90	5.99	1.17	*4.2*
CaO	8.35	8.21	8.06	9.31	*5.9*
Na_2O	2.17	2.04	2.12	3.28	1.44
K_2O	0.62	0.62	0.62	0.88	*0.8*
P_2O_5	0.09	0.09	0.09	0.10	*0.1*
Total	99.87	99.60	99.77	98.58	*1.4*
(LOI)	1.88	2.59	2.74	-	-
Rb	22	23	21	-	-
Sr	585	570	557	-	-
Y	12	12	12	-	-
Zr	57	56	55	-	-
Nb	2	2	2	-	-
Ba	666	724	669	-	-
Pb	7	12	8	-	-
Th	1	1	1	-	-
V	226	216	233	-	-
Cr	24	26	26	-	-
Ni	29	29	28	-	-
Zn	79	70	64	-	-
Ga	20	17	20	-	-

Notes: Glass chemistry of glass shards from mixed-pumice sample SB3065 is quoted as average of 40 analyses, and normalised (anhydrous); original total quoted. Major element data is in wt% (by EPMA), trace element data in ppm (by LA-ICP-MS).

3.3.3 Quartz characteristics

Quartz comprises 20 – 40% of the crystal fraction in Whakamaru and Rangitaiki pumices, and characteristically occurs as large, fractured and partially resorbed crystals ranging from 0.3 – 12 mm in diameter (Fig. 3.3). Quartz crystals are mostly anhedral, which is assumed to be due to resorption caused by changing conditions prior to eruption. They are also extensively fractured, most likely due to fragmentation caused by melt-inclusion explosion during pre-eruptive overheating and/or decompression, and syn-eruptive

shattering (Tait, 1992; Best and Christiansen, 1997; Gualda et al., 2004; Bindeman, 2005). The crystals appear uniform when examined by optical microscopy and BSE imaging (Fig. 3.3) but CL imaging reveals distinct growth zonation, most commonly with a dark CL core and bright rim of varying width (Figs 3.4, 3.5).

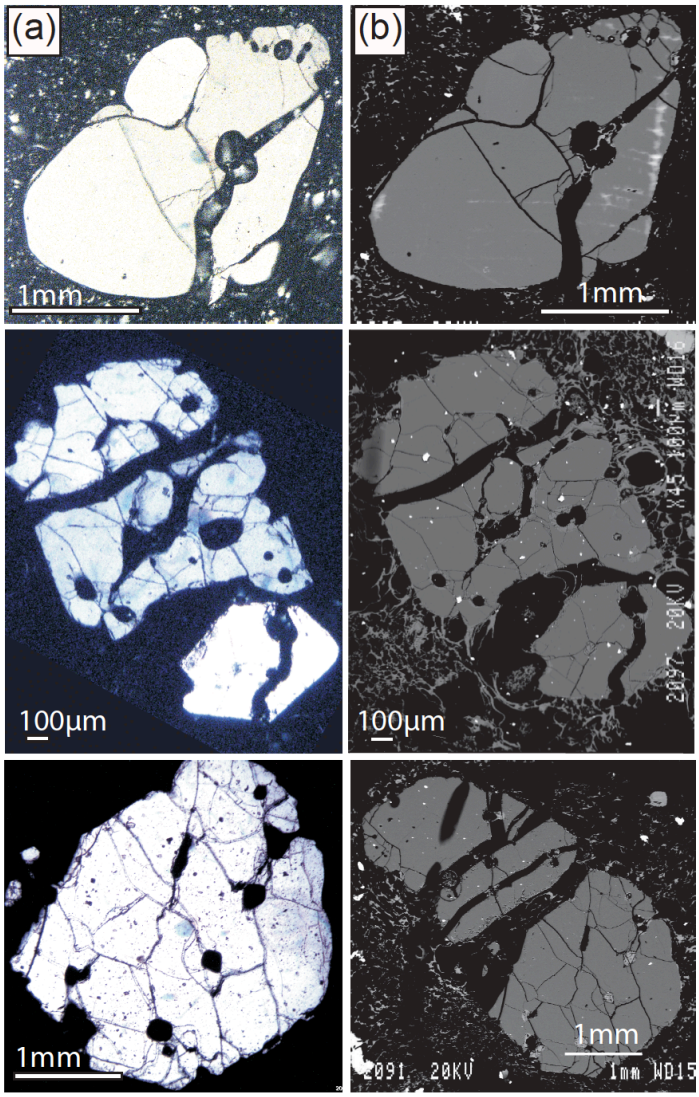

Fig. 3.3: (a) Optical microscope images of quartz from samples P1905 and P1915; (b) Back-scattered electron (BSE)-SEM images of quartz. Note fractured nature of quartz phenocrysts and resorption boundaries.

Oscillatory zoning is a characteristic of all the quartz grains examined (Fig. 3.4), and is marked by zones of alternating higher and lower CL intensity parallel to each other and to

the external crystal faces, unless truncated by resorption surfaces. The most notable feature observed in all quartz crystals is the sharp contrast in CL intensity along the profile, defining a core-rim boundary marked by a dissolution/resorption surface that truncates core growth zones (Figs 3.4, 3.5).

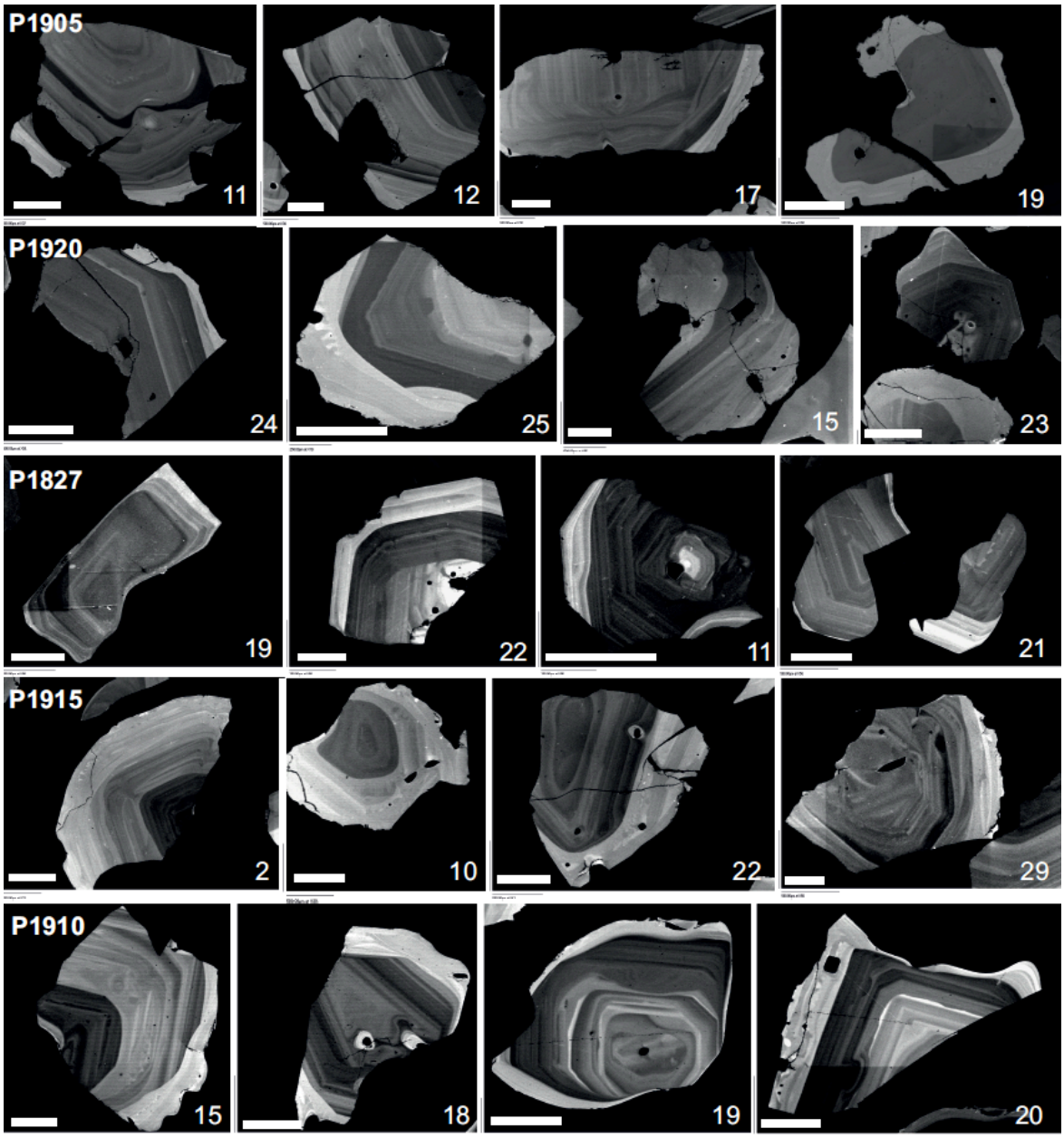

Fig. 3.4: CL images of quartz crystals extracted from the five selected pumice samples; Note bright CL rims and complex internal zoning in dark cores. Scale bar is 500 µm for all images. Codes refer to pumice samples where P1905, P1910, P1915 are Rangitaiki pumice and P1920, P1827 are Whakamaru.

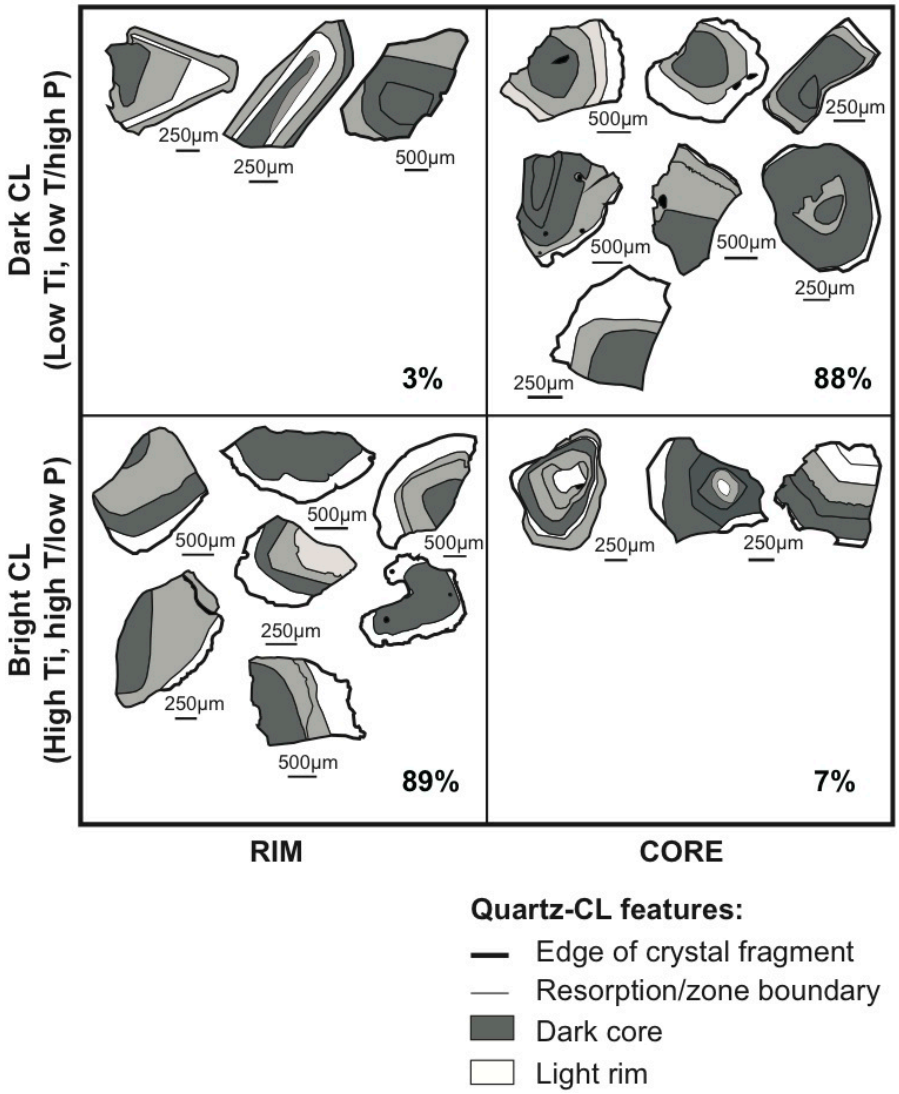

Fig. 3.5: Summary of quartz CL zoning patterns; bright CL rims and dark cores are the most characteristic of Whakamaru and Rangitaiki quartz.

Dark cores commonly host melt inclusions (often associated with local bright CL zones), and these disrupt the zonation pattern with subsequent crystallisation and zoning becoming concordant with the melt inclusion edge (Fig. 3.6). There is no evidence to suggest post-entrapment crystallisation – the melt inclusions are not faceted, and there are no microlites. These inclusions are interpreted as melt pockets, which were connected to the host melt out of the plane of the polished section, and that quartz growth (with the accompanying changes in Ti partitioning into the crystal) continued until the inclusions became trapped or were quenched by eruption. The majority of melt inclusions (~ 85%) are located toward

the interior core of the crystals, within darker zones, with only ~ 15% found in crystal rims. The preferential occurrence of melt inclusions in the dark cores suggests that the dark-CL zones represent periods of rapid crystal growth (Peppard et al., 2001). Melt inclusions are also present in the light-CL rims, however, and the detailed zoning patterns observed in the rims are characteristic of rapid growth structures.

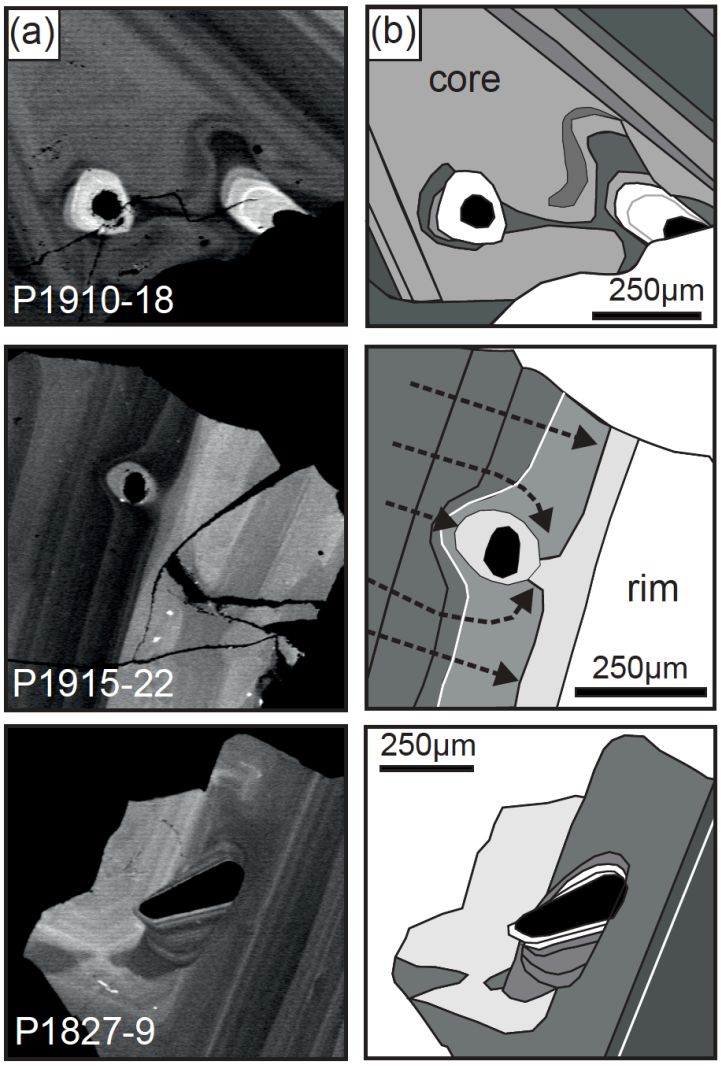

Fig. 3.6: (a) SEM-CL images of melt inclusions in quartz crystals. The inclusion of glass causes a growth embayment and locally disrupts CL zoning, forming a nucleation point for new crystal growth. (b) Sketches of growth zoning around the quartz-hosted melt inclusions. Arrows indicate crystal growth direction.

Resorbed and embayed parts of crystals and dissolution surfaces are found throughout the crystals but are prominent at both the crystal core and near the rim. Resorption surfaces

are typically rounded or display complex dissolution patterns, and are often associated with a bright CL zone. Distinct compositional changes occur across the resorption horizons with marked increases in Ti (up to 100 ± 10 ppm) occurring over distances of < 60 μm (Section 3.4.1). Rims are Ti-rich (bright CL; 90 – 138 ppm Ti) and are generally narrow (< 100 μm, but are sometimes wider at > 200 μm). The true rim is not necessarily observable, however, because the crystal rims may angle outward and extend down into the epoxy mount. Furthermore, resorption would result in some of the rim being missing. This rim-width range should therefore be considered as involving minimum values. Cores display dark CL (Ti-poor: 30 – 96 ppm) with internal zonation truncated by a resorption surface around which the bright rims have crystallised.

3.3.4 Magmatic temperature estimates

Crystallisation temperatures were estimated by four methods based on Fe-Ti oxides, feldspar-melt equilibria, amphibole chemistry, and the TitaniQ method (across CL zones in quartz crystals from core-to-rim), as described in Sections 3.2.3 and 3.2.5 and with results summarised in Table 3.4, Fig. 3.7 and Appendix 10 (amphibole geothermobarometry).

Over all pumice samples, the four suites of temperature estimates have a range of 655 – 975°C, but display a strong mode at 770°C (Fig. 3.7). The inferred eruption temperature for the Whakamaru and Rangitaiki ignimbrites is therefore 770°C, as derived from Fe-Ti oxide compositions using the Ghiorso and Evans (2008) formulation (Figs 3.7, 3.8). Oxygen fugacity was estimated from Fe-Ti oxide equilibria using the method of Ghiorso and Evans (2008). Values for all pumice clasts range from -0.03 to 1.08 log units above the nickel-nickel oxide (NNO) buffer (Table 3.4; Fig. 3.8; Appendix 9), with uncertainties of approximately ± 0.17 log units (1sd).

Table 3.4: ***Geothermometry data (in °C) for the pumice clasts***

Pumice Sample	Fe-Ti oxides					TitaniQ		Feldspar-melt equilibria	
	T **(°C)**	± 1sd	logfO_2 NNO	± 1sd	***n***	**min**	**max**	**min**	**max**
P1905	763	59	+0.41	0.25	20	689	836	763	854
P1910	768	84	+0.30	0.21	26	673	802	788	860
P1915	763	48	+0.39	0.18	21	673	836	757	852
P1920	790	8	+0.35	0.18	66	673	836	785	848
P1827	-	-	-	-	-	655	778	730	884

Notes: Fe-Ti oxide data for equilibrium pairs (determined by the method of Ghiorso and Evans, 2008); Oxygen fugacity is quoted in logfO_2 relative to NNO buffer, values represent averages from number (n) of Fe-Ti oxide pairs (in equilibrium according to the method of Bacon and Hirschmann, 1988) and ± indicates 1 standard deviation. Note that no data from Fe-Ti oxide equilibrium pairs were collected for sample P1827. TitaniQ values using Wark and Watson (2006) equation and an a_{TiO2} of 0.7. Feldspar-melt equilibria calculated using Putirka (2008) formulation and only plagioclase feldspar rim data and co-existing glass (by EPMA).

Feldspar-melt temperatures calculated using plagioclase rim (av. $An_{33\pm7}$, 1sd) and matrix glass (melt) compositions suggest magma temperatures of 817 ± 28°C (1sd) (Fig. 3.7). Plagioclase phenocrysts are commonly resorbed, suggesting that they were not crystallising at the time of eruption and therefore do not record eruption temperatures. Amphibole geothermometry using the Ridolfi et al. (2010) formulation provides a comparable temperature range of 745 – 975°C (uncertainty ± 22°C; Appendix 10). Amphiboles show a bimodal temperature data set with strong modes at 770°C and 860°C (Fig. 3.7). The wide temperature range reflects changing temperature conditions as recorded during amphibole crystallisation. The Fe-Ti oxide temperatures have a strong mode coincident with the lower amphibole temperature mode from the Ridolfi et al. (2010) formulation (Fig. 3.7), similar to that observed for the Oruanui eruption (Wilson et al., 2011).

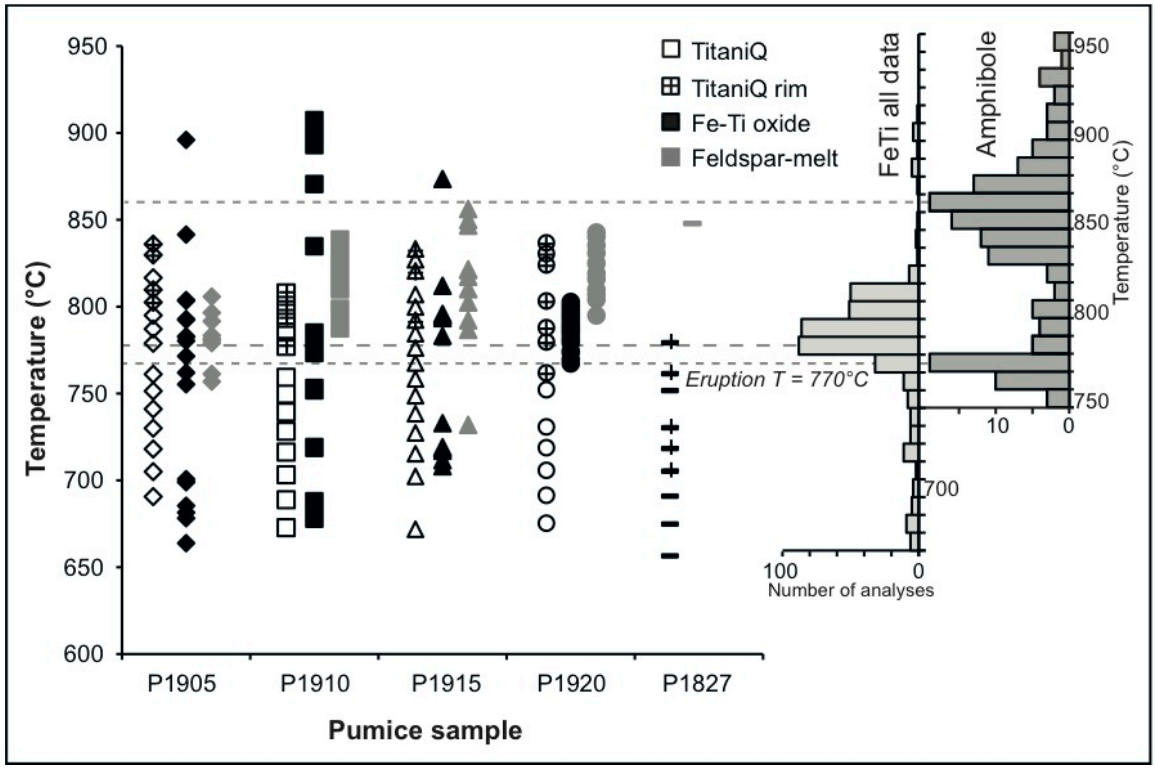

Fig. 3.7: Comparison of temperatures obtained from TitaniQ, Fe-Ti oxides and feldspar-melt geothermometry for selected single Whakamaru pumice clasts. TitaniQ temperatures calculated from Wark and Watson (2006); Fe-Ti oxide temperatures calculated from Ghiorso and Evans (2008) for magnetite-ilmenite equilibrium pairs; Bacon and Hirschmann (1988). Feldspar-melt temperatures from Putirka (2008). The first histogram on the right shows Whakamaru Fe-Ti temperatures recalculated from Brown et al. (1998a) data for comparison. The second histogram displays amphibole temperatures recalculated from Brown et al. (1998a) data using the Ridolfi et al. (2010) formulation. The dashed grey lines show modes for Fe-Ti oxide and amphibole temperatures.

The Ti activity derived from Whakamaru melt compositions, a_{TiO2} = 0.7 (Section 3.2.4), is lower than values estimated for the TVZ Rotoiti and Earthquake Flat magmas (a_{TiO2} = 1; Smith et al., 2010), but similar to the value for the Oruanui rhyolite (0.74 ± 0.07; Wilson et al., 2011). Using a single a_{TiO2} value for all quartz crystal zones is, however, an oversimplification given the inter-dependence with temperature that is changing concurrently. Ti concentrations in Whakamaru quartz range 30 – 138 ppm, corresponding to temperatures of 655 – 836°C (± 15°C, 1sd) using the TitaniQ formulation (Wark and

Watson, 2006; Table 3.5; Fig. 3.7; Appendix 11), and assuming no pressure dependence (cf. Thomas et al., 2010), constant a_{TiO2}, and no other causes for variations in Ti uptake (cf. Wilson et al., 2011). The lowest values are recorded in the crystal core, and typically increase in a fluctuating step-wise pattern towards the rim, as shown in Fig. 3.10. The maximum temperatures recorded from quartz rims are too high for quartz crystallisation in a rhyolite melt (Hammer, 2008), which implies that these high temperatures are misleading and likely to be related to either boundary layer kinetics or errors resulting from the assumption of constant a_{TiO2} and no pressure dependency.

Table 3.5: ***Pressure and temperature estimates for quartz rims and cores using end-member a_{TiO2} values***

Quartz crystal zone	a_{TiO2}	Av. Pressure (MPa)	1sd	Pressure range (MPa)	Av. Temp (°C)	1sd	T range (°C)
RIM	0.5	663	0.81	553 – 837	849	32	757 – 886
CORE	0.5	922	1.99	553 – 1313	767	38	689 – 864
RIM	0.7	830	0.81	720 – 1004	802	30	717 – 836
CORE	0.7	1065	2.37	553 – 1480	727	35	655 – 816
RIM	1	1008	0.81	898 – 1182	756	27	678 – 787
CORE	1	1217	2.85	553 – 16.58	687	32	621 – 770

Notes: Estimates of pressure based on Thomas et al. (2010) formulations (at fixed temperature of 770°C) and temperature based on equations from Wark and Watson (2006) TitaniQ, using rounded end-member a_{TiO2} values from calculations and in comparison with a_{TiO2} values of 0.5 and 1 (providing minimum and maximum temperature estimates respectively).

Whakamaru and Rangitaiki TitaniQ values are broadly consistent with Fe-Ti oxide equilibrium temperatures (Fig. 3.8), although they display a greater temperature range. This is expected since the Ti contents and consequent TitaniQ temperatures are related to individual crystal zones over the growth history of the quartz crystals. This disparity in temperature records can also be attributed to differences in rates of diffusion in the

different mineral phases. Elemental diffusion is faster in Fe-Ti oxides than quartz: diffusion of Ti in quartz is given by equation [3.9] (discussed further in Chapter 4):

$$D_{Ti} = 7 \times 10^{-8} \exp(-273 \pm 12 \text{ kJ mol}^{-1} / RT) \text{ m}^2\text{s}^{-1}, \quad [3.9]$$

(quoted parallel to the 001 axis, over the temperature range 700 – 1150°C; Cherniak et al., 2007) with timescales of years involved (Chapter 4); whereas Fe-Ti oxides re-equilibrate by diffusion on timescales of days to months (Devine et al., 2003). Oxide temperatures thus reflect more the temperature of eruption (or temperatures in the magma system weeks to months prior to eruption; Devine et al., 2003) rather than thermal fluctuations during crystal growth.

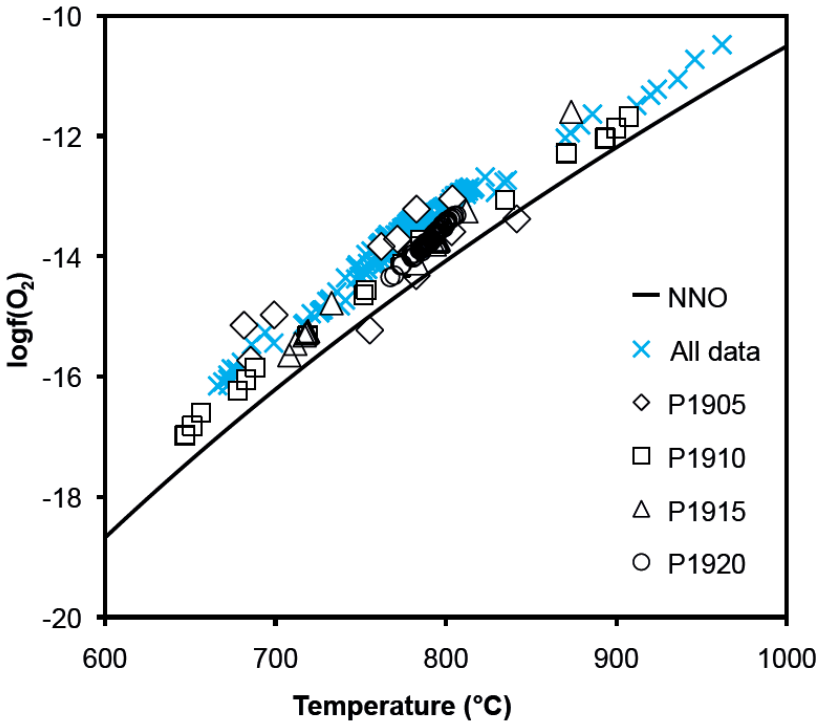

Fig. 3.8: Temperature and oxygen fugacity (log$f$(O_2)) calculated for titanomagnetite-ilmenite pairs from Whakamaru Group pumices, by the method of Ghiorso and Evans (2008). Plotted are results for the five Whakamaru pumice clasts and recalculated values from Brown et al. (1998a). Data are provided in Appendix 9. Samples are identified in key. NNO buffer curve after Huebner and Sato (1970) determined at 1 bar.

The large range in temperature determinations from Fe-Ti oxides observed here (Figs 3.7 and 3.8) is potentially due to pluton recycling (with the lower estimates being subsolidus). The 770°C mode recorded by the Fe-Ti oxides (and amphibole) is thought to reflect the final reheating temperature on eruption, and is not recorded by the quartz rims due to resorption.

3.3.5 Magmatic pressure estimates

The quartz-albite-orthoclase (Qz-Ab-Or) projection of glass major-element analyses from single pumice clasts (Fig. 3.9; Blundy and Cashman, 2001) indicates low closure pressures of 50 – 150 MPa. In silica- and water-saturated magmas like these, this pressure estimate is interpreted as representing the final storage pressure at which quartz and feldspar crystallised and the melt composition was 'frozen'. Assuming an average uppermost crustal density of 2500 kg m^{-3}, these pressures suggest shallow depths (~ 2 – 6 km) of crystallisation of the major mineral phases for Whakamaru and Rangitaiki magmas prior to eruption.

The Putirka (2005, 2008) feldspar-melt geothermometer is pressure sensitive (pH_2O), and calculations provide an average pressure of 235 ± 51 MPa (equivalent to ~ 9 km depth) and H_2O content of 4.01 ± 0.69 wt% (1sd; Putirka, 2008). This is consistent with water contents of 4.3 – 4.7 wt% in inherited Whakamaru-like melt inclusions in Oruanui quartz cores (Liu, Y. et al., 2006). Plagioclase compositions are sensitive to pH_2O, temperature and pressure, however, so the model cannot determine which variables were changing, and it is likely that they were changing simultaneously.

Pressures were also calculated from amphibole compositions using the formulations of Ridolfi et al. (2010) and the full suite of Whakamaru and Rangitaiki samples from Brown et al. (1998a). Calculations yield a unimodal population with a strong mode of 110 ± 14 MPa (with pressures ranging from 70 to 409 MPa), indicating hornblende crystallisation at crustal depths of ~ 5 km.

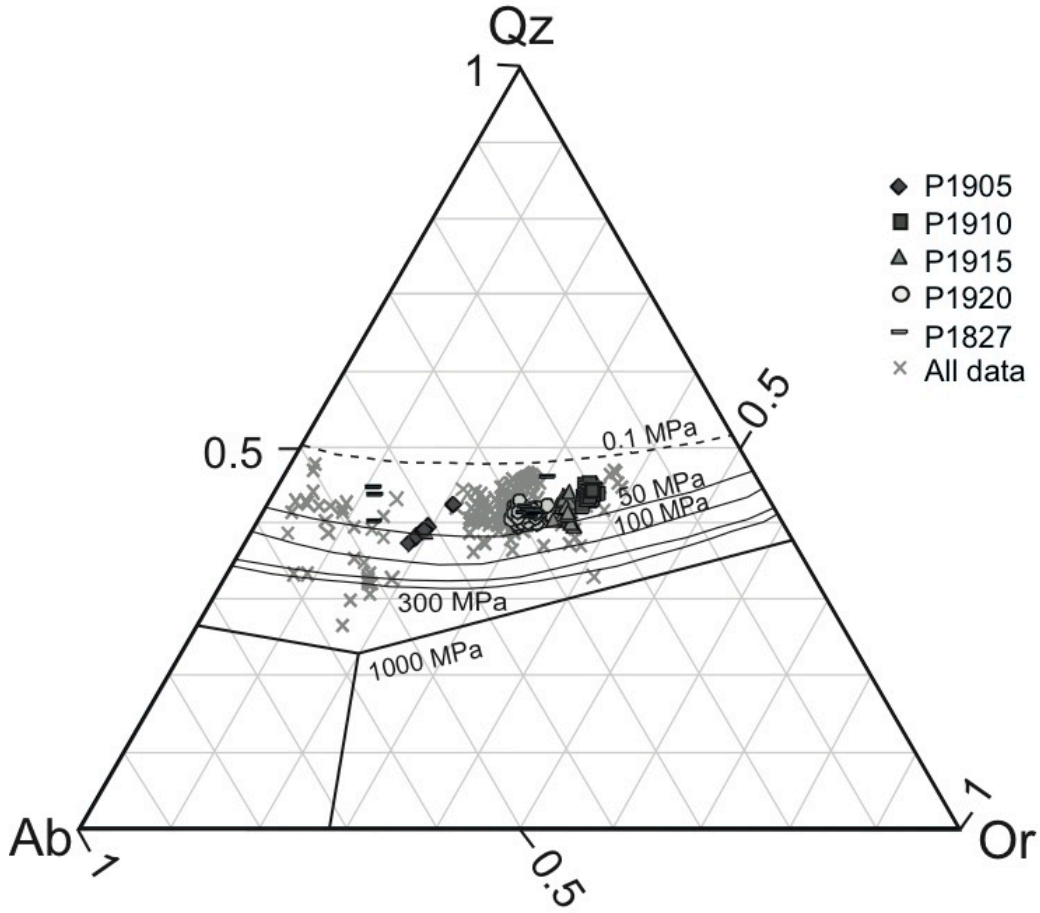

Fig. 3.9: Glass major-element compositions for the selected Whakamaru and Rangitaiki pumice samples plotted on the Qz-Ab-Or-H_2O system following method of Blundy and Cashman (2001). Closure pressure estimates range 50 – 150 MPa. 'All data' refers to the database of Brown et al. (1998a).

3.4 Discussion

3.4.1 Quartz zoning patterns

Quartz CL zoning patterns are illustrated in Fig. 3.5, classified in terms of dark/light rim/core combinations. Contrasting bimodal light/dark zonation is apparent in almost all crystals with 88% showing dark (low-Ti) cores and 89% with light (high-Ti) rims (high-Ti rims and low Ti-cores is classified as "reverse" zoning). The darker cores crystallised at a lower temperature range (655 – 787°C if calculated from TitaniQ; Wark and Watson, 2006), or with higher pressure or higher Ti activities in the melt, whereas rims involved relatively higher-temperature crystallisation, 778 – 836°C by TitaniQ (and/or lower-pressure and/or Ti activities in the melt). Quartz is unstable at the maximum temperatures calculated by TitaniQ here (Hammer and Rutherford, 2002; Hammer 2008), and therefore it is likely that melt composition and the dependence of a_{TiO2} on temperature play important roles in Ti partitioning.

Dark cores are truncated by a resorption horizon, suggesting that changes in melt composition and/or temperature/pressure interrupted crystallisation for a period. This period, by analogy with the Bishop Tuff (Wark et al., 2007), may have been associated with recharge, additionally represented during eruption by the basaltic andesite enclaves and basaltic-mixed pumices. A minority of crystals displays a resorbed light-CL core (7%; Fig. 3.5), suggesting initial crystallisation from higher temperature (and/or lower pressure and/or lower Ti activity) magma, or reflecting mixing of crystals between different zones in a thermally heterogenous magmatic system. Another minor population of crystals was characterised by anhedral dark-CL crystal rims (3%; Fig. 3.5).

Interpolated transects across crystals (Fig. 3.10) suggest abrupt periodic temperature increases (av. 66°C; max 105°C, if pressure and a_{TiO2} are assumed to be uniform). In comparison, at a constant temperature, these average changes would require a large (and unrealistic) pressure decrease (300 MPa, equivalent to a ~ 12 km rise: Thomas et al., 2010) or a sharp decrease of roughly 0.4 in a_{TiO2}. The changes are especially pronounced at the inner margins of the crystal rims, and are characteristic of quartz from the Whakamaru and Rangitaiki ignimbrites. In Fig. 3.10A, for example, the four crystals show sharply defined Ti increases of 53 – 67 ppm, equivalent to temperature increases of 80 – 110°C occurring within 300 μm of the crystal rim, while other samples (Fig. 3.10B) show smaller pulses in increments of 38 – 52 ppm Ti, equivalent to 60 – 90°C closer to the core (300 – 500 μm from rim). In addition, some crystals show separate sequential temperature spikes of up to 100°C further from the rim (> 500 μm). This indicates that the crystals experienced fluctuating conditions throughout their crystallisation histories, but with the most significant thermal event occurring towards the crystal rim. These smaller Ti spikes may, however, be due to kinetics of crystal growth and incorporation of high-Ti from boundary layers, which is feasible if growth rate is more rapid than diffusion. This competition between crystallisation and diffusion timescales can be defined by a Damköhler number (Ruprecht et al., 2008), *Da*, as follows

$$Da = \frac{t_{ad}}{t_{react}}, \qquad [3.10]$$

where t_{ad} is the theoretically derived advection timescale (Linden and Redondo, 1991) and t_{react} is the crystallisation or dissolution timescale. Using estimated quartz growth rates (~ 1 – 3 $\mu m\, y^{-1}$, see calculations in Chapter 4) as t_{react}, and diffusion at 770°C ($1.5 \times 10^{-9}\ \mu m^2\ s^{-1}$; Sections 4.3.4 and 4.4.3) as t_{ad}, then Da ≤ 1, which implies that crystallisation is fast

enough to explain the smaller Ti spikes, rather than being diffusion controlled. The compositional boundary which is the focus of diffusion modelling here is a more significant feature, however, and therefore not affected by the competition between growth rate and diffusion.

Using the Thomas et al. (2010) model and a fixed pressure of 235 MPa (from feldspar-melt calculations; see Section 3.4.2) the range in quartz rim and core temperatures is 681 – 753°C (av. 722 ± 25°C; 1sd) and 582 – 721°C (av. 645 ± 34°C, 1sd), respectively. These are significantly lower than values obtained from TitaniQ. Furthermore, using quartz entrapment pressures recorded from inferred Whakamaru-derived melt inclusions (110 – 140 MPa; Liu, Y. et al., 2006) the temperatures range 654 – 723°C for quartz rims, and 558 – 693°C for quartz cores. These temperatures are below the granite solidus for many pressures equivalent to crustal depths. The temperature ranges yielded by the Thomas et al. (2010) formulation therefore seem implausible at geologically reasonable pressures in the case of the Whakamaru magmas.

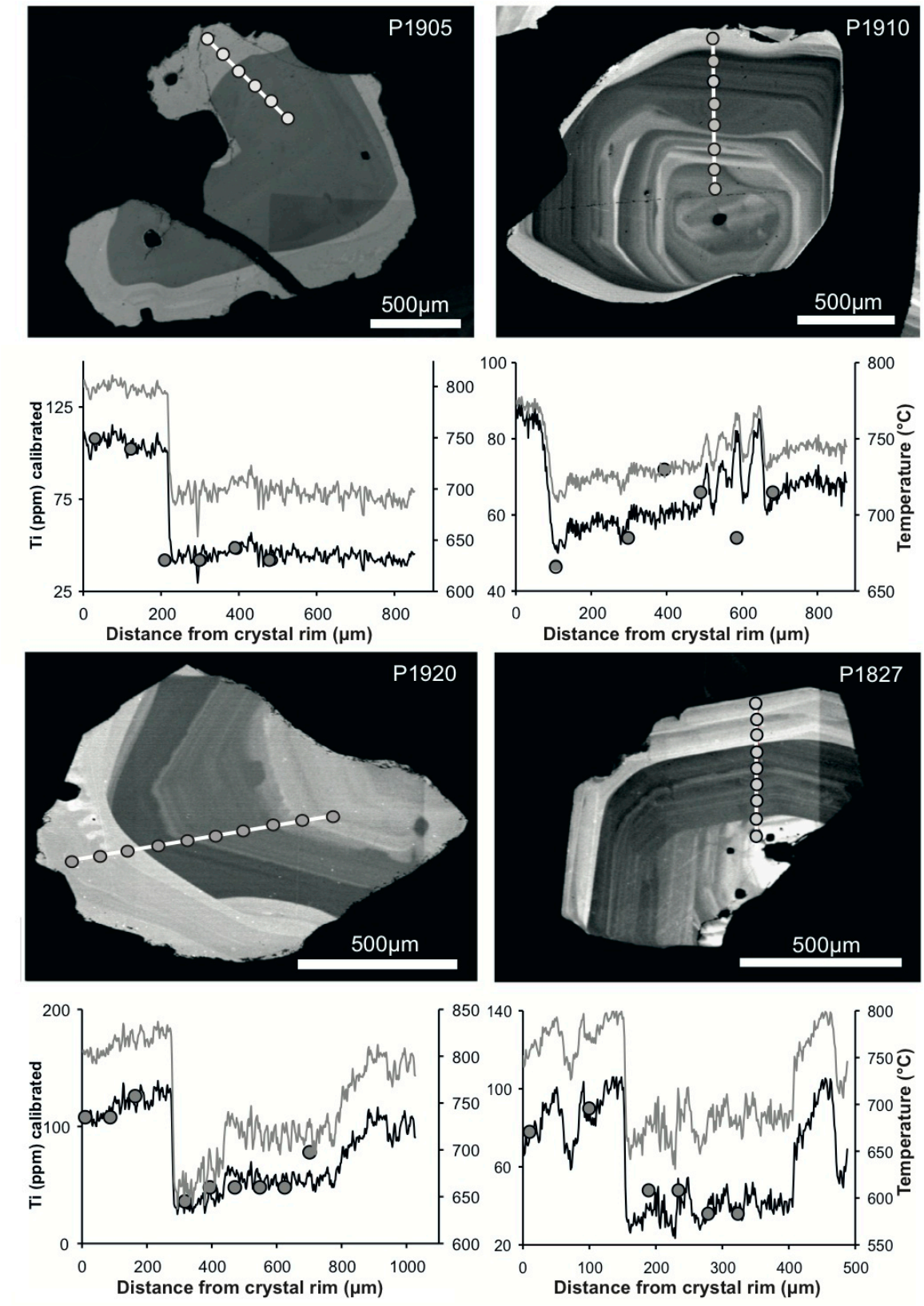

Fig. 3.10A: Selected CL images of quartz crystals showing location of EPMA transect. Profiles show calibrated Ti (black line) and temperature (grey line). The original EPMA Ti analyses used in the calibration are marked by grey circles. The temperatures are estimated from TitaniQ using a single a_{TiO2} of 0.7 and constant Ti concentrations in the melt.

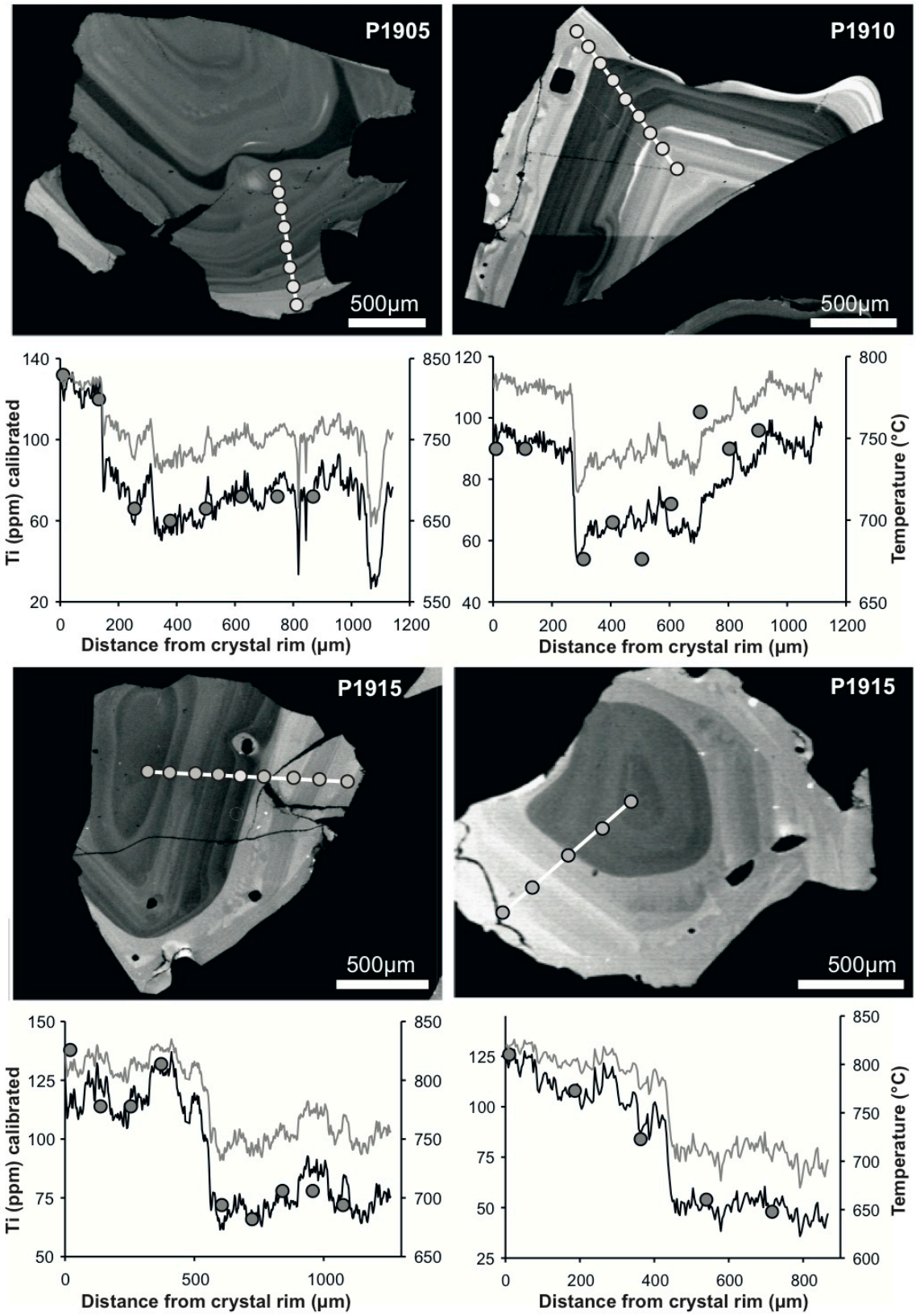

Fig. 3.10B: Selected CL images of quartz crystals showing location of EPMA transect. Profiles show calibrated Ti (black line) and temperature (grey line). The original EPMA Ti analyses used in the calibration are marked by grey circles. The temperatures are estimated from TitaniQ using a single a_{TiO2} of 0.7 and constant Ti concentrations in the melt.

3.4.2 Pressure within the system

As described in Section 3.2.3, new experimental data from Thomas et al. (2010) have demonstrated a pressure effect on Ti solubility in hydrothermally-grown quartz. These authors have suggested that quartz CL zoning could be produced solely by pressure changes at a constant temperature (whereby a decrease in pressure causes an increase in Ti content). Variations in Ti could therefore reflect temperature, pressure, melt composition, or a combination of these variables, affecting previous interpretations of TitaniQ results. Application of the Thomas et al. (2010) pressure-Ti relationships provides a broad pressure range of 800 – 1150 MPa at a fixed temperature (av. 1100 ± 200 MPa; a_{TiO2} = 0.7; calculated at average rim temperature of 825°C; Table 3.4). Quartz rims correspond to pressures of 800 ± 100 MPa (1sd), and dark cores to 1100 ± 200 MPa (1sd) assuming crystallisation at the same temperature, corresponding to depths of 32 – 44 km. These pressures would suggest initial crystallisation in the mantle below TVZ and are thus neither feasible for quartz crystallisation in the TVZ context (e.g., Nairn et al., 2004; Wilson et al., 2006), nor are they consistent with interpretations of crustal structure (Fig. 1.3; e.g., Harrison and White, 2004; Stratford and Stern, 2004). Other data from this study (Section 3.3.5), and others, have been used to constrain pressures of crystallisation within the system by independent means.

Liu, Y. et al. (2006) reported partially resorbed dark-CL cores in some of the quartz in pumices from the 27 ka Oruanui deposits, erupted from Taupo volcano. The trace-element characteristics of the melt inclusions in these dark-CL cores followed a pattern distinctly different to the other quartz-hosted melt inclusions, involving a Ba-compatible phase. The close compositional similarity between these anomalous inclusions in dark-CL quartz to those of Whakamaru type *D* pumice (Analysis SB1119, from Brown et al., 1998a) suggests

that these quartz cores represent recycled Whakamaru-age plutonic material (see also Charlier et al., 2010). Entrapment pressures from water (4.4 ± 0.1 wt%) and CO_2 (62 ± 20 ppm) contents measured by FTIR for the Whakamaru-derived quartz inclusions are 113 – 140 MPa (Liu, Y. et al., 2006), indicative of quartz growth at depths of 4 – 5.5 km. These entrapment pressures are for gas-saturated melts and are thus considered to provide reasonable pressure and depth estimates for the Whakamaru magma body.

Glass chemistry, feldspar-melt and amphibole geothermometry and quartz melt-inclusion data all suggest that crystallisation of the mineral assemblage dominantly occurred at shallow depths, at pressures of 50 – 150 MPa, 120 – 650 MPa (Putirka, 2008), 110 MPa (mode; Ridolfi et al., 2010) and 110 – 140 MPa (Liu, Y. et al., 2006), respectively. These values contradict calculations based on the Thomas et al. (2010) pressure relationship, indicating this does not correctly account for the pressure dependence in this system (Wilson et al., 2011). It is likely that pressure affects Ti solubility in the melt and uptake into the quartz and contributes to some of the zoning, but the relevant model does not yield pressures appropriate for these melts and does not allow adequate quantification of this effect. Similarly, the effects of water and other anions in the melt on Ti solubility and uptake into quartz (Wilson et al., 2011), have not been quantified and therefore it is difficult to assess how the observed Ti changes relate to these parameters.

3.4.3 Heat flow associated with mafic recharge

Results discussed above indicate significant changes in temperature and/or pressure and/or composition occurred prior to eruption (timescales associated with this event are discussed in Chapter 4). The relative consistency of zoning in quartz across all the crystals examined from both the Whakamaru and Rangitaiki ignimbrites suggests that these changes were

widespread in the overall magmatic system that was trapped in pumices sampled for these eruptive phases. This significant change in conditions is inferred to be due to an injection of mafic magma, as this is known to play a significant role in the behaviour of shallow silicic melt-dominant chambers in the TVZ (e.g., Turner and Campbell, 1986; Blake et al., 1992; Brown et al., 1998a; Leonard et al., 2002; Wilson et al., 2006; Shane et al., 2007, 2008b). In addition, some Rangitaiki pumices display mingled textures, with the dominant silicic melt co-existing with hornblende-bearing juvenile mafic material (Tables 3.1, 3.3), showing that the silicic and mafic magmas were in contact during eruption. The preservation of these mingled textures in the Rangitaiki pumice, and the lack of an intermediate mixed composition, are consistent with a sudden injection of mafic magma causing a thermal pulse or magma ascent (and pressure drop) prior to eruption. The observed mafic mixing in Rangitaiki pumices is clearly a syn-eruptive phenomenon, however, and a different event to the recharge event that most likely influenced the earlier growth of bright-CL quartz-crystal rims.

An energy conservation model was used to test the feasibility of raising the magma reservoir temperature by ~ 100°C and causing the observed amount of crystal resorption through mafic underplating. This modelling approach assumes that the change in quartz rim compositions is solely due to temperature rise, while melt composition, pressure and a_{TiO2} remain constant. The calculations also assume that the mafic input magma was basaltic (using the average composition of mixed-basaltic Whakamaru pumices, given in Table 3.3), added in a single pulse, and that it lost heat convectively to the rhyolitic chamber while it cooled and crystallised. These calculations assumed the following: specific heat capacity of rhyolite in the chamber was 1300 J kg^{-1} $°C^{-1}$ (Sutton et al., 2000; Bachmann and Bergantz, 2006; Wark et al., 2007; Michaut and Jaupart, 2011); density of

2350 kg m^{-3} (calculated for crystal-rich rhyolitic magma of av. 25% crystals of 2800 kg m^{-3} density and melt of 2200 kg m^{-3}, after Blake and Ivey, 1986); and that the intruding basalt had a density 2900 kg m^{-3}, specific heat capacity of 1500 J kg^{-1} °C^{-1} (Cottrell et al., 1999), and was injected at a temperature of 900 – 1100°C before cooling to a final temperature of 770°C. Parameters and values used in calculations are outlined in Table 3.6 and calculations discussed below.

MELTS modelling (Ghiorso and Sack, 1995; Asimow and Ghiorso, 1998; Gualda et al., 2010) was used to calculate the variation of crystallinity in the mafic intrusion as it cools, using an average mafic Whakamaru pumice composition (Table 3.3) at 200 MPa and 3 – 4 wt% H_2O. Variation of crystallinity (ϕ) with temperature for the mafic magma can be described by

$$\phi_{\text{int}} = 0.441 erfc(7.9 \times 10^{-3} \times T - 7.55), \qquad [3.11]$$

where *erfc* is the complementary error function (a special function of sigmoidal shape), ϕ_{ini} refers to the crystal content of the mafic intrusion, and T is temperature in °C (Fig. 3.11a). The change in melt fraction in the rhyolitic reservoir between emplacement and eruption temperatures is estimated as 15%, by assuming a reduction in crystallinity from 50% to 35%. This assumes an initial (locked) crystal mush, and uses the crystal-rich (30 – 40 %) type *A* pumice as representing the final crystallinity of the magma (although the exact crystallinity reduction cannot be accurately constrained). Using a simple statement of energy conservation, the amount of enthalpy loss by the intrusion

$$\Delta E_i = V_i \left[\int_{T_{i,ini}}^{T_e} \rho_i c_i dT + \int_{\phi_{i,ini}}^{\phi_{i,f}} \rho_i L_i d\phi \right], \qquad [3.12]$$

can be related to the amount of enthalpy change in the mush

$$\Delta E_m = V_m \left[\int_{T_{m,ini}}^{T_e} \rho_m c_m dT + \int_{\phi_{m,ini}}^{\phi_{m,f}} \rho_m L_m d\phi \right], \quad [3.13]$$

assuming an efficiency ξ (fraction of excess enthalpy of intrusion transferred to the mush)

$$\xi \Delta E_i = \Delta E_m . \quad [3.14]$$

In the equations above, the subscript *i* and *m* refer respectively to the intrusion and the mush, T_{ini}, ϕ_{ini} are respectively the temperature and crystallinity in the given magma at the time of the emplacement of the intrusion, and T_e and ϕ_f are respectively the eruption temperature and final crystallinity (see Table 3.6 for other definitions).

Using the fit of Fig. 3.11a and the parameters listed in Table 3.6, the intrusion efficiency (which refers to the efficiency of the crustal melting process by heat transfer, from Huber et al., 2010a, b) is calculated. The chamber and underlying intrusion are estimated to be ~ 1 km thick (mush thickness = volume/surface area). Results of efficiency calculations are illustrated in Fig. 3.11b, which shows the volume ratio of intrusion to mush as a function of melting efficiency.

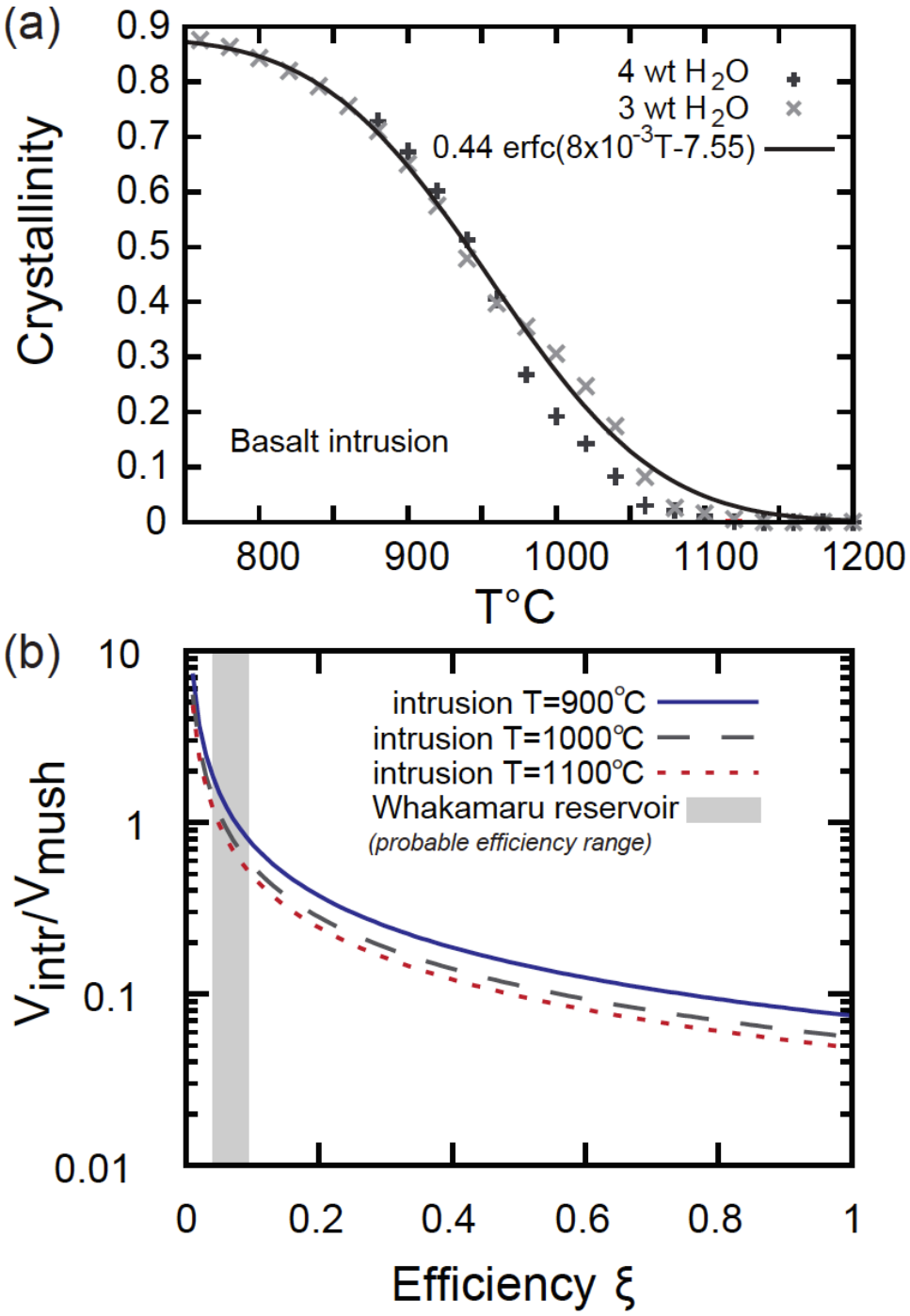

Fig. 3.11: Thermodynamic considerations for the underplating mafic intrusion. (a) Basalt crystallinity decrease with increasing temperature. Curves derived from MELTS (Ghiorso and Sack, 1995) using an average basaltic Whakamaru pumice composition; solid line represents a least-square fit for basaltic magma of 4 wt% H_2O; (b) volume ratio of magma (intrusion : mush) as a function of melting efficiencies; grey shaded region highlights the most probably range of efficiencies (from Dufek and Bergantz, 2005).

A completely efficient melting process can be defined as one where all of the enthalpy associated with cooling and crystallising a volume of intruded magma is used to heat and melt only the magma reservoir below which the intrusion ponds (Dufek and Bergantz, 2005). The most likely range of efficiencies is, however, ~ 5 – 10% where the intrusions are vertically stacked and cool on both sides (from Dufek and Bergantz, 2005) which points to an intrusion to mush ratio of ~ 1:1 (Fig. 3.11b). Therefore an estimated ~ 1000 km^3 of basaltic magma would be required to heat the ~ 1000 km^3 rhyolite magma reservoir by 100°C (assuming that the intruded magma cools to the temperature of the silicic melt), resulting in crystal dissolution followed by high-temperature rim crystallisation.

There are several difficulties with this model of rapid or incremental injection of large volumes of mafic magma however. Physical constraints with respect to the required accommodation space and efficiency of heat transfer through a thick cumulate pile are problematic. Furthermore, the degree of interaction between the underlying basaltic intrusion and rhyolitic chamber is likely to have been minimal due to the density differences between the two magmas. An additional source of energy is required if thermal reactivation of the crystal mush by mafic magma injection alone is invoked. Huber et al. (2010b) suggest that internal overpressurisation of the mush induced by small amounts of melting (10 – 20%) can break the crystalline framework by microfracturing, and thus allow for more efficient unlocking, and accelerating self-assimilation of the chamber and surrounding crustal lithologies. In considering the role of microfracturing, the volume of mafic underplating magma required in these heat balance models could be significantly reduced to values more feasible in terms of crustal accommodation space. It is also possible that although the change in volume may be responsible for unlocking the mush, the critical factor in the reactivation process is the thermal budget.

Streck and Grunder (1999) noted mixing between a mafic melt in the root zone of the Rattlesnake Tuff rhyolite chamber but proposed that the rhyolite formed a low-density cap that trapped the basalt, and thus thermally maintained the rhyolitic magma chamber, promoting internal compositional zonation. This implies that although calculations here indicate the involvement of a substantial volume of mafic magma, physical constraints mean that most of this mafic magma was not erupted, but instead provided the thermal feedback necessary to trigger processes in the overlying silicic reservoir.

Table 3.6: ***List of parameters and symbols used in thermodynamic calculations***

Thermodynamic parameter	Symbol	Value	Units	Ref
Initial melt fraction in the mush (locking point)	ϕ_{ini}	0.5		
Change in crystallinity in mush	ϕ_m	0.15		
Specific heat of intrusion	c_i	1500	$J\,kg^{-1}\,K^{-1}$	1
Specific heat of mush	c_m	1300	$J\,kg^{-1}\,K^{-1}$	1, 2, 3
Density intrusion	ρ_i	2900	$kg\,m^{-3}$	1, 4
Density mush	ρ_m	2400	$kg\,m^{-3}$	1, 5, 6
Latent heat of intrusion	L_i	4×10^5	$J\,kg^{-1}\,K^{-1}$	3
Latent heat of mush	L_m	2.7×10^5	$J\,kg^{-1}\,K^{-1}$	1
Intrusion emplacement temperature	T_{ini}	900-1100	°C	
Eruption temperature (final T intrusion, mush)	T_e	770	°C	
Difference in density that drives convection	$\Delta\rho$	10 – 100	$kg\,m^{-3}$	
Thermal diffusivity	κ	10^{-6}	$m^2\,s^{-1}$	
Viscosity	μ	10^5	Pa s	7, 2, 4
Chamber volume	V	1000	km^3	8
Chamber (mush) thickness (vol/surface area)	H	1	km	
Intrusion thickness	H_i	1	km	
Magma chamber depth	D	5	km	
Acceleration due to gravity	g	9.81	$m^2\,s^{-1}$	
Ideal gas constant	R	8.3145	$J\,K^{-1}\,mol^{-1}$	
Thermal conductivity of host rocks	k	2	$W\,m^{-1}\,K^{-1}$	

Notes: References as follows – (1) Wark et al., 2007; (2) Bachmann and Bergantz, 2006; (3) Michaut and Jaupart, 2011; (4) Cottrell et al., 1999; (5) Tait et al., 1989; (6) Blake and Ivey, 1986; (7) Scaillet et al., 1998a; (8) Brown et al., 1998a.

The 'gas sparging' model of Bachman and Bergantz (2006) may also apply here, whereby the underplating mafic magmas transport heat to the overlying crystal-rich rhyolitic chamber through the upward migration of a hot volatile phase. With volatile fluxes of > 0.1 $m^3 m^{-2} y^{-1}$, a large reservoir would require a significant volume of volatiles, however, which would require multiple sparging episodes in order to rejuvenate the crystal mush, taking up to 100 – 200 ky (Bachmann and Bergantz, 2006). It is clear that generation and differentiation of the silicic magma must have taken a significant period of time, of which the quartz crystals record only the final reheating stage prior to eruption.

3.4.4 Driving mechanisms for quartz zoning patterns: magma chamber models

There is clearly a significant change in late-stage growth conditions affecting a majority of the quartz crystals in the samples analysed. The above calculations assume that temperature is the dominant control on the Ti concentrations in quartz, although the effects of changes in pressure and melt compositional characteristics cannot be discounted or measured.

Similar CL zonation patterns occur in late-erupted Bishop Tuff quartz (and feldspar) and may reflect comparable processes and timings. One model proposed for the Bishop Tuff system, where crystals sink into hotter, less-evolved regions of a compositionally and thermally stratified magma system with subsequent crystallisation of the high temperature rim (Wallace et al., 1999; Anderson et al., 2000), cannot be applied here. This model is discounted for the Whakamaru system because gradual rim-ward changes in CL intensity (and Ti content) were not observed in these quartz crystals (in the crystal-sinking model, the change in Ti content would be a function of how quickly the quartz crystals sank in the chamber). Wark et al. (2007) also discount this model on the basis that they did not record

crystals that grew wholly within the hotter, less evolved melt body (although if temperatures are high enough quartz will not crystallise). The same argument would also apply to the Whakamaru magma body.

The following end-member scenarios are therefore considered to explain the distinct quartz zoning observed: (1) temperature control, with an abrupt increase in temperature; and (2) pressure control, with a significant pressure change; with both scenarios also considering the concomitant role of compositional changes in affecting the TiO_2 activity in the melt. These scenarios invoke an episode (or episodes) of mafic recharge that provides the driving force for subsequent changes in temperature, pressure or composition. The two end-member models are discussed separately in the following sections and summarized in Fig. 3.12.

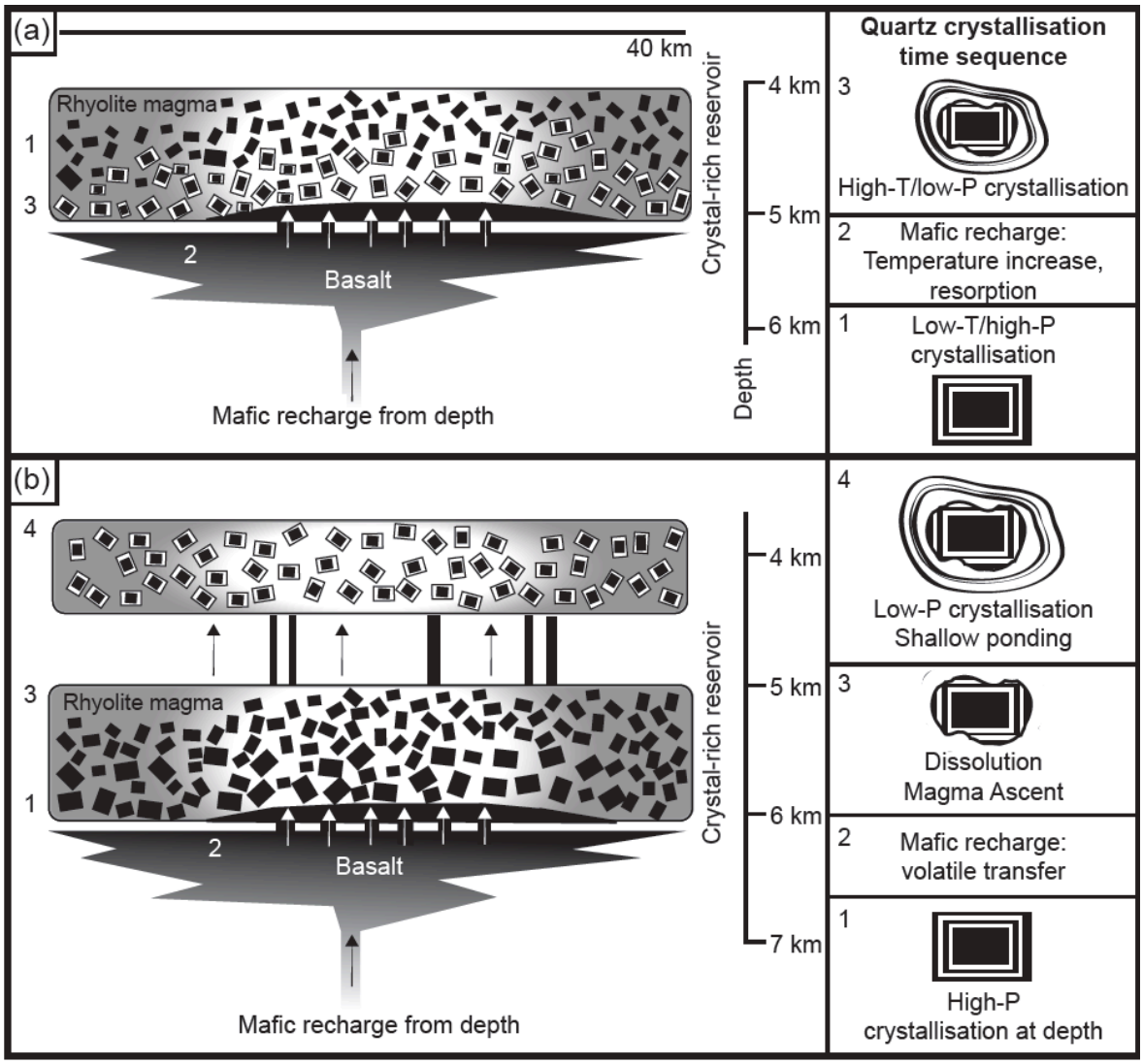

Fig. 3.12: Models for magma chamber processes responsible for generation of quartz crystal zonation patterns. Magma reservoir holds Whakamaru magma of type *A* composition, according to the Brown et al. (1998a) classification. Note: depth scale for magma reservoirs is based on data from quartz melt inclusion volatiles from Liu, Y. et al. (2006) and glass compositions; horizontal scale is derived from estimates of the caldera width from field geology.

(a) Single magma chamber model – Time 1 represents crystallisation at low-temperature/high-pressure within a crystal mush at depth; Time 2: Basaltic magma ponds at depth beneath the voluminous rhyolitic crystal mush, causing a temperature increase and resulting in resorption of quartz; Time 3: High-Ti (high-temperature or low-pressure) crystallisation of quartz rims prior to eruption. High-Ti quartz crystallisation could also be attributed here to a pressure drop associated with a smaller precursor eruption or partial degassing;

(b) Two-stage magma ponding – Time 1 represents crystallisation of high-pressure quartz cores at depth, with some minor fluctuations (in T/P or a_{TiO2}) producing subtle oscillatory zonation; Time 2: mafic recharge and ponding of mafic magma at base of rhyolitic mush causes a pressure change; Time 3: rhyolitic magma ascent accompanied by dissolution/resorption of quartz crystals; Time 4: Low-pressure rims crystallise during ponding and re-equilibration at shallow depths prior to eruption.

3.4.4.1 Temperature control

Mafic melts play an important role in the generation of large silicic magma bodies (e.g., Hildreth, 1981, 2004; Folch and Marti, 1998; Annen et al., 2006; Wark et al., 2007). Models suggest that hot, volatile-rich melts enter the upper crust and induce melting of the crust and any plutonic bodies within it, generating the silicic melt (e.g., Bachmann and Bergantz, 2006; Wark et al., 2007), in addition to the fundamental role of fractional crystallisation of mafic parents in generating silicic melts. In the lifetime of any large silicic magma body there are likely to have been innumerable recharge events that contributed heat and material to the system. Whakamaru quartz crystals appear to record the most significant of these recharge events, in addition to showing evidence for minor oscillations in temperature which shift conditions out of the quartz stability field and result in dissolution.

The bimodal Ti distributions (dark CL cores with truncated oscillatory zoning, surrounded by bright CL rims) observed here in most quartz crystals, and the temperature profiles at fixed pressure (Fig. 3.10), indicate that there were two phases of crystal growth: initially under low-temperature conditions followed by high-temperature crystallisation (assuming no change in melt composition and constant a_{TiO2}). The high-Ti overgrowth boundaries on CL-zoned quartz crystals typically truncate CL growth zoning within the core, and hence represent changes (in temperature, pressure and melt composition) associated with a recharge event. The recharge event would also cause the partial dissolution observed prior to high-temperature crystal-rim growth. The model developed here thus invokes initial lower-temperature crystallisation conditions (with minor fluctuations) followed by a significant recharge event during which hot mafic magma is injected into the deeper parts of the magma system (as proposed for the Bishop Tuff; Hildreth, 1979; Anderson et al.,

2000; Wark et al., 2007). This thermal pulse results in an initial resorption of crystals as quartz becomes unstable. Quartz rims are then able to crystallise at higher temperature either if (a) the pressure drops, or (b) the injected mafic magma is CO_2-rich, which would decrease XH_2O (although if magma is close to water saturation this will only have a minor effect), raise the solidus temperature and affect a_{TiO2} (Wark et al., 2007).

The detailed growth zonation preserved within bright-CL crystal rims (Fig. 3.10) indicates there may have been multiple minor recharge pulses during crystallisation that resulted in crystallisation of the high-temperature rims. This complex oscillatory zoning (Fig. 3.10) may also have been due to fluctuations in a_{TiO2}, small temperature variations, textural instability at the growing crystal front within the melt (Allegre et al., 1981), and the competition between diffusion through the melt and crystal growth rate.

3.4.4.2 Pressure control

Although the Ti/pressure relationships proposed by Thomas et al. (2010) yield unrealistic absolute pressures for Whakamaru quartz crystallisation, there remains the possibility of a relative pressure effect on Ti concentrations in quartz. Given a uniform temperature and assuming uniformity in compositional parameters, the dark-CL quartz cores would imply crystallisation at higher pressures, followed by lower pressure crystallisation of bright-CL rims. The truncated CL zones of quartz cores could be considered to reflect resorption during adiabatic ascent of the magma and its crystal cargo, with ponding and re-equilibration at a shallower level where the bright-CL rims would crystallise (Thomas et al., 2010). Mafic recharge could also be invoked here as the mechanism triggering ascent of the magmas, due to the lowering of density in response to the influx of volatiles or temperature increase (e.g., Folch and Marti, 1998; Snyder, 2000), similar to mechanisms

suggested by Wark et al. (2007) for the Bishop Tuff. However, under such circumstances it is difficult to envisage temperatures and melt compositions remaining uniform, with changes in Ti uptake into quartz being attributable solely to pressure changes.

Drawing on the above temperature and pressure considerations, a mechanism by which the low-Ti followed by high-Ti quartz can be crystallised within a single magma chamber is considered in Fig. 3.12A. This model suggests that initial low-Ti quartz crystallisation occurs at depth (high pressure) within the large crystal-rich magma reservoir. In order for the high-Ti, low-pressure quartz rims to crystallise within the single chamber there must be either (a) a small eruption prior to the main caldera-forming event (although there is no direct evidence for this); or (b) change in volatile species in response to mafic magma interaction (altering the H_2O-CO_2 balance).

A model that includes two-stage evolution of the magma body is also suggested (Fig. 3.12B), paralleling those for the Minoan rhyodacite (Cottrell et al., 1999), the Bandelier magmatic system (Campbell et al., 2009), and the two-stage rhyolite magma-storage model proposed by Smith et al. (2004) for the Rotorua eruption. This model involves crystallisation of dark-cored quartz (and other crystal phases) at depth followed by injection of a volume of mafic magma that underplates the rhyolitic crystal mush and provides enough thermal energy to resorb the quartz crystals and initiate magma chamber stirring. The reactivated mush then rises to shallower depths where quartz re-equilibrates and crystallises lower pressure, higher temperature (higher-Ti) rims prior to eruption. The pressures and depths suggested by the Thomas et al. (2010) model cannot be satisfactorily applied in a TVZ context, as it implies crystallisation in the upper mantle, therefore the depths for the magma reservoirs are derived instead from quartz melt-inclusion volatile

contents (Liu, Y. et al., 2006) and amphibole and glass chemistry pressure estimates, all of which suggest shallow magma storage levels for quartz rim crystallisation of < 6 km.

Thomas et al. (2010) suggest that the dark CL cores of quartz crystals from the Bishop Tuff and Katmai rhyolites grew in a deep-crustal crystal-mush root zone at pressures greater than the final emplacement level, followed by emplacement of a batch of magma to an upper-crustal reservoir where the bright CL rim grew (as depicted here in Fig. 3.12b). This is consistent with models of Hildreth and Wilson (2007) which suggested that large-scale rhyolitic systems may be constructed of crystal-poor, upper-crustal magma chambers that grade down into quartzo-feldspathic crystal-mush zones extending from mid- to lower-crustal regions.

There are complicating issues associated with this model of two-stage magma ponding. Firstly, the reactivated magma which ponds at shallow crustal levels must still be crystal-rich and of high viscosity, which is difficult to explain in terms of a crystal-mush model. Secondly, the thickness of the crust in central TVZ (8 – 10 km; Stratford and Stern, 2004, Stern et al., 2006) means there are significant limitations in terms of the thickness of a magma chamber pile which can be accommodated within the crust. In addition, considering that the timescale for quartz residence in the upper reservoir is < 100 y (see Chapter 4), this would imply that the transfer of 1000 km^3 of crystal-rich, extremely viscous magma was transferred in a shorter timescale from a deeper reservoir to the shallow one. This is a significant mass of magma to be transferred, and would require additional energy sources to account for this phase of magma transport.

Given these limitations of a model whereby pressure changes are the main driving force of quartz zonation, the temperature-controlled scenario (Section 3.4.4.1) is preferred for the Whakamaru magma systems.

3.4.5 Comparison of quartz zoning patterns with other caldera-forming eruption deposits

It is pertinent to consider characteristics of the Whakamaru supereruption in comparison with other large-scale eruptions. Other comparable eruptions for which quartz studies have been conducted are the Bishop Tuff (USA), the Oruanui eruption from Taupo (TVZ), and the significantly smaller Okataina Caldera Complex eruptions (the 120 km^3 Rotoiti and two ~ 5 km^3 eruptions from Tarawera, TVZ).

Whakamaru quartz zoning patterns are similar to those of late-erupted Bishop Tuff quartz, which display bright rims (up to 100 ppm Ti) and dark-CL cores (~ 50 ppm Ti; Wark and Watson, 2006). Despite strong similarities in CL zoning patterns, Bishop Tuff quartz Ti concentrations are lower than values obtained for Whakamaru quartz (bright rims of 90 – 138 ppm Ti and dark-CL cores of 30 – 96 ppm Ti). This contrast might in part be explained by the lower a_{TiO2} values suggested for Bishop Tuff when compared to Whakamaru (0.53 vs. 0.7: Reid et al., 2010; this Chapter). The truncated internal CL growth zoning in quartz cores (Wark et al., 2007) indicates partial crystal dissolution prior to growth of the high-temperature rims. This rimward jump in Ti concentration across the zone boundaries is likely to have been too abrupt (~ 40 ppm change over < 10 μm) to have survived magmatic temperatures for more than ~ 100 y (Wark et al., 2007). It seems then that magma recharge into the Bishop Tuff system within 100 y of the climactic eruption

heated and induced partial dissolution of quartz, followed by the crystallisation of a higher-Ti rim (high temperature rim in the model of Wark et al., 2007).

Oruanui quartz displays four types of CL zoning patterns, which did not correlate with the eruption sequence: oscillatory, irregular cores of bright CL, wide bright-CL zones and jagged cores surrounded by brighter CL rims (Liu, Y. et al., 2006). Whakamaru quartz displays similarly complex zoning but, in contrast, is more consistent in terms of zonation patterns. Melt inclusion data implied that the top of the Oruanui magma body was at ~ 4 km depth, with an increasing amount of total exsolved gas with depth, indicating decreasing density leading to convective instability and mixing (Liu, Y. et al., 2006). The evidence for multiple melt inclusions and reentrants in single quartz crystals suggest that magma mixing probably occurred multiple times, forming a parallel with the complex magma history implied by Whakamaru quartz zoning. The latest mixing events occurred immediately prior to and during the eruption, as indicated by mixed crystal populations and the presence of quenched mafic enclaves (Wilson et al., 2006), but there are no signs of corresponding higher-Ti overgrowths on the Oruanui quartz crystals.

Rotoiti quartz displays very different Ti and CL zoning profiles to those observed for Whakamaru (Smith et al., 2010). These quartz crystals are characterised by a gradual decrease in Ti concentration towards the rim, with only a few crystals (in early eruption phases) showing Ti-rich rims. Similar inferred temperature values have been proposed from TitaniQ for the Rotoiti quartz from the Whakamaru eruption, of 643 – 786°C (Smith et al., 2010). In contrast to the short diffusion timescales experienced by Whakamaru quartz crystals (see Chapter 4), Rotoiti quartz has diffusion-based timescales which vary considerably, from 100 to 2000 y, interpreted as reflecting numerous thermal perturbations

to the system (Smith et al., 2010; see Chapter 4 for discussion of quartz-derived timescales for the Whakamaru system in comparison to other silicic eruptions). Tarawera quartz crystals are also distinct from Whakamaru in that they typically have bright cores with a gradation to darker rims (Shane et al., 2008b). Oscillatory and truncated patterns are also well developed in Tarawera quartz, and some crystals display very bright mid-crystal zones or bands of variable width and irregular texture (Shane et al., 2008b), features similar to those recorded in some granites (Wiebe et al., 2007). CL-brightness zone boundaries in quartz from two Tarawera eruptions were found to be a maximum of 2 μm wide (Shane et al., 2008b), thus constraining zoned quartz residence times to a maximum of 20 y at 750°C, using Ti diffusivities from Cherniak et al. (2007).

It therefore seems that the Whakamaru system involved pre-eruption magma chamber processes that more closely parallel the Bishop Tuff system, consistent with the larger scales in eruption magnitude and magma chamber volumes. In terms of the quartz record of multiple recharge events throughout the crystallisation history, the similarities discussed here indicate that the episodic recharge process is common to many large silicic magma systems, with subtle complexities in terms of intrusion timing and magmatic response that are specific to each system.

3.5 Conclusions

Complex zoning is observed in the volumetrically important quartz crystals in the Whakamaru eruption deposits. Crystals are characterised by cycles of resorption, accompanied by temperature/pressure/compositional fluctuations, as recorded in the CL zonation and Ti concentration profiles. These variations in crystal zoning cannot be

generated solely through closed system process (e.g., crystallisation), and thus indicate that the systems were open to recharge. It is particularly noted that overgrowths encase truncated CL growth zoning within the dark cores, indicating a major period of resorption, heating and subsequent re-growth, consistent with recharge and multi-stage crystallisation. The major step in Ti content (and CL brightness) towards the crystal rims provides evidence for a magma chamber recharge event resulting in elevation of temperature and/or a reduction in pressure and/or a change in melt chemistry due to ponding at shallow crustal levels, and can be modelled as rapid rejuvenation of a crystal mush to a melt-dominant body.

Two 'conventional' end-member mechanisms for the formation of high-Ti quartz rims are (1) a thermal pulse due to mafic underplating of the rhyolitic crystal mush (e.g., Wark et al., 2007), or (2) adiabatic ascent of the magma resulting in a pressure reduction, resorption, and crystallisation of lower-pressure rims during shallow ponding (e.g., Thomas et al., 2010). The presence of mixed basaltic pumices in the Whakamaru and Rangitaiki ignimbrites provides evidence for syn-eruptive mafic recharge and mixing as a driving force during the eruption, and it is inferred that a similar event or events contributed to the resorption and Ti concentration variations recorded in the quartz.

Quartz zoning patterns thus provide evidence that the Whakamaru magma reservoir system experienced a significant heating/decompression event prior to catastrophic eruption, and its evolution over the time span represented by quartz crystals is punctuated by thermal events and/or ponding at different depths with re-equilibration prior to eruption.

Chapter 4

Timescales of magma recharge and reactivation of large silicic systems from Ti diffusion in quartz[2]

4.1 Introduction

Major goals in volcanology are the understanding of how supereruptions are triggered, how voluminous silicic melts are stored, and the timescales over which these processes occur. This chapter is concerned primarily with the timescales of magma recharge and reactivation.

The rates and timing of pre-eruption magmatic processes occurring in large-volume magma chambers are poorly known, yet this information is essential in understanding and quantifying these magmatic systems. Diffusion modelling of chemical gradients in minerals is an important chronological tool that can provide constraints on the timing and duration of thermal, chemical and eruption-triggering events. Kinetic modelling tools have been applied to investigate timescales and processes in a range of volcanic settings (e.g., Nakamura, 1995; Zellmer et al., 1999; Coombs et al., 2000; Klügel, 2001; Costa and Chakraborty, 2004; Morgan et al., 2004; Shaw, 2004; Costa and Dungan, 2005; Morgan and Blake, 2006; Costa et al., 2008; Costa et al., 2010). High-resolution compositional profiles across zoned crystals can be used to determine the residence times of crystals at magmatic temperatures, using known diffusion rates for the element under consideration.

[2] Much of the material in this chapter is in a submitted paper, Matthews et al. (2011c), Journal of Petrology

This temporal information can then be linked with the magmatic processes responsible for generating the compositional changes.

Here the *TitaniQ* geothermometry results (Chapter 3) are developed further, together with interpretations of CL images (Watt et al., 1997; Götze et al., 2001, 2004; Peppard et al., 2001) and high-resolution micro-X-ray Fluorescence (μ-XRF) synchrotron Ti maps of quartz crystals extracted from the Whakamaru Group Ignimbrites and Earthquake Flat (EQF) deposits from the TVZ (Fig. 3.1), and the Youngest Toba Tuff (YTT), Sumatra (Fig. 4.1). Both one-dimensional (1D) and two-dimensional (2D) diffusion modelling techniques (see Huber et al., 2010c, 2011a) are applied to Ti in quartz to model timescales associated with a significant thermal/pressure event recorded in quartz rims. This comparison of quartz-zoning timescales for the Whakamaru eruption with those from the smaller EQF eruption (Okataina Caldera Complex, OCC) and the larger YTT supereruption provides an indication of whether or not the magnitude of eruption and source magma chamber volume correlate with quartz zoning and the related timescales.

The primary objectives of this new study were to: (1) measure the spatially resolved Ti content of representative zoned quartz crystals to further test the assumption that CL zoning in volcanic quartz is caused by compositional zoning of Ti; (2) use spatially resolved (< 4 μm) measurements of Ti across zoned quartz to reconstruct changes in magma chamber conditions prior to eruption; and (3) use diffusion modelling techniques to estimate timescales of magma chamber processes required to explain gradients in Ti content across critical growth zones of volcanic quartz crystals. The information gained enables assessment of timescales of pre-eruption pressure and temperature changes in large-volume magma bodies, and therefore improves understanding of the manner in which these magmatic systems were assembled and triggered.

4.1.1 Eruptions

Quartz-derived diffusion timescales for the Whakamaru supereruption (described in Chapter 1) are compared here with the Earthquake Flat eruption (Section 4.1.1.1) and the Youngest Toba Tuff eruption (Section 4.1.1.2), enabling a comparison across a wide range of eruption magnitudes.

4.1.1.1 Earthquake Flat eruption

The EQF eruption episode occurred at ~ 50 ka, immediately following the Rotoiti eruption (~ 120 km^3) from the OCC (Fig. 3.1). The eruption involved ~ 10 km^3 of rhyolitic magma erupted from vent localities at the southern margin of the Kapenga caldera, which overlaps with the structural boundary of the larger OCC structure (Smith et al., 2005).

The EQF deposits are silicic and crystal-rich (25 – 45%) with a mineral assemblage dominated by plagioclase, quartz, hornblende and biotite (Smith et al., 2010), and with compositional similarities with the earlier Rotoiti magma (Schmitz and Smith, 2004). Zircon age spectra indicate that they had a separate crystallisation history from the Rotoiti magma reservoir (Charlier et al., 2003). Hornblende textural and chemical variations suggest that there was a thermal event immediately prior to the eruption that caused rejuvenation of a crystal-rich system and triggered eruption (Molloy et al., 2008). Volatile contents, plagioclase and quartz zonation of EQF deposits are discussed in Smith et al. (2010) and that dataset is built on here by analysing the same well-characterised crystals.

4.1.1.2 Youngest Toba Tuff eruption

The ~ 74 ka YTT eruption is one of the largest known eruptions on Earth. Approximately 3000 km^3 of magma was erupted from the Toba caldera in central Sumatra, Indonesia,

forming the 100 × 30 km caldera (Fig. 4.1; Rose and Chesner, 1990; Chesner and Rose, 1991; Chesner, 1998; Vazquez and Reid, 2004).

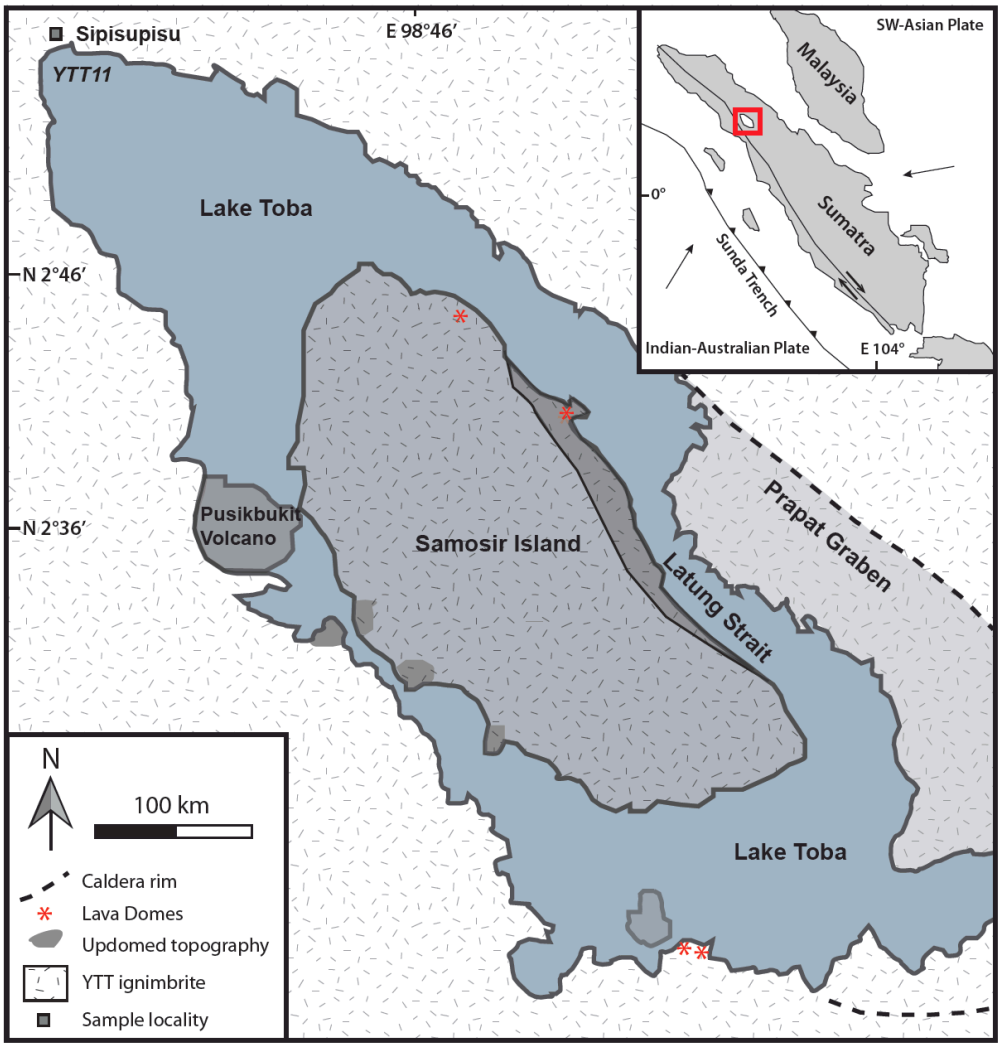

Fig. 4.1: Map showing main structural and topographic features of the Toba Caldera Complex. Inset shows tectonic setting and location map with relative vectors of plate movement indicated by arrows; red box indicates location of detailed map. Recent areas of updoming along the western lake shore are associated with hydrothermal and fumarolic activity. Proximal YTT sample locality marked (at Sipisupisu township). Adapted from Chesner (1998).

Rhyolitic YTT tephra was dispersed throughout the Indian subcontinent, Indian Ocean, the Bay of Bengal, the Andaman Sea, and on land in Malaysia (Shane et al., 1995; Liu, Z. et al., 2006; see Chapter 6 for dispersal modelling results). YTT glass is dominantly of high-

silica rhyolite composition (see Shane et al., 1995; Chesner, 1998; Bühring and Sarnthein, 2000; Song et al., 2000; Liang et al., 2001; Schulz et al., 2002; Liu, Z. et al., 2006; Chesner and Luhr, 2010) and proximal pumice is crystal-rich with up to 40 wt% crystals of quartz, sanidine, plagioclase, biotite and amphibole, with minor magnetite, ilmenite, allanite, zircon, fayalite and orthopyroxene (Chesner, 1998). Magma erupted since 1.2 Ma from the Toba caldera is compositionally zoned, ranging from rhyodacite to rhyolite, attributed to extensive fractional crystallisation in the convecting magma body (Chesner, 1998). Crystallisation of the quartz-bearing magma occurred at 700 – 760ºC at depths of ~ 10 km (Chesner, 1998).

4.2 Samples and methods

The five Whakamaru Group pumice samples (three Rangitaiki and two Whakamaru, selected earlier for detailed quartz CL study as described in Chapter 3; Fig. 3.1) are also the subjects of this Chapter. Pumice samples from the EQF (Fig. 3.1) and the YTT Toba (Fig. 4.1) eruptions were selected (details provided in Smith et al., 2010, 2011 respectively) for comparative analysis. Pumices were selected on the basis of mineralogy, clast size, degree of alteration and major-element geochemistry. Details of the pumice samples referred to in this chapter are provided in Table 4.1.

Normal procedures used for quartz crystal extraction, mounting and imaging were followed, as outlined in Section 3.2. Approximately 40 quartz crystals from each pumice sample were extracted, of which 92 were imaged by CL and analysed by EPMA techniques as described here. A selection of 40 representative crystals was compositionally mapped using synchrotron μ-XRF.

Table 4.1: ***Summary of single pumice samples used for diffusion modelling***

Eruption unit	Sample code	Location	Glass SiO_2 av. (wt%)	a_{TiO2}	Quartz Ti (ppm)	TitaniQ T (°C)
Rangitaiki	P1905	38°52'09.5219" S, 176°03'13.1396" E	76.85	0.54	42 – 138	718 – 874
Rangitaiki	P1910	38°52'09.5219" S, 176°03'13.1396" E	77.87	0.62	36 – 114	686 – 819
Rangitaiki	P1915	38°52'09.5219" S, 176°03'13.1396" E	77.35	0.65	36 – 138	681 – 846
Whakamaru	P1920	38°12'19.9498" S, 175°55'35.4493" E	77.88	0.67	36 – 138	678 – 842
Whakamaru	P1827	38°19'30.6000" S, 175°41'03.5658" E	78.70	0.66	30 – 102	661 – 825
Youngest Toba Tuff	YTT11	02°55'00.6" N, 98°31'20.9" E	74.53	0.50	7 – 128	552 – 875
Earthquake Flat	EQF1	38°15'53.336" S, 176°19'32.892" E	71.28	0.41	41 – 133	750 – 915

Notes: Eruption temperature estimates are calculated from Fe-Ti oxides using the Ghiorso and Evans (2008) geothermometer; a_{TiO2} is calculated using Fe-Ti compositional data, following the method of Reid et al. (2011). EQF eruption temperature and data from Smith et al. (2010); YTT a_{TiO2} calculated using Fe-Ti oxide data from Chesner (1998); SiO_2, all quartz Ti and Whakamaru Fe-Ti oxide compositional data measured by EPMA at University of Oxford. Full glass dataset for selected Whakamaru Group samples provided in Table 3.2.

4.2.1 Glass major and trace elements

Major-element analysis by EPMA, using the JEOL 8600 EMP in the Research Laboratory for Archaeology and the History of Art, University of Oxford, was undertaken on glass shards separated from < 150 μm fractions of crushed pumice and mounted in polished epoxy blocks (details provided in Section 2.2.4). Details of LA-ICP-MS analysis of Whakamaru glass shards are provided in Section 2.2.5.

4.2.2 Ti in quartz

With the discovery that temperature is the principal control on the Ti content of volcanic quartz (Wark and Spear, 2005), many studies have used Ti content of quartz as a geothermometer (e.g., Wark and Watson, 2006; Wark et al., 2007; Wiebe et al., 2007;

Shane et al., 2008b; Smith et al., 2010). This is conventionally achieved by CL imaging of a crystal, and by assuming CL intensity is directly proportional to Ti content (Götze et al., 2001; Wark and Spear, 2005). EPMA of the Ti content of discrete points along a core-rim profile enables use of the Ti-in-quartz *TitaniQ* geothermometer (Wark and Watson, 2006) to reconstruct quartz crystallisation temperatures, as described in Chapter 3. Recent studies (e.g., Thomas et al., 2010; Wilson et al., 2011) have, however, indicated that there may also be a significant pressure and compositional (XH_2O) effect on the Ti partitioning into quartz. Interpretations of temperature/pressure effects from the Ti-in-quartz method must therefore be made with caution, as noted in Chapter 3.

4.2.2.1 Cathodoluminescence and Electron Backscatter Diffraction-SEM analysis

CL images of all quartz crystals were obtained as described in Section 3.2.6. Full crystallographic orientation data for selected quartz crystals were obtained from Electron Backscatter Diffraction patterns (EBSD; Fig. 4.2), using the SEM at the NERC Ion Microprobe Facility, University of Edinburgh. Samples for EBSD-SEM analysis were SYTON-polished (colloidal silica) and carbon coated for analysis. Analytical settings were 20 kV acceleration voltage, 20 mm working distance and a beam current of ~ 1 – 2 nA. EBSD patterns were auto-indexed using the CHANNEL 5.03 software of HKL Technology (Denmark) and all patterns were indexed for quartz (trigonal system).

4.2.2.2 Electron Microprobe Analysis and Laser-Ablation Inductively-Coupled Plasma Mass Spectrometry

EPMA and LA-ICP-MS were used to establish the relationship between quartz growth features and CL and to enable use of the TitaniQ geothermometer (Wark and Watson, 2006; results discussed in Matthews et al., 2011a and Chapter 3). EPMA analysis of Ti-in-

quartz is outlined in Chapter 3, Section 3.2.2. Ti transects were also obtained for selected quartz crystals using LA-ICP-MS. These Ti concentrations from LA-ICP-MS correlate well with those analysed by EPMA (e.g. Fig. 4.3). CL greyscale values were calibrated using discrete EPMA and LA-ICP-MS Ti analyses (Fig. 4.3) as described in Section 3.2.6.

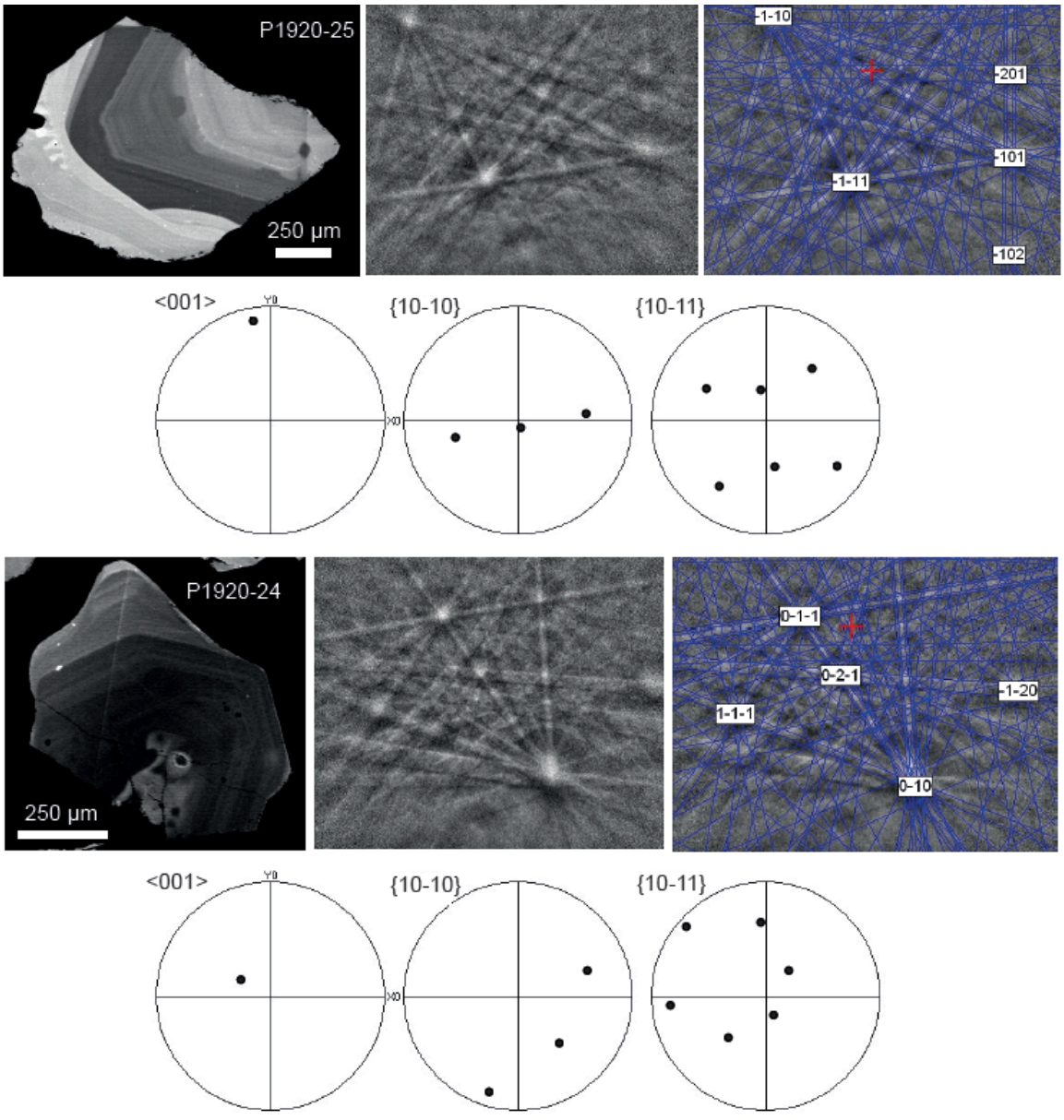

Fig. 4.2: Index diffraction patterns for quartz (trigonal crystal system) by EBSD. Pole figures are plotted using stereographic projection, upper hemispheres.

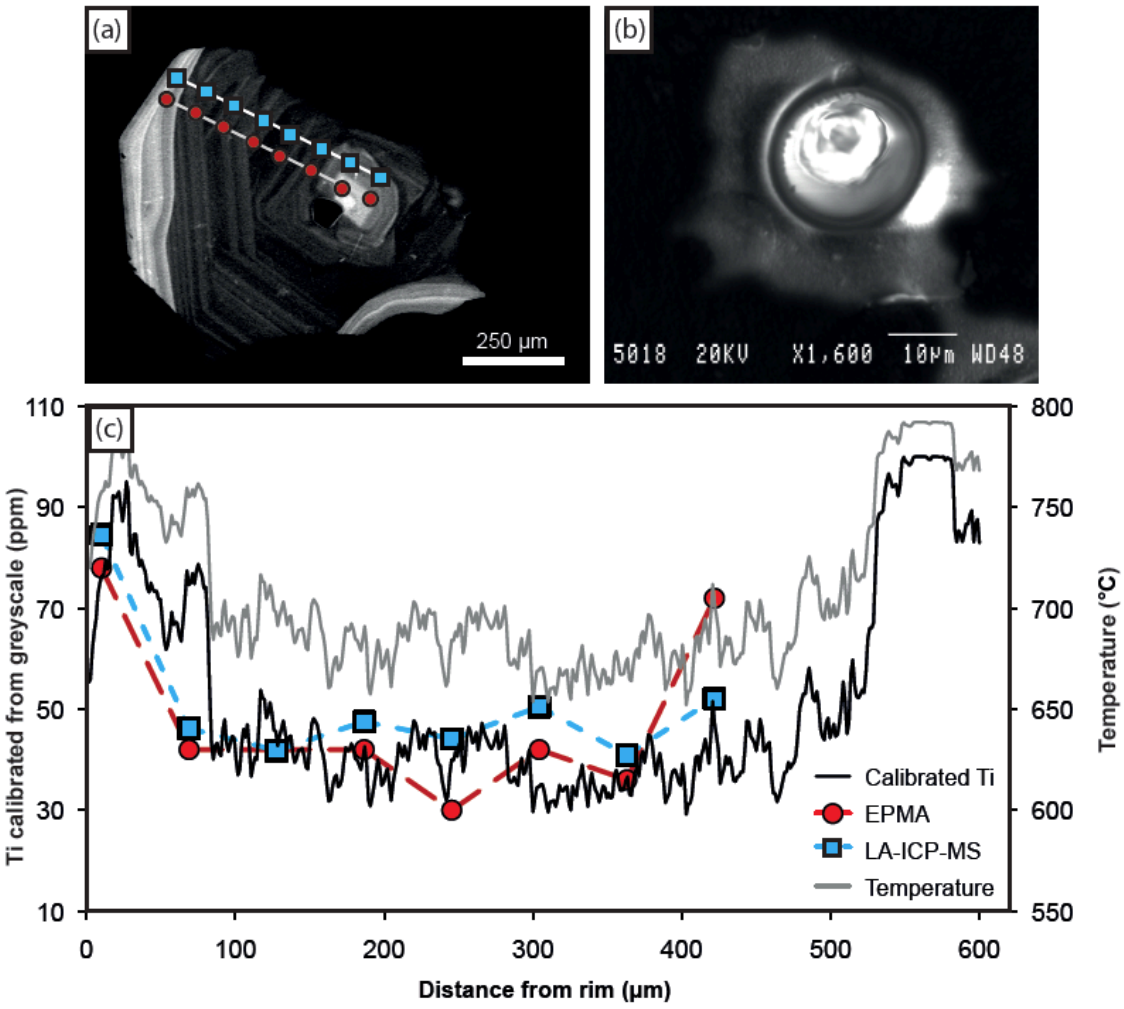

Fig. 4.3: Comparison of Ti-in-quartz analysis by EPMA, CL and LA-ICP-MS. (a) CL image of quartz crystal (P1827-11) with position of Ti analysis transects by EPMA (red) and LA-ICP-MS (blue); (b) SEM image showing detail of a single laser pit; (c) Ti concentrations from core to rim, with CL greyscale profile calibrated by EPMA data ("Calibrated Ti"), and corresponding TitaniQ temperature profile calculated (grey line). Differences between EPMA and LA-ICP-MS analyses on the extreme right spot in the quartz core are due to different zones in the quartz crystal being analysed by the two techniques and not an analytical error

4.2.2.3 Micro- X-ray Fluorescence and X-ray Absorption Near-edge Structure

Synchrotron μ-XRF mapping of Ti in quartz was performed at the Diamond Light Source Ltd (DLS) Microfocus X-ray Spectroscopy Beamline I18, Oxfordshire (Mosselmans et al., 2008, 2009). Detailed description of beamline components, parameters and operating conditions can be found at http://www.diamond.ac.uk/Home/Beamlines/I18.html.

The small spot sizes and rapid spot analyses obtainable with the synchrotron μ-XRF technique are ideal for this study as high-resolution Ti maps spanning core to rim could be rapidly collected (2 s per analysis). The spatially resolved Ti concentrations from synchrotron μ-XRF allow, for the first-time, accurate assessment of the relationship between CL intensity and Ti content, and provide spatially resolved measured Ti concentrations to apply in the Ti-in-quartz geothermometer (Wark and Watson, 2006). High-resolution μ-XRF maps across the core-rim interface in the quartz (described below) display the complex Ti-zonation patterns seen in the CL images, and these can be directly modelled. One drawback with the synchrotron technique in the present context is beam penetration into the crystal (compared to CL and EPMA which are more shallow or surface dominated). Beam penetration depth was ~ 15 μm (see details of X-ray attenuation depth in Appendix A4.1), which results in counts being effectively depth-averaged.

Selected crystals were mounted in epoxy discs and polished prior to μ-XRF mapping. The target areas for mapping were chosen to capture the chemical zoning of the cores and rims of quartz grains, and to accurately define the scale of the boundary zones between core and rim. Crystal transects were mapped at a resolution of 3 × 4 μm, with an analysis time of 2 s per spot which allowed multiple Ti-transects to be analysed per day of beam time. Acquisition time for a typical map, 500 μm long by 50 μm wide, was ~ 75 minutes.

Quartz crystals from selected pumice samples from each eruption (Whakamaru, EQF, YTT, Table 4.1) were analysed - chosen in order to provide the most representative suite of quartz grains which had been previously characterised in terms of their CL zonation, textural features, and Ti contents.

Ti maps were obtained by rastering a polished sample at 45° to the beam and tuning the beam to an incident energy of 5.5 keV. A nine-element Ortec monolithic Ge detector was used. The incident X-ray beamsize was ~ 3 × 4 μm. The μ-XRF spectra were fitted for Ti using the PyMCA package (Solé et al., 2007) and the elemental distribution map was generated from the fitted spectra. The elemental maps show the distribution of Ti from core to rim for each quartz crystal as described below. Quantification of μ-XRF Ti intensity maps involved using a well-characterised homogenous quartz crystal of 90 ppm Ti (analysed by EPMA). The Ti intensity was normalised to the scatter peak, which accounts for incident beam intensity, detector geometry and sample thickness, and to the Ti/scatter ratio of the standard.

Titanium X-ray Absorption Near-edge Structure (XANES) spectra were also measured on beamline I18 at the Diamond Light Source Synchrotron, providing information on the local coordination environment of Ti ions in the same mapped quartz crystals (e.g., Waychunas, 1987). These spectra were compared with a universal standard, volcanic glass, magnetite, clinopyroxene and Ti metal. Results are also described in comparison with results from experimentally grown quartz crystals from Thomas et al. (2010). Spectral data were normalised to account for differences in Ti concentrations between samples, detector and amplifier settings, using Athena software (Ravel and Newville, 2005).

4.2.2.4 TitaniQ

The TitaniQ geothermometer was applied following the equations provided in Section 3.2.3. None of the eruption deposits studied here contained rutile and therefore the activity of Ti in the melt (a_{TiO2}) was estimated to allow use of the TitaniQ geothermometer (as outlined in Section 3.2.4). It was calculated for each eruption assuming ideal exchange equilibria between coexisting Fe-Ti oxides, and using an expanded method of Wark et al. (2007) and Reid et al. (2011). Average geothermometry results for all three eruptions are provided in Table 4.2.

Table 4.2: ***Geothermobarometery data for eruptions***

	Whakamaru	EQF	YTT
Fe-Ti oxide T (°C)	770 ± 46	745 ± 27	760 ± 16
logfO_2	-14.0 ± 1	-15.0 ± 0.8	-15.0 ± 0.6
Amphibole T (°C)	840 ± 50	768 ± 10	828 ± 3
Amphibole P (MPa)	125 ± 66	90 ± 9.5	168 ± 6
Depth (km)	4.7 ± 3	3.4 ± 0.4	6.4 ± 0.2

Notes: Fe-Ti oxide temperatures relate to eruption temperature, and were calculated using the Ghiorso and Evans (2008) geothermometer. Amphibole P, T, and depth were calculated using the geothermometer of Ridolfi et al. (2011). YTT and EQF calculations were made using Fe-Ti oxide data and amphibole compositions reported in Chesner (1998) and Molloy et al. (2008). Whakamaru data and intensive parameters are reported in Matthews et al., 2011a.

4.2.3 Diffusion methodology – calculation of diffusion timescales

The majority of the quartz crystals examined from each eruption show a bright-CL rim, similar to that reported from later-erupted Bishop Tuff samples (Wark et al., 2007). It is thus inferred that a majority of the quartz crystals examined underwent a significant change in physical and/or chemical conditions not long before eruption, as discussed in Chapter 3. The petrographic and chemical evidence for mafic magma involvement during the Whakamaru supereruption (particularly the presence of mixed mafic pumices; Sections 2.3.1 and 3.3.1) suggests that this significant change is likely also to have been associated

with a recharge event. Any linkage between specific magma recharge events and eruption, such that a cause-and-effect relationship might be proposed, depends on constraining the time periods involved.

Diffusion modelling (based on published methods; Morgan et al., 2004; Wark et al., 2007; Huber et al., 2010c) is applied here in order to constrain the recharge timescale, i.e., the time elapsed between recharge/quartz-rim crystallisation and eruption, excluding an unquantifiable period associated with the resorption event itself. The term "diffusion time" is therefore used here as literally meaning the time for which the conditions which allowed the diffusion (following the event which caused the profile change in the first place) prevailed. In the absence of further events affecting the concentration profile, this may be interpreted as being the time between the event (and the onset of renewed crystal growth) and eruption, as discussed below.

Ti gradients along the high-resolution μ-XRF profiles, and corresponding calibrated CL-greyscale profiles (with a resolution of 3 μm), provided data for three independent diffusion modelling techniques to investigate timescales of quartz-Ti zonation. These methods are described here as: "1D", "1D-corrected" and "2D Lattice Boltzmann" techniques as explained in Sections 4.2.3.1 – 4 below.

Diffusion was modelled using quartz Ti diffusivities and activation energies from Cherniak et al. (2007). An activation energy of 273 ± 12 kJ mol^{-1} was assumed for diffusion parallel to the *c*-axis in synthetic quartz, with a Ti diffusion rate of 1.49×10^{-21} m^2 s^{-1} at 770 °C (calculated using equation [4.1] below; Cherniak et al., 2007). As there is only limited anisotropy in quartz Ti diffusion it was not necessary to account for the orientation of the

profile relative to the crystal – diffusivities for the direction normal to *c* have been found not to differ significantly from those parallel to *c* (Cherniak et al., 2007).

The diffusion rate of Ti in quartz ranges from 4.72×10^{-22} m^2 s^{-1} at 700°C to 7.61×10^{-21} m^2 s^{-1} at 900°C (Cherniak et al., 2007). Thermal records are therefore preserved over long periods in quartz crystals in pre-erupted magmas (> 10 ka; Cherniak et al., 2007). Once crystal nucleation has occurred, crystallisation in a melt is controlled by the relative rates of diffusion of components in the melt and by rates of crystal growth (Watt et al., 1997).

The quartz core-rim zone boundary (which marks the compositional step in Ti, e.g., Figs 3.10, 4.3) is assumed to have been initially vertical, but is elongated by elemental diffusion over time after the event. At elevated temperatures, diffusion across compositionally different zones thus produces compositional gradients. Modelling of these gradients enables the elapsed time between thermal events and eruption to be estimated. The sharpness of CL-zoning patterns observed in quartz can thus be used in conjunction with known diffusion parameters to evaluate crystal residence times in the magmatic system since recharge, decompression, and/or sharp changes in chemistry (with each zone reflecting a period of distinct crystallisation conditions, and its width indicating the time period for such conditions). The fine-scale zonation preserved in the crystals studied (Figs 3.4, 3.5, 3.6) therefore indicates relatively short (years to decades) residence times prior to eruption.

4.2.3.1 1D diffusion technique

For 1D diffusion modelling the approach of Morgan et al. (2004) and the method of Wark et al. (2007) was followed. This method uses the width of Ti zone boundaries in quartz (as

this is dependent on Ti diffusion rate under the ambient conditions), with the assumption that the major step in Ti content (and hence CL brightness) was initially vertical and related to the latest major event (Wark et al., 2007) as described above. Results therefore provide a maximum timescale because the compositional gradient is modelled as being solely due to diffusion whereas it may additionally be influenced by the changing conditions of crystal growth, e.g., melt compositions/temperature/pressure conditions (e.g., Costa and Morgan, 2010).

Ti gradients along calibrated profiles (see Section 3.4.1) were modelled focusing on boundaries between the large-magnitude Ti increases from dark CL core to bright CL rim, which occur over distances of 10 – 30 μm in the analysed crystals (Fig. 3.10; where data have a resolution of 2 μm. The following parameters were used in the calculation of diffusion time *t*, s: activation energy (*AEa*) 273 kJ mol^{-1}; a pre-exponential constant (*Do*), 7×10^{-8} m^2 s^{-1} (Cherniak et al., 2007); gas constant (*R*) 8.3145 J K^{-1}; and temperatures of 770 ºC (Whakamaru), 760 ºC (YTT), and 745 ºC (EQF). The eruption temperatures are derived from Fe-Ti oxides, calculated using the geothermometer of Ghiorso and Evans (2008), Table 4.2.

Titanium diffusivity (D_{Ti}, m^2 s^{-1}) at temperature (*T*) is calculated by the Arrhenius relation (for diffusion parallel to (001) in quartz; Cherniak et al., 2007) given in equations [4.1] and [4.2]:

$$D_{Ti} = Do \times \exp\left(\frac{AEa}{R \times T(^{\circ}K)}\right) \qquad [4.1]$$

$$D_{Ti} = 7 \times 10^{-8} \exp\left(\frac{-273 \pm 12 \text{ kJ mol}^{-1}}{R \times T(^{\circ}K)}\right) \text{m}^2 \text{ s}^{-1} \quad [4.2]$$

Diffusion from an initially vertical concentration step is modelled on the basis of Ti concentration at positions on the profile (normalised to relative values between 0 and 1) as calculated by Morgan et al. (2004):

$$C = \frac{1}{2} erfc\left(\frac{x}{2\sqrt{D_{Ti}t}}\right), \quad [4.3]$$

where C is the normalised Ti concentration (between 0 and 1), x is the position along the profile (μm), *erfc* is the complementary error function, and t is the diffusion time. The best-fit solutions to equation [4.3] were determined by modelling Ti-compositional profiles for different timescales and choosing the profile that most closely matched the gradient of the measured greyscale-calibrated Ti profile.

In an ideal situation, the measurement of Ti concentration at distance Δx (in μm) from the step midpoint (where the midpoint concentration, $C_m = 0.5$) also allows calculation of time, t, for Ti diffusion in a quartz crystal:

$$t = \frac{\Delta x^2}{4D_{Ti}(inverfc(2C_n))^2}. \quad [4.4]$$

Here *inverfc* is the inverse complementary error function; and C_n the normalised concentration and Δx its distance from the midpoint of the compositional step.

4.2.3.2 1D-corrected technique

The simple 1D modelling described above can be improved by correcting for cases where the Ti compositional traverses are not perpendicular to crystal margins (see Costa et al., 2008). The "1D-corrected" technique assumes that the concentration profiles of Ti can be modelled with a 1D diffusion equation, but with refinement by incorporation of the angle of the profile with respect to the diffusion gradient. The angle, α, between the measured concentration profile and the core-rim boundary compositional gradient can be accounted for by rescaling Δx (equation [4.4]) with $\Delta x \cos(\alpha)$, as in Fig. 4.4, thus accounting for problems caused by artificial lengthening of the profile due to oblique angles.

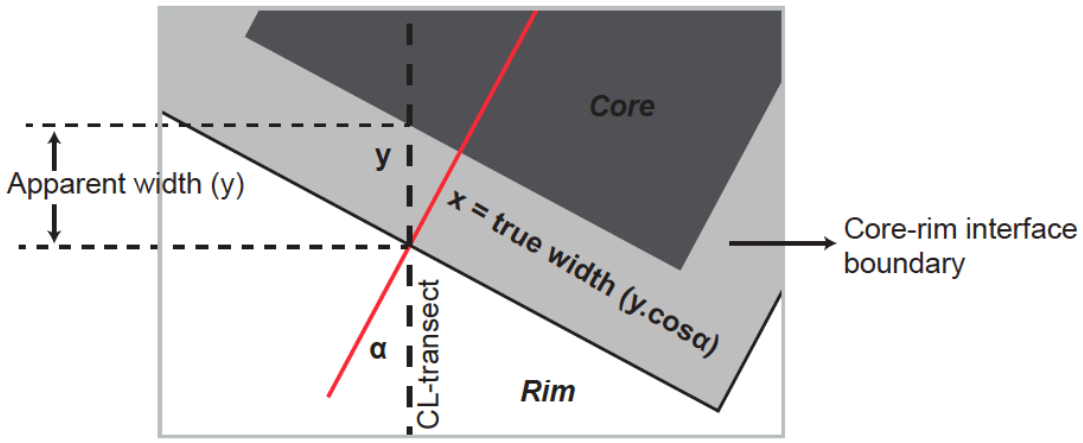

Fig. 4.4: Detail of the quartz core-rim interface (plan view), where the red line indicates the calibrated CL transect, and the black line represents the ideal diffusion modelling profile, oriented perpendicular to the core-rim interface. In order to correct for this angle to the diffusion boundary the 'true' and 'apparent' widths of the transition zone are considered, where the ratio of true:apparent widths is given by x/y = yCosα/y = cosα (where α is the angle to perpendicular from the core-rim boundary; equation [4.5]).

In reality, the actual concentration profiles display complex features that cannot be attributed to solely 1D diffusion, such as 2D effects and local heterogeneities, in addition to analytical errors in the Ti measurements. It was therefore expected that, when applying

equation [4.3] for the few measurements in the vicinity of the step midpoint, the times obtained may differ substantially owing to such complications. The times obtained by the 1D techniques are, however, useful in providing a first rough estimate of the diffusion time, an average time calculated for each profile, and an assessment of the quality of the data to be fitted in the diffusion modelling calculations. This approach also offers simple diagnostics when diffusion times calculated for each point show a large variability (e.g., an asymmetric diffusion profile), which would indicate local heterogeneities associated with structural effects (e.g., individual defects), errors in the concentration measurements, or complex pre-diffusion concentration profiles.

4.2.3.3 2D Lattice Boltzmann technique

To overcome the above shortcomings, a model based on the Lattice Boltzmann (LB) method to solve for diffusion in 2D (Huber et al., 2008; 2010c; 2011a) was employed to account for complex geometries in the physical boundaries of crystals. In the LB method, the diffusion equation incorporates the evolution of particle distribution functions described by simple kinetic rules that allow recovery of the correct dynamics (diffusion) with isotropic or anisotropic diffusion coefficients. Initial calculations are computed in dimensionless time using a Fourier number (*Fo*):

$$Fo = \frac{D_{Ti}t}{L^2}, \qquad [4.6]$$

where D_{Ti} is the diffusivity of Ti, t is the duration of the diffusion event, and L is the length-scale of interest (distance in μm over the compositional change). In isotropic conditions, the *Fo* number fully characterises the state of the system and allows

normalisation of the space-time relationship of the diffusion equation, and thus the solving for time.

The evolution of the particle distribution functions is described by a discretised version of Boltzmann's equation with a simplified collision operator (Bhatnagar et al., 1954; Huber et al., 2011a) given by:

$$f_i(x + v_i dt, v_i, t + dt) - f_i(x, v_i, t) = \omega(f_i^{eq}(x, v_i, t) - f_i(x, v_i, t)) \quad [4.7]$$

where f_i is the distribution function for particles moving along the velocity vector connecting two neighbouring nodes v_i, x is the position on the lattice, and $1/\omega$ is the relaxation time towards an equilibrium described by f_i^{eq}. Diffusivity, D_{Ti}, is related to ω according to equation [4.8] where c_s^2 is the sound speed of the lattice, which depends on the lattice topology (see Huber et al., 2011a, for further details of derivation).

$$D_{Ti} = c_s^2 dt(\frac{1}{\omega} - \frac{1}{2}) \quad [4.8]$$

The equilibrium distribution, f_i^{eq}, is given by:

$$f_i^{eq}(x, v_i, t) = w_i C(x, v_i, t) \quad [4.9]$$

where w_i are the lattice weights. The local concentration is the sum of the distributions, given by:

$$C = \sum_{i=0}^{4} f_i = \sum_{i=0}^{4} f_i^{eq} \quad [4.10]$$

Through a Chapman-Enskog expansion, the set of equations [4.7] – [4.10] retrieves a 2D diffusion equation where the diffusivity is defined by equation [4.8] (Wolf-Gladrow, 2000). A newly developed algorithm by Huber et al. (2010c) was applied, allowing the boundary concentration along the crystal interface to be fixed. For more information of the diffusion model derivation, refer to Chopard and Droz (1998) and Huber et al. (2010c).

Using the modelled elemental gradient which displays the best fit to the real data, the timescale for diffusion is calculated from the Fourier number, *Fo*. Application of equation [4.6] enables the time period for diffusion at any temperature to be calculated. Diffusion times are quoted at an eruption temperature calculated from Fe-Ti oxides (Table 4.2). The angle of the core-rim interface at depth, β, is accounted for by rescaling diffusion results by sinβ (Section 4.3.4.4).

4.3 Results

4.3.1 Eruption temperatures and glass chemistry

Eruption temperatures for the three eruptions are estimated using the Ghiorso and Evans (2008) Fe-Ti oxide geothermometer and compared with the Ridolfi et al. (2010) amphibole geothermobarometer. Published compositional data were used for application of these geothermometers, with YTT data from Chesner (1998) and Liu, Z. et al. (2006), EQF compositions from Molloy et al. (2008), and the Whakamaru dataset presented in Matthews et al. (2011a), Chapter 3. The average eruption temperatures used in the diffusion modelling are: 770°C for Whakamaru, 745°C for EQF, and 760°C for YTT (Table 4.2). All three eruptions are characterised by high-silica rhyolite magma (glass

shards contain 77 – 78 wt% SiO_2, and $Na_2O + K_2O$ = 7.9 – 8.6 wt%; quoted anhydrous). Major- and trace-element glass chemistry data for Whakamaru are presented in Appendix 4. Chapter 6 summarises YTT glass chemistry, and EQF glass chemistry is presented in Smith et al. (2010).

4.3.2 Quartz characteristics

Quartz comprises 20 – 40% of the crystal fraction in Whakamaru pumices and characteristically occurs as coarse (< 12 mm diameter), subhedral to anhedral crystals with resorbed rims as described in Section 3.3.3 (Fig. 4.5), indicating that they were in disequilibrium in their host melt prior to eruption. Quartz crystals are strongly CL-zoned (Figs 3.4, 3.5, 4.5; Matthews et al., 2011a), with EPMA Ti concentrations ranging 30 – 138 ppm (1sd ± 1 – 2 ppm, which equates to ± 1 – 3°C; full datasets are provided in Appendices 11 and 12), implying crystallisation temperatures of 670 – 858°C (using the TitaniQ formulation, an activity of Ti in the melt given by a_{TiO2} = 0.5 – 0.6, and assuming no pressure dependency; Table 4.1). Here, the individual a_{TiO2} values (Table 4.1) were considered rather than the rounded, overall average value (0.7, Section 3.2.4), to ensure consistency of a_{TiO2} estimation for all three eruptions. Under CL, all Whakamaru Group quartz grains show similar features: dark cores (low-Ti; 50 – 90 ppm), and an abrupt Ti concentration increase associated with a bright-CL rim (high-Ti; 102 – 138 ppm; see examples in Figs 4.5, 4.8).

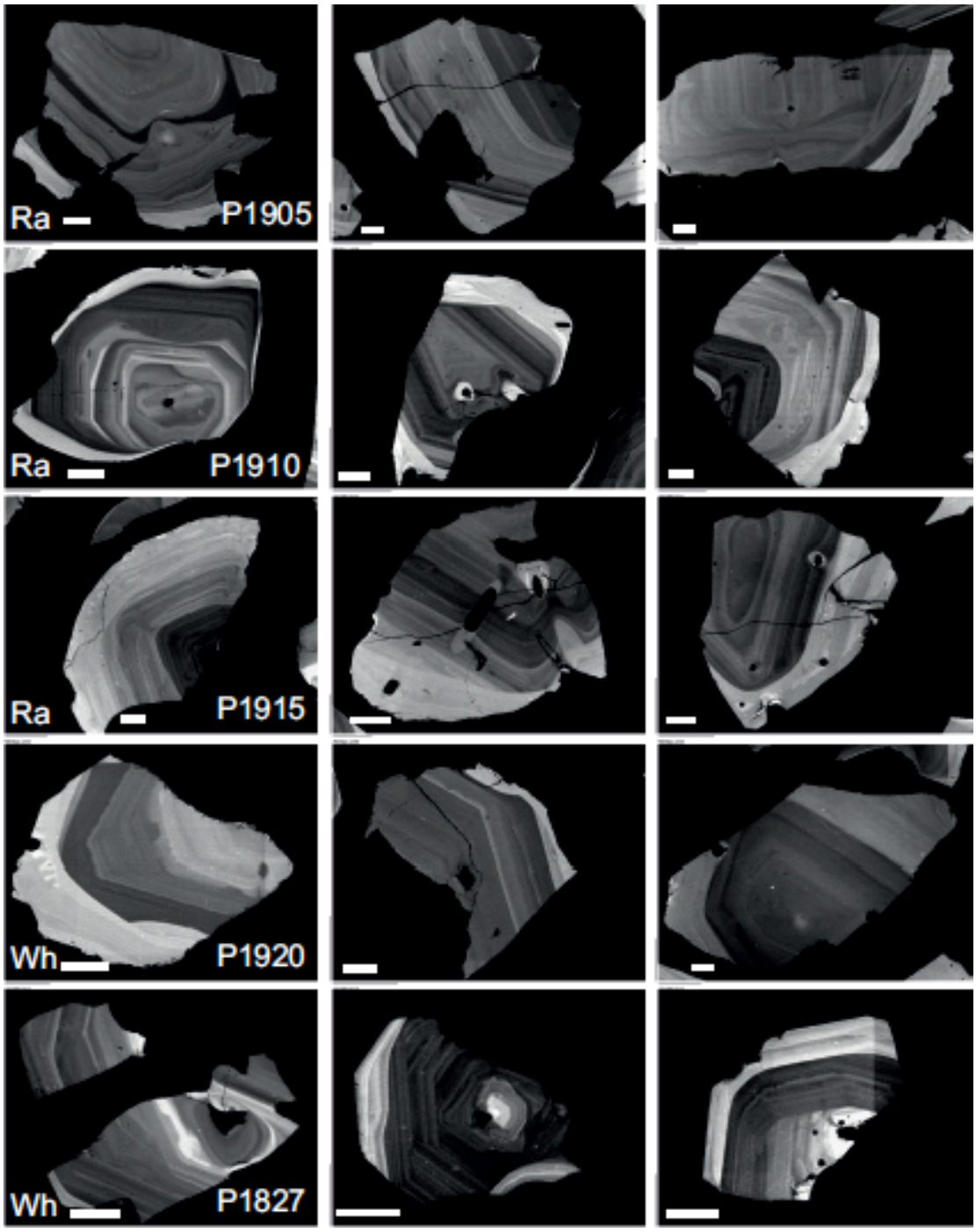

Fig. 4.5: CL images of selected Whakamaru quartz crystals. Scale bar is 250 µm. Whakamaru quartz indicated by Wh, Rangitaiki quartz by Ra. Sample codes marked as: P1905, P1910 and P1915 are basal Rangitaiki pumices, and P1920 and P1827 are Whakamaru. Note the bright CL rims on many of the crystals (up to 250 µm wide) occurring after a significant resorption horizon.

EQF and YTT quartz crystals display more simple zoning patterns. EQF quartz crystals are also characterised by bright CL rims and dark CL cores, with subtle oscillations in CL-greyscale (Fig. 4.6). EQF quartz phenocrysts are 1.5 mm maximum diameter and are anhedral with numerous internal resorption horizons observed in CL imagery. Resorption horizons tend to be associated with Ti-rich (bright-CL) zones, occurring either at the rim or midway along the crystal profiles. Ti in EQF quartz ranges 41 – 133 ppm (Smith et al., 2010; see Appendix 12), with corresponding TitaniQ temperatures of 750 – 915°C (Table 4.1; assuming constant a_{TiO2} of 0.4 calculated using Fe-Ti oxide data from Molloy et al., 2008).

YTT quartz is more similar to Whakamaru quartz, being also characterised by resorption and highly fractured, most likely as a result of quenching and bursting of over-pressurized melt inclusions during pre-eruptive overheating and/or decompression and syn-eruptive shattering (Tait, 1992; Best and Christiansen, 1997; Gualda et al., 2004; Bindeman, 2005). YTT quartz CL zoning displays both reversed and normal patterns and broad zones of homogenous CL (Fig. 4.7), however. All YTT quartz crystals are characterised by an abrupt Ti compositional step near the crystal rim (see Fig. 4.9), which is the focus of diffusion modelling here. Ti in YTT quartz ranges 13 – 128 ppm (Appendix 12), which corresponds to temperatures of 606 – 875°C (Table 4.1; assuming constant a_{TiO2} of 0.5 calculated using Fe-Ti oxide data from Chesner (1998) and consistent with calculations of Gaither et al., 2009).

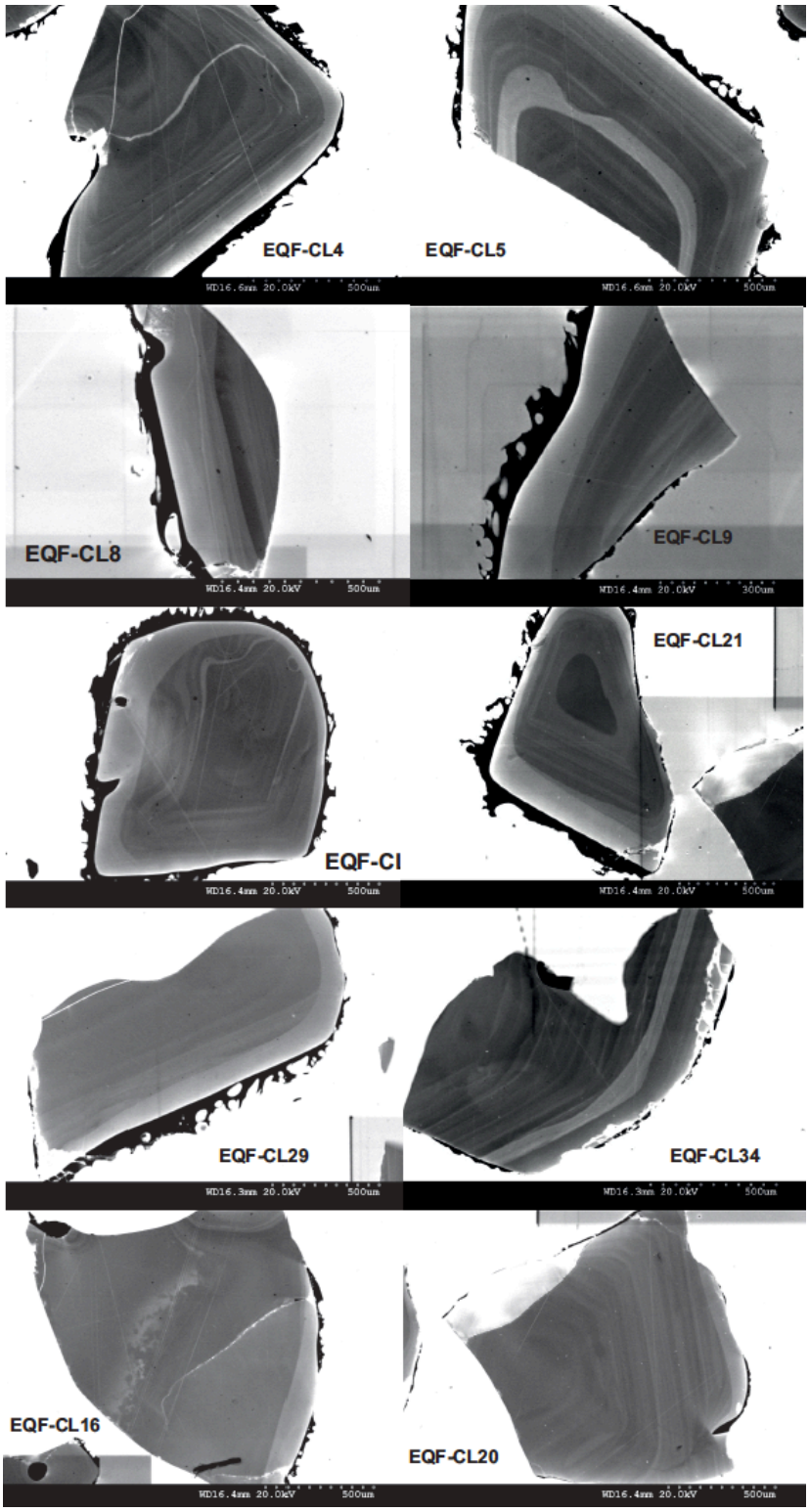

Fig. 4.6: Selected CL images of Earthquake Flat (EQF) quartz crystals (images from Smith et al., 2010); zoning is less complex than Whakamaru quartz, and displays some bright CL rims and internal bright zones.

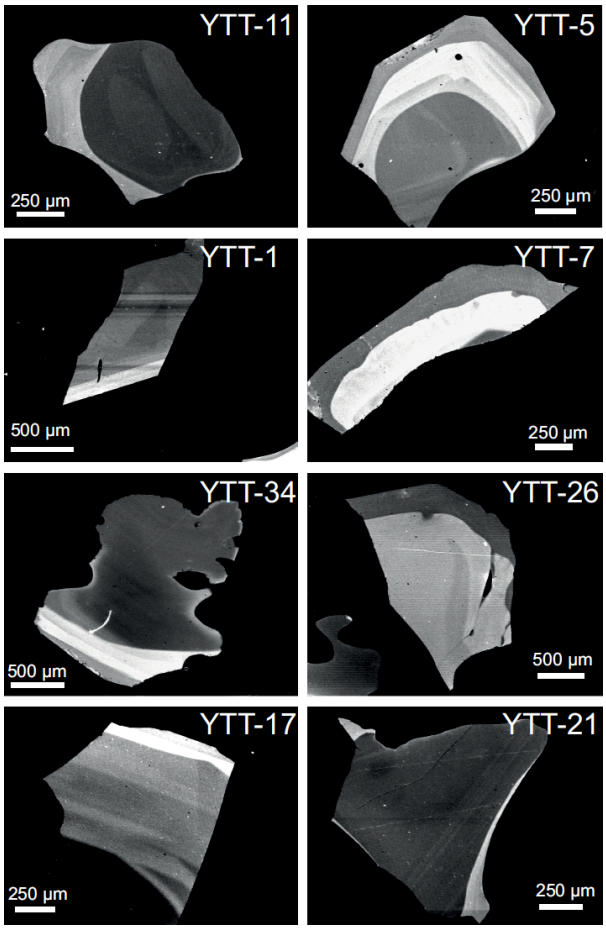

Fig. 4.7: CL images of selected YTT (Toba) quartz crystals; note that very little fine-scale zoning is evident. YTT quartz zoning is characterised by both normal and reverse patterns.

4.3.3 Ti-in-quartz µ-XRF maps

A strong correlation between CL-greyscale values and µ-XRF measurements of Ti concentration in quartz (Figs 4.8, 4.9 and 4.10) was observed. Over all samples, R^2 values were in the range 0.87 – 0.96 (Fig. 4.10). Quartz zonation patterns indicated by the two techniques also compare well, with both the CL and synchrotron profiles showing high-Ti rims and low-Ti cores for Whakamaru and YTT quartz (Figs 4.8, 4.9). The two profiles are offset due to CL being a surface measurement and µ-XRF incurring an angle of penetration effect as described in Sections 4.2.2.3 and 4.3.4.4 (Fig. 4.15). This offset enables calculation of the angle of the core-rim boundary with respect to the analysis surface (Fig. 4.15). In view of the averaging effect caused by µ-XRF beam penetration

(Fig. 4.15), a combination of CL and μ-XRF data is used here for diffusion modelling to provide upper and lower constraints on the diffusion time (Figs 4.12, 4.13).

The degree of agreement between Ti profiles measured by the μ-XRF and CL methods is highlighted in Fig. 4.10, where it can be seen that by applying scaling factors to account for beam offset and depth penetration, virtually identical profiles can be achieved. It is the need for these corrections that makes the μ-XRF unsuitable for the diffusion modelling here, although it is useful in providing the necessary correction angles (Fig. 4.15) for the CL-based modelling. This point is discussed further in Section 4.3.4.3. The unique combination of procedures allows time estimates to be optimised as described here.

4.3.3.1 X-ray absorption near-edge structure

XANES spectra provide information on the Ti co-ordination environment in quartz and enable investigation of possible mechanisms by which Ti enters the quartz structure. XANES spectra were collected from Whakamaru quartz and reference materials including EQF matrix glass, clinopyroxene (Minoan pumice, Santorini), magnetite (Afar, Ethiopia) and Ti foil. The XANES spectra (particularly focusing on the Ti pre-K-edge absorption peak) were compared with experimental results from Thomas et al. (2010), and with previously characterised materials that contain Ti in different coordination positions. The pre-edge feature in spectra of quartz crystals is most notably comprised of a single peak at ~ 4969 eV that is more intense and at lower energies than the multiple pre-edge features observed for rutile (Thomas et al., 2010; Waychunas, 1987). No significant changes in spectra were observed for different Ti concentrations (and corresponding temperature/pressure conditions recorded by core vs. rim), suggesting that the Ti (concentrations < 200 ppm) always sits within the same position within these volcanic quartz crystals. Results are provided in Appendix 13.

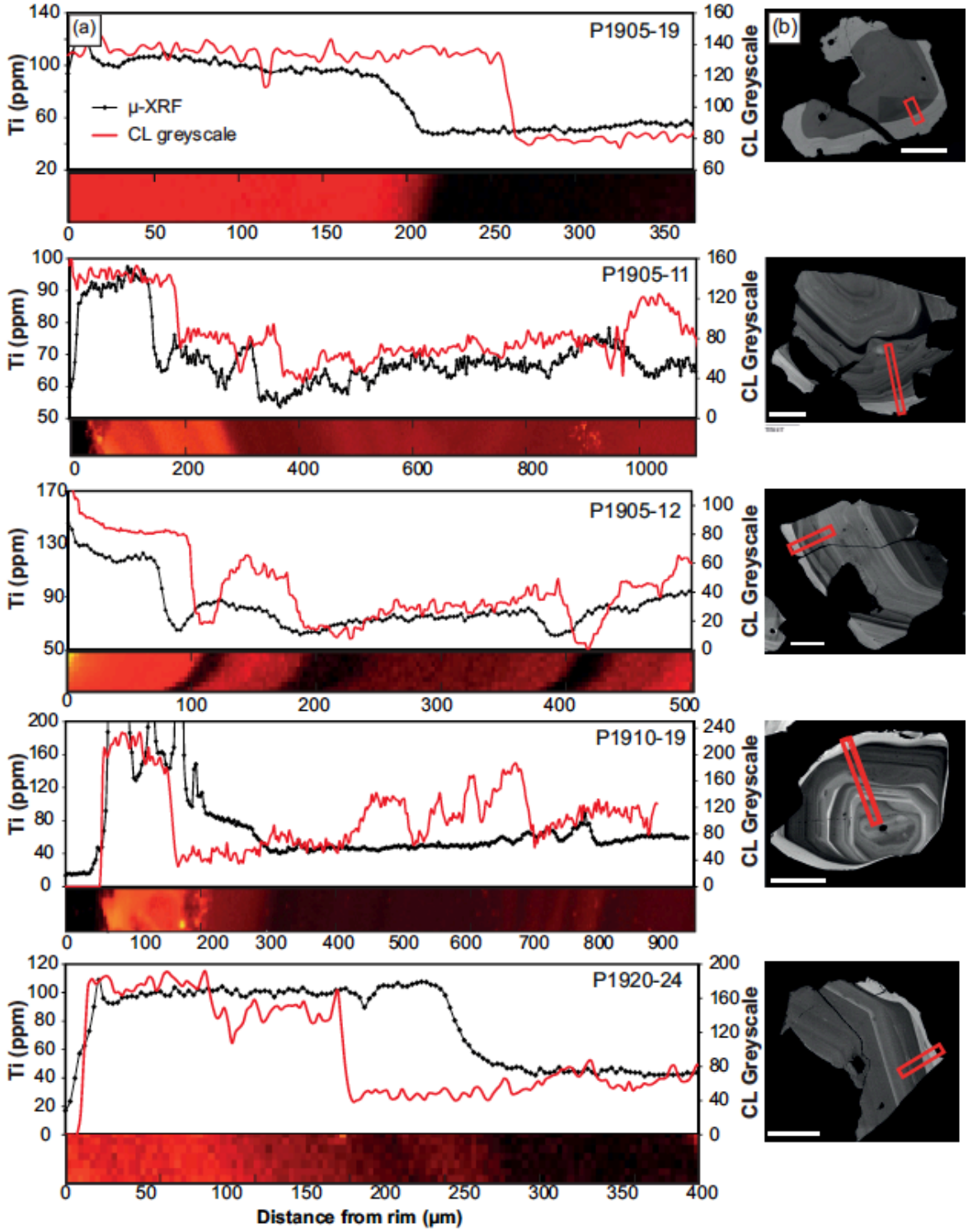

Fig. 4.8: (a) Synchrotron Ti maps of Whakamaru quartz plotted against Ti (ppm) transects (black) with CL greyscale transect (red) for comparison. Transects are areas marked by red rectangles in (b). Intensity of the colour relates to Ti content, where bright reds and yellows indicate high Ti, whereas black records very low Ti values. Note sharp interface between high-Ti (bright-CL) crystal rims and low-Ti (dark-CL) cores. The μ-XRF images have a 3 × 4 μm pixel size; (b) CL images of quartz crystals with μ-XRF map surface area marked by red rectangle; Scale bar is 500 μm.

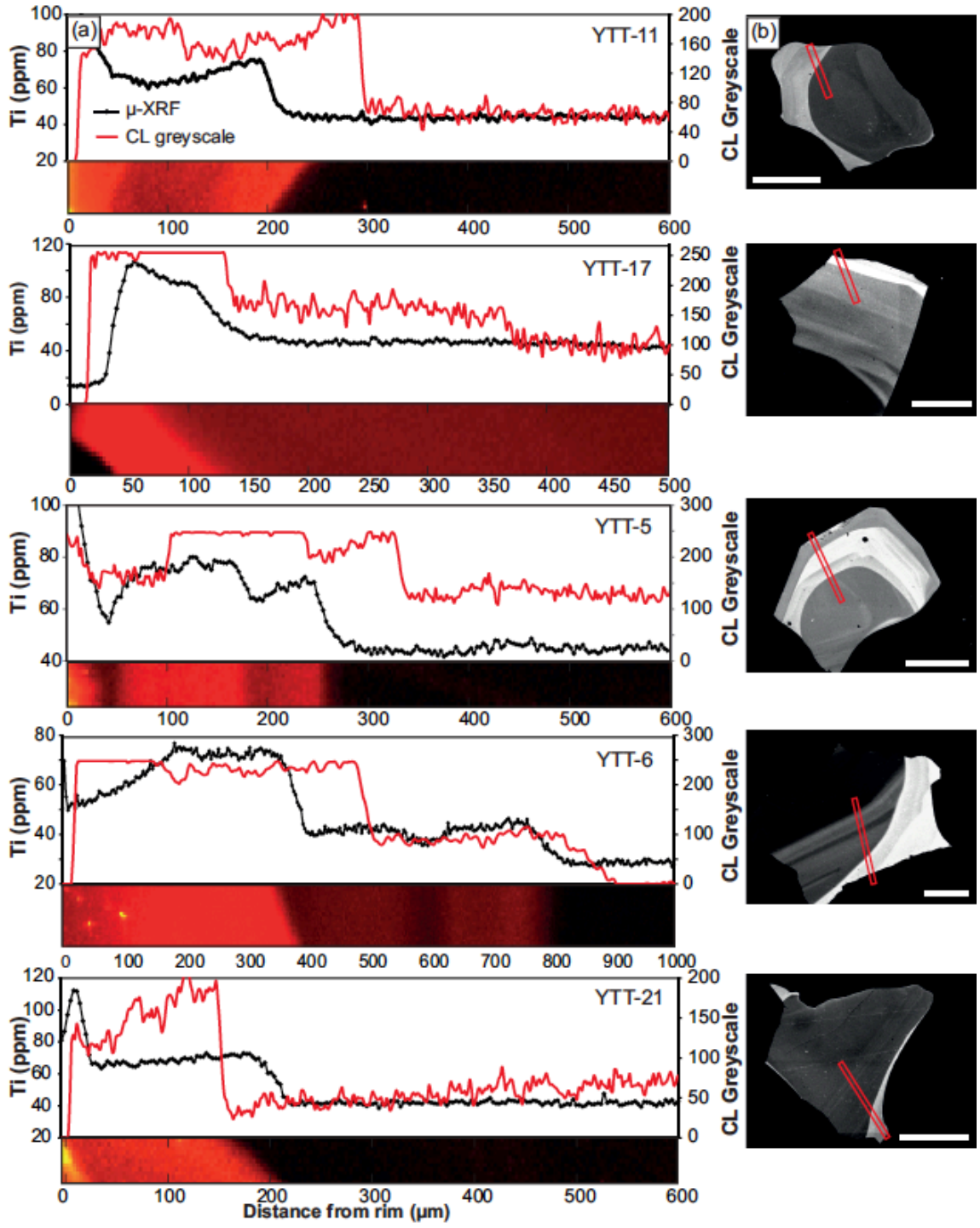

Fig. 4.9: (a) Synchrotron Ti maps of YTT quartz plotted against Ti (ppm) transects (black) with CL greyscale transect (red) for comparison. Transects are areas marked by red rectangles in (b). Note sharp interface between high-Ti (bright-CL) crystal rims and low-Ti (dark-CL) cores. Most YTT quartz are characterised by high-Ti rims of various thickness, but some (e.g. YTT-5) have reverse-zoned patterns. High-Ti recorded at rim in the synchrotron transects is due to adhering glass; (b) CL images of YTT quartz crystals with μ-XRF map surface area marked by red rectangle; Scale bar is 500 μm.

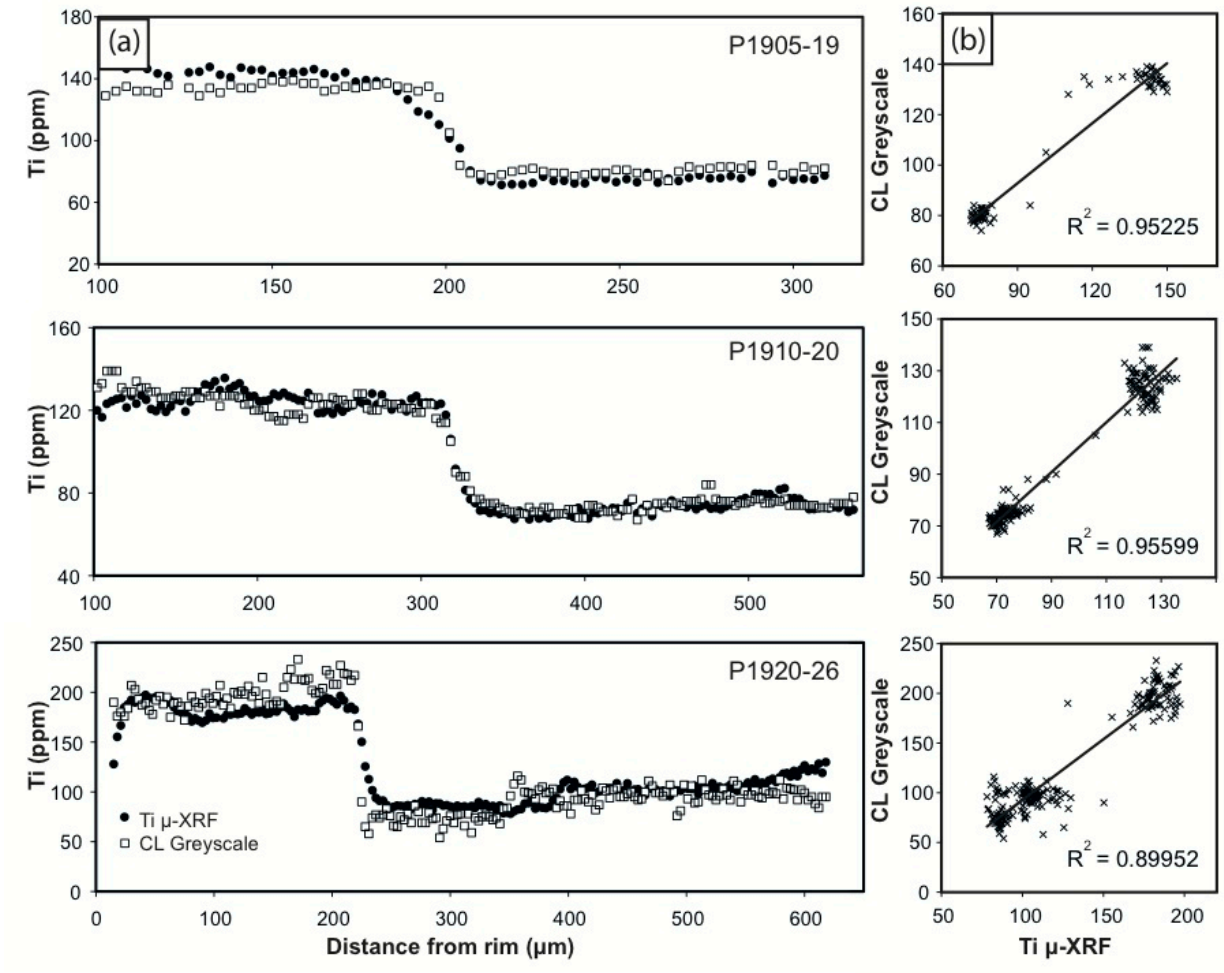

Fig. 4.10: (a) Comparison of Ti µ-XRF data and CL greyscale values for three representative Whakamaru quartz crystals with distance from rim (same y-axis scales apply). These plots show the degree of agreement achievable between µ-XRF and CL techniques in describing the Ti concentration step. Two corrections were required to achieve this comparison: (1) for the offset caused by the angle of µ-XRF beam penetration (by moving one of the profiles sideways); and (2) for the depth-averaging nature of µ-XRF measurements by applying empirical scaling factors (one for each sample). (b) There is a strong correlation between CL and µ-XRF Ti-in-quartz data, with R^2 values of 0.90 – 0.96 for these three quartz crystals. Note that the fits (R^2 values) are effectively two-point lines due to the density of observations.

4.3.4 Diffusion timescales

The presence of abrupt zoning (Ti compositional steps occurring over < 30 μm) in the CL and Ti profiles in all analysed quartz crystals suggests short crystal residence times in the source magma chamber(s). If residence times were sufficiently long after formation of the abrupt compositional step, this would have resulted in a progressively smoother zoning profile until a linear core-to-rim profile was produced (Zellmer et al., 1999; Costa and Chakraborty, 2004; Morgan and Blake, 2006; Wark et al., 2007). It is thus possible to determine the maximum residence times after growth of crystal rims by using the diffusion methods outlined earlier for Ti in quartz. The three diffusion methods for examining the diffusion across the significant core-rim crystal boundary are utilised here to constrain the time required to generate the observed elemental gradient (as outlined in Section 4.2.3). The core-rim interface (using data from both CL greyscale and μ-XRF) was the focus of diffusion modelling here, enabling calculation of the timescales associated with the last significant compositional event recorded by quartz. Results are presented in Table 4.3, which shows differences in diffusion timescales for the 1D methods and 2D LB method and the correction angles used in calculations. The advantages and disadvantages of each method are discussed in detail here.

4.3.4.1 1D and 1D-corrected diffusion methods

Traditional 1D diffusion modelling across a crystal boundary assumes that the profile is along the diffusion gradient (Morgan et al., 2004; Smith et al., 2010) as described earlier, although this is clearly a simplification given the three-dimensional structure of crystals. This approach yields diffusion times, at eruption temperature, for the core-rim boundary in quartz as follows: Whakamaru: 15 – 500 y; YTT: 100 – 450 y; and EQF: 10 – 1000 y (Table 4.3).

Importantly, the 1D-corrected method, which accounts for the angle between the profile and the gradient, provides a more accurate estimation of the range of possible diffusion times. Examples of this approach are shown in Fig. 4.11. On this basis, the core-rim boundary for Whakamaru quartz yields a time range of 5 – 230 y, with an average of ~ 50 y (Table 4.3). YTT rim boundaries provide a range of 4 – 210 y, with an average of 60 y; and EQF rim boundaries are similar, ranging 5 – 190 y, with an average of 60 y and one anomalous boundary of 2000 y (Table 4.3). These timescales are implied as they are long enough to allow for growth of the bright rims, rather than having the recharge event directly physically linked to triggering of the eruption (cf. Sparks et al., 1977).

Both 1D analytical methods enable calculation of time in a purely analytical fashion, with no numerical modelling involved. The 1D-corrected method provides a useful means of individually examining each point across the diffusion boundary with multiple times extracted; thus providing information on how good the fit is, the quality of the data, and the asymmetry of the profile around the midpoint. Anomalous points along the profile relate to structural defects or complexities in initial concentrations.

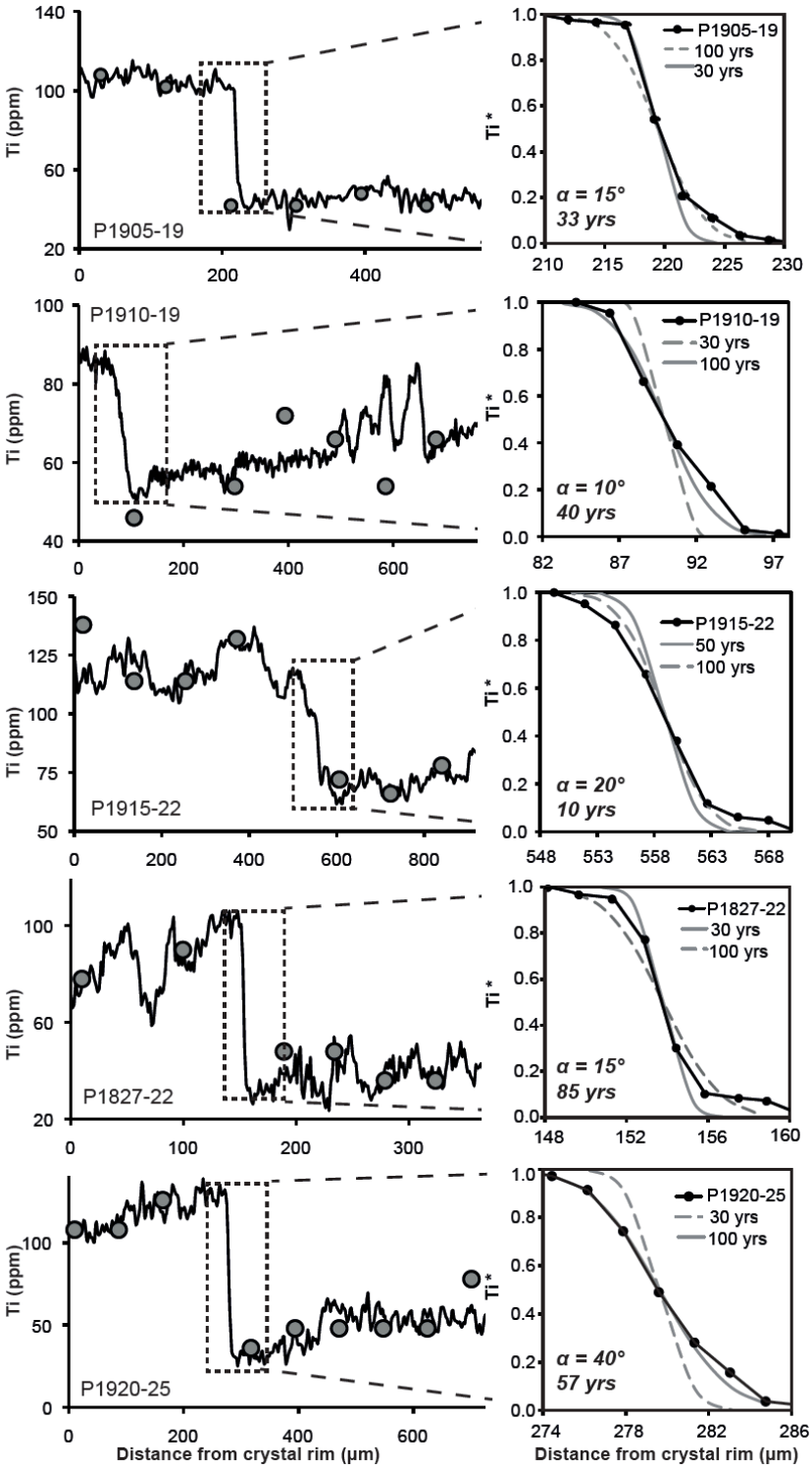

Fig. 4.11: Diffusion modelling for Ti in quartz at eruption temperature of 770°C. Graphs (left) show CL greyscale profiles calibrated to Ti concentration. Modelled diffusion profile (right) for different elapsed times (grey lines) compared to element gradient (black line). Ti content normalised across transition marked by dashed rectangle. Time representing best fit is coded by a solid grey line, and dashed grey line is for comparison. Inset shows results of 1D-corrected method that accounts for the angle (α) between the measured profile and the perpendicular to the boundary of interest. Presented in Matthews et al. (2011a).

4.3.4.2 2D Lattice Boltzmann methodology

Results of 2D LB diffusion modelling, accounting for the angle of core-rim boundary at depth, β, with selected examples of Whakamaru, EQF and YTT quartz diffusion are shown in Figs 4.12 and 4.13. 2D LB diffusion calculations based on calibrated CL greyscale data generate average diffusion times of 71 y for Whakamaru (median 45 y, range 32 – 1150 y), 120 y for EQF (92 – 2750 y), and 95 y for YTT quartz (75 – 210 y; Table 4.3). A minor population of crystals yield longer diffusion times for the core-rim boundary as follows - Whakamaru: 215 (Fig. 4.12j), 265 (Fig. 4.12d) and 1150 y; YTT: 210 y (Fig. 4.13f); and EQF: 2750 y (Fig. 4.13b; Table 4.3).

The main advantage of this numerical method of diffusion modelling is that it accounts for the complex 2D crystal geometry and the angle between profile and the modelled boundary (see modelled areas of quartz crystals in Figs 4.12 and 4.13). Considering the complexities of the core-rim boundary observed for many quartz crystals, this 2D approach is likely to be more accurate than 1D. For example, 2D modelling of diffusion across a corner transect (P1910-20; Fig. 4.12a) provides a significantly shorter timescale than the 1D methods (60 y by 2D vs. 230 y by 1D; Table 4.3). This method also accounts for internal structure adjacent to the crystal boundary (e.g., P1905-23; Fig. 4.12(g), P1905-12 Fig. 4.12j; Fig. 4.8), where structural complexities on the resorption surface result in a significant difference between 2D and 1D diffusion times.

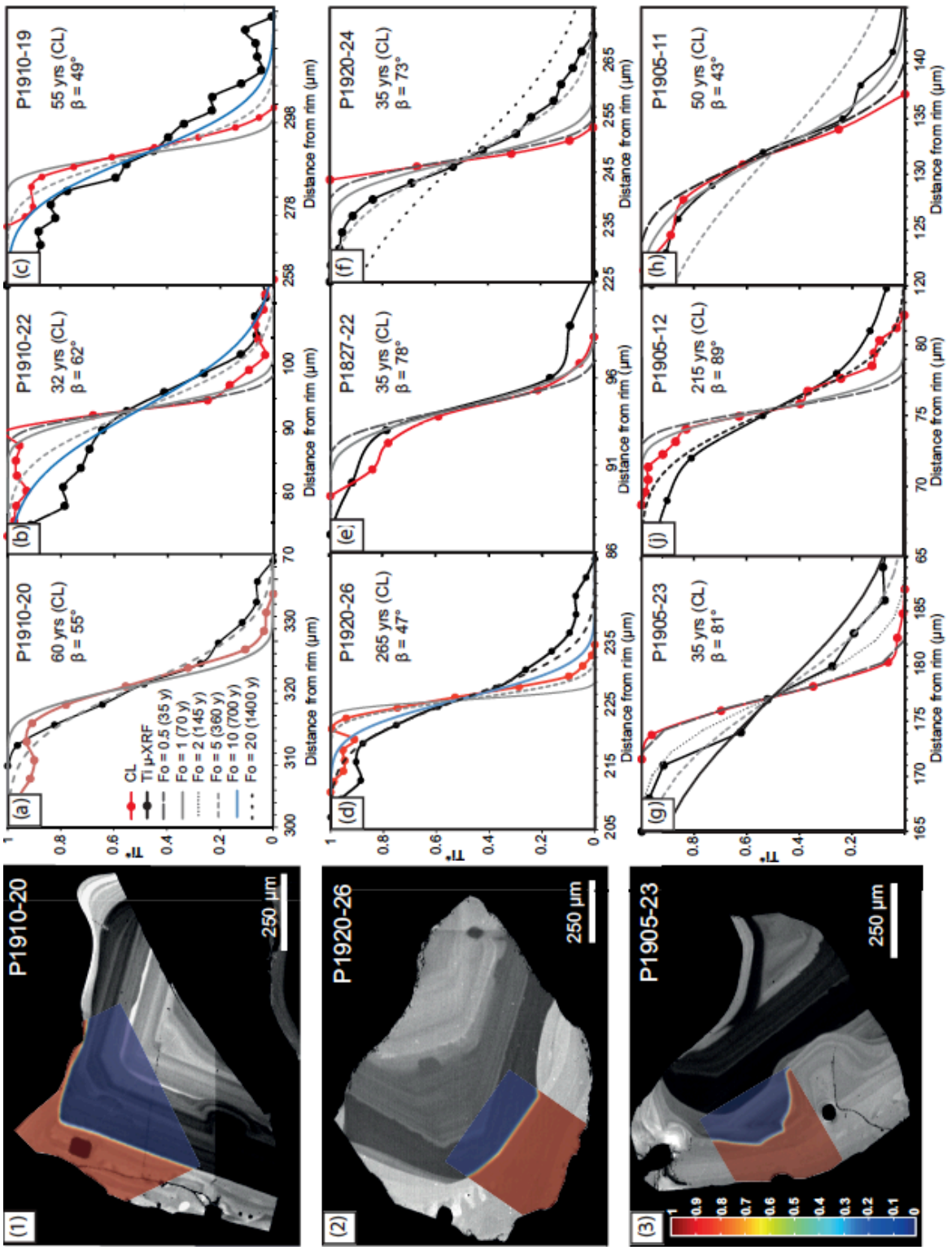

Fig. 4.12: 2D-LB diffusion modelling for Whakamaru quartz. (1-3): CL images of quartz crystals showing area for 2D diffusion modelling, where dark quartz cores (low-Ti) are coded blue, and bright-CL rims are red. Colour scale (3): shows normalised Ti where red *1* indicates maximum Ti concentrations, and blue *0* represents minimum Ti. (a - i): 2D LB diffusion profiles of Ti-in-quartz across the core-rim interface for selected quartz crystals. The black line shows raw (uncorrected) Ti µ-XRF synchrotron data, red line indicates CL-greyscale data and 2D-LB modelled lines are represented by dashed grey and blue lines. Model parameter numbers, Fo, indicated in key (a). Results of 2D-LB diffusion corrected for angle (β) of the core-rim interface at depth are provided in top right inset of each diffusion profile. Note that the µ-XRF data display a lack of smoothness due to the depth-averaging effect.

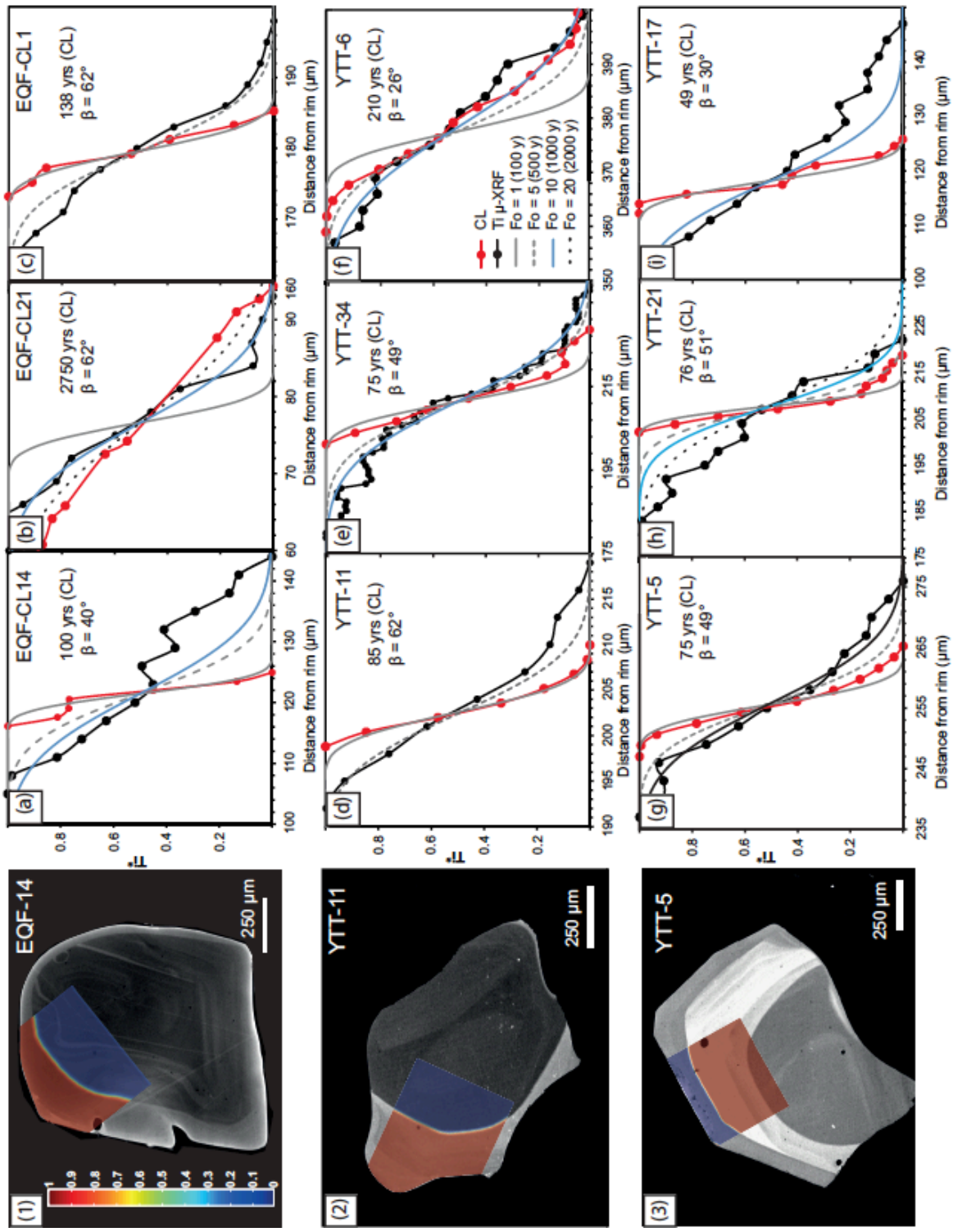

Fig. 4.13: (1-3): CL images of YTT and EQF quartz crystals showing area for 2D diffusion modelling, where dark quartz cores (low-Ti) are coded blue, and bright-CL rims are red. Colour scale in (1) shows normalised Ti where 1 (red) shows maximum Ti concentrations, and 0 (blue) represents minimum Ti. (a - i): 2D LB diffusion profiles of Ti-in-quartz across the core-rim interface for selected EQF and YTT quartz crystals. The black line shows Ti µ-XRF synchrotron data, red line indicates CL-greyscale profile and 2D-LB modelled lines are represented by dashed grey and blue lines. Model parameter numbers, Fo, indicated in key (f). Results of 2D-LB diffusion corrected for angle (β) of the core-rim interface at depth are provided in top right inset of each diffusion profile. Note that the µ-XRF data display a lack of smoothness due to the depth-averaging effect.

4.3.4.3 Synchrotron micro-XRF data for diffusion modelling

As mentioned in Section 4.3.3, there are disadvantages in using μ-XRF data in diffusion modelling. It is pertinent, however, to record a comment on this here.

Although the high spatial resolution of Ti across the zone boundaries acquired by μ-XRF is advantageous, diffusion modelling techniques applied to these data tend to result in longer diffusion times due to the lower gradient often seen for the compositional step (Figs 4.12 and 4.13). For example, the core-rim boundary of crystal P1910-19 (Fig. 4.12c) yields a diffusion time of 55 y from CL-greyscale, while μ-XRF data indicate 700 y. The lower gradients reflect the angle of beam penetration and depth averaging of Ti during synchrotron analysis (Fig. 4.15). Calibrated greyscale CL values therefore appear to more accurately indicate the compositional gradient and have been used here for the diffusion modelling. The spacing of zones observed in CL images is identical to that observed in μ-XRF Ti data however (Figs 4.8, 4.9 and 4.10), confirming that Ti is the main CL activator in quartz. Furthermore, μ-XRF data provide a useful means of calculating the angle of the core-rim interface, using the geometric constraints as outlined in Fig. 4.15. These angles are then incorporated into the diffusion modelling to constrain diffusion times (where the optimal diffusion transect is perpendicular to the core-rim boundary both at the surface and at depth), as mentioned above.

Table 4.3: ***Comparison of diffusion times (y) for core-rim boundaries of Whakamaru, Toba and Earthquake Flat quartz, using both 1D and 2D diffusion methods applied to CL data***

Crystal	1D methods			2D LB from CL-greyscale				
	1D (years)	Corrected 1D av. (years)	Angle α	Angle β	Fo	Years	New Fo (angle)	Years (with angle)
Whakamaru quartz, at 770°C								
P1910-15	275	60	8	33	1	70	0.5	40
P1910-18	200	20	5	34	1	70	0.6	40
P1910-19	100	90	10	49	1	70	0.8	55
P1910-22	100	5	5	62	0.5	35	0.4	32
P1910-20	150	230	0 (corner)	55	1	70	0.8	60
P1915-22	50	40	20	26	1	70	0.4	32
P1920-24	150	25	40	73	0.5	35	0.5	35
P1920-26	100	25	40	47	5	360	3.7	*265*
P1827-7	100	5	30	59	1	70	0.9	60
P1827-22	25	20	15	78	0.5	35	0.5	35
P1905-11	15	5	5	43	1	70	0.7	50
P1905-12	300	35	45	89	3	215	3.0	*215*
P1905-17	500	40	20	40	1	70	0.6	45
P1905-23	60	60	0	81	0.5	35	0.5	35
P1905-19	100	130	15	55	20	*1400*	16.4	*1150*
Average:	**152**	**53**					**Average:**	**71**
Median:	**100**	**35**					**Median:**	**45**
Toba YTT quartz, at 760°C								
YTT-34	450	10	45	49	1	100	0.8	75
YTT-11	100	25	40	62	1	100	0.9	85
YTT-5	100	60	0	49	1	100	0.8	75
YTT-21	100	60	45	51	1	100	0.8	76
YTT-17	100	210	50	30	1	100	0.5	49
YTT-6	300	4	30	26	5	*500*	2.2	*210*
Average:	**192**	**62**					**Average:**	**95**
Median:	**100**	**43**					**Median:**	**75**
Earthquake Flat quartz, at 745°C								
EQF-CL21	1000	2000	0	62	20	*3100*	17.7	*2750*
EQF-CL5	10	5	30	36	1	150	0.6	92
EQF-CL1	100	190	35	62	1	150	0.9	138
EQF-CL8	50	35	40	83	1	150	1.0	154
EQF-CL14	10	10	20	40	1	150	0.6	100
Average:	**43**	**60**					**Average:**	**121**
Median:	**50**	**35**					**Median:**	**138**

Notes: 1D and 2D diffusion modelling is based on CL greyscale as a proxy for Ti content in quartz for core-rim boundaries of selected quartz crystals from each eruption. The angle (α) of the transect perpendicular to the boundary is incorporated in the analytical 1D approach (using xcosα as explained in Fig. 4.4). LB-2D diffusion modelling considers the angle (β) of the core-rim interface to the horizontal, as calculated using CL greyscale, where Fo is the Fourier Number used in diffusion equations (Fig. 4.15). Anomalously long times are indicated in italics and omitted from the average and median calculations.

4.3.4.4 Sources of error in diffusion time calculations

Possible sources of error in the diffusion calculations result from assumptions outlined in the Section 4.2.3. The main source of uncertainty is the choice of temperature, as small variations can result in very different timescales. The relationship between temperature and diffusion time is exponential (Fig. 4.14). For example, 1 y of diffusion at 800°C would take 25 y at 700°C, and 1100 y at 600°C (using equation [4.1]). The temperature error is limited in this study, however, due to constraints from Fe-Ti geothermometry, and the error arising from temperature estimations can be accounted for in the modelling (e.g., refer to Fig. 4.7 of Saunders et al., 2010). The assumption that this temperature is fixed for diffusion is also an oversimplification, however, as diffusion would have continued during any further thermal fluctuations prior to eruption (Shaw, 2004). As Fe-Ti oxide temperatures tend to be lower than TitaniQ rim temperatures for all three eruptions (Table 4.2), timescales calculated using the eruption temperature are also likely to be over-estimated.

Furthermore, the primary assumption that the compositional step was initially vertical introduces an unquantifiable error into diffusion calculations and means that the calculated diffusion times represent the maximum time since rim growth and eruption. The timescales may also be an overestimation of the real times if part of the compositional profile is due to changing conditions during growth rather than diffusion alone (e.g., Costa and Morgan, 2010).

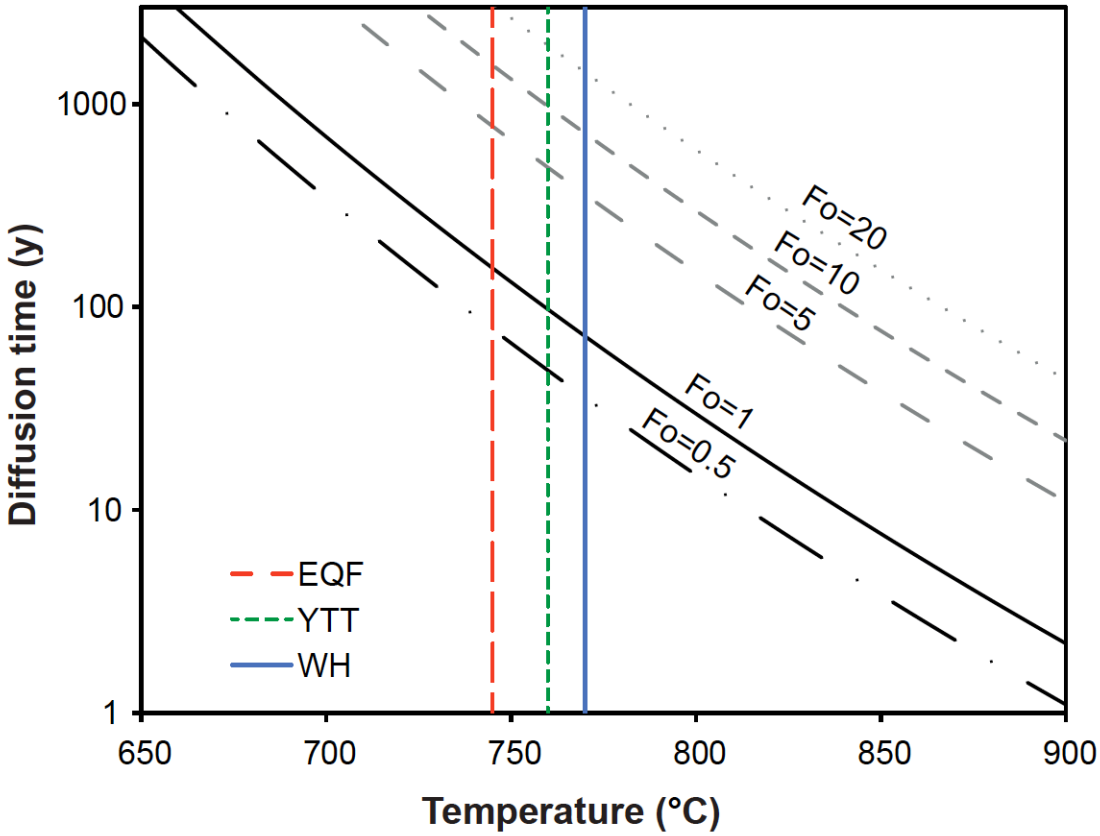

Fig. 4.14: Relationship between temperature and diffusion time for various Fourier (Fo) numbers, using the Arrhenius relationship of Ti diffusion in quartz from Cherniak et al. (2007). Eruption temperatures for Whakamaru (WH), Earthquake Flat (EQF) and Younger Toba Tuff (YTT) are indicated by the coloured lines. Most modelled quartz compositional steps give a Fo of 0.5 to 1 for Whakamaru (from CL greyscale as a proxy for Ti in quartz), corresponding to short diffusion times of 35 – 70 y. For an eruption temperature of 770 °C (relating to Whakamaru), diffusion times are as follows: Fo = 0.5, 35 y; Fo = 1, 70 y; Fo = 5, 360 y; Fo = 10, 720 y, Fo = 20, 1400 y.

The effect of the orientation of the crystal and zonation (due to off-centre sectioning) with respect to the plane of analysis must also be considered. Compositional traverses were taken perpendicular to crystal margins where possible (see Costa et al., 2008), and in 1D modelling the angle between the zonation and the analysis transect (which would result in artificial lengthening of the profile) can be accounted for. 1D diffusion modelling cannot, however, account for the 2D structural complexities. Although 2D structural irregularities in the crystal boundary have been accounted for with the LB modelling, 3D effects are

more difficult to assess and introduce an unquantifiable error. As outlined earlier, the synchrotron data can be used to calculate the angles of the core-rim boundary with respect to the surface, and this is built into the diffusion modelling, assuming that the core-rim interface is a planar feature at depth.

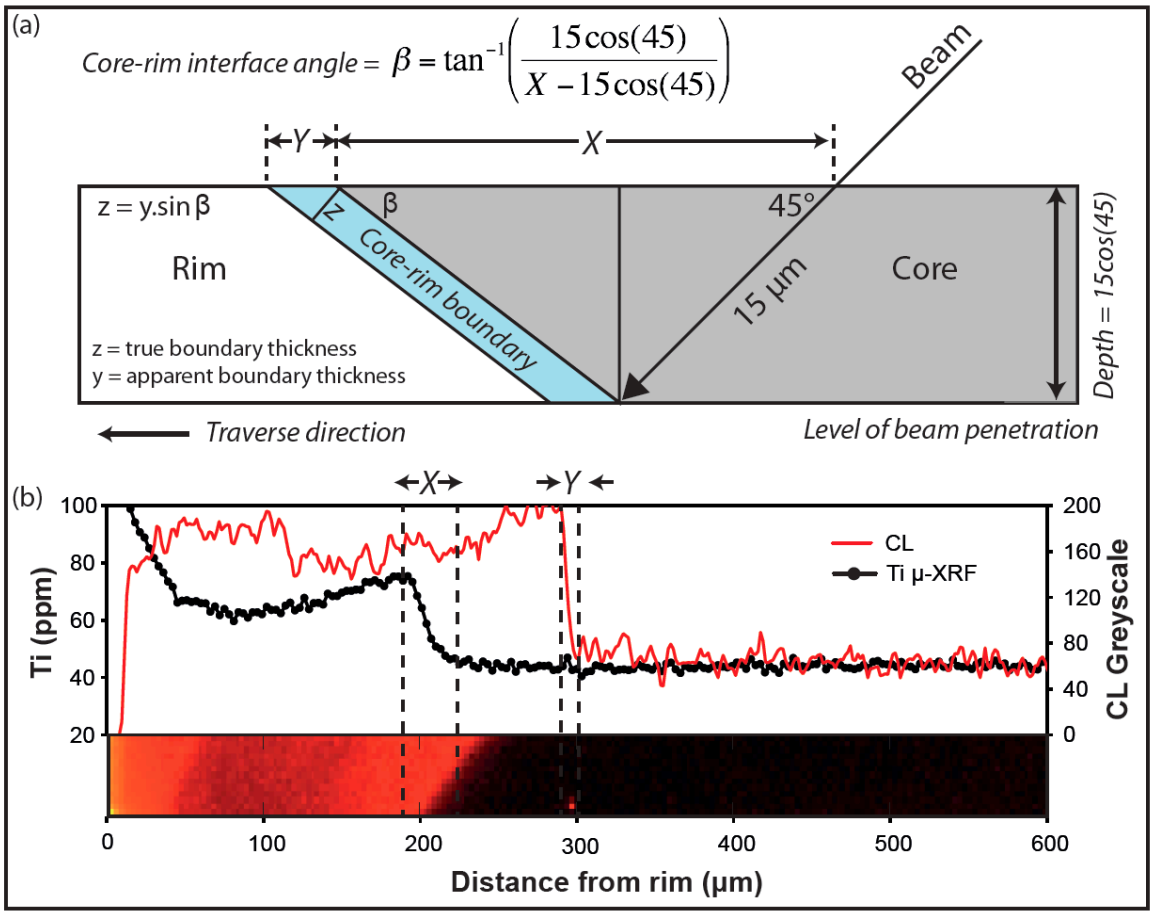

Fig. 4.15: Schematic cross-section through quartz crystal in epoxy mount, showing calculation of the angle (β) of the core-rim boundary with respect to the analysis surface. To account for the angle of the core-rim boundary with respect to the surface CL view of the diffusion boundary, the true distance across which the compositional step takes place (z) is calculated as indicated in fig (a) where the distance Y is determined as indicated by (b). Note the 'averaging-effect' of the synchrotron beam as it penetrates 15 µm into the crystal at a 45° angle of incidence (b), thus depth-averaging Ti concentrations (black), and making the compositional step artificially shallower and less abrupt than shown by CL greyscale (red).

4.3.5 Stirring and reactivation timescales

To extend the record of magma chamber processes derived from quartz two other factors are considered here:

1. timescale of stirring of the rhyolitic chamber - i.e., the time required to homogenise the convecting magma body; and
2. mush reactivation timescale – i.e., the period between the injection of mafic magma under a large crystal-rich reservoir and the time at which the crystal mush is unlocked and open to whole-chamber convection (Huber et al., 2011b).

The stirring timescale (τ_m) is calculated for the Whakamaru magma reservoir assuming steady-state convection, using equation [4.11] from Huber et al. (2009) where 5 – 10 overturns in the chamber is the defined criterion for a stirred chamber; $\dot{\varepsilon}$ is the shear strain induced by convective stirring; H is the magma chamber thickness (volume/surface area, assumed to be 1 km; Section 3.4.3); κ is the thermal diffusivity (10^{-6} m^2 s^{-1}; Turcotte and Schubert, 2002; Huber et al., 2010b, 2011b; Table 3.6); and H^2/κ is the diffusion timescale of interest in the mixing process.

$$\tau_m = \frac{1}{2\dot{\varepsilon}} \times \log\left(\frac{\dot{\varepsilon} H^2}{\kappa}\right) \qquad [4.11]$$

The average shear strain depends on the Rayleigh number (Ra: ratio of diffusive to advective timescales for heat transfer), which for large magma bodies is > 10^9 (Coltice and Schmalzl, 2006). The Rayleigh number is given as

$$Ra = \frac{\Delta\rho g H^3}{\kappa\mu} \qquad [4.12]$$

where $\Delta\rho$ = difference in density that drives convection; g = gravitational constant (9.81 m s^{-2}); and μ = viscosity of the melt (10^5 Pa s; Scaillet et al., 1998a; Cottrell et al., 1999; Bachmann and Bergantz, 2006). Strain is calculated by equation [4.13] for $10^3 \leq Ra \leq 10^9$ (Coltice and Schmalzl, 2006; Huber et al., 2009).

$$\dot{\varepsilon} = 0.023 \times \left(\frac{\kappa}{H^2}\right) \times Ra^{0.685} \qquad [4.13]$$

Alternatively this calculation can be modified using boundary-layer theory ($_{BL}$) to equation [4.14] (Turcotte and Schubert, 2002; Huber et al., 2009).

$$\dot{\varepsilon}_{BL} = 0.271 \times \left(\frac{\kappa}{H^2}\right) \times Ra^{2/3} \qquad [4.14]$$

In these calculations a boundary-layer density difference, $\Delta\rho$, associated with a crystallinity contrast in the rhyolitic magma, of 100 kg m^{-3} is assumed (Blake and Ivey, 1986; Tait et al., 1989).

Using the above method the calculated stirring timescale ($\tau_{m,}$, equation [4.11]) for the Whakamaru magma system is of the order of months to one year. This refers to the time required to homogenise the entire magma chamber in response to the basaltic recharge event, once convection is fully developed (Huber et al., 2009).

The reactivation timescale depends on the size and crystallinity of the magma, the size and frequency of magma intrusion carrying the enthalpy required to induce convection, and also the tectonic setting (in terms of phase assemblage and volatile contents of the crystal

mush and recharge magma; Huber et al., 2010a, 2010b). The reactivation timescale is calculated using equation [4.15]:

$$t_{react} = \frac{H}{\delta c^2}\left(\frac{\kappa \mu Ra_{cr}}{\Delta \rho g}\right)^{2/3}, \qquad [4.15]$$

where δ is the boundary layer thickness of the convecting magma (Huber et al., 2011b); Ra_{cr} is the critical Rayleigh number at which convection starts (of the order of 10^3); and the constant $c \sim 4$ m $y^{-1/2}$ was determined from calculations of Huber et al. (2010a; 2011b) and relates to the rate of opening or 'defrosting' of the mush.

Based on these calculations, the time required for reactivation of the Whakamaru crystal-rich magma reservoir is estimated as being of the order of 10^3 to 10^4 y.

4.4 Discussion

Modelling of quartz zonation patterns for three eruptions of varying magnitude provides information on the evolution of each magmatic system in terms of both physical and chemical changes. Here results of Ti-zoning in quartz and the associated timescales are built into quartz crystallisation pathways in pressure/temperature space.

4.4.1 Ti-zoning in quartz

The bright-CL (high-Ti) rims on all Whakamaru and EQF quartz crystals analysed suggest that both eruptions were preceded by a sudden thermo-chemical change, possibly representing an influx of hotter magmas, crystallisation at reduced pressure (see Thomas et al., 2010; Wilson et al., 2011; Matthews et al., 2011a), and/or shifts in magma chemistry and TiO_2 activity. These variables could also be changing simultaneously, which could dampen or amplify the magnitude of compositional change. Similar features have been observed for quartz from other rhyolitic systems where this reverse zoning pattern is interpreted as resulting from hotter magma inputs and thermal rejuvenation (e.g. Peppard et al., 2001; Wark et al., 2007; Wiebe et al., 2007; Shane et al., 2008b; Campbell et al., 2009). New mafic magma inputs from depth are likely to be hotter than the crystal-rich high-silica rhyolitic chamber, and magma replenishment is thus invoked here as the fundamental process that initiates resorption and overgrowth.

YTT quartz, in contrast, is characterised by both normal and reverse zoning (Fig. 4.7), suggesting that crystals experienced different pre-eruption conditions, most likely due to their spatial separation in the large magmatic system. Parallels can therefore be drawn with the Bishop Tuff (600 km^3, erupted from Long Valley caldera at 760 ka; Hildreth and Wilson, 2007) pre-eruption magmatic processes where a previous study has indicated a

combination of both quartz zoning patterns attributed to the role of crystal sinking in a thermally stratified magma reservoir (Anderson et al., 2000). Alternatively, the system could have comprised different pockets of melt that were isolated and stored under slightly different conditions prior to eruption.

The size of the Whakamaru quartz crystals also indicates that they are likely to be derived from a deeper crustal mush zone, where they experienced an extended period of crystallisation with minor fluctuations in P, T and XH_2O prior to the significant event (or some combination of P, T, XH_2O change) recorded at the core-rim boundary.

4.4.2 Quartz stability

The question of quartz stability is addressed here using the newly calibrated *Rhyolite-MELTS* code (Gualda et al., 2010) to explain the patterns of quartz crystallisation and resorption in P/T space, as shown in Fig. 4.16 (based on Whakamaru pumice sample P1905). This modified calibration of MELTS has been optimised to correctly calculate the quartz + sanidine saturation surface in hydrous silicic systems as a function of pressure, temperature and composition, and has been previously applied to the Bishop Tuff and Peach Spring Tuff magmatic systems (see Gualda et al., 2010).

Pathways (P/T vectors) are envisaged for the Whakamaru quartz crystals to explain their Ti zonation patterns (Fig. 4.16b). The low-Ti quartz cores may be interpreted as representing crystals from a mature crystal mush zone which experiences an abrupt increase in temperature, in parallel with a slight increase in pressure (associated with the injection of hotter mafic magma), until quartz becomes unstable and begins to resorb as conditions move out of the quartz stability field (Fig. 4.16a). This phase would be responsible for

generating the major resorption boundary between the low-Ti cores and the high-Ti rims. In order to crystallise the high-Ti quartz rims, either the pressure then must drop, or there is a combined pressure/temperature change that moves the system back into the quartz stability field to recommence crystallisation prior to the eruption. All Whakamaru quartz crystals show disequilibrium textures (resorbed crystal boundaries with glass re-entrants), however, suggesting that these crystals were in disequilibrium in their host melt shortly before eruption and that there was a final P/T change immediately prior to, or co-incident with, eruption. The minimum timescales (not accounting for resorption time) associated with each of episodes of crystallisation and resorption are outlined in Fig. 4.16c and discussed in the following sections.

Bishop Tuff quartz displays many similarities with Whakamaru, EQF and YTT quartz as discussed here. Wark et al. (2007) suggest that the high-Ti rims are able to crystallise due to reduced water activity in response to an influx of CO_2 from intruding mafic melts, whereas dissolution would occur if the mafic melts were H_2O-rich (Wark and Bachmann, 2005). As H_2O-rich magmas are principally found at convergent plate-margin settings, this suggests the response of quartz to a recharge event may be a function of tectonic setting (Wark and Bachmann, 2005). Here, the Rhyolite-MELTS modelling indicates that high-Ti rims could also crystallise in response to a pressure drop or a pressure drop coincident with a slight temperature rise (see vectors in Fig. 4.16), and changes in water activity (which has negligible effect on quartz stability in comparison to temperature and pressure shifts) do not necessarily have to be invoked.

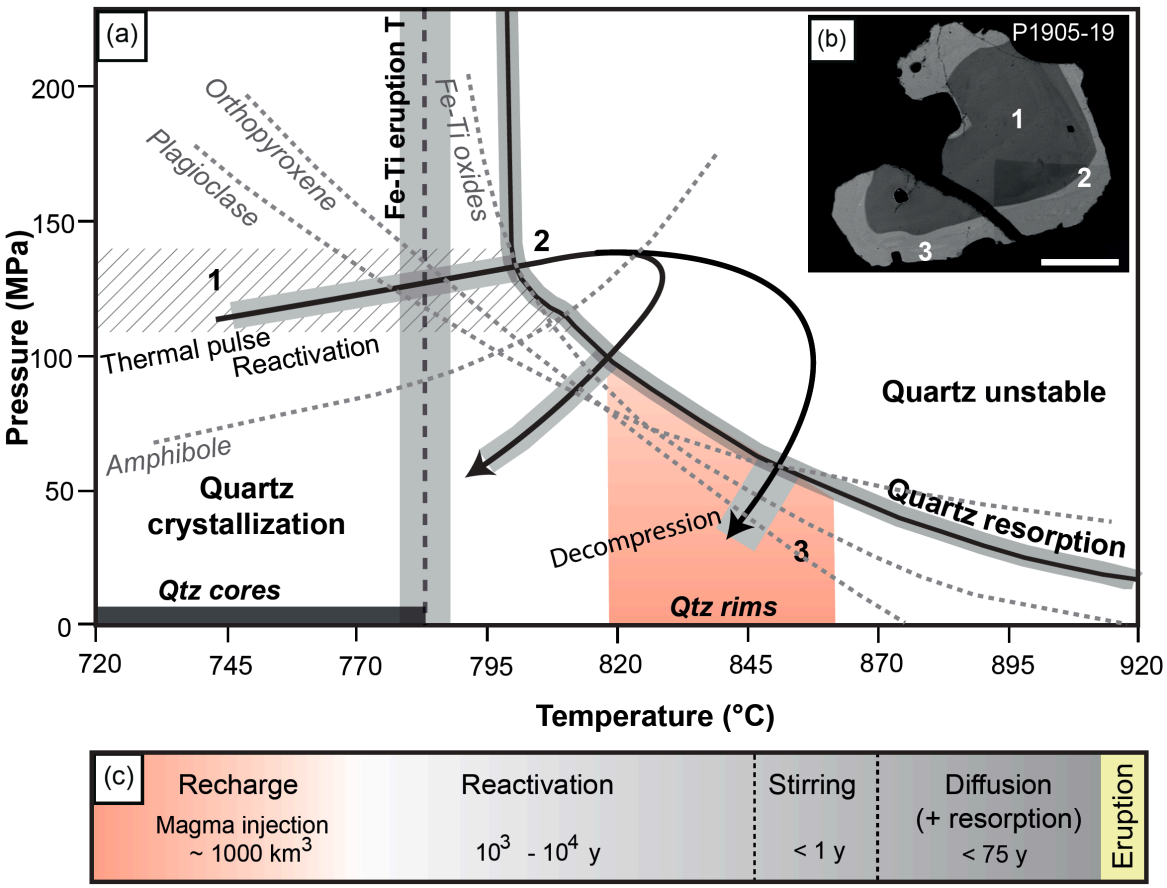

Fig. 4.16: (a) Quartz stability modelled using Rhyolite-MELTS (Gualda et al., 2010) using starting composition from whole-rock XRF data for rhyolitic Whakamaru pumice sample P1905; with 4 wt% H_2O; NNO +0.45 (values chosen from Fe-Ti oxide geothermometry), initial pressures (110 – 140 MPa; field marked by diagonal lines) derived from melt inclusion and amphibole data (see Matthews et al., 2011a); P/T values for quartz stability field as modelled using Rhyolite-MELTS are indicated by black line. Dashed grey lines show phase-equilibria fields for other phases (plagioclase, orthopyroxene, amphibole and Fe-Ti oxides), using data from Coombs and Gardner (2001). Vectors plotted represent P/T pathways during quartz crystallisation, with shaded pathways indicating episodes of quartz crystallisation; (b) CL image of Whakamaru quartz crystal (scale bar 500 µm) showing three major episodes of crystallisation/resorption, where 1 represents the initial thermal pulse and reactivation, 2 thermal pulse results in resorption, taking quartz out of its stability field, and 3 high-Ti quartz rim crystallisation in response to decompression, or temperature drop; and (c) timescales of magma recharge, reactivation, stirring and diffusion prior to eruption; note that these timescales are not presented sequentially.

4.4.3 Timescales of magma recharge

The width of bright-CL quartz rims is variable at < 100 to > 200 μm (Section 3.3.3). With an average diffusion time of ~ 70 y (Table 4.3) the crystal growth rate would be > ~ 1 – 3 μm y^{-1} (0.3 – 1 × 10^{-7} μm s^{-1}). Crystal fragments show no overgrowths or diffusion profiles at fractured margins, implying they had insufficient time to respond to changing P/T conditions and indicating quenching on eruption. The lack of a prolonged diffusive re-equilibration history is, however, suggestive of geologically rapid accumulation of the melt-dominant magma body in its final stages prior to eruption (cf. Brown and Fletcher, 1999; Wilson and Charlier, 2009). These short time intervals suggest that the thermal/pressure/compositional perturbation may represent a mechanism that contributed to the final evacuation of the chamber (most likely associated with a significant magma reservoir recharge event).

The Ti concentration profiles displayed by synchrotron μ-XRF Ti maps (Figs 4.8, 4.9, 4.10) correlate well with CL-greyscale profiles as described above, confirming that CL intensity is directly proportional to Ti content (Wark and Spear, 2005; Götze et al., 2001) and can be used as a proxy for Ti content. The relatively sharp compositional steps in these quartz Ti and CL profiles indicate that the Whakamaru, YTT and EQF magmas experienced a sudden physico-chemical change resulting in the resorption and subsequent overgrowth of high-Ti quartz rims. Timescales derived for these compositional changes are interpreted as the elapsed time between a significant magma recharge event (responsible for generating the thermal pulse indicated by the high-Ti quartz rims) and eruption, minus an unquantifiable period of time associated with rim resportion.

2D LB diffusion modelling across this significant core-rim boundary yields a range of diffusion times, suggesting that some crystals record a unique history. The majority of Whakamaru quartz crystals modelled, however, indicate that the compositional step relates to a significant event that occurred 35 – 60 y prior to eruption (Table 4.3). During this short time span, rapid rim growth must have occurred, followed by partial dissolution of the new quartz zone. This may have been coincident with volatile sparging from underlying mafic magma inputs, which possibly also destabilized the magma reservoir ultimately leading to eruption. Similarly, 2D LB diffusion modelling of YTT quartz rims gives a diffusion timescale of 50 – 85 y, and EQF ~ 120 y (Table 4.3), indicating that these major thermal/pressure/composition events can indeed occur rapidly in large-volume silicic systems.

For all three eruptions some quartz core-rim boundaries yield longer times, which may correspond to earlier events. Three main events are identified in Whakamaru quartz, for example: at 35 – 60 y, 215 – 265 y, and at 1150 y (2D LB data, Table 4.3). An anomalous EQF crystal records an event 2750 y before eruption (EQF-CL21, Table 4.3 and Fig. 4.13b). Toba quartz crystals generally record a 50 – 85 y event, with a single exception that records a 210 y event (YTT-6, Table 4.3 and Fig. 4.13g). Whakamaru quartz crystals therefore record the most complex history of compositional/thermal changes in the chamber, considering the multiple ages recorded. The most significant (and dominant) event for the Whakamaru magma system is, however, closest to eruption (35 – 60 y; Table 4.3) and is thus most likely to represent the event which primed the magma for eruption. These timescales represent a maximum time, given that diffusion calculations use Fe-Ti oxide eruption temperatures, which are significantly lower than those derived from TitaniQ

(Appendix 11), in addition to issues arising from the assumption of an initial vertical step (as outlined earlier, Section 4.3.4.4).

Diffusion timescale results compare well with those presented by Saunders et al. (2010) where Whakamaru quartz core-rim boundaries yield times of 46 – 172 y with a peak likelihood of renewed quartz growth at 50 – 70 y. Although similar, these results from Saunders et al. (2010) do not necessarily compare directly to those presented here because of the different sample types involved.

Timescales calculated here are also similar to the quartz records from the Bishop Tuff and Campanian Ignimbrite, which also display Ti concentration changes considered equivalent to 100°C heating over periods of probably no more than ~ 100 y leading up to the eruption (Wark et al., 2007; Pappalardo et al., 2008). In contrast, Oruanui quartz shows a great variety of CL zonation patterns (Liu, Y. et al., 2006) despite clear evidence for pre- and syn-eruptive mafic recharge (Wilson et al., 2006).

4.4.4 Timescales of stirring and reactivation

Interpretations of magmatic timescales presented here are based on mafic magma recharge of the silicic chamber, causing P/T changes and initiating stirring and reactivation. The thermodynamic calculations (equation [4.15]) suggest that the time required for reactivation (chamber-wide convection) of a voluminous crystal-rich magma reservoir, in response to mafic recharge, is of the order of 10^3 to 10^4 y, whereas stirring timescales (to completely homogenise the chamber; equations [4.11]-[4.14]) are < 1 y (Section 4.3.5). This implies that the magma chamber is much quicker to mix, once it is convecting, than it

is to reactivate. As both processes are concurrent during most of the reactivation process (as soon as the reactivated part is able to convect), reactivated magmas tend to be homogenous (see Huber et al., 2011c). These timescales thus provide a broader view of magma chamber development, which add to the quartz-derived timescale (Fig. 4-16c). In contrast, studies of zircon crystallisation histories for the Whakamaru magma system indicate magma generation and residence times of ~ 100 ky (see Chapter 5; Brown and Fletcher (1999) suggested residence times of > 250 ky), highlighting the overall longevity of the system. The timescales of reheating and eruption-triggering events, as indicated by the quartz zoning, are very rapid in comparison (most likely < 35 y for Whakamaru), indicating that there must be a significant input of energy into the system to prime the large, crystal-rich silicic system for eruption.

As the thermal pulse is recorded shortly before eruption, two possibilities to explain the reactivation timescales are envisaged as follows:

(1) the time elapsed between the end of quartz resorption and the recharge event was long enough to explain reactivation of the mush (this reactivation time is poorly recorded by quartz crystals, which only record the duration of crystallisation during P/T conditions for quartz stability); or

(2) the different timescales recorded in some quartz crystals suggest a protracted history of reactivation by numerous intrusions over the last few thousands of years. The mush is therefore likely to have been mostly reactivated by these different thermal pulses by the time the last thermal pulse reached the rhyolite magma (greater than the shortest time recorded by quartz). The last intrusion may have initiated an eruption trigger.

4.4.5 Recharge episodicity: incremental magma accumulation

The diffusion timescales provide an insight into the episodicity of recharge events responsible for significant P/T changes reflected by quartz crystallisation. The range of timescales is interpreted as providing a chronological record of magma intrusion during the later stages of magma chamber assembly. The final recharge event causes quartz rim resorption, and most likely represents the eruption-triggering event, although the timescale associated with this cannot be quantified by quartz diffusion modelling due to rim resorption. Modelling results of Whakamaru quartz indicate significant recharge events at ~ 35 – 60, 215 – 260 and 1150 y prior to eruption (based on diffusion times for different core-rim boundaries, assuming constant temperature), highlighting the role of incremental magma intrusions in the building of large volumes of silicic magma. The most significant pulse of melt into the crust (recorded by 75% of quartz crystals analysed, Table 4.3) occurred within 32 – 60 y of eruption.

Independent petrographic and geochemical data for the Whakamaru and EQF systems indicate that injections of mafic magma are the most likely explanation for the quartz resorption events and P/T change. Increasingly diffuse resorption horizons are preserved within quartz cores and some rims (e.g., 2750 y, EQF-CL21; 1150 y, WH P1905-19; Table 4.3), and these may be explained as being related to pockets of melt, partially isolated within the mushy system, and recording subtly different crystallisation histories. There is no direct evidence for mafic involvement in the Toba system, however, and it is possible that silicic magma recharge events represent the driving force for the observed quartz zonation patterns. Furthermore, the quartz record indicates that most recharge events only temporarily perturb the system prior to further crystallisation. Whether or not a recharge event results in eruption is likely to depend on differences in melt composition,

crystallinity, temperature, volatile contents and the degree of interaction between the rhyolite and intruding magmas. The presence of mafic-mingled pumices in Whakamaru and EQF eruptions indicates direct interaction between the two magmas as an eruption-triggering mechanism. Similarly complex magmatic histories involving multiple recharge events and mafic-silicic interaction have been observed for magma systems of all sizes (e.g., El Chichón, Mexico, Davidson et al., 2001; Andrews et al., 2008; Tarawera, New Zealand, Shane et al., 2007; and Yellowstone caldera, Girard and Stix, 2009, 2010).

4.5 Conclusions

The new use of synchrotron μ-XRF techniques outlined here has shown that Ti transects correlate directly with CL profiles, providing further evidence that Ti is the main activator of CL in quartz, and adding robustness to the use of the CL-greyscale in Ti-in-quartz diffusion modelling. Chemical and textural zonation of quartz crystals from three major rhyolitic eruptions has indicated that a common feature of such systems is a sudden pre-eruption change in magmatic P/T conditions resulting in high-Ti overgrowths in quartz crystals. As indicated in Section 3.4.3 (Matthews et al., 2011a), an input of a large volume of mafic magma (~ 1000 km^3) would be required to generate the Ti pulse recorded in rims of Whakamaru quartz crystals, if this compositional change were attributed solely to a 100 °C temperature rise. Calculations of timescales here suggest that subsequent rejuvenation of the system occurred over a period of 10^3 – 10^4 y with stirring over < 1 y required to completely homogenise the chamber.

The application of the new 2D diffusion modelling technique provides more accurate estimates of diffusion timescales than traditional 1D approaches. This approach takes into

consideration structural complexities of crystal boundaries and the angle of the diffusion profile to the boundary at depth (provided by the μ-XRF measurements), thus providing more reliable diffusion times. The calculated timescales are on average 70 y for Whakamaru, 95 y for YTT and 120 y for EQF, with modal values for Whakamaru and YTT of 35 and 75 y respectively. These timescales reflect high-Ti crystallisation, with the time between magma replenishment and eruption being longer as the P/T conditions had to change to bring quartz back into its stability field. The range in diffusion timescales provides evidence for episodic magma recharge events and points to incremental growth of large-volume magma reservoirs.

Results of the 2D diffusion modelling applied to CL greyscale data show that the large-volume YTT and Whakamaru eruptions, and the small-volume EQF eruption, are characterised by remarkably similar diffusion times. This indicates that the time between the onset of crystallisation after the reheating event, and prior to eruption, are not dependent on magma volume. This has important implications for magma chamber dynamics and recharge mechanisms. The final recharge event recorded by quartz from all three magmatic systems is likely to have primed the magma for eruption, but the timescale suggests that these events are unlikely to have been the eruption-triggering mechanism.

The results presented here suggest that the spacing of magma recharge events, volatile transfer and rheology of the two magmas are likely to be crucial factors in determining whether a major recharge event will result in caldera-forming eruption, rather than a temporary perturbation of the magmatic system. A comparison of the stirring/mixing and reactivation timescales indicates that the crystal-rich magma is expected to be homogeneous by the time it is fully reactivated before the eruption. This study provides

further evidence that silicic magma bodies are the result of extended periods of stirring, mixing and reactivation of crystal mush bodies, followed by significant thermal pulses attributed to magma recharge events that remobilise the magma and prime it for eruption.

Appendix A4.1

Calculation of μ-XRF synchrotron beam penetration

Calculation of the depth of beam penetration into the crystal specimen is based on equation [A4.1] which describes the attenuation of x-rays by a material:

$$I = Io \exp(-\mu x), \qquad [A4.1]$$

where Io is the original intensity of the signal, I is the resulting intensity after going through the material of thickness x, and μ is the mass attenuation coefficient of the absorber material (T. Geraki, *pers. comm*., 6 Dec 2010). This depends on the atomic numbers of the main constituents, the average density and the energy of the x-rays. This is typically expressed as the maximum depth from which the signal is derived (x) as I/Io = 1/e (which equates to the depth for 65% of the signal).

Using quartz (SiO_2) as the main matrix, with a density of 2.6 g cm^{-3}, energy of the Ti signal of 4.5 keV, and the 45° beam angle, the calculation yields a penetration depth of ~ 15 μm.

Chapter 5

Zircon crystallisation histories: investigating processes and timescales of silicic magma generation[3]

5.1 Introduction

The constraining of pre-eruptive magma storage, assimilation and crystallisation histories, and the identification of magma source components, are crucial for understanding large silicic systems. Zircon ($ZrSiO_4$) is an invaluable tool for unravelling these magmatic histories as it acts as a repository for numerous trace elements, preserving isotopic compositions inherited from the melt, and retaining radiogenic products useful for age determination (Cherniak and Watson, 2007). The application of high-spatial-resolution micro-analytical techniques to zircon is thus helpful in elucidating the assembly and residence timescales of large silicic magma reservoirs. Recent studies of large silicic systems have focused on zircon U-Th and U-Pb analyses to place time constraints on pre-eruptive crystallisation (e.g., Brown and Fletcher, 1999; Vazquez and Reid, 2002; Charlier et al., 2003, 2005; Crowley et al., 2007), and trace-element analyses for reconstructing crystallisation temperatures and inferring petrogenetic processes (e.g., Watson and Harrison 1983, 2005; Hoskin and Schaltegger, 2003; Hiess et al., 2008; Reid et al., 2011). Oxygen isotope ($\delta^{18}O$) zonation in zircon has also been used to reconstruct the pre-eruption histories of crystal recycling, magma mixing and contamination, and to define the

[3] Much of the material presented in this chapter is in Matthews et al., (2011d), Journal of Petrology, *in prep*.

characteristics of melt source regions (e.g., Bindeman and Valley, 2001, 2002; Bindeman et al., 2001).

Here these techniques are applied to the large-volume magma system associated with the ~ 340 ka Whakamaru supereruption (most recent age is 347 ± 4 ka and average age estimate is ~ 346 ± 30 ka; see Table 1.4 and references therein). Zircon is ubiquitous in Whakamaru Group pumices and in principle can provide useful constraints for petrogenesis and timescales of magma assembly and storage. Using this system as a case study, the aim here is to address the processes associated with pre-eruption magma generation and storage in a supervolcano system. Detailed descriptions of zircon growth features, in-situ U-Pb age determinations, and trace element and oxygen isotope data (via SIMS) for Whakamaru zircons are used here to address the following objectives: (1) to quantify magma storage timescales and chemical evolution using dated zircons and CL imagery of growth zonation; (2) to reconstruct the thermal and compositional record of the accumulation and evolution of the magma reservoir(s); and (3) to investigate magma source components and assimilation histories using oxygen isotopes.

5.1.1 Silicic magmatism and residence times

Large-scale silicic magmatism ultimately derives its thermal energy from mantle-derived magmas (e.g., Hildreth, 1981), although the mechanisms and timings whereby silicic magmas are generated and stored prior to eruption remain controversial. Two end-member origins have been proposed for crustal magmatic systems: (1) rhyolitic magma derived by fractionation from mafic mantle-derived magmas; and (2) rhyolite petrogenesis from the remelting of sedimentary or igneous crustal protoliths (Charlier et al., 2005). The range between these is represented by variable amounts of recycling or remobilisation of existing

crustal material, proportions of which can be determined using isotopic evidence where isotopic characteristics of pre-existing crustal material are known and have signatures which contrast with the magmas (e.g., Halliday et al., 1984; Hildreth et al., 1991; Davies et al., 1994; McCulloch et al., 1994; Graham et al., 1995).

Radiogenic isotopic analyses have been interpreted in terms of both prolonged (~ 10^6 y) and short (< 10^2 y) *residence times* for large silicic magmatic systems (Table 5.1; e.g., Halliday et al., 1989; Mahood, 1990; Hawkesworth et al., 2000; Vazquez and Reid, 2002; Bachmann and Bergantz, 2003; Charlier et al., 2005; Miller et al., 2007). The *residence time* can be defined as a *mean lifetime*, which is the time elapsed since the magma was formed and its eruption (e.g., Reid et al., 1997; Schmitt et al., 2002; Vazquez and Reid, 2002; Simon and Reid, 2005; Costa, 2008), or the time period over which a magma body accumulated in the holding chamber from which it was erupted (Charlier et al., 2005).

Uncertainties arise in the estimation of residence times due to the complexities of magma formation, with the final eruption products typically representing a mixture of phases that are likely to have different origins in time and space (comprising xenocrysts and antecrysts in addition to phenocrysts; e.g., Bacon and Lowenstern, 2005; Charlier et al., 2005), therefore providing different temporal records. *Antecrysts* refer to zircon crystallised from an earlier pulse of magma and then incorporated into a later pulse (e.g., Bacon and Lowenstern, 2005; Charlier et al., 2005), and *xenocrysts* are zircons sufficiently older than the intruding magma pulses and/or demonstrably unrelated to the magma system (e.g., metasedimentary wall rock; Johnson, 1989; Kemp et al., 2005). Heterogeneous crystal age populations may therefore result from repeated intrusion, thermal and compositional fluctuations, partial to complete solidification, and entrainment of crystals from mush and

wall rock intrusions during eruption (e.g., Hanchar and Miller 1993; Vazquez and Reid 2002; Miller and Wooden 2004; Bacon and Lowenstern 2005; Claiborne et al., 2006; Walker et al., 2007; Reid, 2008; Claiborne et al., 2010).

Table 5.1: ***Summary of eruption ages and magma residence times and production rates of selected major caldera-forming silicic eruptions***

Caldera / zone	Member or unit	Vol (km^3), DRE	Eruption age	Magma residence time (ky)	Magma production rate (~ $km^3\ y^{-1}$)	Chronometer	Ref.
TVZ	Oruanui	530	26.5 ka	4 – 70	7.5×10^{-3} to 1.3×10^{-1}	Zircon U-Pb, U-Th	1
	Rotoiti	100	63 ka	9 – 40	$(0.2 – 1) \times 10^{-2}$	Zircon U-Th	2
	Whakamaru	1500	347 ka	< 250	$(1 – 4) \times 10^{-3}$	Zircon U-Pb	3
	Ongatiti	400	1.21 Ma	< 240	$(1 – 4) \times 10^{-3}$	Zircon U-Pb	4, 5
Toba	YTT	2800	75 ka	< 160	1.8×10^{-2}	Allanite U-Th	6
Kos	Kos Plateau Tuff	60	161 ka	180	3.3×10^{-4}	Zircon U-Pb Biotite Ar-Ar	7
Yellowstone	Lava Creek	1000	600 ka	19 – 57	$(2 – 5) \times 10^{-2}$	Sanidine Ar-Ar	8
	Mesa Falls	280	1.3 Ma	160 – 170	1.7×10^{-3}	Sanidine Ar-Ar	8
	Huckleberry	2500	2.0 Ma	77 – 234	$(1 – 3) \times 10^{-2}$	Zircon U-Pb	9
Long Valley	Bishop	600	760 ka	50 – 390	$(0.2 – 1) \times 10^{-2}$	Zircon, Allanite U-Th-Pb, Ar-Ar	10,11
La Pacana	Atana, Toconao	2700	4 Ma	500– 750	4×10^{-3}	Zircon U-Th-Pb	12
La Garita	Fish Canyon	5000	28 Ma	80 – 360	$(0.5 – 6) \times 10^{-2}$	Zircon U-Th-Pb	13

Notes: Table adapted from Costa (2008). Eruption ages from $^{40}Ar/^{39}Ar$, K-Ar or ^{14}C methods; Residence time is calculated as the difference between the eruption ages and those of other radioactive clocks (e.g., U-Th-Pb zicron geochronology) using the chronometer indicated; Magma production rate is calculated as magma volume/residence time. References for magma residence time estimates: (1) Wilson and Charlier, 2009; (2) Charlier et al., 2003; (3) Brown and Fletcher, 1999; (4) Brown and Smith, 2004; (5) Wilson et al., 2008; (6) Vazquez and Reid, 2004; (7) Bachmann et al., 2007a, 2010; (8) Gansecki et al., 1998; (9) Bindeman et al., 2001; (10) Davies and Halliday, 1998; (11) Simon and Reid, 2005; (12) Schmitt et al., 2003; (13) Bachmann et al., 2007b. Age for Whakamaru from Leonard et al., 2010 (see also Table 1.4).

Short residence times have been suggested for some rhyolitic supereruptions, e.g., Oruanui (TVZ) zircon ages (in conjunction with stratigraphically-controlled geochemical information) indicate maximum residence times of ~ 40 ky, and model ages for Taupo volcano occur 4 – 40 ky prior to quenching on eruption (Charlier et al., 2005; Wilson and Charlier, 2009). There, zircons with ages of > 60 – 70 ka are considered to be antecrysts recycled from partly to wholly solidified plutonics, and those > 100 Ma are considered xenocrystic and incorporated by melting of metasedimentary host rocks (Charlier et al., 2005). Short residence times have been indicated for the Lava Creek Tuff eruption, Yellowstone (19 – 57 ky; Gansecki et al., 1996, 1998), and residence times of > 150 ky for YTT (based on allanite dating; Vazquez and Reid, 2004). Long residence times of ~ 1.7 Ma were suggested for Bishop Tuff (based on Rb-Sr mineral and glass ages; Halliday et al., 1989; Christensen and DePaolo, 1993; van den Bogaard and Schirnick, 1995), although these have since been discredited (e.g., Winick et al., 2001; Wilson and Hildreth, 2007). Other estimates for Bishop Tuff are significantly shorter, ~ 50 – 390 ky (Table 5.1; Christensen and Halliday, 1996; Davies and Halliday, 1998; Reid and Coath, 2000; Simon and Reid, 2005), and support the view of episodic production of magma batches which form rapidly during thermal pulses (Huppert and Sparks, 1988; Sparks et al., 1990).

New interpretations suggest that zircon model-age populations cannot simply be treated as directly representing magma residence times (Charlier et al., 2005), as the presence of antecrysts and xenocrysts need to be accounted for. Recycling of these zircons during successive magmatic recharge episodes is thought to be the primary cause of zircon age dispersion (Miller et al., 2007), compatible with progressive growth of large, long-lived, crystal mush bodies. Studies of plutonic and volcanic systems have provided evidence for complex histories that require frequent replenishment in order to attain the extended

histories recorded in crystal populations (e.g., Davies et al., 1994; Reid et al., 1997; Brown and Fletcher, 1999; Vazquez and Reid, 2002; Schmitt et al., 2003; Coleman et al., 2004; Miller and Wooden, 2004; Wiebe and Hawkins, 2004; Charlier et al., 2005; Walker et al., 2007; Claiborne et al., 2010). Zircon age spectra taken in isolation (for a magma which consists of a mix of components of multiple ages and sources) therefore only provide information about the cycles of crystallisation in the source materials for the magmas, rather than a definitive 'residence time'. Charlier et al. (2005) suggest that bimodality in zircon model-age spectra indicates remobilisation of zircons from mush rather than a prolonged evolutionary history in a continuously existing magma body. Unimodal zircon age spectra, in contrast, are thought to provide a more accurate estimate of residence time in a continuous, mostly liquid magma body (Charlier et al., 2005). Nevertheless, different chronometers (e.g., Table 5.1) will give different model residence times and caution must therefore be exercised in interpretation of age spectra. The new zircon data presented here are interpreted within this framework.

5.1.2 TVZ basement

The TVZ basement lithology, widely used in models of assimilation for TVZ magmas, comprises Mesozoic metasedimentary greywackes of the Gondwana accretionary wedge: the Torlesse and Waipapa Terranes (Fig. 5.1; 100 – 170 Ma; Mortimer, 1994; Mortimer, 2004; Adams et al., 2009). In addition, plutonics associated with TVZ magmatism (< 2 Ma) also contribute to silicic magma generation (Charlier et al., 2010). Granitic xenoliths have been recorded in several silicic deposits in central TVZ which are either co-genetic with the host eruption magma or incorporated from the crust during caldera collapse (e.g., Brown et al., 1998b; Burt et al., 1998; Charlier et al., 2003). Dating of zircons can provide a direct record of assimilated material, with geochemical/isotopic characteristics distinct from the host magmas (e.g., McCormack et al., 2009; Charlier et al., 2010).

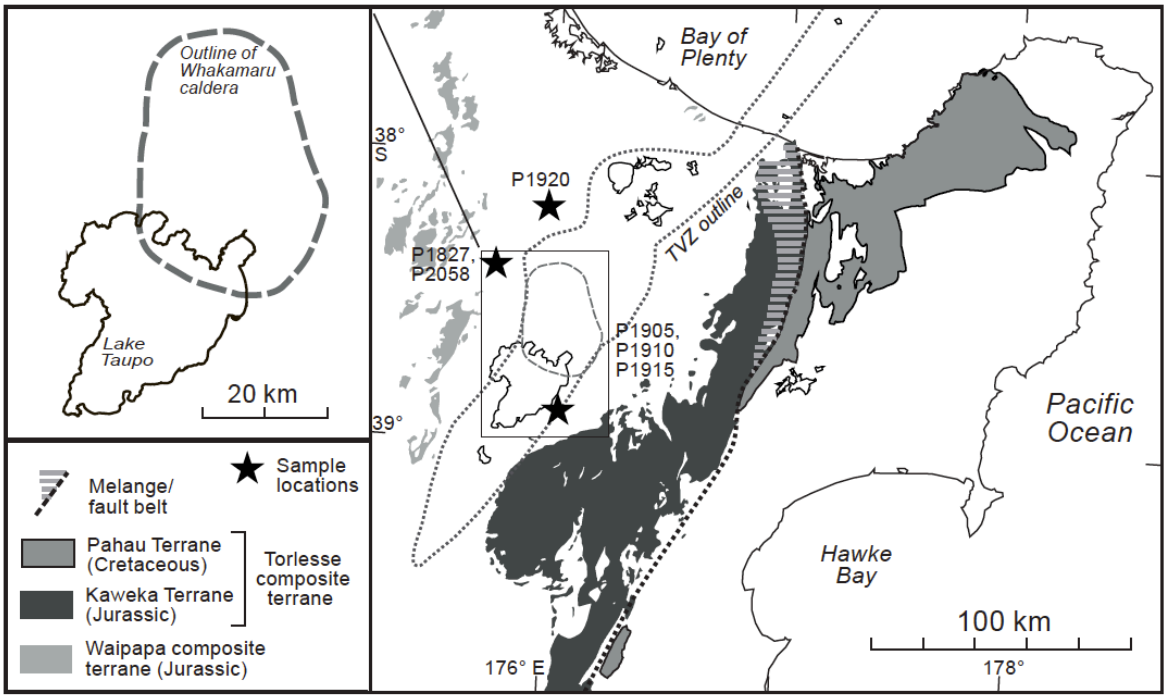

Fig. 5.1: Map of the eastern central North Island, with basement Torlesse and Waipapa Terranes. Pumice sample localities referred to in this chapter are marked by black stars, with sample codes indicated. Inset map shows the outline of the Whakamaru caldera from Wilson et al. (1995a) and Brown et al. (1998a). Modified from Charlier et al. (2010).

Oxygen isotopic ($\delta^{18}O$) signatures also provide insight into the degree of crustal contamination, with Torlesse and Waipapa Terranes being $\delta^{18}O$-rich, with average values of 12.5 ‰ and 9.5 ‰, respectively (McCulloch et al., 1994), or ranging between 9.5 – 12.5 ‰ and 7.8 – 12 ‰, respectively (Graham et al., 1995). Torlesse greywackes are characterised by SiO_2 > 65 wt%, whereas Waipapa has lower SiO_2 of ~ 55 – 60 wt% (Roser and Korsch, 1999). Isotopic ratios for the two terranes are as follows: $^{143}Nd/^{144}Nd$ = 0.51; $^{87}Sr/^{86}Sr$ = 0.71 – 0.72; $^{207}Pb/^{204}Pb$ = 15.64 – 15.66 for Torlesse; and $^{143}Nd/^{144}Nd$ = 0.51; $^{87}Sr/^{86}Sr$ = 0.70 – 0.71; $^{207}Pb/^{204}Pb$ = 15.61 – 15.63 for Waipapa (Graham et al., 1992, 1995). Results of an earlier isotopic study indicate that TVZ rhyolites are produced by contamination of an initially basaltic magma with 15 – 25% Torlesse crustal component, followed by essentially closed-system fractionation (McCulloch et al., 1994).

5.2 Methods

Pumice from the Whakamaru and Rangitaiki ignimbrites was sampled extensively (260 samples; Appendix 1) and characterised by whole-rock XRF (Section 2.3.2), matrix-glass (Section 2.3.3), mineral chemistry (Section 2.3.4) and Fe-Ti oxide compositional data (Section 3.3.4; see Matthews et al., 2011a). The other ignimbrite units are too welded, vapour-phase altered, and too pumice-poor for extraction of pumices large enough to enable zircon separation.

5.2.1 Samples and standards

Zircons were extracted from six representative pumice samples from the Whakamaru and Rangitaiki ignimbrite units selected on the basis of mineralogy, clast size, lack of alteration and major-element geochemistry (Fig. 5.1; Table 5.2). Three of the selected samples (P1905, P1920 and P2058) were analysed for zircon U-Pb ages (Section 5.2.3) and trace elements (Section 5.2.4), while five samples were analysed for $\delta^{18}O$ (P1905, P1910, P1915 P1920 and P1827; Section 5.2.5). A summary of analyses undertaken for each sample is provided in Table 5.2. Petrographic descriptions and chemistry for each pumice sample are outlined in Section 2.3.1 (and Appendix 2) and glass chemistry results for the selected pumice samples are given in Appendix 4.

Zircon standards used were the R33 zircon for U-Pb analysis, Madagascar Green (MAD) zircon for trace-element analyses, and a kimberlite zircon standard 'Laura' for oxygen isotope analysis. Matrix-matched standards were used for $\delta^{18}O$ analysis. Full trace-element characteristics of MAD zircon are provided in Mazdab and Wooden (2006), and Barth and Wooden (2010). The R33 zircon standard (from 419 Ma monzodiorite, Braintree complex, Vermont, USA; Black et al., 2004) is characterised by $\delta^{18}O$ of 5.5 ‰ (University of

Wisconsin, Stable Isotope Lab; Valley, 2003) and 'Laura' has $\delta^{18}O$ of 5.3 ‰ (J. Craven, Edinburgh Ion Microprobe Facility, *pers comm.,* 3 Jun 2011). $\delta^{18}O$ values are reported in standard 'per mil' notation relative to VSMOW (Valley et al., 1994; Valley, 2003). A silica sand (NBS-28) was used as the quartz standard for $\delta^{18}O$ quartz analysis, with $\delta^{18}O$ = 9.57 ‰ (Hut, 1987). A 'Sierra' feldspar standard was used, with $\delta^{18}O$ = 6.28 ‰ and An = 62 (J. Craven, Edinburgh Ion Microprobe Facility, *pers comm.,* 3 Jun 2011). $\delta^{18}O$ values for Laura and Sierra standards were measured at East Kilbride (J. Craven, Edinburgh Ion Microprobe Facility, *pers comm.,* 3 Jun 2011). Refer to Section 5.2.5 for variability encountered in standards during analytical sessions.

Table 5.2: ***Details of the samples used for zircon, quartz and feldspar analysis***

Sample	**P1905**	**P1910**	**P1915**	**P1920**	**P1827**	**P2058**
Ignimbrite unit	**Rangitaiki**	**Rangitaiki**	**Rangitaiki**	**Whakamaru**	**Whakamaru**	**Whakamaru**
Pumice type	***A***	***A***	***Mixed***	***A***	***D***	***D***
Location (°lat, long)	-38.8693, 176.0536	-38.8693, 176.0536	-38.8693, 176.0537	-38.2055, 175.9265	-38.3252, 175.6843	-38.3252, 175.6843
SiO_2 (wt%)	76.85	77.87	77.27	77.88	78.70	77.86
Zr (ppm)	167	141	139	161	168	83
Zrc sat. T (˚C)	796	797	792	793	779	789
M	1.52	1.41	1.61	1.35	1.27	1.17
FM	1.74	1.59	2.01	1.55	1.42	1.17
Zrc (U-Pb), *n*	60	-	-	87	-	44
Zrc (REE), *n*	100	-	-	108	-	58
Zrc ($\delta^{18}O$), *n*	39	68	30	40	23	-
Qtz ($\delta^{18}O$), *n*	43	53	47	52	73	-
Feld ($\delta^{18}O$), *n*	-	-	50	-	-	-

Notes: Pumice type refers to classification outlined in Brown et al. (1998a) on the basis of whole-rock geochemistry, where the Whakamaru eruption was fed by five magma types: A, B, C, D and mixed-basaltic (refer to Section 1.5.3). All pumices characterised by the following mineral assemblage: feldspar, quartz > orthopyroxene, amphibole, biotite >> magnetite, ilmenite. SiO_2 data is from EPMA analysis of glass shards. FM and M are melt compositional parameters (cation fractions) calculated from glass compositions using formulations from Hanchar and Watson (2003). Zrc Sat. T refers to zircon saturation temperature. Zircon (Zrc) crystals from samples P1905, P1920 and P2058 were analysed for U-Pb and trace elements; zircon and quartz (Qtz) from samples P1905, P1910, P1915, P1920 and P1827 were analysed for $\delta^{18}O$; Feldspar (Feld) was analysed from sample P1915 only; n refers to number of analyses of each type.

5.2.2 Mineral separation

Pumice samples were cleaned of organic material and weathering rind, cleaned ultrasonically, and dried at 100˚C for 24 h. Each sample was thin-sectioned prior to crushing, and a fraction retained for further analysis. Standard zircon extraction procedures were followed (Charlier et al., 2005), involving crushing to < 400 μm, grinding, sieving to < 250 μm, hydrodynamic separation by Wilfley table, and removal of the magnetic fraction by hand magnet followed by passing the remaining heavy fraction through a Frantz isodynamic magnetic separator. Zircons were hand-picked under a binocular microscope from the non-magnetic > 2.86 SG fraction and mounted in epoxy resin. Approximately 300 zircon crystals from each pumice sample were extracted.

Zircon and quartz standard grains were mounted in each epoxy mount. Mounts were polished to reveal the midsection of grains, and carbon coated for imaging. All zircon grains were thoroughly imaged in reflected light and by SEM-CL to facilitate analysis of magmatic growth domains (where darker CL zones are more U-rich). Zircon mounts were cleaned by washing with a mild soap, rinsed with distilled water, acid rinsed in 1M HCl for 5 min with a final distilled water rinse, followed by oven drying under vacuum at ~ 50°C. Mounts were then gold coated for isotopic analysis. Quartz crystals were also extracted from the same pumice clasts, mounted and imaged by CL prior to analysis (as outlined in Section 3.2.6).

5.2.3 Zircon U-Pb geochronology

The SHRIMP-RG SIMS instrument at the U.S. Geological Survey - Stanford joint facility was used for U-Pb zircon age determination, following standard techniques (Dalrymple et al., 1999; Lowenstern et al., 2000; Charlier et al., 2005; Lindsay et al., 2005), with data collected over three analytical sessions. Prior to data acquisition, the primary beam was rastered for 240 s on a 150 μm^2 area. Secondary ions were sputtered from zircons with a 5 – 6 nA primary $^{16}O_2^-$ beam focused to a 25 × 35 μm spot. The mass spectrometer was cycled six times through peaks corresponding to $^{90}Zr_2{}^{16}O$, ^{204}Pb, background, ^{206}Pb, ^{207}Pb, ^{208}Pb, ^{238}U, $^{232}Th^{16}O$ and $^{238}U^{16}O$, with a total analysis time of 948 s. Ages based on isotopic ratios were standardized against R33 zircon, which was analysed after every fourth analysis of the unknowns (see Barth and Wooden, 2010).

Whakamaru zircons tend to be U-rich, ranging from ~ 100 – 10000 ppm (average 1500 ppm, compared to the more typical range of 10 – 1000 ppm; Parish and Noble, 2003), thus allowing application of U-Pb dating techniques despite their relatively young ages. U-rich zones of zircon crystals were preferentially chosen for analysis as they provide better counting statistics (although zones with U > ~ 4000 – 5000 ppm were avoided). An earlier study found dates of cores and rims from individual zircons were distinguished using longer than usual ^{206}Pb count times (due to high U contents of zircons; Brown and Fletcher, 1999). Extended count times of 30 s for ^{206}Pb and 20 s for ^{207}Pb were therefore used, with six scans through the mass sequence, and 3 min raster to help remove any common Pb from surface contamination (including the Au coat). The presence of common Pb was monitored using ^{204}Pb, and a correction applied using the recorded $^{207}Pb/^{206}Pb$ values and an average common Pb isotopic composition for TVZ rhyolites (Graham et al., 1992). Analyses with > 20% common Pb were excluded from the data set. Values for the

percentage of the ^{206}Pb attributable to common Pb are given in Table 5.3 (the full dataset is provided in Appendix 14).

5.2.4 Zircon trace-element analysis

Trace-element concentrations in zircon (Table 5.4, Appendix 15) were measured with the SHRIMP-RG. Mounts were repolished and coated following U-Pb analysis. Spots for trace-element analyses were selected on the basis of CL zoning, and to avoid inclusions visible in reflected-light images. Preference was given to locations that had been previously analysed for U-Pb ages, although trace-element spots did not coincide exactly with age spots (instead an adjacent part of the crystal in nominally the same growth zone was analysed). Both core and rim zones of these dated zircons were analysed where possible, to assess core-rim relationships and establish normal or reverse temperature trends and compositional changes. SIMS analyses were performed using a 1.5 – 3 nA primary beam current and 15 – 20 μm spot size. Trace-element concentrations were standardised against MAD zircon, with replicate analyses of MAD over multiple analytical sessions to establish precision of the trace-element analyses (following procedures of Mazdab and Wooden, 2006).

5.2.5 Oxygen isotope analysis

A Multi-Collector CAMECA ims-1270 SIMS instrument at the University of Edinburgh was used to obtain precise oxygen isotope ratios for zircon, quartz and feldspar (Appendices 16, 17 and 18 respectively). $\delta^{18}O$ values for zircon and quartz in the same pumice clasts, and for feldspar from one pumice (Table 5.2), were determined to establish whether the crystals grew in isotopic equilibrium (i.e. from the same melt, under the same conditions) or were entrained from isotopically distinct sources. Crystals were mounted in

epoxy resin, polished, photographed in reflected light and BSE-SEM, and imaged by CL. The mounts were cleaned and coated with 100 nm of Au and left in the IMS-1270 chamber overnight prior to analysis to reach full vacuum. A total of 200 zircon, 274 quartz and 50 feldspar $\delta^{18}O$ analyses were performed on the five pumice samples (Table 5.2).

High-mass-resolution and dual faraday detectors (precision ~ 0.3%; Cavosie et al., 2005) were used, with samples sputtered with a 10 kV Cs+ primary beam of ~ 5 nA current focused to 20 – 25 μm spots. 'Contiguous bracketing' of the zircon, quartz and feldspar standards was employed in order to correct for instrumental drift within any analytical session. Five to ten individual $\delta^{18}O$ measurements on standard grains were run at the beginning and end of each block of data collection. To correct raw feldspar data for instrumental mass fractionation (IMF; Eiler et al., 1997) an average value of IMF in a given block of data was used. Small instrumental drifts of 0.05 – 0.1‰ per h were detected, and a linear parameterization as a function of time was applied to correct for this.

Oxygen isotope analyses were standardised by replicate analyses of standards, on the same day. Typical precision for these analyses is ± 0.05 ‰ (1sd) and accuracy relative to the standards is as follows: Laura zircon ± 0.11 ‰ (1sd); R33 zircon ± 0.10 ‰ (1sd); NBS28 quartz standard ± 0.14 ‰ (1sd); and Sierra feldspar ± 0.08 ‰ (1sd). A careful protocol for analysis was adopted in each study, with standard analyses bracketing unknowns and representing 25 – 50% of all analyses in each analytical session. Day-to-day $\delta^{18}O$ values for standards were within +0.05 ‰ to -0.2 5‰ of their empirical value, and unknown samples were adjusted to correct for this small variability on the VSMOW scale. The total variability encountered for the zircon standards across all analytical sessions were as follows: R33 5.06 ± 0.47 ‰; and Laura: 5.3 ± 0.36 ‰; and variability in quartz standard

NBS-28 was 9.43 ± 0.45 ‰, and feldspar Sierra 6.09 ± 0.24 ‰. The external reproducibility calculated from ten analyses of unknown quartz grains was 0.2 – 0.3 ‰ (1sd). Probe drift during each day of analysis was assessed by sample/standard bracketing, and correcting for assumed linear drift.

Oxygen isotope analyses of populations of individual zircon crystals in the pumice clasts were compared using four statistical parameters: mean, standard deviation, standard error and t-test. The mean and standard error describe how well the average value is known (Bindeman and Valley, 2002); the standard deviation is useful to predict reproducibility of additional analyses in a sample population, and the t-test is used to determine whether core and rim $\delta^{18}O$ signatures represent statistically different populations. The use of these parameters assumes that analyses are distributed normally, and this is demonstrated here by plotting results as histograms (Section 5.3.4). Most crystals are homogenous in $\delta^{18}O$ within analytical uncertainty, and an average value is reported for single crystals where multiple analyses were made.

5.3 Results

5.3.1 Zircon textural types

Zircon types are classified on the basis of crystal morphology and CL imaging (e.g., Pupin, 1980; Corfu et al., 2003), with a simple textural classification with types as follows: complex cores; homogenous cores; oscillatory zoning; and sector zoning (Fig. 5.2). Whakamaru and Rangitaiki zircon crystals are typically euhedral prismatic grains occurring as free crystals in vesicular glass, often containing inclusions of apatite, pyroxene, opaques and/or melt inclusions, or are themselves inclusions in ferromagnesian minerals. Grains are commonly preserved with adhering vesicular glass selvages indicating that most represent free phenocrysts. CL images of selected zircons are shown in Figs 5.2, 5.3, 5.4 and 5.5.

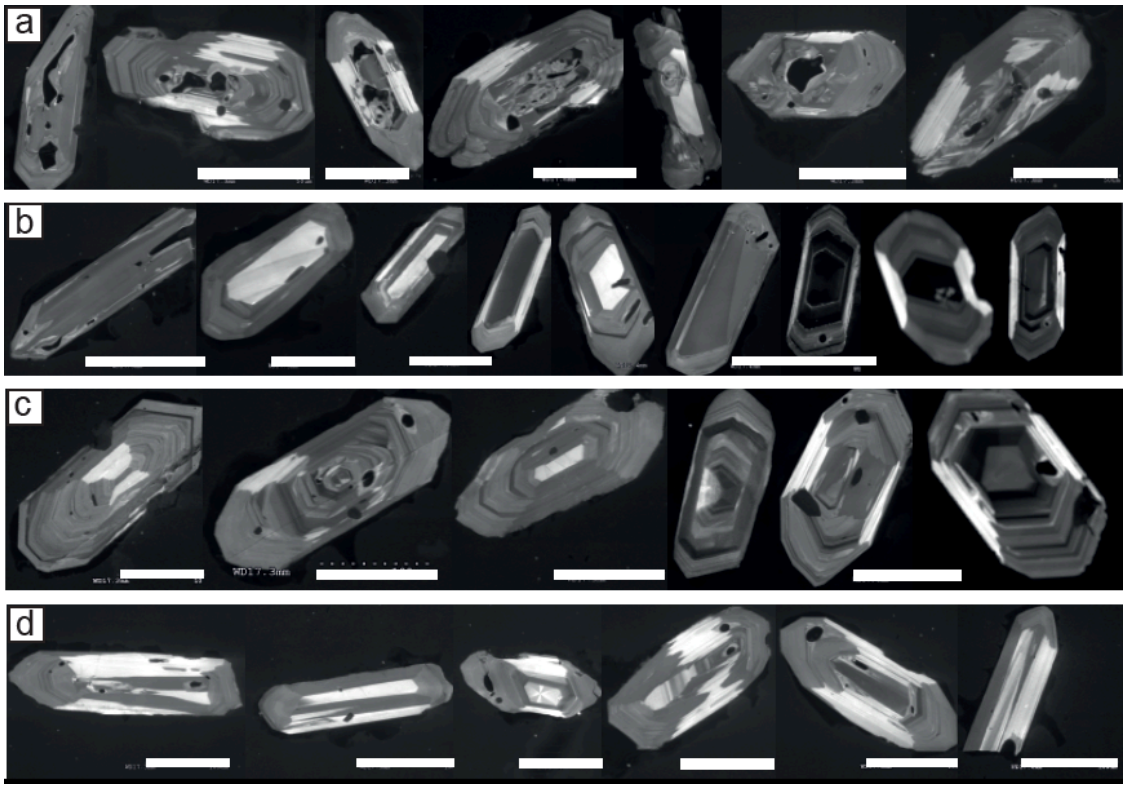

Fig. 5.2: CL images of zircon crystals showing classification by zonation type; a) complex cores with melt inclusions; b) homogenous cores; c) oscillatory zoning; d) sector zoning. Scale bar is 100 µm.

Zircon crystals are < 250 µm in length and typically elongate, with aspect ratios ranging from 1.5:1 (stubby) to 3:1 (length:width). CL imaging reveals distinct euhedral zoning, with discrete zones and bands of oscillatory zoning, while some display distinct resorbed cores or xenocrystic cores (Fig. 5.3). These features were also noted by Brown and Fletcher (1999), and are interpreted as being indicative of a complex magmatic crystallisation history. Zircon zoning patterns and textures are described here in terms of core morphology (Fig. 5.2a, b), oscillatory zoning (Fig. 5.2c) and sector zoning (Fig. 5.2d).

5.3.1.1 Complex cores

Resorbed zircon cores with complex CL zoning (Figs 5.2a, 5.4a-f) are common in all pumice samples. These cores are truncated by a resorbed margin and mantled by younger euhedral zircon growth, and are interpreted as being regions of early growth around which oscillatory-zoned external domains formed (although in some cases these may be xenocrystic cores, based on measured differences in U-Pb ages; see Section 5.3.2).

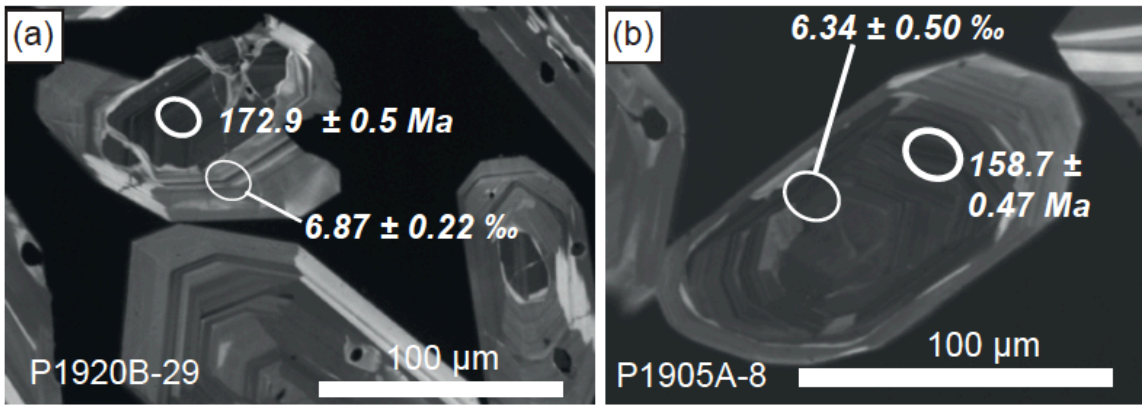

Fig. 5.3: CL images of complex zircon cores (assimilated greywacke; see Section 5.3.2)

Some zircons contain irregular melt inclusions which form tubes along most of the crystal length (e.g., Fig. 5.4c), and are likely to reflect an initial period of rapid skeletal growth. Irregular, sieved and resorbed overgrowths, either at the crystal rim or surrounding the crystal core also occur, but are uncommon.

5.3.1.2 Homogenous cores

Distinct homogenous cores are also observed (Figs 5.2b), with euhedral to subhedral outer boundaries, followed rimwards by oscillatory zoning. A sub-population of Whakamaru and Rangitaiki zircons displays dark U-rich cores (e.g., Figs 5.4a,f and 5.5e,f,m,n). Dark zircon cores were also noted by Brown and Fletcher (1999) who observed that high-U zircon and glass inclusion-rich zones immediately surround irregular and resorbed zircon cores in Whakamaru zircons. Bright- or mid-CL cores are however, more common, and are typically mantled by rims of euhedral oscillatory zoning (e.g., Figs 5.5g,h,k,p).

5.3.1.3 Oscillatory zoning

Oscillatory zoning (e.g., Figs 5.2c, 5.4i-l) typically consists of very narrow cyclic variations (1 – 3 μm zones), or larger oscillatory zones (10 – 20 μm) which are termed 'growth bands' in various studies (e.g., Gagnevin et al., 2010). Rims of 5 – 10 μm width are typically of uniform CL around zoned interiors with 1 – 5 μm scale growth zones defined by alternating bright and dark CL. A characteristic feature of Whakamaru and Rangitaiki zircon crystals is the dark-CL narrow growth band near the outer rim of the crystal (e.g., Fig. 5.4i), preferentially targeted for U-Pb dating due to high-U content (Section 5.2.3).

5.3.1.4 Sector zoning

Sector zoning is a common characteristic of zircons from all pumice samples, defined by patches of relative CL brightness (Figs 5.2d, 5.4m-p). The symmetric bright CL patches are typically associated with fine oscillatory zoning. Sector zonation occurs in all zircon categories and is associated with zircons displaying both homogenous and complex cores. The development of sector zoning in zircon has been attributed to kinetic factors and rapid

changes in the growth environment during crystal development (where sectors show variable trace-element enrichment; e.g., Paterson and Stephens, 1992; Corfu et al., 2003).

5.3.2 Zircon ages: ^{238}U - ^{206}Pb data

Timescales of assembly of the Whakamaru magma reservoir system are investigated here using zircon U-Pb age spectra. Single-crystal dating provides an effective means of showing the timescales over which parental magma chambers produce eruptible (melt-dominant) silicic magma (Charlier and Wilson, 2010). The data are presented as age histograms, with probability distribution function (PDF) curves fitted using Isoplot (Ludwig, 2003) in Figs 5.6 and 5.8. Selected SHRIMP spot ages for Whakamaru and Rangitaiki magmatic zircons are presented in Table 5.3, and the full dataset is available in Appendix 14.

Zircon age spectra indicate a unimodal age distribution - with a dominant peak at ~ 0.42 Ma (Fig. 5.6). All three pumice samples (Table 5.2) also contain zircons with crystallisation ages of 0.5 – 0.7 Ma, and P2058 shows a subordinate peak at 0.44 Ma (Fig. 5.6). The age distribution is from 0.30 to 0.74 Ma, with a mean crystallisation age of 0.40 ± 0.05 Ma (2sd, Fig. 5.6). The youngest ten zircon ages for each sample give a weighted average age of 0.32 ± 0.01 Ma which agrees well with the assumed eruption age of 0.346 ± 0.03 Ma (Table 1.4; Fig. 5.7; although is younger than the latest estimate of 0.347 ± 0.004 Ma; Leonard et al., 2010), indicating that zircon crystallisation was occurring up until eruption. The characteristic dark outer rim (before final light-CL rim; Figs 5.4 and 5.5) gives near-eruption age of ~ 0.44 Ma.

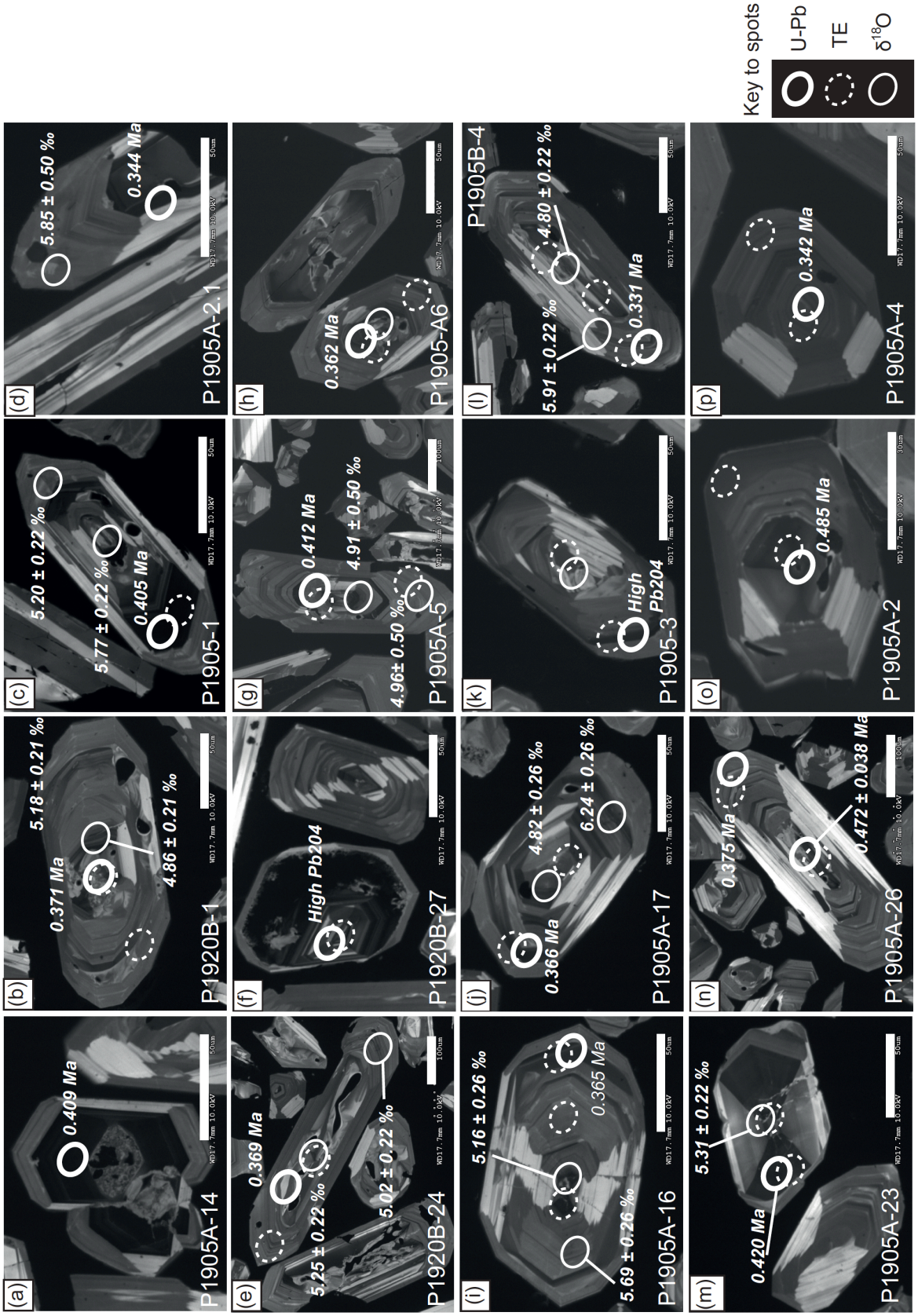

Fig. 5.4: CL images of zircons (P1905 and P1920) with circles indicating SHRIMP spots analysed for U-Pb age and trace elements (TE), and dashed SIMS spots for $\delta^{18}O$. Scale bar for all images is 50 µm.

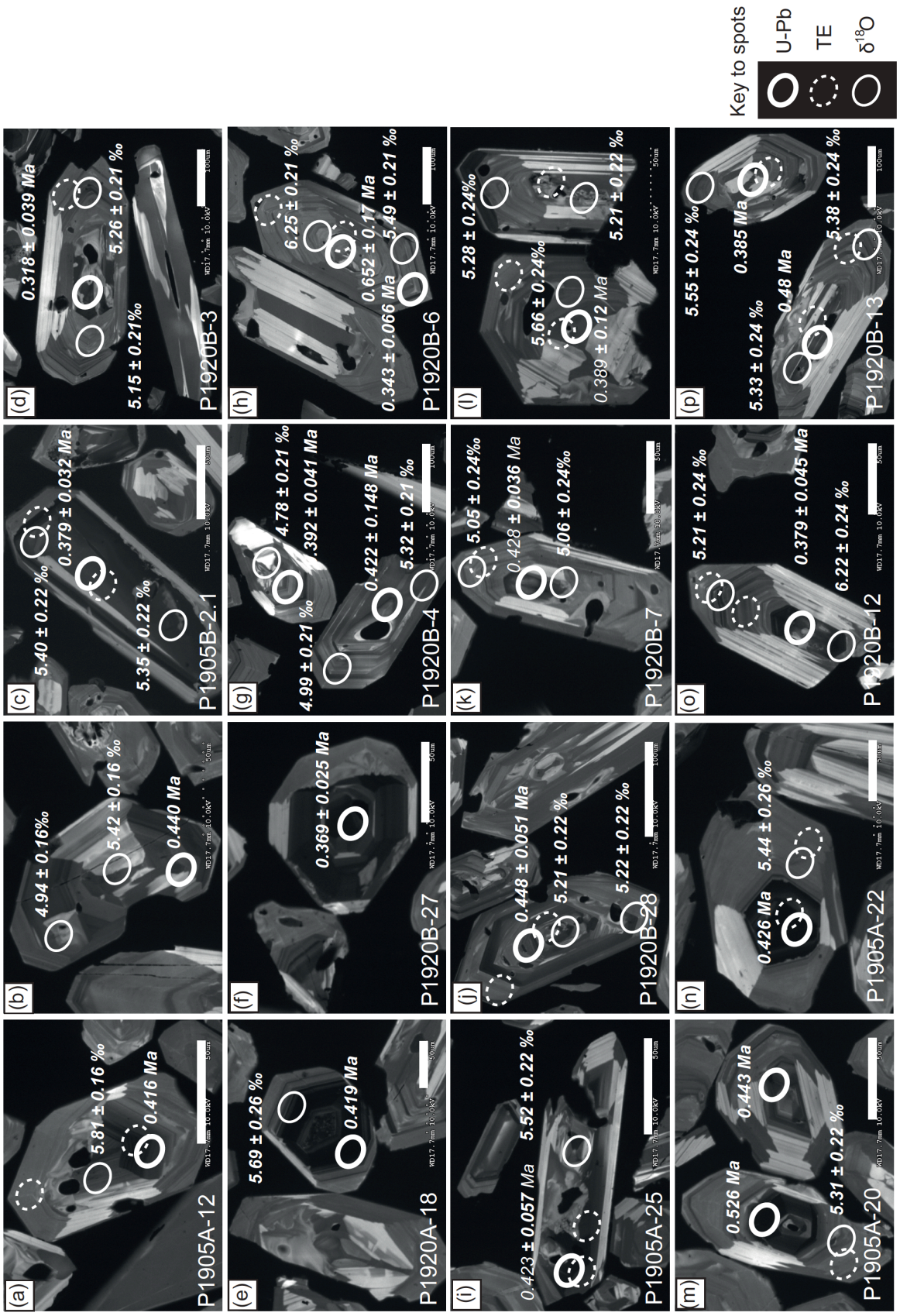

Fig. 5.5: Further examples of CL images of zircons (P1905 and P1920) with circles indicating SHRIMP spots analysed for U-Pb age and trace elements (TE), and dashed SIMS spots for $\delta^{18}O$. Scale bar for all images is 50 µm

Table 5.3: ***Selected U-Pb data for Whakamaru and Rangitaiki zircons (^{238}U - ^{206}Pb ages corrected for ^{207}Pb and initial ^{230}Th disequilibrium)***

Spot name	U, ppm	Th, ppm	% common ^{206}Pb	Age (Ma)	2sd
P1905A-38.1	1302	2403	0.6	0.364	0.032
P1905A-16.1	1267	1019	7.4	0.365	0.033
P1905A-46.1	1547	1541	6.9	0.368	0.031
P1905B-1.1	3558	7532	2.9	0.371	0.020
P1905A-19.1	1322	1763	12.1	0.385	0.037
P1905A-40.1	1866	1979	2.6	0.391	0.027
P1905A-36.1	1897	2143	5.8	0.397	0.028
P1905A-1.1	2241	3124	11.7	0.405	0.031
P1905A-12.1	3497	4206	8.3	0.416	0.024
P1905A-22.1	9051	11814	5.0	0.426	0.015
P1905A-15.1	1273	1912	5.6	0.440	0.040
P1905A-21.1	2508	2238	3.4	0.443	0.033
P1905A-26.1	1117	1565	10.4	0.472	0.038
P1905A-20.1	7843	13654	4.0	0.526	0.018
P1920A-08.1	697	499	4.9	0.342	0.041
P1920A-22.1	900	1080	13.6	0.353	0.040
P1920B-03.2	498	335	9.1	0.362	0.051
P1920A-26.1	638	506	8.1	0.379	0.053
P1920A-01.1	407	422	2.2	0.402	0.061
P1920A-13.1	331	217	13.6	0.422	0.078
P1920B-36.1	308	266	6.3	0.439	0.068
P1920B-45.1	3342	5000	2.6	0.444	0.022
P1920B-38.1	403	380	3.5	0.453	0.063
P1920B-60.1	2354	3156	11.9	0.460	0.068
P1920B-32.1	1759	3273	29.7	0.496	0.110
P1920B-2.1	1089	2049	1.9	0.527	0.045
P1920B-6.2	138	87	29.0	0.652	0.170
P1920B-48.1	2365	2955	1.3	0.739	0.037
P2058A-14	1062	803	4.5	0.334	0.033
P2058A-08	293	226	26.3	0.336	0.067
P2058A-11	760	638	7.6	0.348	0.038
P2058A-12	736	672	16.9	0.354	0.038
P2058A-10	639	585	3.0	0.361	0.044
P2058A-05	1272	1187	4.9	0.369	0.034
P2058A-16	1317	2068	1.2	0.375	0.032
P2058A-02	2156	2042	39.8	0.377	0.034
P2058A-06	970	1333	22.0	0.383	0.043
P2058A-03	1779	1644	7.1	0.406	0.028
P2058A-17	4339	11811	2.6	0.412	0.020
P2058A-07	303	238	30.1	0.474	0.091
P2058A-09	637	576	23.7	0.593	0.346

Note: Analysis by SHRIMP-RG. Full dataset provided in Appendix 14.

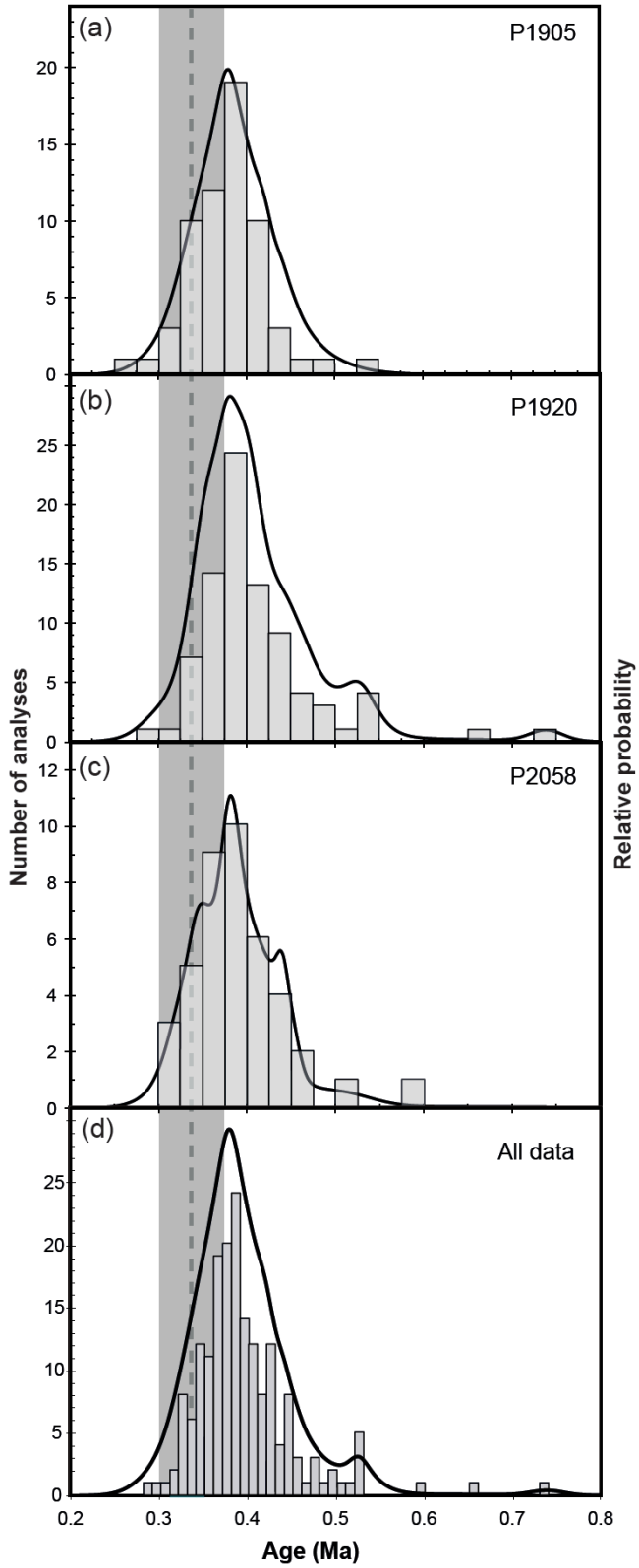

Fig. 5.6: Comparison of age histograms and PDF curves for Whakamaru zircons (plotted using Ludwig, 2003); (a) Rangitaiki pumice sample P1905; (b) Whakamaru pumice sample P1920; (c) Whakamaru pumice sample type *D* P2058; (d) All data combined. Grey dashed line shows Whakamaru eruption age (average 0.346 ± 0.03 Ma; see Table 1.4), with 1sd error indicated by shaded grey bar.

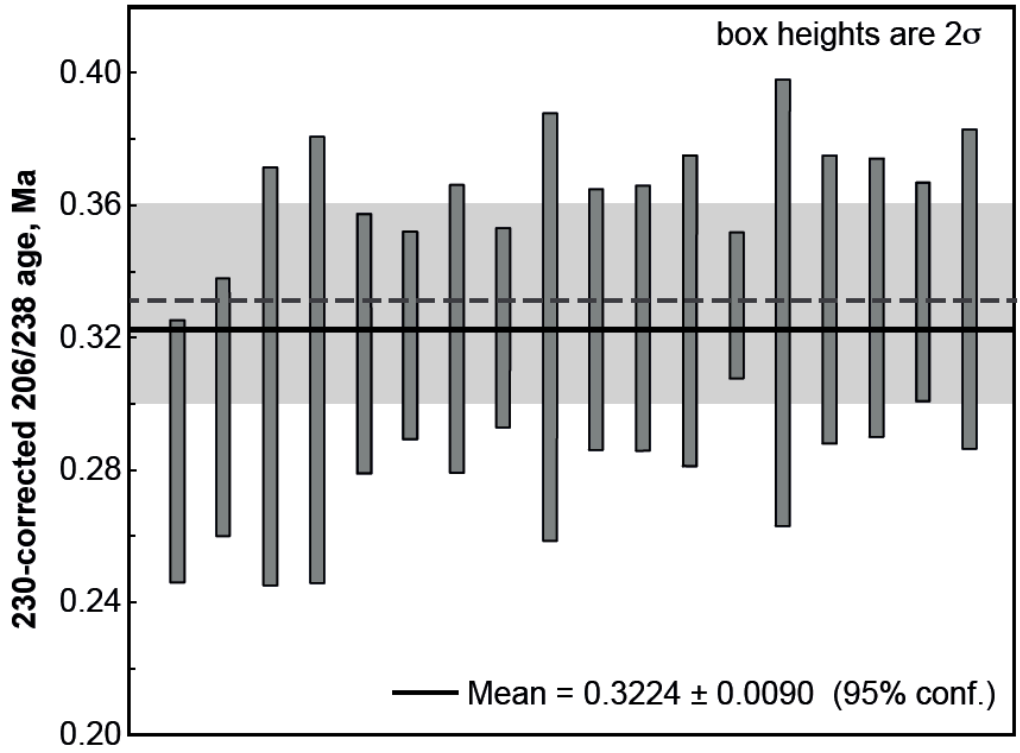

Fig. 5.7: Compilation of youngest zircon ages from all three samples; Mean age is 0.32 ± 0.01 Ma (indicated by solid black horizontal line) which agrees well with the Whakamaru eruption age (dashed black line, ± 1sd shown by grey band).

In terms of core versus rim relationships, some cores return ages within uncertainty (2sd) of eruption age and are therefore not consistently older than rims at the stated level of analytical precision (Appendix 14). Zircon U-Pb age spectra are shown in Fig. 5.8 in terms of rims, interiors and cores for each sample, showing that rims tend to be youngest (0.34 – 0.37 Ma; within uncertainty of eruption age), interiors are older (0.37 – 0.38 Ma), and cores show complex bimodal or polymodal PDF curves. Zircon cores for sample P1905 show a dominant peak at 0.40 Ma (Fig. 5.8a); P1920 shows a broad peak coinciding with the interiors at 0.39 Ma and subsidiary peaks at 0.45 and 0.52 Ma (Fig. 5.8b); P2058 has a dominant peak at 0.43 Ma and a subsidiary peak at 0.39 Ma (Fig. 5.8c). Older zircons with ages > 0.5 Ma (up to 0.74 Ma), are thought to represent inherited magmatic zircons, while inherited greywacke cores return ages of > 100 Ma (Appendix 14).

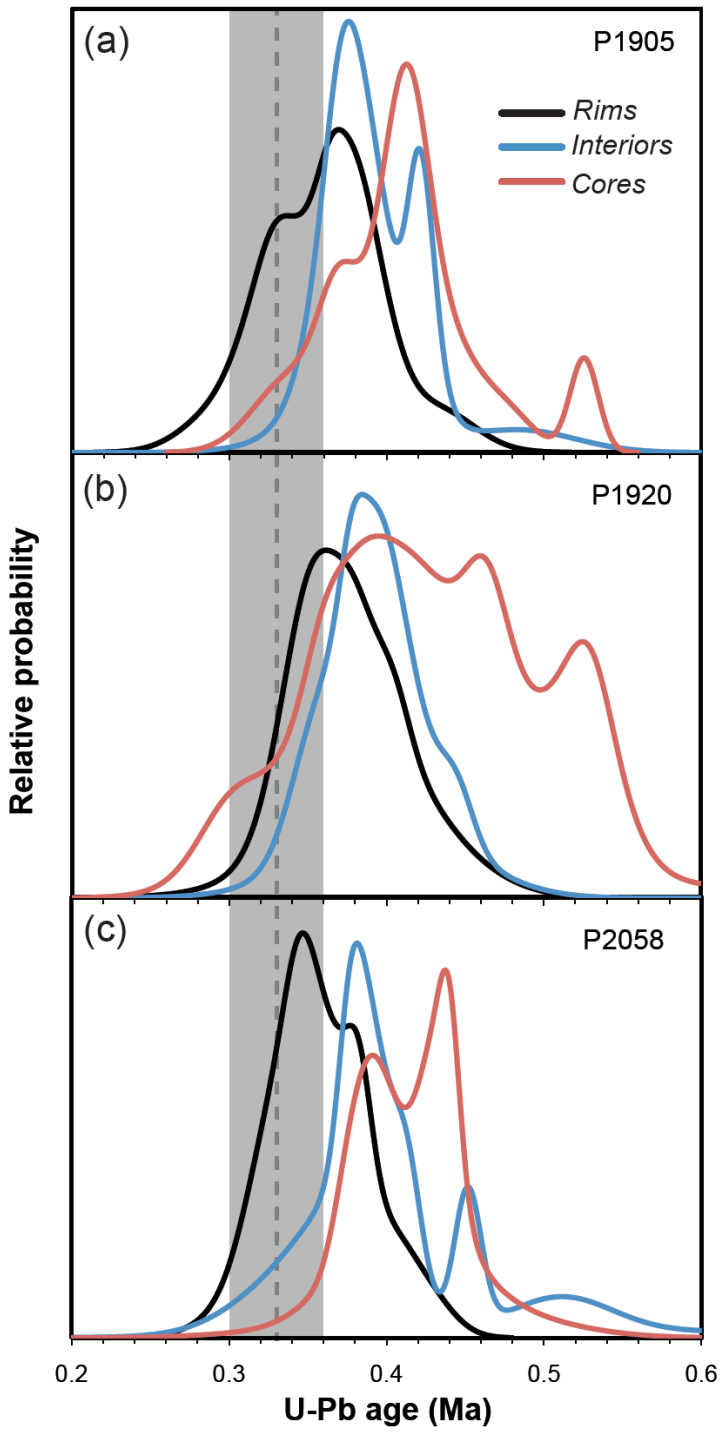

Fig. 5.8: Zircon U-Pb age spectra classified in terms of rim, interior and core for each sample. PDF curves for each crystal zone category shown for samples (a) P1905; (b) P1920; and (c) P2058. Grey shaded bar indicates eruption age for the Whakamaru supereruption (0.346 ± 0.03 Ma, 1sd; Table 1.4).

5.3.3 Zircon trace elements

Whakamaru and Rangitaiki zircons are characterised by large intra- and inter-grain trace-element compositional variations (Table 5.4; the full trace-element dataset is provided in Appendix 15). Zircons from all three pumice samples exhibit similar chondrite-normalised rare earth element (REE) patterns with a steeply increasing trend over five orders of magnitude, strong HREE enrichment relative to LREE, and negative Eu and positive Ce anomalies (Fig. 5.9; normalised to C1 chondrite; McDonough and Sun, 1995). The following ranges were recorded: U 78 – 9392 ppm, Th 31 – 15421 ppm, Ce 6 – 446 ppm and Eu 0.06 – 7.23 ppm, across all samples. Dark-CL zones are characterised by higher U (2200 – 9392 ppm), Th (2200 – 15421 ppm), and Y (2200 – 14700 ppm), as also noted by Brown and Fletcher (1999). Hf in zircon ranges from 5327 – 13572 ppm, with the highest concentrations typically recorded in rims (Fig. 5.10), corresponding to lower Ti concentrations and lower (apparent) temperatures (see Section 5.3.3.1). Ti ranges from 2.4 – 20.7 ppm, with lower Ti typically characteristic of most zircon rims. Decreasing Ti (and apparent Ti-in-zircon temperature) correlates with Hf-enrichment for all samples (Fig. 5.10).

Zircon trace-element data can be examined in terms of Eu and Ce anomalies (see Fig. 5.9). The magnitude of the Eu anomaly is expressed as the Eu/Eu* ratio calculated using equation [5.1] where Eu* is the expected value for a smooth normalised pattern. Similarly, the Ce anomaly is calculated using equation [5.2] where Ce* is the smoothed expected value. Equations [5.1] and [5.2] are from Hoskin and Schaltegger (2003):

$$Eu/Eu^* = \frac{Eu_N}{\sqrt{Sm_N \times Gd_N}} \qquad [5.1]$$

$$Ce/Ce^* = \frac{Ce_N}{\sqrt{La_N \times Pr_N}} \qquad [5.2]$$

where Sm_N, Gd_N, Eu_N, Ce_N, La_N and Pr_N refer to chondrite-normalised values. Zircon cores typically exhibit a smaller Eu anomaly (Eu/Eu*; equation [5.1]) and greater HREE enrichment than rims (Fig. 5.9; ~ 60% of rims show a greater Eu/Eu* than core). The magnitudes of the Ce (equation [5.2]) and Eu anomalies do not vary systematically between samples or within individual zircon crystals. For sample P1920, for example, ~ 60% of zircons analysed show a larger rim Eu/Eu*, 14% show larger core anomaly, and 26% show no change core to rim. All of the analysed zircon crystals from sample P2058 show larger Eu/Eu* for rims than cores. In comparison, for sample P1905 44% of zircons show a larger rim anomaly, 40% larger core anomaly, and 16% show no core-to-rim difference in Eu/Eu*.

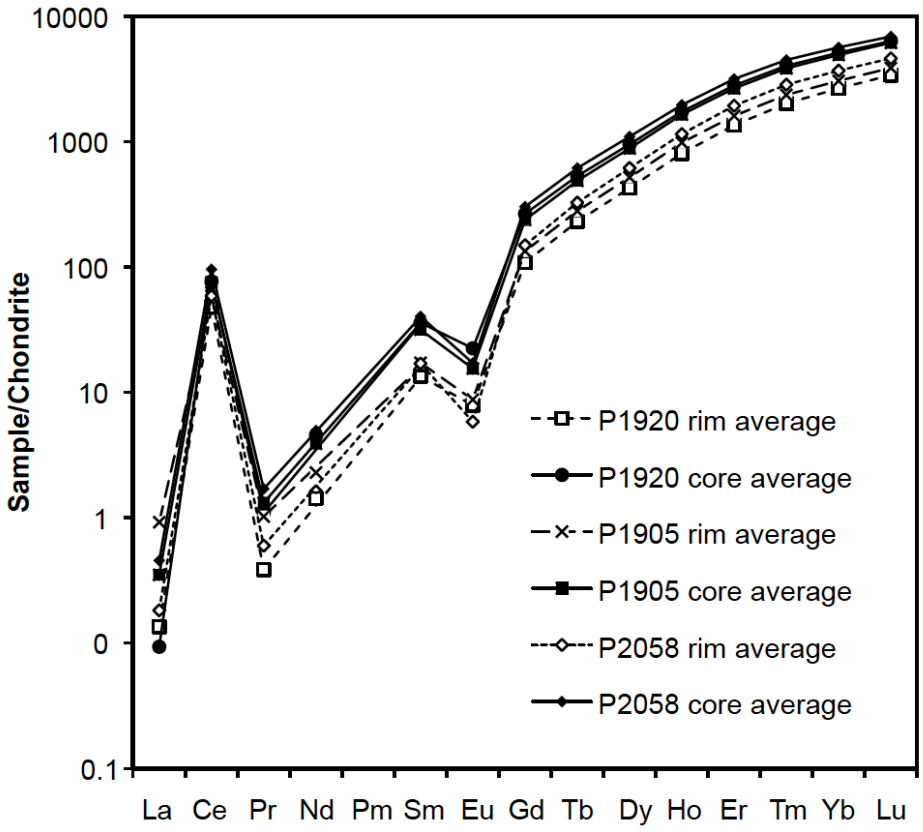

Fig. 5.9: Chondrite-normalised REE plot for zircon cores and rims from each pumice sample analysed (zircon REE data normalised to C1 chondrite; McDonough and Sun, 1995).

Plots of Hf and Ti against zircon U-Pb age show random scatter (Fig. 5.11) with no evident systematic compositional change with time. ∑REE becomes less diverse over time, with the youngest zircons showing the lowest ∑REE values (Fig. 5.11c). Examination of compositional change with time in single crystals tends to show decreasing apparent temperature and increasing Hf trends (as discussed in Section 5.3.3.1; Fig. 5.13). For example, zircon P1920-B6 shows a decrease of ~ 60°C which occurred over 0.309 Ma (see Fig. 5.13c), and P1920-B1 shows a ~ 40°C decrease over 0.059 Ma (Fig. 5.13d).

Table 5.4: ***Summary of trace-element data for zircons from each pumice sample***

Sample	**P1905**				**P1920**				**P2058**			
Element (ppm)	***Mean (n=100)***	***1sd***	***Min***	***Max***	***Mean (n=108)***	***1sd***	***Min***	***Max***	***Mean (n=58)***	***1sd***	***Min***	***Max***
Y	2438	1992	370	12538	2477	2401	260	12737	3122	2773	561	14674
La	0.20	1.08	0.00	9.65	0.03	0.14	0.00	1.47	0.29	1.42	0.00	10.72
Ce	54.35	66.9	6.50	446.0	52.27	65.37	5.67	322.5	66.78	68.40	8.94	307.0
Nd	1.85	2.63	0.08	16.60	1.82	2.52	0.08	12.68	2.43	3.87	0.12	22.35
Sm	4.76	5.67	0.38	39.06	5.01	6.11	0.27	33.53	6.21	7.29	0.54	31.37
Eu	0.91	1.03	0.10	7.23	1.13	1.41	0.06	6.29	0.90	0.89	0.12	4.82
Gd	48	50	4	335	51	57	3	322	65	69	7	328
Dy	222	200	28	1317	232	234	22	1218	301	289	48	1483
Ho	96	81	14	521	98	95	9	501	125	113	21	586
Er	442	350	72	2253	458	420	56	2129	581	502	121	2663
Yb	846	605	161	3842	876	736	123	3512	1083	841	262	4588
Lu	159	107	33	665	164	130	26	619	198	142	54	776
Th	1118	1799	42	12180	1137	1709	31	9211	1902	3261	65	15421
U	929	951	103	4648	901	997	78	4427	1497	1896	140	9392
Hf	10385	803	8147	12841	164	130	5327	12714	11097	1148	8698	13572
∑REE	1991	1542	351	9940	2060	1840	259	9068	2581	2157	554	11454
$(Sm/La)_N$	561	633	0	3599	525	416	2	2271	609	757	2	3302
Ce/Ce*	542	507	2	2247	513	430	9	2330	566	577	8	2746
Eu/Eu*	0.20	0	0.03	0.36	0.22	0.1	0.1	1.0	0.2	0.1	0.0	0.4

Note: Zircon trace-element data by SHRIMP-RG analysis. Full zircon trace-element dataset provided in Appendix 15.

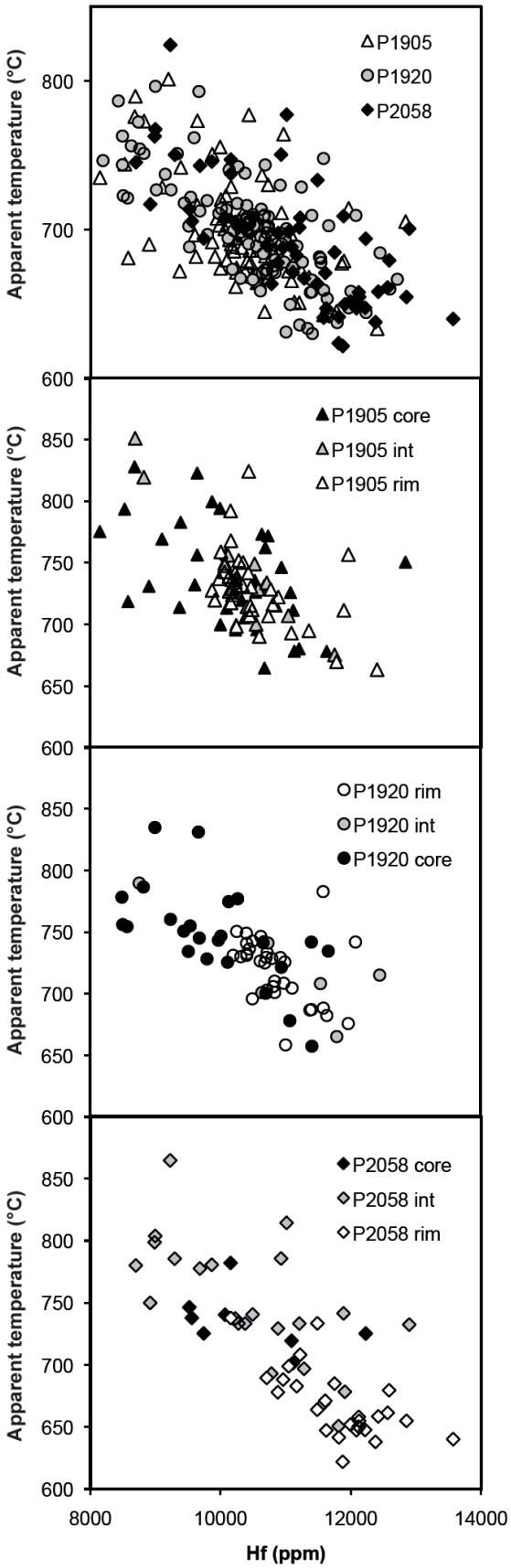

Fig. 5.10: Hf concentration versus Ti-in-zircon 'apparent' temperatures for each sample by core, interior (mid), and rim crystal zone (using geothermometer of Ferry and Watson (2007), assuming a_{TiO2} = 0.7, and a_{SiO2} = 1). Uncertainties on temperatures are < 10°C (2sd).

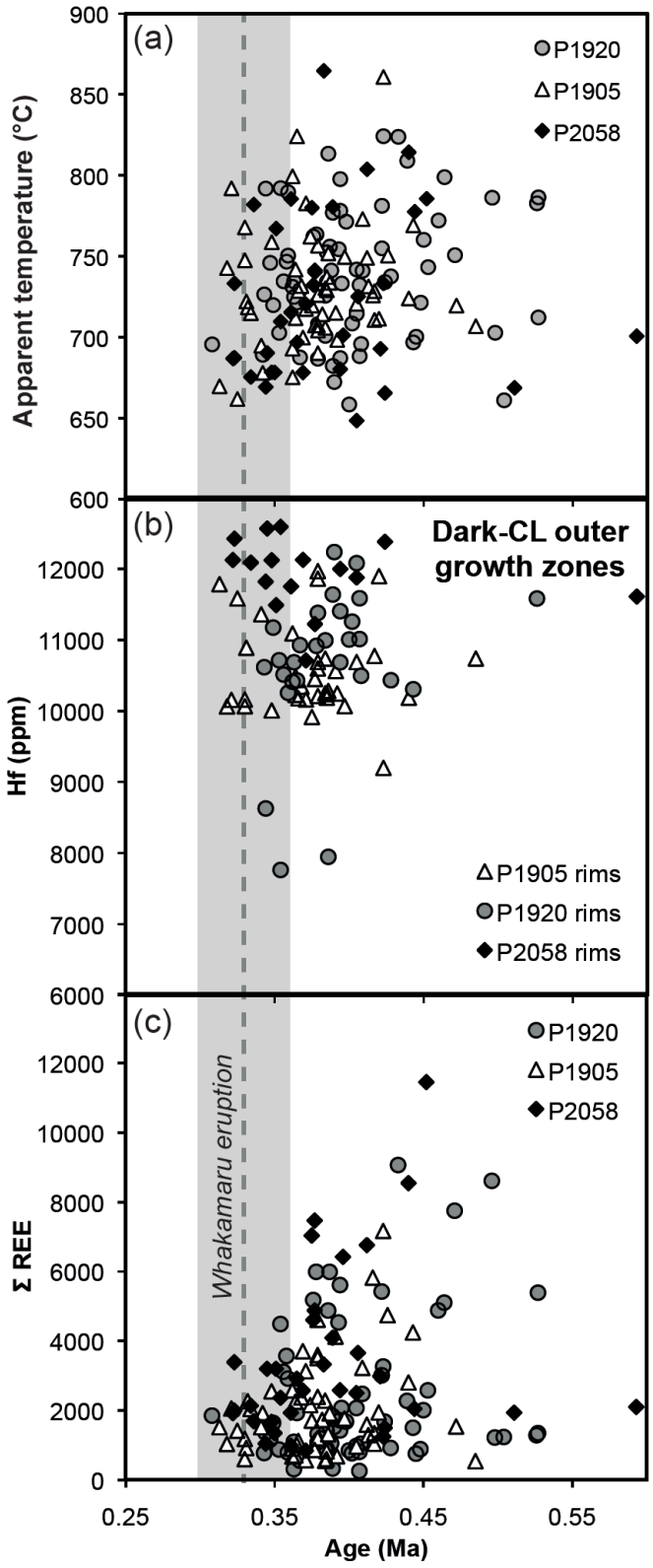

Fig. 5.11: Trends in zircon trace-element chemistry with U-Pb age: (a) Apparent temperatures calculated from Ti-in-zircon geothermometer (Ferry and Watson, 2007); (b) Hf (ppm) for the dark CL outer zircon growth zone; (c) ΣREE plotted versus U-Pb corrected zircon ages for the three pumice samples. The approximate eruption age for the Whakamaru supereruption is marked with the grey bar (references in Table 1.4).

5.3.3.1 Ti-in-zircon temperature estimates

The dependence of Ti concentration in zircon on crystallisation temperature was first described by Watson and Harrison (2005) on the basis of experimental results and well-characterised natural samples. Ti has low diffusivity in zircon under geologic conditions (Cherniak et al., 2007) and therefore can yield valuable information on magmatic thermal evolution. The Ti-in-zircon geothermometer was revised by Ferry and Watson (2007) to incorporate variability in Ti and Si activities (a_{TiO2} and a_{SiO2}), and allow for under-saturation in quartz and rutile, as given by equation [5.3]:

$$T(K) = \frac{-4800 \pm 86}{\log Ti(ppm) + \log a_{SiO2} - \log a_{TiO2} - (5.711 \pm 0.072)} \qquad [5.3]$$

Application of the Ti-in-zircon geothermometer therefore requires knowledge of a_{TiO2} and a_{SiO2} at the time of zircon crystallisation. Samples indicate simultaneous crystallisation of quartz, zircon and ilmenite, suggesting $a_{SiO2} = 1$ and $a_{TiO2} < 1$ (Matthews et al., 2011a). Here, the Ti-in-zircon temperatures (T_{TiZ}) assume a fixed a_{TiO2} of 0.7 and a_{SiO2} of 1.0 (see Section 3.2.4 for a full discussion of a_{TiO2}). Values of a_{TiO2} and a_{SiO2} can be difficult to constrain, however, particularly if zircons were not in equilibrium with their final host magma, and as crystallisation is likely to cause both activities to change during magma evolution (Claiborne et al., 2010). Ti also varies quasi-systematically with other indicators of melt evolution (e.g., Hf, or Zr/Hf), and temperatures cannot be allocated unless a single value of a_{TiO2} is adopted. Furthermore, zircon stability and crystallisation can depend on water contents and pressure (Reid et al., 2011). Ti-in-zircon geothermometry also has a moderate pressure dependence (~ 5 – 10°C kbar^{-1}; Ferry and Watson, 2007; Ferriss et al., 2008). This implies that temperatures calculated using Ferry and Watson's (2007) formulation may be tens of degrees too high for shallow crustal conditions, and tens of

degrees too low at deep-crustal/upper-mantle pressures (Claiborne et al., 2010). The problems associated with application of the TitaniQ geothermometer (as discussed in Chapter 3) also apply to Ti-in-zircon geothermometry. In view of these uncertainties, Ti-in-zircon temperatures are presented here as '*apparent T*' rather than as absolute values (terminology also used by Ickert et al., 2011).

Table 5.5: ***Ti-in-zircon 'apparent' temperatures for core, intermediate and rim zircon growth zones***

Sample	Crystal zone	Av. T (°C)	1sd	Min T (°C)	Max T (°C)	*n*
P1905	Core	738	42	665	828	*36*
	Int	743	54	675	851	*10*
	Rim	729	29	663	824	*42*
P1920	Core	752	41	657	835	*26*
	Int	720	42	665	790	*6*
	Rim	720	26	659	783	*33*
P2058	Core	745	24	701	782	*8*
	Int	748	51	651	865	*23*
	Rim	698	30	649	772	*58*

Notes: Average (Av.) of n analyses (with 1sd), minimum (Min) and maximum (Max) temperatures were calculated using Ferry and Watson's (2007) geothermometer assuming fixed a_{TiO2} of 0.7 and a_{SiO2} of 1.0. Uncertainties are < 10°C (2sd).

Apparent Ti-in-zircon temperatures are presented in Table 5.5 and Figs 5.10, 5.11a, 5.12, 5.13. The range of Ti-in-zircon temperatures for all samples is 649 – 865°C (assuming constant a_{TiO2} = 0.7 and a_{SiO2} = 1; 266 analyses, Table 5.5). Intra-sample variability is ~ 177 – 216°C. The majority of zircons (76% of core-rim pair analyses) in all three samples show an apparent temperature trend which is the inverse of the Hf trend and decreases from core to rim (Fig. 5.13c, d) although rare zircons show a slight increase from the interior to rim (Fig. 5.13a). Zircon rims from sample P2058 consistently show lower Ti-in-zircon temperatures than the corresponding cores (Fig. 5.12; Table 5.5; 93% of core-rim pairs show higher-T cores).

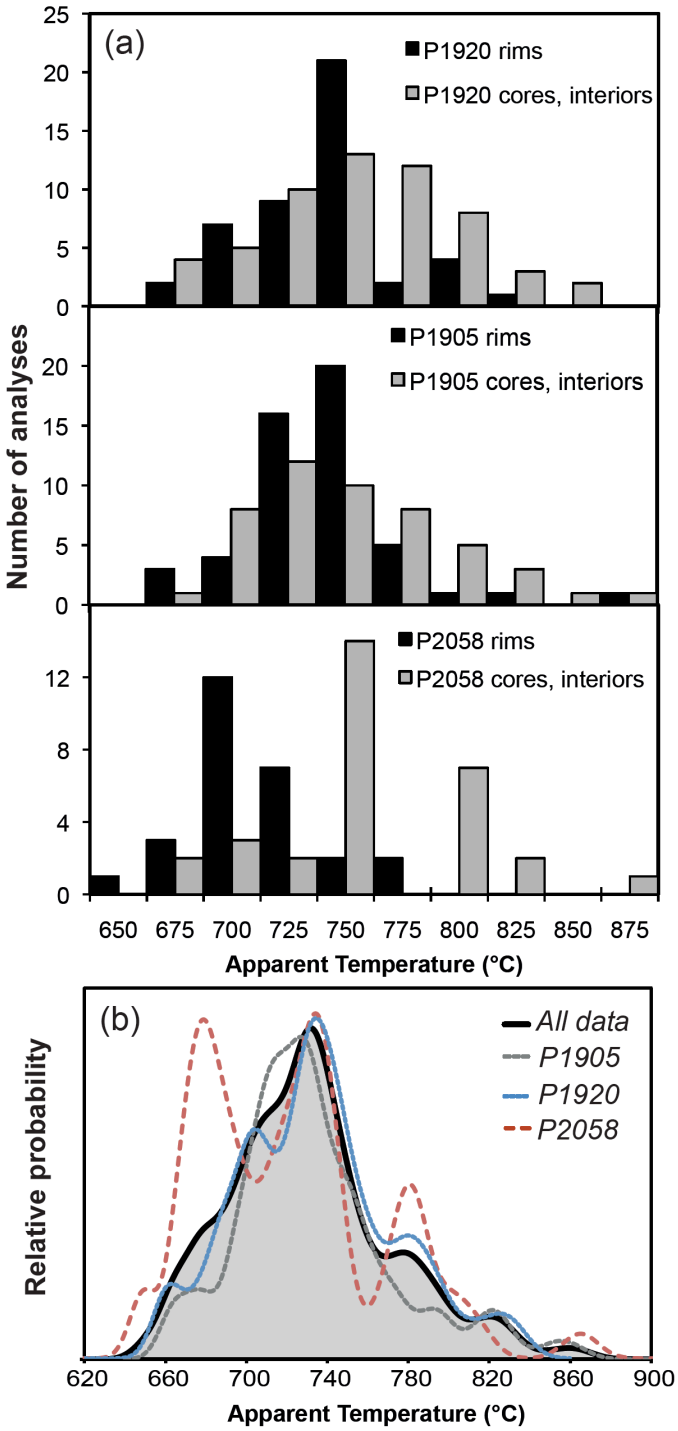

Fig. 5.12: (a) Histograms showing distribution of apparent temperatures from Ti-in-zircon thermometry for each sample (using geothermometer of Ferry and Watson, 2007) by rim (dark-CL outer growth band) and core/interior. Note that samples P1905 and P1920 (type *A* pumice) show very similar Ti-in-zircon apparent temperature signatures, whereas P2058 (type *D*) is characterised by rims of cooler temperatures, and different core vs rim temperature distributions (statistically different at 95% confidence). (b) PDF curves for Ti-in-zircon *apparent* temperature data for each sample, showing bimodal peak for P2058, and strong unimodal curve for other samples, with mode of ~ 740°C.

The apparent temperature decrease from core to rim is of variable magnitude, with temperature fluctuations usually > 100°C for individual zircons. For example, zircon crystal P1920A-26.3 records core and rim temperatures of 835°C and 687°C respectively, corresponding to a 148°C temperature drop to subsolidus temperatures, while P1905-30.4 shows a temperature decrease of 55°C (823°C core to 768°C rim); Appendix 15.

For comparison, pre-eruptive temperatures of magmas were also estimated on the basis of zircon saturation geothermometry using glass chemistry data (Appendix 4) and equation [5.4] (Watson and Harrison, 1983; Hanchar and Watson, 2003; see parameters in Table 5.2):

$$\ln D_{Zr}^{zircon/melt} = (-3.80 - [0.85(M-1)]) + 12900/T \qquad [5.4]$$

where $D_{Zr}^{zircon/melt}$ is the concentration of Zr in zircon relative to Zr in the melt, M is the cation ratio (Na+K+2Ca)/(Al × Si), and T is temperature (Kelvin; see parameters in Table 5.6). These calculations indicate pre-eruptive temperatures of 779 – 797°C (Table 5.6), which are comparable to the average Fe-Ti oxide eruption-temperature of 770°C (Section 3.2.4; Matthews et al., 2011a).

Table 5.6*: Zircon saturation temperatures calculated from glass chemistry*

Sample	SiO_2	Zr (ppm)	1sd	M factor	Zircon saturation T (°C)	Ti (ppm)	FM
P1905	76.85	139	14	1.19	796	775	1.10
P1920	77.88	148	16	1.22	793	786	1.26
P2058	77.86	83	10	1.17	789	328	1.17
P1910	77.87	141	17	1.10	797	785	1.10
P1915	77.27	139	10	1.15	792	960	1.24
P1827	78.70	124	23	1.19	779	561	1.20

Notes: Melt composition is based on in situ glass analysis (EPMA) and results are quoted anhydrous and as average values from n analyses (shown in Table 5.2).

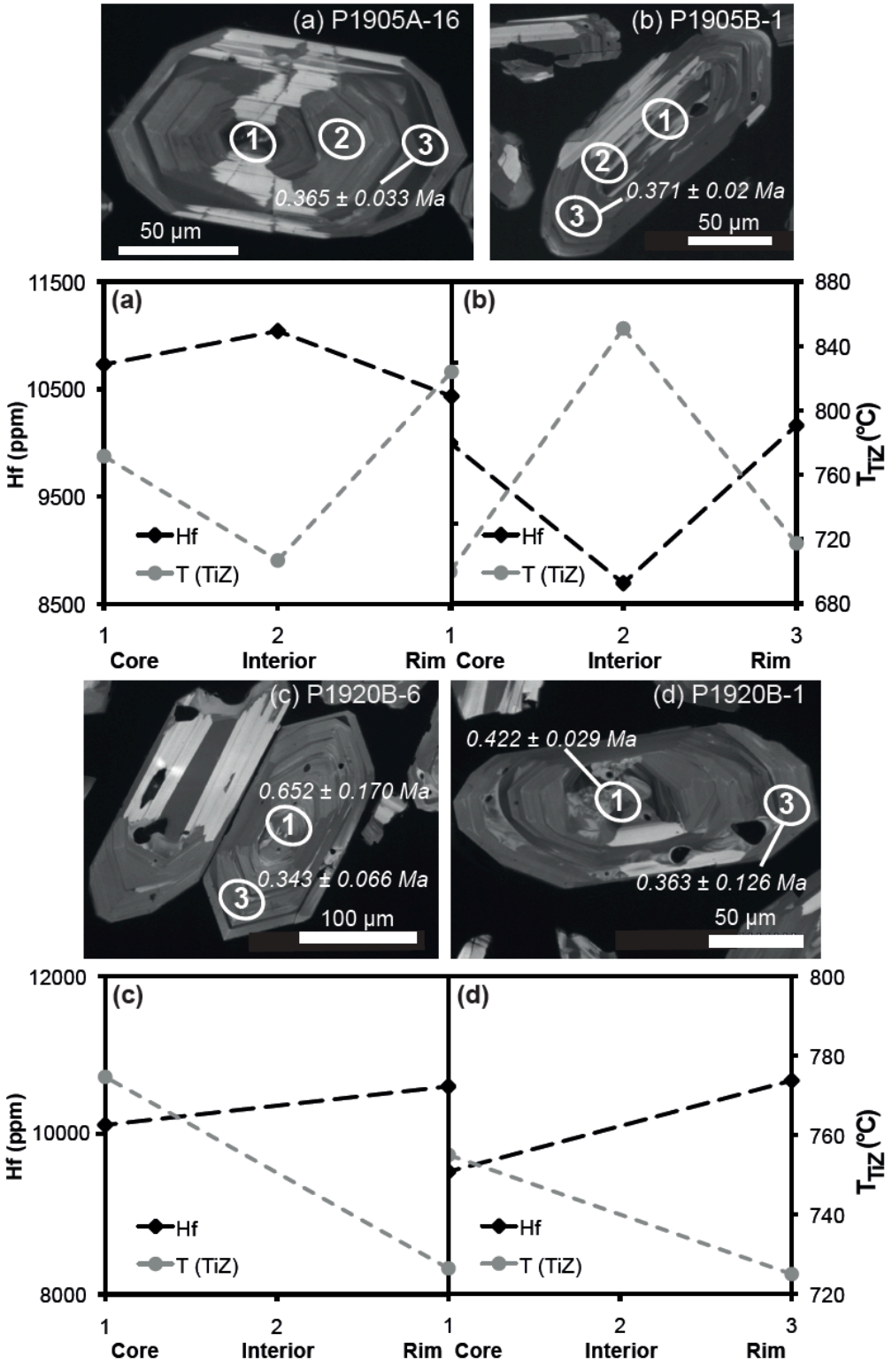

Fig. 5.13: CL images of zircon grains from samples P1905 and P1920 showing U-Pb ages and analysis spots, and Hf and apparent Ti-in-zircon (T_{TiZ}) temperature (geothermometer of Ferry and Watson, 2007) profiles (shown by black and grey dashed lines respectively).

5.3.3.2 Melt composition

Reconstruction of the temporal evolution of the melt is possible if it is assumed that zircon trace-element contents are primarily controlled by equilibrium zircon-melt partitioning at the time of mineral growth (Hoskin and Schaltegger, 2003; Cavosie et al., 2006). With REEs, however, interpretations of reconstructed melt compositions are hampered by the complexities of REE incorporation into zircon (Hanchar and van Westrenenen, 2007), and by variable distribution coefficient (D_{REE}) estimates for zircon-melt partitioning (e.g., Dickinson et al., 1980; Watson, 1980; Sano et al., 2002; Thomas et al., 2002; Rubatto and Hermann, 2007). Here, REE partition coefficient (D_{REE}) values, based on measurements of natural samples from Sano et al. (2002), have been used to reconstruct the composition of melts from which zircon crystallised.

Melt composition calculations suggest that the parental melt from which zircon crystallised is typically more LREE-enriched than the composition of the final pumice glass, with a Eu anomaly of variable magnitude (Fig. 5.14). Plots of Eu/Eu* and La/Yb (HREE:LREE) for reconstructed melt compositions versus age show random scatter (Fig. 5.15; although Eu/Eu* vs age shows a weak positive trend), indicating a lack of significant trace-element evolutionary trends over the time period from 0.5 Ma until eruption.

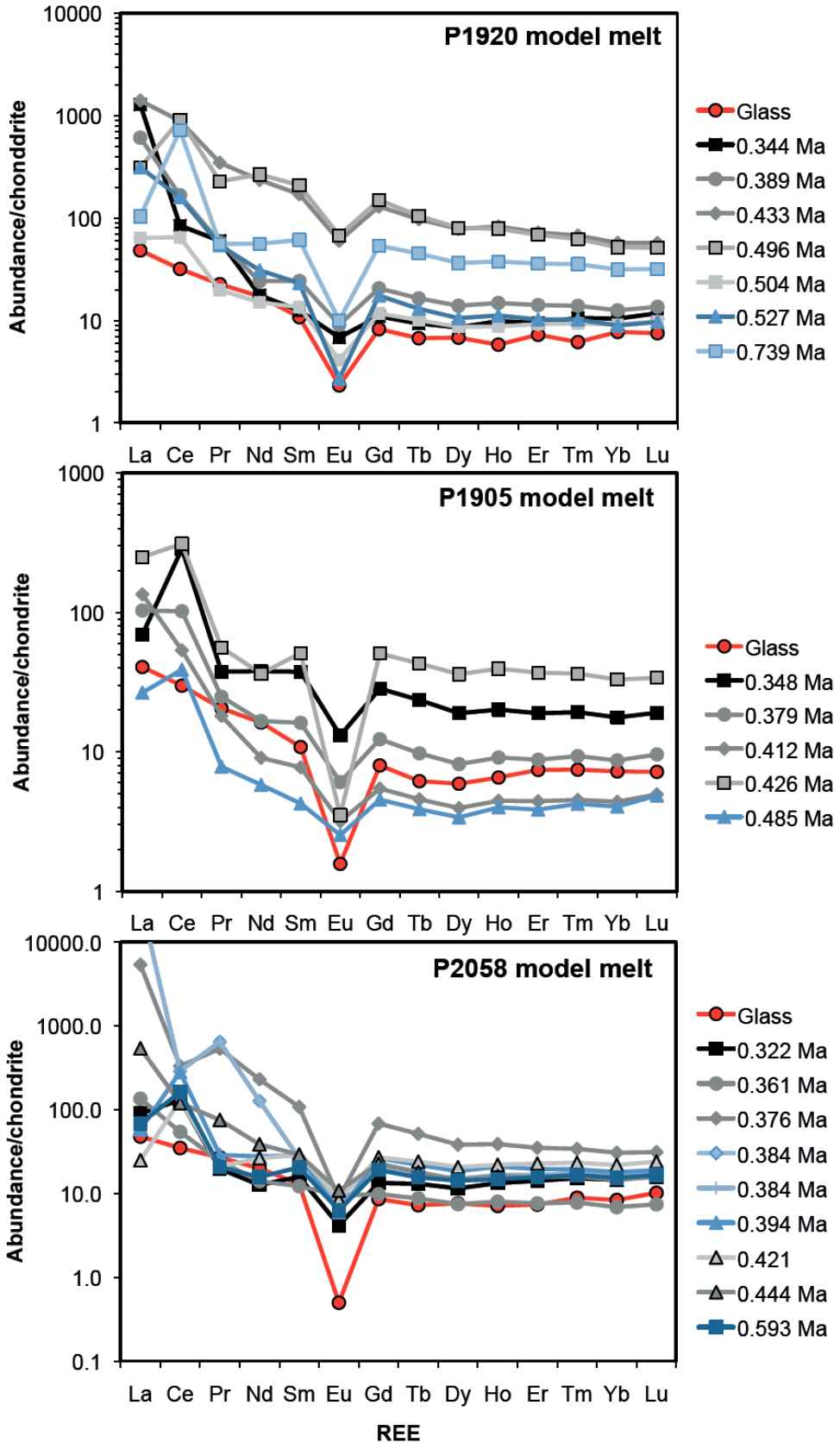

Fig. 5.14: Selected melt compositions reconstructed from zircon-melt partitioning (using partition coefficients from Sano et al., 2002), showing evolutionary trends in melt composition with time compared to final glass REE compositions.

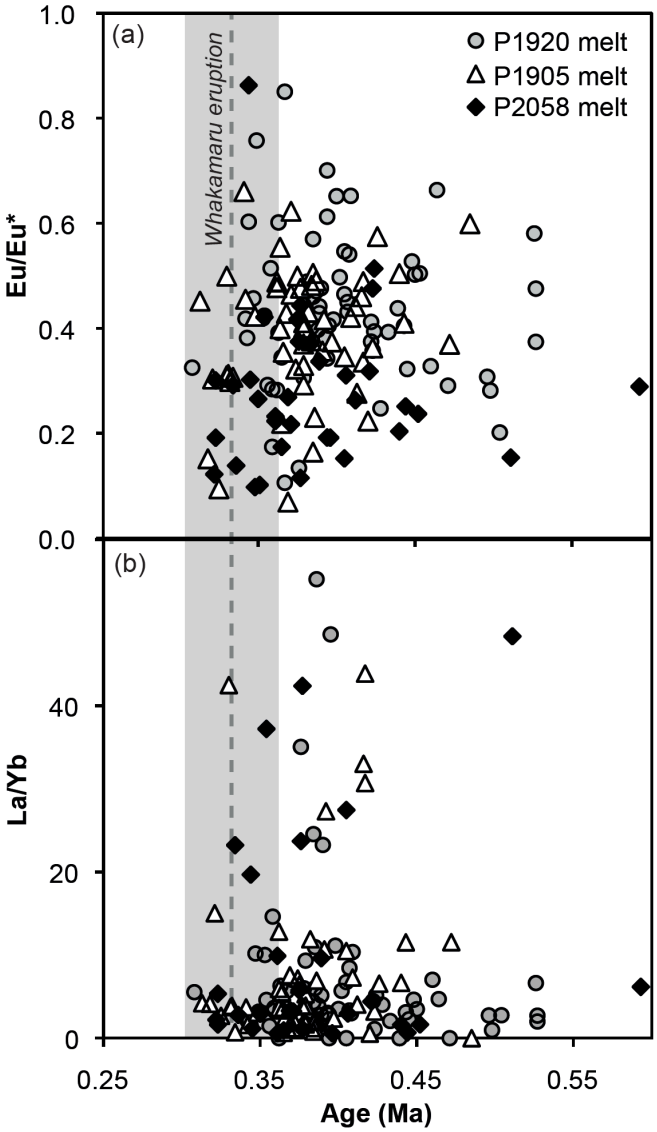

Fig. 5.15: (a) Eu anomaly (Eu/Eu*) and (b) La/Yb with time for melt reconstructed from zircon partition coefficients. The approximate eruption age for the Whakamaru supereruption is marked with the grey bar (references in Table 5.1).

5.3.4 $\delta^{18}O$ data

Results of $\delta^{18}O$ analysis for zircon ($\delta^{18}O_{Zrc}$) and quartz ($\delta^{18}O_{Qtz}$) are presented in Table 5.7, and Figs 5.16 and 5.17. Taken together, the data yield averages $\delta^{18}O_{Zrc}$ = 5.78 ± 0.27 ‰ (1sd) and $\delta^{18}O_{Qtz}$ = 8.15 ± 0.26 ‰ (1sd) for all pumice samples (Table 5.7; full data set in Appendix 16 and 17 respectively). Most Whakamaru zircons have near mantle $\delta^{18}O_{Zrc}$ values (5.3 ± 0.3 ‰; Valley et al., 1994), although older (> 100 Ma) zircon cores have

elevated $\delta^{18}O$ values of up to 7.21 ‰ (Fig. 5.17; Appendix 16). Feldspar $\delta^{18}O$ data are provided in Appendix 17.

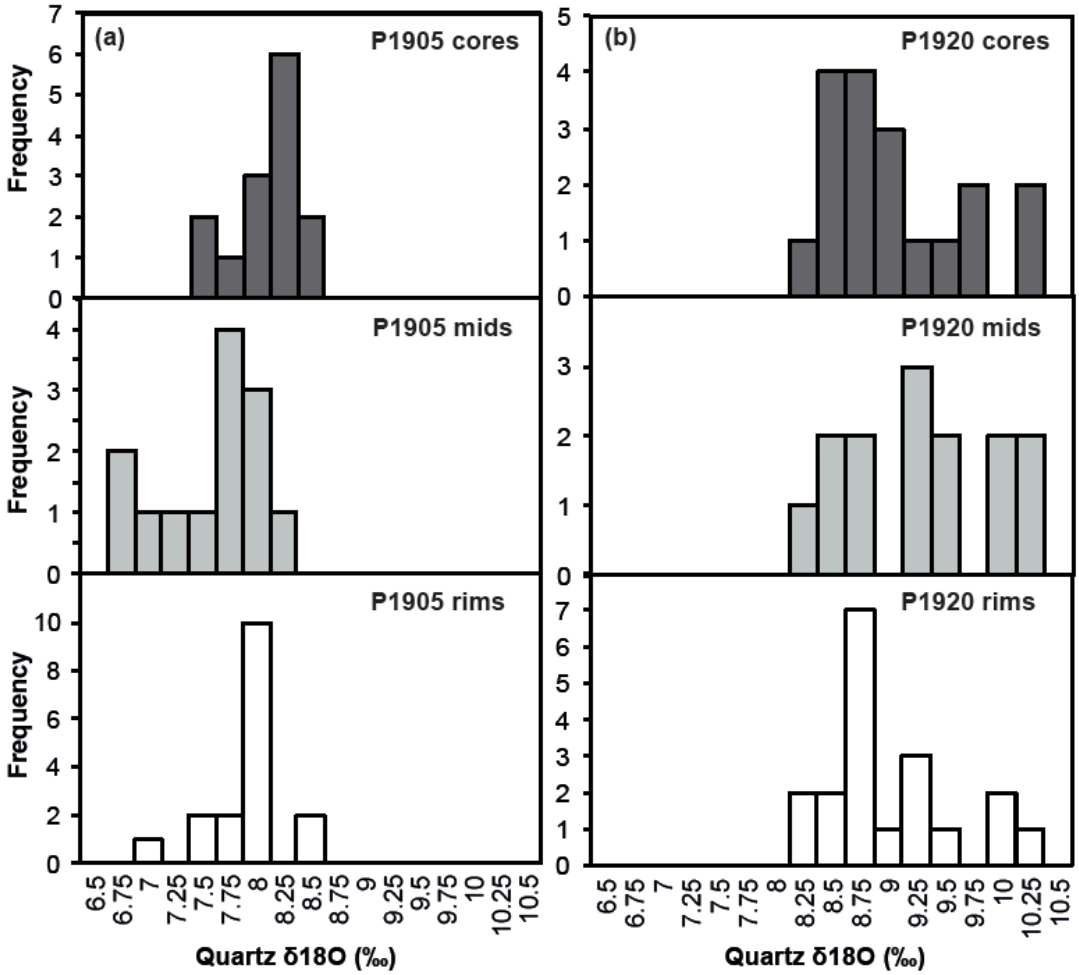

Fig. 5.16: Quartz $\delta^{18}O$ histograms for (a) Rangitaiki sample P1905; and (b) Whakamaru sample P1920; showing core, mid and rim $\delta^{18}O$ signatures.

For quartz, cores, mid-sections and rims show no systematic patterns of $\delta^{18}O$ variation within any particular sample (Fig. 5.16). Individual quartz crystals show $\delta^{18}O$ variation of ± 0.7 ‰ with variability within a single pumice sample of ± 1.5 – 2.9 ‰ (e.g., $\delta^{18}O_{Qtz}$ range for sample P1915: 7.3 – 8.8 ‰, and sample P1920: 8.2 – 11.1 ‰; see Appendix 16). There were no statistically significant differences between core and rim mean $\delta^{18}O$ values (t-test, 95% confidence) for zircon, quartz and feldspar.

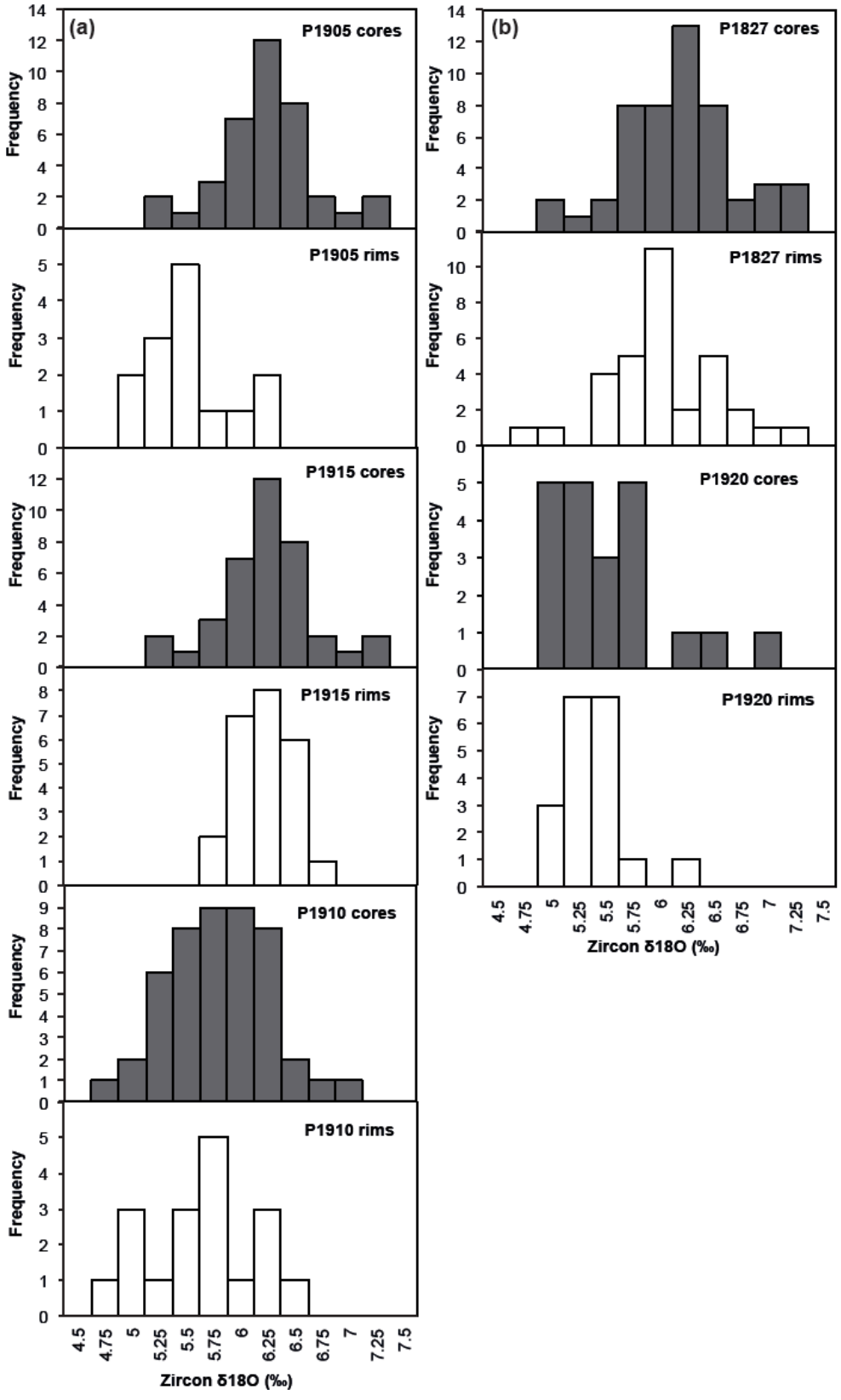

Fig. 5.17: Zircon $\delta^{18}O$ histograms for pumice samples, showing different population distributions for cores versus rims; (a) Rangitaiki samples, (b) Whakamaru samples.

Table 5.7: ***Summary of $\delta^{18}O$ results for Whakamaru quartz, zircon and feldspar***

Sample	Crystal zone	$\delta^{18}O$ mean (‰)	error (± ‰)	1sd	*n*
Quartz					
P1905	Core	**7.95**	0.19	0.32	*14*
(Ra)	Mid	**7.46**	0.22	0.53	*13*
	Rim	**7.79**	0.18	0.32	*17*
P1910	Core	**8.75**	0.31	0.40	*19*
(Ra)	Mid	**8.73**	0.33	0.45	*16*
	Rim	**8.73**	0.33	0.42	*17*
P1915	Core	**8.06**	0.25	0.21	*15*
(Ra)	Mid	**7.94**	0.19	0.34	*18*
	Rim	**7.98**	0.20	0.38	*16*
P1920	Core	**9.05**	0.34	0.75	*19*
(Wh)	Mid	**9.17**	0.34	0.65	*14*
	Rim	**8.88**	0.36	0.54	*19*
P1827	Core	**7.68**	0.22	0.99	*29*
(Wh)	Mid	**7.48**	0.24	0.61	*18*
	Rim	**7.24**	0.26	1.03	*30*
Zircon					
P1905	Core	**5.46**	0.29	0.51	*25*
	Rim	**5.44**	0.32	0.39	*14*
P1910	Core	**5.68**	0.30	0.47	*47*
	Rim	**5.50**	0.32	0.50	*18*
P1915	Core	**6.13**	0.17	0.44	*38*
	Rim	**6.09**	0.17	0.24	*24*
P1920	Core	**5.41**	0.52	0.22	*21*
	Rim	**5.27**	0.22	0.26	*19*
P1827	Core	**6.12**	0.32	0.60	*51*
	Rim	**5.92**	0.32	0.50	*33*
Feldspar					
P1915	Core	**7.54**	0.14	1.38	*16*
	Mid	**7.15**	0.12	0.28	*13*
	Rim	**7.66**	0.12	1.6	*21*

Notes: Summary of $\delta^{18}O$ measurements by SIMS. Standards used were: kimberlite zircon ('Laura'), NBS-28 quartz and Sierra-60 feldspar; Full datasets provided in Appendix 16 and 17.

5.3.4.1 Isotopic fractionation

An empirically predicted equilibrium zircon $\delta^{18}O$ value for Whakamaru magma is $\delta^{18}O_{Zrc}$ = 6.25 ± 0.48 ‰, as calculated by equation [5.5] (Valley et al., 1994; Valley et al., 2005):

$$\delta^{18}O_{Zrc} - \delta^{18}O_{WR} = -0.0612 \times [SiO_2] + 2.5 \qquad [5.5]$$

where WR refers to whole-rock ($\delta^{18}O_{WR}$ = 8.15 ± 0.36 ‰; Blattner et al., 1996) and [SiO_2] is wt% SiO_2 (average whole-rock value 72 wt%; Appendix 3; calculation is valid at magmatic temperatures). Measured zircon rim values range 5.27 – 6.09 ‰, with an average of 5.74 ± 0.48 ‰ (Fig. 5.17; Table 5.7), which is slightly lower but within uncertainty of the predicted value for equilibrium with the host Whakamaru melt.

Oxygen isotopic fractionation between two minerals has a temperature dependency, as indicated by equation [5.6] which describes the equilibrium fractionation between quartz and zircon in terms of an experimentally determined constant, *A*, and temperature (*T* °K, for conditions $T > 773$ K; Valley et al., 2003; Trail et al., 2009):

$$\delta^{18}O_{Qtz} - \delta^{18}O_{Zrc} = \Delta^{18}O_{Qtz\text{-}Zrc} \approx 1000 \ln(\alpha_{Qtz-zrc}) = A_{Qtz-zrc} 10^6 / T^2 \qquad [5.6]$$

where the 'fractionation factor', $\alpha_{Qtz\text{-}zrc}$, is the $^{18}O/^{16}O$ ratio in quartz divided by the $^{18}O/^{16}O$ ratio in zircon (Trail et al., 2009). The $A_{Qtz\text{-}Zrc}$ value has been estimated as 2.33 ± 0.24 (Trail et al., 2009) and 2.64 ± 0.08 (Valley et al., 2003), assuming linearity of 1000lnα vs $1/T^2$ (Bottinga and Javoy, 1973; Valley et al., 2003). Experimental and analytical studies of fractionation between quartz and zircon show no clear dependence on oxygen fugacity or pressure (Trail et al., 2009).

Table 5.8: ***Average $\delta^{18}O$ for rims of zircons and coexisting quartz and calculated fractionation factors ($\alpha_{Qtz\text{-}zrc}$) and oxygen isotope temperatures***

Sample	Zrc $\delta^{18}O$ (‰)	1sd (‰)	*n*	Qtz $\delta^{18}O$ (‰)	1sd (‰)	*n*	$\Delta^{18}O$ (Qtz-zrc)	1sd	$\alpha_{Qtz\text{-}Zrc}$	*T*, (°C)	*T max*, (°C)	*T min*, (°C)	*A*
P1905	5.44	0.32	*14*	7.79	0.18	*17*	2.35	0.37	1.002	723	811	653	2.45
P1910	5.50	0.32	*18*	8.73	0.33	*17*	3.23	0.46	1.003	*526*	*644*	*522*	*3.37*
P1915	6.09	0.17	*24*	7.98	0.20	*16*	1.89	0.26	1.002	837	923	767	1.97
P1920	5.27	0.22	*19*	8.88	0.36	*19*	3.61	0.42	1.004	*530*	*582*	*487*	*3.77*
P1827	5.92	0.32	*33*	7.24	0.26	*30*	1.32	0.41	1.001	*1055*	*1329*	887	1.38
Av.	**5.64**	**0.27**	**-**	**8.12**	**0.27**	**-**	**2.48**	**0.38**	**1.003**	**696**	**781**	**629**	**2.59**

Note: $\delta^{18}O$ values are presented as averages of n analyses with 1sd. Temperatures calculated from oxygen isotope geothemometry (using formulations of Valley et al., 2003; Trail et al., 2009) are feasible magmatic temperatures with the exception of those in italics which are subsolidus, and the high values calculated for sample P1827. 'A' coefficients estimated using equation [5.6], $\Delta^{18}O_{Qtz\text{-}Zrc}$, and an eruption temperature of 770°C (from Fe-Ti oxide geothermometry using the Ghiorso and Evans (2008) geothermometer; see Chapter 3 and Matthews et al., 2011a).

Intra-sample variation of $\delta^{18}O_{Qtz}$ is significantly larger than that for zircon, and $\alpha_{Qtz\text{-}zrc}$ varies slightly between samples (Table 5.8). The average isotopic fractionation between zircon and quartz rims is $\alpha_{Qtz\text{-}zrc}$ = 1.003 across all five pumice samples analysed (Table 5.8), which is consistent with values constrained by analyses of equilibrium quartz-zircon pairs from felsic volcanic rocks at temperatures of 671 – 978°C (Valley et al., 2003) and experimentally constrained values (at 700 to 1000°C; Trail et al., 2009). Results here therefore provide evidence that the rims of both zircon and quartz crystallised simultaneously and under isotopic equilibrium conditions. Temperatures based on oxygen isotope equilibrium between quartz and zircon (using equation [5.6] with A ~ 2.33) range from 530 – 1055°C (Table 5.8) where the lowest two estimates (for samples P1910 and P1920) are subsolidus conditions. Estimates of *A* for the selected pumices range from 1.38 – 3.77, with an average of 2.59 (Table 5.8; using equation [5.6] and the eruption temperature of 770°C; Section 3.3.4; Matthews et al., 2011a); consistent with experimental and analytical values of 2.64 and 2.33 (respectively from Valley et al., 2003; Trail et al.,

2009). Nevertheless, these estimates are clearly limited by the choice of temperature. It is assumed here that the use of eruption temperature is appropriate as Ti-in-zircon apparent temperatures show little temperature change during crystal growth (core-to-rim; Table 5.5).

5.4 Discussion

5.4.1 Zircon crystallisation ages and timescales of silicic magma systems

Whakamaru (sample P1920) and Rangitaiki (sample P1905) zircon crystals show similar age spectra (Fig. 5.6) indicating that these ignimbrite units were likely to have been erupted from the same voluminous magma reservoir (dominantly type *A* magma; Section 1.5.3). Data from Huckleberry Ridge Tuff pumices have indicated, however, that clasts with different compositional characteristics can have similar age populations, even when the compositional and isotopic data show that they must have come from different reservoirs (C. Wilson, *pers. comm.*, 23 July 2011). The age spectrum for type *D* magma (sample P2058) differs slightly from the type *A* pumices in that it shows fewer zircons of young ages (within uncertainty of eruption age ~ 0.32 Ma) and a secondary peak of crystallisation at 0.44 Ma, with the majority of crystals recording ~ 0.40 Ma ages (Fig. 5.6). The ages suggest that this magma body ceased to crystallise before type *A* and was therefore isolated during the final stages prior to eruption in an independent (and subsidiary) magma reservoir (also supported by the contrasting glass major- and trace-element chemistry (Appendix 4) and fractionation trends which differ from type *A* magma; Chapter 2). The incorporation of distinct magma bodies (represented by type *A* and *D* pumices) may contribute to the scattering of zircon trace-element patterns with age (Fig. 5.11).

The variety of zircon textures and CL zoning patterns observed in all samples (Section 5.3.1) indicates multi-stage zircon growth, with complex histories of growth and resorption during the waxing/waning of the parental magma reservoirs. The dark-CL/high-U zircon growth zones near the majority of zircon rims show a variety of ages (from eruption age to 0.59 Ma, although dominantly ~ 0.44 Ma). These growth zones are interpreted as representing a short-lived range of magmatic conditions that start and finish abruptly (due to the sharp boundaries between the dark zones and the earlier and later lighter-CL zones). These conditions are all in the 'early' history of the grains, as no crystals show dark-CL as their outermost rims. 'Early' in this context is within uncertainty of eruption age to > 0.1 Ma older (up to a maximum of 0.526 Ma for sample P1920, 0.485 Ma for P1905, and 0.593 Ma for P2058). It is likely that these high-U growth zones represent zircon crystallisation during or following an event that changed the physicochemical conditions within the chamber, possibly due to magma replenishment, or mixing of more evolved parts of the magma system (also noted by Brown and Fletcher, 1999).

An earlier U-Pb ion-microprobe study of Whakamaru zircons gave a rim and outer growth zone age of up to 0.45 ± 0.02 Ma (1sd), with core ages of 0.61 ± 0.02 Ma (Brown and Fletcher, 1999). These differences in age between cores and rims were interpreted as evidence for magmatic residence times exceeding 0.25 Ma (Brown and Fletcher, 1999). The new data here show a unimodal age distribution with a dominant zircon peak for both Whakamaru and Rangitaiki zircon populations at ~ 0.40 – 0.44 Ma (Fig. 5.6), suggesting that most zircon crystallisation occurred ~ 0.05 – 0.1 Ma prior to eruption (Table 5.3). While these data might not be directly interpretable in terms of residence times, they do not support the > 0.25 Ma estimate of Brown and Fletcher (1999). Interpreting the residence time is difficult, however, due to the mix of antecrysts and xenocrysts, in

addition to phenocrysts. The zircon age spectra are broader than $^{40}Ar/^{39}Ar$ ages which are fixed at the time of eruption. For zircon the U-Pb system closes as soon as the zircon grows and crystallisation persists once nuclei exist, therefore age spectra show the full range of crystallisation ages, in addition to reflecting assimilation of antecrysts. If it is assumed that the residence time of Whakamaru magma is ~ 100 ky (assuming that the peak in zircon crystallisation indicates that the large-volume reservoir existed at this time), the magma production rate would be 1.5×10^{-2} km^3 y^{-1}, which is consistent with estimates for other large silicic magmatic systems (Table 5.1).

The observed greywacke zircon cores (Fig. 5.3; six xenocrystic cores out of 188 analyses, of which one is from Rangitaiki and five are from Whakamaru pumice) have ages of 159 – 920 Ma (Appendix 14), corresponding to U-Pb detrital zircon ages for the Torlesse and Waipapa Terranes (e.g., Adams et al., 1998; Pickard et al., 2000; Adams et al., 2009). The presence of these xenocrysts in Whakamaru and Rangitaiki pumices indicates that assimilation of older crustal material (Waipapa and/or Torlesse Terrane) must have played a role in the petrogenesis of the Whakamaru magma body (cf. Brown and Fletcher, 1999, did not record any 100 – 300 Ma zircon cores). The rarity of xenocryst zircons may reflect limited assimilation of basement material, dilution of a small number of zircons in the large-volume magma reservoir, or resorption of zircon by Zr-undersaturated magma in the crust (as also observed for Mangakino, Ongatiti and Oruanui ignimbrites; Brown and Smith, 2004; Charlier et al., 2005; McCormack et al., 2009). Additional analyses (targeting anhedral zircon cores) are required, however, to address this issue fully.

Zircons which record ages of 0.5 – 0.7 Ma are also presumed to be inherited in this system (10 analyses, Figs 5.6 and 5.8; Appendix 14) and are most likely derived from older

plutonic bodies recycled into the magmatic system. Older plutonic bodies have also been identified as contributors to other rhyolitic TVZ eruptions (e.g., Charlier et al., 2010). Furthermore, the zircons with a Whakamaru modal age (0.42 – 0.44 Ma) have been observed in the 20 ka Omega Dome unit (Charlier et al., 2010), suggesting that the Whakamaru plutonic body was itself also quarried and recycled by younger Quaternary eruptions (i.e. Whakamaru-aged zircons of ~ 0.42 Ma formed part of the country rock assimilated for the younger magmas; Charlier et al., 2010). This history of assimilation of older plutonics is similar to the protracted magma storage and recycling recorded by Mt St. Helens zircons (Claiborne et al., 2010), suggesting that assimilation and plutonic recycling is a process common to volcanic systems of all sizes (also noted by Wilson and Charlier, 2009).

The zircon age population is also consistent with Oruanui zircon ages where a mixture of phenocrysts, antecrysts and xenocrysts is also shown (Charlier et al., 2005). The xenocrysts here are assumed to be derived from Quaternary plutonic and Mesozoic-Palaeozoic metasedimentary rocks; and the antecrysts from older silicic mush and plutonic rocks; while the youngest zircon ages represent zircons which are phenocrysts (*autocrysts*; Miller et al., 2007) that grew in the magma body immediately prior to eruption (Charlier et al., 2005). Other recent studies of TVZ zircons highlight the complex evolution of silicic magma systems, with zircons surviving earlier eruptive events and becoming incorporated into later-developed magmas (e.g., Charlier et al., 2003, 2005; McCormack et al., 2009; Wilson and Charlier, 2009; Charlier and Wilson, 2010; Storm et al., 2011).

5.4.2 Zircon chemistry as a recorder of melt evolution

Zircon trace-element data are discussed here in terms of concentrations of Hf (controlled by zircon fractionation in the melt; Linnen and Keppler, 2002), Ti (reflecting crystallisation temperatures; Watson et al., 2006), REE patterns, and Eu and Ce anomalies. Ti-in-zircon temperatures and Hf concentrations serve as effective indicators of zircon fractionation and thus magma evolution (e.g., Linnen and Keppler, 2002; Grimes et al., 2009). The zircon temperature versus Hf relationships (Fig. 5.10) show a typical fractionation trend for rhyolitic magmas, with increasing Hf corresponding to decreasing Ti concentrations (Hf abundance in zircon increases with magmatic differentiation; Hoskin and Schaltegger, 2003). The lack of systematic compositional change in Hf and Ti with zircon U-Pb age (Fig. 5.11) indicates the complexity of compositional changes in the magma reservoir and is indicative of complex recycling, assimilation and recharge processes which disrupt fractional crystallisation processes and perturb the system.

The decreasing ionic radii of the REE with increasing atomic number results in partitioning behavior that produces characteristic patterns to chondrite-normalised values in zircon (Fig. 5.9; e.g., Hinton and Upton, 1991; Hoskin, 1998; Hoskin and Ireland, 2000; Belousova et al., 2002; Hoskin and Schaltegger, 2003). Negative Eu and positive Ce anomalies are characteristic of magmatic zircons (Hoskin and Schaltegger, 2003), with the Ce anomaly interpreted as indicating oxidising conditions (which allow Ce^{4+} to substitute more readily for Zr^{4+}; Berry et al., 2006), and the Eu anomaly being attributed to reducing conditions (Eu^{2+} in the melt) and/or feldspar as an important fractionating phase. Many zircons exhibit both positive Ce and negative Eu anomalies (Hoskin and Schaltegger, 2003).

Burnham and Berry (2011) provide evidence that both Ce and Eu anomalies vary systematically with the magnitude of oxidising conditions, with temperature and melt compositions also having a significant effect. The magnitude of these anomalies is, however, also dependent on whether other phases are co-crystallising e.g., Ce is partitioned into allanite and monazite, and Eu into feldspar (Hoskin and Schaltegger, 2003). Furthermore, Ce/Ce* values should be treated with caution because their calculation depends on La and Nd values which have very low concentrations in zircons (< 1 ppm) and correspondingly high analytical errors, and are very susceptible to contamination from small LREE minerals or trapped melt at the sub-micron scale (cf. Hoffman et al., 2009). Plagioclase fractionation may deplete Eu from the melt prior to or during zircon crystallisation, and this process most likely dominates over fO_2 (Snyder et al., 1993; Hoskin, 1998; Hoskin et al., 2000). The Eu-anomaly in zircon is then both inherited from the Eu-depleted melt as well as being influenced by fO_2 conditions. The more significant Eu anomalies are recorded by zircon rims for sample P2058 indicating that magmatic conditions for type *D* magma became more reducing over time, or that plagioclase crystallisation increased as the magma body evolved. This inference is supported by the extremely pronounced Eu anomaly for P2058 glass, suggestive of strong plagioclase fractionation.

The compositional diversity of Whakamaru and Rangitaiki zircons may also be explained by two separate compositional trends due to melt fractionation, with mixing between these compositional series at many different stages as pictured in Fig. 5.18. The role of mixing of melts in the petrogenesis of the Whakamaru magma reservoir is still under investigation. Using reconstructed melt compositions based on zircon-melt partitioning calculations (Fig. 5.14), all samples taken together indicate that the melt Eu anomaly increases with age.

This suggests that the effect of plagioclase fractionation decreased with time prior to eruption. These melt compositions also show significant variation with time (Fig. 5.15), which may be related to new inputs of magma into the system during the assembly and growth of the magma reservoir(s). The high-U zircon growth zones also support periodic influxes of new magma into the system (or mixing of more evolved magma). Furthermore, records of Whakamaru quartz and feldspar zonation also indicate complex compositional changes throughout their crystallisation, reflecting P/T changes in response to magma recharge and pointing to incremental magma chamber assembly (see Saunders et al., 2010; Matthews et al., 2011a).

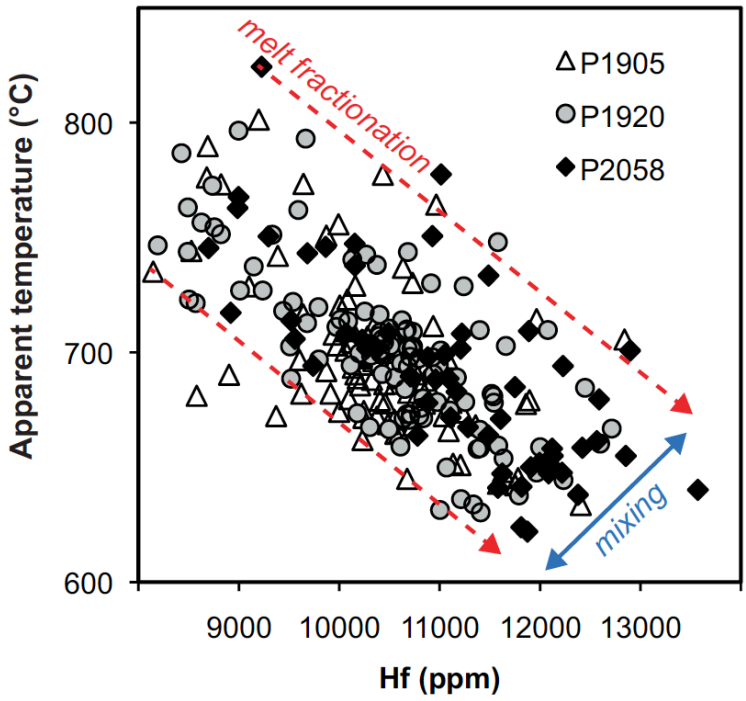

Fig. 5.18: Plot of Hf versus apparent Ti-in-zircon temperatures (assuming fixed a_{TiO2} = 0.7) annotated with suggested melt fractionation trends for two magma bodies with mixing between the two creating compositional and thermal diversity of zircons.

5.4.2.1 Magmatic thermal evolution

The long-term record of magmatic temperatures recorded by zircon crystallisation (using Ti-in-zircon geothermometry, Section 5.3.3.1) indicates that temperatures fluctuated within the range 650 – 865 °C, around an average of 734 ± 38 °C (1sd), with no significant trend over the 0.3 – 0.55 Ma period (Fig. 5.11). There is no clear core-mid-rim temperature trend, except for the type *D* pumice (sample P2058) which shows lower temperature rims (Fig. 5.10). Nor do rims from P2058 record ages as young as those of P1905 and P1920, suggesting crystallisation ceased earlier for type *D* magma. In conjunction with the independent temperature histories, this provides further evidence that the type *D* magma was isolated from the more dominant type *A* magma reservoir, and evolved independently prior to eruption. Individual zircon crystals record variable growth histories primarily as a function of whether or not they are exposed to the melt during a particular event. For example, crystals may be enclosed in other minerals or in a portion of the mineral mass that did not melt.

Ti-in-zircon geothermometry provides *apparent* magma temperatures consistent with the broad range of estimates derived from Fe-Ti oxide, amphibole, feldspar-melt, and TitaniQ geothermometry (647 – 968°C; eruption temperature of 770°C; see Matthews et al., 2011a). The large range in Fe-Ti oxide temperature estimates (including subsolidus values), is interpreted as being due to pluton recycling, rather than reflecting solely magmatic temperatures. Values of < 600°C at grain edges (mainly from the dark-CL outer growth zone) may reflect a_{TiO2} dropping to values as low as 0.2, or conditions being no longer silicate melt (and are instead H_2O-rich). Ti-in-zircon temperature values < 700°C indicate subsolidus conditions and may be better explained by sources of inaccuracy in the temperature estimates (with the assumed fixed a_{TiO2} and a_{SiO2} values), further indicating

that all such temperature estimates should be treated with caution. This has similarly been observed for Ti-in-zircon temperatures for the Bishop Tuff (Reid et al., 2011).

Significant magma temperature fluctuations of > 100°C occur over short timescales of < 7 ky (e.g., temperature rise from 659 to 836°C between 0.433 Ma and 0.426 Ma; Fig. 5.13). This could be due to new pulses of magma entering the system which was growing incrementally for thousands of years prior to eruption (consistent with fluctuating melt REE patterns; Section 5.3.3.2). Fluctuations in temperature (and melt composition) are consistent with a repeatedly replenished system which is reheated and potentially rejuvenated by introduction of new melt, mixing with other magmas, and subsequent crystallisation and fractionation (Claiborne et al., 2010).

Individual zircon crystals commonly show a decrease in temperature towards the rim (Fig. 5.13), although a minor population shows an increase, indicating that different crystals recorded separate thermal events as a function of age. These diverse *apparent* temperature trends, and the lack of systematic variations in zircon Hf and Ti contents with age, provides further evidence for complex mixing of zircons from different parts of the magma body (assimilation of antecrystic and xenocrystic zircons with contrasting trace-element signatures and ages could also be involved). These complexities may also reflect cooling history with local high-temperature anomalies within the large magma reservoir(s) (also noted by Hiess et al., 2008, for Greenland Archaean zircons).

Ti-in-quartz geothermometry (Chapter 3), in contrast, shows a consistent apparent temperature rise at the crystal rims (~ 100°C increase across core-rim boundary, assuming constant a_{TiO2} and no pressure change; see Matthews et al., 2011a). The disparity in

temperature patterns between the two geothermometers can be explained by the different timescales that zircon and quartz record, with quartz more likely to record events immediately prior to eruption (due to more rapid crystal growth; Kirkpatrick, 1975). In contrast, zircons can retain several generations of chemical and thermal information, due to their slower growth, insolubility in crustal melts and fluids, resistance to chemical and physical breakdown (Watson, 1996; Cherniak and Watson, 2007), and the slow diffusion rates of Ti in zircon (for comparison, Ti diffusion rates in zircon and quartz at 770 °C are 5.8×10^{-36} m^2 s^{-1} and 1.5×10^{-21} m^2 s^{-1}, respectively; Cherniak and Watson, 2007; Cherniak et al., 2007).

5.4.3 Zircon oxygen isotope constraints on magma sources

Oxygen istope signatures of zircons can be used to constrain source melt compositions, due to zircon being resistant to physical and chemical breakdown (Trail et al., 2009). The dominance of mantle $\delta^{18}O$ signatures for zircon cores and rims suggests that the host melt was differentiated directly from the mantle, or remelted or equilibrated at high temperatures with such rocks (e.g., Valley et al., 1998; 2003). This is an apparent contradiction to the Sr-isotopic evidence, presented by Brown et al. (1998a), which shows a strong crustal influence. Older zircon cores (158.7 ± 0.5 to 172.9 ± 0.5 Ma; Fig. 5.3), however, have elevated $\delta^{18}O$ (6.34 ± 0.50 ‰ to 8.31 ± 0.26 ‰; Appendix 15), corresponding to values for Waipapa Terrane greywacke (McCulloch et al., 1994) and suggesting crustal contamination had a role in the petrogenesis of the parental magma body (although it must be noted that the existing data sets for the basement terranes are sparse and may not represent deeper crustal rocks). Ages are also consistent with detrital studies for the Torlesse and Waipapa Terranes (Mortimer, 1994; 2004; Adams et al., 2009; Section 5.1). Furthermore, the lack of isotopic intra- and inter-grain variability suggests that

evolving melt composition and magmatic differentiation were limited during zircon crystallisation, and that magma source components remained constant during magma assembly (i.e. mantle versus crustal signature).

The heterogeneous $\delta^{18}O$ values in individual quartz crystals and within the pumice samples studied (Appendix 17) can partly be explained by interaction with meteoric groundwater or hydrothermal exchange. Bindeman and Valley (2002) explain such variation in Bishop Tuff quartz as being due to alteration by meteoric water during and shortly after eruption (also proposed for Yellowstone magma $\delta^{18}O$ depletion; Hildreth, 1984). Meteoric waters of the TVZ are characterised by $\delta^{18}O$ = -7 ‰ (Blattner et al., 1996) and therefore may be responsible for the lower $\delta^{18}O_{Qtz}$ values recorded by some crystal zones (Appendix 17). Some Whakamaru and Rangitaiki quartz crystals are, however, characterised by elevated $\delta^{18}O$ values, which are likely to be due to crustal contamination as outlined below.

Increasing $\delta^{18}O$ correlates roughly with increasing SiO_2 content and therefore provides a measure of the degree of magmatic differentiation, although extreme fractionation is required to produce small changes in $\delta^{18}O$ (e.g., Chivas et al., 1982). Crustal contamination could partly explain the elevated $\delta^{18}O$ quartz and rhyolite signatures (Waipapa Terrane has $\delta^{18}O$ 7.6 – 9.7 ‰, and Torlesse Terrane 10.0 – 14.0 ‰; McCulloch et al., 1994). This is consistent with conclusions of Blattner and Reid (1982) and McCulloch et al. (1994) which highlight the role of crustal assimilation in the petrogenesis of TVZ rhyolite.

5.4.3.1 Isotopic fractionation

The fractionation of oxygen isotopes between zircon and coexisting minerals (quartz and feldspar here) provides information on magmatic processes, including crystallisation, re-

melting, assimilation and fractional crystallisation (Valley et al., 2003). Isotopic equilibrium is conserved if cooling is relatively rapid, due to rapid ascent, with diffusion being the rate-limiting process in the transfer of ^{18}O between minerals (Bottinga and Javoy, 1975). Disequilibrium between isotopic composition of mineral pairs may arise due to late-stage hydration and open-system processes (Bottinga and Javoy, 1975), introducing additional uncertainties.

Zircon $\delta^{18}O$ data together with quartz and feldspar crystals extracted from the same pumice clasts, illustrate that co-erupted mineral phases crystallised together in isotopic equilibrium (Fig. 5.19; based on predicted equilibrium rhyolite-melt values and equilibrium values of $\alpha_{Qtz\text{-}Zrc}$; Section 5.3.4.1; Table 5.8). Quartz and zircon thus crystallised from isotopically homogenous magma sources which fed the magma reservoir system over time prior to eruption. Quartz is in equilibrium with whole-rock $\delta^{18}O$ (see Fig. 5.19 for calculated rhyolite-melt $\delta^{18}O$ in equilibrium with measured quartz values, compared to the measured Whakamaru glass signature of 8.15 ± 0.36 ‰; Blattner and Reid, 1982; Blattner et al., 1996), and is therefore consistent with crystallisation in the host Whakamaru magma in equilibrium conditions.

The magnitude and direction of $\delta^{18}O$ changes between crystal cores and rims for both quartz and zircon is variable suggesting complex pre-eruptive mixing and partial homogenization processes in the large silicic reservoir. This contradicts the simplistic view of a ~ 100 ky magma residence time and suggests that the magma was incrementally added throughout this time period. These observations are consistent with the model of rapid pre-eruptive heating, recharge and rejuvenation of the magmatic system (sections 3.4.4 and 4.4.5; Matthews et al., 2011a), based on mineral thermobarometry.

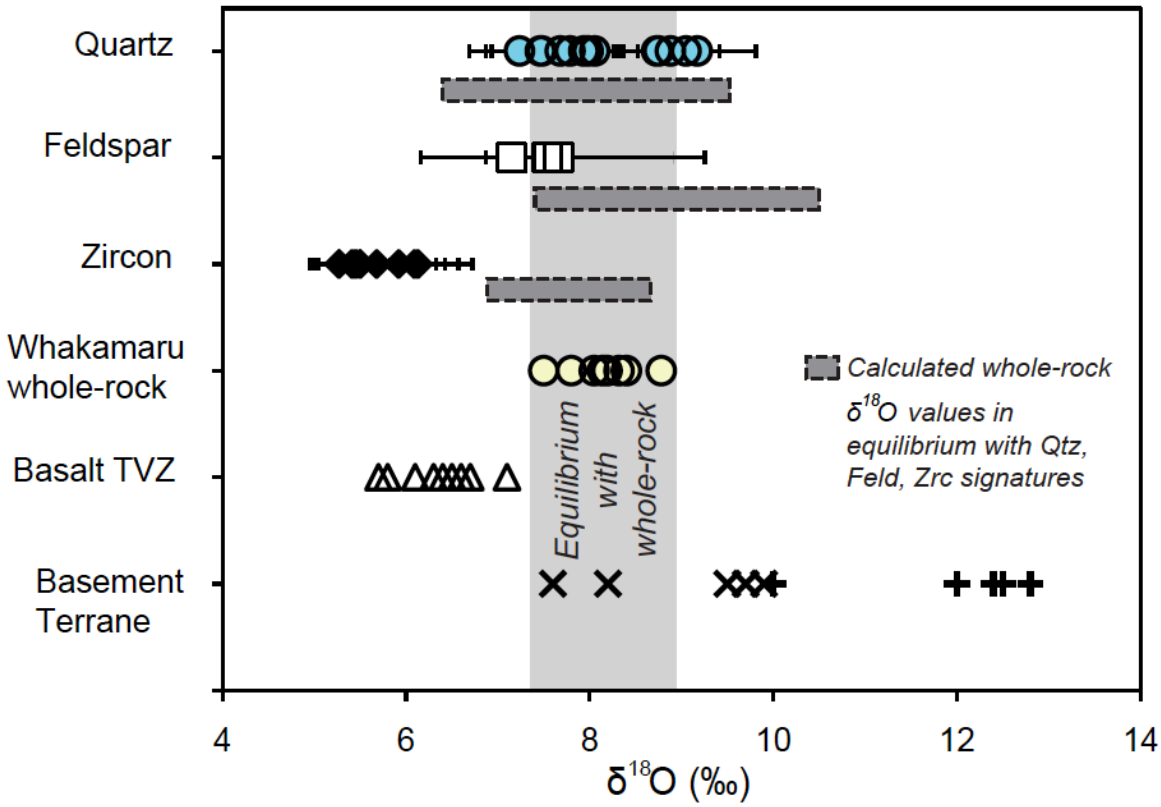

Fig. 5.19: Isotopic $\delta^{18}O$ signatures for Whakamaru quartz, zircon and feldspar compared with published values for whole-rock, TVZ basalt and basement terranes. Data are presented as averages, with 1sd error bars (see Table 5.7). Predicted values for Whakamaru rhyolite melt are marked by grey dashed lines, calculated on the basis of mineral-melt oxygen isotope fractionation. Zircon-melt equilibrium fractionation calculated using equation [5.5] (from Valley et al., 2003; see Section 5.3.4.1). Quartz-melt $\delta^{18}O$ fractionation calculated using a fractionation factor of ~ 0.6 ‰ from Bindeman and Valley (2002). Feldspar-melt fractionation factor from Palin et al. (1996). Calculations at magmatic temperatures (~ 770°C). Mineral-specific data from this study; Whakamaru whole-rock data from Blattner et al. (1996); TVZ basalt and basement terranes from Blattner and Reid (1982) and McCulloch et al. (1994). Grey vertical band represents measured $\delta^{18}O$ values for whole-rock Whakamaru.

5.5 Conclusions

Geochemical evolution recorded by zircon trace elements, coupled with U-Pb geochronology, provides evidence for repeated replenishment, fractionation, and recycling of material in the assembly of the large-volume, silicic Whakamaru magma reservoir. Zircon ages record the role of inheritance of basement rocks into the magmatic system (with older zircons present as antecrysts and xenocrysts), and provide evidence for protracted crystallisation in the magma reservoir prior to eruption. The exact residence time is, however, difficult to constrain due to the presence of antecrsysts and xenocrysts in the magma system, although data here do not support the interpretation of a > 250 ky residence time proposed by Brown and Fletcher (1999). The dominant unimodal peak in zircon age spectra at ~ 0.4 Ma is suggestive of relatively short residence times of < 50 ky. The new zircon U-Pb ages also indicate an age for the Whakamaru eruption, of 0.32 ± 0.01 Ma (2σ, 95% conf., from the youngest zircon phenocryst ages), which is consistent with earlier age estimates, but 25 ky younger than the latest published estimate (Leonard et al., 2010). The data presented here are consistent with some assimilation of basement metasediments and the incorporation of xenocrystic and antecrystic zircon prior to eruption. The apparent ~ 50 – 100 ky assembly period may therefore be an artefact of different magma batches, rather than representing the residence time of the Whakamaru magma system.

Zircon Hf is inversely correlated with Ti for all samples, and concentrations indicate large fluctuations in melt composition and apparent temperature, T_{TiZ} (with increases of > 100°C recorded) for individual zircons. Such variations are consistent with U-Pb geochronology indicating a protracted (> 100 ky) history of repeated replenishment, fractionation, and extraction of melt from an isotopically homogenous source zone, with limited assimilation

of crustal material. Type *D* magma incorporates slightly older zircons, with less eruption-age zircon crystallisation, lower T_{TiZ} rims and larger Eu/Eu* anomalies suggestive of extensive plagioclase fractionation. These differences provide further evidence that the Whakamaru eruption episode involved at least two isolated bodies of magma which evolved independently, but from the same source components at a later stage prior to eruption. No significant differences between Whakamaru and Rangitaiki zircon U-Pb age, trace elements and oxygen isotope signatures were observed, and hence these two ignimbrites were presumably fed by the same large-volume silicic chamber.

The chemical and thermal scatter recorded by zircons over a period of > 100 ky provides evidence for repeated recharge of the system during incremental magma chamber assembly. The fluctuating trace-element patterns with age are consistent with multiple periods of zircon growth in pre-eruptive pluton conditions. Variable zircon growth histories recorded by individual grains may reflect different melt environments (zircons as free crystals or inclusions) and crystallisation in different parts of a large-volume chamber, which was experiencing periodic thermochemical changes in response to recharge. Results for the Whakamaru magma system are consistent with those for other plutonic and volcanic systems which accumulate and evolve over protracted periods of time, with complex histories that require frequent replenishment in order to attain the thermal and compositional fluctuations and recycling of crystals into the system. Whakamaru zircon ages and trace-element characterisitics therefore provide evidence for incremental emplacement of the large silicic magma reservoir, with complex process of recharge and assembly occurring over 100 ky timescales.

Oxygen isotope data for zircon, quartz and feldspar from the selected Whakamaru and Rangitaiki pumices show that the magma system was fed by relatively homogeneous source components. Results also show that these co-erupted mineral phases crystallised together in isotopic equilibrium. Variability in $\delta^{18}O$ zonation within single crystals is suggestive of complex pre-eruptive mixing and partial homogenization processes in the large silicic reservoir.

The data indicate here that Whakamaru zircons do not record a systematic history of linear evolution of a closed magmatic system, but may instead represent multiple processes associated with recharge, mixing and P/T/compositional changes and magma chamber assembly over a ~ 100 ky timescale.

Chapter 6

Ultra-distal tephra deposits from supereruptions: examples from Toba and Whakamaru[4]

6.1 Introduction

Rhyolitic tephra deposits associated with large-magnitude volcanic eruptions provide crucial age control for geological sequences and are therefore a valuable tool for stratigraphic, geomorphological and archaeological studies. This chapter presents an investigation of the characteristics of distal tephra deposits associated with two supereruptions: the ~ 74 ka Youngest Toba Tuff (YTT) eruption, Sumatra; and the ~ 340 ka Whakamaru eruption. Quaternary tephra deposits from both eruptions are widely used as tools for regional correlation of sedimentary archives. Distal ash deposits from such eruptions are particularly valuable as they can be deposited up to thousands of km from the vent, forming discrete layers in sedimentary sequences that are useful for chronological purposes providing they can be traced to a specific eruption of a particular volcanic source (e.g., Self and Sparks, 1981). Information obtained from distal deposits can also be used to constrain eruption parameters (e.g., Pyle, 1999; Pyle et al., 2006). It is difficult to estimate tephra volumes associated with such large-magnitude eruptions and usually rough approximations are adopted, which inevitably involve extrapolation based on observations.

[4] Much of the material in this chapter is presented in an accepted paper: Matthews, N.E., Smith, V.C., Costa, A., Durant, A.J., Pyle, D.M., Pearce, N.J.G., 2011b. Ultra-distal tephra deposits from super-eruptions: examples from Toba and New Zealand. Quaternary International, Special Issue; The Toba Super-eruption: Impact on Ecosystems and Hominins. In press, doi:10.1016/j.quaint.2011.07.010.

The application of computational models of ash dispersal enables alternative estimates for erupted volumes to be produced, as discussed in this chapter.

Geochemical characteristics of distal and ultra-distal deposits of the two supereruptions are also reported and described here. Glass shards, which typically comprise > 95% of these deposits, usually have characteristic compositions which enable the matching of deposit and eruption. Glass chemistry data from proximal and distal exposures of both tephra units are used to determine whether the correlations of distal deposits to the particular eruptions are robust. Physical parameters of the deposits at ultra-distal terrestrial sites, such as grain size and tephra thicknesses, are also documented to help in the understanding of reworking of the ash at these sites. These data are coupled with tephra thickness data from sedimentary archives up to thousands of kilometres from source (e.g., references listed in Tables 6.2 and 6.3), and input into the HAZMAP (Macedonio et al., 2005) ash dispersal model to help constrain tephra dispersal and estimate eruption parameters, and to provide insight into eruption plume dynamics and deposition.

The potential for other large caldera-forming eruptions to occur with global consequences (e.g., from Uturuncu, Bolivia; Sparks et al*.,* 2008) makes it imperative that possible climatic and environmental effects are investigated. The new constraints developed here on ash dispersal from two supereruptions provide detail on areas affected and help evaluate the impact of large volumes of fine ash on the environment and human health at great distances from the source volcano.

6.1.1 Youngest Toba Tuff

The ~ 74 ka YTT supereruption is the youngest of four large eruptions in northern Sumatra, with the earlier three being ~ 1.2 Ma Haranggoal Dacite Tuff, ~ 840 ka Oldest Toba Tuff (OTT), and ~ 501 ka Middle Toba Tuff (MTT) (Chesner et al., 1991). It formed the 100 × 30 km Toba caldera (Fig. 6.1; Rose and Chesner, 1987; Chesner, 1998), erupting ~ 2800 km^3 (DRE) of rhyolitic magma - making it the largest eruption to have occurred globally during the last 2 Ma (Rose and Chesner, 1987; Rose and Chesner, 1990; Chesner et al., 1991).

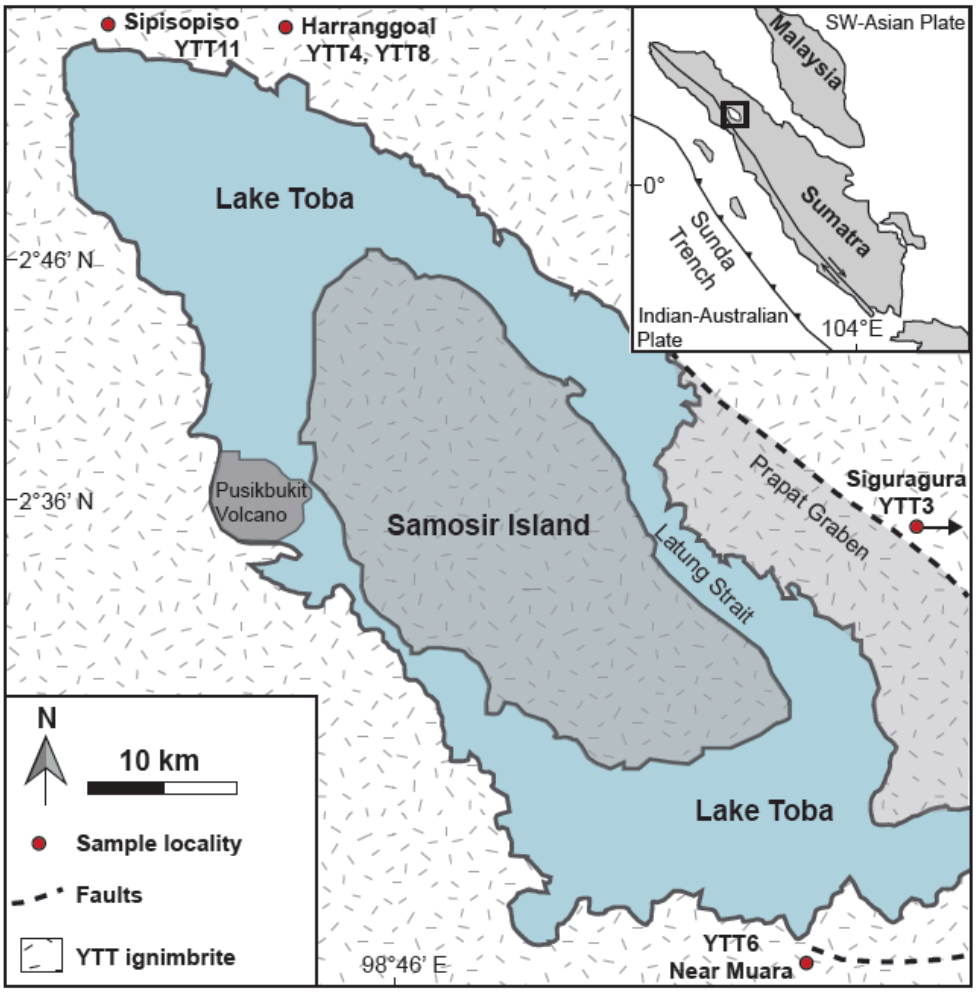

Fig. 6.1: Toba caldera complex (adapted from Chesner, 1998). Red circles mark sampling locations (see Table 6.1 for details). Samosir Island forms part of the post-YTT resurgent dome and consists of densely welded YTT caldera fill (Chesner, 1998). Pusikbukit volcano is a prominent post-YTT edifice on the western edge of the lake (Smith et al., 2011).

The minimum mass of the tephra deposit has previously been estimated as 2×10^{15} kg, equivalent to 800 km^3 DRE, representing ~ 30% of the total mass of erupted material (Rose and Chesner, 1987). The eruption resulted in deposition of thick ignimbrite sequences proximally (covering up to 30,000 km^2 of Sumatra; Rose and Chesner, 1987; Bühring et al., 2000) and widespread distribution of ash westward over the Indian subcontinent and the Arabian Sea (Schulz et al., 1998; Pattan et al., 1999, 2001), and eastward over the South China Sea (~ 1500 – 1800 km NE of Toba; Bühring et al., 2000; Song et al., 2000; Liang et al., 2001; Fig. 6.2).

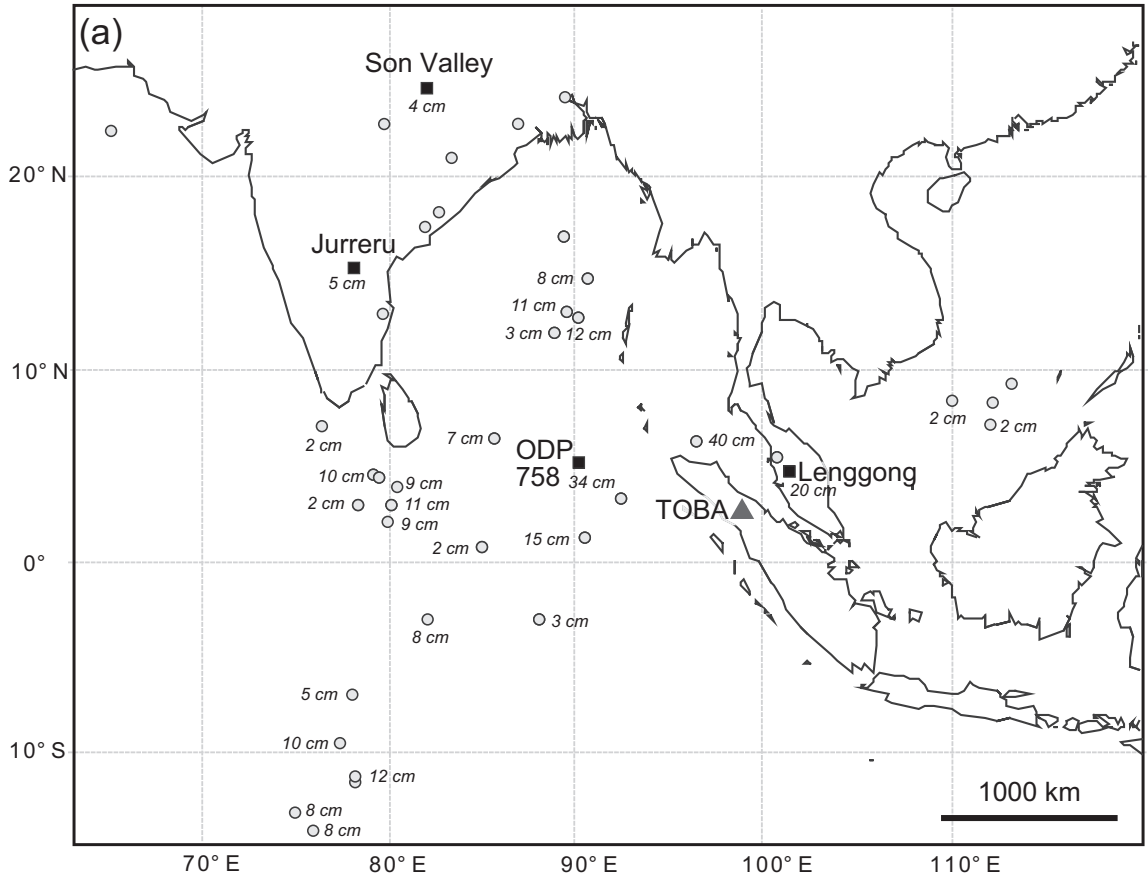

Fig. 6.2: Distribution of recovered YTT deposits and location of Toba caldera. Open circles indicate marine cores with YTT identified; black squares show terrestrial YTT localities discussed in this chapter and ODP core 758; grey triangle marks Toba caldera. Map adapted from Pattan et al. (1999) and Liu, Z. et al. (2006). Location of marine cores with annotated YTT thickness data are provided in Table 6.2 (Ninkovich et al., 1978a,b; Rose and Chesner, 1987; Acharyya and Basu, 1993; Shane et al., 1995; Schulz et al., 1998; Pattan et al., 1999, 2001; Bühring et al., 2000; Gasparotto et al., 2000; and Song et al., 2000).

Distal YTT was first documented in Malaysia by Scrivenor (1930) and subsequently reported in the Bay of Bengal (Ninkovich et al., 1978a, b; Ninkovitch, 1979; Gasparotto et al., 2000) and the Indian subcontinent (Acharyya and Basu, 1993; Shane et al., 1995; Westgate et al., 1998; Pattan et al., 1999). YTT deposits in the Middle Son Valley, Madhya Pradesh, India, were first identified by Williams and Royce (1982) and Basu et al. (1987). Further south at Jwalaparum, Kurnool District of Andhra Pradesh, the tephra was first reported by Rao and Rao (1992) and geochemically identified as YTT by Petraglia et al. (2007). Localities of deposits referred to here are listed in Table 6.1 and mapped in Figs 6.1 and 6.2.

Analyses of glass compositions of tephra throughout the Indian peninsula provide evidence for direct correlation with Toba (Shane et al., 1995, 1996; Westgate et al., 1998). The magmas that drove the OTT, MTT and YTT eruptions were, however, compositionally similar (Smith et al., 2011) and the glass chemistry normally used to distinguish between eruption units cannot solely be relied on to identify chronostratigraphic markers in their distal deposits. Correlations using biotite compositions confirm, however, that the ash found in Malaysia and in archaeological sites in India was from the ~ 74 ka YTT eruption (Smith et al., 2011).

6.1.2 Rangitawa Tephra

The Rangitawa Tephra unit has previously been linked to the ~ 340 ka Whakamaru supereruption on the basis of glass shard major-element chemistry, ferromagnesian mineralogy, and similarity of paleomagnetic dates and zircon fission-track ages (Section 1.5.2; Kohn et al., 1992; Alloway et al., 1993; Pillans et al., 1996). Glass and mineral geochemistry is discussed in detail in Chapter 2. The volume of ashfall dispersed across

the Pacific Ocean is estimated to be ~ 700 km^3 (Froggatt et al., 1986), which was deposited primarily in the SSW–ESE sector from the source caldera. Deposits are also recorded to the northwest of the vent area in the Waikato region, and > 500 km beyond New Zealand at ODP 591 in the Tasman Sea (Fig. 6.3; Nelson et al., 1985; Lowe et al., 2001).

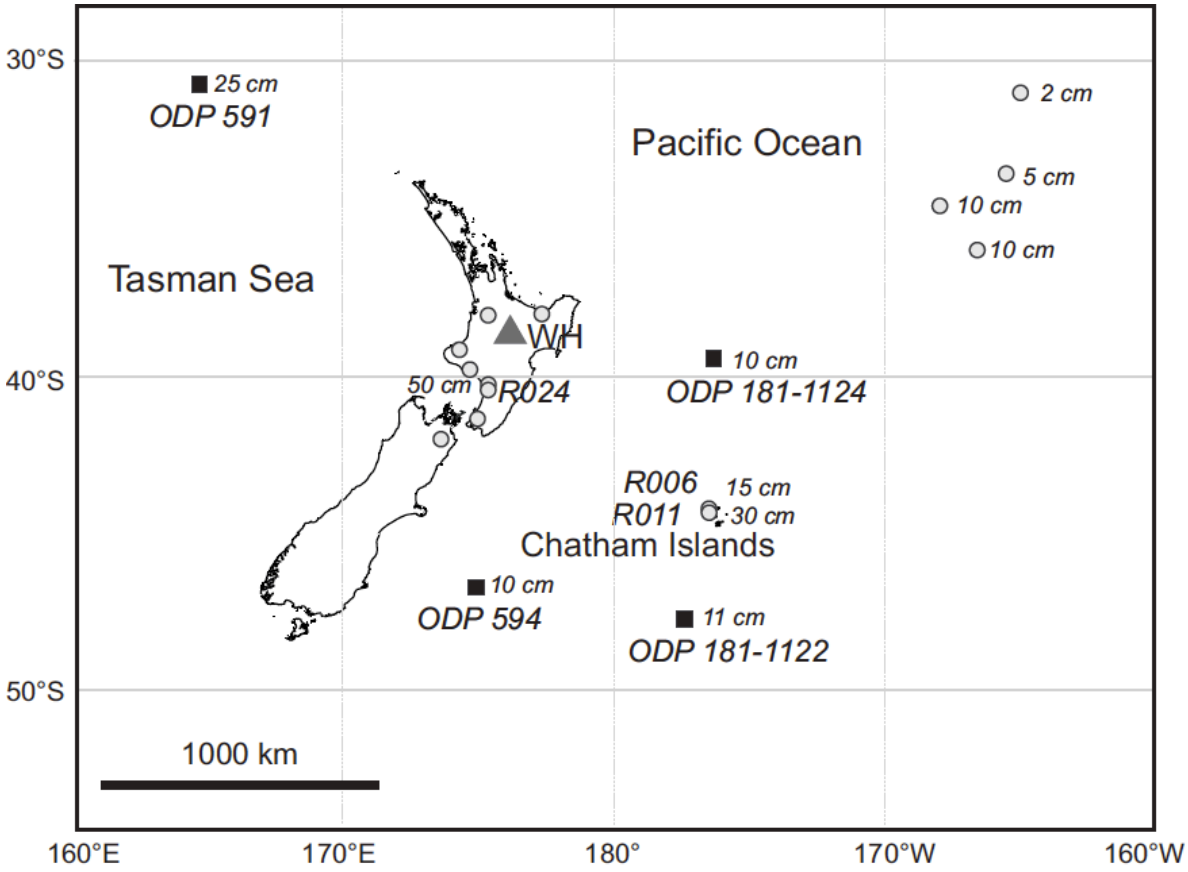

Fig. 6.3: Locations and thicknesses of documented Rangitawa Tephra in terrestrial exposures and ocean cores. Whakamaru caldera marked by grey triangle (WH). Samples marked as follows: R024, Rangitawa Stream; R011, Red Bluffs and R006, Mairangi North (Chatham Island); black squares, ODP cores; grey circles, other ocean cores (RC9 – RC12). Refer to Table 6.3 for location details and references.

The Rangitawa Tephra represents an important stratigraphic marker in mid-Pleistocene marine and terrestrial sequences in New Zealand and has been fission-track dated at ~ 340 ± 40 ka (near the end of OIS 10; Kohn et al., 1992; Pillans et al., 1996; Lowe et al., 2001; Holt et al., 2010; see Table 1.4), corresponding to the age of the Whakamaru eruption. The

crystal-rich nature of the ashfall deposit is thought to preclude it from being a simple co-ignimbrite ashfall (Kohn et al., 1992), although previous work has been unable to establish how this fallout is related to the ignimbrites. One major aim of this work is to use grain-size analysis, glass chemistry (Section 2.3.3) and ash dispersal modelling to establish which phase emplaced the Rangitawa Tephra.

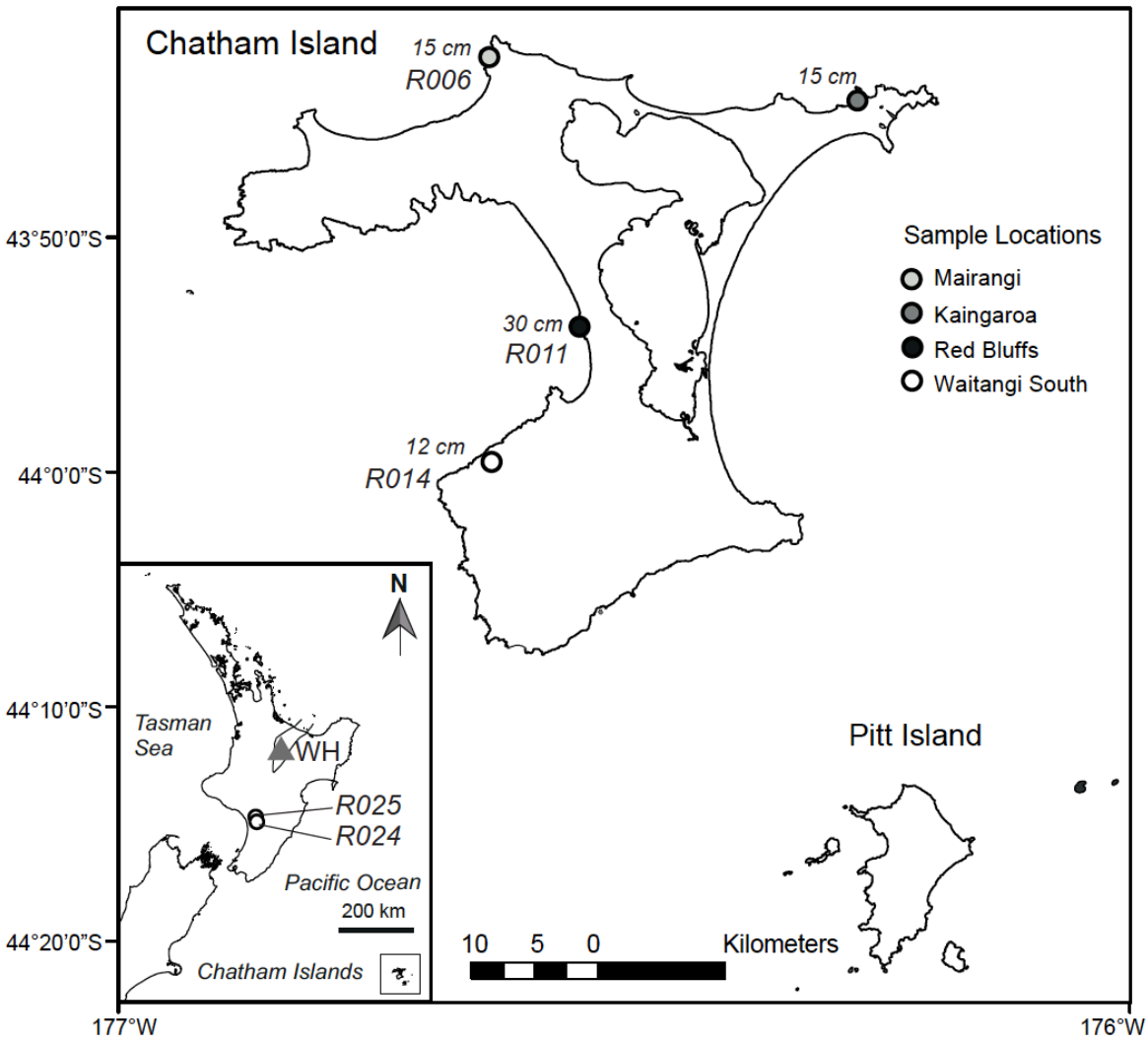

Fig. 6.4: Map of Chatham Island, New Zealand, showing distal Rangitawa Tephra sampling localities and measured thickness (legend shows sample codes); Inset shows Chatham Islands location in relation to mainland New Zealand, Rangitawa Stream (locality R024) and Mount Curl (R025) localities marked by open circles, and Whakamaru caldera marked by grey triangle (WH). Base map from Forsyth et al. (2008).

Localities of samples referred to here are listed in Table 6.1 and mapped in Figs 6.3 and 6.4. The type locality is the Rangitawa Stream exposure (Site R024; Fig. 6.3) near Mt Curl in the Wanganui region, North Island (Te Punga, 1952). The most distal on-land exposures of the Rangitawa Tephra are preserved on the Chatham Islands (Holt et al., 2010; Fig. 6.4) where it is present as a distinctive macroscopic tephra horizon within terrestrial deposits, commonly preserved within peat and outcrops at coastal exposures. Distal ash deposits of the large Oruanui eruption from Taupo caldera (Wilson, 2001; Wilson et al., 2006), the Kawakawa Tephra, are also preserved on the Chatham Islands (Holt et al., 2010) and were collected and analysed for comparative purposes.

6.2 Materials and methods

6.2.1 Sampling

Representative pumice samples from proximal deposits of the Toba and Whakamaru eruptions were selected for analysis, in addition to samples of the distal tephra deposits pictured in Figs 6.5 and 6.6 respectively. The sample codes and localities are provided in Table 6.1.

Proximal YTT samples were collected from Sumatra and provided for this study by N. Pearce (Fig. 6.1; Table 6.1; see also Smith et al., 2011). Distal YTT samples were collected from archaeological sites situated in two localities: the Jurreru river valley near Jwalaparum in the Kurnool area in southern India, and Son Valley, Ghogara, in NE India (Fig. 6.2), respectively ~ 2600 km and 3000 km from the Toba caldera. Sampling focused on the basal primary ash, but samples were also collected at a high resolution through the complete reworked tephra sequence (Fig. 6.5).

The five ignimbrite members associated with the Whakamaru supereruption are exposed in proximal locations (where proximal here refers to deposits at distances of < ~ 50 km from source as explained in Section 1.5.2). No ashfall deposits are preserved in proximal locations, and it is likely that the energetic emplacement of the ignimbrites eroded these units. Distal Rangitawa Tephra samples (Fig. 6.6) were collected from Rangitawa Stream (site R024 in Table 6.1 and Fig. 6.3), Mt Curl (R025 Table 6.1, near R024 Fig. 6.3) and Chatham Island (Red Bluffs, R011 Table 6.1; Fig. 6.4), New Zealand, ~ 200 km SSW and ~ 900 km SE of the source Whakamaru caldera respectively. Samples were taken at 1 – 2 cm increments vertically through the ash deposits. Geochemical and physical characteristics of Rangitawa Tephra are also compared to those of distal exposures of the Kawakawa Tephra (site R006, Table 6.1, Fig. 6.4; Holt et al., 2010).

Thickness data for both tephra deposits are supplemented by previous measurements of tephra identified in ODP and DSDP cores (Tables 6.2, 6.3).

6.2.2 Glass chemistry

The glass phase was separated from proximal pumices and distal tephra using standard procedures (Section 2.2.4). Glass shards from tephra and pumices were analysed using EPMA and LA-ICP-MS techniques, as outlined in Sections 2.2.4 and 2.2.5. Totals of glass analyses were > 95% and, due to variable secondary hydration, all analyses presented here are normalised to 100%.

6.2.3 Particle size analysis

Laser-diffraction particle-size analysis (LDPSA) was carried out on tephra samples from both eruptions in order to reconstruct the deposit particle-size distribution (PSD). Laser-

scatter analysis was undertaken to determine grain sizes using the Malvern Mastersizer 2000 at the Geography Department, University of Oxford. This technique measures particles in the 0.02 – 4000 μm size range, assuming spherical particle shape, using low-angle laser-light scattering (Blott and Pye, 2001; Blott et al., 2004; Bonadonna and Houghton, 2005). Tephra samples were decalcified using HCl, centrifuged, treated with a deflocculant (calgon), then wet sieved and disaggregated in an ultrasonic bath for 90 s prior to grain-size analysis. A refractive index of 1.6 was assumed for both tephra deposits based on rhyolitic glass compositions (Section 6.3.3; Ewart, 1963; Horwell, 2007). Grain size for basal ash samples was measured at regular stratigraphic intervals of 1 – 2 cm from the base to the top of the eruption deposits at each locality.

6.2.4 Whole-rock chemistry by scanning- X-ray Fluorescence

The bulk elemental composition of the basal ash samples was analysed at high stratigraphic resolution using the Itrax X-ray Fluorescence Core Scanner (Cox Analytical Instruments) at Aberystwyth University. Intact blocks of basal YTT and Chatham Island Rangitawa Tephra were cut to size to fit the core-scanner. The complete stratigraphic profile from the Rangitawa Stream section was reconstructed from incremental bulk ash samples at a 2 cm resolution. The scanner was operated at 1 mm resolution, with the exception of the Rangitawa Stream core that was scanned at 2 cm resolution. Scan parameters were as follows: 5 s scan times using a Mo X-ray excitation source set to 30 kV and 15 mA, and X-ray beam dimensions of 20 × 0.1 mm. The scanner is particularly useful in investigating variations in elements with atomic numbers greater than 19 (primarily Ba, Sr, Rb, K and Ca).

Table 6.1: ***Details of proximal and distal samples for YTT and Rangitawa Tephra***

Sample	Eruption unit	Location	Lat/long	Sample type	Thickness (cm)
YTT3	YTT ignimbrite	Sigguragura, Sumatra	02°31'19.999" N, 099°16'14.000" E	Pumice	-
YTT4	YTT ignimbrite	Harranggoal, Sumatra	02°53'11.000" N, 098°39'41.000" E	Pumice	-
YTT6	YTT ignimbrite	Near Muara, Sumatra	02°18'33.999" N, 099°00'51.999" E	Pumice	-
YTT7	YTT ignimbrite	Sipisopiso, Sumatra	02°55'00.600" N, 98°31'20.900" E	Pumice	-
YTT8	YTT ignimbrite	Harranggoal, Sumatra	02°53'53.000" N, 098°39'29.999" E	Pumice	-
YTT11	YTT ignimbrite	Sipisopiso, Sumatra	02°55'00.600" N, 98°31'20.900" E	Pumice	-
JV2	YTT tephra	Jwalapuram, Kurnool, India	15°19'29.856" N, 078°07'49.872" E	Tephra	4
JV7	YTT tephra	Jwalapuram, Kurnool, India	15°19'29.856" N, 078°7'49.872" E	Tephra	4
JV13	YTT tephra	Jwalapuram, Kurnool, India	15°19'29.856" N, 078°7'49.872" E	Tephra	4
JV22	YTT tephra	Jwalapuram, Kurnool, India	15°19'29.856" N, 078°7'49.872" E	Tephra	4
JWP138	YTT tephra	Jwalapuram, Kurnool, India	15°19'21.240" N, 078°07'59.160" E	Tephra	4
GG1	YTT tephra	Ghogara, Middle Son, India	24°30'7.776" N, 082°1'2.748" E	Tephra	4–5
G05209	YTT tephra	Ghogara, Middle Son, India	24°30'7.776" N, 082°1'2.748" E	Tephra	5
P1905, P1910, P1912, P1915	Rangitaiki	Hinemaiaia Dam, TVZ	38°52’09.522" S, 176°03'13.140" E	Pumice *A*	-
P1920, P1921	Whakamaru	Northern Lake Taupo, TVZ	38°12'19.950" S, 175°55'35.450" E	Pumice *A*	-
P1885, P1886	Whakamaru	Waipapa Rd, TVZ	38°19'30.612" S, 175°41'03.552" E	Pumice *A*	-
P1917f	Whakamaru	Northern Lake Taupo, TVZ	38°37'18.840" S, 175°49'32.268" E	Pumice *B*	-
T5/4	Whakamaru	Tokoroa Forestry, TVZ	38°13'26.328" S, 175°56'44.052" E	Pumice *C*	-
SB1119P 1827	Whakamaru	Waipapa Rd, TVZ	38°19'30.600" S, 175°41'03.566" E	Pumice *D*	-
R025	Rangitawa Tephra	Mt Curl, New Zealand	39°58'14.284" S, 175°27'03.039" E	Tephra	70
R024	Rangitawa Tephra	Rangitawa Stream	40°07'53.414" S, 175°27'34.960" E	Tephra	55
R011	Rangitawa Tephra	Red Bluffs, Chatham Island	43°54'05.220" S, 176°32'33.060" W	Tephra	30
R006	Kawakawa Tephra	Mairangi Nth, Chatham Is.	43°42'19.740" S, 176°38'14.100" W	Tephra	8

Notes: YTT thicknesses recorded in India refer to the primary ash thickness, not the over-thickened, reworked deposits; Whakamaru pumice sample SB1119 collected by Brown et al. (1998a); Whakamaru pumices listed as types A, B, C and D, as referred to in text. Localities quoted using WGS84 coordinates.

6.2.5 Field constraints on eruption source parameters

Tephra dispersal from both eruptions was modelled using tephra-thickness data from ODP cores and terrestrial exposures (Tables 6.2, 6.3). Data for YTT proximal thicknesses in Malaysia and distal thicknesses from ocean cores were collated (using data from Ninkovich et al., 1978a, b; Acharyya and Basu, 1993; Song et al., 2000; Liang et al., 2001; Lee et al., 2004) and supplemented by field measurements of basal primary ash in India (Table 6.1).

Rangitawa Tephra thicknesses were measured in the field at the North Island and Chatham Island exposures (Table 6.1) and supplemented by thicknesses recorded in ocean cores and additional terrestrial exposures (from Seward, 1974; Pillans and Kohn, 1981; Froggatt, 1983; Nelson et al., 1985; Froggatt et al., 1986; Nelson, 1988; Kohn et al., 1992; Manning, 1996; Pillans et al., 1996; Lowe et al., 2001; Alloway et al., 2005; Holt et al., 2010; Table 6.3).

Bulk density of samples is assumed to be 1100 kg m^{-3} for YTT and 1200 kg m^{-3} for Rangitawa (Ninkovich et al., 1978a; Watkins et al., 1978), although it is possible that deposit density varies between sites (Durant et al., 2009). Such an uncertainty in density variation introduces proportional uncertainty in the final estimation of the total mass. The limited grain-size data available were used as a semi-quantitative indicator to characterise the total grain-size distribution (TGSD; Bonadonna and Houghton, 2005; Rose and Durant, 2009). Much material from these eruptions was deposited over ocean areas, and their full extent has yet to be identified. This limits the number of deposit samples available. Additionally, many of the terrestrial exposures have been eroded and reworked (e.g., Alloway et al., 2005; Jones, 2010).

6.2.6 Ash dispersal modelling

Ash dispersal from a point source (source volcano) was simulated using the HAZMAP model, which solves equations for advection, diffusion and sedimentation of particles in two dimensions (Macedonio et al., 2005). The model assumes atmospheric dispersion of particles through effective turbulent diffusion and wind transport, with fallout being controlled by gravitational settling velocity and air drag (Macedonio et al., 2005). Isopach maps were generated by modelling the ash deposition in terms of mass loading (kg m^{-2}) and converting to thicknesses using the bulk densities in Section 6.2.5.

Input parameters required for the dispersal model include: total erupted mass, eruption column height, mass distribution along the column, TGSD, wind profile, and horizontal diffusion coefficient. Since there is no direct way to estimate all these parameters pertaining to the time of the eruptions, they were reconstructed by best-fitting field observations of tephra thickness through minimising the difference between observed and modelled thickness (Costa et al., 2009; Bonasia et al., 2010) using equation [6.1]:

$$\sigma^2 = \sum_{i=1}^{N} w_i \left[T_i(obs) - T_i(mod) \right]^2 \qquad [6.1]$$

where w_i is a weighting factor, N is the number of data points, and $T_i(obs)$ and $T_i(mod)$ represent observed and calculated thickness values respectively. Weighting factors w_i depend upon the distribution of random errors in the dependent variable. When $w_i = 1$ is used, all values have same weight (i.e., absolute squared error), and when $w_i = 1/T_i^2(obs)$ the relative squared errors are minimised (i.e., proportional weight). The use of $w_i = 1/T_i(obs)$ is a compromise between minimising the absolute and relative squared errors.

In the modelling, the total erupted mass was calculated analytically to minimise the difference between the modelled and observed loads (equation [6.1]). Total column heights in the range 20 – 50 km were trialled in one-kilometre steps. The mass distribution within the eruption column was assessed using a modified empirical parameterisation proposed by Suzuki (1983) with a Suzuki parameter selected to reproduce observations (e.g., Costa et al., 2009; Macedonio et al., 2005, 2008). Since dispersal is over large distances (> 1000 km) the model assumes deposition was from a filiform eruption column extending from the volcanic source area. There were five granulometric size classes assumed in the eruption source parameters, with four representing particles falling as single particles and, following Cornell et al. (1983), the last representing aggregates formed of fine particles (or single particles having an equivalent settling velocity). Furthermore, as there was insufficient field data to allow full reconstruction of the TGSD, assumptions were based on the analysis of Rose and Durant (2009), and assumed ~ 50 – 60% of the deposit was finer than 63 μm (which represents an extreme end-member of co-ignimbrite-dominated activity).

The wind profile at the time of the eruption is unknown and can only be vaguely reconstructed from field data, and thus palaeo-winds cannot be accounted for in this modelling approach. The inversion was based on the assumption that the wind field was horizontally uniform, which holds well for a domain of up to a few hundred km from vent but is problematic for the dispersal distances involved here. For such large domains, modelling is based on an average wind profile over the entire domain and not the actual wind field. A unidirectional profile with wind speed increasing from zero at sea level to a maximum at the tropopause was assumed, with a subsequent decrease to 75% of maximum intensity at higher altitudes (Cornell et al., 1983). In this way, the effective wind direction

and wind intensity could be found that best fitted observed deposits (roughly representing the actual mean wind field).

The horizontal diffusion coefficient, K, was approximated by fitting to the observed thickness data, and represents an empirical parameter accounting for the physical effects that dispersed the volcanic particles (atmospheric turbulence, eruption column turbulence, wind shear; Macedonio et al., 2005; Pfeiffer et al., 2005). The order of magnitude of the apparent diffusion coefficient due to atmospheric turbulence varies with dispersal distance (L, m) with $K \propto L^{6/5}$ (Suzuki, 1983). For sub-Plinian and Plinian eruptions, tephra dispersal domains of 50 – 100 km indicate diffusion coefficients of ~ 5000 m^2 s^{-1} (Macedonio et al., 2008; Costa et al., 2009); and with domains of ~ 3000 km, as in this study, scaling gives $K > 10^5$ m^2 s^{-1}.

Table 6.2: ***YTT thicknesses used in tephra dispersal modelling, compiled from terrestrial exposures and ocean cores***

Sample	Location	Latitude	Longitude	Tephra thickness (cm)	Distance from vent (km)	Ref
-	**Toba caldera (source)**	**2°36'10.81"N**	**98°47'2.75"E**	**-**	**0**	
JV2-JV22	Jwalapuram, Kurnool, India	15°19' 29.856"N	78°7' 49.872"E	5	2669	
GC1	Ghogara, Son Valley, India	24°30' 7.776"N	82°1' 2.748"E	4	3028	
GOC1	Ghogara, Son Valley, India	24°30' 7.776"N	82°1' 2.748"E	4	3028	
Malaysia	Lenggong, Malaysia	5°7'9.07"N	100°59'9.12"E	20	371	1
NPm	Tampan, Malaysia	2°27'56.72"N	102°12'59.87"E	150	382	2
RC12-343	Bay of Bengal	15°9'60.00"N	90°33'60.00"E	8	1662	3
RC12-341	Bay of Bengal	13°3'0.00"N	89°34'60.00"E	11	1541	3
RC12-340	Bay of Bengal	12°42'2.35"N	90°1'0.83"E	12	1480	3
V29-15	Bay of Bengal	11°57'2.54"N	88°44'14.99"E	3	1518	3
V29-14	Bay of Bengal, DSDP XXII 218	8°0'25.20"N	86°16'58.08"E	7	1508	3
V19-176	Laccadive Sea, W of Sri Lanka	7°7'54.17"N	76°33'47.38"E	2	2512	3
V29-24	Bay of Bengal	4°58'28.10"N	79°26'47.06"E	10	2161	3
V29-31	Bay of Bengal	3°48'0.00"N	78°39'0.00"E	3	2239	3
V29-23	Bay of Bengal	4°37'11.26"N	80°1'48.16"E	9	2093	3
V19-175	Bay of Bengal	4°11'30.36"N	80°37'1.24"E	11	2024	3
RC17-128	Bay of Bengal	3°43'51.54"N	80°7'32.44"E	9	2075	3
RC14-37	Bay of Bengal, DSDP XX11 216	1°28'31.17"N	90°13'9.11"E	15	960	3
RC17-145	Andaman Sea, North of Sumatra	6°24'0.00"N	96°16'1.20"E	40	506	2,3
CR-02	Central Indian Ocean Basin	3°0'0.00"S	82°15'0.00"E	8	1940	4,5,6
CR-05	Central Indian Ocean Basin	3°0'0.00"S	88°0'0.00"E	3	1351	7
NR-01	Central Indian Ocean Basin	9°56'0.00"S	77°42'0.00"E	10	2719	7
NR-21	Central Indian Ocean Basin	11°30'0.00"S	78°31'60.00"E	10	2734	7
NR-35	Central Indian Ocean Basin	11°56'0.00"S	78°29'0.00"E	12	2765	7
NR-54	Central Indian Ocean Basin	7°0'0.00"S	78°15'0.00"E	5	2517	7
SK-226	Central Indian Ocean Basin	13°8'0.00"S	75°0'0.00"E	8	3155	7
SS-657	Central Indian Ocean Basin	14°0'0.00"S	75°0'0.00"E	8	3117	7
MD972151	ODP 1143, South China Sea	8°43'43.80"N	109°52'10.20"E	2	1403	2
-	Bay of Bengal	3°2'4.98"N	90°15'58.25"E	15	900	2
-	Bay of Bengal	2°24'1.14"N	85°19'41.50"E	2	1495	2
-	ODP-758, layer A	5°23'2.40"N	90°21'40.32"E	34	984	2

Notes: Latitude and longitude given in WGS84. YTT thickness data compiled from the following references - 1: Smith et al., 2011; 2: Acharayya and Basu, 1993; 3: Ninkovich et al., 1978a,b; 4: Song et al., 2000; 5: Westgate et al., 1998; 6: Liang et al., 2001; 7: Pattan et al., 2002.

Table 6.3: ***Rangitawa Tephra thicknesses used in tephra dispersal modelling, compiled from terrestrial exposures and ocean cores***

Sample	Location	Latitude	Longitude	Tephra thickness (cm)	Distance from vent (km)	Ref
-	**Whakamaru caldera (source)**	**38°34'7.24"S**	**175°56'30.86"E**	**-**	**0**	
-	Matarakau, Chatham Island	43°44'15.11"S	176°20'51.67"W	15	864	1
R011	Red Bluff, Chatham Island	43°54'5.27"S	176°32'31.04"W	40	864	1
R006	Mairangi, Chatham Island	43°42'19.41"S	176°38'14.15"W	15	864	1
R014	Waitaingi Sth, Chatham Island	43°59'36.06"S	176°38'9.00"W	12	864	1
BP-144	Omahina Road, Wanganui basin	39°41'43.572"S	174°41'13.639"E	10	166	2,3,4
R025	Mt Curl, Wanganui basin	39°58'14.78"S	175°27'3.12"E	70	162	3,4
R024	Rangitawa Stream, Wanganui	40° 7'53.45"S	175°27'34.86"E	50	179	2,5,6
-	Kakariki, Wanganui basin	40° 7'6.96"S	175°27'4.32"E	50	177	7
-	Spur Road West, Wanganui	40°12'37.29"S	175°39'36.63"E	60	184	7
-	Stormy Point, Wanganui basin	40° 0'12.61"S	175°38'33.72"E	40	162	7
-	Pahiatua Refuse dump	40°26'23.42"S	175°49'25.41"E	40	208	7
-	Pahiatua Ridge Road South	40°27'37.77"S	175°47'21.19"E	30	211	7
-	Kimbolton, Wanganui basin	40° 2'43.31"S	175°46'49.22"E	60	165	7
-	Ahiaruhe Rd, Wanganui basin	41° 5'25.39"S	175°35'21.73"E	40	282	7
-	Linton Quarry, Wanganui basin	40°26'6.65"S	175°36'2.40"E	30	210	7
-	Ohinewai Ash, Hamilton	37°29'17.55"S	175°09'57.80"E	57	138	8
-	Aratora Tephra Formation, Te Kuiti	38°21'26.667"S	175°14'33.13"E	~65*	65	9, 10
-	Horokiri Stream, Wellington area	41°03'25.345"S	174°56'47.981"E	6	290	11
UT1161	Waitara River Valley	39°03'42.599"S	174°17'49.085"E	~50*	153	3
Kohioawa Tephra	Opotiki, Bay of Plenty	37°59'27.728"S	177°12'39.046"E	350	128	12
-	Awatere Valley, South Island	42° 5'6.72"S	173°15'39.87"E	<10*	452	13
RC9-113	RC9 deep sea core, Pacific	36°44'12.00"S	167° 2'54.00"W	10	1509	14
RC9-114	RC9 deep sea core, Pacific	33°41'24.00"S	165° 2'48.00"W	5	1788	14
RC9-115	RC9 deep sea core, Pacific	31°22'60.00"S	163°43'6.00"W	2	2012	14
RC12-215	RC12 deep sea core, Pacific	35°28'0.00"S	167°53'30.00"W	15	1473	15, 16
AT-413-415,483	ODP 181 site 1124, Rekohu Drift	39°29'53.16"S	176°31'53.40"W	10	658	17, 18
AT-282	ODP 181 site 1122, Bounty Fan	46°34'46.92"S	177°23'37.32"W	11	1044	18, 19
-	ODP 591, Lord Howe Rise	31°35'3.48"S	164°26'56.40"E	25	1301	17, 19, 20
-	DSDP 594, Chatham Rise	45°31'24.60"S	174°56'52.80"E	10	778	4, 21

*Notes: Latitudes and longitude given in WGS84. Rangitawa Tephra thickness data compiled from - 1: Holt et al., 2010; 2: Pillans and Kohn, 1981; 3: Pillans et al., 1996; 4: Kohn et al., 1992; 5: Te Punga, 1952; 6: Milne, 1973; 7: Palmer, A., pers. comm. (21 April 2011); 8: Lowe et al., 2001; 9: Vucetich et al., 1981; 10: Birrell et al., 1981; 11: Mildenhall and Alloway, 2008; 12: Manning, 1996; 13: Froggatt, 1983; 14: Ninkovitch, 1968; 15: Seward, 1974; 16: Watkins and Huang, 1977; 17: Carter et al., 2004; 18: Alloway et al., 2005; 19: Froggatt et al., 1986; 20: Nelson et al., 1985; 21: Nelson, 1988. Rangitawa Tephra identified by glass chemistry, ferromagnesian assemblages, and geochronology. Thicknesses marked by * represent estimates based on extrapolation from nearby localities.*

6.3 Results

6.3.1 Tephra stratigraphy

Distal YTT tephra has been identified at numerous localities in India (Table 6.1). At Jurreru, Kurnool (~ 2600 km from the source caldera), YTT is characterised by ~ 2.55 m of redeposited tephra and 3 – 5 cm of primary volcanic ash (Fig. 6.5a; Oppenheimer, 2004; Petraglia et al., 2007) stratigraphically located within a well-documented archaeological sequence. The basal 3 – 5 cm of ash forms a continuous layer, characterised by abrupt lower and upper contacts and an absence of internal sedimentary structures. Reworking of the ash above this layer is extensive, with sedimentary structures including cross-bedding, fine laminations, mud cracks and fine-scale load structures (Fig. 6.5b) indicative of fluvial, lacustrine and aeolian reworking processes. Seven hardpan layers are identified at regular intervals within the deposit (Figs 6.5c,d), which may correspond to the effects of weathering conditions at the end of successive monsoon seasons (Jones, 2010). An abundance of fossilised tree debris was observed throughout the reworked YTT sequence, including well-preserved leaf fossils within the basal ash. Evidence for extensive bioturbation includes worm casts, trace fossils and termitaries (Haslam et al., 2010b).

The YTT horizon preserved at Ghogara (Fig. 6.5e), Son Valley (~ 3000 km from the source caldera; Fig. 6.2), is stratigraphically located above a fine clay unit with an abrupt well-defined lower boundary (Fig. 6.5f), and with the upper contact grading into a silty paleosol. The very fine to fine-grained white primary ash layer has a sharp planar to wavy upper contact (Fig. 6.5f), with increased sediment input up-section indicated by a progressive colour change. Cross-bedding and herringbone structures are particularly well preserved (Fig. 6.5g) above the basal 4 – 5 cm, indicative of deposition within a fluvial environment. Worm casts, escape structures and pellet structures within the cross-bedded

strata suggest that life persisted in this area. These sedimentary structures and complex layering also indicate seasonality in exposure and cycles of deposition.

Rangitawa Tephra stratigraphy at Mount Curl (Fig. 6.6a) and the Rangitawa Stream (Fig. 6.6b) localities (~ 200 km from the source caldera) has been documented by Te Punga (1952), Milne and Smalley (1979), Pillans et al. (1996), and revised by Pillans et al. (2005). The Rangitawa Stream exposure is ~ 55 cm thick and occurs within the upper part of the Aldworth loess (Fig. 6.6b). It consists of a crystal-rich coarse basal layer (Fig. 6.6c), fining upwards, with a distinct accretionary lapilli or ash pellet band near the upper contact (38 – 42 cm above the basal contact; Fig. 6.6d). The coarse basal layer contains glass shards and crystals of quartz (< 2 mm diameter), feldspar, orthopyroxene, and minor biotite, titanomagnetite, hornblende, clinopyroxene and zircon. Similar mineralogical features have been recognised at other localities (e.g., Lowe et al., 2001). The tephra is mineralogically zoned, with orthopyroxene dominating the ferromagnesian mineral assemblage at the base and biotite being introduced gradually up-section (also observed within the proximal Whakamaru ignimbrite; Brown et al., 1998a). The basal contact is a very well defined paleosol, and the upper contact grades into jointed pink-brown loess material that represents sheet wash and wind-reworked tephra. No break within the tephra is observed, suggesting continuous sedimentation resulting from a single eruption phase (also noted by Milne, 1973; Kohn et al., 1992).

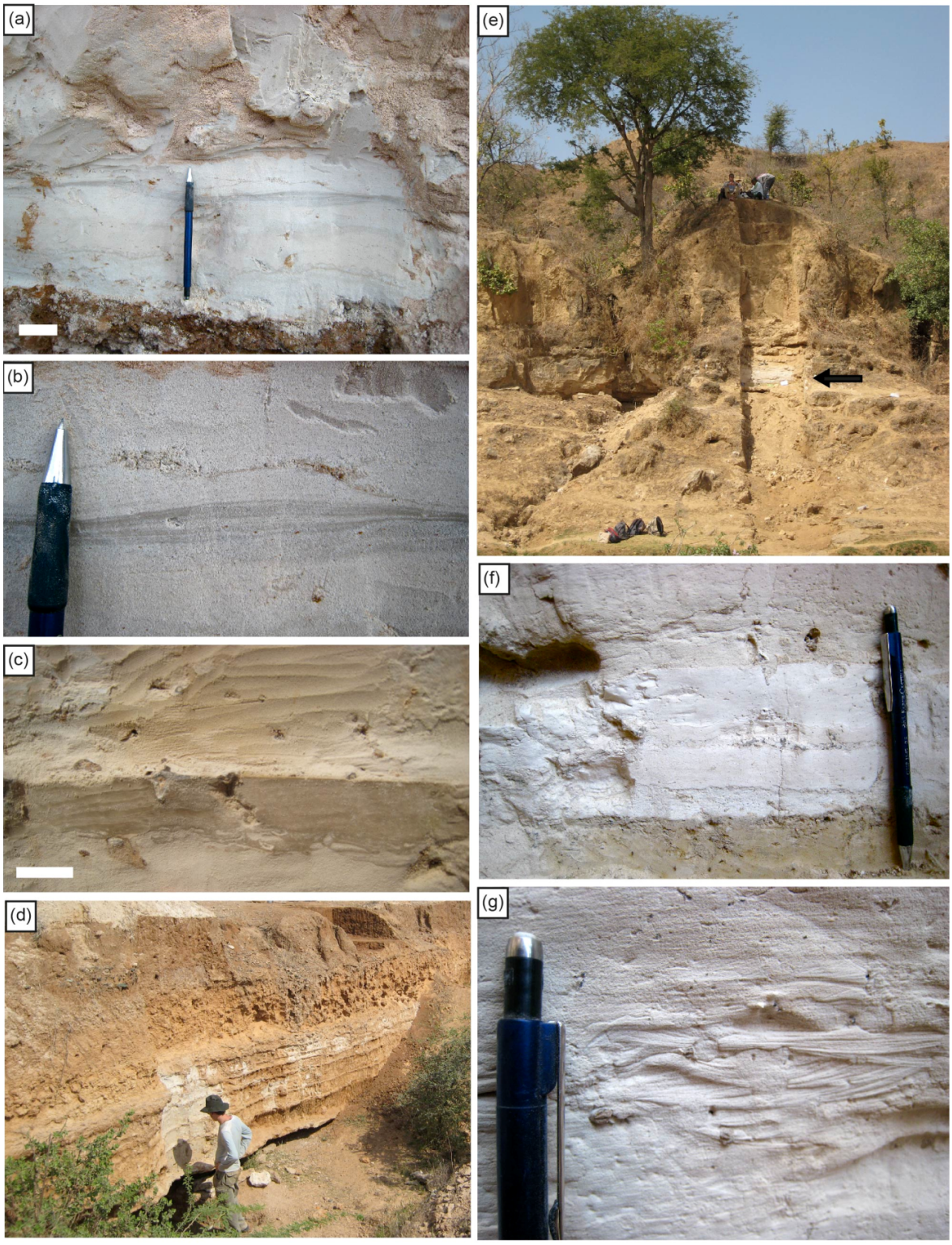

Fig. 6.5: Field photographs of YTT in India. (a)-(d) Jurreru locality, (e)-(g) Son Valley; (a) basal YTT, scale bar 2 cm; (b) cross-bedding structures 15 cm above basal ash contact; (c) detail of hard pan layer with load structures, scale bar 2 cm; (d) 7 hard pan layers visible in reworked YTT sequence; (e) sequence at Ghogara, arrow indicates YTT layer; (f) basal YTT, primary deposit thickness ~ 4 – 5 cm; (g) cross-bedding and herringbone structures above basal primary YTT.

Fig. 6.6: Field photographs of Rangitawa Tephra. (a)-(d) Mount Curl and Rangitawa Stream localities, Nth Island, (e)-(g) Chatham Island, New Zealand; (a) Rangitawa Tephra horizon at Mount Curl locality; (b) 55 cm thick tephra horizon at Rangitawa Stream; (c) detail of the crystal-rich basal tephra, scale bar 1 cm; (d) detail of accretionary lappilli layer at top of tephra horizon; (e) distal Rangitawa Tephra at Red Bluffs, Chatham Island; (f) tephra horizon between peat layers, Kaingaroa, Chatham Island; (g) Kawakawa Tephra horizon at Mairangi North, Chatham Island.

Distal Rangitawa Tephra preserved on Chatham Island (~ 900 km from source; Fig. 6.4) is characterised by variable thickness, ranging from ~ 8 cm at Mairangi North, 14 cm at Mairangi South, 15 cm at Kaingaroa, and to a maximum of 30 cm at Red Bluffs (Fig. 6.6e; see Table 6.3 and Holt et al., 2010). The tephra is usually a pinkish-grey or yellow-white colour and is bracketed by peat (Fig. 6.6f) or overlain by a paleosol. The extent of weathering varies (alteration affects glass composition, Section 2.3.3.3), and texturally the tephra is fine to very-fine ash in grain-size when fresh (Section 6.3.3). Mineral assemblage is biotite, orthopyroxene, bi-pyramidal quartz, hornblende, oxides and zircon. The crystal-rich basal layer is absent in these distal exposures.

6.3.2 Glass chemistry

Anhydrous (normalised) glass compositions of proximal YTT range 72.4 – 77.4 wt% SiO_2, 4.8 – 5.3 wt% K_2O, 2.9 – 3.2 wt% Na_2O, 0.7 – 0.9 wt% CaO, 0.8 – 0.9 wt% FeO^T (*n = 118*; averages provided in Table 6.4) and 135–302 ppm Rb, 12 – 100 ppm Sr, 47 – 102 Zr, 66 –785 ppm Ba, 33 – 76 ppm Ce and 13 – 34 ppm Nd (trace element data from Smith et al., 2011).

Glass shards within distal ash deposits in Jurreru and the Son Valley, India, are pristine, colourless, bubble-wall shards (Smith et al., 2011). Within India, distal tephra compositions range 76.41 – 77.77 wt% SiO_2, 4.60 – 5.63 wt% K_2O, 2.79 – 3.81 wt% Na_2O, 0.69 – 1.17 wt% CaO, 0.69 – 1.17 wt% FeO^T (*n = 220*; Fig. 6.7a,b; Table 6.4); and 175 – 317 ppm Rb, 14 – 70 ppm Sr (Fig. 6.7c,d), 41 – 111 ppm Zr, 53 – 842 ppm Ba, 36 – 68 ppm Ce and 15 – 27 ppm Nd (Smith et al., 2011). The composition of the distal tephra in India, is similar to tephra sampled in Lenggong, Malaysia (Smith et al., 2011) and proximal YTT (Table 6.4; Fig. 6.7).

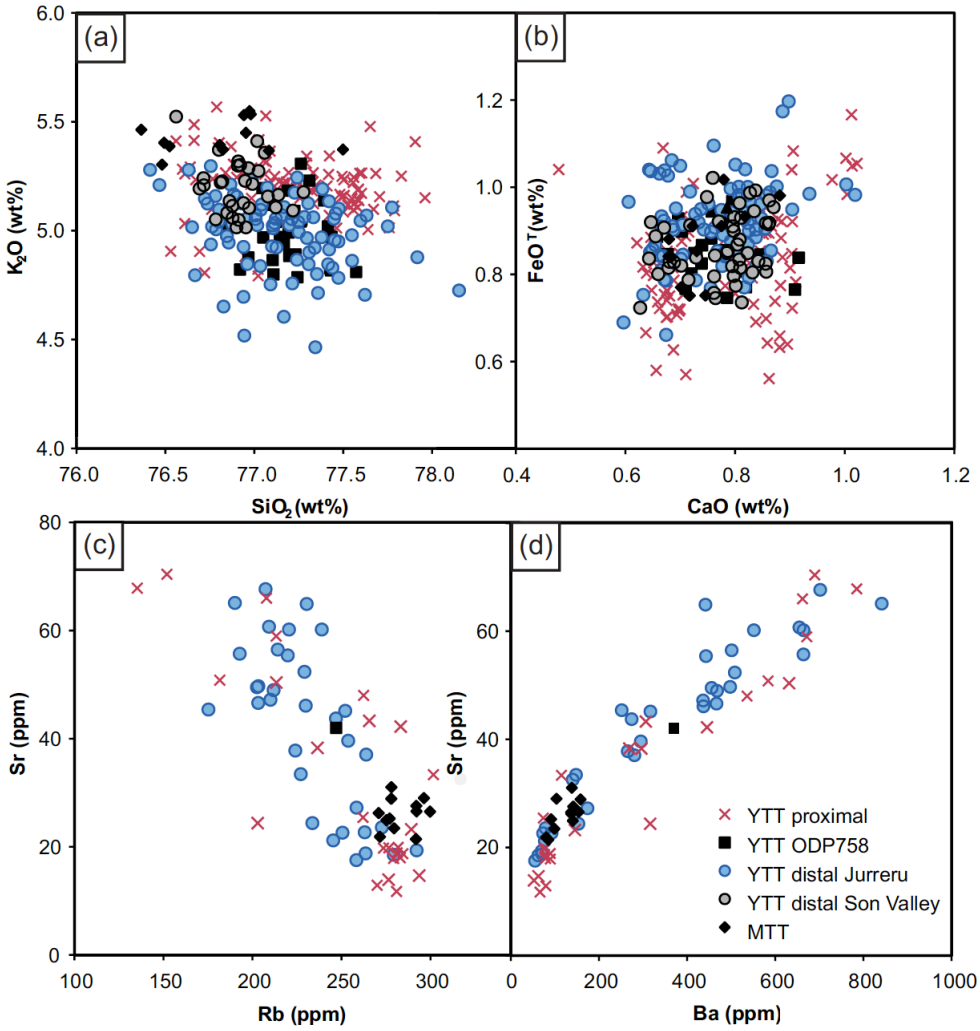

Fig 6.7: Compositions of glass shards at distal sites in India compared with proximal data from Malaysia YTT pumice, and published data of YTT from Layer A, ODP 758 (see Westgate et al., 1998; Smith et al., 2011).

Anhydrous glass compositions of pumices from the proximal Whakamaru and Rangitaiki ignimbrites and Rangitawa Tephra are provided in Sections 2.3.3.1 and 2.3.3.2. The composition of the Rangitawa Tephra is similar to the two members of the Whakamaru Group Ignimbrites sampled. It has a closer chemical affinity to type *A* Whakamaru and Rangitaiki pumices, however, with high CaO and Sr (Fig. 2.6). Similarities in glass geochemistry between distal Rangitawa and the Whakamaru Group Ignimbrites enable the distal deposits to be correlated (see Section 2.4.1, Tables 2.4 and 2.5).

Table 6.4: ***Proximal and distal YTT glass chemistry (by EPMA)***

	Toba YTT (proximal pumices)											
	YTT7 Sipisopiso		YTT3 Sigguragura (855m)		YTT4 Haranggom (1360m)		YTT6 Muara		YTT8 Harrangoal		YTT6 Muara	
EPMA (wt%)	(n=17)	*1sd*	(n=22)	*1sd*	(n=22)	*1sd*	(n=18)	*1sd*	(n=21)	*1sd*	(n=18)	*1sd*
SiO_2	76.91	0.34	77.44	0.19	77.33	0.34	76.88	0.21	77.41	0.24	76.88	0.21
TiO_2	0.08	0.03	0.05	0.03	0.05	0.02	0.07	0.02	0.05	0.02	0.07	0.02
Al_2O_3	12.62	0.11	12.51	0.15	12.47	0.18	12.70	0.12	12.40	0.16	12.70	0.12
FeO	0.97	0.13	0.84	0.08	0.83	0.11	0.77	0.12	0.80	0.08	0.77	0.12
MnO	0.07	0.05	0.08	0.04	0.06	0.05	0.06	0.04	0.08	0.06	0.06	0.04
MgO	0.07	0.02	0.05	0.01	0.05	0.02	0.06	0.02	0.04	0.01	0.06	0.02
CaO	0.89	0.11	0.73	0.08	0.77	0.07	0.86	0.05	0.69	0.02	0.86	0.05
Na_2O	3.12	0.15	2.98	0.13	2.99	0.12	3.19	0.11	3.23	0.15	3.19	0.11
K_2O	5.11	0.20	5.17	0.08	5.29	0.12	5.29	0.09	5.17	0.09	5.29	0.09
H_2O*	3.09	0.51	0.93	0.39	1.40	0.60	3.63	0.31	3.22	0.39	3.63	0.31

	Distal YTT, Jurreru						Distal YTT, Son Valley					
	JV22 YTT		JV7 YTT		JV13 YTT		GOC1 YTT (Son)		G05309 YTT (Son)		GOC1 YTT (Son)	
EPMA (wt%)	(n=24)	*1sd*	(n=23)	*1sd*	(n=20)	*1sd*	(n=35)	*1sd*	(n=19)	*1sd*	(n=35)	*1sd*
SiO_2	76.80	0.18	77.29	0.22	77.21	0.24	77.03	0.17	76.92	0.18	77.03	0.17
TiO_2	0.05	0.02	0.05	0.03	0.06	0.02	0.05	0.02	0.06	0.03	0.05	0.02
Al_2O_3	12.66	0.15	12.52	0.17	12.57	0.18	12.56	0.12	12.55	0.11	12.56	0.12
FeO	0.92	0.05	0.91	0.08	0.91	0.08	0.87	0.07	0.88	0.07	0.87	0.07
MnO	0.07	0.05	0.07	0.04	0.07	0.04	0.07	0.04	0.07	0.03	0.07	0.04
MgO	0.06	0.02	0.05	0.02	0.05	0.02	0.05	0.02	0.05	0.02	0.05	0.02
CaO	0.83	0.08	0.74	0.08	0.75	0.07	0.78	0.06	0.76	0.08	0.78	0.06
Na_2O	3.36	0.14	3.24	0.09	3.24	0.14	3.24	0.19	3.38	0.17	3.24	0.19
K_2O	5.07	0.18	4.98	0.12	4.98	0.11	5.17	0.15	5.16	0.11	5.17	0.15
H_2O*	4.15	0.42	3.55	0.94	4.24	1.12	4.00	0.57	3.79	0.44	4.00	0.57

*Note: Numbers are quoted as averages of n analyses, with 1 standard deviation (1sd), and results are presented as anhydrous. *H_2O by difference. All major elements determined by EPMA at University of Oxford. Glass chemistry data for distal Rangitawa Tephra is provided in Table 2.5.*

6.3.3 Particle size distribution

Selected particle size distributions (PSDs) for YTT and Rangitawa Tephra are provided in Table 6.5 and illustrated in Figures 6.8 and 6.9, together with profile-averaged cumulative frequency distributions (Fig. 6.10). Both YTT and Rangitawa tephra deposits are

texturally classified as fine ash, with unimodal PSDs. The ash is dominantly fine, with all particles at distal localities in India and Chatham Islands being < 1000 μm in diameter, including significant fractions of fine (< 63 μm) and very-fine ash (< 32 μm). Both ash deposits also comprise a significant fraction of the respirable sub-10 μm fraction (PM_{10}: Particulate Matter < 10 μm aerodynamic diameter; Expert Panel on Air Quality Standards, 2001).

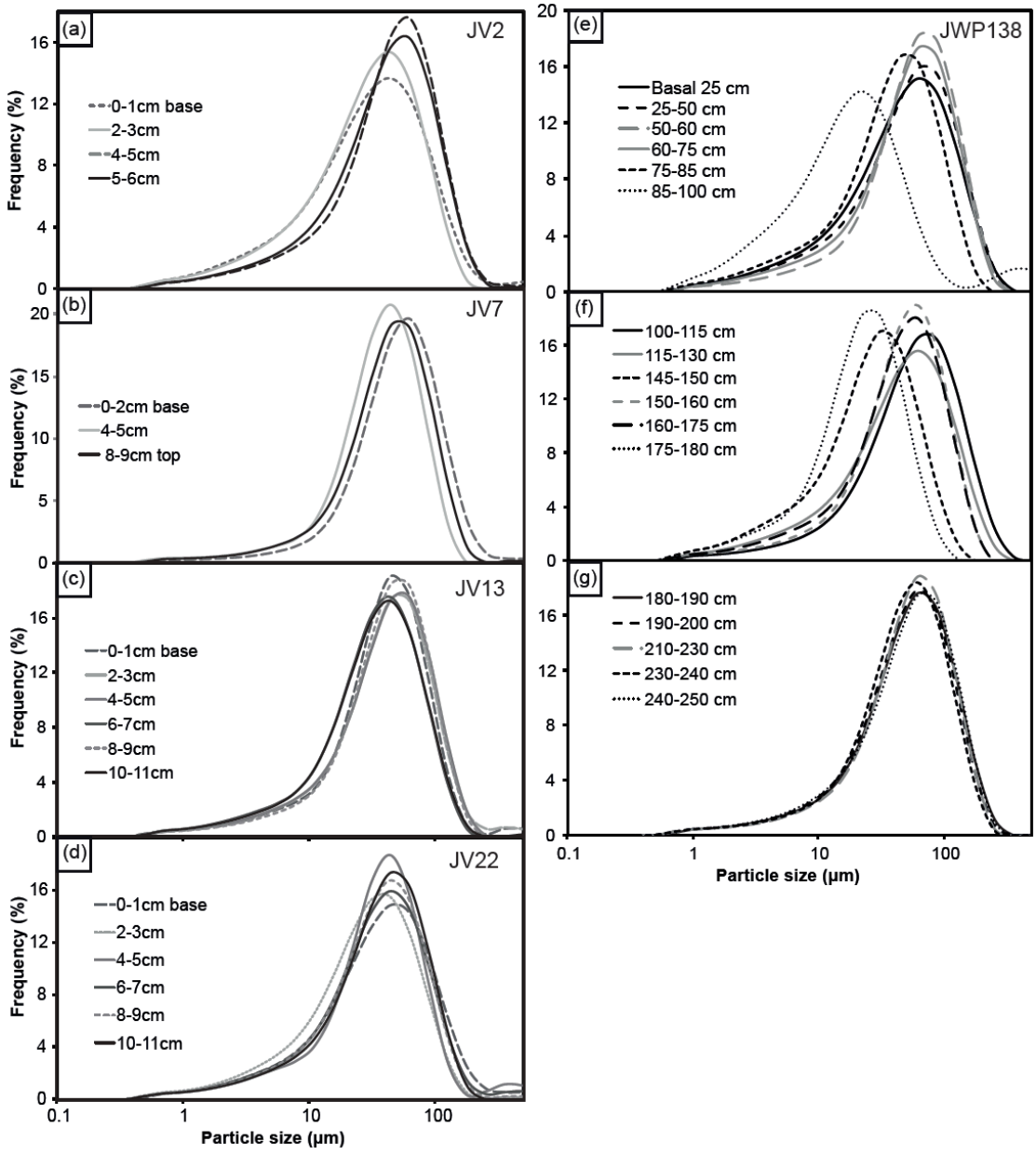

Fig. 6.8: YTT grain-size characteristics (PSD), all samples from Jurreru Valley, India; (e)-(g) grain-size characteristics for complete reworked YTT sequence (2.5 m thick) at archaeological site JWP138, Jurreru Valley.

Table 6.5: ***Selected Particle Size Distribution (PSD) parameters for distal YTT ash and Rangitawa Tephra***

(a)	Distal YTT, Kurnool			
PSD Parameter	**JV2-M1 0 – 1cm**	**JV7-M1 0 – 2cm**	**JV13-M1 0 – 1cm**	**JV22-M1 0 – 1cm**
Mean (μm)	64.36	78.13	63.63	67.97
Mode (μm)	53.35	75.45	53.35	53.35
Fraction < 2000 μm (ash total fraction, %)	100	100	100	100
Fraction < 63 μm (fine ash fraction, %)	82	70	81	78
Fraction < 30 μm (very-fine ash fraction, %)	56	32	45	49
Fraction < 10 μm (respirable size fraction, %)	24	7	13	18
Fraction < 2.5 μm (ultra-fine fraction, %)	6	2	4	4
Fraction < 1 μm (%)	2	1	1	1
Distance from source (km)	2669	2669	2669	2669

(b)	Rangitawa	Kawakawa	Rangitawa	Rangitawa
PSD Parameter	**R011/1 0 – 2cm**	**R006/2 0 – 2cm**	**R024/1 0 – 2cm**	**R024/25 48 – 50cm**
Mean (μm)	51.58	41.72	228.25	41.77
Mode (μm)	75.45	53.35	426.8	75.45
Fraction < 2000 μm (ash total fraction, %)	100	100	100	100
Fraction < 63 μm (fine ash fraction, %)	66	75	15	74
Fraction < 30 μm (very-fine ash fraction, %)	41	46	9	44
Fraction < 10 μm (respirable size fraction, %)	16	17	4	17
Fraction < 2.5 μm (ultra-fine fraction, %)	4	6	1	4
Fraction < 1 μm (%)	1	2	0	1
Distance from source (km)	864	864	179	179

Notes: Grain-size distributions measured on Malvern Mastersizer 2000, data quoted as average of 5 analyses per sample. All samples are characterised by a unimodal PSD and are fine skewed. Mean particle size quoted as geometric mean following methodology of Blott and Pye (2001). Particle fractions are chosen based on ash grain-size classification divisions and health-pertinent fractions.

Basal YTT ash at the Jurreru locality, India, shows unimodal grain-size populations, with a mean of 64 – 78 μm (Fig. 6.8; Table 6.5a). The basal primary YTT distal ash in India is all < 2000 μm, of which 70 – 82% is fine ash (< 63 μm), 32 – 56% is very-fine ash (< 32 μm), and 7 – 24% is potentially respirable ash (< 10 μm; Table 6.5a; Fig. 6.10c). All localities show the same PSD, with the exception of site JV7 which is coarser (likely to represent sample contamination; Table 6.5a). Grain-size characteristics at 25 cm increments through

the 2.5 m reworked tephra sequence at archaeological site JWP138, Jurreru, are provided in Fig. 6.8(e-g). Each layer is characterised by normal grading, capped by a hard pan layer which is typically finer than the reworked ash (mean 22 μm).

Distal Rangitawa Tephra on Chatham Island is texturally very-fine to fine ash, and shows a grain-size mean of 52 μm at the base (Table 6.5b), that grades to 44 μm at the upper contact (Fig. 6.9c). All ash particles are < 2000 μm, 66% of the total deposit is fine ash (< 63 μm), 41% is very-fine ash (< 32 μm), and 16% is the potentially respirable fraction (< 10 μm; Table 6.5b; Fig. 6.10d). The more proximal Rangitawa Stream locality is characterised by particularly pronounced normal grading, with the coarse crystal-rich base (Fig. 6.10a, pictured in 6.4c; primarily comprised of quartz, feldspar and biotite crystals) characterised by a mean of 228 μm (Table 6.5b), and the upper contact dominated by grain-sizes of 42 μm (Fig. 10b). The very-fine-grained ash component increases with stratigraphic height, from 9% to 44% (< 32 μm; Table 6.5b and Fig. 6.10) and the respirable fraction increases from 4 – 17% (< 10 μm).

In comparison, distal Kawakawa Tephra shows similar grain-size characteristics to distal Rangitawa, with 75% < 63 μm, 46% < 32 μm and 17% < 10 μm (Table 6.5b). Distal YTT and Rangitawa Tephra are characterised by similar median grain-sizes (Fig. 6.10a), and deposits exponentially thin away from source (Fig. 6.11).

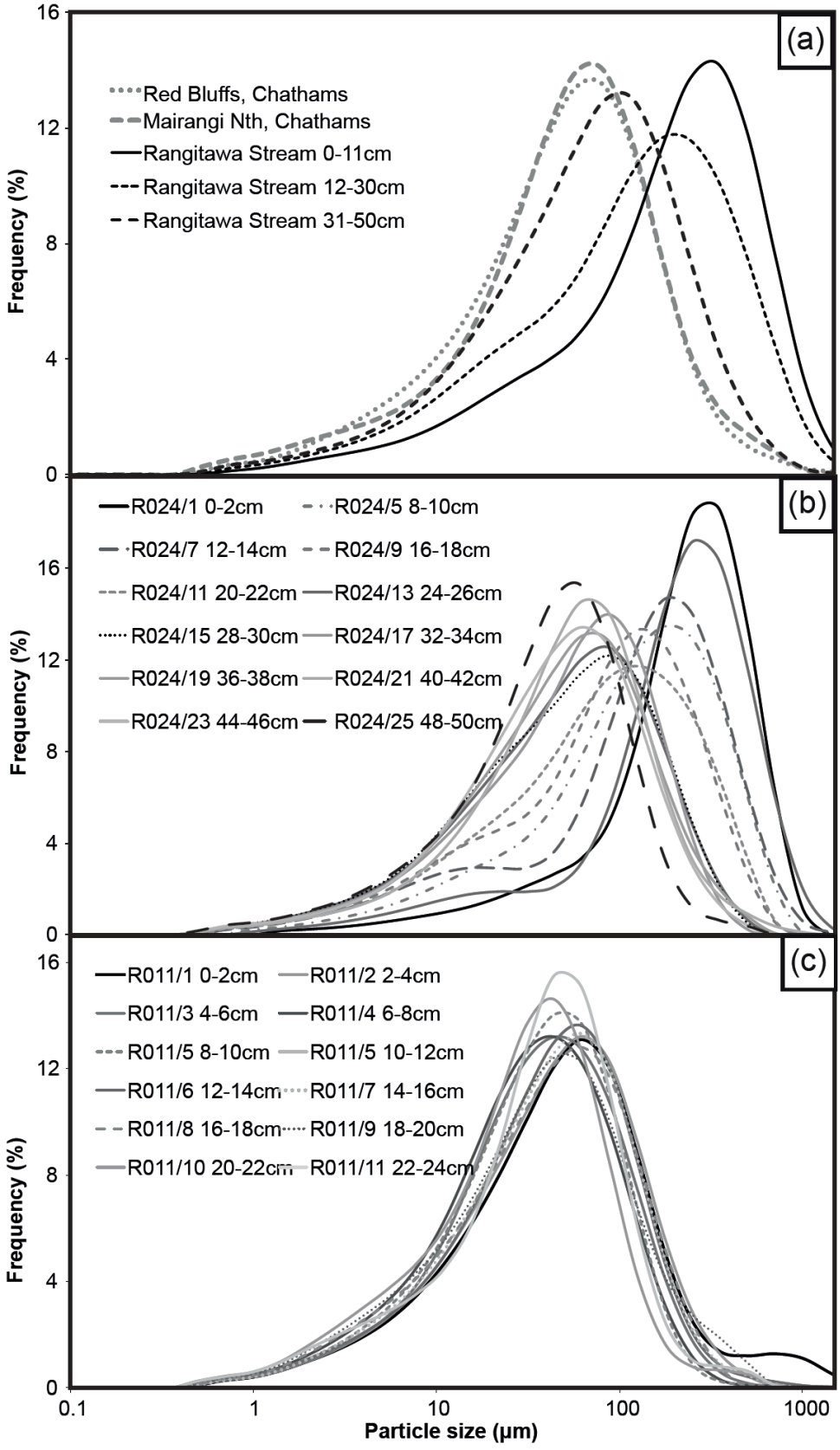

Fig. 6.9: Grain-size characteristics of distal Rangitawa Tephra, (a) summary of particle size distributions (PSDs) for Rangitawa Stream and Chatham Island localities; (b) Rangitawa Stream tephra; (c) Red Bluffs Tephra

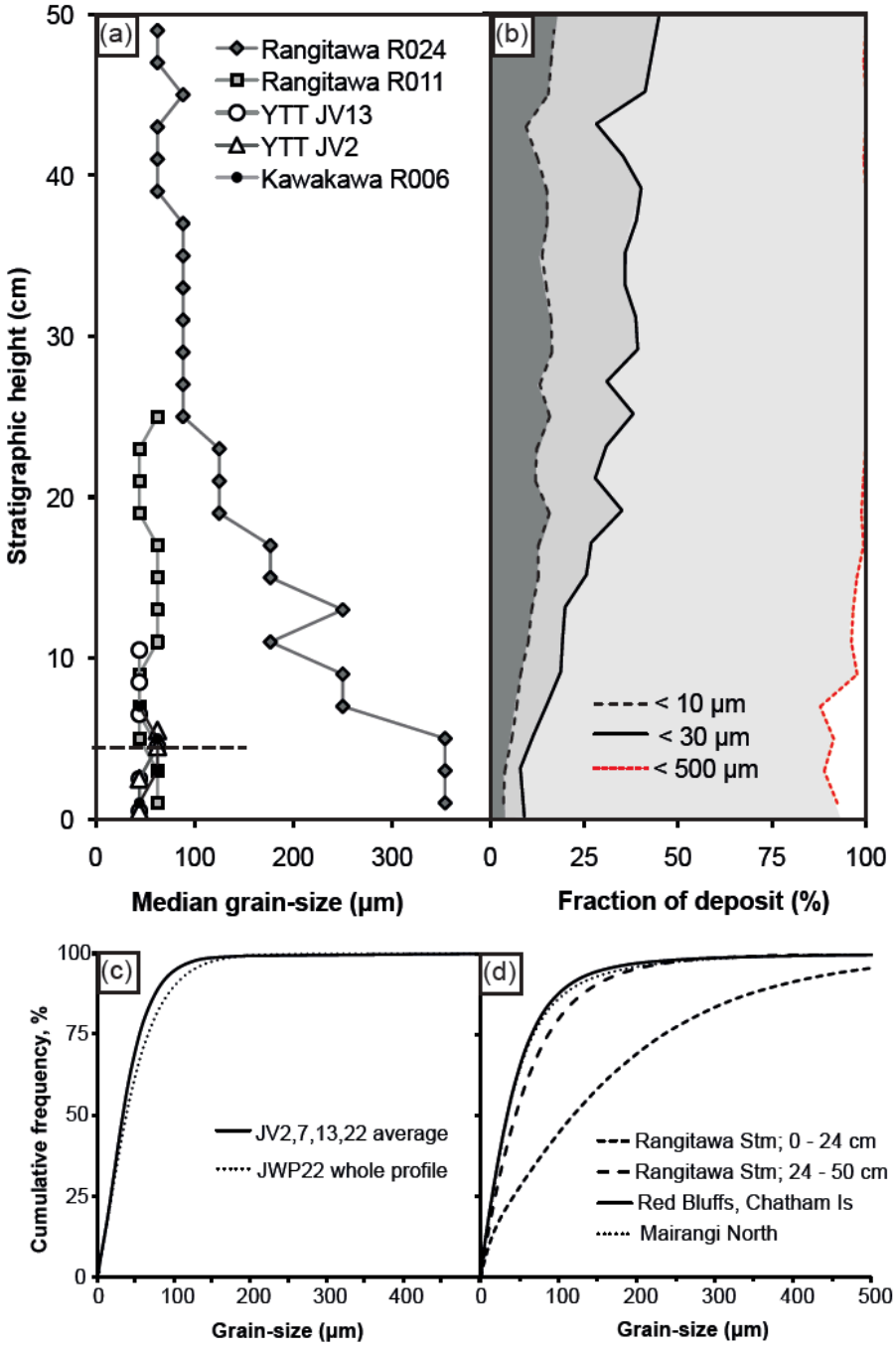

Fig. 6.10: (a) Median grain-size with stratigraphic height for Rangitawa Tephra and basal YTT; Note that both distal YTT and Rangitawa Tephra show similar median grain-size characteristics, and the more proximal R024 Rangitawa sample shows strong normal grading. Dashed black line at 4.5 cm height marks the upper contact of the YTT primary ash layer, with reworked ash above as indicated by sedimentary structures within the deposit. Kawakawa tephra is shown for comparison; (b) Median grain-size in terms of fraction of whole deposit with stratigrahic height at Rangitawa Stream locality (R024); all ash is < 1000 µm; (c) cumulative frequency plot of YTT grain-size; (d) cumulative frequency plot of Rangitawa Tephra grain-size.

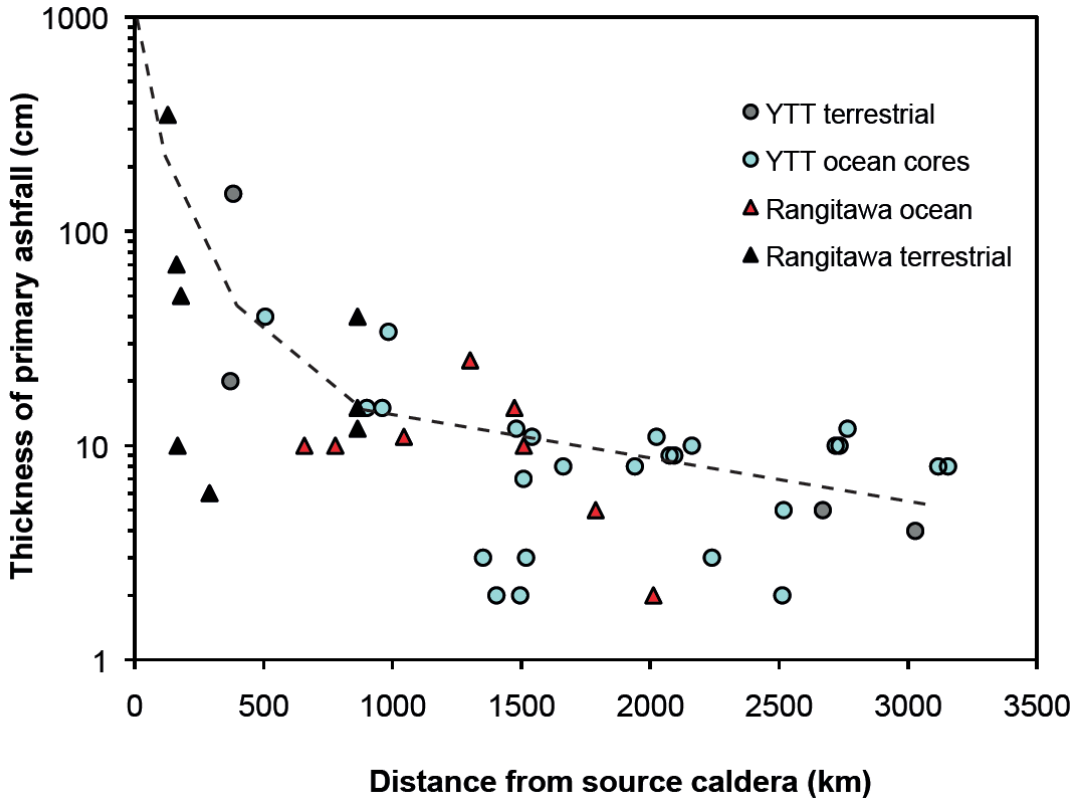

Fig. 6.11: Thickness versus distance for terrestrial and deep-sea tephra layers in cores of the Toba and Rangitawa Tephra layers, data reported in Table 6.2 and 6.3. Dashed black line shows generalised model for thickness variations in tephra fall deposit with segmentation into four domains as described by Bonadonna et al. (1998), where the proximal segment is formed from deposition of high Reynolds number particles, and the distal segment is formed from deposition of low Reynolds number particles (while the transitional region has a mixture of the two particle populations).

6.3.4 Ash dispersal modelling and eruption parameters

Results of the ash dispersal modelling for both eruptions are provided in Table 6.6 and Figs 6.12, 6.13, 6.14 and 6.15.

6.3.4.1 YTT modelling

Two different ash dispersal scenarios were considered for YTT (Figs 6.12a and 6.13), models "YTT1" and "YTT2" (Figs 6.12 and 6.13), using best-fit parameters obtained from minimising equation [6.1] assuming either statistical or proportional weighting. Statistical weighting was better at reproducing observations (Fig. 6.14a) and a satisfactory HAZMAP solution was found within the assigned parameter ranges. Proportional weighting (which tends to give more weight to the distal sections) showed no convergence within the assigned parameter range and a maximum column height of 40 km was assigned. Modelled best-fit eruption volumes of ~ 1500 km^3 (DRE) and ~ 1900 km^3 (DRE) were estimated for the models YTT1 and YTT2 (with statistical and proportional weighting), respectively. Both these estimates are larger than the assumed ashfall volume of ~ 800 km^3 (with 2000 km^3 of ignimbrite; Chesner and Rose, 1991) which was based on proximal extent and thickness of the deposits. It is worth noting, however, that the actual deposit densities may differ from the average values assumed here (e.g., deposits of the Mt St Helens 1980 eruption show up to 40% density variation; Durant et al., 2009).

Dispersal isopachs for both models are presented in Figs 6.12 and 6.13, with fit shown in Fig. 6.14 and model parameters provided in Table 6.6. For model YTT1, the best-fit wind direction was towards WSW (bearing 258°) with a maximum wind velocity of 21 m s^{-1} at 17 km altitude (tropospheric height in equatorial region). The best-fit column height was 35 km with mass concentrated at the very top of the column. In model YTT2 the best-fit

wind direction was towards the NW (347°) and the maximum wind intensity was 19 m s^{-1}. The estimated apparent diffusion coefficient was > 10^7 m^2 s^{-1}, which is two orders of magnitude above that expected for atmospheric turbulence alone (Section 6.2.6). This suggests that the near-column turbulence was from a broad source and wind shear may have spread the plume more effectively than diffusion. The size and density of the aggregate was determined through best fit, assuming values closer to those suggested by Cornell et al. (1983), i.e., an aggregate diameter of 200 μm and density ~ 200 kg m^{-3}. Results of the inversion suggested that at least 60% of the mass fell as particles having a settling velocity of about 0.1 m s^{-1} (corresponding to particles of 200 μm and density of 100 kg m^{-3} or to single particles having an equivalent settling velocity). With this set of assumed parameters satisfactory agreement was generally obtained, and the modelled thicknesses are all within a factor of five of the observations (Fig. 6.14).

Table 6.6: ***Results of HAZMAP tephra dispersal modelling for Toba and Whakamaru eruptions***

Modelled Dispersion Parameters	Explored range	YTT1	YTT2	RANG1	RANG2
Volume (DRE; km^3)	Calculated analytically	1500	1900	400**	400
Max wind velocity at 17 km altitude for YTT and 11 km for Rangitawa (m s^{-1})	5 – 50	21	19	35	42
Wind azimuth (° clockwise from Nth)	0 – 360	102	15	125	125
Column height (H, km)	20 – 50	35	40*	45	44
Suzuki coefficient	2 – 9	9	9	4	4
Diffusion coefficient (K, m^2 s^{-1})	10^4–10^7	1×10^7	1×10^7	6×10^5	6×10^5
Percentage of aggregates with respect total mass (%)	50 – 60	60	60	60	60
Settling velocity of aggregates (m s^{-1})	Calculated	0.1	0.1	0.2	0.2
Deposit density (kg m^{-3})	-	1100	1100	1200	1200

*Notes: Model YTT1 uses all data points (terrestrial and ocean-cores) with statistical weighting; YTT2 uses all data points with proportional weighting; comparison of these two illustrates uncertainty in the total mass erupted (1500 – 1900 km^3 DRE). Whakamaru model RANG1 uses all data points with statistical weighting (omitting the 25 cm from ODP 591) and assuming a maximum wind intensity of 35 m s^{-1}; Whakamaru model RANG2 uses the best-fit wind intensity of 42 m s^{-1}. *Maximum column height of 40 km for YTT is the upper limit imposed in the modelling; **Rangitawa Tephra volume is underestimated due to ash deposition which also occurred in sectors away from the main SE dispersal axis.*

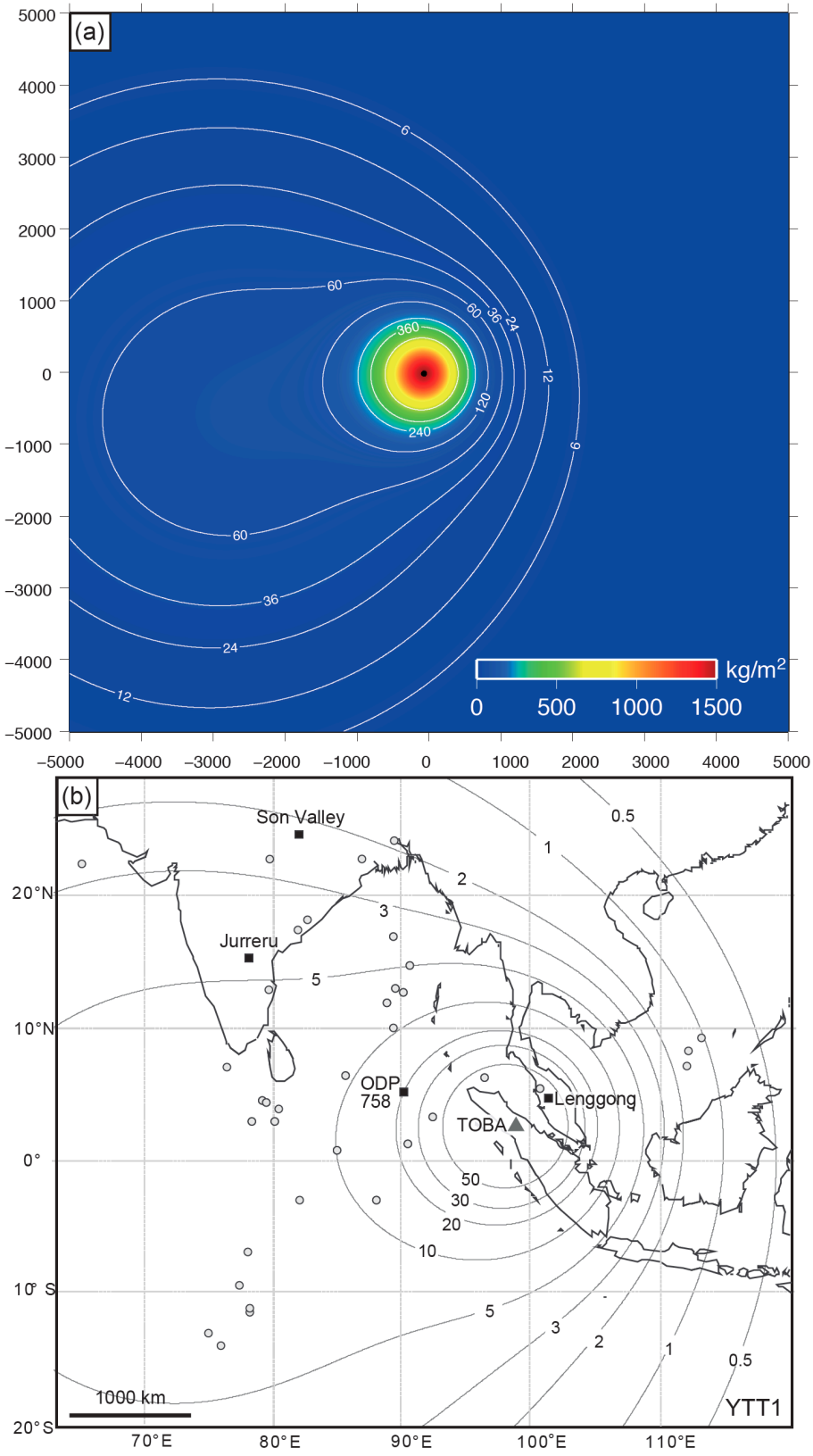

Fig. 6.12: (a) Isomass plot showing modelled ash loading (in kg m^{-2}) for model YTT1, domain size is 10000 km; (b) Isopach map showing modelled ash thickness (in cm; intervals 1, 5, 10, 20, 30, 40 cm etc.), as modelled using HAZMAP based on measured thicknesses and grain-size data for the distal localities in India. See parameters in Table 6.6. Details of the models and the assumptions are discussed in the text. Input dataset provided in Table 6.2.

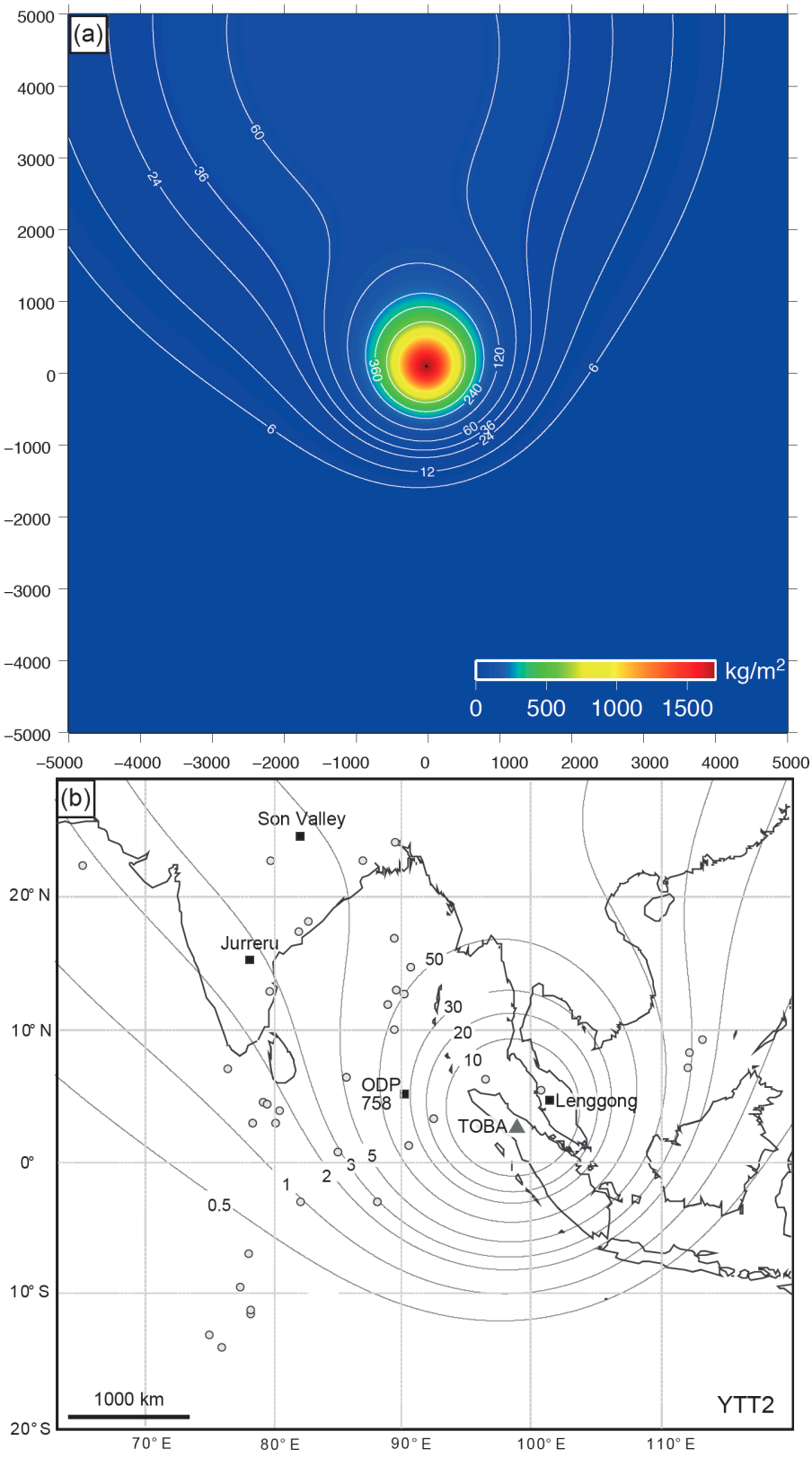

Fig. 6.13: (a) Isomass plot showing modelled ash loading (in kg m^{-2}) for model YTT2, domain size is 10000 km; (b) Isopachs show YTT ash thickness (intervals 1, 5, 10, 20, 30, 40 cm etc.), as modelled using HAZMAP based on measured thicknesses and grain-size data for the distal localities in India, see parameters in Table 6.6. Details of the models and the assumptions are discussed in the text. Input dataset provided in Table 6.2.

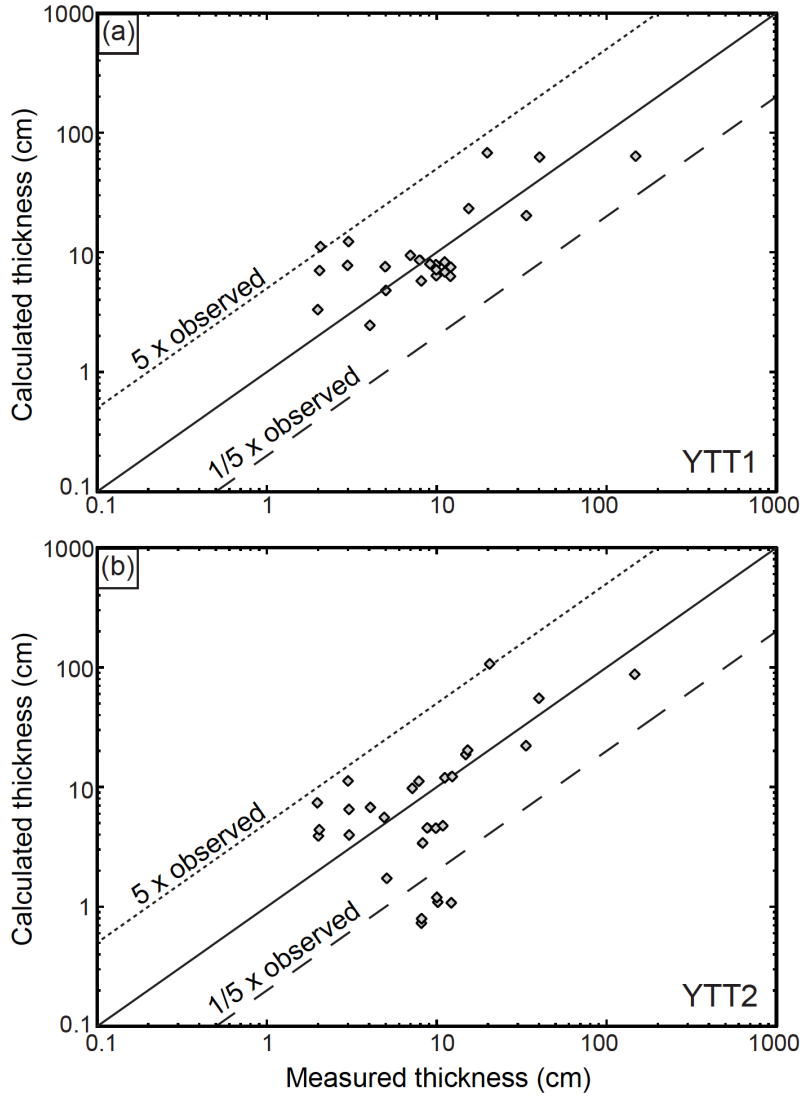

Fig. 6.14: Comparison between the HAZMAP simulation for YTT using the values obtained by best-fit procedure and the field data at each sampling point (where tephra thickness is equivalent to ash loading divided by 11, using a deposit density of 1.1 g cm^{-3}). The equiline (black solid line) represents an ideal line if a perfect agreement existed, and the dotted and dashed black lines mark the region between 5 and 1/5 times the observed thickness at each location; (a) Modelling results for YTT1; (b) Modelling results for YTT2 (parameters provided in Table 6.6).

6.3.4.2 Rangitawa modelling

Two scenarios were also considered for the Whakamaru eruption, referred to here as models "RANG1" and "RANG2". Both were based on Rangitawa ash dispersal and the limited dataset for tephra thickness (Table 6.3), but with different wind speeds. Modelling generally indicated that the eruption was dominated by a Plinian phase, with a plume height of ~ 44 – 46 km. The estimated erupted volume is ~ 400 km^3 (DRE).

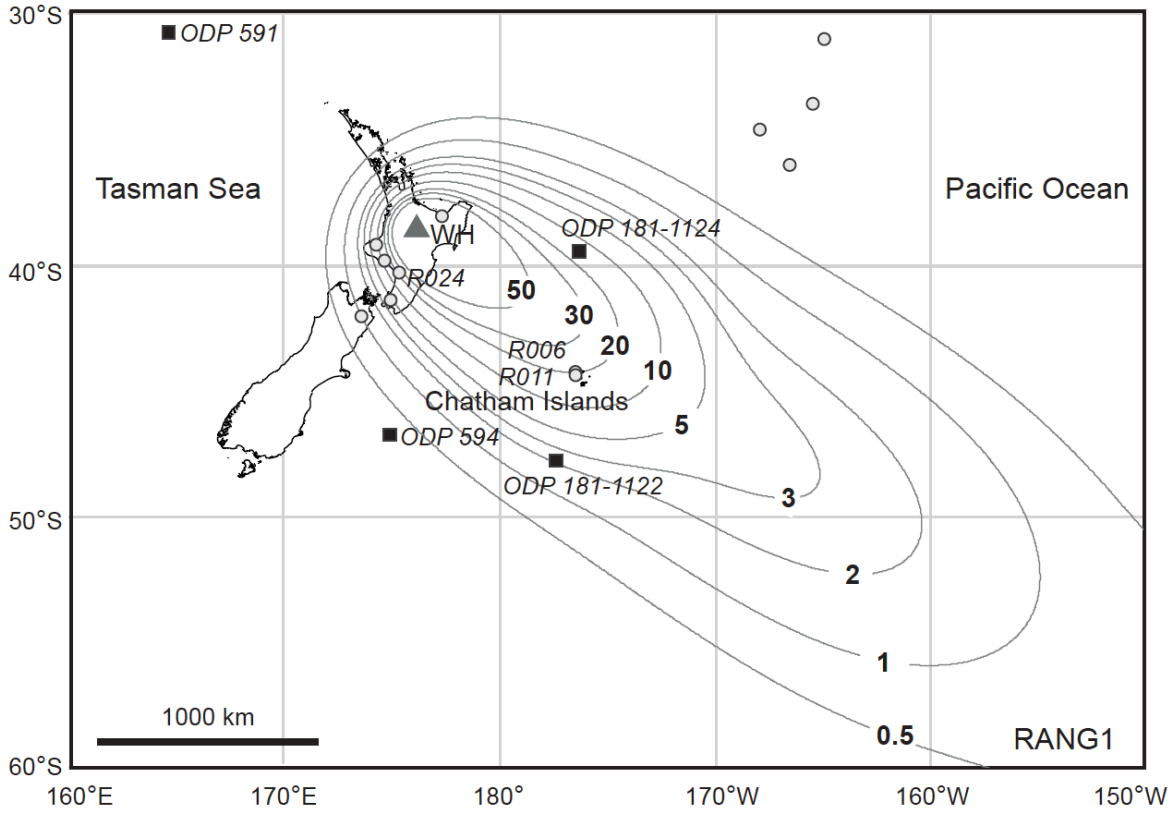

Fig. 6.15: Isopach map for Rangitawa Tephra showing modelled tephra thickness (model RANG1); isopachs labeled in cm of primary ashfall thickness. All data points included with equal weighting (with the exception of ODP 591 to the NW of New Zealand, see text). Parameters are summarised in Table 6.6. Input dataset provided in Table 6.3.

In model RANG1, results excluding points in the NE sector (samples RC9 – 12, Table 6.3 - outside of the main dispersal direction), gave an erupted volume of 380 km^3 (DRE), while inclusion of all sample points gave a volume of 420 km^3 (DRE). Extrapolations

accounting for mass dispersed to the NE sector indicate a total volume of ~ 500 km^3 (DRE). Inversion results for wind intensity indicate that there were very strong wind conditions, with a best-fit intensity of 42 m s^{-1} to the SE (105°). Isopachs for model RANG1 are shown in Fig. 6.15.

Model RANG2 assumed a maximum wind intensity of 35 m s^{-1}, which is more consistent with typical modern high-altitude wind conditions in this area (Prata and Grant, 2001; Fig. 6.16). In this case statistical weighting only was used as the proportional weighting favours distal points, and most of these were outside of the main dispersal sector (towards the SE; Fig. 6.16; fit shown in Fig. 6.17). The modelled diffusion coefficient was 6×10^5 m^2 s^{-1}, consistent with the estimation of an apparent diffusion coefficient on a dispersion scale of ~ 3000 km (Section 6.2.6), reflecting a typical dispersion dominated by advection from a Plinian column (at least for the distal deposits). Concerning the TGSD, results suggested that at least 60% of the mass fell as particles with a settling velocity of about 0.2 m s^{-1} (corresponding to particles of 200 μm and density of 200 kg m^{-3} or to single particles having an equivalent settling velocity).

Observed tephra layers in sites located outside of the main dispersal direction, such as those in the NW and NE sectors, cannot be reproduced within the framework of a unidirectional wind profile as assumed in the dispersion model here. It is likely that these deposits are related to different phases of the eruption with deposition occurring on different days. Changes in wind direction are also likely to occur during a long-lasting eruption (e.g., Chaitén eruption; Watt et al., 2009a).

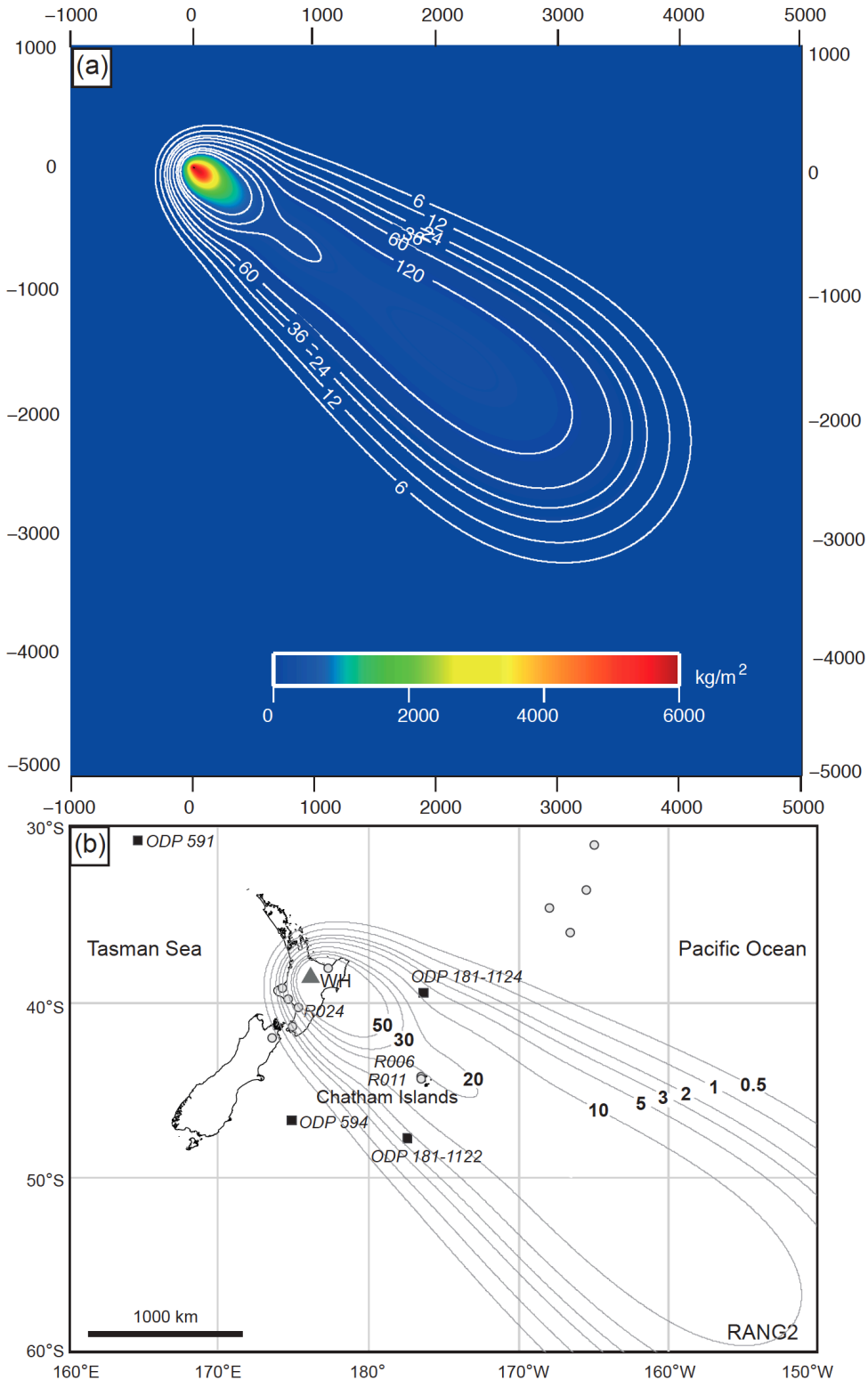

Fig. 6.16: (a) Isomass map for model RANG2, domain 6000 km. (b) Isopach map for Rangitawa Tephra showing modelled tephra thickness; isopachs labeled in cm of primary ashfall thickness. Modelled by exluding data from ODP cores to the NE of New Zealand, parameters are summarised in Table 6.6. Input dataset provided in Table 6.3.

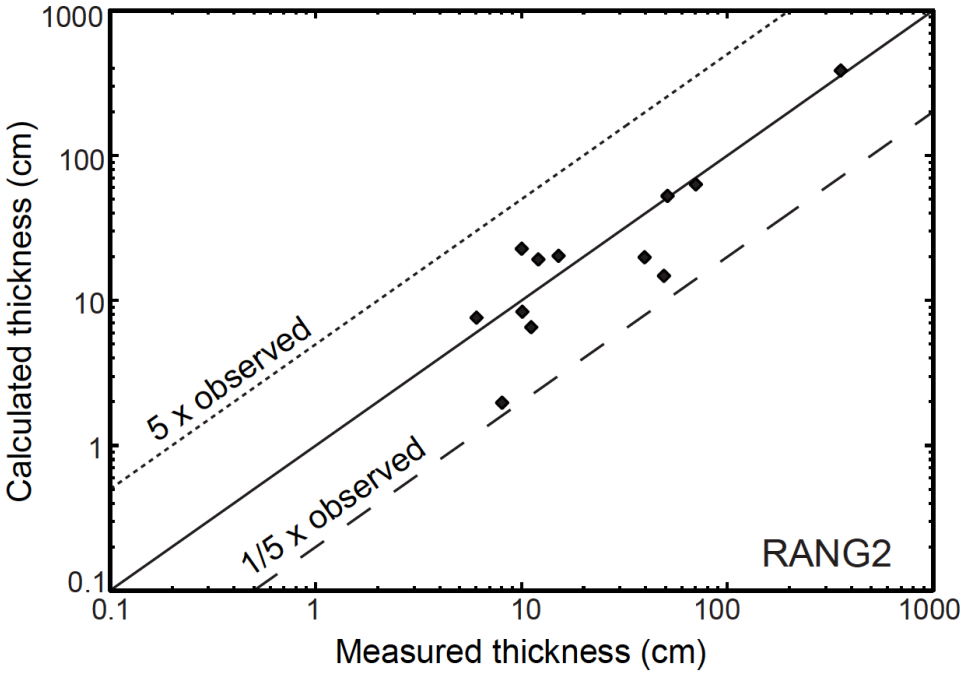

Fig. 6.17: Comparison between the HAZMAP simulation (RANG2) for Rangitawa Tephra using the values obtained by best-fit procedure and the field data at each sampling point (where tephra thickness is equivalent to ash loading divided by 12, using a deposit density of 1.2 g cm^{-3}). The equiline (black solid line) represents an ideal line if a perfect agreement exists, and the dotted and dashed lines mark the region between 5 and 1/5 times the observed thickness at each location (parameters provided in Table 6.6).

6.4 Discussion

6.4.1 Glass chemistry

The similarities in major- and trace-element glass chemistry for the large Toba eruptions (Smith et al., 2011) suggest that tephra horizons in deep-sea cores may have been miscorrelated in the past, particularly in sequences which do not have independent chronological control (although the chronology is adequately constrained in most marine examples). Existing uncertainty in records concerning thicknesses of terrestrial YTT deposits (primary versus reworked tephra) has been clarified by the recent identification of

the basal primary ash layer (Petraglia et al., 2007), although the primary deposit may have been thicker prior to erosion. The potential for miscorrelations and incorrect tephra thickness measurements (particularly for marine occurrences; Manville and Wilson, 2004a) introduces an unquantifiable error into dispersal modelling, particularly given the dependence on a limited dataset. Glass chemistry of distal deposits in India is consistent with proximal YTT chemistry and this, in conjunction with matching biotite compositions (see Smith et al., 2011), confirms that the distal deposits at the sites discussed here were sourced from the YTT eruption.

Rangitawa glass chemistry is discussed extensively in Chapter 2. The glass and mineral compositions of distal Rangitawa Tephra deposits (Figs 2.6, 2.8) indicate that the magma that fed the Plinian phase was similar to that which generated the proximal type *A* pumices that dominate the Rangitaiki and Whakamaru ignimbrites (as discussed in Chapter 2). The low CaO glass population observed at the Rangitawa Stream locality (see Fig. 2.8) most likely relates to Rangitaiki type *A* magma, and Whakamaru types *B*, *C* and *D* do not appear to contribute significantly to the distal tephra. The distal tephra displays less compositional diversity than the proximal ignimbrite deposits, suggesting that some of the material erupted during some phases was not widely dispersed.

The dispersal modelling suggests that the deposit on Chatham Island was from a Plinian column (Section 6.3.4.2) but no ashfall deposits are preserved in proximal locations. The chemical similarity between the Rangitawa and volumetrically-dominant type *A* magma indicates that the distal tephra is certainly associated with the eruption, and provides evidence that the proximal ashfall deposits were eroded prior to or during ignimbrite emplacement.

As the eruptions from Toba all share the same glass chemistry (Fig. 6.7; Smith et al., 2011), the composition of Rangitawa Tephra was compared to the deposits of the Oruanui eruption from TVZ, the Kawakawa Tephra, to assess whether large eruptions from New Zealand also share the same chemical affinity. Rangitawa Tephra is clearly different from the Kawakawa Tephra - it is more evolved with higher K_2O, Rb and Ba, and lower CaO, FeO^T and Sr compositions, forming a separate compositional group on major- and trace-element plots (Section 2.3.3.1; Fig. 2.6). It therefore appears that the TVZ is unlike Toba as at least two of the large eruptions have distinct glass chemistries.

6.4.2 Sedimentological characteristics: post-depositional reworking

The YTT exposures in India were significantly over-thickened through reworking after deposition. Many earlier reports simply identified the full reworked thickness, which ranges from < 1 m to 5 m, rather than the thickness of the primary ash layer (e.g., compilation in Table 1 in Jones, 2007). However, in the field there is strong evidence for fluvial and aeolian reworking of the deposit above the basal 4 – 5 cm, and it is likely that only this basal layer represents the primary ashfall deposit (see also Petraglia et al., 2007).

The field observations outlined in section 6.3.1 suggest that the occurrences of YTT at both Jurreru and the Son Valley are primary ash deposits. The criteria used here for identifying an ash unit as a primary deposit are as follows: the unit may have weakly-developed planar bedding but no cross-bedding features; it forms a continuous, uniformly-bedded deposit which blankets pre-existing topography with only minor lateral variations in thickness locally; and it is characterised dominantly by glass shards and an absence of detrital (non-volcanic) material. The basal 4 – 5 cm of tephra at archaeological pit sites JV2, JV13, JV22 and JWP138, Jurreru, and at Ghogara, Son Valley, are therefore thought

to represent primary ash. In contrast, on the basis of the above criteria, the sedimentary characteristics of the thick deposits of ash above this basal layer indicate that they are reworked. Grain-size characteristics of the basal ash at site JV7 also suggest that this material has been reworked. Itrax data (see Appendix A6.1) do not distinguish any significant compositional changes through the basal ~ 10 cm of distal ash at the Jurreru and Son Valley localities, other than a peak in Ca (at 6.5 cm above the basal contact) which may indicate either post-depositional diagenesis or terrigenous input with carbonate material being worked into the deposit. The consistency of grain size throughout the complete YTT stratigraphy at the India localities prevents distinction between primary and reworked tephra on the basis of grain size alone. This uniformity in grain size also suggests that reworking processes occurred relatively rapidly, before any significant external sediment had been incorporated into the depositional system.

The Rangitawa Tephra has previously been considered as representing the product of a phreatoplinian phase of the Whakamaru eruption (Brown et al., 1998a). The identification of accretionary lapilli or armoured lapilli (Fig. 6.6d) within this unit at both the Mt Curl and Rangitawa Stream localities supports a phreatomagmatic origin (although there is no evidence for phreatomagmatic activity in the proximal ignimbrite facies). These features can also be explained by a co-ignimbrite plume origin with fallout of ash pellets occurring within a ~ 200 km radius of the source caldera. The fine-grained upper ash is suggestive of co-ignimbrite deposition. Rangitawa Tephra exposures on Chatham Island are very fine-grained and contain low levels of crystal material (1 – 2 g kg^{-1}; Holt et al., 2010) due to atmospheric sorting and long-range transport (> 900 km from source). Particle-size distributions for Rangitawa Tephra therefore exhibit a coarse particle sub-population that fines with distance from the volcano (Pyle, 1989), in addition to a finer subpopulation

(mode at 31 – 62 μm diameter, average mode is 53 μm; Fig. 6.9; Table 6.5) that retains consistent size characteristics but becomes proportionally-dominant in distal regions of the deposit (Durant et al., 2008).

Post-depositional processes such as winnowing of fine material by wind or water erosion and compaction due to burial, may have affected the grain-size distributions and altered thickness measurements for both tephra deposits. These processes are also likely to have been more significant given the distal nature of the deposits under consideration here. This clearly introduces errors into ash dispersal modelling (see Section 6.4.3), as the approach used here assumes that the measured primary ashfall thicknesses and PSDs reflect initial deposition. Degrees of ash reworking are expected to vary significantly based on the particular environment of the ash exposure, especially with respect to terrestrial versus ocean-floor localities (e.g., Manville and Wilson, 2004a).

6.4.3 Ash dispersal patterns

The modelled dispersal patterns for YTT reproduce the recorded thickness distribution within an order of magnitude, with modelled thickness values being between 0.2 and 5 times the observed thickness at each location (Fig. 6.14). The YTT isopach maps (Figs 6.12 and 6.13) show the extensive offshore dispersal of ash, verified by the distal terrestrial exposures in India and further occurrences in cores from the Bay of Bengal and South China Sea (e.g., Bürhring et al., 2000). The distribution patterns indicated by terrestrial and offshore tephra occurrences outline a generally westward dispersal, and hence model YTT1 (Fig. 6.12a) is favoured. These isopachs (Fig. 6.12b) must be considered as approximations only, as they assume a uniform average wind profile over a very large domain and due to the other reasons outlined in Section 6.3.4.

The column height for the YTT eruption provided by the best-fit model (Section 6.3.4.1) is ~ 35 km, comparable to earlier estimates of Woods and Wohletz (1991) and this, together with a very large diffusion coefficient (10^7 m^2 s^{-1} upper limit) and the high proportion of very fine ash (Fig. 6.8), indicates that the YTT event was mainly a co-ignimbrite eruption. The diffusion parameter controls the spreading of the plume and the high value, apart from the atmospheric turbulence, could be due to wind shear on the entire domain, turbulence due to the co-ignimbrite column itself, and the possibility of an extended source. It is likely that the column extended from vents scattered over an area, emanating from a ring fracture or fissure. Deposits on Sumatra are all ignimbrite, instead of ashfall, thus providing further evidence that the distal deposition was mostly associated with the co-ignimbrite ash cloud (Rose and Chesner, 1987). Previous work by Ninkovich et al. (1978a, b), Chesner and Rose (1991) and Woods and Wohletz (1991) also concluded that YTT ash is entirely of co-ignimbrite origin, drawing on the lack of significant Plinian-fall deposits underlying the proximal ignimbrite. Furthermore, bubble-wall shards are common in the deposit and these typically have high drag coefficients and therefore are not transported into the upper reaches of eruption columns, thus restricting dispersal to around the source (Rose and Chesner, 1987).

The Rangitawa Tephra dispersal modelling suggests a higher eruption column of ~ 45 km, with maximum mass distribution within the column at 3/4 of the total column height (Suzuki coefficient equal to 4; Macedonio et al., 2005; Pfeiffer et al., 2005), which is a typical value for Plinian columns (Costa et al., 2009). The erupted volume is estimated to be ~ 400 km^3 DRE, although this accounts for only the mass deposited in the main dispersal direction (towards the SE; Fig. 6.16) and will be an underestimate because the uniform wind field approximation cannot capture the thin (2 – 10 cm; Fig. 6.3) deposits

that lie outside this area. Temporal and spatial variability in the real wind patterns could not be incorporated in the simplified modelling approach, and more elaborate, fully time-dependent, three-dimensional models (e.g., Folch et al., 2010) would require full wind field descriptions at the time of eruption, which are unknown. Preliminary simulations restricted to the more proximal region (< 300 km from source) and using a larger number of sections on the mainland, indicate lower column heights (~ 22 km) and low volumes (~ 220 km^3), suggesting that the proximal deposits were dominated by co-ignimbrite deposition, whereas distal deposits were mainly from the Plinian phase.

Relationships between measured tephra thickness and those calculated by HAZMAP modelling for YTT (Fig. 6.12) and Rangitawa (Fig. 6.16) are shown in Figs 6.14 and 6.17 respectively. The model reproduces measured Rangitawa thicknesses > 10 cm but, because a uniform wind field is assumed, it cannot reproduce points in sectors outside the main SE dispersal direction. The erupted volume is a maximum of ~ 500 km^3 DRE if results are roughly extrapolated by moving the NE points at equivalent distances in the main dispersal sector. The 25 cm thickness recorded at ODP site 591 (Froggatt et al., 1986; Carter et al., 2004) was omitted as it lies in the NW sector and is inconsistent with other measurements (and may thus represent a miscorrelation or an over-thickened tephra horizon). These thicknesses to the NW cannot be reproduced here as the model does not consider changes in wind direction during long-lasting eruptions (hence the mass calculated by modelling here represents a lower-bound estimation). It is likely that these deposits were produced during a wind direction change which shifted the main dispersion axis. As mentioned above, in order to capture this kind of wind variation and account for realistic wind fields (which are unknown), more elaborate, fully time-dependent, three-dimensional models are needed (e.g., Folch et al., 2010). The occurrence of Rangitawa

Tephra in ocean cores to the NE of North Island (Table 6.3; Figs 6.3 and 6.16) could also have been caused by a change in wind direction at some point beyond the Chatham Islands, dispersing a significant amount of tephra northwards. The value of the diffusion coefficient obtained for Rangitawa (6×10^5 m^2 s^{-1}) is consistent with the previous estimation on this dispersal scale, reflecting a typical dispersal dominated by advection, and indicative of a fully developed Plinian eruption column.

6.4.3.1 Sources of uncertainty in modelling

Caution should be exercised in interpreting modelling results as their accuracy depends on the adequacy of the assumptions made (as outlined in Section 6.2.5). Inaccuracies here may arise through the limited datasets available for model input; assumption of an average deposit density on such large domains; miscorrelation of tephra horizons in ocean cores; incompleteness of stratigraphic records and spatially; inadequacy of characterisation data of potential correlatives; lack of recognition of non-unique chemical fingerprints (particularly for Toba; see Smith et al., 2011); inappropriate geochemical analysis leading to faulty characterisation; and reworking of tephra to different stratigraphic positions (e.g., Dugmore et al., 2004; Shane et al., 2006; Payne and Gehrels, 2010; Lowe, 2011). Further errors could be introduced from tephra thickness data, with possible over-thickened estimates from terrestrial exposures, and minimum thicknesses from ODP cores due to the role of bioturbation and erosion by ocean currents (see Ninkovich and Ruddiman, 1977; Watkins et al., 1978; Ninkovich, 1979; Kyle and Seward, 1984; Manville and Wilson, 2004a).

Furthermore, the modelling approach used here assumes a discrete number of point sources above the vent, which is an oversimplification given that a co-ignimbrite column could

have a broad source (large caldera collapse structure, and extensive ignimbrite outflow sheets) or multiple sources over an area of ten to a hundred km in diameter (Toba caldera is ~ 100 × 30 km, Rose and Chesner, 1987; and Whakamaru is ~ 45 km diameter; Brown et al., 1998a). Finally, the verification of model outputs is hampered by the incompleteness of stratigraphic records, so the isopachs generated must be treated as estimates only. They do, however, provide useful information as discussed here and, as further data become available, they will form a useful basis for future simulations using more sophisticated approaches for describing aggregation and dispersion processes (Costa, A. et al., 2010; Folch et al., 2010).

6.4.4 Eruption environmental impacts

Based on the likely ash dispersal patterns indicated by the modelling here, it is clear that the Toba and Whakamaru eruptions may have had contrasting environmental impacts. Examples of how they differ include the area of land surface covered by ash (~ 3×10^6 km^2 for India in distal regions, and < 10^5 km^2 in the vent-proximal area for New Zealand); possible larger-scale water vapour transport to the lower stratosphere by the Toba eruption (Joshi and Jones, 2009); and potential for ash in the two cases to have affected the two hemispheres differently (e.g., Baines et al., 2008; Whakamaru eruption occurred at mid-latitudes (38°S), compared to the equatorial YTT eruption (2°N)).

The YTT supereruption led to deposition of large quantities of ash across the Indian subcontinent. Such deposition would have caused significant changes to regional surface-water, groundwater and sedimentary systems, resulting in the choking of river valleys and lakes, and catastrophic flooding and burial of land surfaces (c.f. Park and Schmincke, 1997; Manville and Wilson, 2004; Manville et al., 2009). The hypothesised effects of this

eruption have included severe climatic change with the onset of a six-year "volcanic winter" and global glaciation (the eruption occurred at the end of OIS 4; Rampino and Self, 1992; Robock et al., 2009; Williams et al., 2009) and the extinction of human populations (Ambrose, 1998; Rampino and Ambrose, 2000); although more recent studies have suggested that the global consequences of such eruptions may have been less severe than initially assumed (e.g., Bekki et al., 1996; Oppenheimer, 2002; Jones et al., 2007; Timmreck et al., 2010) and that human and animal populations survived the Toba eruption (e.g., Gathorne-Hardy and Harcourt-Smith, 2003; Petraglia et al., 2007).

Proximal terrestrial environmental impacts would have been significant for both eruptions, with a considerable land area (> 10^4 km^2) affected by pyroclastic flows and proximal ashfall in both cases. Following the Whakamaru eruption, instantaneous changes in sedimentary systems over large areas of North Island are likely to have occurred, with burial of existing environments, obliteration of topography and loading of the landscape with large volumes of unconsolidated particulate material (e.g., Park and Schmincke, 1997). Large-scale post-eruption remobilisation of this material, with mass flows and the re-establishment of fluvial systems would have characterised the proximal area. Similar effects have been postulated for the 1.8 ka Taupo eruption, and may have continued for decades subsequently (Manville et al., 2009). Potential terrestrial responses to such a large-scale eruption are likely to depend on a complex interplay between volume, nature and distribution of pyroclastic material, the topography and hydrology of the affected landscape, and the availability of accommodation space (Manville et al., 2009). In contrast to the Whakamaru scenario (where most distal ash was deposited over the Pacific Ocean and Tasman Sea), the YTT eruption impacted a greater total land area, principally because of the deposition of distal ash across India.

The excess humidity in the lower stratosphere likely to have been caused by the YTT eruption would have acted to warm the tropospheric climate and balance the cooling induced by volcanic aerosol (Robock, 2000; Joshi and Jones, 2009). The water vapour transport, which accompanied the eruption, would have been increased with the proximity of the ocean, with the moist co-ignimbrite plumes caused by pyroclastic flows travelling over large expanses of ocean. This would have been less significant for the Whakamaru eruption, with its central North Island location and more buoyant Plinian eruption plume, resulting in less water entrainment from the ocean.

The broader environmental impacts of both eruptions would have depended on the quantities of volatile species released in each case (e.g., SO_2, HCl and HF), but while there are a few constraints on the likely volatile release from the Toba eruption, there are none at all for the Whakamaru eruption. Zielinski et al. (1996) proposed that a sulphate peak observed in the Greenland ice cores (GISP2) at 71 ± 5 ka was generated by the YTT eruption, and suggest a stratospheric loading of sulphate aerosols of 100 – 10000 Mt (e.g., Rose and Chesner, 1990; Scaillet et al., 1998a; Jones et al., 2005). Using melt inclusion constraints, however, Chesner and Luhr (2010) suggest that the YTT eruption most likely generated ~ 150 Mt H_2SO_4 aerosols. While this amount is significant (perhaps four times larger than that of the 1991 Pinatubo eruption; Bluth et al., 1992), it is considerably less than some earlier estimates, and of the same magnitude as that ejected during large basaltic fissure eruptions from Iceland (e.g., ~ 250 Mt H_2SO_4 associated with 1783 – 1784 Laki eruption; Thordarson et al., 1996). The sulphate spike in the Greenland ice cores is therefore more likely associated with a small eruption of sulphur-rich magma from a volcano nearby (e.g. Iceland), than with the sulphur-poor YTT melt. The low sulphur yield from the YTT eruption would suggest that the climatic impact of the eruption may

have been little different from the short-term impacts due to the much smaller volume historical eruptions of Tambora (1815; Self et al., 2004) or Pinatubo (e.g., Robock, 2002).

The high proportion of very fine ash (particularly PM_{10}: 7 – 24% for YTT and 16% for Rangitawa, and ultra-fine particles: 2 – 6% for YTT and 4% for Rangitawa; Table 6.5) in distal deposits from both eruptions indicates that there would exist high potential for human health impacts in such eruptions. PM_{10} ash particles affect humans by causing lung irritation, inflammation, asthma and bronchitis (Horwell and Baxter, 2006; Horwell, 2007). In comparison, deposits of the 1991 Plinian eruption of Mt Pinatubo contain ~ 18% PM_{10} at ~ 30 km from source, while the deposits of the AD79 eruption of Vesuvius contained 33% PM_{10} at 4 km from vent (Horwell, 2007).

It is likely that this fine unconsolidated ash would have prevailed in the environment for months to years after eruption, being re-suspended by wind, with revegetation being the key factor that determined how long the ash remained unconsolidated. The possible monsoonal cycles observed in the reworked YTT sequence in India suggest long-term (> 7 y) recovery of fluvial systems in response to the increased sediment input and indicate the longevity of fine ash in the environment. The amount of re-suspension would have been more significant in sparsely-vegetated fluvial and lacustrine environments (more dust emission; Tegen et al., 2002), thus significantly impacting on populations inhabiting these areas. It is also these areas that would have been attractive to humans existing at ~ 74 ka due to the "hunter-gatherer" mode of existence (Haslam et al., 2010a, b; Jones, this volume) and the daily requirements for drinking water. Potential long-term exposure to resuspended ash would therefore have been high, resulting in heath impacts such as silicosis.

Latitude and atmospheric circulation patterns are significant factors which may influence whether or not an eruption has a global impact. Ash clouds rely on atmospheric winds for their wide dispersal, and the nature and extent of dispersal is dependent primarily on the level within the atmosphere at which the ash is transported (Pyle, 1999). As indicated by the modelling here, ash-rich plumes for both YTT and Whakamaru were injected into the stratosphere. At equatorial latitudes, aerosol and fine tephra are transported rapidly around the globe, before being mixed across both hemispheres, as shown by aerosol studies following the 1991 Pinatubo eruption (e.g., McCormick and Veiga, 1992; Trepte et al., 1993; Hitchman et al., 1994). In contrast, stratospheric aerosol and fine ash from mid- to high-latitude eruptions are more likely to be transported poleward, rather than across both hemispheres, thus limiting their global impact. The Whakamaru supereruption is likely only to have had a significant environmental impact in the Southern Hemisphere, and was thus unlikely to have seriously impacted hominin populations existing at this time. The 26.5 ka Oruanui super-eruption may, however, have had impacts on hominin populations (for example the Aboriginal population in Australia) although these have not yet been studied in any detail.

6.5 Conclusions

The distal YTT and Rangitawa Tephra deposits are both characterised by rhyolitic compositions. The distal deposits have the same major- and trace-element glass composition as the proximal deposits of the eruptions they were correlated to previously. Subtle compositional variations are observed between the Rangitaiki and the Whakamaru members of the Whakamaru Group Ignimbrites. As discussed in Chapter 2, the similar chemical affinity of the distal Rangitawa to the type *A* Whakamaru and Rangitaiki pumices suggests the ashfall deposits are primarily associated with the fallout phase that was associated with the eruption of these ignimbrites. Some of the proximal Whakamaru pumices are altered, while distal tephra deposits are more pristine. This alteration is common in proximal, thick ignimbrite deposits, e.g., Older Toba Tuff (Smith et al., 2011), and potentially hinders correlation of tephra deposits. The lack of compositional variation within and through the distal deposits indicates that they are from a compositionally homogenous eruption phase.

Ash deposited at distal localities during both YTT (> 2000 km from Toba caldera) and Whakamaru (> 900 km from source) eruptions is fine, with > 70% fine particles (< 63 μm) and unimodal particle size distributions with means of 64 – 78 μm and 52 μm respectively. The fine grain sizes for both eruption deposits are suggestive of deposition from the co-ignimbrite plume. Rangitawa Tephra at < 200 km from source is characterised by a coarse crystal-rich basal layer (mean 228 μm), which is absent in distal regions, suggesting that Plinian ashfall dominated in the proximal area. The high proportion of very-fine ash (PM_{10}; 7 – 24% and 16% for YTT and Rangitawa respectively) indicates these large-magnitude silicic eruptions would have had significant impact on human health and the environment in any distant inhabited areas.

Application of the ash dispersal model, HAZMAP, to thickness data of the distal tephra deposits in India and in ocean cores indicates that distal YTT ash is likely to have been derived from the co-ignimbrite eruption column, that reached stratospheric heights of ~ 35 km. Conversely, the observed thicknesses of the Rangitawa Tephra, at distances of > 900 km from the source caldera, are more consistent with deposition from a Plinian column that reached an altitude of ~ 45 km. Two dispersal scenarios are indicated for YTT: one with dispersal dominantly to the west over the Bay of Bengal and India, and the second to the north. Rangitawa Tephra dispersal is to the southwest with more elongated isopachs due to high wind speeds. Significant thicknesses of Rangitawa ashfall (most likely produced during a different phase of the eruption) occur to the northwest of the source area, but these have not been incorporated into modelling here which assumes a uniform wind profile. The modelling also suggests that a large fraction of erupted mass (~ 60%) fell as aggregates of fine ash. It is emphasised that the model output should be interpreted only in terms of potential dispersal scenarios rather than absolute patterns, given the number of assumptions necessary to model dispersal over such a wide area.

Environmental impact for both these supereruptions would have been severe given the mass of material erupted and the widespread dispersal of fine ash. Environmental effects would have differed for the two eruptions, particularly as the terrestrial impact in New Zealand would have been largely in the proximal areas, whereas large areas of distal landmass were impacted for the YTT eruption. These eruptions would have significantly affected sedimentary systems and impacted on human health and other living organisms at distal localities at distances of over a thousand km from the source volcano.

Appendix A6.1: Itrax data for basal YTT and Rangitawa Tephra

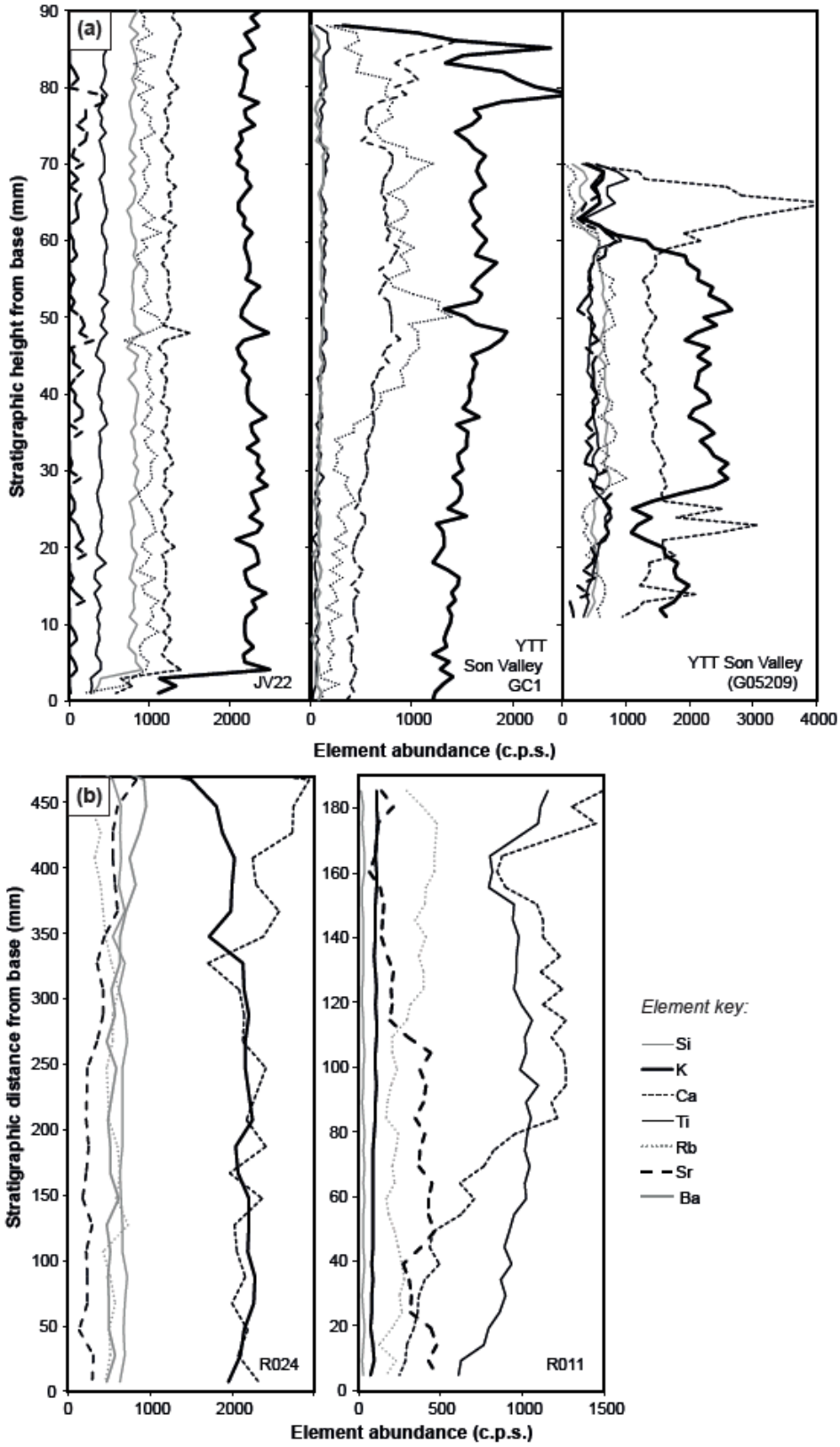

Fig. A6.1: XRF data (by Itrax scanning-XRF) for (a) YTT at Jurreru and Middle Son Valley localities, note reworking starts at ~ 4 – 5 cm above the basal contact; (b) Rangitawa Tephra at Rangitawa Stream and Chatham Island.

Chapter 7

Summary and Conclusions

7.1 Summary of chapter conclusions

The aim of this thesis has been to obtain a better understanding of large silicic magma systems by using crystal-specific micro-analytical techniques in conjunction with field studies, petrological observations and numerical modelling approaches applied to deposits of the ~ 340 ka Whakamaru supereruption, TVZ, New Zealand. Crystal-specific analysis using high-spatial-resolution techniques enables linkages between compositional and temporal records, and reconstruction of pre-eruptive magmatic evolution, and this approach has been the focus of this thesis. The mineral phases analysed in detail here have provided different temporal records which can be integrated to develop a more complete history of assembly and dynamics of a large-volume magma reservoir system (see Section 7.2). Detailed analysis of ashfall deposits, in addition to proximal ignimbrites, further enhances understanding of eruption dynamics, magnitude and environmental impacts.

7.1.1 Petrography and geochemistry of proximal and distal Whakamaru deposits

Petrography and geochemistry of proximal and distal deposits were investigated with the aims of characterising the magma, correlating the distal ashfall units with specific phases of the supereruption, and improving understanding of magma storage and eruption processes (Chapter 2). Whakamaru Group pumices are moderately crystal-rich (up to ~

25%), and contain a mineral assemblage of plagioclase, quartz, orthopyroxene, amphibole, biotite, Fe-Ti oxides and zircon. Mafic-mingled and mixed pumices provide direct evidence for a basaltic recharge event prior to eruption. Plutonic inclusions in pumices indicate that completely crystalline parts of the magma chamber were remobilised and incorporated into the main reservoir (possibly from side-wall crystal mush or assimilated older plutonics).

The high-silica, crystal-rich rhyolite magma which fed the Whakamaru supereruption is characterised by five separate pumice types on the basis of whole-rock geochemistry, classified as types *A, B, C, D* (as defined on the basis of whole-rock chemistry by Brown et al., 1998a) and *mixed-basaltic*. The mixed and mingled basaltic pumice clasts identified within the proximal Rangitaiki and Whakamaru ignimbrites are thought to relate to mafic magma being injected into the base of the chamber immediately prior to eruption, resulting in significant thermo-chemical changes which primed the magma for eruption (see Sections 7.1.2 and 7.1.3).

Type *A* is the most dominant pumice type (~ 89%) and shows the widest compositional variation, most likely due to mixing with basaltic magma. Pumice types *B*, *C* and *D* are similar in terms of glass chemistry, but are characterised by different crystal contents and compositional variation of the crystal cargo (as indicated by the variations in whole-rock chemistry and Sr isotope systematics, Brown et al., 1998a), which suggest that they represent different magma types. Type *D* pumice is the most evolved (high-Rb contents), attributed to its crystal-rich nature and the incorporation of xenocrysts into the magma. Fractional crystallisation modelling fits the range in pumice chemistry for pumice types *A, B, C*, although cannot explain type *D* chemistry. The Whakamaru magmatic system therefore seems to be dominantly a single magma body (97% types *A* and subsidiary *B* and

C, zoned in terms of crystal content and mineralogy), possibly containing a subsidiary melt pocket or side-wall crystal mush (type *D*) which was isolated from fractional crystallisation processes occurring in the main reservoir and evolved separately at a late stage prior to eruption.

On the basis of glass major- and trace-element compositions, the Rangitawa Tephra ashfall deposit correlates with Whakamaru type *A* magma with a minor contribution of Rangitaiki type *A* (identification based on the low CaO glass population). Biotite chemistry for proximal and distal deposits strengthens the correlation to type *A* magma and the eruption phase which produced the Whakamaru and Rangitaiki ignimbrites. Rangitawa Tephra displays little compositional variation with stratigraphy, indicating that relatively homogenous magmas fed the ashfall phase of the eruption.

7.1.2 Magmatic thermal evolution

Various geothermometers were applied to proximal pumices to establish the pre-eruptive state of the magma reservoir system and provide a thermal record of pre-eruptive conditions (Chapter 3). Application of Fe-Ti oxide, feldspar-melt, amphibole and Ti-in-quartz (TitaniQ) geothermometers provide a temperature range of 655 – 975°C for the Whakamaru magmatic system. The eruption temperature is ~ 770°C, as derived from the Fe-Ti oxide and amphibole temperature modes, suggesting that the whole magma body homogenized to this temperature prior to eruption. The wide range in Fe-Ti oxide temperatures is interpreted as due to pluton recycling, and the lower temperature estimates from TitaniQ geothermometry are most likely associated with the assumption of constant a_{TiO2}/pressure/composition throughout crystallisation. Magmatic pressures derived from amphibole geothermometry and quartz melt inclusion data average ~ 110 MPa, equivalent

to shallow levels of magma ponding (at crustal depths of ~ 5 km).

Complex Ti-zoning is observed in the volumetrically important quartz crystals (20 – 40% of the crystal fraction) in Whakamaru and Rangitaiki pumices, with crystals characterised by cycles of resorption, accompanied by temperature/pressure/compositional fluctuations. Application of the TitaniQ geothermometer indicated a ~ 100 °C temperature increase at the crystal rims (assuming constant P, a_{TiO2} and melt composition). The high-resolution thermal record derived from quartz indicates that the system was open to recharge, with multi-stage crystallisation (initial low-T/high-P crystallisation followed by high-T/low-P conditions). Two 'conventional' end-member mechanisms for the formation of high-Ti quartz rims are proposed: (1) a thermal pulse due to mafic underplating of the rhyolitic crystal mush and crystallisation within a single chamber; or (2) adiabatic ascent of the magma resulting in a pressure reduction, resorption, and crystallisation of low-pressure rims during shallow ponding. The presence of mixed basaltic pumices in the Whakamaru and Rangitaiki ignimbrites provides evidence for syn-eruptive mafic recharge and mixing as a driving force during the eruption, and it is inferred that a similar event or events contributed to the resorption and Ti concentration variations recorded in the quartz. Similar quartz zoning patterns have been observed for other large silicic systems such as the Bishop Tuff.

In contrast to the coherent record of P/T changes recorded by quartz crystals, feldspars show complex compositional zoning patterns, indicative of fluctuating temperature, pressure and oxygen fugacity conditions and changing melt compositions throughout crystallisation. Plagioclase crystals are also characterised by numerous resorption horizons, which may relate to successive magma recharge events. High-An plagioclase is most likely derived from hotter, more primitive mafic magma associated with these events.

These complexities in compositional zoning patterns make correlation between individual plagioclase crystals from within a single pumice clast and between pumice clasts difficult. Furthermore, correlation of magmatic conditions and melt composition information from plagioclase with similar records derived from other mineral phases is unlikely to be feasible in such complex, crystal-rich systems.

7.1.3 Timescales of recharge and assembly

Diffusion modelling techniques were applied to trace-element micro-zonation patterns in quartz with the aim of reconstructing recharge and eruption-triggering timescales (Chapter 4). High-resolution synchrotron μ-XRF mapping of quartz shows that Ti transects correlate directly with CL profiles, providing further evidence that Ti is the main activator of CL in quartz, and adding robustness to the use of the CL-greyscale in Ti-in-quartz diffusion modelling. A new 2D Lattice Boltzmann diffusion modelling technique was applied to core-rim boundaries in quartz crystals from the Whakamaru, Younger Toba Tuff (YTT) and Earthquake Flat (EQF) eruptions to establish time periods over which conditions were maintained following a significant change in magmatic P/T conditions prior to eruption (inferred as being the time between the onset of renewed crystal growth and eruption). This modelling approach takes into consideration structural complexities of crystal boundaries, thus providing more reliable diffusion times than traditional 1D approaches. The calculated timescales are, on average, 70 y for Whakamaru, 95 y for YTT and 120 y for EQF, with modal values for Whakamaru and YTT of 35 and 75 y respectively. These represent maximum timescales as modelling is based on the assumption that the compositional step was initially vertical in the modelled profile.

The calibrated Ti CL profiles indicate episodic magma recharge events occurring over extended time periods, pointing to incremental growth of the large-volume magma

reservoir over thousands of years prior to eruption. The final recorded magma recharge event (associated with the event which produced mafic-mingled pumice clasts) may represent the eruption trigger. Both Whakamaru and EQF eruptions show evidence for mafic magma in the petrogenesis of the system, in contrast to YTT where silicic magma may have been the recharge magma and driving force for quartz zonation patterns. Whether or not a recharge event results in eruption is likely to depend on differences in melt composition, crystallinity, temperature, volatile contents and the degree of interaction between the rhyolite and intruding magmas. The similarity of diffusion times for these eruptions indicates that the time between the onset of crystallisation after the reheating event, and prior to eruption, are not dependent on magma volume.

Thermodynamic calculations indicate that an input of a large volume of mafic magma (~ 1000 km^3) would be required to generate the Ti pulse recorded in rims of Whakamaru quartz crystals, if this compositional change were attributed solely to a 100°C temperature rise. Calculations also suggest that rejuvenation of the system, in response to mafic recharge, occurred over a period of $10^3 – 10^4$ y with stirring timescales of < 1 y required to completely homogenise the chamber. The final recharge event recorded by quartz from all three magmatic systems (Whakamaru, YTT and Earthquake Flat) is likely to have primed the magma for eruption, but the timescales suggest that these events are unlikely to have been the eruption-triggering mechanism. The spacing of magma recharge events, volatile transfer and rheology of the intruding and reservoir magmas are likely to be crucial factors in determining whether a major recharge event will result in caldera-forming eruption, rather than a temporary perturbation of the magmatic system. The presence of mixed and mingled pumice clasts in the Whakamaru Group Ignimbrites suggests that a basaltic recharge event occurred as a syn-eruptive or eruption-triggering event (possibly responsible for the resorbed quartz rims).

7.1.4 Zircon-derived magma storage timescales and evolution

Zircon U-Pb dating was undertaken to constrain the magma residence time of the Whakamaru magma system and to address the long-term history of magma assembly and storage (Chapter 5). Whakamaru and Rangitaiki zircons show unimodal age distributions, with a dominant ~ 400 ka peak and ages back to 700 ka, with some recording ages > 100 Ma. The youngest peak represents phenocrysts that grew in the magma body prior to eruption. The older zircon populations are interpreted as representing antecrysts and xenocrysts inherited from older silicic mush or plutonic rocks and assimilated basement material, providing direct evidence for the involvement of crustal material in the Whakamaru storage region. The zircon age spectra indicate that multiple reservoir recharge events and complex mixing and recycling of zircons into the large-volume reservoir occurred over a period of < 100 ky (with continuous growth of the magma reservoir, suggesting a magma accumulation rate of 1.5×10^{-2} km^3 y^{-1}). The exact residence time is, however, difficult to constrain due to the presence of antecrysts and xenocrysts, and it is likely that the reservoir was growing incrementally over this ~ 100 ky period prior to eruption.

Trace-element micro-zonation patterns in dated zircon crystals were investigated with the aim of reconstructing the history of pre-eruptive conditions within the source magma chamber. The variety of zircon textures and CL zoning patterns is indicative of multi-stage zircon growth with complex histories of growth and resorption during waxing/waning parental magma reservoirs. The lack of systematic changes in Hf and Ti with zircon age highlights the complexity of compositional changes in the magma reservoir(s) and provides further evidence for multiple periods of zircon growth and recharge events in pre-eruptive pluton conditions. Variable zircon growth histories recorded by individual grains may also reflect different melt environments and/or crystallisation in different parts of a

large-volume chamber which was experiencing periodic thermochemical changes in response to recharge. Ti-in-zircon thermometry shows fluctuations of > 100°C over short timescales of < 7 ky, attributed to magma recharge during incremental growth and replenishment of the reservoir system.

Oxygen isotope signatures of zircon, quartz and feldspar were analysed to determine the degree of isotopic fractionation and crystal recycling, to constrain core-rim variations, and to identify magma sources. $\delta^{18}O$ data for the dated zircons, in addition to quartz and feldspar crystals extracted from the same pumice clasts, illustrate that the mineral phases crystallised together in isotopic equilibrium (which conflicts with earlier interpretations based on Sr-isotopic evidence; Brown et al., 1998a), and suggest that isotopically homogenous magma sources fed the magma reservoir system over time prior to eruption. Older zircons (> 100 Ma) have elevated $\delta^{18}O$, corresponding to Waipapa and Torlesse greywacke values, and provide further evidence for the role of crustal contamination in TVZ rhyolite petrogenesis. The lack of isotopic intra- and inter-grain $\delta^{18}O$ variability in zircons would suggest that evolving melt composition and magmatic differentiation were limited during crystallisation (with magma source components not changing significantly during magma assembly), although this is inconsistent with the variability in zircon trace-element data.

The zircon crystal record extends the magmatic history derived from quartz-zoning studies and provides evidence for repeated replenishment, fractionation, mixing, and recycling of material in the assembly of the large-volume silicic magma reservoir. Zircon data for the Whakamaru magma system are consistent with other plutonic and volcanic systems which accumulate and evolve over protracted periods of time, with complex histories that require frequent replenishment in order to attain the indicated thermal and compositional fluctuations and the recycling of antecrysts and xenocrysts into the system.

7.1.5 Tephra dispersal and environmental impact

Stratigraphy and grain-size characteristics of ultra-distal ashfall deposits from both the Whakamaru (the Rangitawa Tephra) and YTT supereruptions were investigated with the objective of constraining eruption depositional processes, magnitudes and tephra dispersal mechanisms, and to enhance understanding of the likely environmental impacts of a supereruption (Chapter 6). Glass chemistry enabled correlation of distal deposits to the specific eruption (YTT correlation was strengthened by biotite chemistry on same samples, as presented in Smith et al., 2011). Distal YTT exposures in India (> 2000 km from source) are overthickened through reworking, but show a distinct primary basal ash layer ~ 5 cm thick. Distal Rangitawa Tephra at > 900 km from source is 15 – 30 cm thick. At distances of ~ 200 km from source, Rangitawa Tephra shows pronounced normal grading, a crystal-rich basal layer, and accretionary lapilli (suggestive of a phreatomagmatic origin, although there is no evidence for phreatomagmatic activity in the proximal ignimbrite facies). The fine grain sizes for both eruption deposits at distal locations are suggestive of deposition from co-ignimbrite plumes.

Field observations, stratigraphy and grain-size data for these distal tephra deposits provided input for the semi-analytical ash dispersal model (HAZMAP), with assumptions concerning average wind direction and strength during eruption, column shape and vent size. Modelling based on observed YTT distal tephra thicknesses indicated a relatively low (~ 35 km high), very turbulent eruption column, consistent with deposition from a co-ignimbrite cloud extending over a broad region (primarily to the west over the Bay of Bengal and India), with an eruptive volume of 1500 – 1900 km^3 (DRE). The Whakamaru eruption was modelled as producing a predominantly Plinian column (~ 45 km high), with dispersal to the southeast by strong prevailing winds, and minimum volume of ~ 400 km^3.

The widespread dispersal of large volumes of fine ash from both eruptions would have had global environmental consequences, acutely affecting areas up to thousands of kilometres from vent. The two eruptions differ in terms of the likely environmental impacts due to the area of land surface covered in ash, the latitude of the source volcano, and atmospheric circulation patterns. The near-equatorial YTT eruption would have affected both hemispheres (with potential climatic impacts due to volatile and particulate release), whereas the impacts of the mid-latitude Whakamaru eruption would have been largely restricted to the Southern Hemisphere. Both eruptions would have resulted in the burial of land surfaces and impact on groundwater and sedimentary systems, conditions which would have prevailed for decades after eruption. In particular, the high proportion of very-fine ash (PM_{10}) indicates that such large-magnitude silicic eruptions would have significant impact on human health in any inhabited areas, even at great distances from source.

7.2 Whakamaru magma reservoir model

The detailed field, geochemical, and numerical modelling data presented in this thesis, as summarised above, provide insight into the dynamics of the Whakamaru magmatic system. In particular, the geochemical records derived from volcanic glass, feldspar, quartz and zircon crystals provide evidence that the large-volume silicic magma reservoir system was the result of extended periods of stirring, mixing and reactivation of crystal mush bodies, followed by significant thermal pulses attributed to magma recharge events that remobilised the magma and primed it for eruption over timescales of hundreds to thousands of years. The records and timescales of pre-eruptive magmatic processes derived from different mineral phases are visualised in Fig. 7.1.

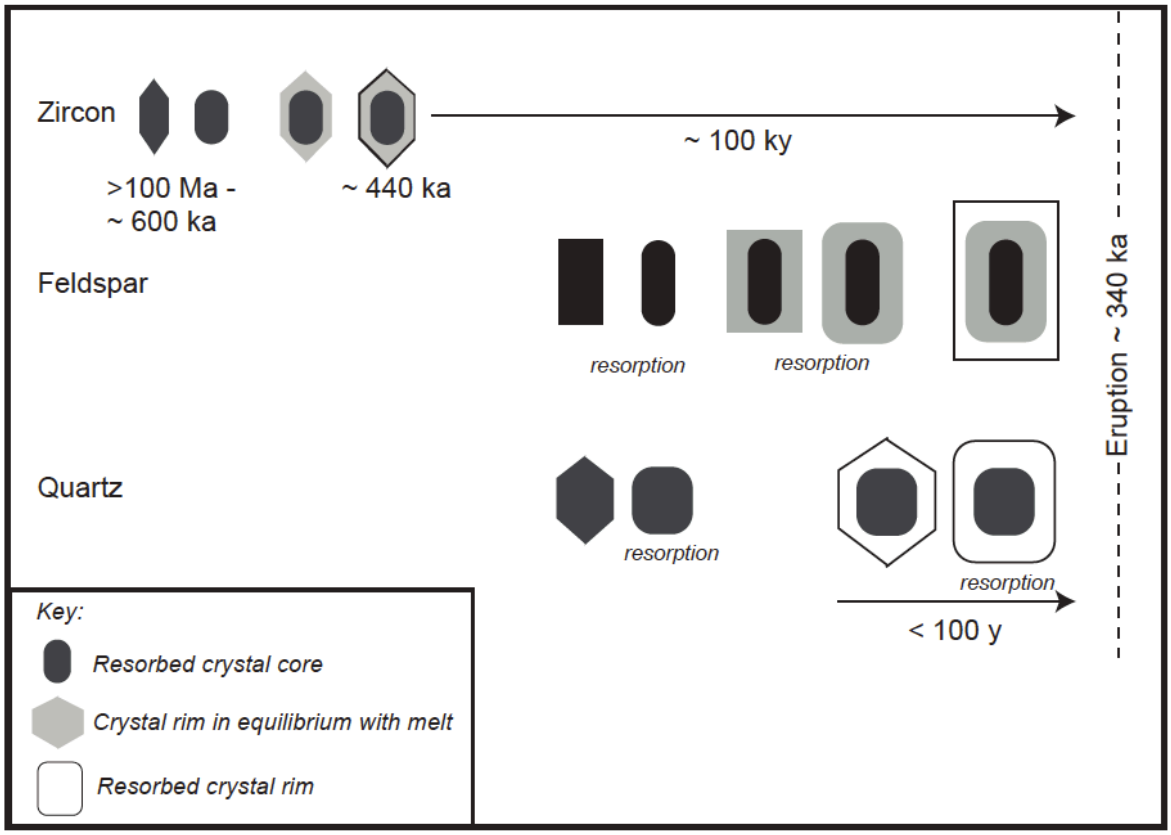

Fig. 7.1: Temporal records derived from different mineral phases (zircon, feldspar and quartz) extracted from pumices from the Whakamaru Group Ignimbrites. Note that different greyscale shades represent discrete crystal zones separated by resorption horizons. Zircon cores are depicted here as xenocrysts and antecrysts (> 100 Ma and ~ 600 ka respectively).

A schematic model for the Whakamaru magmatic system is presented in Fig. 7.2, which brings together the diverse strands of data presented in this thesis. This magma reservoir model incorporates TVZ crustal structure data from Stern and Davey (1987) and Stern et al. (2006). The depth of magma ponding is ~ 5 – < 10 km, derived from pressure estimates from amphibole geothermobarometry and quartz melt inclusion data. The Whakamaru magma reservoir system is depicted as dominantly one large reservoir of type *A* magma, which is stratified in terms of mineralogy (with types *B* and *C* derived from type *A* by fractional crystallisation processes). Type *D* shows related glass and mineral chemistry and similar zircon age spectra and is therefore clearly related to the main magma reservoir.

It is depicted here as forming a subsidiary melt pocket on the basis of its evolved glass geochemistry, crystal-rich nature and isotopic characteristics. Fractional crystallisation modelling for type *D* suggests that this magma body was evolving separately prior to eruption.

Petrography and pumice geochemistry provide evidence for mafic magma recharge events fed from the large-volume reservoir of mafic magma which underplates the TVZ at depths of < ~ 15 km (from Stern et al., 2006), and involving mixing and mingling with the rhyolitic reservoir (being able to penetrate the density contrast at the reservoir base). The role of mafic recharge in the petrogenesis of the Whakamaru magma is also illustrated by quartz Ti-zoning patterns and diffusion timescales which show episodic thermal pulses which shift quartz out of its stability field (changing P/T conditions) over timescales of < 100 to thousands of years prior to eruption. Zircon data indicates that assimilation of pre-existing plutonic material and basement Torlesse and/or Waipapa Terrane also played a role in Whakamaru petrogensisis, and suggests that mixing, fractionation and incremental assembly of the large-volume reservoir occurred over a roughly 100 ky timescale. These factors are incorporated into the Whakamaru system model depicted in Fig. 7.2, with associated timescales shown in Fig. 7.3.

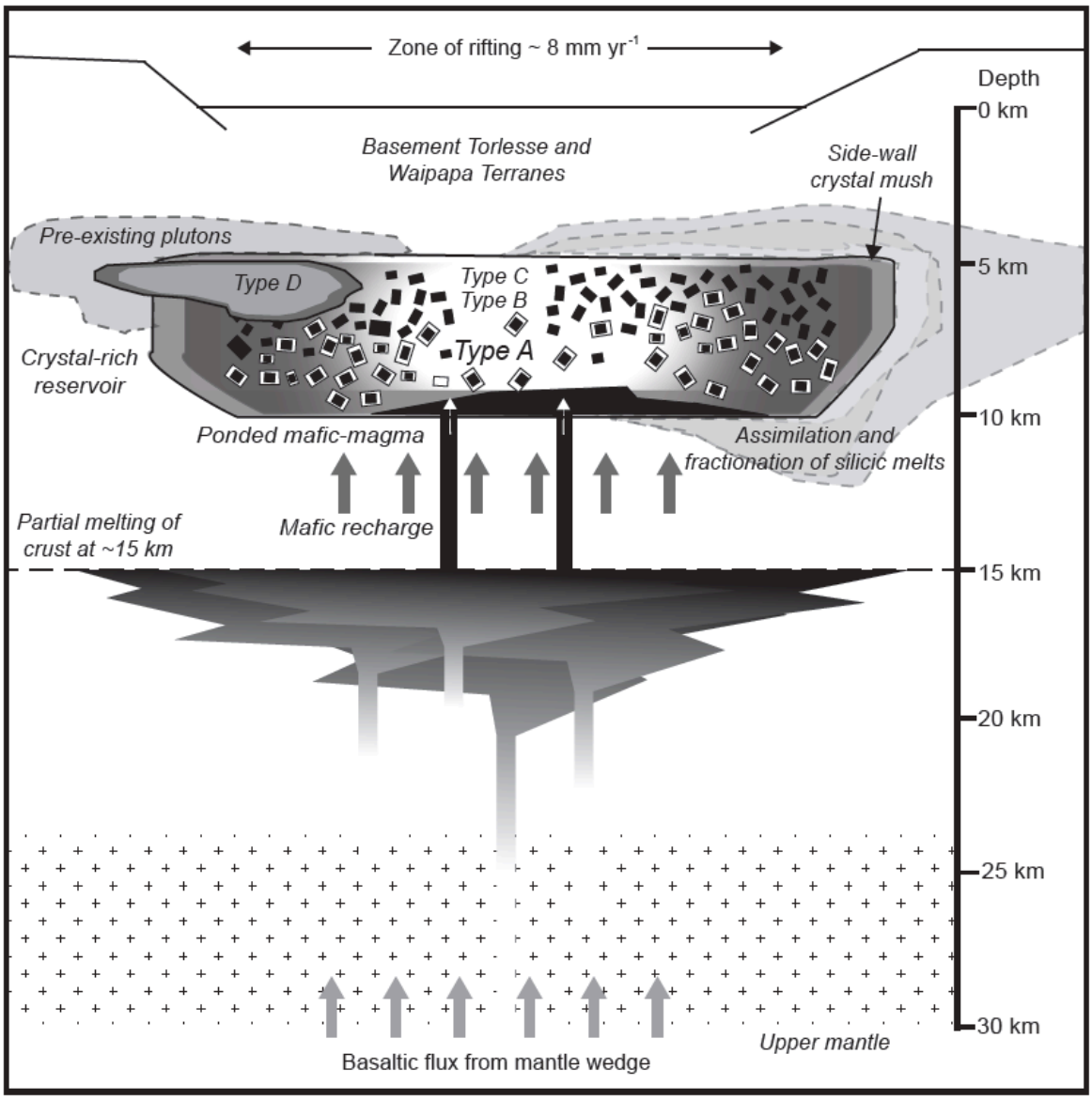

Fig. 7.2: Schematic cross-section of the Whakamaru magmatic system prior to eruption, and crustal structure of central TVZ. The ~ 15 km deep interface between the quartzo-feldspathic crust and denser mafic material below is based on values from Stern and Davey (1987) and Stern et al. (2006). Crustal structure is based on model proposed by Harrison and White (2004, 2006) and Charlier et al. (2005). Fractional crystallisation modelling based on glass chemistry (Chapter 2) shows that type *B* and *C* magmas were derived from the dominantly type *A* magma, whereas type *D* was evolving separately and is therefore indicated as an associated separate chamber. Petrographic evidence indicates assimilation of side-wall crystal mush into the main reservoir (Chapter 2). Depths of the magma reservoir are derived from amphibole, feldspar-melt and quartz melt inclusion pressure estimates (Chapter 3). Evidence for mafic recharge is provided by petrography and glass chemistry (Chapter 2) and quartz zoning patterns (Chapter 3). Diffusion modelling indicates that recharge occurred over multiple episodes with the final event occurring ~ 35 y (or < 100 y) prior to eruption (Chapter 4). Zircon data (Chapter 5) indicate that the basement Torlesse and/or Waipapa metasediment, and material from pre-existing plutons, were incorporated into the Whakamaru magmatic system. Refer also to Fig. 3.13 (e.g., for crystal symbol descriptions).

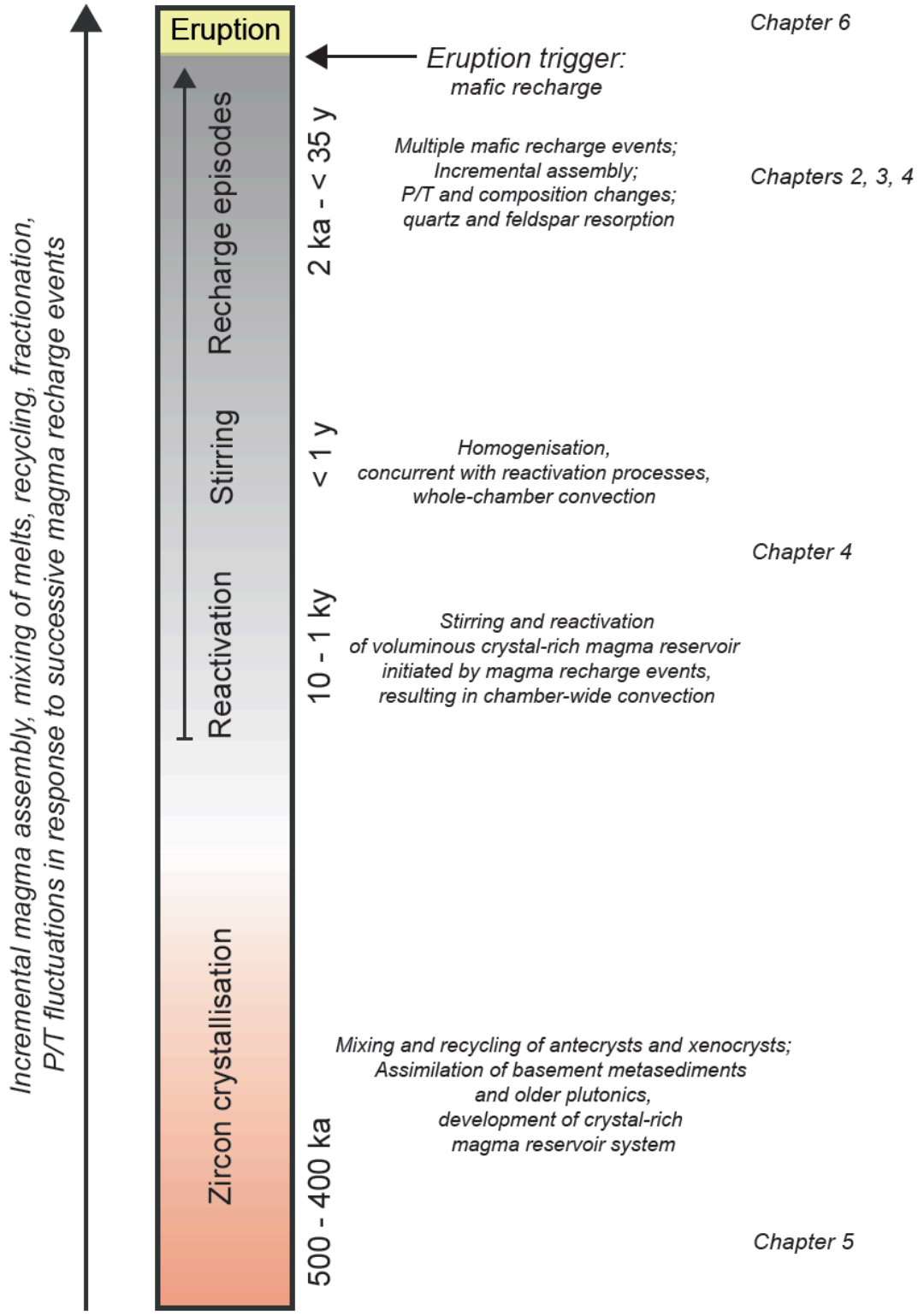

Fig. 7.3: Processes and associated timescales of magma reservoir assembly and development for the Whakamaru magma reservoir system (as pictured in Fig. 7.2). The 'reactivation' process is initiated by influxes of mafic magma below the rhyolitic reservoir. The timescales of 'recharge episodes' are derived from quartz-Ti records. Note that reactivation, stirring and recharge timescales are not presented sequentially but are concurrent processes.

7.3 Future directions

The Whakamaru system is obviously a fruitful area for study and there remains much that could be done. Particular areas which warrant further investigation include the integration of disparate crystal records from large-volume silicic systems; integration of zircon-age and trace-element data with crystal-size distribution studies; addressing the inconsistency between zircon $\delta^{18}O$ and trace element variability; reconstruction of the total-grain-size distribution of the Whakamaru and YTT supereruptions to enable more comprehensive ash dispersal modelling; and research into the long-term environmental and human impacts of supereruptions. Development of tools to compare zonation patterns and textural features for large numbers of crystals would greatly benefit this crystal-specific work (e.g., crystal cladistics). High-resolution mapping of amphibole crystals from the same pumice clasts, with application of geothermobarometry techniques, would provide a valuable comparative record for the quartz zoning patterns discussed in this thesis. Additional high-spatial-resolution trace-element data for feldspar crystals would also allow for the development of more robust P/T/compositional histories which could then be linked to the quartz-derived record. Diffusion modelling applied to other mineral phases (e.g., feldspar and pyroxene) would provide further insight into the timescales of pre-eruptive processes and eruption-triggering mechanisms. Analysis of quartz and zircon-hosted melt inclusions would also provide further constraints on the physical conditions in the pre-eruptive magma reservoir.

In terms of future directions, this work should be integrated with the results of similar research focusing on two other TVZ supereruptions (~ 26.5 ka Oruanui, and ~ 1.0 Ma Kidnappers/Rocky Hill). Analysis of crystal zonation patterns in parallel for all three TVZ supereruptions would enhance present understanding of TVZ magmatism and the dynamics and eruption-triggering processes of supervolcanoes.

References

Acharyya, S. and Basu, P., 1993. Toba ash and the Indian subcontinent and its implications for correlation of Late Pleistocene alluvium. Quaternary Research, 40: 10-19.

Adams, C.J., Barley, M.E., Fletcher, I.P. and Pickard, A.L., 1998. Evidence from U-Pb zircon and $^{40}Ar/^{39}Ar$ muscovite detrital mineral ages for movement of the Torlesse suspect terrane around the eastern margin of Gondwanaland. Terra Nova, 10: 183-189.

Adams, C.J., Mortimer, N., Campbell, H.J. and Griffin, W.L., 2009. Age and isotopic characterisation of metasedimentary rocks from the Torlesse Supergroup and Waipapa Group in the central North Island, New Zealand. New Zealand Journal of Geology and Geophysics, 52: 149-170.

Allegre, C.J., Provost, A. and Jaupart, C., 1981. Oscillatory zoning: a pathological case of crystal growth. Nature, 294: 223-228.

Alloway, B.V., Pillans, B.J., Sandhu, A.S. and Westgate, J.A., 1993. Revision of the marine chronology in the Wanganui Basin, New Zealand, based on the isothermal plateau fission track dating of tephra horizons. Sedimentary Geology, 82: 299-310.

Alloway, B.V., Pillans, B.J., Carter, L., Naish, T.R. and Westgate, J.A., 2005. Onshore-offshore correlation of Pleistocene rhyolitic eruptions from New Zealand: implications for TVZ eruptive history and paleoenvironmental construction. Quaternary Science Reviews, 24: 1601-1622.

Ambrose, S.H., 1998. Late Pleistocene human population bottlenecks, volcanic winter, and differentiation of modern humans. Journal of Human Evolution, 34: 623–651.

Anderson, AT.., 1976. Magma mixing - petrological process and volcanological tool. Journal of Volcanology and Geothermal Reseach, 1: 3-33.

Anderson, A.T., Davis, A.M. and Lu, F., 2000. Evolution of Bishop Tuff rhyolitic magma based on melt and magnetite inclusions and zoned phenocrysts. Journal of Petrology, 41: 449-473.

Andrews, B.J., Gardner, J.E. and Housh, T.B., 2008. Repeated recharge, assimilation, and hybridization in magmas erupted from El Chichón as recorded by plagioclase and amphibole phenocrysts. Journal of Volcanology and Geothermal Research, 175: 415-426.

Annen, C. and Sparks, R.S.J., 2002. Effects of repetitive emplacement of basaltic intrusions on thermal evolution and melt generation in the crust. Earth and Planetary Science Letters, 203: 937-955.

Annen, C., Blundy, J. and Sparks, R.S.J., 2006. The genesis of intermediate and silicic magmas in deep crustal hot zones. Journal of Petrology, 47: 505–539.

Asimow, P.D. and Ghiorso, M.S., 1998. Algorithmic modifications extending MELTS to calculate subsolidus phase relations. American Mineralogist, 83: 1127-1131.

Bachmann, O., 2010. The petrologic evolution and pre-eruptive conditions of the rhyolitic Kos Plateau Tuff (Aegean arc). Central European Journal of Geosciences, 2: 270-305.

Bachmann, O. and Bergantz, G., 2003. Rejuvenation of the Fish Canyon magma body: a window into the evolution of large-volume silicic magma systems. Geology, 31: 789-792.

Bachmann, O. and Bergantz, G.W., 2004. On the origin of crystal-poor rhyolites: extracted from batholithic crystal mushes. Journal of Petrology, 45: 1565-1582.

Bachmann, O. and Bergantz, G.W., 2006. Gas percolation in upper-crustal silicic crystal mushes as a mechanism for upward heat advection and rejuvenation of near-solidus magma bodies. Journal of Volcanology and Geothermal Research, 149: 85-102.

Bachmann, O. and Bergantz, G., 2008. The magma reservoirs that feed supereruptions. Elements, 4: 17-21.

Bachmann, O., Dungan, M.A. and Lipman, P.W., 2002. The Fish Canyon magma body, San Juan volcanic field, Colorado: rejuvenation and eruption of an upper-crustal batholith. Journal of Petrology, 43: 1469-1503.

Bachmann, O., Charlier, B.L.A. and Lowenstern, J.B., 2007a. Zircon crystallisation and recycling in the magma chamber of the rhyolitic Kos Plateau Tuff (Aegean arc). Geology, 35: 73-76.

Bachmann, O., Oberli, F., Dungan, M.A., Meier, M., Mundil, R. and Fischer, H., 2007b. $^{40}Ar/^{39}Ar$ and U-Pb dating of the Fish Canyon magmatic system, San Juan Volcanic field, Colorado: evidence for an extended crystallisation history. Chemical Geology, 236: 134-166.

Bachmann, O., Schoene, B., Schnyder, C. and Spikings, R., 2010. The $^{40}Ar/^{39}Ar$ and U/Pb dating of young rhyolites in the Kos-Nisyros volcanic complex, Eastern Aegean Arc, Greece: age discordance due to excess ^{40}Ar in biotite. Geochemistry, Geophysics, Geosystems, 11: Q0AA08, doi:10.1029/2010GC003073.

Bacon, C.R. and Hirschmann, M.M., 1988. Mg/Mn partitioning as a test for equilibrium between coexisting Fe-Ti oxides. American Mineralogist, 73: 57-61.

Bacon, C.R. and Lowenstern, J.B., 2005. Late Pleistocene granodiorite source for recycled zircon and phenocrysts in rhyodacite lava at Crater Lake, Oregon. Earth and Planetary Science Letters, 233: 277–293.

Bailey, R.A., Dalrymple, G.B. and Lanphere, M.A., 1976. Volcanism, structure, and geochronology of Long Valley caldera, Mono County, California. Journal of Geophysical Research, 81: 725-744.

Bailey, R.A., and Carr, R.G., 1994. Matahina Ignimbrite, Taupo Volcanic Zone: physical geology and eruptive history. New Zealand Journal of Geology and Geophysics, 37: 319-344.

Baines, P.G., Jones, M.T. and Sparks, R.S.J., 2008. The variation of large-magnitude volcanic ash cloud formation with source latitude. Journal of Geophysical Research, 113: D21204.

Baker, D.R., 2008. The fidelity of melt inclusions as records of melt composition. Contributions to Mineralogy and Petrology 156: 377-395.

Barth, A.P. and Wooden, J.L., 2010. Coupled elemental and isotopic analyses of polygenetic zircons from granitic rocks by ion microprobe, with implications for

melt evolution and the sources of granitic magmas. Chemical Geology, 277: 149-159.

Basu, P.K., Biswas, S. and Acharayya, S.K., 1987. Late Quaternary ash beds from Son and Narmada basins, Madhya Pradesh. Indian Minerals, 41: 66-72.

Bekki, S., Pyle, J.A., Zhong, W., Toumi, R., Haigh, J.D. and Pyle, D.M., 1996. The role of microphysical and chemical processes in prolonging the climate forcing of the Toba eruption. Geophysical Research Letters, 23: 2669-2672.

Belousova, E.A., Griffin, W.L., O'Reilly, S.Y. and Fisher, N.I., 2002. Igneous zircon: trace element composition as an indicator of source rock type. Contributions to Mineralogy and Petrology, 143: 602–622.

Beresford, S.W., and Cole, J.W., 2000. Kaingaroa Ignimbrite, Taupo Volcanic Zone, New Zealand: Evidence for asymmetric caldera subsidence of the Reporoa Caldera. New Zealand Journal of Geology and Geophysics, 43: 471-481.

Bergantz, G.W., 1989. Underplating and partial melting: implications for melt generation and extraction. Science, 245: 1093-1094.

Berry, A.J., O'Neill, H.S., Scott, D.R., Foran, G.J. and Shelley, J.M.G., 2006. The effect of composition on Cr^{2+}/Cr^{3+} in silicate melts. American Mineralogist, 91: 1901-1908.

Berryman, K.R., Villamor, P., Nairn, I.A., Van Dissen, R.J., Begg, J.G. and Lee, J., 2008. Late Pleistocene surface rupture history of the Paeroa Fault, Taupo Rift, New Zealand. New Zealand Journal of Geology and Geophysics, 51: 135-158.

Best, M.G. and Christiansen, E.H., 1997. Origin of broken phenocrysts in ash-flow tuffs. Geological Society of America Bulletin, 109: 63-73.

Bhatnagar, P., Gross, E. and Krook, A., 1954. A model for collisional processes in gases I: small amplitude processes in charged and neutral one component systems. Physical Review, 94: 511-525.

Bibby, H.M., Caldwell, T.G., Davey, F.J. and Webb, T.H., 1995. Geophysical evidence on the structure of the Taupo Volcanic Zone and its hydrothermal circulation. Journal of Volcanology and Geothermal Research, 68: 29-58.

Bindeman, I.N., 2005. Fragmentation phenomena in populations of magmatic crystals. American Mineralogist, 90: 1801-1815.

Bindeman, I.N. and Valley, J.W., 2001. Low-$\delta^{18}O$ rhyolites from Yellowstone: magmatic evolution based on analyses of zircons and individual phenocrysts. Journal of Petrology, 42: 1491-1517.

Bindeman, I.N., and Valley, J.W., 2002. Oxygen isotope study of the Long Valley magma system, California: isotope thermometry and convection in large silicic magma bodies. Contributions to Mineralogy and Petrogy, 144: 185-205.

Bindeman, I.N., Davis, A.M. and Drake, M.J., 1998. Ion microprobe study of plagioclase-basalt partition experiments at natural concentration levels of trace elements. Geochimica et Cosmochimica Acta, 62: 1175-1193.

Bindeman, I.N., Valley, J.W., Wooden, J.L. and Persing, H.M., 2001. Post-caldera volcanism: in situ measurement of U-Pb age and oxygen isotope ratio in Pleistocene zircons from Yellowstone caldera. Earth and Planetary Science Letters, 189: 197-206.

Birrell, K.S., Stevens, K.F. and Vucetich, C.G., 1981. Late Quaternary sections containing tephra and loess in the Te Kuiti district, New Zealand. Geology Department, Victoria University of Wellington Publication, 20: 5-10.

Black, L.P., Kamo, S.L., Allen, C.M., Davis, D.W., Aleinikoff, J.N., Valley, J.W., Mundil, R., Campbell, I.H., Korsch, R.J., Williams, I.S., and Foudoulis, C., 2004. Improved $^{206}Pb/^{238}U$ microprobe geochronology by the monitoring of a trace-element-related matrix effect; SHRIMP, ID-TIMS, ELA-ICP-MS and oxygen isotope documentation for a series of zircon standards. Chemical Geology, 205: 115–140.

Blake, S., 1984. Volatile oversaturation during the evolution of silicic magma chambers as an eruption trigger. Journal of Geophysical Research, 89: 8237-8244.

Blake, S. and Ivey, G.N., 1986. Magma-mixing and the dynamics of withdrawal from stratified reservoirs. Journal of Volcanology and Geothermal Research, 27: 153-178.

Blake, S., Wilson, C.J.N., Smith, I.E.M. and Walker, G.P.L., 1992. Petrology and dynamics of the Waimihia mixed magma eruption, Taupo Volcano, New Zealand. Journal of the Geological Society of London, 149: 193-207.

Blank, H.R., 1965. Ash flow deposits of the central King Country, New Zealand. New Zealand Journal of Geology and Geophysics, 8: 588-607.

Blattner, P. and Reid, F., 1982. The origin of lavas and ignimbrites of the Taupo Volcanic Zone, New Zealand, in the light of oxygen isotope data. Geochemica et Cosmochimica Acta, 46: 1417-1429.

Blattner, P., Rui-Zhong, H., Graham, I.J. and Houston-Eleftheriadis, C., 1996. Temperatures and isotopic evolution of silicic magmas, Taupo Volcanic Zone and Coromandel, New Zealand. New Zealand Journal of Geology and Geophysics, 39: 353-362.

Blott, S.J. and Pye, K., 2001. Gradistat: a grain size distribution and statistics package for the analysis of unconsolidated sediments. Earth Surface Processes and Landforms, 26: 1237–1248.

Blott, S.J., Croft, D.J., Pye, K., Saye, S.E. and Wilson, H.E., 2004. Particle size analysis by laser diffraction. Geological Society of London Special Publications, 232: 63-73.

Blundy, J.D and Cashman, K., 2001. Ascent-driven crystallization of dacite magmas at Mount St Helens, 1980-1986. Contributions to Mineralogy and Petrology, 140: 631-650.

Blundy, J.D. and Cashman, K., 2008. Petrologic reconstruction of Magmatic System Variables and Processes. Reviews in Mineralogy and Geochemistry, 69: 179-239.

Blundy, J. D. and Shimizu, N., 1991. Trace element evidence for plagioclase recycling in calc-alkaline magmas. Earth and Planetary Science Letters, 102: 178-197.

Blundy, J.D. and Wood, B.J., 1991. Crystal-chemical controls on the partitioning of Sr and Ba between plagioclase feldspar, silicate melts, and hydrothermal solutions. Geochimica et Cosmochimica Acta, 55: 193-209.

Bluth, G.J.S., Doiron, S.D., Schnetzler, C.C., Krueger, A.J. and Walter, R.S., 1992. Global tracking of the SO_2 clouds from the June 1991 Mount Pinatubo eruptions. Geophysical Research Letters, 19: 151-154.

Boellstorff, J.D. and Te Punga, M.T., 1977. Fission-track ages and correlation of upper and lower Pleistocene sequences from Nebraska and New Zealand. New Zealand Journal of Geology and Geophysics, 20: 47-58.

Bonadonna, C., Ernst, G.G.J. and Sparks, R.S.J., 1998. Thickness variations and volume estimates of tephra fall deposits: the importance of particle Reynolds number. Journal of Volcanology and Geothermal Research, 81: 173-187.

Bonadonna, C. and Houghton, B.F., 2005. Total grain-size distribution and volume of tephra-fall deposits. Bulletin of Volcanology, 67: 441-456.

Bonasia, R., Macedonio, G., Costa, A., Mele, D. and Sulpizio, R., 2010. Numerical inversion and analysis of tephra fallout deposits from the 472 AD sub-Plinian eruption at Vesuvius (Italy) through a new best-fit procedure. Journal of Volcanology and Geothermal Research, 189: 238-246.

Bottinga, Y. and Javoy, M., 1973. Comments on oxygen isotope geothermometry. Earth and Planetary Science Letters, 20: 250-265.

Bottinga, Y. and Javoy, M., 1975. Oxygen isotope partitioning among the minerals in igneous and metamorphic rocks. Reviews of Geophysics and Space Physics, 13: 401-418.

Bowen, N.L., 1928. The Evolution of the Igneous Rocks. Princeton University Press, Princeton, NJ.

Branney, M.J. and Kokelaar, P., 1992. A reappraisal of ignimbrite emplacement: progressive aggradation and changes from particulate to non-particulate flow during emplacement of high-grade ignimbrite. Bulletin of Volcanology, 54: 504-520.

Branney M.J. and Kokelaar B.P., 2003. Pyroclastic Density Currents and the Sedimentation of Ignimbrites. Geological Society of London Memoir, 27: pp 152.

Briggs, N.D., 1973. Investigations of New Zealand pyroclastic flow deposits. Ph.D. thesis, Victoria University, Wellington, New Zealand.

Briggs, N.D., 1976a. Recognition and correlation of subdivisions within the Whakamaru ignimbrite, central North Island, New Zealand. New Zealand Journal of Geology and Geophysics, 19: 463-501.

Briggs, N.D., 1976b. Welding and crystallization zonation in Whakamaru ignimbrite, central North Island, New Zealand. New Zealand Journal of Geology and Geophysics, 19: 189-212.

Briggs R.M., Gifford, M.G., Moyle, A.R., Taylor, S.R., Norman, M.D., Houghton, B.F. and Wilson, C.J.N. 1993. Geochemical zoning and eruptive mixing in ignimbrites from Mangakino volcano, Taupo Volcanic Zone, New Zealand. Journal of Volcanology and Geothermal Research, 56: 175-203.

Briggs, R.M., Houghton, B.F., McWilliams, M. and Wilson, C.J.N., 2005. $^{40}Ar/^{39}Ar$ ages of silicic volcanic rocks in the Tauranga-Kaimai area, New Zealand: dating the transition between volcanism in the Coromandel Arc and the Taupo Volcanic Zone. New Zealand Journal of Geology and Geophysics, 48: 459-469.

Brown, S.J.A., 1994. Geology and geochemistry of the Whakamaru group ignimbrites, and associated rhyolite domes, Taupo Volcanic Zone, New Zealand. PhD thesis, University of Canterbury, Christchurch, New Zealand.

Brown, S.J.A. and Fletcher, I., 1999. SHRIMP U-Pb dating of the preeruption growth history of zircons from the 340 ka Whakamaru Ignimbrite, New Zealand: Evidence for > 250 k.y. magma residence times. Geology, 27(11): 1035-1038.

Brown, S.J.A. and Smith, R.T., 2004. Crystallisation history and crustal inheritance in a large silicic magma system: $^{206}Pb/^{238}U$ ion probe dating of zircons from the 1.2 Ma Ongatiti ignimbrite, Taupo Volcanic Zone. Journal of Volcanology and Geothermal Research, 135: 247-257.

Brown, S.J.A., Wilson, C.J.N., Cole, J.W. and Wooden J., 1998a. The Whakamaru group ignimbrites, Taupo Volcanic Zone, New Zealand: evidence for reverse tapping of a zoned silicic magmatic system. Journal of Volcanology and Geothermal Research, 84: 1-37.

Brown, S.J.A, Burt, R.M., Cole, J.W., Krippner, S.J.P., Price, R.C. and Cartwright, I., 1998b. Plutonic lithics in ignimbrites of Taupo Volcanic Zone, New Zealand; sources and conditions of crystallisation. Chemical Geology, 148: 21-41.

Bryan, C.J., Sherburn, S., Bibby, H.M., Bannister, S. and Hurst, A.W., 1999. Shallow seismicity of the central Taupo Volcanic Zone, New Zealand: its distribution and nature. New Zealand Journal of Geology and Geophysics, 42: 533-542.

Bühring, C., Sarnthein, M. and Leg 184 Shipboard Scientific Party, 2000. Toba ash layers in the South China Sea: Evidence of contrasting wind directions during eruption ca. 74 ka. Geology, 28: 275-278.

Burnham, A.P. and Berry, A.J., 2011. Zircon as a probe of the oxidising environment of magmas. Unpublished report for Edinburgh Ion Microprobe Facility, IMF 409/0510.

Burt, R.M., Brown, S.J.A., Cole, J.W., Shelley, D. and Waight, T.E., 1998. Glass-bearing plutonic fragments from ignimbrites of the Okataina caldera complex, Taupo Volcanic Zone, New Zealand: remnants of a partially molten intrusion associated with preceding eruptions. Journal of Volcanology and Geothermal Research, 84: 209-237.

Campbell, M.E., Hanson, J.B., Minarik, W.G. and Stix, J., 2009. Thermal history of the Bandelier magmatic system: evidence for magmatic injection and recharge at 1.61 Ma as revealed by cathodoluminescence and titanium geothermometry. Journal of Geology, 117: 469-485.

Carey, S. and Sparks, R.S.J., 1986. Quantitative models of the fall out and dispersal of tephra from volcanic eruption columns. Bulletin of Volcanology, 48: 109–125.

Carter, L., Alloway, B., Shane, P. and Westgate, J., 2004. Deep-ocean record of major late Cenozoic rhyolitic eruptions from New Zealand. New Zealand Journal of Geology and Geophysics, 47: 481–500.

Cavosie, A.J., Valley, J.W., Wilde, S.A. and E.I.M.F, 2005. Magmatic $\delta^{18}O$ in 4400-3900 Ma detrital zircons: A record of the alteration and recycling of crust in the Early Archean. Earth and Planetary Science Letters, 235: 663-681.

Cavosie, A.J., Valley, J.W., Wilde, S.A., and E.I.M.F., 2006. Correlated microanalysis of zircon: trace element, $\delta^{18}O$, and U–Th–Pb isotopic constraints on the igneous origin of complex >3900 Ma detrital grains. Geochimica et Cosmochimica Acta, 70: 5601–5616.

Charlier, B.L.A. and Wilson, C.J.N., 2010. Chronology and evolution of caldera-forming and post-caldera magma systems at Okataina Volcano, New Zealand from zircon U-Th model-age spectra. Journal of Petrology, 51: 1121-1141.

Charlier, B.L. and Zellmer, G., 2000. Some remarks on U-Th mineral ages from igneous rocks with prolonged cystallisation histories. Earth and Planetary Science Letters, 183: 457-469.

Charlier, B.L.A., Peate, D.W., Wilson, C.J.N., Lowenstern, J.B., Storey, M. and Brown, S.J.A., 2003. Crystallisation ages in coeval silicic magma bodies: ^{238}U–^{230}Th-disequilibrium evidence from the Rotoiti and Earthquake Flat eruption deposits, Taupo Volcanic Zone, New Zealand. Earth and Planetary Science Letters, 206: 441-457.

Charlier, B.L.A., Wilson, C.J.N., Lowenstern, J.B., Blake, S., van Calsteren, P.W. and Davidson, J.P., 2005. Magma generation at a large, hyperactive silicic volcano (Taupo, New Zealand) revealed by U-Th and U-Pb systematics in zircons. Journal of Petrology, 46: 3-32.

Charlier, B.L.A., Bachmann, O., Davidson, J.P., Dungan M.A. and Morgan, D.J., 2007. The upper crustal evolution of a large silicic magma body: evidence from crystal-scale Rb–Sr isotopic heterogeneities in the Fish Canyon magmatic system, Colorado. Journal of Petrology, 48: 1875-1894.

Charlier, B.L.A., Wilson, C.J.N. and Davidson, J.P., 2008. Rapid open-system assembly of a large silicic magma body: time-resolved evidence from cored plagioclase crystals in the Oruanui eruption deposits, New Zealand. Contributions to Mineralogy and Petrology, 156: 799-813.

Charlier, B.L.A., Wilson, C.J.N. and Mortimer, N., 2010. Evidence from zircon U-Pb age spectra for crustal structure and felsic magma genesis at Taupo volcano, New Zealand. Geology, 38: 915-918.

Chase, C.G., 1978. Plate kinematics: the Americas, East Africa and the rest of the world. Earth and Planetary Science Letters, 37: 355-368.

Cherniak, D.J. and Watson, E.B., 2007. Ti diffusion in zircon. Chemical Geology, 242: 470-483.

Cherniak, D.J., Watson, E.B. and Wark, D.A., 2007. Ti diffusion in quartz. Chemical Geology, 236: 65-74.

Chesner, C.A., 1998. Petrogenesis of the Toba Tuffs, Sumatra, Indonesia. Journal of Petrology, 39: 397-438.

Chesner, C.A. and Luhr, J.F., 2010. A melt inclusion study of the Toba Tuffs, Sumatra, Indonesia. Journal of Volcanology and Geothermal Research, 197: 259-278.

Chesner, C.A. and Rose, W.I., 1991. Stratigraphy of the Toba Tuffs and the evolution of the Toba Caldera Complex, Sumatra, Indonesia. Bulletin of Volcanology, 53: 343-356.

Chesner, C.A., Rose, W.I., Deino, A., Drake, R. and Westgate, J.A., 1991. Eruptive history of Earth's largest Quaternary caldera (Toba, Indonesia) clarified. Geology, 19: 200-203.

Chivas, A.R., Andrew, A.S., Sinha, A.K. and O'Neil, J.R., 1982. Geochemistry of a Pliocene-Pleistocene oceanic-arc plutonic complex, Guadalcanal. Nature, 300: 139-143.

Chopard, B. and Droz, M., 1998. Cellular automata and modeling of physical systems. Cambridge University Press, Cambridge, UK.

Christensen, J.N. and DePaolo, D.J., 1993. Time scales of large volume silicic magma systems: Sr isotopic systematics of phenocrysts and glass from the Bishop Tuff, Long Valley, California. Contributions to Mineralogy and Petrology, 113: 100-114.

Christensen, J.N. and Halliday, A.N., 1996. Rb–Sr ages and Nd isotopic compositions of melt inclusions from the Bishop Tuff and the generation of silicic magma. Earth and Planetary Science Letters, 144: 547-561.

Christiansen, R.L., 2001. The Quaternary and Pliocene Yellowstone Plateau Volcanic

Field of Wyoming, Idaho, and Montana. U.S. Geological Survey Professional Paper 729-G.

Claiborne, L.L., Miller, C.F., Walker, B.A., Wooden, J.L., Mazdab, F.K. and Bea, F., 2006. Tracking magmatic processes through Zr/Hf rations in rocks and Hf and Ti zoning in zircons: an example from the Spirit Mountain batholith, Nevada. Mineralogical Magazine, 70: 517-543.

Claiborne, L.L., Miller, C.F., Flanagan, D.M., Clynne, M.A. and Wooden, J.L., 2010. Zircon reveals protracted magma storage and recycling beneath Mount St. Helens. Geology, 38: 1011-1014.

Cole, J.W., 1990. Structural control and origin of volcanism in the Taupo Volcanic Zone, New Zealand. Bulletin of Volcanology, 52: 445-459.

Cole, J.W. and Lewis, K.B., 1981. Evolution of the Taupo-Hikurangi subduction system. Tectonophysics, 72: 1-21.

Coleman, D.S., Gray, W. and Glazner, A.F., 2004. Rethinking the emplacement and evolution of zoned plutons: geochronologic evidence for incremental assembly of the Tuolumne Intrusive Suite, California. Geology, 32: 433-436.

Coltice, N. and Schmalzl, J., 2006. Mixing times in the mantle of the early Earth derived from 2-D and 3-D numerical simulations of convection. Geophysical Research Letters 33, L23304, doi:10.1029/2006GL027707.

Coombs, M.L., Eichelberger, J.C. and Rutherford, M.J., 2000. Magma storage and mixing conditions for the 1953-1974 eruptions of Southwest Trident volcano, Katmai National Park, Alaska. Contributions to Mineralogy and Petrology, 140: 99-118.

Coombs, M.L. and Gardner, J.L., 2001. Shallow-storage conditions for the rhyolite of the 1912 eruption at Novarupta, Alaska. Geology, 29: 775-778.

Corfu, F., Hanchar, J.M., Hoskin, P.W.O. and Kinny, P., 2003. Atlas of zircon textures. Reviews in Mineralogy and Geochemistry, 53: 469-500.

Cornell, W., Carey, S. and Sigurdsson, H., 1983. Computer simulation of transport and deposition of the Campanian Y-5 ash. Journal of Volcanology and Geothermal Research, 17: 89-109.

Costa, A., Dell'Erba, F., Di Vito, M.A., Isaia, R., Macedonio, G., Orsi, G. and Pfeiffer, T., 2009. Tephra fallout hazard assessment at the Campi Flegrei caldera (Italy). Bulletin of Volcanology, 71: 259-273.

Costa, A., Folch, A. and Macedonio, G., 2010. A model for wet aggregation of ash particles in volcanic plumes and clouds: 1. Theoretical formulation. Journal of Geophysical Research, 115, B09201.

Costa, F., 2008. Residence times of silicic magmas associated with calderas. Developments in Volcanology, 10: 1-55.

Costa, F. and Chakraborty, S., 2004. Decadal time gaps between mafic intrusion and silicic eruption obtained from chemical zoning patterns in olivine. Earth and Planetary Science Letters, 227: 517–530.

Costa, F. and Dungan, M., 2005. Short time scales of magmatic assimilation from diffusion modeling of multiple elements in olivine. Geology, 33: 837-840.

Costa, F. and Morgan, D., 2010. Time constraints from chemical equilibration in magmatic crystals. *In:* Timescales of magmatic processes: from core to atmosphere, Dosseto, A., Turner, S.P., Van Orman, J.A. (Editors). Wiley-Blackwell: Chichester UK.

Costa, F., Dohmen, R. and Chakraborty, S., 2008. Time scales of magmatic processes from modeling the zoning patterns of crystals. Reviews in Mineralogy and Geochemistry, 69: 545–594.

Costa, F., Coogan, L.A. and Chakraborty, S., 2010. The timescales of magma mixing and mingling involving primitive melts and melt-mush interaction at mid-ocean ridges. Contributions to Mineralogy and Petrology, 159: 371-387.

Cottrell, E., Gardner, J.E. and Rutherford, M.J., 1999. Petrologic and experimental evidence for the movement and heating of the pre-eruptive Minoan rhyodacite (Santorini, Greece). Contributions to Mineralogy and Petrology, 135: 315-331.

Crowley, J.L., Schoene, B. and Bowring, S.A., 2007. U-Pb dating of zircon in the Bishop Tuff at the millennial scale. Geology, 35: 1123-1126.

Dalrymple, G.B., Grove, M., Lovera, O.M., Harrison, T.M., Hulen, J.B. and Lanphere, M.A., 1999. Age and thermal history of the Geysers plutonic complex (felsite unit),

Geysers geothermal field, California: a $^{40}Ar/^{39}Ar$ and U–Pb study. Earth and Planetary Science Letters, 173: 285–298.

Davey, F.J., Henrys, S.A. and Lodolo, E., 1995. Asymmetric rifting in a continental back-arc environment, North Island, New Zealand. Journal of Volcanology and Geothermal Research, 68: 209-238.

Davidson, J.P. and Tepley, F.J., 1997. Recharge in volcanic systems: Evidence from isotope profiles of phenocrysts. Science, 275: 826-829.

Davidson, J.P., Tepley, F., Palacz, Z. and Meffan-Main, S., 2001. Magma recharge, contamination and residence times revealed by in situ laser ablation isotopic analysis of feldspar in volcanic rocks. Earth and Planetary Science Letters, 184: 427-442.

Davies, G.R. and Halliday, A.N., 1998. Development of the Long Valley rhyolite magma system: strontium and neodymium isotope evidence from glasses and individual phenocrysts. Geochimica et Cosmochimica Acta, 62: 3561-3574.

Davies, G.R., Halliday, A.N., Mahood, G.A. and Hall, C.M., 1994. Isotopic constraints on the production rates, crystallization histories and residence times of pre-caldera silicic magmas, Long Valley, California. Earth and Planetary Science Letters, 125: 17–37.

Davis, M., Koenders, M.A. and Petford, N., 2007. Vibro-agitation of chambered magma. Journal of Volcanology and Geothermal Research, 167: 24-36.

de la Cruz-Reyna, S., Tárraga, M., Ortiz, R. and Martínez-Bringas, A., 2010. Tectonic earthquakes triggering volcanic seismicity and eruptions. Case studies at Tungurahua and Popocatépetl volcanoes. Journal of Volcanology and Geothermal Research, 193: 37-48.

de Silva, S.L. and Francis, P.W., 1989. Correlation of large ignimbrites: two case studies from the Central Andes of north Chile. Journal of Volcanology and Geothermal Research, 37: 133-149.

de Silva, S., Bachmann, O., Miller, C., Yoshida, T. and Knesel, K., 2007. Large silicic magma systems. Journal of Volcanology and Geothermal Research, 167: vii-ix.

de Silva, S., Salas, G. and Schubring, S., 2008. Triggering explosive eruptions - The case for silicic magma recharge at Huaynaputina, southern Peru. Geology, 36: 387-390.

Devine, J.D., Rutherford, M.J., Norton, G.E. and Young, S.R., 2003. Magma storage region processes inferred from geochemistry of Fe-Ti oxides in andesitic magma, Soufriere Hills volcano, Montserrat, W.I. Journal of Petrology, 44: 1375-1400.

Dickinson, J.E., Hess, P.C. and Rutherford, M.J., 1980. REE partitioning between zircon, whitlockite and two liquids. EOS, Transactions of the American Geophysical Union, 61: 397.

Donoghue, E., Troll, V.R., Harris, C., O'Halloran, A., Walter, T.R. and Torrado, F.J.P., 2008. Low-temperature hydrothermal alteration of intra-caldera tuffs, Miocene Tejeda caldera, Gran Canaria, Canary Islands. Journal of Volcanology and Geothermal Research, 176: 551-564.

Dufek, J. and Bergantz, G.W., 2005. Lower crustal magma genesis and preservation: a stochastic framework for the evaluation of basalt-crust interaction. Journal of Petrology, 46: 2167-2195.

Dugmore, A.J., Larsen, G. and Newton, A.J., 2004. Tephrochronology and its application to late Quaternary environmental reconstruction, with special reference to the North Atlantic islands. *In:* Buck, C.E., Millard, A.R. (Eds), Tools for Constructing Chronologies: Crossing Disciplinary Boundaries. Lecture Notes in Statistics, vol. 177. Springer, London, pp. 173-188.

Dunbar, N.W., Hervig, R.L., Kyle, P.R., 1989. Determination of pre-eruptive H_2O, F and Cl contents of silicic magmas using melt inclusions: Examples from Taupo volcanic centre, New Zealand. Bulletin of Volcanology, 51: 177–184.

Durant, A.J., Shaw, R.A., Rose, W.I., Mi, Y. and Ernst, G.G.J., 2008. Ice nucleation and overseeding of ice in volcanic clouds. Journal of Geophysical Research, 113: D09206.

Durant, A.J., Rose, W.I., Sarna-Wojcicki, A.M., Carey, S. and Volentik, A.C.M., 2009. Hydrometeor-enhanced tephra sedimentation: Constraints from the 18 May 1980 eruption of Mount St. Helens. Journal of Geophysical Research, 114: B03204.

Eiler, J.M., Graham, C. and Valley, J.W., 1997. SIMS analysis of oxygen isotopes: matrix effects in complex minerals and glasses. Chemical Geology, 138: 221-244.

Evison, F.F., Robinson, R. and Arabasz, W.J., 1976. Microearthquakes, geothermal activity, and structure, central North Island, New Zealand. New Zealand Journal of Geology and Geophysics, 19: 625–637.

Ewart, A., 1963. Petrology and petrogenesis of the Quaternary pumice ash in the Taupo area, New Zealand. Journal of Petrology, 4: 392-431.

Ewart, A. 1965. Mineralogy and petrogenesis of the Whakamaru ignimbrite in the Maraetai area of the Taupo Volcanic Zone, New Zealand. Journal of Geology and Geophysics, 8: 611-677.

Ewart, A. and Cole, J.W., 1967. Textural and mineralogical significance of granitic xenoliths from the central volcanic region, North Island, New Zealand. New Zealand Journal of Geology and Geophysics, 10: 31–54.

Ewart, A. and Healy, J., 1965. Te Whaiti Ignimbrites at Murapara. *In:* Thompson, B.N., Kermode, L.O., Ewart, A. (Editors), New Zealand Volcanology, Central Volcanic Region. New Zealand Department of Scientific and Industrial Research, Information Series, 50: 121-125.

Ewart, A., Hildreth, W. and Carmichael, I.S.E., 1975. Quaternary acid magma in New Zealand. Contributions to Mineralogy and Petrology, 51: 1-27.

Expert Panel on Air Quality Standards, 2001. Airborne particles: what is the appropriate measurement on which to base a standard? A discussion document. Department for Environment, Food & Rural Affairs, London: http://www.defra.gov.uk/environment/airquality/aqs/air_measure/index.htm.

Ferriss, E.D.A., Essene, E.J. and Becker, U., 2008. Computational study of the effect of pressure on the Ti-in-zircon thermometer. European Journal of Mineralogy, 20: 745–755.

Ferry, J.M. and Watson, E.B., 2007. New thermodynamic models and revised calibrations for the Ti-in-zircon and Zr-in-rutile thermometers. Contributions to Mineralogy and Petrology, 154: 429-437.

Folch, A and Marti, J., 1998. The generation of overpressure in felsic magma chambers by replenishment. Earth and Planetary Science Letters, 163: 301-314.

Folch, A., Costa, A., Durant, A. and Macedonio, G., 2010. A model for wet aggregation of ash particles in volcanic plumes and clouds: 2. Model application. Journal of Geophysical Research, 115: B09202.

Folkes, C.B., de Silva, S.L., Schmitt, A.K. and Cas, R.A.F., 2011. A reconnaissance of U-Pb ages in the Cerro Galan system, NW Argentina: prolonged magma residence, crystal recycling, and crustal assimilation. Journal of Volcanology and Geothermal Research, *in press.*

Forsyth, P.J.; Barrell, D.J.A. and Jongens, R. (compilers), 2008. Geology of the Christchurch area: scale 1:250,000. Lower Hutt: GNS Science. Institute of Geological & Nuclear Sciences 1:250,000 geological map 16. 67 p. + 1 folded map.

Francis, P. and Oppenheimer, C., 2004. Volcanoes. Oxford University Press, Oxford, UK.

Froggatt, P.C., 1982. Review of methods of estimating rhyolitic tephra volumes; applications to the Taupo Volcanic Zone, New Zealand. Journal of Volcanology and Geothermal Research, 14: 301-318.

Froggatt, P.C, 1983. Towards a comprehensive Upper Quaternary tephra and ignimbrite stratigraphy in New Zealand using electron microprobe analysis of glass shards. Quaternary Research, 19: 188-200.

Froggatt, P.C., Nelson, C.S., Carter, L., Griggs, G. and Black, K.P., 1986. An exceptionally large late Quaternary eruption from New Zealand. Nature, 319: 578-582.

Gagnevin, D., Daly, J.S., and Kronz, A., 2010. Zircon texture and chemical composition as a guide to magmatic processes and mixing in a granitic environment and coeval volcanic system. Contributions to Mineralogy and Petrology, 159: 579–596.

Gaither, T., Reid, M.R. and Vazquez, J.A., 2009. Geochemistry and temperatures recorded by zircon during the final stages of the Youngest Toba Tuff magma chamber,

Sumatra, Indonesia. American Geophysical Union Fall Meeting 2009, abstract V51E-1779.

Gamble, J.A., Smith, I.E.M., McCulloch, M.T., Graham, I.J. and Kokelaar, B.P., 1993. The geochemistry and petrogenesis of basalts from the Taupo Volcanic Zone and Kermadec Island Arc, S.W. Pacific. Journal of Volcanology and Geothermal Research, 54: 265-290.

Gansecki, C.A., Mahood, G.A. and McWilliams, M.O., 1996. $^{40}Ar/^{39}Ar$ geochronology of rhyolites erupted following collapse of the Yellowstone caldera, Yellowstone Plateau volcanic Field: implications for crustal contamination. Earth and Planetary Science Letters, 142: 91-107.

Gansecki, C.A., Mahood, G.A. and McWilliams, M.O., 1998. New ages for the climatic eruptions at Yellowstone: single crystal $^{40}Ar/^{39}Ar$ dating identifies contamination. Geology, 26: 343-346.

Gasparotto, G., Spadafora, E., Summa, V. and Tateo, F., 2000. Contribution of grain size and compositional data from the Bengal Fan sediment to the understanding of Toba volcanic event. Marine Geology, 162: 561-572.

Gathorne-Hardy, F. and Harcourt-Smith, W., 2003. The super-eruption of Toba, did it cause a human bottleneck? Journal of Human Evolution, 45: 227-230.

Ghiorso, M.S. and Evans, B.W., 2008. Thermodynamics of rhombohedral oxide solid solutions and a revision of the Fe-Ti two-oxide geothermometer and oxygen-barometer. American Journal of Science, 308: 957-1039.

Ghiorso, M.S. and Sack, R.O., 1995. Chemical mass transfer in magmatic processes. IV. A revised and internally consistent thermodynamic model for the interpolation and extrapolation of liquid-solid equilibria in magmatic systems at elevated temperatures and pressures. Contributions to Mineralogy and Petrology, 119: 197-212.

Ginibre, C., Kronz, A. and Wörner, G., 2002a. High-resolution quantitative imaging of plagioclase composition using accumulated backscattered electron images: new constraints on oscillatory zoning. Contributions to Mineralogy and Petrology, 142: 436-448.

Ginibre, C., Wörner, G. and Kronz, A., 2002b. Minor- and trace-element zoning in plagioclase: implications for magma chamber processes at Parinacota volcano, northern Chile. Contributions to Mineralogy and Petrology, 143: 300-315.

Girard, G. and Stix, J., 2009. Magma recharge and crystal mush rejuvenation associated with early post-collapse Upper Basin Member rhyolites, Yellowstone Caldera, Wyoming. Journal of Petrology, 50: 2095-2125.

Girard, G. and Stix, J., 2010. Rapid extraction of discrete magma batches from a large differentiating magma chamber: the Central Plateau Member rhyolites, Yellowstone Caldera, Wyoming. Contributions to Mineralogy and Petrology, 160: 441-465.

Glazner, A.F., Bartley, J.M., Coleman, D.S., Gray, W. and Taylor, R.Z., 2004. Are plutons assembled over millions of years by amalgamation from small magma chambers? GSA Today, 14(4/5): 4-11.

Götze, J., Plötze, M. and Habermann, D., 2001. Origin, spectral characteristics and practical applications of the cathodoluminescence (CL) of quartz - a review. Mineralogy and Petrology, 71: 225-250.

Götze, J., Plötze, M., Graupner, T., Hallbauer, D.K. and Bray, C.J., 2004. Trace element incorporation into quartz: A combined study by ICP-MS, electron spin resonance, cathodoluminescence, capillary ion analysis, and gas chromatography. Geochimica et Cosmochimica Acta, 68: 3741-3759.

Graham, I.J., 1987. Petrography and origin of metasedimentary xenoliths in lavas from Tongariro Volcanic centre. New Zealand Journal of Geology and Geophysics, 30: 139–157.

Graham, I.J., Grapes, R.H. and Kifle, K., 1988. Buchite metagreywacke xenoliths from Mount Ngauruhoe, Taupo Volcanic Zone, New Zealand. Journal of Volcanology and Geothermal Research, 35: 205–216.

Graham, I.J., Gulson, B.L., Hedenquist, J.W. and Mizon, K., 1992. Petrogenesis of late Cenozoic volcanic rocks from the Taupo Volcanic Zone, New Zealand, in the light of new lead isotope data. Geochimica et Cosmochimica Acta, 56: 2797–2819.

Graham, I.J., Cole, J.W., Briggs, R.M., Gamble, J.A. and Smith, I.E.M., 1995. Petrology and petrogenesis of volcanic rocks from the Taupo Volcanic Zone: a review. Journal of Volcanology and Geothermal Research, 68: 59-87.

Gravley, D.M., and Wilson, C.J.N., 2006. An ignimbrite flare-up event at 340–240 ka in the Taupo Volcanic Zone, New Zealand: implications for magmatic, volcanic, tectonic linkages. 5th Biennial Workshop on Subduction Processes emphasizing the Japan–Kuril–Kamchatka–Aleutian Arcs (JKASP-5) and International Volcanology Field School for Graduate Students, Programme and Abstracts vol. A201.

Gravley, D.M., Wilson, C.J.N., Leonard, G.S. and Cole, J.W., 2007. Double trouble: paired ignimbrite eruptions and collateral subsidence in the Taupo Volcanic Zone, New Zealand. Geological Society of America Bulletin, 119: 18–30.

Grimes, C.B., John, B.E., Cheadle, M.J., Mazdab, F.K., Wooden, J.L., Swapp, S. and Schwartz, J.J., 2009. On the occurrence, trace element geochemistry, and crystallization history of zirocn from in situ ocean lithosphere. Contributions to Mineralogy and Petrology, 158: 757-783.

Grindley, G.W., 1960. Sheet 8 - Taupo. Geological Map of New Zealand 1:250,000, Wellington, New Zealand: Department of Scientific and Industrial Research.

Grindley, G.W., 1965. The geology, structure, and exploitation of the Wairakei Geothermal Field, Taupo, New Zealand. New Zealand Geological Survey Bulletin, 75: 131 pp.

Grindley, G.W. and Hull, A.G., 1986. Historical Taupo earthquakes and earth deformation. Royal Society of New Zealand Bulletin, 24: 173–186.

Grunder, A. and Russell, J.K., 2005. Welding processes in volcanology: insights from field, experimental, and modeling studies. Journal of Volcanology and Geothermal Research, 142: 1-9.

Gualda, G.A.R., Cook, D.L., Chopra, R., Qin, L., Anderson, A.T. and Rivers, M., 2004. Fragmentation, nucleation and migration of crystals and bubbles in the Bishop Tuff rhyolitic magma. Transactions of the Royal Society of Edinburgh: Earth Sciences, 95: 375-390.

Gualda, G.A.R., Ghiorso, M.S., Vaum, R. and Carley, T.L., 2010. Rhyolite-MELTS: a modified calibration of MELTS optimized for silica-rich, fluid-bearing magmatic systems. American Geophysical Union, Fall Meeting 2010, abstract V43A-2352.

Halliday, A.N., Fallick, A.E., Hutchinson, J. and Hildreth, W., 1984. A Nd, Sr and O isotopic investigation into the causes of chemical and isotopic zonation in the Bishop Tuff, California. Earth and Planetary Science Letters, 68: 379-391.

Halliday, A.N., Mahood, G.A., Holden, P., Metz, J.M., Dempster, T.J. and Davidson, J.P., 1989. Evidence for long residence times of rhyolitic magma in the Long Valley magmatic system: the isotopic record in precaldera lavas of Glass Mountain. Earth and Planetary Science Letters, 94: 274-290.

Hammer, J.E., 2008. Experimental studies of the kinetics and energetics of magma crystallization. Reviews in Mineralogy and Geochemistry, 69: 9–59.

Hammer, J.E. and Rutherford, M.J., 2002. An experimental study of the kinetics of decompression-induced crystallization in silicic melt. Journal of Geophysical Research, 107: 2021.

Hanchar, J.M. and Miller, C.F., 1993. Zircon zonation patterns as revealed by cathodoluminescence and backscattered electron images: implications for interpreation of complex crustal histories. Chemical Geology, 110: 1-13.

Hanchar, J.M. and van Westrenen, W., 2007. Rare earth element behaviour in zircon-melt systems. Elements, 3: 37-42.

Hanchar, J.M. and Watson, E.B., 2003. Zircon saturation thermometry. Reviews in Mineralogy and Geochemistry, 53: 89-112.

Harrison, A.J. and White, R.S., 2004. Crustal structure of the Taupo Volcanic Zone, New Zealand: stretching and igneous intrusion. Geophysical Research Letters, 31: L13615.

Harrison, A. and White, R.S., 2006. Lithospheric structure of an active backarc basin: the Taupo Volcanic Zone, New Zealand. Geophysical Journal International, 167: 968-990.

Haslam, M., Clarkson, C., Petraglia, M., Korisettar, R., Bora, J., Boivin, N., Ditchfield, P., Jones, S. and Mackay, A., 2010a. Indian lithic technology prior to the 74,000 BP Toba super-eruption: searching for an early modern human signature. *In:* Boyle, C., Gamble, G.A. and Bar-Yosef, O. (Editors), Upper Palaeolithic Revolution in Global Perspective: Essays in honour of Paul Mellars, McDonald Institute for Archaeological Research, Cambridge, pp 73-84.

Haslam, M., Clarkson, C., Petraglia, M., Korisettar, R., Jones, S., Shipton, C., Ditchfield, P. and Ambrose, S.H., 2010b. The 74 ka Toba super-eruption and southern Indian hominins: archaeology, lithic technology and environments at Jwalapuram Locality 3. Journal of Archaeological Science, 37: 3370-3384.

Hatherton, T., 1954. The magnetic properties of the Whakamaru ignimbrites. New Zealand Journal of Science and Technology, 35: 421-431.

Hawkesworth, C., Blake, S., Evans, P., Hughes, R., Macdonald, R., Thomas, L. and Turner, S., 2000. Time scales of crystal fractionation in magma chambers - Integrating physical, isotopic and geochemical perspectives. Journal of Petrology, 41: 991-1006.

Hayden, L.A. and Watson, E.B., 2007. Rutile saturation in hydrous siliceous melts and its bearing on Ti-thermometry of quartz and zircon. Earth and Planetary Science Letters, 258: 561-568.

Hayden, L.A., Watson, E.B. and Wark, D.A., 2005. Rutile saturation and TiO_2 diffusion in hydrous siliceous melts. EOS, Transactions of the American Geophysical Union, 86 (52, Fall Meeting Supplement): MR13A-0076.

Heise, W., Bibby, H.M., Caldwell, T.G., Bannister, S.C., Ogawa, Y., Takakura, S. and Uchida, T., 2007. Melt distribution beneath a young continental rift: the Taupo Volcanic Zone, New Zealand. Geophysical Research Letters, 34: L14313.

Henrys, S., Reyners, M. and Bibby, H., 2003. Exploring the plate boundary in New Zealand. EOS, Transactions of the American Geophysical Union, 84: 289, 294-295.

Herzer, R.H., 1995. Seismic stratigraphy of a buried volcanic arc, Northland, New Zealand and implications for Neogene subduction. Marine and Petroleum Geology, 12: 511–531.

Herzer, R.H. and Mascle, J., 1996. Anatomy of a continent–backarc transform — the Vening Meinesz fracture zone northwest of New Zealand. Marine Geophysical Researches, 18: 401–427.

Hiess, J., Nutman, A.P., Bennett, V.C. and Holden, P., 2008. Ti-in-zircon thermometry applied to contrasting Achaean metamorphic and igneous systems. Chemical Geology, 247: 323-338.

Hildreth, W., 1979. The Bishop Tuff: evidence for the origin of compositional zonation in silicic magma chambers. *In:* Chapin C.E., Elston W.E. (Editors), Ash-flow tuffs. Geological Society of America Special Paper, 180: 43-75.

Hildreth, W., 1981. Gradients in silicic magma chambers: implications for lithospheric magmatism. Journal of Geophysical Research, 86:10153-10192.

Hildreth, W., 1983. The compositionally zoned eruption of 1912 in the Valley of Ten Thousand Smokes, Katmai National Park, Alaska. Journal of Volcanology and Geothermal Research, 18: 1-56.

Hildreth, W., 2004. Volcanological perspectives on Long Valley, Mammoth Mountain, and Mono Craters: several contiguous but discrete systems. Journal of Volcanology and Geothermal Research, 136: 169-198.

Hildreth, W. and Mahood, G.A., 1985. Correlation of ash-flow tuffs. Geological Society of America Bulletin, 96: 396-403.

Hildreth, W. and Wilson, C.J.N., 2007. Compositional zoning of the Bishop Tuff. Journal of Petrology, 48: 951-999.

Hildreth, W., Christiansen, R.L. and O'Neil, J.R., 1984. Catastrophic isotopic modification of rhyolitic magma at times of caldera subsidence, Yellowstone Plateau volcanic field. Journal of Geophysical Research, 89: 8339-8369.

Hildreth, W., Halliday, A.N. and Christiansen, R.L., 1991. Isotopic and chemical evidence concerning the genesis and contamination of basaltic and rhyolitic magma beneath the Yellowstone Plateau volcanic field. Journal of Petrology, 32: 63–138.

Hildyard, S.C., Cole, J.W., and Weaver, S.D., 2000. Tikorangi Ignimbrite: a 0.89 Ma mixed rhyolite-andesite ignimbrite from Matahana Basin, Taupo Volcanic Zone, New Zealand. New Zealand Journal of Geology and Geophysics, 43: 95-107.

Hinton, R.W. and Upton, B.G.J., 1991. The chemistry of zircon: variations within and between large crystals from syenite and alkali basalt xenoliths. Geochimica et Cosmochimica Acta, 55: 3287–3302.

Hitchman, M.H., McKay, M. and Trepte, C.R., 1994. A climatology of stratospheric aerosol. Journal of Geophysical Research, 99: 20689-20700.

Hochstein, M.P., 1995. Crustal heat transfer in the Taupo Volcanic Zone (New Zealand): comparison with other volcanic arcs and explanatory heat source models. Journal of Volcanology and Geothermal Research, 68: 117-151.

Hochstetter. F. von, 1864. Geologie von Neu Seeland. Beitrage zur Geologie der Provinzen Auckland und Nelson. (Novara Expedition, Geological Part l(1)): 274 pp. (English translation by C.A. Fleming, Government Printer, Wellington, 1959).

Hoffman, A.E., Valley, J.W., Watson, E.B., Cavosie, A.J. and Eiler, J.M., 2009. Sub-micron scale distributions of trace elements in zircon. Contributions to Mineralogy and Petrology, 158: 317-355.

Holland, T.J.B. and Powell, R., 1998. An internally consistent thermodynamic data set for phases of petrological interest. Journal of Metamorphic Geology, 16: 309-343.

Holt, K.A., 2008. The Quaternary history of Chatham Island, New Zealand. PhD thesis, Massey University, Palmerston North, New Zealand.

Holt, K.A., Wallace, R.C., Neall, V.E., Kohn, B.P. and Lowe, D.J., 2010. Quaternary tephra marker beds and their potential for palaeoenvironmental reconstruction on Chatham Island, east of New Zealand, southwest Pacific Ocean. Journal of Quaternary Science, 25: 1169-1178.

Horwell, C.J., 2007. Grain-size analysis of volcanic ash for the rapid assessment of respiratory health hazard. Journal of Environmental Monitoring, 9: 1107-1115.

Horwell, C.J. and Baxter, P.J., 2006. The respiratory health hazards of volcanic ash: a review for volcanic risk mitigation. Bulletin of Volcanology, 69: 1-24.

Hoskin, P.W.O., 1998. Minor and trace element analysis of natural zircon ($ZrSiO_4$) by SIMS and laser ablation ICPMS: a consideration and comparison of two broadly competitive techniques. Journal of Trace Microprobe Techniques, 16: 301–326.

Hoskin, P.W.O. and Ireland, T.R., 2000. Rare earth element chemistry of zircon and its use as a provenance indicator. Geology, 28: 627–630.

Hoskin, P.W.O. and Schaltegger, U., 2003. The composition of zircon and igneous and metamorphic petrogenesis. Reviews in Mineralogy and Geochemistry, 53: 27-55.

Hoskin, P.W.O., Kinny, P.D., Wyborn, D. and Chappell, B.W., 2000. Identifying accessory mineral saturation during differentiation in granitoid magmas: an integrated approach. Journal of Petrology, 41: 1365-1396.

Houghton, B.F., Wilson, C.J.N., McWilliams, M.O., Lanphere, M.A., Weaver, S.D., Briggs, R.M. and Pringle, M.S., 1995. Chronology and dynamics of a large silicic magmatic system: central Taupo Volcanic Zone, New Zealand. Geology, 23: 13-16.

Huber, C., Parmigiani, A., Chopard, B., Manga, M. and Bachmann, O., 2008. Lattice Boltzmann model for melting with natural convection, International Journal of Heat and Fluid Flow, 29: 1469-1480.

Huber, C., Bachmann, O. and Manga, M., 2009. Homogenization processes in silicic magma chambers by stirring and mushification (latent heat buffering). Earth and Planetary Science Letters, 283: 38-47.

Huber, C., Bachmann, O. and Dufek, J., 2010a. The limitations of melting on the reactivation of silicic mushes. Journal of Volcanology and Geothermal Research, 195: 97-105.

Huber, C., Bachmann, O. and Manga, M., 2010b. Two competing effects of volatiles on heat transfer in crystal-rich magmas: thermal insulation vs. defrosting. Journal of Petrology, 51: 847-867

Huber, C., Chopard, B. and Manga, M., 2010c. A lattice Boltzmann model for coupled diffusion. Journal of Computational Physics, 229: 7956-7976.

Huber, C., Cassata, W.S. and Renne, P.R., 2011a. A lattice-Boltzman model for noble gas diffusion in solids. Part 1: The importance of domain shape and diffusive anisotropy and implications for thermochronometry. Geochimica et Cosmochimica Acta, *in press*, doi:10.1016/j.gca.2011.01.039.

Huber, C., Bachmann, O. and Dufek, J., 2011b. Thermo-mechanical reactivation of locked crystal mushes: melting-induced internal fracturing and assimilation processes in magmas. Earth and Planetary Science Letters, 304: 443–454.

Huber, C., Dufek, J. and Bachmann, O., 2011c. Crystal-poor vs. crystal-rich supervolcanic deposits: a competition between recharge-induced stirring and mush reactivation in shallow reservoirs, s*ubmitted to Geology*.

Huebner, J.S. and Sato, M., 1970. The oxygen fugacity-temperature relationships of manganese oxide and nickel oxide buffers. American Mineralogist, 55: 934-952.

Humphreys, M.C.S., Blundy, J.D. and Sparks, R.S.J., 2006. Magma evolution and open-system processes at Shiveluch volcano: insights from phenocryst zoning. Journal of Petrology, 47: 2303-2334.

Huppert, H.E. and Sparks, R.S.J., 1988. The generation of granitic magmas by intrusion of basalt into continental crust. Journal of Petrology, 29: 599-624.

Hut, G., 1987. Stable isotope reference samples for geochemical and hydrological investigations. Report of the Consultants Group Meeting, Vienna, 1985, International Atomic Energy Agency, Vienna, p. 1-47.

Ickert, R.B., Williams, I.S. and Wyborn, D., 2011. Ti in zircon from the Boggy Plain zoned pluton: implications for zircon petrology and Hadean tectonics. Contributions to Mineralogy and Petrology, 162: 447-461.

Jellinek, A.M. and DePaolo, D.J., 2003. A model for the origin of large silicic magma chambers: precursors of caldera-forming eruptions. Bulletin of Volcanology, 65: 363-381.

Jochum, K.P., Stoll, B., Herwig, K., Willbold, M., Hofmann, A.W., Amini, M., Aarburg, S., Abochami, W., Hellebrand, E., Mocek, B., Raczek, I., Stracke, A., Alard, O., Bouman, C., Becker, S., Dücking, M., Brätz, H., Klemd, R., de Bruin, D., Canil,

D., Cornell, D., de Hoog, C., Dalpé, C., Danyushevsky, L., Eisenhauer, A., Gao, Y., Snow, J.E., Groschopf, N., Günther, D., Latkoczy, C., Guillong, M., Hauri, E., Lahaye, Y., Horz, K., Jacob, D.E., Kasemann, S.A., Kent, A.J.R., Ludwig, T., Zack, T., Mason, P.R.D., Meixner, A., Rosner, M., Misawa, K., Nash, B.P., Premo, W.R., Sun, W.D., Tiepolo, M., Vannucci, R., Vennemann, T. and Woodhead, J.D., 2006. MPI-DING reference glasses for in situ microanalysis: new reference values for element concentrations and isotope ratios. Geochemistry Geophysics Geosystems, 7: Q02008.

Johnson, C.M., 1989. Isotopic zonations in silicic magma chambers. Geology, 17: 1136–1139.

Johnson, E.R., Kamenetsky, V.S., McPhie, J. and Wallace, P.J., 2011. Degassing of the H_2O-rich rhyolites of the Okataina Volcanic Centre, Taupo Volcanic Zone, New Zealand. Geology, 39: 311-314.

Jones, G.S., Gregory, J.M., Stott, P.A., Tett, S.F.B. and Thorpe, R.B., 2005. An AOGCM simulation of the climate response to a volcanic super-eruption. Climate Dynamics, 25: 725-738.

Jones, M.T., Sparks, R.S.J. and Valdes, P.J., 2007. The climatic impact of supervolcanic ash blankets. Climate Dynamics, 29: 553-564

Jones, S., 2007. The Toba supervolcanic eruption: Tephra-fall deposits in India and paleoanthropological implications. *In:* Petraglia, M.D. and Allchin. B. (Editors), The Evolution and History of Human Populations in South Asia, Springer, Berlin, pp. 173–200.

Jones, S.C., 2010. Palaeoenvironmental response to the 74 ka Toba ash-fall in the Jurreru and Middle Son valleys in southern and north-central India. Quaternary Research, 73: 336-350.

Jones, S.C., 2011. Local- and regional-scale impacts of the ~74 ka Toba supervolcanic eruption on hominin populations and habitats in India. Quaternary International, Special Issue; The Toba Super-eruption: Impact on Ecosystems and Hominins, s*ubmitted*.

Joshi, M.M. and Jones, G.S., 2009. The climatic effects of the direct injection of water vapour into the stratosphere by large volcanic eruptions. Atmospheric Chemistry and Physics, 9: 6109-6118.

Karhunen, R.A., 1993. The Pokai and Chimp Ignimbrites of the NW Taupo Volcanic Zone. PhD thesis, University of Canterbury, Christchurch, New Zealand.

Keall, J.M., 1988. Volcanology and ignimbrite stratigraphy along the Paeroa Fault, Taupo Volcanic Zone. MSc Thesis, Victoria University, Wellington, New Zealand.

Kemp, A.I.S., Whitehouse, M.J., Hawkesworth, C.J. and Alarcon, M.K., 2005. A zircon U/Pb study of metaluminous (I-type) granites of the Lachlan fold belt, southeastern Australia; implications for the high-low temperature classification and magma differentiation processes. Contributions to Mineralogy and Petrology, 150: 230–249.

Kirkpatrick, R.J., 1975. Crystal growth from the melt: a review. American Mineralogist, 60: 798-814.

Klügel, A., 2001. Prolonged reactions between harzburgite xenoliths and silica-undersaturated melt: implications for dissolution and Fe-Mg interdiffusion rates of orthopyroxene. Contributions to Mineralogy and Petrology, 141: 1–14.

Knesel, K.M. and Duffield, W.A., 2007. Gradients in silicic eruptions caused by rapid inputs from above and below rather than protracted chamber differentiation. Journal of Volcanology and Geothermal Research, 167: 181-197.

Kohn, B.P., 1973. Some studies of New Zealand pyroclastic rocks. PhD thesis, Victoria University, Wellington, New Zealand.

Kohn, B.P., Pillans, B. and McGlone, M.S., 1992. Zircon fission-track age for middle Pleistocene Rangitawa Tephra, New Zealand - stratigraphic and paleoclimatic significance. Palaeogeography, Palaeoclimatology, Palaeoecology, 95: 73-94.

Krippner, S.J.P., Briggs, R.M., Wilson, C.J.N. and Cole, J.W., 1998. Petrography and geochemistry of lithic fragments in ignimbrites from the Mangakino volcanic centre: implications for the composition of the subvolcanic crust in western Taupo

Volcanic Zone, New Zealand. New Zealand Journal of Geology and Geophysics, 41: 187–199.

Kyle, P.R. and Seward, D., 1984. Dispersed rhyolitic tephra from New Zealand in deep-sea sediments of the Southern Ocean. Geology 12, 487-490.

Lamarche, G. and Froggatt, P.C., 1993. New eruptive vents for the Whakamaru ignimbrite (Taupo Volcanic Zone) identified from magnetic fabric study. New Zealand Journal of Geology and Geophysics, 36: 213-222.

Lee, M-Y., Chen, C-H., Wei, K-Y., Iizuka, Y. and Carey, S., 2004. First Toba supereruption revival. Geology, 32: 61-64.

Legros, F. and Marti, J., 2001. Formation of inversely graded basal layers in ignimbrites by progressive aggradation. Journal of Volcanology and Geothermal Research, 111: 25-33.

Leonard, G.S., Cole, J.W., Nairn, I.A. and Self, S., 2002. Basalt triggering of the c. AD 1305 Kaharoa rhyolite eruption, Tarawera Volcanic Complex, New Zealand. Journal of Volcanology and Geothermal Research, 115: 461-486.

Leonard, G.S., Begg, J.G. and Wilson, C.J.N. (compilers), 2010. Geology of the Rotorua area: scale 1:250,000. Lower Hutt: Institute of Geological & Nuclear Sciences Limited. Institute of Geological & Nuclear Sciences 1:250,000 geological map 5. 102 p. + 1 folded map.

Liang, X., Wei, G., Shao, L., Li, X. and Wang, R., 2001. Records of Toba eruptions in the South China Sea: chemical characteristics of the glass shards from ODP 1143A. Science in China (Series D), 44: 871–878.

Linde, A.T. and Sacks, I.S., 1998. Triggering of volcanic eruptions. Nature, 395: 888-890.

Linden, P.F. and Redondo, J.M., 1991. Molecular mixing in Rayleigh-Taylor instability. Part I: Global mixing. Physics of Fluids A, 3: 1269-1277.

Lindsay, J., Trumbull, R., and Siebel, W., 2005. Geochemistry and petrogenesis of late Pleistocene to recent volcanism in Southern Dominica, Lesser Antilles. Journal of Volcanology and Geothermal Research, 148: 253-294.

Lindsay, J.M., de Silva, S.L., Trumbull, R., Emmermann, R. and Wemmer, K., 2011. La Pacana caldera, N. Chile: a relevaluation of the stratigraphy and volcanology of one of the world's largest resurgent calderas. Journal of Volcanology and Geothermal Research, 106: 145-173.

Linnen, R.L. and Keppler, H., 2002. Melt composition control of Zr/Hf fractionation in magmatic processes. Geochemica et Cosmochimica Acta, 66: 3293-3301.

Lipman, P., Dungan, M. and Bachmann, O., 1997. Comagmatic granophyric granite in the Fish Canyon Tuff, Colorado: Implications for magma-chamber processes during a large ash-flow eruption. Geology, 25: 915-918.

Liu, Y., Anderson, A.T., Wilson, C.J.N., Davis, A.M. and Steele, I.M., 2006. Mixing and differentiation in the Oruanui rhyolitic magma, Taupo, New Zealand: evidence from volatiles and trace elements in melt inclusions. Contributions to Mineralogy and Petrology, 151: 71-87.

Liu, Z., Colin, C. and Trentesaux, A., 2006. Major element geochemistry of glass shards and minerals in the Youngest Toba Tephra in the southwestern China Sea. Journal of Asian Earth Sciences, 27: 99-107.

Lowe, D.J., 2011. Tephrochronology and its application: a review. Quaternary Geochronology, 6: 107-153.

Lowe, D.J., Tippett, J.M., Kamp, P.J.J., Liddell, I.J., Briggs, R.M. and Horrocks, J.R. 2001. Ages on weathered Plio-Pleistocene tephra sequences, western North Island, New Zealand. *In*: Juvigné, E.T., Raynal, J.P. (Editors), 'Tephra: Chronology, Archeaology", CDERAD editeur, Goudet. Les Dossiers de l'Archéo-Logis, 1: 45-60.

Lowe, D.J., Shane, P.A.R., Alloway, B.V. and Newnham, R.M. 2008. Fingerprints and age models for widespread New Zealand tephra marker beds erupted since 30,000 years ago: a framework for NZ-INTIMATE. Quaternary Science Reviews, 27: 95-126.

Lowe, D.J., Wilson, C.J.N., Newnham, R.M. and Hogg, A.G., 2010. Dating the Kawakawa/Oruanui eruption: comment on "Optical luminescence dating of a loess section containing a critical tephra marker horizon, SW North Island of New Zealand" by R. Grapes et al. Quaternary Geochronology, 5: 493-496.

Lowenstern, J.B. and Hurwitz, S., 2008. Monitoring a supervolcano in repose: Heat and volatile flux at the Yellowstone caldera. Elements, 4: 35-40.

Lowenstern, J.B., Persing, H.M., Wooden, J.L., Lanphere, M., Donnelly-Nolan, J. and Grove, T.L., 2000. U-Th dating of single zircons from young granitoid xenoliths: new tools for understanding volcanic processes. Earth and Planetary Science Letters, 183: 291-302.

Ludwig, K.R., 2003. Isoplot/Ex version 3.41, a geochronological toolkit for Microsoft Excel, Berkeley Geochronology Center Special Publication, 4.

Macedonio, G., Costa, A. and Longo, A., 2005. A computer model for volcanic ash fallout and assessment of subsequent hazard. Computers and Geosciences, 31: 837-845.

Macedonio, G., Costa, A. and Folch, A., 2008. Ash fallout scenarios at Vesuvius: Numberical simulations and implications for hazard assessment. Journal of Volcanology and Geothermal Research, 178: 366-377.

Mahood, G.A., 1990. Evidence for long residence times of rhyolitic magma in the Long Valley magmatic system - the isotopic record in the precaldera lavas of Glass Mountain - reply. Earth and Planetary Science Letters, 99: 395-399.

Mahood, G.A. and Hildreth, W., 1983. Large partition coefficients for trace elements in high-silica rhyolites. Geochimica et Cosmochemica Acta, 47: 11-30.

Manning, D.A., 1996. Middle-Late Pleistocene tephrostratigraphy of the eastern Bay of Plenty, New Zealand. Quaternary International, 34-36: 3-12.

Manville, V. and Wilson, C.J.N., 2004a. The 26.5 ka Oruanui eruption, New Zealand: a review of the roles of volcanism and climate in the post-eruptive sedimentary response. New Zealand Journal of Geology and Geophysics, 47(3): 525-547.

Manville, V. and Wilson, C.J.N., 2004b. Vertical density currents: a review of their potential role in the deposition and interpretation of deep-sea ash layers. Journal of the Geological Society, London, 161: 947-958.

Manville, V., Segschneider, B., Newton, E., White, J.D.L., Houghton, B.F. and Wilson, C.J.N., 2009. Environmental impact of the 1.8 ka Taupo eruption, New Zealand:

Landscape responses to a large-scale explosive rhyolite eruption. Sedimentary Geology, 220: 318-336.

Martin, R.C., 1961. Stratigraphy and structural outline of the Taupo Volcanic Zone. New Zealand Journal of Geology and Geophysics, 4: 449-478.

Martin, R.C., 1965. Lithology and eruptive history of the Whakamaru Ignimbrites in the Maraetai area of the Taupo Volcanic Zone, New Zealand. New Zealand Journal of Geology and Geophysics, 8: 680-701.

Martin, V.M., Morgan, D.J., Jerram, D.A., Caddick, M.J., Prior, D.J. and Davidson, J.P., 2008. Bang! Month-scale eruption triggering at Santorini Volcano. Science, 321: 1178.

Mason, B.G., Pyle, D.M. and Oppenheimer, C., 2004. The size and frequency of the largest explosive eruptions on earth. Bulletin of Volcanology, 66: 735-748.

Matthews, N.E., Pyle, D.M., Smith, V.C., Wilson, C.J.N., Huber, C. and van Hinsberg, V., 2011a. Quartz zoning and the pre-eruptive evolution of the ~340 ka Whakamaru magma systems, New Zealand. Contributions to Mineralogy and Petrology, i*n press,* doi: 10.1007/s00410-011-0660-1.

Matthews, N.E., Smith, V.C., Costa, A., Durant, A.J., Pyle, D.M. and Pearce, N.J.G., 2011b. Ultra-distal tephra deposits from super-eruptions: examples from Toba and New Zealand. Quaternary International, Special Issue; The Toba Super-eruption: Impact on Ecosystems and Hominins, *in press*, doi: 10.1016/j.quaint.2011.07.010.

Matthews, N.E., Huber, C., Pyle, D.M. and Smith, V.C., 2011c. Timescales of magma recharge and reactivation of large silicic systems from Ti diffusion in quartz. Journal of Petrology, s*ubmitted February 2011*.

Matthews, N.E., Wilson, C.J.N., Charlier, B.L.A., Wooden, J. and Pyle, D.M. 2011d. Zircon crystallisation histories: investigating processes and timescales of silicic magma generation, Whakamaru, New Zealand. Journal of Petrology. *Manuscript in prep.*

Mazdab, F.M. and Wooden, J.L., 2006. Trace element analysis in zircon by ion microprobe (SHRIMP-RG); technique and applications. Geochimica et Cosmochmica Acta, 70: A40.

McCormack, K.D., Gee, M.A.M., McNaughton, N.J., Smith, R. and Fletcher, I.R., 2009. U–Pb dating of magmatic and xenocryst zircons from Mangakino ignimbrites and their correlation with detrital zircons from the Torlesse metasediments, Taupo Volcanic Zone, New Zealand. Journal of Volcanology and Geothermal Research, 183: 97-111.

McCormick, M.P. and Veiga, R.E., 1992. SAGE II measurements of early Pinatubo aerosols. Geophysical Research Letters, 19: 155-158.

McCulloch, M.T., Kyser, T.K., Woodhead, J.D. and Kinsey, L., 1994. Pb-Sr-Nd-O isotopic constraints on the origin of rhyolites from the Taupo Volcanic Zone of New Zealand: evidence for assimilation followed by fractionation from basalt. Contributions to Mineralogy and Petrology, 115: 303-312.

McDonough, W.F. and Sun, S.S., 1995. The composition of the earth. Chemical Geology, 120: 223-253.

McIntire, W.L., 1963. Trace element partition coefficients – a review of theory and applications to geology. Geochimica et Cosmochemica Acta, 27: 1209-1264.

Michaut, C. and Jaupart, C., 2011. Two models for the formation of magma reservoirs by small increments. Tectonophysics, 500: 34-49.

Mildenhall, D.C. and Alloway, B.V., 2008. A widespread ca. 1.1 Ma TVZ silicic tephra preserved near Wellington, New Zealand: implications for regional reconstruction of mid-Pleistocene vegetation. Quaternary International, 178: 167–182.

Miller, C.F. and Wark, D.A., 2008. Supervolcanoes and their explosive supereruptions. Elements, 4: 11-15.

Miller, J.S. and Wooden, J.L., 2004. Residence, resorption and recycling of zircons in Devils Kitchen rhyolite, Coso Volcanic field, California. Journal of Petrology, 45: 2155-2170.

Miller, J.S., Matzel, J.E.P., Miller, C.F., Burgess, S.D. and Miller, R.B., 2007. Zircon growth and recycling during the assembly of large, composite arc plutons. Journal of Volcanology and Geothermal Research, 167: 282-299.

Milne, J.D.G., 1973. Mount Curl Tephra, a 230,000 year-old marker bed in New Zealand, and its implications for Quaternary chronology. New Zealand Journal of Geology and Geophysics, 16: 519-532.

Milne, J.D.G. and Smalley, I., 1979. Loess deposits in the southern part of the North Island of New Zealand: an outline stratigraphy. Acta Geologica Academiae Scientiarum Hungaricae, 22: 197-204.

Milner, D.M., Cole, J.W. and Wood, C.P., 2003. Mamaku Ignimbrite: a caldera-forming ignimbrite erupted from a compositionally zoned magma chamber in Taupo Volcanic Zone, New Zealand. Journal of Volcanology and Geothermal Research, 122: 243-264.

Molloy, C., Shane, P. and Nairn, I., 2008. Pre-eruption thermal rejuvenation and stirring of a partly crystalline pluton revealed by the Earthquake Flat Pyroclastics deposits, New Zealand. Journal of the Geological Society, London, 165: 435-447.

Morgan, D. and Blake, S., 2006. Magmatic residence times of zoned phenocrysts: introduction and application of the binary element diffusion modelling (BEDM) technique. Contributions to Mineralogy and Petrology, 151: 58-70.

Morgan, D.J., Blake, S., Rogers, N.W.B., DeVivo, B., Rolandi, G., Macdonald, R. and Hawkesworth, C.J., 2004. Time scales of crystal residence and magma chamber volume from modelling of diffusion profiles in phenocrysts: Vesuvius 1944. Earth and Planetary Science Letters, 222: 933-946.

Mortimer, N., 1994. Origin of the Torlesse Terrane and coeval rocks, North Island, New Zealand. International Geology Review, 36: 891–910.

Mortimer, N., 2004. New Zealand's geological foundations. Gondwana Research, 7: 261–272.

Mosselmans, J.F.W., Quinn, P.D., Roque-Rosell, J., Atkinson, K.D., Dent, A.J., Cavill, S.I., Hodson, M.E., Kirk, C.A. and Schofield, P.F., 2008. The first environmental

science experiments on the new microfocus spectroscopy beamline at Diamond. Mineralogical Magazine, 72: 197–200.

Mosselmans, J.F.W., Quinn, P.D., Dent, A.J., Cavill, S.A., Diaz Moreno, S., Peach, A., Leicester, P.J., Keylock, S.J., Gregory, S.R., Atkinson, K.D. and Roque Rosell, J., 2009. I18 - microfocus spectroscopy beamline at the Diamond light source. Journal of Synchrotron Radiation, 16: 818-824.

Murphy, M.D., Sparks, R.S.J., Barclay, J., Carroll, M.R. and Brewer, T.S., 2000. Remobilization of andesite magma by intrusion of mafic magma at the Soufrière Hills volcano, Montserrat, West Indies. Journal of Petrology, 41: 21-42.

Nairn, I.A., 1972. Rotoehu Ash and the Rotoiti Breccia Formation, Taupo Volcanic Zone, New Zealand. New Zealand Journal of Geology and Geophysics, 15: 251–261.

Nairn, I.A., Wood, C.P. and Bailey, R.A., 1994. The Reporoa caldera, Taupo Volcanic Zone: source of the Kaingaroa Ignimbrites. Bulletin of Volcanology, 56: 529-537.

Nairn, I.A., Shane, P.R., Cole, J.W., Leonard, G.J., Self, S. and Pearson, N., 2004. Rhyolite magma processes of the ~AD 1315 Kaharoa eruption episode, Tarawera volcano, New Zealand. Journal of Volcanology and Geothermal Research, 131: 265-294.

Nairn, I.A., Hedenquist, J.W., Villamor, P., Berryman, K.R. and Shane, P.A., 2005. The ~AD1315 Tarawera and Waiotapu eruptions, New Zealand: contemporaneous rhyolite and hydrothermal eruptions driven by an arrested basalt dike system? Bulletin of Volcanology, 67: 186–193.

Nakamura, M., 1995. Continuous mixing of crystal mush and replenished magma in the ongoing Unzen eruption. Geology, 23: 807–810.

Nash, W.P. and Crecraft, H.R., 1985, Partition coefficients for trace elements in silicic magmas. Geochimica et Cosmochimica Acta, 49: 2309-2322.

Nelson, C., 1988. Revised age of a late Quaternary tephra at DSDP site 584 off eastern South Island and some implications for correlation. Geological Society of New Zealand Newsletter, 82: 35-40.

Nelson, C.S., Hendy, C.H., Cuthbertson, A.M. and Jarrett, G., 1985. Late Quaternary carbonate and isotope stratigraphy, subantarctic site 594, southwest Pacific. *In:* Kennett, J.P., von der Borch, C.C. (Editors). Initial Reports of the Deep Sea Drilling Project, 90: 1425-1436.

Newhall, C.G. and Self, S., 1982. The Volcanic Explosivity Index (VEI): an estimate of the explosive magnitude for historical volcanism. Journal of Geophysical Research, 87: 1231–1238.

Ninkovich, D., 1968. Pleistocene volcanic eruptions in New Zealand recorded in deep-sea sediments. Earth and Planetary Science Letters, 4: 89-102.

Ninkovich, D., 1979. Distribution, age and chemical composition of tephra layers in deep-sea sediments off western Indonesia. Journal of Volcanology and Geothermal Research, 5: 67-86.

Ninkovich, D. and Ruddiman, W., 1977. Bioturbation of volcanic ash layers in deep-sea sediments. X INQUA Congress Proceedings (abstract): p. 326.

Ninkovich, D., Sparks, R.S.J. and Ledbetter, M.T., 1978a. The exceptional magnitude and intensity of the Toba eruption, Sumatra: An example of the use of deep-sea tephra layers as a geological tool. Bulletin Volcanologique, 41: 286-298.

Ninkovich, D., Shackleton, N., Abdel-Monem, A., Obradovich, J. and Izett, G., 1978b. K/Ar age of the late Pleistocene eruption of Toba, north Sumatra. Nature, 276: 574-577.

Nixon, G.T. and Pearce, T.H., 1987. Laser-interferometry study of oscillatory zoning in plagioclase: The record of magma mixing and phenocryst recycling in calc-alkaline magma chambers, Iztaccihuatl Volcano, Mexico. American Mineralogist, 72: 1144-1162.

O'Hara, M.J., 1977. Geochemical evolution during fractional crystallisation of a periodically refilled magma chamber. Nature, 266: 503-507.

O'Hara, M.J. and Matthews, R.E., 1981. Geochemical evolution in an advancing periodically replenished, periodically tapped, continously fractionated magma chamber. Journal of the Geological Society, London, 138: 237-277.

Oppenheimer, C., 2002. Limited global change due to the largest known Quaternary eruption, Toba ~74 kyr BP? Quaternary Science Reviews, 21: 1593–1609.

Oppenheimer, C., 2004. Jwalapuram Project 2004: Tephrastratigraphy. Unpublished report; Geography Department, University of Cambridge.

Otway, P.M., 1986. Vertical deformation associated with the Taupo earthquake swarm, June 1983. Royal Society of New Zealand Bulletin, 24: 187–200.

Otway, P.M., Blick, G.H. and Scott, B.J., 2002. Vertical deformation at Lake Taupo, New Zealand, from lake leveling surveys, 1979–99. New Zealand Journal of Geology and Geophysics, 45: 121–132.

Palin, J.M., Epstein, S. and Stolper, E.M., 1996. Oxygen isotope partitioning between rhyolitic glass/melt and CO_2: an experimental study at 550-950°C and 1 bar. Geochimica et Cosmochimica Acta, 60: 1963-1973.

Pallister, J.S., Hoblitt, R.P. and Reyes, A.G., 1992. A basalt trigger for the 1991 eruptions of Pinatubo volcano? Nature, 356: 426-428.

Pappalardo, L., Ottolini, L. and Mastrolorenzo, G., 2008. The Campanian Ignimbrite (southern Italy) geochemical zoning: insight on the generation of a super-eruption from catastrophic differentiation and fast withdrawal. Contributions to Mineralogy and Petrology, 156: 1-26.

Park, C. and Schmincke, H.U., 1997. Lake formation and catastrophic dam burst during the late Pleistocene Laacher See eruption (Germany). Naturwissenschaften, 84: 521-525.

Parrish, R.R. and Noble, S.R., 2003. Zircon U-Th-Pb geochronology by isotope dissolution – Thermal Ionization Mass Spectrometry (ID-TIMS). Reviews in Mineralogy and Geochemistry, 53: 183-213.

Paterson, B.E. and Stephens, W.E., 1992. Kinetically induced compositional zoning in titanite: Implications for accessory-phase/melt partitioning of trace elements. Contributions to Mineralogy and Petrology, 109: 373-385.

Pattan, J., Shane, P. and Banakar, V., 1999. New occurrence of Youngest Toba Tuff in abyssal sediments of the Central Indian Basin. Marine Geology, 155: 243-248.

Pattan, J.N., Shane, P., Pearce, N.J.G., Banakar, V.K. and Parthiban, G., 2001. An occurrence of ~ 74 ka Youngest Toba Tephra from the western continental margin of India. Current Science, 80: 1322-1326.

Pattan, J.N., Pearce, N.J.G., Banakar, V.K. and Parthiban, G., 2002. Origin of ash in the Central Indian Ocean Basin and its implication for the volume estimate of the 74,000 year BP Youngest Toba eruption. Current Science, 83: 889-893.

Payne, R.J. and Gehrels, M.J., 2010. The formation of tephra layers in peatlands: an experimental approach. Catena 81, 12-23.

Pearce, J.A. and Norry, M.J., 1979. Petrogenetic implications of Ti, Zr, Y and Nb variations in volcanic rocks. Contributions to Mineralogy and Petrology, 69: 33-47.

Pearce, N.J.G., Westgate, J.A. and Perkins, W.T., 1996. Developments in the analysis of volcanic glass shards by laser ablation ICP-MS: quantitative and single internal standard-multi-element methods. Quaternary International, 34–36: 213–227.

Pearce, N.J.G., Perkins, W.T., Westgate, J.A., Gorton, M.P., Jackson, S.E., Neal, C.R. and Chenery, S.P., 1997. A compilation of new and published major and trace element data for NIST SRM 610 and NIST SRM 612 glass reference materials. Geostandards Newsletter, 21: 115–144.

Pearce, N.J.G., Westgate, J.A., Perkins, W.T., Eastwood, W.J. and Shane, P.A.R., 1999. The application of laser ablation ICP-MS to the analysis of volcanic glass shards from tephra deposits: bulk glass and single shard analysis. Global and Planetary Change, 21: 151–171.

Pearce, N., Westgate, J., Perkins, W. and Preece, S., 2004. The application of ICP-MS methods to tephrochronological problems. Applied Geochemistry, 19: 289-322.

Pearce, N.J.G., Denton, J.S., Perkins, W.T., Westgate, J.A. and Alloway, B.V., 2007. Correlation and characterisation of individual glass shards from tephra deposits using trace element laser ablation ICP-MS analyses: current status and future potential. Journal of Quaternary Research, 22: 721-736.

Pearce, N.J.G., Perkins, W.T., Westgate, J.A. and Wade S.C., 2011. Trace-element microanalysis by LA-ICP-MS: the quest for comprehensive chemical

characterisation of single, sub-10 μm volcanic glass shards. Quaternary International, s*ubmitted*.

Peppard, B.T., Steele, I.M., Davis, A.M., Wallace, P.J. and Anderson, A.T., 2001. Zoned quartz phenocrysts from the rhyolitic Bishop Tuff. American Mineralogist, 86: 1034-1052.

Perkins, W.T. and Pearce, N.J.G., 1995. Mineral microanalysis by laserprobe inductively coupled plasma mass spectrometry. *In:* Potts, P.J., Bowles, J.F.W., Reed, S.J.B., Cave, M.R. (Editors), Microprobe Techniques in the Earth Sciences. The Mineralogical Society, London: pp. 000-000

Perkins, W.T., Pearce, N.J.G. and Westgate, J.A., 1997. The development of laser ablation ICP-MS and calibration strategies: examples from the analysis of trace elements in volcanic glass shards and sulphide minerals. Geostandards Newsletter, 21: 175–190.

Petford, N. and Gallagher, K., 2001. Partial melting of mafic (amphibolitic) lower crust by periodic influx of basaltic magma. Earth and Planetary Science Letters, 193: 483-499.

Petraglia, M., Korisettar, R., Boivin, N., Clarkson, C., Ditchfield, P., Jones, S., Koshy, J., Lahr, M.M., Oppenheimer, C., Pyle, D.M., Roberts, R., Schwenninger, J., Arnold, L. and White, K., 2007. Middle Paleolithic assemblages from the Indian subcontinent before and after the Toba Super-Eruption. Science, 317: 114-116.

Pfeiffer T., Costa A. and Macedonio G., 2005. A model for the numerical simulation of tephra fall deposits. Journal of Volcanology and Geothermal Research, 140: 273-294.

Pickard, A.L., Adams, C.J. and Barley, M.E., 2000. Australian provenance for Upper Permian to Cretaceous rocks forming accretionary complexes on the New Zealand sector of the Gondwanaland margin. Australian Journal of Earth Sciences, 47: 987–1007.

Pillans, B. and Kohn, B.P., 1981. Rangitawa Pumice: a widespread(?) Quaternary marker bed in Taranaki-Wanganui. Geology Department, Victoria University of Wellington Publication, 20: 94-104.

Pillans, B.J., Kohn, B.P., Berger, G.W., Froggatt, P.C., Duller, G.A.T., Alloway, B.V. and Hesse. P.P., 1996. Multi-method dating comparison for mid-Pleistocene Rangitawa Tephra, New Zealand. Quaternary Science Reviews, 15: 641-653.

Pillans, B.J., Alloway, B.V., Naish, T.R., Westgate, J.A., Abbott, S.A. and Palmer, A., 2005. Silicic tephras in Pleistocene shallow-marine sediments of Wanganui Basin, New Zealand. Journal of the Royal Society of New Zealand, 35: 43-90.

Prata, A.J. and Grant, I.F., 2001. Retrieval of microphysical and morphological properties of volcanic ash plumes from satellite data: application to Mt Ruapehu, New Zealand. Quarterly Journal of the Royal Meteorological Society, 127: 2153–2179.

Price, R.C., Gamble, J.A., Smith, I.E.M., Stewart, R.B., Eggins, S. and Wright, I.C., 2005. An integrated model for the temporal evolution of andesites and rhyolites and crustal development in New Zealand's North Island. Journal of Volcanology and Geothermal Research, 140: 1–24.

Pringle, M.S., McWilliams, M., Houghton, B.F., Lamphere, M.A. and Wilson, C.J.N., 1992. $^{40}Ar/^{39}Ar$ dating of Quaternary feldspar: examples from the Taupo Volcanic Zone, New Zealand. Geology, 20: 531-534.

Pupin, J.P., 1980. Zircon and granite petrology. Contributions to Mineralogy and Petrology, 73: 207-220.

Putirka, K.D., 2005. Igneous thermometers and barometers based on plagioclase + liquid equilibria: tests of some existing models and new calibrations. American Mineralogist, 90: 336-346.

Putirka, K.D., 2008. Thermometers and barometers for volcanic systems. Reviews in Mineralogy and Geochemistry, 69: 61-120.

Pyle, D.M., 1989. The thickness, volume and grain size of tephra fall deposits. Bulletin of Volcanology, 51: 1-15.

Pyle, D.M., 1999. Widely dispersed Quaternary tephra in Africa. Global and Planetary Change, 21: 95-112.

Pyle, D.M., 2000. The sizes of volcanic eruptions. *In:* Sigurdsson, H., Houghton, B.F., McNutt, S.R., Rymer, H. Stix, J. (Eds), Encyclopedia of Volcanoes. Academic Press, London, pp. 263-269.

Pyle, D.M., Ricketts, G.D., Margari, V., van Andel, T.H., Sinitsyn, A.A., Praslov, N.D. and Lisitsyn, S., 2006. Wide dispersal and deposition of distal tephra during the Pleistocene 'Campanian Ignimbrite/Y5' eruption, Italy. Quaternary Science Reviews, 25: 2713-2728.

Rampino, M. and Ambrose, S.H., 2000. Volcanic winter in the Garden of Eden: the Toba supereruption and the late Pleistocene human population crash. *In:* McCoy, F.W., Heiken, G. (Editors), Volcanic Hazards and Disasters in Human Antiquity. Geological Society of America Special Paper, 345: 71-82.

Rampino, M. and Self, S., 1992. Volcanic winter and accelerated glaciation following the Toba super-eruption. Nature, 359: 50-52.

Ramsey, M.H., Potts, P.J., Webb, P.C., Watkins, P., Watson, J.S. and Coles, B.J., 1995. An objective assessment of analytical method precision: comparison of ICP-AES and XRF for the analysis of silicate rocks. Chemical Geology, 124: 1–19.

Rao, V. and Rao, C.V.N.K., 1992. Palaeontological studies of the cave fauna of Kurnool district, Andhra Pradesh. Records of the Geological Survey of India, 135: 240-241.

Ravel, B. and Newville, M., 2005. ATHENA, ARTEMIS, HEPHAESTUS: data analysis for X-ray absorption spectroscopy using IFEFFIT. Journal of Synchrotron Radiation, 12: 537–541.

Reid, M.R., 2008. How long does it take to supersize an eruption? Elements, 4(1): 23-28.

Reid, M.R. and Coath, C.D., 2000. In situ U-Pb ages of zircons from the Bishop Tuff: no evidence for long crystal residence times. Geology, 28: 443-446.

Reid, M.R., Coath, C.D., Harrison, T.M. and McKeegan, K.D., 1997. Prolonged residence times for the youngest rhyolites associated with Long Valley Caldera: $^{230}Th/^{238}U$ ion microprobe dating of young zircons. Earth and Planetary Science Letters, 150: 27-39

Reid, M.R., Vazquez, J.A. and Schmitt, A.K., 2011. Zircon-scale insights into the history

of a Supervolcano, Bishop Tuff, Long Valley, California, with implications for the Ti-in-zircon geothermometer. Contributions to Mineralogy and Petrology, 161: 293-311.

Ridolfi, F., Renzulli, A. and Puerini, M., 2010. Stability and chemical equilibrium of amphibole in calc-alkaline magmas: an overview, new thermobarometric formulations and application to subduction-related volcanoes. Contributions to Mineralogy and Petrology, 160: 45-66.

Riehle, J.R., Miller, T.F. and Bailey, R.A., 1995. Cooling, degassing and compaction of rhyolitic ash-flow tuffs: a computational model. Bulletin of Volcanology, 57: 319-336.

Robock, A., 2000. Volcanic eruptions and climate. Reviews of Geophysics, 38: 191-219.

Robock, A., 2002. Pinatubo eruption – the climatic aftermath. Science, 295: 1242-1244.

Robock, A., Ammann, C.M., Oman, L., Shindell, D., Levis, S. and Stenchikov, G., 2009. Did the Toba volcanic eruption of ~74 ka B.P. produce widespread glaciation? Journal of Geophysical Research, 114: D10107.

Rogan, A.M., 1982. A geophysical study of the Taupo Volcanic Zone, New Zealand. Journal of Geophysical Research, 87: 4073-4088.

Rollinson, H., 1993. Using geochemical data: evaluation, presentation, interpretation. Longman Group, London, UK.

Rose, W.I. and Chesner, C.A., 1987. Dispersal of ash in the great Toba eruption, 75 ka. Geology, 15: 913-917.

Rose, W.I. and Chesner, C.A., 1990. Worldwide dispersal of ash and gases from earth's largest known eruption: Toba, Sumatra, 75 ka. Palaeaogeography, Palaeoclimatology, Palaeoecology, 89: 269-275.

Rose, W.I., Durant, A.J., 2008. El Chichón volcano, 4 April 1982: volcanic cloud history and fine ash fallout. Natural Hazards, 51: 363-374.

Rose, W.I. and Durant, A.J., 2009. Fine ash content of explosive eruptions. Journal of Volcanology and Geothermal Research, 186: 32-39.

Roser, B.P. and Korsch R.J., 1999. Geochemical characterization, evolution and source of a Mesozoic accretionary wedge: The Torlesse terrane, New Zealand. Geological Magazine, 136: 493–512.

Ross, C.S. and Smith, R.L., 1961. Ash-flow tuffs: their origin, geologic relations, and identification. US Geological Survey Professional Paper, 366: 81 pp.

Rowland, J.V. and Sibson, R.H., 2001. Extensional fault kinematics within the Taupo Volcanic Zone, New Zealand: soft-linked segmentation of a continental rift system. New Zealand Journal of Geology and Geophysics, 44: 271–283.

Rowland, J.V., Wilson, C.J.N. and Gravley, D.M., 2010. Spatial and temporal variations in magma-assisted rifting, Taupo Volcanic Zone, New Zealand. Journal of Volcanology and Geothermal Research, 190: 89-108.

Rubatto, D. and Hermann, J., 2007. Experimental zircon/melt and zircon/garnet trace element partitioning and implications for the geochronology of crustal rocks. Chemical Geology, 241: 38–61.

Ruprecht, P., Bergantz, G.W. and Dufek, J., 2008. Modeling of gas-driven magmatic overturn: Tracking of phenocryst dispersal and gathering during magma mixing. Geochemistry, Geophysics, Geosystems, 9: Q07017.

Rusk, B.G., Lowers, H.A. and Reed, M.H., 2008. Trace elements in hydrothermal quartz: relationships to cathodoluminescence textures and insights into vein formation. Geology, 36: 547-550.

Sano, Y., Terada, K. and Fukuoka, T., 2002. High mass resolution ion microprobe analysis of rare earth elements in silicate glass, apatite and zircon: lack of matrix dependency. Chemical Geology, 184: 217-230.

Saunders, K.E., Morgan, D.J., Baker, J.A. and Wysoczanski, R.J., 2010. The magmatic evolution of the Whakamaru supereruption, New Zealand, constrained by a microanalytical study of plagioclase and quartz. Journal of Petrology, 51: 2465-2488.

Scaillet, B., Holtz, F. and Pichavant, M., 1998a. Phase equilibrium constraints on the viscosity of silicic magmas 1. Volcanic-plutonic comparison. Journal of Geophysical Research, 103: 257-266.

Scaillet, B., Clemente, B., Evans, B.W. and Pichavant, M., 1998b. Redox control of sulfur degassing in silicic magmas. Journal of Geophysical Research, 103: 23937–23949.

Schipper, C.I., 2004. Chemical and mineralogical characterization of pyroclastic deposits from the ca. 1 Ma Kidnappers and Rocky Hill eruptions, Taupo Volcanic Zone, New Zealand. MSc thesis, Otago University, Dunedin, New Zealand.

Schmitt, A.K., Lindsay, J.M., de Silva, S. and Trumbull, R.B., 2003. U–Pb zircon chronostratigraphy of early-Pliocene ignimbrites from La Pacana, North Chile; implications for the formation of stratified magma chambers. Journal of Volcanology and Geothermal Research, 120: 43–53.

Schmitz, M.D. and Smith, I.E.M., 2004. The petrology of the Rotoiti eruption sequence, Taupo Volcanic Zone: an example of fractionation of a rhyolitic system. Journal of Petrology, 45: 2045-2066.

Schulz, H., von Rad, U. and Erlenkeuser, H., 1998. Correlation between Arabian Sea and Greenland climate oscillations of the past 110,000 years. Nature, 393: 54-57.

Schulz, H., Emeis, K., Erlenkeuser, H., von Rad, U. and Rolf, C., 2002. The Toba volcanic event and interstadial/stadial climates at the Marine Isotopic Stage 5 to 4 transition in the Northern Indian Ocean. Quaternary Research, 57: 22-31.

Scott, R.B., 1971. Alkali exchange during devitrification and hydration of glasses in ignimbrite cooling units. Journal of Geology, 79: 100-110.

Scott, W.E., Hoblitt, R.P., Torres, R.C., Self, S., Martinez, M.M.L., and Nillos, T., 1996. Pyroclastic flows of the June 15, 1991 climactic eruption of Mount Pinatubo. *In:* Newhall, C.G., Punongbayan, R.S. (Editors), Fire and Mud: Eruptions and Lahars of Mount Pinatubo, Philippines. University of Washington Press, Seattle: pp. 545–570.

Scrivenor, J.B., 1930. A recent rhyolite-ash with sponge-spicules and diatoms in Malaysia. Geological Magazine, 67: 385-393.

Self, S., 2006. The effects and consequences of very large explosive volcanic eruptions. Royal Society of London, Philosophical Transactions A364: 2073-2097.

Self, S. and Sparks, R.S.J. (Editors), 1981. Tephra studies. D. Reidel, Dordrecht, Netherlands: 481 pp.

Self, S., Gertisser, R., Rampino, M.R. and Wolff, J.A., 2004. Magma volume, volatile emissions, and stratospheric aerosols from the 1851 eruption of Tambora. Geophysical Research Letters, 31: L20608.

Seward, D., 1974. Age of New Zealand Pleistocene substages by fission track dating of glass shards from tephra horizons. Earth and Planetary Science Letters, 24: 242-248.

Shane, P., 1998. Correlation of rhyolitic pyroclastic eruptive units from the Taupo volcanic zone by Fe-Ti oxide compositional data. Bulletin of Volcanology, 60: 224-238.

Shane, P., Westgate, J., Williams, M. and Korisettar, R., 1995. New geochemical evidence for the Youngest Toba Tuff in India. Quaternary Research, 44: 200-204.

Shane, P., Westgate, J., Williams, M. and Korisettar, R., 1996. Reply: New geochemical evidence for the Youngest Toba Tuff in India. Quaternary Research, 46: 342-343.

Shane, P., Smith, V. and Nairn, I., 2003. Biotite composition as a tool for the identification of Quaternary tephra beds. Quaternary Research, 59: 262-270.

Shane, P., Nairn, I.A. and Smith, V.C., 2005. Magma mingling in the ~50 ka Rotoiti eruption from Okataina Volcanic Centre: implications for geochemical diversity and chronology of large volume rhyolites. Journal of Volcanology and Geothermal Research, 139: 295-313.

Shane, P., Sikes, E.L. and Guilderson, T.P., 2006. Tephra beds in deep-sea cores off northern New Zealand: implications for the history of Taupo volcanic zone, Mayor Island and White Island volcanoes. Journal of Volcanology and Geothermal Research, 154: 276-290.

Shane, P., Martin, S.B., Smith, V.C., Beggs, K.F., Darragh, M.B., Cole, J.W. and Nairn, I.A., 2007. Multiple rhyolite magmas and basalt injection in the 17.7 ka

Rerewhakaaitu eruption episode from Tarawera volcanic complex, New Zealand. Journal of Volcanology and Geothermal Research, 164: 1-26.

Shane, P., Nairn, I.A., Smith, V.C., Darragh, M., Beggs, K.F. and Cole, J.W., 2008a. Silicic recharge of multiple rhyolite magmas by basaltic intrusion during the 22.6 ka Okareka eruption episode, New Zealand. Lithos, 103: 527–549.

Shane, P., Smith, V.C. and Nairn, I.A., 2008b. Millenial timescale resolution of rhyolite magma recharge at Tarawera volcano: insights from quartz chemistry and melt inclusions. Contributions to Mineralogy and Petrology, 155: 397-411.

Shaw, C., 2004. The temporal evolution of three magmatic systems in the West Eifel volcanic field, Germany. Journal of Volcanology and Geothermal Research, 131: 213–240.

Simon, J.I. and Reid, M.R., 2005. The pace of rhyolite differentiation and storage in an 'archetypical' silicic magma system, Long Valley, California. Earth and Planetary Science Letters, 235: 123-140.

Smith, E.G.C. and Webb, T.H., 1986. The seismicity and related deformation of the Central Volcanic Region, North Island, New Zealand. Royal Society of New Zealand Bulletin, 23: 112–133.

Smith, E.G.C., Williams, T.D. and Darby, D.J., 2007. Principal component analysis and modeling of the subsidence of the shoreline of Lake Taupo, New Zealand, 1983-1999: evidence for the dewatering of a magmatic intrusion? Journal of Geophysical Research, 112: B08406.

Smith, R.L., 1960. Zones and zonal variations in welded ash-flows. U.S. Geological Survey Professional Paper 354-F, 149–158.

Smith, R.L., 1979. Ash flow magmatism. Geological Society of America Special Paper, 180: 5-27.

Smith, V.C., Shane, P. and Nairn, I.A., 2004. Reactivation of a rhyolitic magma body by a new rhyolitic intrusion before the 15.8 ka Rotorua eruptive episode: implications for magma storage in the Okataina Volcanic Centre, New Zealand. Journal of the Geological Society, London, 161: 757-772.

Smith, V.C., Shane, P. and Nairn, I.A., 2005. Trends in rhyolite geochemistry, mineralogy, and magma storage during the last 50 kyr at Okataina and Taupo volcanic centres, Taupo Volcanic Zone, New Zealand. Journal of Volcanology and Geothermal Research, 148: 372-406.

Smith, V.C, Blundy, J.D. and Arce, J.L., 2009. A temporal record of magma accumulation and evolution beneath Nevado de Toluca, Mexico, preserved in plagioclase phenocrysts. Journal of Petrology, 50: 405-426.

Smith, V., Shane, P. and Nairn, I., 2010. Insights into silicic melt generation using plagioclase, quartz and melt inclusions from the caldera-forming Rotoiti eruption, Taupo Volcanic Zone, New Zealand. Contributions to Mineralogy and Petrology, 160: 951-971.

Smith, V.C., Pearce, N.J.G., Matthews, N.E., Westgate, J., Petraglia, M., Haslam, M., Lane, C., Korisettar, R. and Pal, J., 2011. Geochemical fingerprinting of the widespread Toba tephra using biotite compositions. Quaternary International, *in press*, doi:10.1016/j.quaint.2011.05.012.

Snyder, D., 2000. Thermal effects of the intrusion of basaltic magma into a more silicic magma chamber and implications for eruption triggering. Earth and Planetary Science Letters, 175: 257-273.

Snyder, G.A., Taylor, L.A. and Crozaz, G., 1993. Rare earth element selenochemistry of immiscible liquids and zircon at Apollo 14: an ion probe study of evolved rocks on the Moon. Geochimica et Cosmochimica Acta, 57: 1143-1149.

Solé, V.A., Papillon, E., Cotte, M., Walter, Ph. and Susini, J., 2007. A multiplatform code for the analysis of energy-dispersive X-ray fluorescence spectra. Spectrochimica Acta B, 62: 63–68.

Song, S.R., Chen, C.H., Lee, M.Y., Yang, T.F., Iizuka, Y. and Wei, K.Y., 2000. Newly discovered eastern dispersal of the youngest Toba Tuff. Marine Geology, 167: 303–312.

Sparks, R.S.J., 1976. Grain size variations in ignimbrites and implications for the transport of pyroclastic flows. Sedimentology, 23: 147-188.

Sparks, R.S.J., 1978. Gas release rates from pyroclastic flows: an assessment of the role of fluidization in their emplacement. Bulletin Volcanologique, 41: l-9.

Sparks, R.S.J., 1986, The dimensions and dynamics of volcanic eruption columns. Bulletin of Volcanology, 48: 3-15.

Sparks, R.S.J. and Walker, G.P.L., 1977. The significance of vitric-enriched air-fall ashes associated with crystal-enriched ignimbrites. Journal of Volcanology and Geothermal Research, 2: 329–341.

Sparks, R.S.J. and Wilson, L., 1976. A model for the formation of ignimbrite by the gravitational column collapse. Journal of the Geological Society, London, 132: 441-451.

Sparks, R.S.J., Self, S. and Walker, G.P.L., 1973. Products of ignimbrite eruptions. Geology, 1: 115-118.

Sparks, R.S.J., Sigurdsson, H. and Wilson, L., 1977. Magma mixing: a mechanism for triggering explosive eruptions. Nature, 267: 315-318.

Sparks, R.S.J., Huppert, H.E. and Wilson, C.J.N., 1990. Comment on "Evidence for long residence times of rhyolitic magma in the Long Valley magmatic system: the isotopic record in pre-caldera lavas of Glass Mountain" by A.N. Halliday, G.A. Mahood, P. Holden, J.M. Metz, T.J. Dempster and J.P. Davidson. Earth and Planetary Science Letters, 99: 387-389.

Sparks, R.S.J., Tait, S. and Yanev, Y., 1999. Dense welding caused by volatile resorption. Journal of the Geological Society, London, 156: 217-225.

Sparks, R.S.J., Self, S., Grattan, J.P., Oppenheimer, C., Pyle, D.M. and Rymer, H., 2005. Supereruptions: global effects and future threats. The Geological Society, London.

Sparks. R.S.J., Folkes, C., Humphreys, M., Barfod, D., Clavero, J., Sunagua, M., McNutt, S. and Pritchard, M., 2008. Uturuncu volcano, Bolivia: Volcanic unrest due to mid-crustal magma intrusion. American Journal of Science, 308: 727-769.

Spinks, K., Acocella, V., Cole, J. and Bassett, K., 2005. Structural control of volcanism and caldera development in the transtensional Taupo Volcanic Zone, New Zealand. Journal of Volcanology and Geothermal Research, 144: 7-22.

Stern, T.A., 1979. Regional and residual gravity fields, central North Island, New Zealand. New Zealand Journal of Geology and Geophysics, 22: 479-485.

Stem, T.A., 1985. A back-arc basin formed within continental lithosphere: the Central Volcanic Region of New Zealand. Tectonophysics, 112: 385-409.

Stern, T.A., 1987. Asymmetric back-arc spreading, heat flux and structure associated with the Central Volcanic Region of New Zealand. Earth and Planetary Science Letters, 85: 265-276.

Stern, T.A., Stratford, W.R. and Salmon, M.L., 2006. Subduction evolution and mantle dynamics at a continental margin: central North Island, New Zealand. Reviews of Geophysics, 44: RG4002.

Stern, T., Stratford, W., Seward, A., Henderson, M., Savage, M., Smith, E., Benson, A., Greve, S. and Salmon, M., 2010. Crust–mantle structure of the central North Island, New Zealand, based on seismological observations. Journal of Volcanology and Geothermal Research, 190: 58-74.

Stratford, W.R. and Stern, T.A., 2004. Strong seismic reflections and melts in the mantle of a continental back-arc basin. Geophysical Research Letters, 31: L06622.

Stratford, W.R. and Stern, T.A., 2006. Crust and upper mantle structure of a continental backarc: central North Island, New Zealand. Geophysical Journal International, 166: 469–484.

Streck, M.J. and Grunder, A.L., 1997. Compositional gradients and gaps in high-silica rhyolites of the Rattlesnake Tuff, Oregon. Journal of Petrology, 38: 133-163.

Streck, M.J. and Grunder, A., 1999. Enrichment of basalt and mixing of dacite in the rootzone of a large rhyolite magma chamber: inclusions and pumices from the Rattlesnake Tuff, Oregon. Contributions to Mineralogy and Petrology, 136: 193-212.

Storm, S., Shane, S., Schmitt, A.K. and Lindsay, J.M., 2011. Contrasting punctuated zircon growth in two syn-erupted rhyolite magmas from Tarawera volcano: Insights to crystal diversity in magmatic systems. Earth and Planetary Science Letters, 301: 511-520.

Sutton, A.N., Blake, S., Wilson, C.J.N. and Charlier, B.L.A., 2000. Late Quaternary evolution of a hyperactive rhyolite magmatic system: Taupo volcanic centre, New Zealand. Journal of Geological Society, London, 157: 537-552.

Suzuki, T., 1983. A theoretical model for dispersion of tephra. *In:* Shimozuru, D., Yokoyama, I. (Editors), Arc Volcanism: Physics and Tectonics. Terra Scientific Publishing Company (TERRAPUB), Tokyo: pp. 93–113.

Tait, S., 1992. Selective preservation of melt inclusions in igneous phenocrysts. American Mineralogist, 77: 146-155.

Tait, S.R., Worner, G., van den Bogaard, P. and Schmincke, H., 1989. Cumulate nodules as evidence for convective fractionation in a phonolite magma chamber. Journal of Volcanology and Geothermal Research, 37: 21-37.

Tegen, I., Harrison, S.P., Kohfeld, K., Prentice, C., Coe, M. and Heimann, M., 2002. Impact of vegetation and preferential source areas on global dust aerosol: Results from a model study. Journal of Geophysical Research, 108: 4576.

Te Punga, M.T., 1952. The Geology of Rangitikei Valley. New Zealand Geological Survey, Memoir 8: 1-43.

Thomas, J.B., Bodnar, R.J., Shimizu, N. and Sinha, A.K., 2002. Determination of zircon/melt trace element partition coefficients from SIMS analysis of melt inclusions in zircon. Geochimica et Cosmochimica Acta, 66: 2887–2901.

Thomas, J.B., Watson, E.B., Spear, F.S., Shemella, P.T., Nayak, S.K. and Lanzirotti, A., 2010. TitaniQ under pressure: the effect of pressure and temperature on the solubility of Ti in quartz. Contributions to Mineralogy and Petrology, 160: 743-759.

Thordarson, T., Self, S., Oskarsson, N. and Hulsebosch, T., 1996. Sulfur, chlorine, and fluorine degassing and atmospheric loading by the 1783–1784 AD Laki (Skaftár Fires) eruption in Iceland. Bulletin of Volcanology, 58: 205–225.

Timmreck, C., Graf, H.F., Lorenz, S.J., Niemeier, U., Zanchettin, D., Matei, D., Jungclaus, J.H. and Crowley, T.J., 2010. Aerosol size confines climate response to volcanic super-eruptions. Geophysical Research Letters, 37: L24705.

Trail, D., Bindeman, I.N., Watson, E.B. and Schmitt, A.K., 2009. Experimental calibration of oxygen isotope fractionation between quartz and zircon. Geochimica et Cosmochimica Acta, 73: 7100-7126.

Trepte, C.R., Veiga, R.E. and McCormick, M.P., 1993. The poleward dispersal of Mount Pinatubo aerosol. Journal of Geophysical Research, 98: 18563-18573.

Turcotte, D.L. and Schubert, G., 2002. Geodynamics, 2nd ed. Cambridge University Press, Cambridge, UK.

Turner, J.S. and Campbell, I.H., 1986. Convection and mixing in magma chambers. Earth-Science Reviews, 23: 255-352.

Valentine, G.A. and Wohletz, K.H., 1989. Numerical models of Plinian eruption columns and pyroclastic flows. Journal of Geophysical Research, 94: 1876-1887.

Valley, J., 2003. Oxygen isotopes in zircon. Reviews in Mineralogy and Geochemistry, 53: 343-385.

Valley, J.W., Chiarenzelli, J.R. and McLelland, J.M., 1994. Oxygen isotope geochemistry of zircon. Earth and Planetary Science Letters, 126: 187-206.

Valley, J.W., Kinny, P.D., Schulze, E.J. and Spicuzza, M.J., 1998. Zircon megacrysts from kimberlite: oxygen isotope variability among mantle melts. Contributions to Mineralogy and Petrology, 133: 1-11.

Valley, J.W., Bindeman, I.N. and Peck, W.H., 2003. Empirical calibration of oxygen isotope fractionation in zircon. Geochimica et Cosmochimica Acta, 67(17): 3257-3266.

Valley, J.W., Lackey, J.S., Cavosie, A.J., Clechenko, C.C., Spicuzza, M.J., Basei, M.A.S., Bindeman, I.N., Ferreira, V.P., Sial, A.N., King, E.M., Peck, W.H., Sinha, A.K. and Wei, C.S., 2005. 4.4 billion years of crustal maturation: oxygen isotope ratios of magmatic zircon. Contributions to Mineralogy and Petrology, 150: 561-580.

van den Bogaard, P. and Schirnick, C., 1995. $^{40}Ar/^{39}Ar$ laser probe ages of Bishop Tuff quartz phenocrysts substantiate long-lived silicic magma chamber at Long Valley, United States. Geology, 23: 759-762.

Vazquez, J.A. and Reid, M.R., 2002. Time scales of magma storage and differentiation of voluminous high-silica rhyolites at Yellowstone caldera, Wyoming. Contributions to Mineralogy and Petrology, 144: 274-285.

Vazquez, J.A. and Reid, M.R., 2004. Probing the accumulation history of the voluminous Toba magma. Science, 305: 991-994.

Venezky, D.U. and Rutherford, M.J., 1999. Petrology and Fe-Ti oxide reequilibration of the 1991 Mount Unzen mixed magma. Journal of Volcanology and Geothermal Research, 89: 213-230.

Villamor, P. and Berryman, K.R., 2001. A late Quaternary extension rate in the Taupo Volcanic Zone, New Zealand, derived from fault slip data. New Zealand Journal of Geology and Geophysics, 44: 243-270.

Vucetich, C.G., Kohn, B.P. and Pullar, W.A., 1981. Correlation of Aratora Tephra, Ahuroa cover bed type section, Te Kuiti. Geology Department, Victoria University of Wellington Publication, 20: 116-130.

Walker, B.A., Miller, C.F., Claiborne, L.L., Wooden, J.L. and Miller, J.S., 2007. Batholith construction: new insights concerning timescales and physical processes from the Spirit Mountain batholith, southern Nevada. Journal of Volcanology and Geothermal Research, 167: 239-262.

Wallace, P.J., Anderson, A.T. and Davis, A.M., 1999. Gradients in H_2O, CO_2, and exsolved gas in a large-volume silicic magma system: interpreting the record preserved in melt inclusions from the Bishop Tuff. Journal of Geophysical Research, 104: 20097-20122.

Wallace, L.M., Beavan, J., McCaffrey, R. and Darby, D.J., 2004. Subduction zone coupling and tectonic block rotations in the North Island, New Zealand. Journal of Geophysical Research, 109: B12406.

Wark, D.A. and Bachmann, O., 2005. Contrasting Ti zoning patterns in quartz phenocrysts from the Bishop and Fish Canyon Tuffs: An expression of volatile composition in recharge melts: EOS, Transactions of the American Geophysical Union, 86: Fall meeting supplement, abstract V13B–0523.

Wark, D.A. and Spear, F.S., 2005. Titanium in quartz: cathodoluminescence and thermometry. Geochimica et Cosmochimica Acta, 69: A592.

Wark, D.A. and Watson, E.B., 2006. TitaniQ: a titanium-in-quartz geothermometer. Contributions to Mineralogy and Petrology, 152: 743-754.

Wark, D.A., Hildreth, W., Spear, F.S., Cherniak, D.J. and Watson, E.B., 2007. Pre-eruption recharge of the Bishop magma system. Geology, 35: 235-238.

Watkins, N.D. and Huang, T.C., 1977. Tephras in abyssal sediments east of the North Island, New Zealand: chronology, paleowind velocity, and paleoexplosivity. New Zealand Journal of Geology and Geophysics, 20: 179-198.

Watkins, N.D., Sparks, R.S.J., Sigurdsson, H., Huang, T.C., Federman, A., Carey, S. and Ninkovich, D., 1978. Volume and extent of the Minoan tephra from Santorini Volcano: new evidence from deep-sea sediment cores. Nature, 271: 122-126.

Watson E. B., 1980. Some experimentally determined zircon-liquid partition-coefficients for the rare-earth elements. Geochimica et Cosmochimica Acta, 44: 895–897.

Watson, E.B., 1996. Dissolution, growth and survival of zircons during crustal fusion: Kinetic principles, geological models and implications of isotopic inheritance. Transactions of the Royal Society of Edinburgh, Earth Sciences, 87: 43-56.

Watson, E.B. and Harrison, T.M., 1983. Zircon saturation revisited: temperature and composition effects in a variety of crustal magma types. Earth and Planetary Science Letters, 64: 295-304.

Watson, E.B. and Harrison, T.M., 2005. Zircon thermometer reveals minimum melting conditions on earliest Earth. Science, 308: 841-844.

Watson, E.B., Wark, D.A. and Thomas, J.B., 2006. Crystallization thermometers for zircon and rutile. Contributions to Mineralogy and Petrology, 151: 413-433.

Watt, G.R., Wright, P., Galloway, S. and McLean, C., 1997. Cathodoluminescence and trace element zoning in quartz phenocrysts and xenocrysts. Geochimica et Cosmochimica Acta, 61: 4337-4348.

Watt, S.F.L., Pyle, D.M., Mather, T.A., Martin, R.S. and Matthews, N.E., 2009a. Fallout and distribution of volcanic ash over Argentina following the May 2008 explosive eruption of Chaitén, Chile. Journal of Geophysical Research 113, B04207.

Watt, S.F.L., Pyle, D.M. and Mather, T.A., 2009b. The influence of great earthquakes on volcanic eruption rate along the Chilean subduction zone. Earth and Planetary Science Letters, 277: 399-407.

Waychunas, G.A., 1987. Synchrotron radiation XANES spectroscopy of Ti in minerals: effects of Ti bonding distances, Ti valence and site geometry on absorption edge structure. American Mineralogist, 72: 89-101.

Webb, T.H., Ferris, B.C. and Harris, J.S., 1986. The Lake Taupo, New Zealand, earthquake swarms of 1983. New Zealand Journal of Geology and Geophysics, 29: 377–389.

Westgate, J.A., Shane, P., Pearce, N.J.G., Perkins, W.T., Korisettar, R., Chesner, C.A., Williams, M.A.J. and Acharyya, S.K., 1998. All Toba Tephra occurrences across peninsular India belong to the 75,000 yr B.P. eruption. Quaternary Research, 50: 107–112.

White, R.W., Powell, R., Holland, T.J.B. and Worley, B.A., 2000. The effect of TiO_2 and Fe_2O_3 on metapelitic assemblages at greenschist and amphibolite facies conditions: mineral equilibria calculations in the system K_2O-FeO-MgO-Al_2O_3-SiO_2-H_2O-TiO_2-Fe_2O_3. Journal of Metamorphic Geology, 18: 497-511.

White, R.W., Powell, R. and Clarke, G.L., 2002. The interpretation of reaction textures in Fe-rich metapelitic granulites of the Musgrave Block, central Australia: constraints from mineral equilibria calculations in the system K_2O-FeO-MgO-A_2O_3-SiO_2-H_2O-TiO_2-Fe_2O_3. Journal of Metamorphic Geology, 20: 41-55.

Wiebe, R.A. and Hawkins, D.P., 2004. Multiple replenishments in an evolving silicic magma chamber: the Vinalhaven intrusive complex, Maine, USA. Geochimica et Cosmochimica Acta, 68: A672.

Wiebe, R.A., Wark, D.A. and Hawkins, D.P., 2007. Insights from quartz cathodoluminescence zoning into crystallization of the Vinalhaven granite, coastal Maine. Contributions to Mineralogy and Petrology, 154: 439-453.

Williams, M.A.J. and Royce, K., 1982. Quaternary geology of the Middle Son Valley, North Central India: Implications for prehistoric Archaeology. Palaeogeography, Palaeoclimatology, Palaeoecology, 38: 139-162.

Williams, M., Ambrose, S.H., van der Kaars, S., Ruehlemann, C., Chattopadhyaya, U.C., Pal, J.N. and Chauhan, P., 2009. Environmental impact of the 73 ka Toba super-eruption in south Asia. Palaeogeography, Palaeoclimatology, Palaeoecology, 284: 295-314.

Wilson, C.J.N., 1980. The role of fluidization in the emplacement of pyroclastic flows: an experimental approach. Journal of Volcanology and Geothermal Research, 8: 231 - 249.

Wilson, C.J.N., 2001. The 26.5 ka Oruanui eruption, New Zealand: an introduction and overview. Journal of Volcanology and Geothermal Research, 112: 133-174.

Wilson, C.J.N., 2008. Supereruptions and supervolcanoes: processes and products. Elements, 4: 29-34.

Wilson, C.J.N. and Charlier, B.L.A., 2009. Rapid rates of magma generation at contemporaneous magma systems, Taupo volcano, New Zealand: insights from U-Th model-age spectra in zircons. Journal of Petrology, 50: 875-907.

Wilson, C.J.N. and Hildreth, W., 2003. Assembling an ignimbrite: mechanical and thermal building blocks in the Bishop Tuff, California. Journal of Geology, 111: 653-670.

Wilson, C.J.N. and Hildreth, W. 2007. Compositional zoning of the Bishop Tuff. Journal of Petrology, 48: 951-999.

Wilson, C.J.N. and Walker, G.P.L., 1985. The Taupo eruption, New Zealand, I. General aspects. Philosophical Transactions of the Royal Society of London, A314: 199-228.

Wilson, C.J.N., Houghton, B.F. and Lloyd, E.F., 1986. Volcanic history and evolution of the Maroa-Taupo area, central North Island. Royal Society of New Zealand Bulletin, 23: 194-223.

Wilson, C.J.N., Houghton, B.F., McWilliams, M.O., Lanphere, M.A., Weaver, S.D. and Briggs, R.M., 1995a. Volcanic and structural evolution of Taupo Volcanic Zone, New Zealand: a review. J Volcanology and Geothermal Research, 68: 1-28.

Wilson, C.J.N., Houghton, B.F., Kamp, P.J.J. and McWilliams, M.O., 1995b. An exceptionally widespread ignimbrite with implications for pyroclastic flow emplacement. Nature, 378: 605-607.

Wilson, C.J.N., Blake, S., Charlier, B.L.A. and Sutton, A.N., 2006. The 26.5 ka Oruanui eruption, Taupo volcano, New Zealand: development, characteristics and evacuation of a large rhyolitic magma body. Journal of Petrology, 47: 35-69.

Wilson, C.J.N., Charlier, B.L.A., Fagan, C.J., Spinks, K.D., Gravley, D.M., Simmons, S.F. and Browne, P.R.L., 2008. U-Pb dating of zircon in hydrothermally altered rocks as a correlation tool: application to the Mangakino geothermal field, New Zealand. Journal of Volcanology and Geothermal Research, 176: 191-198.

Wilson, C.J.N., Gravley, D.M., Leonard, G.S. and Rowland, J.V., 2009. Volcanism in the Central Taupo Volcanic Zone, New Zealand: tempo, styles and controls. *In:* Thordarson, T., Self, S., Larsen, G., Rowland, S.K., Hoskuldsson, A. (Eds), Studies in Volcanology: The Legacy of George Walker. Special Publications of IAVCEI, 2: pp. 225-247.

Wilson, C.J.N., Seward, T.M., Allan, A.S.R., Charlier, B.L.A., Bello, L. and Hildreth, W., 2011. A comment on: TitaniQ under pressure: the effect of pressure and temperature on the solubility of Ti in quartz, by Jay B. Thomas, E. Bruce Watson, Frank S. Spear, Philip, T. Shemella, Saroj K. Nayak & Antonio Lanzirotti. Contributions to Mineralogy and Petrology, s*ubmitted.*

Wilson, L., 1976. Explosive volcanic eruptions: III. Plinian eruption columns. Geophysical Journal of the Royal Astronomical Society, 45: 543–556.

Wilson, L. and Walker, G.P.L., 1987. Explosive volcanic eruptions: VI. Ejecta dispersal in plinian eruptions: the control of eruption conditions and atmospheric properties. . Geophysical Journal of the Royal Astronomical Society, 89: 657–679.

Wilson, L., Sparks, R.S.J., Huang, T.C. and Watkins, N.D., 1978. The control of volcanic column height dynamics by eruption energetics and dynamics. Journal of Geophysical Research, 83: 1820-1836.

Winick, J.A., McIntosh, W.C. and Dunbar, N.W., 2001. Melt-inclusion-hosted excess 40Ar in quartz crystals of the Bishop and Bandelier magma systems. Geology, 29: 275-278.

Wolf-Gladrow, D.A., 2000. Lattice-Gas Cellular Automata and Lattice Boltzmann models: An introduction. Springer, Berlin: pp. 308.

Woods, A.W., 1988, The fluid dynamics and thermodynamics of eruption columns. Bulletin of Volcanology, 50: 169–193.

Woods, A.W. and Bursik, M.I., 1991. Particle fallout, thermal disequilibrium and volcanic plumes. Bulletin of Volcanology, 53: 559–570.

Woods A.W. and Wohletz, K., 1991. Dimensions and dynamics of co-ignimbrite eruption columns. Nature, 350: 225-227.

Yokoyama, I., 1981. A geophysical interpretation of the 1883 Krakatau eruption. Journal of Volcanology and Geothermal Research, 9: 359-378.

Zellmer, G.F., Blake, S., Vance, D., Hawkesworth, C. and Turner, S., 1999. Plagioclase residence times at two island arc volcanoes (Kameni Islands, Santorini and Soufriere. St. Vincent) determined by Sr diffusion systematics. Contributions to Mineralogy and Petrology, 136: 345–357.

Zielinski, G.A., Mayewski, P.A., Meeker, L.D., Whitlow, S. and Twickler, M.S., 1996. Potential atmospheric impact of the Toba mega-eruption ~71,000 years ago. Geophysical Research Letters, 23: 837-840.